

# 1D Nanomaterials: Synthesis, Properties, and Applications

Journal of  
Nanomaterials

Guest Editors: Yun Zhao, Haiping Hong, Qianming Gong, and Lijun Ji





---

# **1D Nanomaterials: Synthesis, Properties, and Applications**

# **1D Nanomaterials: Synthesis, Properties, and Applications**

Guest Editors: Yun Zhao, Haiping Hong, Qianming Gong,  
and Lijun Ji



---

Copyright © 2013 Hindawi Publishing Corporation. All rights reserved.

This is a special issue published in "Journal of Nanomaterials." All articles are open access articles distributed under the Creative Commons Attribution License, which permits unrestricted use, distribution, and reproduction in any medium, provided the original work is properly cited.

## Editorial Board

Katerina E. Aifantis, Greece  
Nageh K. Allam, USA  
Margarida Amaral, Portugal  
Xuedong Bai, China  
Lavinia Balan, France  
Enrico Bergamaschi, Italy  
Theodorian Borca-Tasciuc, USA  
C. Jeffrey Brinker, USA  
Christian Brosseau, France  
Xuebo Cao, China  
Shafiq Chowdhury, USA  
Kwang-Leong Choy, UK  
Cui ChunXiang, China  
Miguel A. Correa-Duarte, Spain  
Shadi A. Dayeh, USA  
Claude Estourns, France  
Alan Fuchs, USA  
Lian Gao, China  
Russell E. Gorga, USA  
Hongchen Chen Gu, China  
Mustafa O. Guler, Turkey  
John Zhanhu Guo, USA  
Smrati Gupta, Germany  
Michael Harris, USA  
Zhongkui Hong, China  
Michael Z. Hu, USA  
David Hui, USA  
Y.-K. Jeong, Republic of Korea  
Sheng-Rui Jian, Taiwan  
Wanqin Jin, China  
Rakesh K. Joshi, UK  
Zhenhui Kang, China  
Fathallah Karimzadeh, Iran  
Alireza Khataee, Iran  
Do Kyung Kim, Republic of Korea  
Alan K. T. Lau, Hong Kong  
Burtrand Lee, USA  
Jun Li, Singapore  
Benxia Li, China  
Xing-Jie Liang, China  
Shijun Liao, China  
Gong Ru Lin, Taiwan  
J.-Y. Liu, USA  
Tianxi Liu, China  
Jue Lu, USA  
Songwei Lu, USA  
Daniel Lu, China  
Ed Ma, USA  
Gaurav Mago, USA  
Santanu K. Maiti, India  
Sanjay R. Mathur, Germany  
Vikas Mittal, UAE  
Weihai Ni, Germany  
Sherine Obare, USA  
Atsuto Okamoto, Japan  
Abdelwahab Omri, Canada  
Edward Andrew Payzant, USA  
Kui-Qing Peng, China  
Anukorn Phuruangrat, Thailand  
Suprakas Sinha Ray, South Africa  
Ugur Serincan, Turkey  
Huaiyu Shao, Japan  
Donglu Shi, USA  
Vladimir Sivakov, Germany  
Marinella Striccoli, Italy  
Bohua Sun, South Africa  
Saikat Talapatra, USA  
Nairong Tao, China  
Titipun Thongtem, Thailand  
Somchai Thongtem, Thailand  
Alexander Tolmachev, Ukraine  
Valeri P. Tolstoy, Russia  
Tsung-Yen Tsai, Taiwan  
Takuya Tsuzuki, Australia  
Raquel Verdejo, Spain  
Mat U. Wahit, Malaysia  
Zhenbo Wang, China  
Ruiping Wang, Canada  
Shiren Wang, USA  
Cheng Wang, China  
Yong Wang, USA  
Jinquan Wei, China  
Ching-Ping Wong, Hong Kong  
Xingcai Wu, China  
Guodong Xia, Hong Kong  
Zhi Li Xiao, USA  
Ping Xiao, UK  
Yangchuan Xing, USA  
Shuangxi Xing, China  
N. Xu, China  
Doron Yadlovker, Israel  
Yingkui Yang,  
Khaled Youssef, USA  
Kui Yu, Canada  
William W. Yu, USA  
Haibo Zeng, China  
Tianyou Zhai, Japan  
Renyun Zhang, Sweden  
Bin Zhang, China  
Yanbao Zhao, China  
Lianxi Zheng, Singapore  
Chunyi Zhi, Hong Kong

# Contents

**ID Nanomaterials: Synthesis, Properties, and Applications**, Yun Zhao, Haiping Hong, Qianming Gong, and Lijun Ji

Volume 2013, Article ID 101836, 1 page

**Effect of Wrapped Carbon Nanotubes on Optical Properties, Morphology, and Thermal Stability of Electrospun Poly(vinyl alcohol) Composite Nanofibers**, Naoual Diouri, Mimouna Baitoul, and Malik Maaza

Volume 2013, Article ID 949108, 6 pages

**Shape Effects of Iron Nanowires on Hyperthermia Treatment**, Wei-Syuan Lin, Hong-Ming Lin, Hsiang-Hsin Chen, Yeu-Kuang Hwu, and Yuh-Jing Chiou

Volume 2013, Article ID 237439, 6 pages

**Correlation Effects in Kinetics of One-Dimensional Atomic Systems**, V. D. Borman, I. V. Tronin, V. N. Tronin, V. I. Troyan, and O. S. Vasiliev

Volume 2013, Article ID 682832, 43 pages

**Electrical Resistivity of Pristine and Functional Single-Wall Carbon Nanotubes**, Yijiang Lu, Jing Li, and Haiping Hong

Volume 2013, Article ID 635673, 5 pages

**Synthesis and Characterisation of Calcium Carbonate Aragonite Nanocrystals from Cockle Shell Powder (*Anadara granosa*)**, Abdullahi Shafiu Kamba, Maznah Ismail, Tengku Azmi Tengku Ibrahim, and Zuki Abu Bakar Zakaria

Volume 2013, Article ID 398357, 9 pages

**Improved Processing of Carbon Nanotube Yarn**, Chaminda Jayasinghe, Trent Amstutz, Mark J. Schulz, and Vesselin Shanov

Volume 2013, Article ID 309617, 7 pages

**A Comparative Study of Three Different Chemical Vapor Deposition Techniques of Carbon Nanotube Growth on Diamond Films**, Betty T. Quinton, Paul N. Barnes, Chakrapani V. Varanasi, Jack Burke, Bang-Hung Tsao, Kevin J. Yost, and Sharmila M. Mukhopadhyay

Volume 2013, Article ID 356259, 9 pages

**Photoluminescence of Hexagonal ZnO Nanorods Hydrothermally Grown on Zn Foils in KOH Solutions with Different Values of Basicity**, Nuengruethai Ekthammathat, Titipun Thongtem, Anukorn Phuruangrat, and Somchai Thongtem

Volume 2013, Article ID 208230, 4 pages

**Growth and Physical Property Study of Single Nanowire (Diameter ~45 nm) of Half Doped Manganite**, Subarna Datta, Sayan Chandra, Sudeshna Samanta, K. Das, H. Srikanth, and Barnali Ghosh

Volume 2013, Article ID 162315, 6 pages

**Spin-Filtering Effects in Würtzite and Graphite-Like AlN Nanowires with Mn Impurities**, G. A. Nemnes

Volume 2013, Article ID 408475, 5 pages



---

**Investigation and Estimation of Structure of Web from Electrospun Nanofibres**, Jolanta Malašauskiene.  
and Rimvydas Milašius  
Volume 2013, Article ID 416961, 6 pages

## Editorial

# 1D Nanomaterials: Synthesis, Properties, and Applications

**Yun Zhao,<sup>1</sup> Haiping Hong,<sup>2</sup> Qianming Gong,<sup>3</sup> and Lijun Ji<sup>4</sup>**

<sup>1</sup> School of Chemical Engineering and Environment, Beijing Institute of Technology, Beijing 100081, China

<sup>2</sup> Department of Materials and Metallurgical Engineering, South Dakota School of Mines and Technology, Rapid City, SD 57701, USA

<sup>3</sup> Department of Mechanical Engineering, Tsinghua University, Beijing 100084, China

<sup>4</sup> College of Chemistry and Chemical Engineering, Yangzhou University, Yangzhou, Jiangsu 225009, China

Correspondence should be addressed to Yun Zhao; zhaoyun@bit.edu.cn

Received 12 June 2013; Accepted 12 June 2013

Copyright © 2013 Yun Zhao et al. This is an open access article distributed under the Creative Commons Attribution License, which permits unrestricted use, distribution, and reproduction in any medium, provided the original work is properly cited.

One-dimensional (1D) nanostructured materials, including nanotubes, nanofibers, and nanowires, have attracted much attention due to their interesting properties and wide range of potential applications. Considerable research has been conducted on new routes to controllable synthesis of 1D nanomaterials. The unique properties of as-obtained 1D nanomaterials can lead to applications in various fields such as electronics, magnetism, optics, and catalysis. Therefore, researchers working in the 1D nanomaterials are constantly striving to develop new fundamental science as well as potential applications. The importance of a platform that allows active researchers in this field to present their new development in a timely and efficient manner is, therefore, necessary.

This special issue focuses on the recent progress in production techniques, novel properties, and applications of various 1D nanomaterials including oxides/metals/nitrides with 1D nanostructures, carbon nanotubes, and nanofibers.

A total of 11 articles are presented in the current issue and they are all research papers. They involve spin transport properties of AlN nanowires, photoluminescence of ZnO nanorods, heating efficiency of iron nanowires, optical properties and thermal stability of poly(vinyl alcohol) composite nanofibers, electrical properties of half-doped manganite single nanowire, carbon nanotube yarns, and pristine and functional single-wall carbon nanotubes. Production techniques include a hydrothermal reaction, reducing method, chemical vapor deposition, spinning method, and microemulsion system. Carbon nanotubes have attracted most research interest, maintaining their comfortable leading positions.

We are pleased to see the progress in synthesis and properties of 1D nanomaterials. We hope that this special issue will promote further development of large-scale economically feasible 1D nanomaterial-making technologies and also contribute to their wide use.

## Acknowledgments

The editors gratefully thank the authors for their contributions to this special issue and the reviewers for their constructive comments and dedication.

Yun Zhao  
Haiping Hong  
Qianming Gong  
Lijun Ji

## Research Article

# Effect of Wrapped Carbon Nanotubes on Optical Properties, Morphology, and Thermal Stability of Electrospun Poly(vinyl alcohol) Composite Nanofibers

Naoual Diouri,<sup>1</sup> Mimouna Baitoul,<sup>1</sup> and Malik Maaza<sup>2,3</sup>

<sup>1</sup> University USMBA, Faculty of Sciences Dhar El Mahraz, Laboratory of Solid State Physics, Group Polymers and Nanomaterials, Regional University Center of the Interface (CURI), P.O. Box 1796 Atlas, 30000 Fez, Morocco

<sup>2</sup> iThemba LABS, National Research Foundation, NANOAFNET, 1 Old Faure Road, Somerset West 7129, P.O. Box 722, Somerset, Western Cape Province, South Africa

<sup>3</sup> UNESCO, UNISA Africa Chair in Nanosciences/Nanotechnology, College of Graduate Studies, University of South Africa (UNISA), Muckleneuk Ridge, P.O. Box 392, Pretoria, South Africa

Correspondence should be addressed to Mimouna Baitoul; [baitoul@yahoo.fr](mailto:baitoul@yahoo.fr)

Received 29 October 2012; Accepted 19 May 2013

Academic Editor: Haiping Hong

Copyright © 2013 Naoual Diouri et al. This is an open access article distributed under the Creative Commons Attribution License, which permits unrestricted use, distribution, and reproduction in any medium, provided the original work is properly cited.

Electrospinning was used to elaborate poly(vinyl alcohol) (PVA) nanofibers in the presence of embedded multiwall carbon nanotubes (MWCNTs) in surfactant and polymer. MWCNTs were dispersed in aqueous solution using both sodium dodecyl sulfate (SDS) as surfactant and Poly(vinyl pyrrolidone) (PVP). Changing the surfactant and polymer concentration reveals that the maximum dispersion achievable is corresponding to the mass ratios MWCNTs:SDS—1:5 and MWCNTs:SDS:PVP—1:5:0.6 in the presence of the PVP. After the optimization of the dispersion process, the SEM image of the PVA/PVP/SDS/MWCNTs electrospun fibers presents high stability of the fibers with diameter around 224 nm. Infrared spectroscopy and thermal gravimetric analysis elucidate the type of interaction between the PVA and the coated carbon nanotube. The presence of PVP wrapped carbon nanotubes reduced slightly the onset of the degradation temperature of the electrospun nanofibers.

## 1. Introduction

Electrospun nanofibers present an exciting avenue for development of novel nanomaterials with well-defined functionalities which have attracted researchers' interest. Because of their unique physical, chemical properties and a specific surface approximately two order larger than flat films, nanofibers have great potential use in sensors [1–3], filtration for bacteria, medical applications, tissue scaffolding [4–8], textile fabric [9], and other applications in nanoscience and nanotechnology. Due to their electronic, mechanical, and thermal properties, CNTs enjoy an incomparable status in the panoply of nanomaterials finding large range of applications in composites. However, the fabrication of high quality polymer-CNTs nanocomposites with predictable and optimal performance requires homogenous dispersion of the CNTs in polymer matrix. This is a challenging task for their

utilization due to the highly nonwetting character of CNTs surface and strong tendency to form bundles by van der Waals attractive forces. Currently, different approaches are used to disperse CNTs, such as covalent or noncovalent functionalization. From the nondestructive point of view, in situ polymerization, polymers, and also surfactants are used to obtain homogenous CNTs dispersion in various solvents or matrices [10–12]. A series of cationic, anionic, and nonionic surfactants and polymers have been studied for their ability to suspend individual CNTs [13, 14]. The present work confronts the dispersion assisted by surfactant as well as polymer. In the first step, we investigate the dispersion of MWCNTs in aqueous solution using SDS as an anionic surfactant. Different concentrations of SDS compared to those of MWCNTs were used, and the second step consisted in improving the dispersion and it is stabilization while using the PVP. After the optimization of the dispersion of MWCNTs, we elaborated

the nanocomposite fibers via electrospinning process. The optical properties and thermal stability of the electrospun nanofibers will be presented.

## 2. Experimental

**2.1. Materials.** Poly(vinyl alcohol) (Mw: 70000, 99% hydrolyzed), poly(vinyl pyrrolidone), and sodium dodecyl sulfate were purchased from Sigma Aldrich. Multiwall carbon nanotubes (CCVD method, purity >95%, outer mean diameter 10–15 nm, and length 0.1–10  $\mu\text{m}$ ) were purchased from Arkema France.

**2.2. Dispersion of MWCNTs.** In a typical dispersion procedure, two steps were realized in order to achieve better dispersion in the one hand and for preparing three suspensions of MWCNTs. The anionic surfactant SDS,  $\text{NaC}_{12}\text{H}_{25}\text{SO}_4$ , is first used for the exfoliation of the CNTs by varying the concentration to 10 wt% of MWCNTs aqueous solution. It can penetrate easily inside the aggregates of MWCNTs, and it was useful for improving the dispensability. After the characterization with the UV-Vis spectroscopy, the solution with the ratio 1:5 of MWCNTs:SDS was chosen. However, this surfactant does not prevent individual nanotubes from agglomeration after sonication process. In order to achieve better stabilization of the dispersion, different amounts of the nonionic PVP ( $\text{C}_6\text{H}_9\text{ON}$ )<sub>n</sub>, which possesses both hydrophilic and hydrophobic groups have been added to this solution to further improve the dispersion. The temperature was around room temperature, and all solutions were ultrasonicated for 60 min. Moreover, rings in PVP contain a proton accepting carbonyl moiety, while PVA presents hydroxyl groups as side groups. Indeed, interactions by hydrogen bonding can be expected between hydroxyl groups of PVA and carboxyl groups of PVP.

**2.3. Preparation of PVA/MWCNTs/SDS/PVP Nanofibers.** PVA was dissolved in warm water by heating at 80°C under a continuous slight stirring for 2 h to prepare PVA solution with the desired concentration. The PVP/SDS/MWCNTs suspension was added to an aqueous solution of PVA to obtain a final solution of 12 wt% PVA and 0.3 wt% of MWCNTs. The solution of PVA/MWCNTs/SDS/PVP was briefly sonicated and stirred to remove trapped air bubbles and for effective mixing prior to electrospinning. After the complete homogenization of the nanocomposite, the solution was poured into the syringe. A voltage of 15 Kv was applied to the solution, and the solution jet emerging from the needle was collected on the stationary electrode (Figure 1).

**2.4. Characterization.** The dispersions of MWCNTs in the surfactant and polymer were characterized using UV-visible spectrophotometer—Cecil 2000 series which cover the full 190–1000 nm wavelength range with a narrow 1.8 nm optical bandwidth. The baseline correction was carried out using a quartz cuvette.

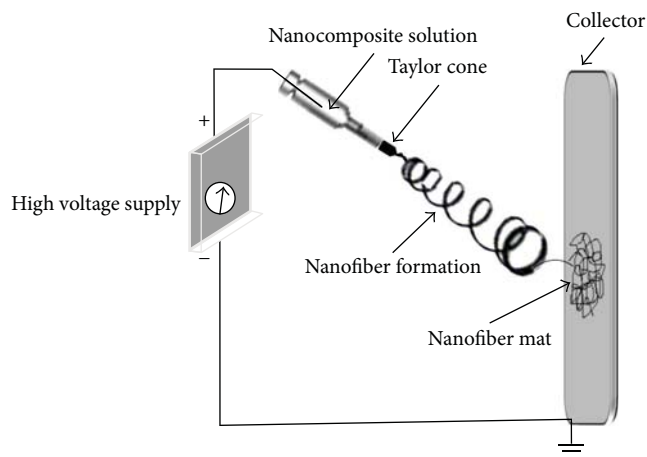


FIGURE 1: Scheme of the electrospinning process.

The morphology of electrospun nanofibers and their average diameter were characterized using environmental scanning electronic microscopy (ESEM) equipped with sonde EDAX for the surface microanalysis.

An analysis was carried out by ATR using PerkinElmer, Spotlight 400 FTIR Imaging system, while thermal analysis was accomplished using SETSYS Evolution.

## 3. Results and Discussion

**3.1. Ultraviolet-Visible Spectroscopy.** It has been demonstrated that carrier dynamics in carbon nanotubes bundles are dominated by the tunnel coupling between carbon nanotubes. These bundled carbon nanotubes are not active in the UV-Vis region and only individual carbon nanotubes absorb in the UV-Vis region [15]. Here, we describe combination of two concepts for dispersing MWCNTs by using SDS as surfactant and PVP.

To disperse MWCNTs, both maintaining stabilization and intrinsic properties of carbon nanotubes are required. We used the ionic surfactant to disperse MWCNTs because it is known to disperse them in aqueous solution via noncovalent method without affecting MWCNTs properties [16]. Since SDS molecules have featureless absorbance in the region, we were interested in this work. The mechanism of MWCNTs dispersion according to the duration and power of sonication has been studied by other researchers [15].

To obtain better dispersion, the solutions were resounded after the variation of the mass of SDS compared to that of the MWCNTs using the same conditions of sonication during all experiments.

The UV-Vis absorbance spectra (Figure 2(A)) show the prepared MWCNTs dispersion with different amounts of SDS. The MWCNTs have characteristic absorption peak around the wavelength of 290 nm corresponding to the intrinsic optical properties of graphite [17] and will thus be present in MWCNTs. Unlike optical transitions in a particle, the carbon nanotubes present different collective excitations of electrons, called  $\pi$ -plasmon, which involve the electron orbitals  $\sigma$  and exist at much higher energy. Since the size of carbon nanotubes is less than the wavelength of excitation in

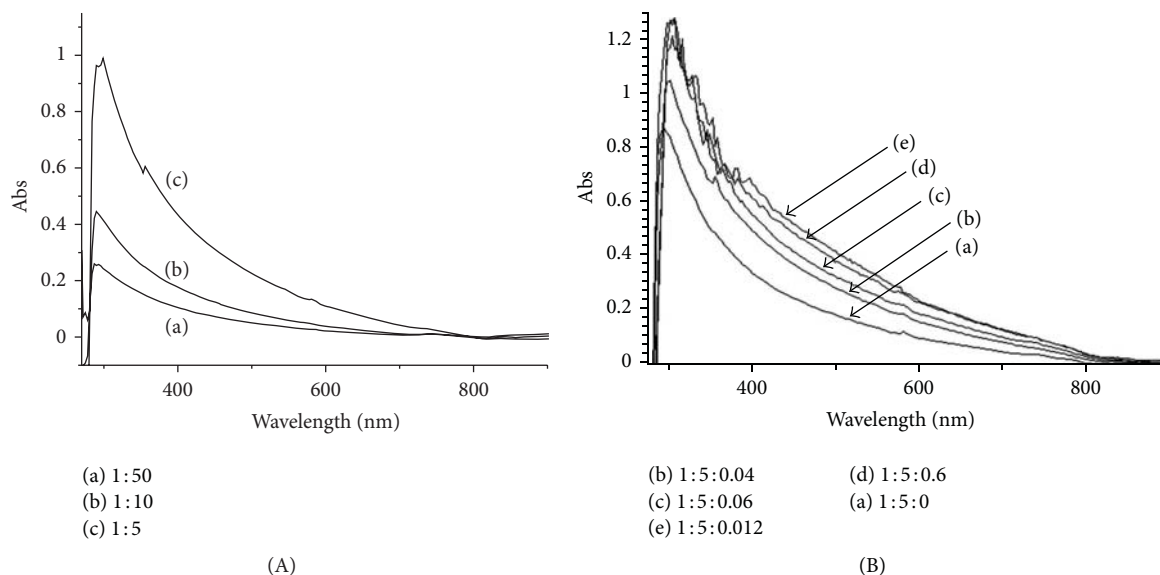


FIGURE 2: (A) UV-Vis optical absorbance spectra of aqueous solution of MWCNTs with different concentrations of SDS. (B) UV-Vis optical absorbance spectra of aqueous solution of MWCNTs-SDS with different concentrations of PVP.

the UV-Vis, there is a movement phase of the charge density and charge accumulation at the surface, and therefore  $\pi$ -plasmon carbon nanotubes can be coupled with light. But the distribution of charges at the surface of carbon nanotubes is not in mechanical equilibrium and oscillates around the equilibrium position. The plasmon resonance corresponds to a strong increase in absorption at the resonant frequency. Indeed, when we reduced the mass of SDS compared to that of MWCNTs which was fixed at 1 mg, from 50 mg to 5 mg of SDS, the intensity of absorbance was significantly increased, and the best absorbance was achieved for the mass ratio of MWCNTs : SDS—1 : 5.

To study the effect of the PVP on the dispersion of MWCNTs in the presence of SDS, we have taken the same quantities used for the MWCNTs : SDS, 1 : 5, which gave the best dispersion, and different amounts of PVP were added. All suspensions of MWCNTs-SDS-PVP were prepared in the same conditions as the previous suspensions.

The UV-Vis spectra of all suspensions (Figure 2(B)) show that when the mass of PVP increased from 0.04 mg to 0.6 mg compared to the mass of MWCNTs : SDS—1 : 5 the solutions absorbance has improved considerably and the characteristic absorbance band of the MWCNTs is shifted to higher wavelengths. This redshift can be explained by the improvement of the density fluctuations of  $\pi$ -plasmon of internal and external surfaces of MWCNTs [18]. So, we can deduce that the dispersion of MWCNTs is enhanced with the addition of the PVP until a certain threshold. For the mass increasing from 0.6 mg to 1.2 mg, the absorbance is found to saturate with even a slight drop. These optimized concentrations were used for the solutions used in electrospinning process.

**3.2. SEM Analysis.** The characteristics of the fibrous structures produced via the electrospinning process were observed by SEM micrograph.

Nanofibers diameter and morphology can be controlled by several processing parameters including solution viscosity (as controlled by changing the polymer concentration), voltage, feed solution conductivity, and capillary-to-collector distance. In addition, the spinning process is expected to align CNTs or their bundles along the fiber direction due to combination of dielectrophoretic forces caused by dielectric or conductivity mismatch between the CNTs and the polymer solution and high shear forces induced by spinning.

The selected SEM representative images (Figure 3) show the as-spun PVA (Figure 3(a)), PVA/SDS/MWCNTs (Figure 3(b)), and PVA/SDS/PVP/MWCNTs (Figure 3(c)) fibers deposited on the glass substrate at 20 000x magnification. The treatment of the images with Image J software shows that the diameter average was varying from 230 nm for the pure PVA to 210 nm for PVA/SDS/MWCNTs. The decrease of the fibers diameter indicates that the incorporation of the MWCNTs into the fibers increases the conductivity of the matrix solution, which favors the stretching of the solution under electric field during the electrospinning. Furthermore, for PVA/SDS/PVP/MWCNTs composite nanofibers, the fibers diameter decreases to be 224 nm due to the increase of solution viscosity. It should be noted that the fibers structures were completely stabilized and any beads were observed.

**3.3. FTIR Spectroscopy.** To determine the interaction between PVA, MWCNTs, and PVP, FTIR measurements of pure PVA, PVA/SDS/MWCNTs, and PVA/SDS/PVP/MWCNTs fibers were conducted.

The FTIR spectrum of pure PVA fibers (Figure 4(a)) shows the main characteristic bonds as follows.

The C–H stretching vibration is observed at  $3283\text{ cm}^{-1}$ . The symmetric and antisymmetric  $-\text{CH}_2$  vibrations appear at, respectively,  $2940\text{ cm}^{-1}$  and  $2912\text{ cm}^{-1}$ . The peaks located

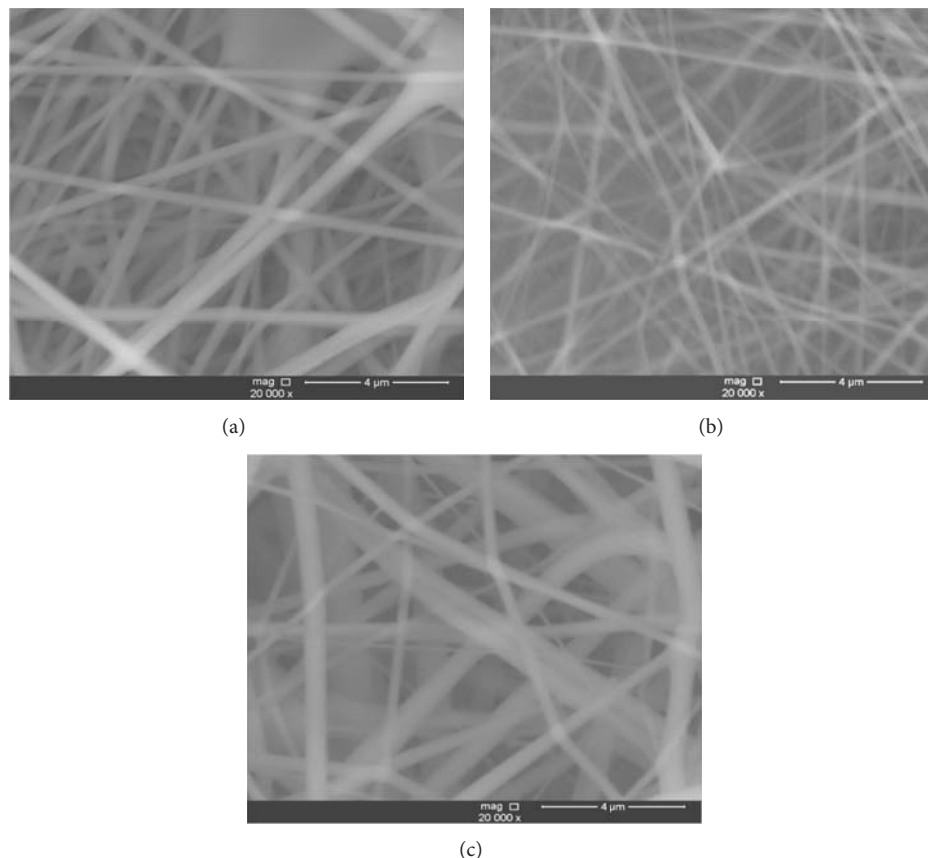


FIGURE 3: SEM images of PVA fibers (a), PVA/SDS/MWCNTs (b), and PVA/SDS/PVP/MWCNTs (c).

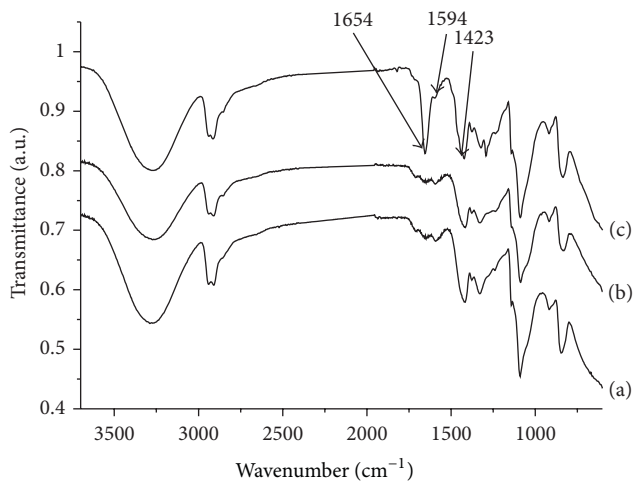


FIGURE 4: FTIR spectra of PVA (a), PVA/SDS/MWCNTs (b), and PVA/SDS/PVP/MWCNTs (c).

at 1417 cm<sup>-1</sup> and 1330 cm<sup>-1</sup> are attributed to the -CH deformation vibration. At 1089 cm<sup>-1</sup>, we observe a characteristic peak of C-O stretching vibration. In addition, the peak of O-H stretching vibration appears at 919 cm<sup>-1</sup> [19, 20].

Compared to the PVA spectrum (Figure 4(a)), it could be observed that any additional band was observed in the PVA/SDS/MWCNTs spectra (Figure 4(b)). This indicates

that any covalent bond was created between PVA and MWCNTs coated with SDS. Consequently, we confirmed that MWCNTs were dispersed in the PVA via noncovalent functionalization.

Concerning the PVA/SDS/PVP/MWCNTs nanocomposite fibers, the FTIR spectra of the fibers (Figure 4(c)) showed a characteristic peak of PVP at 1423 cm<sup>-1</sup> which is assigned to the deformation of CH<sub>2</sub> in PVP. The shoulder at 1594 cm<sup>-1</sup> is characteristic of C=C (aromatic) and C-N stretching. The additional peak located at 1654 cm<sup>-1</sup> is assigned to the C=O vibration [21–23]. The appearance of this band is due to the interaction of MWCNTs with PVP.

**3.4. Thermal Analysis.** Thermal gravimetric analysis (TGA) was carried out at a heating rate of 10°C·min<sup>-1</sup> in nitrogen atmosphere.

The thermal decomposition of the three samples was multistage processes; it exhibits two degradation steps. In the first region, as can be seen, the three samples displayed a similar behavior with degradation temperature close to 240°C. In fact, the degradation of isobutyl groups [24, 25] was located at about 246°C for the neat PVA fibers (Figure 5(a)). This temperature was decreased slightly for the PVA/SDS/MWCNTs fibers (Figure 5(b)) to be 239°C, and the shift is due to the presence of SDS in the bulk PVA polymer matrix [26], while the PVA/SDS/PVP/MWCNTs fibers (Figure 5(c)) degradation temperature was decreased

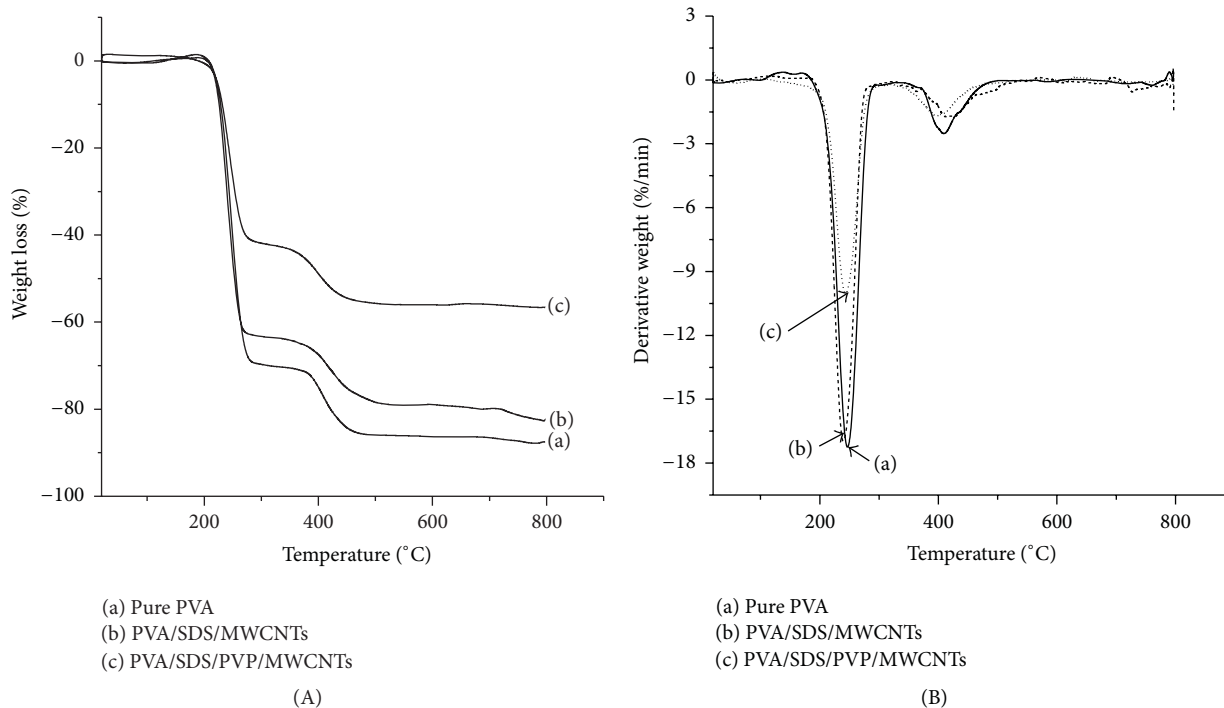


FIGURE 5: TGA and derivative TGA curves of (a) pure PVA, (b) PVA/SDS/MWCNTs and (c) PVA/SDS/PVP/MWCNTs.

TABLE 1: TGA results of weight loss of pure PVA, PVA/SDS/MWCNTs, and PVA/SDS/PVP/MWCNTs fibers.

|                  | Pure PVA fibers |       | PVA/SDS/MWCNTs fibers |      | PVA/SDS/PVP/MWCNTs fibers |     |
|------------------|-----------------|-------|-----------------------|------|---------------------------|-----|
| Temperature (°C) | 246.5           | 408.9 | 239.8                 | 413  | 242.7                     | 396 |
| Weight loss (%)  | 70              | 17    | 63.5                  | 18.7 | 43.7                      | 14  |

from 246°C to 242°C compared to the pure PVA fibers. This change reflects the specific multiple hydrogen bonding interaction between PVA and PVP [27].

The second stage appearing around 400°C is corresponding to the cleavage of C–C backbone of side and main chains of PVA [25]. According to Figure 4, all these transitions were accompanied with a weight loss as listed in Table 1.

All samples show a small loss in weight at around 100°C which is assigned to the detachment of residual water (from fibers preparation). For the neat PVA, the major weight loss (70 wt%) is at 193°C, and this continued to increase rapidly with temperature, until a stable plateau region appeared between 351 and 477°C, while the difference between the weight loss of pure PVA and PVA/SDS/MWCNTs fibers indicated the interfacial interaction between the matrix and MWCNTs. When the PVP was incorporated into the composite, the weight loss decreased considerably due to the interaction of PVA with the MWCNTs coated by the PVP through hydrogen bonding interaction between PVA and PVP.

#### 4. Conclusion

PVA electrospun nanofibers containing SDS/PVP/MWCNTs were fabricated, using different concentrations of the SDS

and PVP in order to achieve a stable dispersion lasting for several months. Our results showed clearly that the absorption of the wrapped MWCNTs in aqueous solution increased with the concentration of SDS and PVP and the best absorption was achieved for MWCNTs : SDS : PVP = 1 : 5 : 0.6. SEM images of PVA/SDS/PVP/MWCNTs nanofibers showed that the diameter was decreasing to around 224 nm and the interaction between the PVA and the coated carbon nanotubes with PVP was elucidated by FTIR and TGA.

#### Conflict of Interests

The authors declare no conflict of interests.

#### References

- [1] B. Ding, M. Wang, J. Yu, and G. Sun, "Gas sensors based on electrospun nanofibers," *Sensors*, vol. 9, no. 3, pp. 1609–1624, 2009.
- [2] R. Dersch, M. Steinhart, U. Boudriot, A. Greiner, and J. H. Wendorff, "Nanoprocessing of polymers: applications in medicine, sensors, catalysis, photonics," *Polymers for Advanced Technologies*, vol. 16, no. 2-3, pp. 276–282, 2005.
- [3] M. Bognitzki, T. Frese, M. Steinhart et al., "Preparation of fibers with nanoscaled morphologies: electrospinning of polymer

- blends," *Polymer Engineering and Science*, vol. 41, no. 6, pp. 982–989, 2001.
- [4] Q. Li, S. Mahendra, D. Y. Lyon et al., "Antimicrobial nanomaterials for water disinfection and microbial control: potential applications and implications," *Water Research*, vol. 42, no. 18, pp. 4591–4602, 2008.
  - [5] K. H. Hong, J. L. Park, I. N. Hwan Sul, J. H. Youk, and T. J. Kang, "Preparation of antimicrobial poly(vinyl alcohol) nanofibers containing silver nanoparticles," *Journal of Polymer Science B*, vol. 44, no. 17, pp. 2468–2474, 2006.
  - [6] K. Yoon, K. Kim, X. Wang, D. Fang, B. S. Hsiao, and B. Chu, "High flux ultrafiltration membranes based on electrospun nanofibrous PAN scaffolds and chitosan coating," *Polymer*, vol. 47, no. 7, pp. 2434–2441, 2006.
  - [7] J. Jagur-Grodzinski, "Polymers for tissue engineering, medical devices, and regenerative medicine. Concise general review of recent studies," *Polymers for Advanced Technologies*, vol. 17, no. 6, pp. 395–418, 2006.
  - [8] Z. Rožek, W. Kaczorowski, D. Lukáš, P. Louda, and S. Mitura, "Potential applications of nanofiber textile covered by carbon coatings," *Journal of Achievements in Materials and Manufacturing Engineering*, vol. 27, pp. 35–38, 2008.
  - [9] J. Nader, C. Bhuvanesh, M. Apparao et al., "Functional fabric with embedded nanotube actuators/sensors," Tech. Rep., National Textile Center Annual Report, 2004.
  - [10] A. Martinez, S. Uchida, Y.-W. Song, T. Ishigure, and S. Yamashita, "Fabrication of Carbon nanotube-poly-methylmethacrylate composites for nonlinear photonic devices," *Optics Express*, vol. 16, no. 15, pp. 11337–11343, 2008.
  - [11] B. Vigolo, A. Penicaud, C. Coulon et al., "Macroscopic fibers and ribbons of oriented carbon nanotubes," *Science*, vol. 290, no. 5495, pp. 1331–1334, 2000.
  - [12] H. Aarab, M. Baitoul, J. Wéry et al., "Electrical and optical properties of PPV and single-walled carbon nanotubes composite films," *Synthetic Metals*, vol. 155, no. 1, pp. 63–67, 2005.
  - [13] O. Matarredona, H. Rhoads, Z. Li, J. H. Harwell, L. Balzano, and D. E. Resasco, "Dispersion of single-walled carbon nanotubes in aqueous solutions of the anionic surfactant NaDDBS," *Journal of Physical Chemistry B*, vol. 107, no. 48, pp. 13357–13367, 2003.
  - [14] L. Liu, F. Zhao, F. Xiao, and B. Zeng, "Improved voltammetric response of malachite green at a multi-walled carbon nanotubes coated glassy carbon electrode in the presence of surfactant," *International Journal of Electrochemical Science*, vol. 4, no. 4, pp. 525–534, 2009.
  - [15] J. Yu, N. Grossiord, C. E. Koning, and J. Loos, "Controlling the dispersion of multi-wall carbon nanotubes in aqueous surfactant solution," *Carbon*, vol. 45, no. 3, pp. 618–623, 2007.
  - [16] N. Diouri and M. Baitoul, "Studies of multiwall carbon nanotubes dispersion in poly vinyl alcohol," *Mediterranean Journal of Electronics and Communications*, vol. 6, pp. 127–131, 2010.
  - [17] M. E. Hughes, E. Brandin, and J. A. Golovchenko, "Optical absorption of DNA-carbon nanotube structures," *Nano Letters*, vol. 7, no. 5, pp. 1191–1194, 2007.
  - [18] L. Zeng, W. Wang, J. Liang et al., "The changes of morphology, structure and optical properties from carbon nanotubes treated by hydrogen plasma," *Materials Chemistry and Physics*, vol. 108, no. 1, pp. 82–87, 2008.
  - [19] X. M. Sui, C. L. Shao, and Y. C. Liu, "White-light emission of polyvinyl alcohol/ZnO hybrid nanofibers prepared by electrospinning," *Applied Physics Letters*, vol. 87, no. 11, Article ID 113115, 2005.
  - [20] L. Zhang, P. Yu, and Y. Luo, "Dehydration of caprolactam-water mixtures through cross-linked PVA composite pervaporation membranes," *Journal of Membrane Science*, vol. 306, no. 1-2, pp. 93–102, 2007.
  - [21] R. F. Bhajantri, V. Ravindrachary, B. Poojary, I. Ismayil, A. Harisha, and V. Crasta, "Studies on fluorescent PVA + PVP + MPDMAPP composite films," *Polymer Engineering and Science*, vol. 49, no. 5, pp. 903–909, 2009.
  - [22] S. F. Wei, J. S. Lian, and Q. Jiang, "Controlling growth of ZnO rods by polyvinylpyrrolidone (PVP) and their optical properties," *Applied Surface Science*, vol. 255, no. 15, pp. 6978–6984, 2009.
  - [23] S. Sethia and E. Squillante, "Solid dispersion of carbamazepine in PVP K30 by conventional solvent evaporation and supercritical methods," *International Journal of Pharmaceutics*, vol. 272, no. 1-2, pp. 1–10, 2004.
  - [24] Y.-W. Chang, E. Wang, G. Shin, J.-E. Han, and P. T. Mather, "Poly(vinyl alcohol) (PVA)/sulfonated polyhedral oligosilsesquioxane (sPOSS) hybrid membranes for direct methanol fuel cell applications," *Polymers for Advanced Technologies*, vol. 18, no. 7, pp. 535–543, 2007.
  - [25] E. D. Wang, T. S. Zhao, and W. W. Yang, "Poly (vinyl alcohol)/3-(trimethylammonium) propyl-functionalized silica hybrid membranes for alkaline direct ethanol fuel cells," *International Journal of Hydrogen Energy*, vol. 35, no. 5, pp. 2183–2189, 2010.
  - [26] C. Bartholome, P. Miaudet, A. Derré et al., "Influence of surface functionalization on the thermal and electrical properties of nanotube-PVA composites," *Composites Science and Technology*, vol. 68, no. 12, pp. 2568–2573, 2008.
  - [27] A. B. Seabra and M. G. De Oliveira, "Poly(vinyl alcohol) and poly(vinyl pyrrolidone) blended films for local nitric oxide release," *Biomaterials*, vol. 25, no. 17, pp. 3773–3782, 2004.

## Research Article

# Shape Effects of Iron Nanowires on Hyperthermia Treatment

Wei-Syuan Lin,<sup>1</sup> Hong-Ming Lin,<sup>1</sup> Hsiang-Hsin Chen,<sup>2</sup>  
Yeu-Kuang Hwu,<sup>2</sup> and Yuh-Jing Chiou<sup>3</sup>

<sup>1</sup> Department of Materials Engineering, Tatung University, Taipei 104, Taiwan

<sup>2</sup> Institute of Physics, Academia Sinica, Nankang, Taipei 115, Taiwan

<sup>3</sup> Department of Chemical Engineering, Tatung University, Taipei 104, Taiwan

Correspondence should be addressed to Hong-Ming Lin; [hmlin@ttu.edu.tw](mailto:hmlin@ttu.edu.tw)

Received 7 October 2012; Accepted 12 May 2013

Academic Editor: Haiping Hong

Copyright © 2013 Wei-Syuan Lin et al. This is an open access article distributed under the Creative Commons Attribution License, which permits unrestricted use, distribution, and reproduction in any medium, provided the original work is properly cited.

This research discusses the influence of morphology of nanomagnetic materials (one-dimensional iron nanowires and zero-dimensional iron nanoparticles) on heating efficiency of the hyperthermia treatment. One-dimensional iron nanowires, synthesized by reducing method in external magnetic field, are explored in terms of their material properties, magnetic anisotropy, and cytotoxicity of EMT-6 cells. The magnetic anisotropy of an array of nanowires is examined in parallel and perpendicular magnetic fields by VSM. For the magnetic hyperthermia treatment tests, iron nanowires and nanoparticles with different concentrations are heated in alternating magnetic field to measure their actual heating efficiency and SLP heating properties. The shape effects of iron nanomaterials can be revealed from their heating properties. The cytotoxicity of nanowires with different concentrations is measured by its survival rate in EMT-6 with the cells cultivated for 6 and 24 hours.

## 1. Introduction

According to the World Health Organization (WHO), cancers were the top causes of death all over the world. In 2008 alone, 7.6 million victims died from cancers, accounting for 13% of the total death toll [1]. Currently, cancer can be treated by chemotherapy, radiation therapy, surgery, gene therapy, and immunotherapy, and so forth. Conventional hyperthermia treatments include ultrasound, radiofrequency, microwaves, infrared radiation, and tubes with hot water. Some of them will cause side effect all over the patients' bodies during the treatment [2–4].

This research is focused on the magnetic targeted hyperthermia treatments. This treatment can directly eliminate the cancer cells without damaging the normal ones. Most importantly, the medication applied on the surfaces of magnetic materials can directly perform the treatment [5, 6]. Magnetic targeted hyperthermia treatments are conducted by placing magnetic targeted medicines on the tumor and imposing the alternating magnetic field (~kHz–~MHz) on it [7, 8].

To generate heat in an alternating field, magnetic materials activate more than four different known mechanisms, which are generation of eddy currents, hysteresis losses,

relaxation losses, and frictional losses, and so forth. There are two modes, rotational (Brownian) and Neel, in which the relaxation losses in single-domain MNPs occur. The magnetic moment fixed along the crystal easy axis revolves away towards the external field in the Neel mode. Similar to the hysteresis loss in multidomain magnetic particles, the Neel mechanism can also generate heat by means of “internal friction” caused by the movement of the magnetic moment in an external field. In the Brownian mode, however, the interaction between a thermal force and viscous drag in the suspending medium will influence the particle movement significantly. The whole particle moves towards the external field with the moment locked along the crystal axis instead. This phenomenon serves to account for the mechanical friction component in a given suspending medium. Applying the mechanism mentioned above, the local temperature of the tumor can rise up to 42–50°C, with that the cancer cells will be killed [9–11].

The important factor for magnetic heating is the specific loss power (SLP) (also called the specific absorption rate (SAR)). SLP is equal to  $C \times m_{\text{sample}}/m_{\text{metal}} \times \Delta T/\Delta t$ , where  $C$  is the specific heat capacity of sample ( $C_{\text{water}} = 4.185 \text{ J/g}^\circ\text{C}$ ),

$m_{\text{sample}}$  is the mass of sample,  $m_{\text{metal}}$  is the mass of the magnetic material in sample, and  $\Delta T/\Delta t$  is the slope of the heating curve. And SLP is very sensitive to the material properties [7, 12, 13].

The factors that affect the biodistribution of polymeric iron nanoparticles (NPs) include the size, shape, hydrophobic/hydrophilic balance of the surface, and surface charge [14]. Thus, this experiment explores the characteristic differences of heating effectiveness between 1D iron nanowires (NWs) and commercial iron nanoparticles (NPs) in hyperthermia treatments. Iron NWs reveal a special property that may easily destroy the cancer cells by its 1D spinning radius. The cellular toxic tests of the nanoiron are also conducted for the iron NWs in further studies.

## 2. Experimental

Iron (III) chloride hexahydrate ( $\text{FeCl}_3 \cdot 6\text{H}_2\text{O}$ , 98%, assay) and sodium borohydride (98%, assay) are purchased from Sigma-Aldrich Company and Acros Organics Company, respectively. Ethanol (99.5%, assay) was obtained from Shimakyu Pure Chemicals Company. Iron NWs are fabricated by the reduction of iron (III) chloride under high magnetic field. The aqueous iron (III) chloride hexahydrate (0.5 M, 0.2 mL) is diluted with 5 mL of aqueous dextran (40 ppm) and the iron (III) precursor is kept in an external magnetic field of about 2000 gauss. The argon gas is bubbling through the solution to purge the dissolved oxygen. The reducing agent,  $\text{NaBH}_4$ , is added dropwisely under Ar. After 5 minutes, the products are washed with ethanol for several times and dried at  $95^\circ\text{C}$  [15]. The iron nanoparticles are obtained from Yong-Zhen Technomaterial Co., Ltd. with 10–60 nm in diameter for comparison.

X-ray powder diffraction (XRD) analysis of samples is carried out at NSRRIC beam line. High-resolution images of samples are examined by field emission transmission electron microscope (FE-TEM), JEOL 2100F. Magnetic hysteresis loop is measured by using vibration sample magnetization (VSM, Lakeshore) at room temperature.

The hyperthermia device (Power cube 64/900) used in this study is produced by AREZZO, President Honor Ind. Co., Ltd., Taiwan. The experimental samples are placed in the inductive coil heater of 3 cm diameter with an optic fiber (Luxtron One, Lambda Photometrics, UK) to measure the raise of temperature.

The biocompatibility of iron NWs is evaluated by murine breast cancer cells, EMT-6 cells. EMT-6 cells are cultured in DMEM/F12 medium with 10% of the fetal bovine serum (FBS) and 1% of penicillin-streptomycin in 5% of  $\text{CO}_2$  humidified chamber at  $37^\circ\text{C}$ . After the cells are seeded on multiple plates for overnight, iron NWs dispersed in culture medium are applied to each well of culture plates. The cells are treated with different concentrations of nanoiron for 6 and 24 hours. The control cell is treated in the normal culture medium without adding iron nanowires. After incubation, the cells are directly counted by trypan blue exclusion assay for assaying cellular viability.

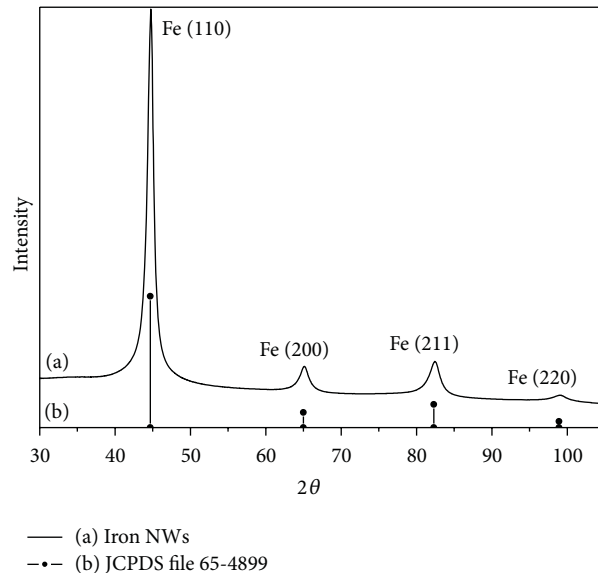


FIGURE 1: X-ray diffraction patterns of (a) iron NWs; (b) JCPDS file 65-4899.

## 3. Results and Discussion

XRD pattern of iron NWs and JCPDS file 65-4899 are shown in Figure 1. The diffraction angles of JCPDS file 65-4899 at  $2\theta = 44.662^\circ$ ,  $65.006^\circ$ , and  $82.311^\circ$  are related to (110), (200), and (211) planes of pure iron, respectively. This pattern shows clearly that a strong diffraction peak corresponds to the (110) plane. The growth orientation of iron NWs is highly dependent on applied magnetic field. According to these results, preferred crystal orientation of the iron NWs is in (110) direction. The lattice parameters of iron NWs are less than theoretical lattice constants. This may be due to lattice defects.

Figures 2(a)–2(d) show HR-TEM images of iron NWs. The diameter of iron NWs is around 60 nm with length of about 2–6  $\mu\text{m}$  as indicated in Figure 2(a). The selective area diffraction (SAD) of circle area in Figure 2(a) is shown in Figure 2(d). It indicates that iron NWs exhibit bcc crystal structure. The diffraction planes are assigned to (110), (200), (220), (310), and (222) from inside to outside diffraction rings. Figure 2(c) indicates an oxide layer of about 4 nm is passivated on the surface of iron NWs. The oxide layer on iron NWs results from magnetite formation during the reduction process. TEM images show that the iron NWs are synthesized by pearl-linking of iron NPs due to external magnetic field. Figures 2(c)-2.1 to 2(c)-5.1 are the atoms resolution related to c1, c2, c3, c4, and c5 positions in Figure 2(c), respectively. The d-spacing of Figures 2(c)-1.1, 2(c)-2.1, 2(c)-3.1, 2(c)-4.1, and 2(c)-5.1 are 1.889 Å, 1.879 Å, 1.888 Å, 2.022 Å, and 1.884 Å, respectively.

The magnetic hysteresis curve of iron NWs at room temperature is shown in Figure 3. The results indicate that the saturation magnetization and coercive force of iron NWs are 157.93 emu/g and 9.74 Oe, respectively. The saturation magnetization of iron NWs is lower than that of bulk iron (220 emu/g) due to the existence of a high surface/volume

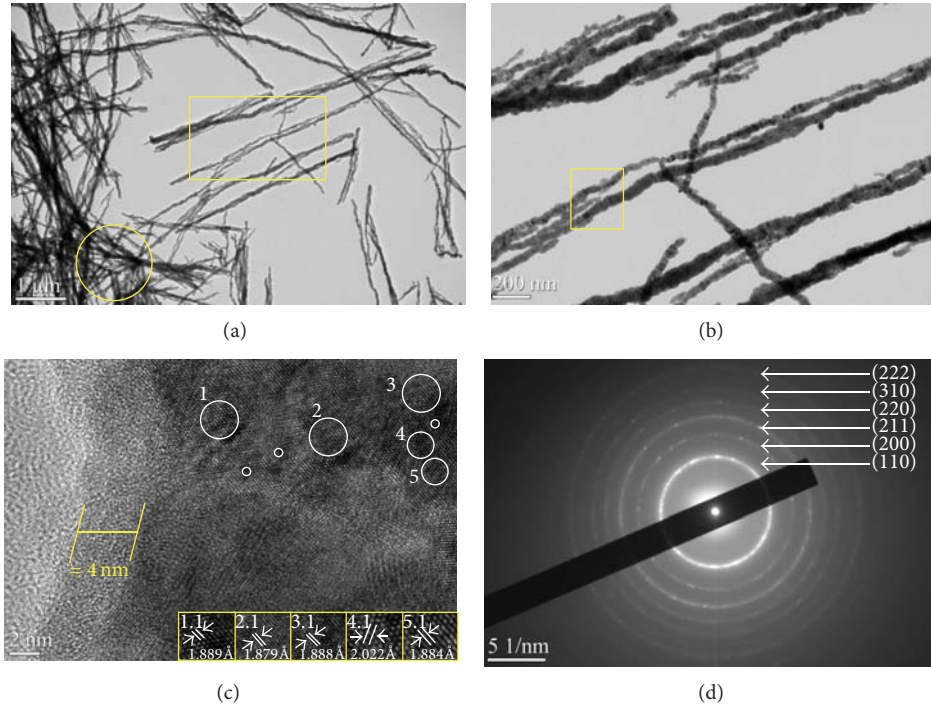


FIGURE 2: HR-TEM images of iron NWs: (a) low-magnification image; (b) high-magnification image at square area of (a); (c) HR-TEM images of iron NWs, 1.1, 2.1, 3.1, 4.1, and 5.1 are atomic resolution related to 1, 2, 3, 4, and 5 positions in (c), respectively; and (d) electron diffraction pattern at circle area of (a).

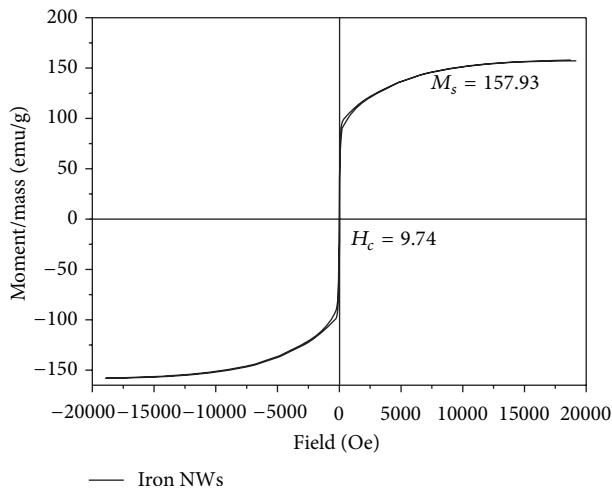


FIGURE 3: The hysteresis loops of iron NWs at 300 K.

ratio. And structural defects may be one of the possible causes for decreasing magnetization of iron NWs.

As shown in Figure 4, the formations of an array of nanowires under (a) parallel and (b) perpendicular magnetic fields at room temperature are measured for their magnetic properties such as coercive force and squareness ratio (remnant magnetization/saturation magnetization). In Table 1, the arrayed nanowires under the parallel magnetic field have greater squareness ratio (about 64.20%), while those under the perpendicular magnetic field have less squareness ratio

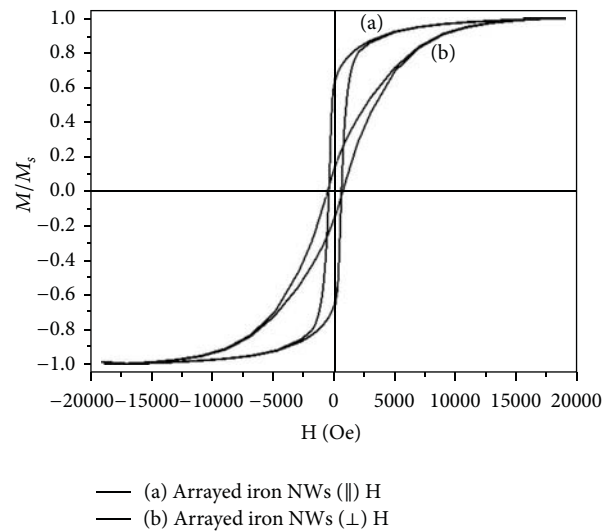


FIGURE 4: The hysteresis loops of an array of nanowires under parallel and perpendicular magnetic fields at room temperature are shown in (a) and (b), respectively.

(about 14.20%). The former's coercive force is 100 Oe less than the latter one.

Two sets of different amounts of iron NWs (0.1 mg, 0.25 mg, and 0.5 mg) and commercial iron nanoparticles (0.5 mg) are dispersed in 1 mL of deionized water. SEM image of commercial iron nanoparticles produced by Yong-Zhen Technomaterial Co., Ltd. is shown in Figure 5.

TABLE 1: The Hc (coercive force) and Mr/Ms (squareness ratio) of an array of nanowires under parallel and perpendicular magnetic fields.

|                                    | Hc (Oe) | Mr/Ms  |
|------------------------------------|---------|--------|
| Arrayed iron NWs ( $\parallel$ ) H | 520.3   | 64.20% |
| Arrayed iron NWs ( $\perp$ ) H     | 628     | 14.20% |

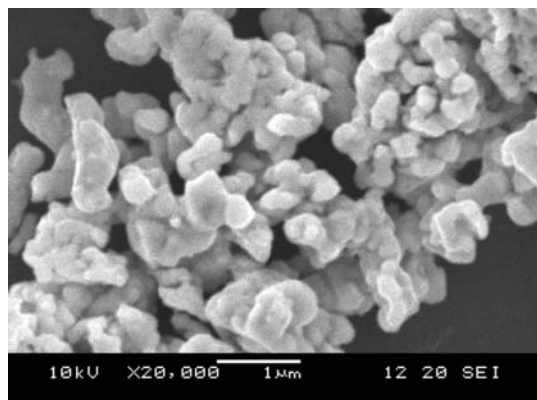


FIGURE 5: The SEM image of commercial iron nanoparticles.

Three different concentrations (100, 250, and 500 ppm) of iron NWs or commercial iron nanoparticles (500 ppm) solution in centrifuge tube is placed in the coil of inductive heater for an hour. The rising temperature of solution with time is shown in Figure 6. The maximal temperatures of iron NWs of 500, 250, and 100 ppm can be 73.8°C, 49.6°C, and 36.0°C, respectively. The heating rates of commercial iron nanoparticles of 500 ppm are 0.006°C/sec and are listed in Table 2. When the iron nanowires and commercial iron nanoparticles have the same concentration of 500 ppm, the heating rates of iron NWs are much higher than those of the commercial iron nanoparticles. The average of SLP values for different concentrations of iron NWs and commercial iron nanoparticles are also listed in Table 2. For iron NWs, the SLP values are 619.7 W/g, 535.8 W/g, and 920.8 W/g; and for commercial iron nanoparticles (500 ppm), the SLP values are 50.2 W/g. The highest SLP value (920.8 W/g) is obtained at 100 ppm of iron NWs. From the heating results of the iron nanowires and commercial iron nanoparticles with the same concentration of 500 ppm, the former have higher saturated temperature and efficiency than the latter one.

As mentioned above, this study presents the hypothesis in Figure 7 as an imaginary rundown. Because the iron nanowires, as compared to iron nanoparticles, have more spinning radii, the materials which are heated and stirred in the alternating magnetic field have larger reactive areas. This fact leads iron NWs to better heating efficiency than that of the iron nanoparticles.

When one-dimensional iron nanowires are applied to the tumor hyperthermia treatment, they can provide larger frictional reactive areas than zero-dimensional iron nanoparticles. This enables one-dimensional iron nanowires to have a better heating efficiency, which reduces the treatment time of the cancer patients.

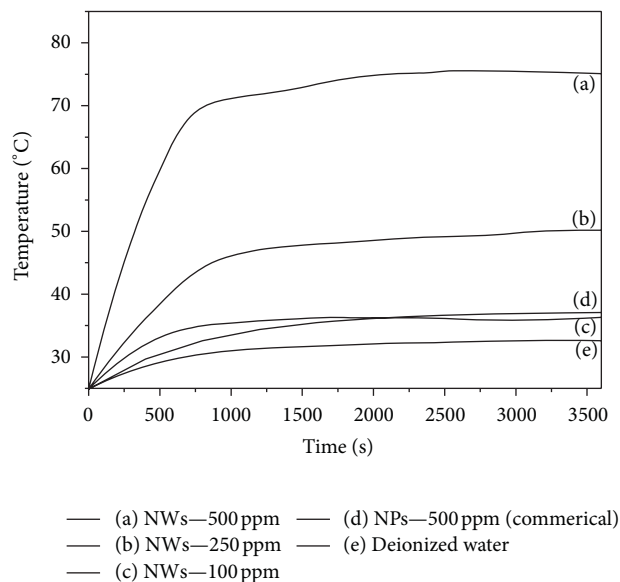


FIGURE 6: The heating effectiveness of the iron NWs in different concentrations, (a) 500 ppm of iron NWs (0.5 mg/mL), (b) 250 ppm of iron NWs (0.25 mg/mL), (c) 100 ppm of iron NWs (0.1 mg/mL), (d) 250 ppm of commercial iron NPs (0.5 mg/mL), and (e) deionized water is shown for reference.

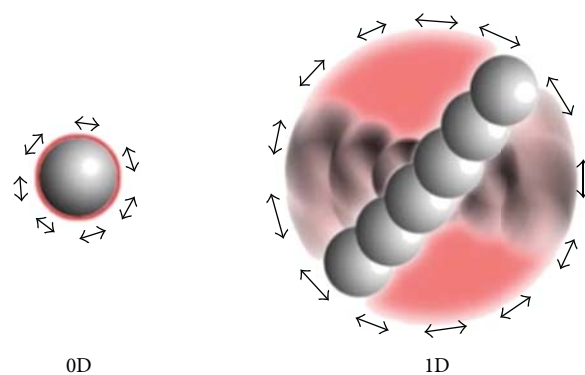


FIGURE 7: One-dimensional materials have large spinning radii.

TABLE 2: Heating effectiveness of iron NWs and commercial iron NPs.

| Samples (ppm) | Max. Temp. (°C) | Heating rate (°C/sec) | SLP (W/g) |
|---------------|-----------------|-----------------------|-----------|
| NWs—500       | 73.8            | 0.074                 | 619.7     |
| NWs—250       | 49.6            | 0.032                 | 535.8     |
| NWs—100       | 36.0            | 0.022                 | 920.8     |
| NPs—500*      | 37.1            | 0.006                 | 50.2      |

\* NPs—500: commercial iron nanoparticles.

The cytotoxicity in response to iron NWs in different concentrations (1, 10, 250, and 500 ppm) is performed by directly counting the number of live cells after incubation. Figure 8 shows the results of cytotoxicity of iron NWs in EMT-6 cells. The number of cellular vesicles appearing in the cytoplasm increases due to being exposed to iron NWs

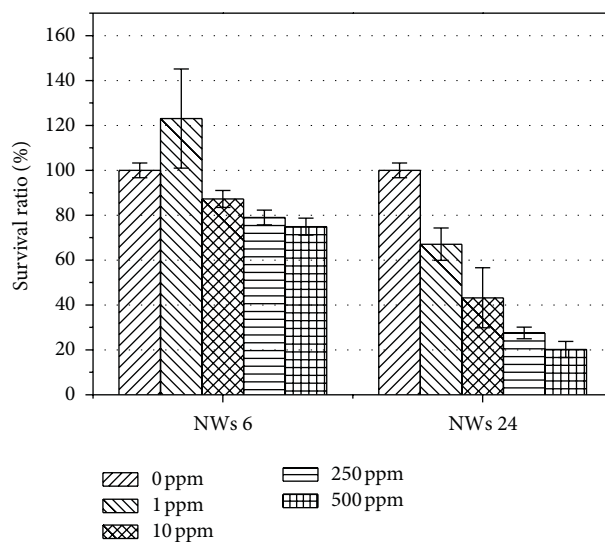


FIGURE 8: Survival ratio of iron NWs and NPs coculture with EMT-6 cells in concentrations of 0, 1, 10, 250, and 500 ppm for 6 and 24 hours.

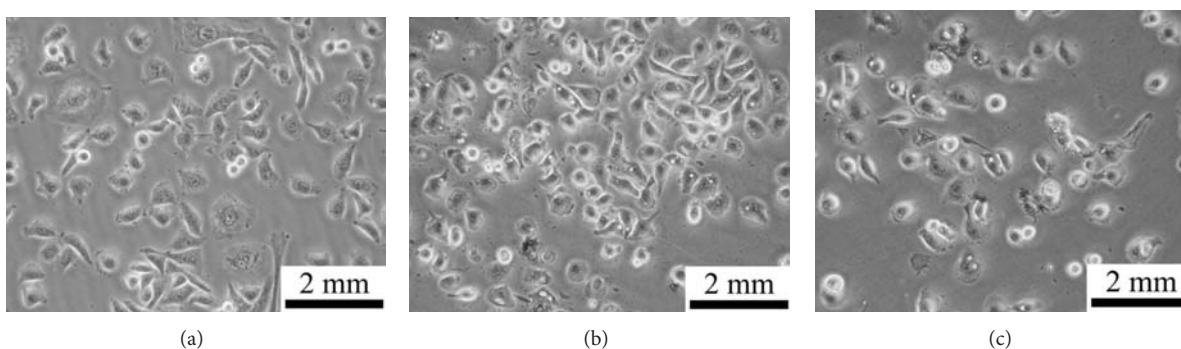


FIGURE 9: The optical images of (a) untreated EMT-6 cells; (b) and (c) cocultured iron NWs (10 ppm) and EMT-6 cells in 6 and 24 hours, respectively.

at lower concentrations in shorter time. After 6 hours of incubation, iron NWs shows cell survivability of more than 80%. Figures 9(b) and 9(c) show the optical images of EMT-6 cocultured with iron NWs for 6 and 24 hours, respectively. The untreated cells are shown in Figure 9(a). It is also noted that the cell morphology is transformed into spherical shape.

#### 4. Conclusions

This study synthesizes the iron nanowires with diameter of about 60 nm and length of approximately 2–6  $\mu\text{m}$ . Their saturation magnetization is about 157.9 emu/g while their coercive force is about 9.7 Oe. They have greater squareness ratio of about 64.2% under the parallel external magnetic field, whereas it is only about 14.20% under the perpendicular magnetic field. With regard to heating efficiency, one-dimensional iron nanowires have a better heating efficiency at the external alternating magnetic field than that of zero-dimensional ones at the same concentration of 500 ppm. The one-dimensional

iron nanowires have the saturated heating temperature at about 73.8°C (that of the nanoparticles is only 40°C) and their heating efficiency is about 0.074 (that of the nanoparticles is about 0.006). These results indicate the strong shape effects of nanomaterials on its heating efficiency. The cytotoxicity of the iron nanowires (10 ppm) in EMT-6 cells undergoing 6 hours of toxic test has the mortality rate of about 80%. These results indicate that with further study the iron nanowires are feasible to be used in hyperthermia therapy.

#### Conflict of Interests

The authors declare that they have no conflict of interests with the chemical companies (Sigma-Aldrich Company, Acros Organics Company, Shimadzu Pure Chemicals Company, and Yung-Zhen Technomaterial Co., Ltd.), instrument providers (Lakeshore, AREZZO President Honor Ind. Co., Ltd., Taiwan, Luxtron one, Lambda Photometrics, UK, NSRRC, NISP Lab in Maryland University, and Composites Lab in NTU), and research funding (NSC of Taiwan).

## Acknowledgments

The authors acknowledge the Grant from NSC of Taiwan, the support from SRRC, Taiwan, TEM/SEM from NISP Lab in Maryland University, and hyperthermia test from Bioceramics and Composites Lab in NTU, Taiwan.

## References

- [1] Globocan 2008, IARC, 2010, <http://www.iarc.fr/>.
- [2] B. E. Billard, K. Hynynen, and R. B. Roemer, "Effects of physical parameters on high temperature ultrasound hyperthermia," *Ultrasound in Medicine and Biology*, vol. 16, no. 4, pp. 409–420, 1990.
- [3] P. Wust, B. Hildebrandt, G. Sreenivasa et al., "Hyperthermia in combined treatment of cancer," *The Lancet Oncology*, vol. 3, no. 8, pp. 487–497, 2002.
- [4] C. J. Diederich and K. Hynynen, "Ultrasound technology for hyperthermia," *Ultrasound in Medicine and Biology*, vol. 25, no. 6, pp. 871–887, 1999.
- [5] P. Cherukuri, E. S. Glazer, and S. A. Curley, "Targeted hyperthermia using metal nanoparticles," *Advanced Drug Delivery Reviews*, vol. 62, no. 3, pp. 339–345, 2010.
- [6] D. L. Zhao, X. X. Wang, X. W. Zeng, Q. S. Xia, and J. T. Tang, "Preparation and inductive heating property of Fe<sub>3</sub>O<sub>4</sub>-chitosan composite nanoparticles in an AC magnetic field for localized hyperthermia," *Journal of Alloys and Compounds*, vol. 477, no. 1–2, pp. 739–743, 2009.
- [7] C. S. S. R. Kumar and F. Mohammad, "Magnetic nanomaterials for hyperthermia-based therapy and controlled drug delivery," *Advanced Drug Delivery Reviews*, vol. 63, no. 9, pp. 789–808, 2011.
- [8] G. Zhang, Y. Liao, and I. Baker, "Surface engineering of core/shell iron/iron oxide nanoparticles from microemulsions for hyperthermia," *Materials Science and Engineering C*, vol. 30, no. 1, pp. 92–97, 2010.
- [9] R. Kötitz, W. Weitschies, L. Trahms, and W. Semmler, "Investigation of Brownian and Néel relaxation in magnetic fluids," *Journal of Magnetism and Magnetic Materials*, vol. 201, no. 1–3, pp. 102–104, 1999.
- [10] G. Nedelcu, "Magnetic nanoparticles impact on tumoral cells in the treatment by magnetic fluid hyperthermia," *Digest Journal of Nanomaterials and Biostructures*, vol. 3, no. 3, pp. 103–107, 2008.
- [11] G. Nedelcu, "The heating study of two types of colloids with magnetite nanoparticles for tumours therapy," *Digest Journal of Nanomaterials and Biostructures*, vol. 3, no. 2, pp. 99–102, 2008.
- [12] R. Hergt, S. Dutz, R. Müller, and M. Zeisberger, "Magnetic particle hyperthermia: nanoparticle magnetism and materials development for cancer therapy," *Journal of Physics Condensed Matter*, vol. 18, no. 38, pp. S2919–S2934, 2006.
- [13] F. Mohammad, G. Balaji, A. Weber, R. M. Uppu, and C. S. S. R. Kumar, "Influence of gold nanoshell on hyperthermia of superparamagnetic iron oxide nanoparticles," *Journal of Physical Chemistry C*, vol. 114, no. 45, pp. 19194–19201, 2010.
- [14] F. Sonvico, S. Mornet, S. Vasseur et al., "Folate-conjugated iron oxide nanoparticles for solid tumor targeting as potential specific magnetic hyperthermia mediators: synthesis, physico-chemical characterization, and in vitro experiments," *Bioconjugate Chemistry*, vol. 16, no. 5, pp. 1181–1188, 2005.
- [15] W. S. Lin, Z. J. Jian, H. M. Lin et al., "Synthesis and characterization of iron nanowires," *Journal of the Chinese Chemical Society*, vol. 60, pp. 85–91, 2013.

## Research Article

# Correlation Effects in Kinetics of One-Dimensional Atomic Systems

**V. D. Borman, I. V. Tronin, V. N. Tronin,  
V. I. Troyan, and O. S. Vasiliev**

*National Research Nuclear University, MEPhI, Kashirskoye Sh. 31, Moscow 115409, Russia*

Correspondence should be addressed to V. D. Borman; [vdborman@mephi.ru](mailto:vdborman@mephi.ru)

Received 10 January 2013; Accepted 7 March 2013

Academic Editor: Yun Zhao

Copyright © 2013 V. D. Borman et al. This is an open access article distributed under the Creative Commons Attribution License, which permits unrestricted use, distribution, and reproduction in any medium, provided the original work is properly cited.

The paper is devoted to the analysis of the correlation effects and manifestations of general properties of 1D systems (such as spatial heterogeneity that is associated with strong density fluctuations, the lack of phase transitions, the presence of frozen disorder, confinement, and blocked movement of nuclear particle by its neighbours) in nonequilibrium phenomena by considering the four examples. The anomalous transport in zeolite channels is considered. The mechanism of the transport may appear in carbon nanotubes and MOF structures, relaxation, mechanical properties, and stability of nonequilibrium states of free chains of metal atoms, non-Einstein atomic mobility in 1D atomic systems. Also we discuss atomic transport and separation of two-component mixture of atoms in a 1D system—a zeolite membrane with subnanometer channels. We discuss the atomic transport and separation of two-component mixture of atoms in a 1D system—zeolite membrane with subnanometer channels. These phenomena are described by the response function method for nonequilibrium systems of arbitrary density that allows us to calculate the dynamic response function and the spectrum of relaxation of density fluctuations 1D atomic system.

## 1. Introduction

In recent years, one-dimensional objects became available and actively investigated due to their unique properties. They are free chains of metals just one atom thick (Au, Ag, Pt, In, Mn, Li, and Ni) [1–13], chains on specially prepared surfaces of crystals with high crystalline indices [14–19], the molecules (atoms) in subnanometer channels of complex oxides, zeolites [20–22], carbon nanotubes [23–27], and in some metal organic frameworks (MOF).

According to modern concepts, the common feature of one-dimensional objects as statistical systems is spatially inhomogeneous state and density fluctuations. These fluctuations are caused by the crucial role of many-particle correlations in 1D systems. This feature is connected with the absence of phase transitions in 1D systems of particles of one kind with short-range potential of the interparticle interaction (see van Hove Theorem [28, 29]). In this case, for certain values of the density the susceptibility of 1D system has a maximum but stays finite in contrast to 3D systems,

where susceptibility becomes infinite in vapour-liquid and liquid-solid phase transitions [30].

The absence of phase transition means that stable nuclei of a new phase are not formed, and the one-dimensional clusters nuclei that are formed in a system have a finite lifetime and are the density fluctuations. 1D systems are characterized by frozen disorder because the atomic particles cannot be exchanged with their neighbours and block the movement of each particle neighbors. For kinetic phenomena in atomic 1D confinement system, the role of confinement is not only to preserve the geometry of the system, but also the system relaxation by phonons. Relaxation of the system in confinement due to strong interparticle correlations depends on the ratio of the energy of particle interaction with confinement and interparticle interaction [31].

This paper is devoted to the analysis of correlation effects and manifestations of these general properties of nonequilibrium phenomena in the four examples. The anomalous transport in zeolite channels is considered. The mechanism

of the transport may appear in carbon nanotubes and MOF structures, relaxation, mechanical properties, and stability of nonequilibrium states of free chains of metal atoms, non-Einstein atomic mobility in 1D atomic systems. Also we discuss atomic transport and separation of two-component mixture of atoms in a 1D system—a zeolite membrane with subnanometer channels.

These phenomena are described below using the response function method for nonequilibrium systems of arbitrary density [31]. This method allows us to calculate the dynamic response function and the spectrum of relaxation of density fluctuations of 1D atomic system. The spectrum contains diffusion and hydrodynamic modes. In the latter case, the relaxation of the system and the nuclear transport occurs through the distribution of density waves and not by the diffusion of particles. This relaxation mechanism becomes the determining by increasing the density that allows one to explain the abnormally high rate of atomic transport in subnanometer channels. The change of relaxation mechanism by increase of the density is associated with the observed non-Einstein character of mobility of atomic particles (the law for the mean square displacement  $x^2 = 2Dt$  is violated ( $D$  is the diffusion coefficient, and  $t$  is the time of observation) [32]). The found spectrum of relaxation allows to calculate the probability of decay of 1D free clusters of various lengths [30] and to explain the dependence of the stability of clusters of metal atoms on the chain atoms properties, the mechanical state of a cluster under the influence of an external force, and the number of particles in a stable cluster. These values were measured simultaneously in experiments [13].

The response function method was used to describe the practically important transport of two-component mixture in membranes with subnanometer channels.

It was shown that a phase transition in an inhomogeneous state may occur in 1D system of particles of two kinds with the increase of filling factor. Such a phase transition occurs due to an effective particle attraction and is characterised by the formation of clusters of a finite size [33]. The amplitude of the fluctuations in the density corresponding to the formation of such a state is the order parameter. An equation for the order parameter for a mixture of particles in the channels is derived. In contrast to the well-known phenomenological Landau-Ginzburg equation [34], the coefficients of the equation are calculated for a known interparticle interaction potential depending on the density and temperature. The analysis of this equation allows us to describe the observed increase in the separation factor with increasing flux through 1D channels at their closing by a stable clusters with a certain concentration of the components and determine the dependence of the separation on the concentration, temperature, and density.

## 2. Materials and Methods

**2.1. Molecular Transport in Subnanometer Channels.** Molecular transport in nanometer and subnanometer channels in porous bodies is currently drawing a great deal of interest

from the standpoint of fundamental science [35–39] and because of the many applications of membrane and nanotechnologies in various fields ranging from nuclear power to ecology [40, 41]. Polycrystalline ceramic membranes consisting of complex oxides (zeolites), possessing subnanometer channels ranging in diameter from 0.3 to 1.4 nm, have been synthesized recently [40]. On account of the high selectivity of molecular transport in zeolite membranes, as compared with the well-known polymeric membranes [41–43], new technologies for separation, reprocessing, and utilization of materials are being intensively developed on the basis of zeolite membranes [41–43].

When the channel diameters in membranes decrease to the nanometer scale, molecular transport is determined by the Knudsen flow in the central zone of the channel, free of interaction of molecules with walls, and particle diffusion in the surface force field [39]. In subnanometer channels, the interaction potentials between molecules and the opposite walls overlap, and molecular transport occurs under conditions of a constant interaction of molecules with a solid. Consequently, the diffusion coefficient in the limit of small filling numbers of a channel is determined by the relaxation of particles on phonons and surface defects [37]. For molecules, with the exception of light particles (H, He), the channel walls are impenetrable, and consequently molecular transport is possible only along the channel axes. In this sense, it is different from diffusion in solids and may be assumed to be one-dimensional. In contrast to surface diffusion in channels with diameter  $d > 1$  nm, a fundamentally new property of molecular transport should appear in subnanometer channels. As the filling factor of a channel or the diameter ( $\sigma$ ) of molecules increases, so that  $d < 2\sigma$ , each molecule can block the motion of two molecules. Consequently, it can be expected that as the diameter of the molecules or the external gas pressure increases, the molecular flux in membranes with subnanometer channels should decrease. However, experiments have shown that the diffusion flux of a number of molecules ( $\text{CH}_4$ ,  $\text{C}_2\text{H}_6$ , and others) in a ZSM-5 zeolite membrane with channel diameters 0.54–0.57 nm does not decrease but rather increases as the external gas pressure increases [43]. It has also been established that the diffusion coefficient for these gases increases by more than an order of magnitude as the filling factor of the channels with molecules increases. It has been found that for a number of gases, the temperature dependence of the flux possesses a maximum and a minimum.

In this section, the transport of a single-component molecular gas (system of atomic particles) in subnanometer-diameter channels is investigated theoretically.

**2.1.1. Sorption Isotherm in a 1D Channel.** Let us consider a surface in contact with an ideal single-component gas with temperature  $T$  and pressure  $p$ . Let us assume that particles located on the surface do not interact with one another. We will also assume that the energy of the gas molecules on the surface is  $\varepsilon_0$ . Let there be  $N$  adsorption centers on the surface. Then the average number  $\bar{N}_1$  of particles adsorbed on

the surface as a function of the gas pressure and temperature has the form (Langmuir isotherm)

$$\begin{aligned} \frac{\bar{N}_1}{N} &= \frac{p}{p + p_0(T)}, \\ p_0(T) &\equiv T \left( \frac{\hbar^2}{2m\pi T} \right)^{-3/2} \exp(-\beta\epsilon_0), \end{aligned} \quad (1)$$

where  $m$  is the mass of a gas molecule,  $\hbar$  is Planck's constant, and  $\beta = T^{-1}$  is the reciprocal of the temperature. The method used to derive the Langmuir isotherms (1) admits wide extensions. Specifically, this method can be used to solve the problem of the filling factor of a cylindrical channel with diameter  $d$  taking into account the interparticle interaction in the channel. Let the channel diameter be comparable to the maximum diameter of a gas molecule. Let us consider the equilibrium of the gas with the surface on which  $k$  of the channels described previously emerge. Let  $\epsilon_1$  be the binding energy of a particle at the entrance to the channel. If the energy  $\epsilon_1$  is negative, then it is energetically favorable for the gas molecule to enter the channel. Let  $q$  be the total number of particles in a channel of length  $L$ ,  $n$  the total number of particles in the channel and on the surface, and  $N_0$  the number of settling locations in the channel. Then the partition function for the grand canonical ensemble, taking into account the interaction of the gas particles in the channel, is

$$\begin{aligned} \Theta &= \sum \frac{(N-k)! \exp[\beta\epsilon_0(N_1-n)]}{(N_1-n)!(N-k-(N_1-n))!} \\ &\times \frac{k! \exp[\beta\epsilon_1(n-q)]}{(n-q)!(k-(n-q))!} \\ &\times \frac{N_0! \exp(\beta\epsilon_2 q)}{q!(N_0-q)!} \exp(\beta\mu N_1) Z_{\text{int}}(q), \\ N_1 + q &= n. \end{aligned} \quad (2)$$

Here  $\epsilon_2$  is the binding energy of the particles in the channel and  $Z_{\text{int}}(q)$  is the partition function, corresponding to taking account of the interaction of the gas particles in the channel. Since  $Z_{\text{int}}$  depends on the number  $q$  of particles in the channel, it is impossible to calculate the partition function (2) in the grand canonical ensemble in the general case. However, in the problem of filling of a channel, the states for which the number of particles in the channel  $q \gg 1$  should make the main contribution to the partition function (2). Then the quantity  $Z_{\text{int}}(q)$  can be replaced by the partition function of interacting particles in the channel, calculated with the average number  $\bar{q}$  of particles in the channel:

$$Z_{\text{int}}(q) \approx Z_{\text{int}}(\bar{q}). \quad (3)$$

The approximation (3) corresponds to the thermodynamic limit ( $q \gg 1$ ) for gas (system of atomic particles) molecules located in the channel. Using the relation (3), the partition function (2) can be easily calculated. Using the condition for

equilibrium between the gas and the surface, we obtain for the average number  $\bar{q}$  of particles in the channel

$$\begin{aligned} \frac{\bar{q}}{N_0} &= \frac{p}{p + \bar{p}(T, \bar{q})}, \quad \bar{p}(\bar{q}, T) = \frac{\exp[-\beta\epsilon(\bar{q}, T)]}{\alpha(T)}, \\ (\alpha(T))^{-1} &= T \left( \frac{\hbar^2}{2m\pi T} \right)^{-3/2}, \quad \epsilon = \epsilon_1 - F_{\text{int}}(\bar{q}, T), \\ F_{\text{int}}(\bar{q}, T) &\equiv -T \ln Z_{\text{int}}(\bar{q}, T). \end{aligned} \quad (4)$$

Here  $F_{\text{int}}(\bar{q}, T)$  is the free energy of interaction per atomic particle in the channel. Instead of the number  $N_0$  of settling locations in the channel, it is convenient to introduce the average distance between settling locations in the channel ( $\eta = L/N_0$ ) and to replace  $\bar{q}$  by the filling factor  $\theta \equiv \bar{q}\sigma/L$  of particles in the channel. Then, we obtain from (4) an equation determining the pressure and temperature dependences of the filling factor  $\theta$  of the channel:

$$\frac{\eta\theta}{\sigma} = \frac{p}{p + \bar{p}(T, \theta)}. \quad (5)$$

The relations (4) show that the problem of obtaining the equation for the adsorption  $\theta(p, T)$ , determining the filling factor at various pressures and temperatures of the gas above the surface, reduces to calculating the quantity  $F_{\text{int}}(\theta, T) \equiv -T \ln Z_{\text{int}}(\theta, T)$ , determining the "correction" to the pressure as a result of the interaction of the particles in the channel. Thus, to obtain the adsorption isotherms in the system under study, it is necessary to calculate the total free energy of the particles in a subnanometer channel taking into account their interaction with the channel wall and with one another. For this, we will consider  $N$  particles in a channel whose size is comparable to the average particle diameter. In the general case, the total potential energy of such a system can be written as

$$E(\mathbf{r}_1, \dots, \mathbf{r}_N) = \sum_{i,j=1}^N V(\mathbf{r}_i - \mathbf{r}_j) + \sum_{i=1}^N U(\mathbf{r}_i). \quad (6)$$

Here  $V(\mathbf{r}_i - \mathbf{r}_j)$  is the potential energy of the pair interaction of the particles located at points with coordinates  $\mathbf{r}_i$  and  $\mathbf{r}_j$ ;  $U(\mathbf{r}_i)$  is the interaction energy between a particle located at the point  $\mathbf{r}_i$  and the channel walls. We will transform the expression for the pair interaction potential of the particles using the fact that the channel diameter is comparable to the particle diameter. Then the interaction potential depends only on the particle coordinates along the channel  $r$ . We write the expression for  $V(\mathbf{r}_i - \mathbf{r}_j)$  in the form

$$\begin{aligned} V(\mathbf{r}_i - \mathbf{r}_j) &\equiv V(x_i - x_j, y_i - y_j, r_i - r_j) \\ &\approx V(r_i - r_j, 0, 0) \equiv \Phi(r_i - r_j). \end{aligned} \quad (7)$$

This relation holds when the channel diameter is comparable to the particle diameter, and the pair interaction potential  $V(\mathbf{r}_i - \mathbf{r}_j)$  of the particles is not a long-range potential.

It is convenient to represent the interaction energy between a particle and the channel walls in the form

$$U(\mathbf{r}_i) = U(\mathbf{r}'_i, r_i). \quad (8)$$

Here  $\mathbf{r}'_i$  is a dimensionless two-dimensional radius vector in a plane perpendicular to the channel. It is convenient to write the partition function of such a system in the form

$$Z_N \propto \int d\mathbf{r}'_1 \cdots d\mathbf{r}'_N dz_1 \cdots dz_N \exp(-\beta U_N) \times \exp\left[-\beta \sum_{i=1}^N U(\mathbf{r}'_i, r_i)\right]. \quad (9)$$

Here

$$U_N = \sum_{1 \leq i, j \leq N} \Phi(r_i - r_j). \quad (10)$$

The integration over the particle coordinates in a plane perpendicular to the channel can be performed exactly:

$$\begin{aligned} & \int d\mathbf{r}'_1 \cdots d\mathbf{r}'_N \exp\left[-\beta \sum_{i=1}^N U(\mathbf{r}'_i, r_i)\right] \\ &= \int d\mathbf{r}'_1 \exp[-\beta U(\mathbf{r}'_1, r_1)] \int d\mathbf{r}'_2 \exp[-\beta U(\mathbf{r}'_2, r_2)] \\ & \quad \times \cdots \times \int d\mathbf{r}'_N \exp[-\beta U(\mathbf{r}'_N, r_N)] \\ &\equiv \exp\left[-\beta \sum_{i=1}^N \Psi(r_i)\right]. \end{aligned} \quad (11)$$

Here  $\Psi(r_i)$  is the effective potential in which a particle moves in the channel as a result of the interaction of the particle with the walls:

$$\exp[-\beta \Psi(r)] \equiv \int \exp[-\beta U(\mathbf{r}', r)] d\mathbf{r}'. \quad (12)$$

Let us assume that the energy of a gas molecule interacting with the channel surface is constant and equal to  $\varepsilon_1 = \Psi(r_{\min}) = \Psi(0)$ . Then

$$Z'_N \propto \exp(-\beta N \varepsilon_2) \int dr_1 \cdots dr_N \exp(-\beta U_N). \quad (13)$$

The energy  $\varepsilon_1$  physically corresponds to the binding energy of a particle in the surface potential  $\Psi(r)$ . Thus, under the assumptions made previously, the gas in the channel can be assumed to be one-dimensional (the channel diameter is comparable to the maximum diameter of an atomic particle). It is well known [44, 45] that the partition function of a one-dimensional gas with an arbitrary interaction potential can be calculated exactly under certain assumptions, which are formulated in the following. Indeed, let us consider an equilibrium system of  $N$  particles in a channel which possesses only one degree of freedom per particle that are

located in the segment  $[0, L]$  of the  $r$  axis. The total partition function of the system has the form

$$\tilde{Z}_N = \left(\frac{mT}{2\pi\hbar^2}\right) \frac{Q_N}{N!} \exp(-\beta N \varepsilon_1), \quad (14)$$

where

$$\begin{aligned} Q_N &= \int_0^L \cdots \int_0^L \exp(-\beta U_N) dr_1 \cdots dr_N \\ U_N &= \sum_{1 \leq y \leq N-1} \Phi(r_{y+1} - r_y). \end{aligned} \quad (15)$$

Here  $\Phi(r)$  is the pair interaction potential of the particles in the channel. To calculate  $F_{\text{int}}$ , the cofactor responsible for the partition function of an ideal gas must be eliminated from the partition function (14). In our problem, the cofactor corresponding to a gas of particles in a channel without a pair interaction potential between the particles is already included in the expression (2). Thus, since the partition function of a one-dimensional gas without an interaction has the form

$$Z_{\text{int}} = \left(\frac{mT}{2\pi\hbar^2}\right)^{N/2} \frac{L^N}{N!} \exp(-\beta N \varepsilon_2), \quad (16)$$

we obtain from (2)

$$F_{\text{int}} = -T \frac{\ln \tilde{Z}_N(\theta, T)}{Z_{\text{id}}} = -T \ln \left(\frac{Q_N}{L^N}\right). \quad (17)$$

Thus, the problem has been reduced to calculating the configuration integral

$$\begin{aligned} Q_N &= \int \cdots \int \exp[-\beta \{\Phi(\xi_1) + \Phi(\xi_2) \\ & \quad + \cdots + \Phi(\xi_N)\}] d\xi_1 \cdots d\xi_N, \quad (18) \\ \xi_i &\equiv r_{i+1} - r_i. \end{aligned}$$

In studying the configuration space of a system of particles in a one-dimensional channel, it should be kept in mind that the quantities  $\xi_i$  are not independent. They are related as

$$\sum_{j=1}^N \xi_j = L, \quad (19)$$

where  $L$  is the total length of the channel. Physically, this relation corresponds to the impossibility of particles penetrating one another and the condition of "blocking" of particles with diameter  $\sigma$  in a channel whose diameter  $d < 2\sigma$ . An explicit expression for the configuration integral can be obtained if the explicit form of the pair interaction potential of the particles is known. We will consider a simple but nontrivial case: a system of hard spheres with diameter  $\sigma$ . The expression for the interatomic interaction energy in this case is

$$\Phi_i(\xi) = \begin{cases} \infty & \text{for } \xi < \sigma, \\ 0 & \text{for } \xi \geq \sigma. \end{cases} \quad (20)$$

We obtain for  $F_{\text{int}}$  in the hard-sphere approximation

$$F_{\text{int}}(\theta, T) = -T \ln(1 - \theta). \quad (21)$$

Thus, in the hard-sphere approximation, the adsorption isotherm for a gas in a subnanometer channel has the form

$$\frac{\eta\theta}{\sigma} = \frac{(1 - \theta)p}{(1 - \theta)p + \tilde{p}_0(T)}, \quad (22)$$

$$\tilde{p}_0(T) \equiv T \left( \frac{\hbar^2}{2\pi m T} \right)^{-3/2} \exp(-\beta\epsilon_1).$$

The relation (22) makes it possible to construct the dependence of the filling factor on the gas pressure for various molecules. It should be kept in mind that the sign of the energy  $\epsilon_1$  determines the possibility or impossibility of a particle entering a channel: for  $\epsilon_1 > 0$ , it is energetically favorable for a gas particle to enter the channel for any external pressure greater than  $p_0$ . For  $\epsilon_1 < 0$ , the particles must overcome a potential barrier to enter the channel. The configuration integral can be calculated exactly for an arbitrary interaction between the particles in the channels [45]. This makes it possible to obtain an equation of state of a 1D gas for an arbitrary interaction. Thus, for an interparticle interaction potential of the form

$$\Phi(z) = \begin{cases} +\infty & \text{for } r \leq \sigma, \\ -\epsilon & \text{for } \sigma < r \leq \sigma + R, \\ 0 & \text{for } r < R + \sigma, \end{cases} \quad (23)$$

where  $r$  is the effective radius of attraction, the equation of state of a one-dimensional gas is

$$p_{1D}\sigma \left( \frac{1}{\theta} - 1 \right) = T - p_{1D}R \left[ \frac{\exp(\beta p_{1D}R)}{1 - \exp(-\beta\epsilon)} - 1 \right]^{-1}. \quad (24)$$

In the limits  $\epsilon \rightarrow 0$  and  $R \rightarrow 0$ , this equation becomes the equation of state of a system of hard spheres. The isotherms calculated numerically starting from (24) are presented in Figure 1. It is also evident in this figure that at high temperatures the gas behaves almost as an ideal gas ( $p_{1D} \propto \theta$ ). At low temperatures the isotherms seem to consist of two parts. For high density  $\theta \approx \text{const}$ , which is typical for a condensed phase, whereas at pressure less than a characteristic value a gas-like phase for which  $p_{1D} \propto \theta$  appears.

It can be shown that at a transition from one regime to another, the free energy of the system has no singularities. For this reason, there is no exact analogy with phase transitions. This assertion agrees completely with the Landau-van Hove Theorem [44], according to which any one-dimensional model of a gas with a finite interaction radius does not undergo phase transitions. On the other hand, it should be expected that for sufficiently low temperatures, as the filling factor  $\theta$  increases, the gas in the channel tends to form clusters whose size increases with the filling factor. The number and size of the clusters grow with the total number of particles in the system in a manner so as to ensure the existence

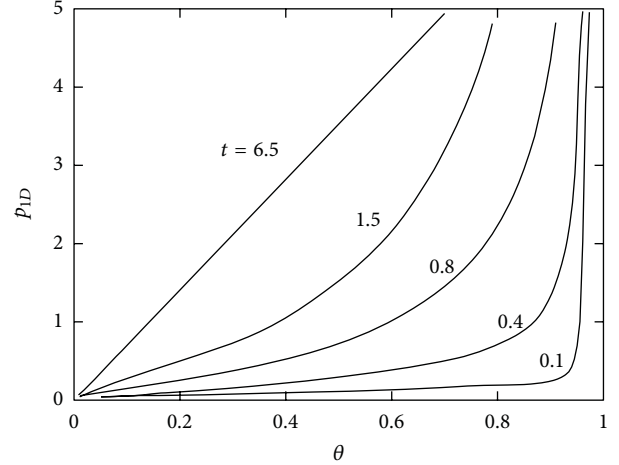


FIGURE 1: Reduced “pressure” ( $p_{1D}$ ) (24) of a one-dimensional gas in a channel versus the filling factor ( $\theta$ ) of the channel at various temperatures  $t = T/T_0$ .

of such clusters in the thermodynamic limit, where  $N \rightarrow \infty$ ,  $L \rightarrow \infty$ , and  $N/L = \text{const}$ . This agrees completely with the formation of nuclei of a new phase in three-dimensional systems with first-order phase transitions [34, 46]. On the other hand, in our one-dimensional system, in contrast to three-dimensional systems, a continuous behavior of thermodynamic quantities determined as derivatives of the free energy of the system with respect to the temperature, pressure, and filling factor should be expected in the entire range of variation of the thermodynamic parameters. For example, the specific heat calculated using the relation (24) will possess a maximum at the “critical” point. This fact has been observed experimentally [35], which attests to the applicability of the one-dimensional model employed previously.

**2.1.2. Transport in a Dense 1D System.** The gas flux through a membrane is the main experimentally measurable parameter (Section 2.1.3). Particle transport is usually described using a relation between the outgoing particle flux and the parameters of the problem, such as, for example, the difference of the gas pressures on different sides of the membrane. This description is based on Fick’s relation between the gas flux density  $\mathbf{J}$ , the gradient of the gas concentration, and the diffusion coefficient  $\tilde{D}$ , using the conservation law for the number of particles:

$$\mathbf{J} = -\tilde{D}\nabla n, \quad (25)$$

$$\frac{\partial n}{\partial t} + \text{div } \mathbf{J} = 0. \quad (26)$$

In the relations (25) and (26),  $\mathbf{J}$  is the flux,  $\tilde{D}$  is the diffusion coefficient, and  $\nabla n$  is the gradient of the particle concentration. The relation (25) is actually a definition of the diffusion coefficient  $\tilde{D}$ . Thus, the problem of determining the particle flux through a channel reduces to calculating the diffusion coefficient. A more general method of describing

transport is to calculate the characteristic relaxation time of density fluctuations arising or specially created in the system under study [47]. Formally, the problem of determining this time reduces to calculating the characteristic frequency or spectrum  $\omega(\mathbf{k})$  for the system under study. Thus, when the particle density is low and there is no interparticle interaction, an explicit expression for the spectrum  $\omega(\mathbf{k})$  can be easily obtained from the relation (25). Indeed, let  $n_0$  be the average particle concentration in the system. From (25), we obtain an equation determining the dynamics of the density fluctuations  $\delta n(\mathbf{r}, t) = n - n_0$ :

$$\frac{\partial (\delta n)}{\partial t} = \bar{D} \Delta (\delta n). \quad (27)$$

Switching to a Fourier representation of the density fluctuations

$$\delta n(\mathbf{r}, t) = \frac{1}{(2\pi)^4} \int d\mathbf{k} d\omega \exp(-i\mathbf{k} \cdot \mathbf{r} - i\omega t) \delta n(\mathbf{k}, \omega), \quad (28)$$

we obtain an expression determining the reciprocal of the relaxation time of the density fluctuations  $\delta n$  in the case at hand:

$$\omega_0(\mathbf{k}) = -i \bar{D} k^2. \quad (29)$$

It is obvious that a spectrum of this type is characteristic for systems where relaxation to equilibrium occurs by diffusion. Let us consider a system of interacting particles with arbitrary density. Assume that we have been able to calculate the characteristic relaxation time  $\omega^{-1}$  of density fluctuations in the system. If the spectrum of relaxation times in such a system has the form

$$\omega(\mathbf{k}) = -iD(\mathbf{k}, n_0) k^2, \quad (30)$$

then it is natural to consider the quantity  $D(\mathbf{k}, n_0)$  to be the diffusion coefficient in the system, provided that in the limit of low densities  $n_0$  the quantity  $D(\mathbf{k}, n_0)$  becomes the diffusion coefficient for a low-density system of particles:

$$\lim_{n_0 \rightarrow 0} D(\mathbf{k}, n_0) = \bar{D}. \quad (31)$$

This definition of the diffusion coefficient means that the system possesses a diffusion characteristic mode. Proceeding from the definition (30), to calculate the diffusion coefficient  $D(\mathbf{k}, n_0)$ , it is necessary to know the characteristic modes of a weakly nonequilibrium system. If these characteristic modes have the form (30), then  $D(\mathbf{k}, n_0)$  will be the diffusion coefficient of the system. It is obvious that the diffusion coefficient in the general case is nonlocal and is a functional of the density of the diffusing particles. The expression for the flux of diffusing particles will have a form generalizing equation (25):

$$\mathbf{J} = - \int d\mathbf{r}' D(\mathbf{r}, \mathbf{r}', n(\mathbf{r}', t)) \nabla n(\mathbf{r}', t). \quad (32)$$

The equation, obtained using this relation, for the particle number density in the system is in general a nonlinear

integrodifferential equation. When studying the diffusion of a single-component gas in subnanometer channels, it should be kept in mind that the pair interaction potential between the particles is of short range, and no phase transitions occur in the system of particles in the channel (see the preceding section). In this case, it can be assumed that the diffusion coefficient  $D(\mathbf{r}, \mathbf{r}', n(\mathbf{r}, t))$  is local:

$$D(\mathbf{r}, \mathbf{r}', n(\mathbf{r}, t)) = D(n(\mathbf{r}, t)) \delta(\mathbf{r} - \mathbf{r}'). \quad (33)$$

The corresponding expression for the flux of diffusing particles and the equation for their density become

$$\begin{aligned} \mathbf{J} &= -D(n) \nabla n, \\ \frac{\partial n}{\partial t} &= \nabla (D(n) \nabla n). \end{aligned} \quad (34)$$

For low densities, the relation (34) becomes (25), which is the first term in the expansion of the flux in odd powers of the density gradient. Thus, for systems where the relaxation spectrum of the fluctuations is of the form (30), the diffusion coefficient can be determined starting from the explicit form of this spectrum. The expression obtained for the diffusion coefficient in this case is a generalization of the expressions obtained for the diffusion coefficient in various models, specifically, in the Maxwell-Stefan model [43].

It is convenient to calculate the relaxation spectrum using the response functions [31, 48, 49]. Let us formulate the basis of this formalism. Consider the system of the atomic particles, which can interact with each other as well as the environment such as liquid, solid, or surface. Let us show, following [49], that many-particles distribution functions of such a system are the density functionals. Assume that each particle at the coordinate  $\mathbf{r}$  interacts with time-dependent external field  $v(\mathbf{r}, t)$ . In order to describe such a system, one can use Liouville equation for many-particle distribution function  $F(x_1, x_2, \dots, x_N, t)$ , where  $x_i = (\mathbf{r}_i, \mathbf{p}_i)$  are the coordinates and th momentum of the particles. Solving the Liouville equation with the fixed initial distribution function and for the different external potentials  $V(\mathbf{r}_1, \mathbf{r}_2, \dots, t) = \sum_i v(\mathbf{r}_i, t)$ , one can obtain one-to-one conformance between  $F(x_1, x_2, \dots, x_N, t)$  and  $V(\mathbf{r}_1, \mathbf{r}_2, \dots, t)$ . On the other hand, introducing the density of the particles

$$n(\mathbf{r}, t) = \int d\Gamma \hat{n} F(x_1, x_2, \dots, x_N, t), \quad (35)$$

where  $d\Gamma$  is the phase space element, and  $\hat{n}$  is the density operator, one can obtain one-to-one conformance between the external field  $V(\mathbf{r}_1, \mathbf{r}_2, \dots, t)$  and the density  $n(\mathbf{r}, t)$ . From this it directly follows that many-particles distribution functions are density functionals:

$$F(x_1, x_2, \dots, x_N, t) = F(x_1, x_2, \dots, x_N, t, [n]). \quad (36)$$

Following [49], let us write the action for the Liouville equation in the form

$$S = \frac{1}{t_2 - t_1} \int_{t_1}^{t_2} dt \int d\Gamma L F, \quad (37)$$

where  $L$  is the Lagrangian of the system, which is equal to the difference between the kinetic and potential energy of the particles. It follows from (36) and (37) that the action  $S$  is the density functional:

$$S = \Delta[n] = \frac{1}{t_2 - t_1} \int_{t_1}^{t_2} dt \int d\Gamma LF(x_1, x_2, \dots, x_N, t, [n]). \quad (38)$$

Functional  $\Delta[n]$  has an extrema for the equilibrium state of the system [48, 49]. Due to the linearity of the (38) by the potential energy, system of the particles interacting with the external field  $v(\mathbf{r}, t)$  corresponds to the functional  $\Delta[n, v]$ , which can be expressed as

$$\Delta[n, v] = \Delta[n] + \frac{1}{t_2 - t_1} \int_{t_1}^{t_2} v(\mathbf{r}, t) n(\mathbf{r}, t) d\mathbf{r} dt. \quad (39)$$

Functional (39) has an extrema for the stationary or quasi-stationary  $n(\mathbf{r}, t) = n_0(\mathbf{r}, t) \equiv n^{(0)}$  state of the system [48, 49]

$$\left. \frac{\delta \Delta[n]}{\delta n} \right|_{n=n^{(0)}} = 0 \quad (40)$$

and represents the time average of the free energy functional  $F[n(\mathbf{r}, t), t]$ :

$$\Delta[n] = \tau^{-1} \int_0^\tau F[n(\mathbf{r}, t), t] dt. \quad (41)$$

The functional  $\Delta[n]$  was for the first time introduced in such a form in the papers [31, 48]. Equation (40) determines the density of the atomic particles  $n(\mathbf{r}, t)$ . Let us express the free energy using the response functions defined as follows. Consider the system in the external field  $ev_{\text{ext}}(\mathbf{r}, t)$  ( $e$  - external field amplitude). The response function  $\beta(\mathbf{r}, \mathbf{r}', t, t')$  of such a system couples the density fluctuation  $\delta n(\mathbf{r}, t)$  with the external field  $ev_{\text{ext}}(\mathbf{r}, t)$ , which generate this fluctuation [31, 48] at  $e \rightarrow 0$ :

$$\delta n(\mathbf{r}, t) = \int d\mathbf{r}' dt' \beta(\mathbf{r}, \mathbf{r}', t, t') ev_{\text{ext}}(\mathbf{r}', t') \Big|_{e \rightarrow 0}. \quad (42)$$

It is obvious that in the case of the linear response and  $e \rightarrow 0$ , the response function  $\beta(\mathbf{r}, \mathbf{r}', t, t')$  is independent on  $e$ . Let us rewrite the definition (42) in the operator form

$$\delta n = ev_{\text{ext}} \beta. \quad (43)$$

Such a form (43) will be used further in the paper. In the presence of the external field, the functional  $\Delta[n, v]$  at  $e \rightarrow 0$  is determined by the relation (39):

$$\Delta[n, ev_{\text{ext}}] = \Delta[n] + \frac{1}{t_2 - t_1} \int_{t_1}^{t_2} ev_{\text{ext}}(\mathbf{r}, t) n(\mathbf{r}, t) d\mathbf{r} dt. \quad (44)$$

Here  $\Delta[n]$  is the functional at  $e = 0$ , determined by the formula (38). In order to obtain linear response function, let us use the relation (39). One can rewrite the solution of the (39) at  $e \rightarrow 0$  with the sum  $n(\mathbf{r}, t) = n^{(0)}(\mathbf{r}, t) + \delta n(\mathbf{r}, t)$ . In

this case, one can obtain, in the first order and with respect to (39),

$$\left. \frac{\delta \Delta[n]}{\delta n} \right|_{n=n^{(0)}} + \left. \frac{\delta^2 \Delta[n]}{\delta n^2} \right|_{n=n^{(0)}} \delta n + ev_{\text{ext}} = 0 \quad (45)$$

or

$$-\left( \left. \frac{\delta^2 \Delta[n]}{\delta n^2} \right|_{n=n^{(0)}} \right)^{-1} ev_{\text{ext}} = \delta n. \quad (46)$$

At  $e \rightarrow 0$ , the quantity

$$\left. \frac{\delta^2 \Delta[n]}{\delta n^2} \right|_{n=n^{(0)}} \equiv \frac{\delta^2 \Delta}{\delta n(\mathbf{r}, t) \delta n(\mathbf{r}', t')} \quad (47)$$

is independent on  $e$ . Comparison of the relations (43) and (46) gives the following form of the response function  $\beta(\mathbf{r}, \mathbf{r}', t, t')$ :

$$\begin{aligned} \beta(\mathbf{r}, \mathbf{r}', t, t') &= -\left( \left. \frac{\delta^2 \Delta[n]}{\delta n^2} \right|_{n=n^{(0)}} \right)^{-1} \\ &= -\left( \frac{\delta^2 \Delta}{\delta n(\mathbf{r}, t) \delta n(\mathbf{r}', t')} \right)^{-1}. \end{aligned} \quad (48)$$

It follows from the functional  $\Delta[n]$  definition that it can be expressed as

$$\Delta[n] = \Delta_0[n] + \Delta_{\text{int}}[n]. \quad (49)$$

Here  $\Delta_0[n]$  corresponds to the functional of the particles without their interaction with each other, and  $\Delta_{\text{int}}[n]$  corresponds to the functional (38), which represents particle-particle interactions. Two times variation of the (49), with respect to (48), gives the following:

$$-\beta^{-1} = -\beta_0^{-1} + R, \quad (50)$$

where

$$\beta_0^{-1}(\mathbf{r}, \mathbf{r}', t, t') = -\left. \frac{\delta^2 \Delta_0[n]}{\delta n^2} \right|_{n=n^{(0)}} = -\frac{\delta^2 \Delta_0}{\delta n(\mathbf{r}, t) \delta n(\mathbf{r}', t')} \quad (51)$$

is the response function of the noninteracting particles

$$R(\mathbf{r}, \mathbf{r}', t, t') = -\left. \frac{\delta^2 \Delta_{\text{int}}[n]}{\delta n^2} \right|_{n=n^{(0)}} = -\frac{\delta^2 \Delta_{\text{int}}}{\delta n(\mathbf{r}, t) \delta n(\mathbf{r}', t')}. \quad (52)$$

It is shown in the paper [31, 48] that the function  $R(\mathbf{r}, \mathbf{r}', t, t')$  is connected to the effective lagged interaction between the particles. Multiplying the relation (45) on the  $\beta$  in the left and on the  $\beta_0$  in the right, one can obtain the equation on the response function. In the case of the homogeneous quasi-stationary state of the atomic system, the functions  $\beta_0(\mathbf{r}, \mathbf{r}', t, t')$ ,  $\beta(\mathbf{r}, \mathbf{r}', t, t')$  и  $R(\mathbf{r}, \mathbf{r}', t, t')$  depend only on the differences  $\mathbf{r} - \mathbf{r}'$  и  $t - t'$ , so (50) can be rewritten as

$$\beta(\mathbf{k}, \omega) = \beta_0(\mathbf{k}, \omega) + \beta_0(\mathbf{k}, \omega) R(\mathbf{k}, \omega) \beta(\mathbf{k}, \omega), \quad (53)$$

where  $\beta(\mathbf{k}, \omega)$ ,  $\beta_0(\mathbf{k}, \omega)$  и  $R(\mathbf{k}, \omega)$  are the Fourier transform of the response functions  $\beta(\mathbf{r} - \mathbf{r}', t - t')$ ,  $\beta_0(\mathbf{r} - \mathbf{r}', t - t')$ , and  $R(\mathbf{r} - \mathbf{r}', t - t')$ , respectively; for example,

$$\beta_0(\mathbf{r} - \mathbf{r}', t - t') = \int d\mathbf{k} d\omega e^{-i\omega(t-t') + i\mathbf{k}(\mathbf{r}-\mathbf{r}')} \beta_0(\mathbf{k}, \omega). \quad (54)$$

Equation (53) allows us (when the  $R$  function is known) to determine the response function of the system of interacting particles and relaxation spectrum of the system [31, 48].

In order to determine the relaxation spectrum, let us note, that the expression  $\beta^{-1}\delta n = ev_{\text{ext}}$  follows directly from (43). Due to the response function definition (as the response of the system on the arbitrary small external field), one can write  $\beta^{-1}\delta n = 0$ . This equation has the nontrivial solutions  $\delta n \neq 0$  only if  $\beta^{-1} = 0$ . So, we can write that the relaxation spectrum of the system  $\omega(\mathbf{k})$  is determined by the relation [31, 48]

$$\beta^{-1}(\mathbf{k}, \omega) = 0. \quad (55)$$

We will use the response function formalism to calculate the response function and the diffusion coefficient of a dense system of atomic particles in a subnanometer channel. We will calculate first the response function  $\beta_0(k, \omega)$  and the relaxation spectrum of such a gas when there is no interaction between the particles. We write the diffusion equation for the filling factor  $\theta$  of the channel with molecules in the presence of a weak perturbing external field  $ev_{\text{ext}}(x, t)$  in the form

$$\frac{\partial \theta}{\partial t} = D_0 \nabla \left( \nabla \theta + \frac{\theta}{T} \nabla ev_{\text{ext}} \right), \quad \nabla \equiv \frac{\partial}{\partial x}. \quad (56)$$

Here  $D_0$  is the diffusion coefficient for noninteracting particles. Let  $\theta_0$  be the equilibrium filling factor of the channel. We will seek the solution of (56) in the form

$$\theta = \theta_0 + \delta\theta(x, t). \quad (57)$$

Then, we obtain from (56), assuming the external field  $e_{\text{ext}}$  to be weak, an equation for  $\delta\theta(r, t)$ :

$$\frac{\partial \delta\theta}{\partial t} = D_0 \Delta \delta\theta + \frac{D_0 \theta_0 \Delta ev_{\text{ext}}}{T}. \quad (58)$$

In deriving (58), only first-order infinitesimals in  $\delta\theta$  and  $ev_{\text{ext}}$  were retained in all terms. We will seek the solution of (58) in the form of a Fourier integral

$$\begin{aligned} \delta\theta(x, t) &= \frac{1}{(2\pi)^2} \int e^{ikx} e^{i\omega t} \delta\theta(k, \omega) dk d\omega, \\ ev_{\text{ext}}(x, t) &= \frac{1}{(2\pi)^2} \int e^{ikx} e^{i\omega t} ev_{\text{ext}}(k, \omega) dk d\omega. \end{aligned} \quad (59)$$

Substituting the expressions (59) into (58) and solving the resulting linear equation for  $\delta\theta(k, \omega)$ , we obtain

$$\delta\theta(k, \omega) = \beta_0(k, \omega) ev_{\text{ext}}(k, \omega). \quad (60)$$

Here

$$\beta_0(k, \omega) = -\frac{\theta_0 k^2 D}{T(i\omega + k^2 D_0)} \quad (61)$$

is the response function of a gas of noninteracting diffusing particles. Indeed, as  $\omega \rightarrow 0$ , the function  $\beta_0(k, \omega)$  reduces to the well-known response function of an ideal equilibrium gas with density  $\theta_0$  at temperature  $T$  [38, 47]:

$$\beta_0(k, 0) = -\frac{\theta_0}{T}. \quad (62)$$

The relaxation spectrum of such a gas is determined from the relation (55) and has the form

$$\omega_0(k) = -iD_0 k^2. \quad (63)$$

In accordance with the definition (26), the quantity  $D_0$  is the diffusion coefficient. The relations obtained make it possible to calculate the relaxation spectrum  $\omega(k)$  by solving (54). Thus, we find for the response function of a one-dimensional system

$$\beta(k, \omega) = \frac{\beta_0(k, \omega)}{1 - \beta_0(k, \omega) R(k, \omega)}. \quad (64)$$

Using the relations (61) and (64), we obtain an equation determining the relaxation spectrum of the system under study:

$$1 + \frac{\theta_0}{T} \frac{\omega_0}{\omega + \omega_0} R(k, \omega) = 0. \quad (65)$$

Equation (65) can be solved in a general form in the quasistatic case  $\omega \rightarrow 0$ . Indeed, in this case, we find from (65)

$$\omega(k) = -iD(\theta_0, k) k^2, \quad (66)$$

$$D(\theta_0, k) = D_0 \left[ 1 + \frac{\theta_0}{T} R(k, 0) \right]. \quad (67)$$

It is convenient to rewrite the relation (67), introducing the pair distribution function  $n_2(x - x') = \theta_0^2 [1 + \nu(x - x')]$ :

$$T\beta(k, 0) = -\theta_0 (1 + \theta_0 \nu(k)). \quad (68)$$

Then we obtain from relations (53) and (61)

$$R(k, 0) = -\frac{T\nu(k)}{1 + \theta_0 \nu(k)}. \quad (69)$$

Substituting the expression (69) into (67) gives a relation determining the relaxation spectrum of a dense gas in a one-dimensional channel:

$$\omega(k) = -\frac{iD_0 k^2}{1 + \theta_0 \nu(k)}. \quad (70)$$

We will now calculate the diffusion coefficient of a gas in a one-dimensional channel taking into account the interaction between hard-sphere particles. In this case, the correlation function  $n_2(x) = \theta_0^2 [1 + \nu(x)]$  has been calculated exactly [45] with an arbitrary filling factor of the channel:

$$\begin{aligned} n_2(x) &= \begin{cases} 0, & r < \sigma, \\ \frac{1}{\theta_0} \sum_m \frac{(x\sigma^{-1} - m)^{m-1}}{(m-1)!(\theta_0^{-1} - 1)^m} \exp\left(-\frac{x\sigma^{-1} - m}{\theta_0^{-1} - 1}\right), & x > \sigma. \end{cases} \end{aligned} \quad (71)$$

Using the relations (70) and (71), we find

$$\begin{aligned}\omega(k) &= -iD(\theta_0)k^2, \\ D(\theta_0) &= D_0 \left( \frac{1}{(1-\theta_0)^2} \right).\end{aligned}\quad (72)$$

It follows from (72) that the general equation describing particle transport in a dense 1D system, in accordance with (34), has the form

$$\frac{\partial \theta}{\partial t} = \frac{\partial}{\partial x} \left[ D_0 \left( \frac{1}{(1-\theta)^2} \right) \frac{\partial \theta}{\partial x} \right]. \quad (73)$$

This equation can be obtained from (72) if the characteristic local equilibration times in a dense system of particles in a channel are short compared with the characteristic propagation times of disturbances along such a system. For the cases considered in the following, this assumption obviously holds. We will consider solutions of (73) in the case where complete equilibrium has been established in the channel and the filling factor  $\theta = \theta_0(p, T)$ , with the function  $\theta_0(p, T)$  being determined by the relation (23). Transport in a channel in this case will be determined by the dynamics of the motion of disturbances of the filling factor. The solution of (73) in this case should be sought in the form  $\theta = \theta_0(p, T) + \delta\theta(x, t)$ . It follows from (73) that the relaxation spectrum of disturbances in this case has the form (72), where  $\theta = \theta_0(p, T)$ . Thus, taking account of the interaction of hard-sphere particles in a channel does not change the character of the relaxation of its weakly nonequilibrium state: the relaxation spectrum (72) remains a diffusion spectrum with diffusion coefficient  $D(\theta_0)$ . However, it is important to underscore that transport in the channel in this case is a collective effect and proceeds via transport of disturbances of the equilibrium density  $\theta_0(p, T)$ . The diffusion coefficient  $D(\theta_0)$  in this case is the diffusion coefficient of disturbances of the equilibrium density. It is convenient to rewrite the relation (72) for the diffusion coefficient in a different form. Using the Arrhenius character of the diffusion coefficient for noninteracting particles

$$D_0 = \tilde{D}_0 \exp\left(-\frac{E}{T}\right) \quad (74)$$

( $\tilde{D}_0$  is proportional to the product of the squared lattice constant of the wall material of the channel and the relaxation frequency of particles in a channel on defects and lattice phonons and is calculated in [37], and  $E \approx \Psi(r_{\max})$  (13) is the activation energy of diffusing of noninteracting particles in the channel), we will rewrite (72) in the form

$$\begin{aligned}D(\theta_0) &= \tilde{D}_0 \exp\left(-\frac{\tilde{E}(\theta_0)}{T}\right), \\ \tilde{E}(\theta_0) &\equiv E - T \ln\left(\frac{1}{(1-\theta_0)^2}\right).\end{aligned}\quad (75)$$

This way of writing the diffusion coefficient for a gas of interacting particles in a channel makes it possible to give

a physical interpretation for the change in the diffusion coefficient accompanying a change in the filling factor  $\theta_0$ . The relation (75) shows that the interaction of particles in a channel decreases the activation energy  $E$  of the motion of particles, even in the hard-sphere model. For an interaction between hard-sphere particles such that there is no direct attraction between the particles, the diffusion activation energy decreases with increasing filling factor  $\theta_0$  as a result of the effective interaction (see the following). Physically, this corresponds to a change because of the presence of another particle in a neighboring potential well, in the parameters of the potential in which a gas particle moves. Since the gas particles are assumed to be indistinguishable, diffusion with the filling factor  $\theta_0 \sim 1$  (when the effective diffusion activation energy  $\tilde{E}(\theta_0)$  becomes comparable to the temperature of the system) can be interpreted as a transfer of “excitation” of the density along a chain of close gas particles. It is obvious that the motion of such an “excitation” will occur with substantial velocities. This leads to a large increase in the diffusion coefficient when  $\theta_0 \sim 1$ . For  $E = 0$ , the possibility of such a diffusion mechanism is played out in [36]. We note that for all gases investigated, the barrier  $E$  is different from 0. This is indicated by the presence of a maximum in the temperature dependence of the flux in a zeolite membrane [43]. It can be assumed that the increase in the diffusion coefficient in a channel observed with filling factors  $\theta_0 \geq 0.5$  is related to the formation of clusters in the channel whose sizes increase with the filling factor. The transport of gas in the channel containing such clusters is determined by the motion of “excitation” in a finite-size cluster. The formation of clusters in a gas consisting of particles with a hard-sphere pair interaction potential is related to the well-known [46] appearance of an effective attraction between such particles. This effect is manifested in the appearance of a maximum in the correlation function  $n_2(x)$ , describing the probability of finding the “first” particle at a distance  $x$  from the “second” particle.

The relaxation spectra of the system for an arbitrary wave vector  $k$  can be found from (70) and (71). It is found that the spectrum  $\omega(k)$  contains a real part, which corresponds to transport of an “excitation” in the system. The imaginary part of the spectrum obtained has a minimum at a definite value of the wave vector  $k = k_{\min}$ , which depends on the filling factor  $\theta_0$ . It is natural to interpret the value  $R = 2\pi/k_{\min}(\theta_0)$  as the characteristic size of a cluster with a given filling factor and the value  $\tau = \text{Im} \omega^{-1}(k_{\min}(\theta_0))$  as its characteristic lifetime. As the filling factor increases, the value of the effective attraction between the particles increases [46]; this could lead to the appearance of clusters consisting of two or more particles. However, it is found that as a result of the one-dimensionality of the channel, the lifetime of the clusters that are formed is finite, which corresponds to the absence, as noted previously, of a phase transition in such systems. The dependences of the lifetime and size of the clusters formed on the filling factor  $\theta_0$  are presented in Figure 2.

It is evident in the figure that increasing the filling factor increases the lifetime and the size of the clusters formed. In finite-size channels, for a definite value of the filling factor

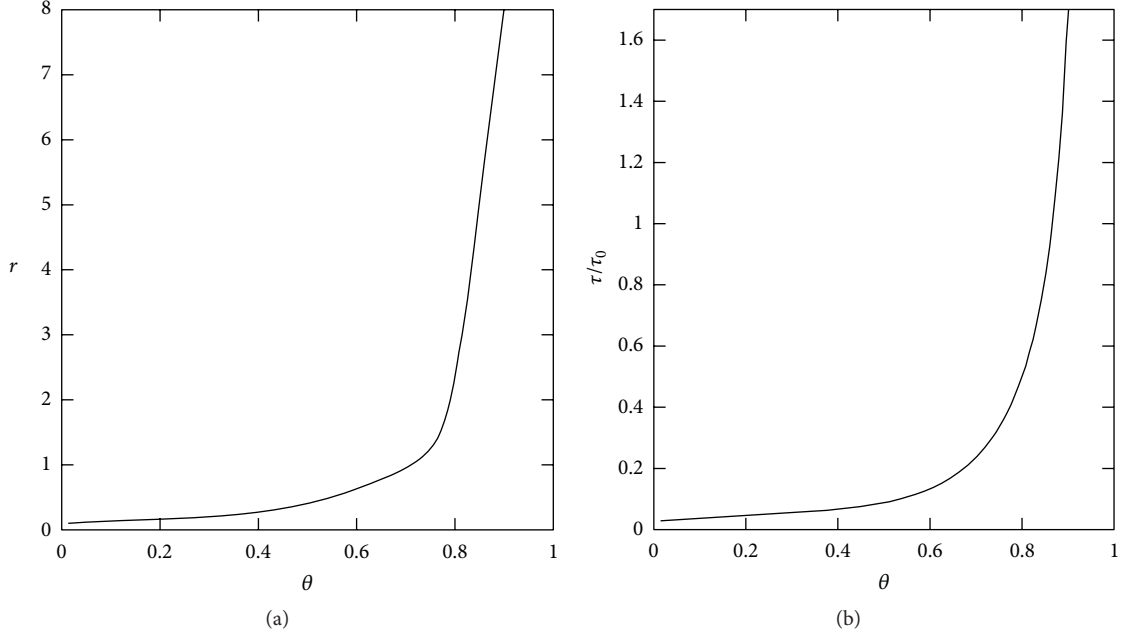


FIGURE 2: Size ( $r = R/\sigma$ ) (a) and lifetime ( $\tau/\tau_0, \tau_0 = \sigma^2/D_0$ ) (b) of clusters versus the filling factor.

$\theta_0 = \theta_c$ , a cluster equal in size to the length of the channel is formed. It is obvious that the diffusion coefficient in such a channel increases without bound as  $\theta_0 \rightarrow \theta_c$ , even though the lifetime of such a cluster is finite. If the range of relaxation frequencies  $\omega(k)$  is known, then an expression that defines the relaxation of the Fourier components of the particle density in the channel  $n(k, t)$  in the case of arbitrary density  $n(k, t)$  is given by

$$\dot{n}(k, t) = i\omega(k) n(k, t). \quad (76)$$

From (76), we can get that the equation for the amplitude of the fluctuations can be written as

$$\delta \dot{n}(k, t) = i\omega(k) \delta n(k, t). \quad (77)$$

Equation (77) describes the relaxation of  $k$  component of the density fluctuation at arbitrary wave vector. In particular, at  $k \neq 0$ , this equation allows to describe the relaxation of density fluctuations and propagation of disturbances on the cluster of finite size in the case of the formation of the cluster. At  $k \rightarrow 0$ , the equation describes the relaxation of density fluctuations on large spatial scales. This value is related to the macroscopic flux. Let us write the equation of continuity to calculate the flux  $j$ :

$$\dot{n} + \frac{\partial j}{\partial x} = 0. \quad (78)$$

After applying the Fourier transform, (78) takes the form

$$ikj(k, t) = -\dot{n}(k, t). \quad (79)$$

Using (76) and (79), one can get for  $j(k)$

$$j(k, t) = \frac{n(k, t) \omega(k)}{k}. \quad (80)$$

Using the relation (70) we find that  $\nu(k)$  and therefore the spectrum contains both real and imaginary parts, corresponding to the “hydrodynamic” (real part of  $\omega(k)$ ) and diffusive (imaginary part of  $\omega(k)$ ) transport of particles. Therefore, (80) for the flux  $j(k, t)$  contains terms relating to hydrodynamic transport of particles in a cluster and diffusive transport of particles in the space between clusters. We note that the response function method can be used to take into account the interaction of particles in a channel for a potential that is different from a hard-spheres interaction, similarly to the way this was done previously.

Analysis of the experimental data showed that for high filling factors  $\theta_0 \sim 1$ , the dependence of the diffusion coefficient  $D(\theta_0)$ , calculated from the relation (72), leads to a discrepancy between theory and experiment (Section 2.1.3). This discrepancy could be due, in our opinion, to the above-described influence of a finite channel length, the asphericity of the gas molecules, and the possible breakdown of one dimensionality of the problem. These effects lead to the following dependence of the diffusion coefficient on the filling factor:

$$D(\theta_0) = D_0 \left( \frac{1}{(1 - \zeta\theta_0)^2} \right). \quad (81)$$

Here  $\zeta$  is a coefficient that takes into account the finite size of the channel, the possible deviation of the channel from one-dimensionality, and the asphericity of the molecules. The relations (72), (81), and (52) make it possible to describe transport in a subnanometer channel for different values of parameters such as the gas pressure and the pressure difference outside the membrane, the temperature of the membrane, and the type of gas molecules. As an example, we present the dependence, calculated according

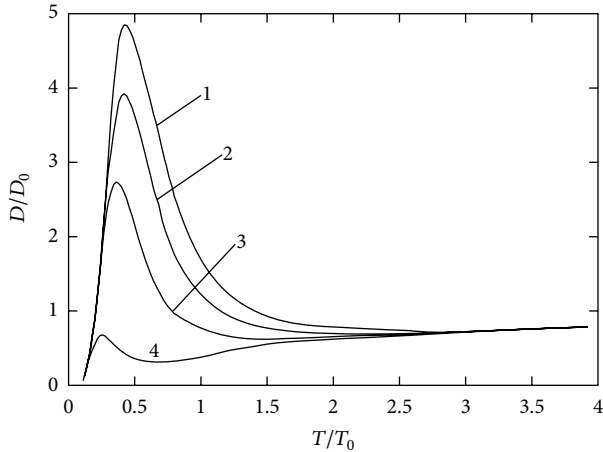


FIGURE 3: Theoretical curves of the relative diffusion coefficient  $D/D_0$  versus the relative temperature  $T/T_0$  for various values of the relative pressure  $p/p_0$ : (1)  $p/p_0 = 3$ , (2)  $p/p_0 = 2$ , (3)  $p/p_0 = 1$ , and (4)  $p/p_0 = 0.1$ .

to (72), (81), and (23), of the diffusion coefficient in a subnanometer channel on the relative temperature  $T/T_0$  for various relative pressures  $p/p_0$  (Figure 3).

It is evident in the figure that the character of the temperature dependence of the relative diffusion coefficient in subnanometer channels is substantially different at different pressures  $p$ . For example, if the pressure is high ( $p/p_0 > 1$ ), the dependence of  $D/D_0$  on  $T/T_0$  has a pronounced maximum at temperatures  $T \sim 0.5T_0$  (curve 1). As pressure decreases, the magnitude of this maximum decreases and the maximum itself shifts into the region of lower temperatures (curves 2, 3). A further decrease of pressure to values  $p/p_0 < 1$  results in the appearance of a minimum in the dependence of  $D/D_0$  on  $T/T_0$  in the temperature range  $T \sim 0.5T_0$ . The maximum occurs at  $T \sim 0.3T_0$ . Since for  $p/p_0 < 1$ , the flux depends on  $p$  and the average distance between particles in the channel is much greater than the diameter of the particles, the increase in the diffusion coefficient for  $T \sim 0.5T_0$  is due to the temperature dependence of the diffusion coefficient  $D_0$  on individual molecules in the channel. At high temperatures, all curves saturate at a value corresponding to  $D/D_0 = 1$ . In the next section, the theoretical laws obtained previously will be compared with the experimental data.

**2.1.3. Analysis of the Experimental Data: Comparison of Theory with Experiment.** Quite extensive experimental investigations of the sorption and transport properties of a series of organic molecules ( $\text{CH}_4$ ,  $\text{C}_2\text{H}_6$ ,  $n\text{-C}_4\text{H}_{10}$ ,  $i\text{-C}_4\text{H}_{10}$ , and others) and the inert gases Ar, Ne, and Kr in ZSM-5 zeolite membranes (MFI, silicate-1) have now been performed. The results are presented in [42, 50, 51]. According to [52], ZSM-5 zeolite membranes have a complicated chemical and crystalline structure. The chemical structure of zeolite membranes is given by the formula



For small values of  $n$ , zeolite membranes of this type are called silicate-1 membranes. The crystalline structure of ZSM-5 membranes has been studied quite well. It consists of a 3D structure, consisting of sinusoidal channels with a circular cross section ( $0.54 \pm 0.02 \text{ nm}$ ) parallel to the  $a$  axis [53], which intersect straight channels with an elliptical cross section ( $0.57\text{-}0.58 \times 0.51\text{-}0.52 \text{ nm}^2$ ) parallel to the  $b$  axis [010] [50, 54]. Cavities  $\sim 0.9 \text{ nm}$  in size form at the intersection of the channels. The sorption capacity of ZSM-5 zeolite is determined by the number of sorbed (entering the channels) molecules per cell of a crystal. According to [50, 55], the cell parameters are  $a = 2.007 \text{ nm}$ ,  $b = 1.992 \text{ nm}$ , and  $c = 1.342 \text{ nm}$ . A single cell is a structure consisting of four segments of  $0.46 \text{ nm}$  linear channels, four segments of  $0.66 \text{ nm}$  sinusoidal channels, and four  $0.54 \text{ nm}$  intersections. Depending on the structure of a molecule, sorption of one or two molecules per intersection is possible. In [50], the sorption capacity of ZSM-5 was measured for a number of molecules. It was concluded that the molecules  $\text{CH}_4$ ,  $\text{C}_3\text{H}_8$ , and  $n\text{-C}_4\text{H}_{10}$  are sorbed with one molecule per intersection, while nitrogen,  $n$ -hexane, and  $p$ -xylene are sorbed with two molecules per intersection. Thus, for gases of the type  $\text{CH}_4$ ,  $n\text{-C}_3\text{H}_8$ , and  $\text{C}_4\text{H}_{10}$ , channels in the crystal structure of ZSM-8 can be treated as one dimensional. For nitrogen-type molecules, two molecules can be arranged at an intersection, and therefore molecules can change places at an intersection (absence of blocking). Nonetheless, since there are significantly more nitrogen molecules in a channel (24 molecules per unit cell [50]), the one-dimensional model can also be used for this gas. Analysis of the experimental data presented [43, 55–58] shows that all gases investigated can be conditionally divided into two groups. The first group of gases, containing, specifically, Ar, Kr, Ne, and  $\text{CH}_4$ , is characterized by a linear pressure dependence of the filling factor  $\theta$ ; that is, Henry's law holds for them [43]. For these gases, the pressure dependence of the flux is nearly linear, and the diffusion coefficient is essentially independent of the filling factor [55]. The temperature dependence of the flux is characterized by the presence of a minimum at temperatures  $T \sim 400 \text{ K}$  (e.g., for Ar and Kr), while a maximum is not observed in the diffusion coefficient [57, 58]. Here neon, whose diffusion coefficient increases with temperature [58], is an exception. The second group of gases, containing, specifically,  $i\text{-C}_4\text{H}_{10}$ ,  $\text{C}_2\text{H}_4$ ,  $\text{C}_2\text{H}_6$ , and  $\text{C}_4\text{H}_8$ , is characterized by a dependence of the filling factor  $\theta$  on the pressure  $p$  in the form of a curve that saturates [43]. For these gases, the pressure dependence of the flux is likewise characterized by a curve that emerges at a value that is pressure independent [55]. For this group of gases, the diffusion coefficient depends strongly on the filling factor [56]. The temperature dependence of the flux is characterized by the existence of a maximum and minimum at high ( $T > 500 \text{ K}$ ) temperature [57]. The model, constructed in this paper, of the sorption and transport properties makes it possible to describe these dependences of transport in one-dimensional channels on the basis of general assumptions. Figure 4 shows the dependence of the diffusion coefficient  $D$  on the filling factor  $\theta$  (solid line), calculated using (81) and the experimental data obtained in [57] for various gases.

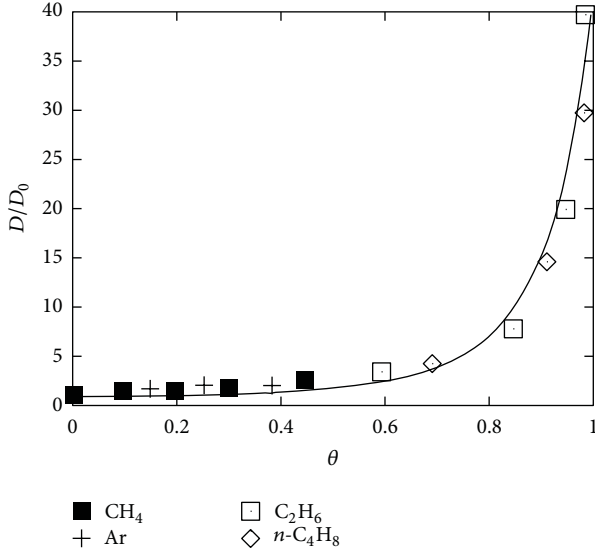


FIGURE 4: Relative diffusion coefficient versus the filling factor. Solid curve—theoretical dependence (81) with  $\zeta = 0.86$ ; dots—experimental data from [57].

We note that the dependence (81) presented in Figure 4 takes into account the asphericity of the molecules, equal to  $\zeta = 0.86$ . For inert gases and methane (first group of gases), the diffusion coefficient measured in the range of filling factors  $\theta_0 < 0.5$  depends weakly on  $\theta_0$ . A large increase in the diffusion coefficient at  $\theta_0 \sim 1$  is observed for gases of the type C<sub>2</sub>H<sub>6</sub> and n-C<sub>4</sub>H<sub>8</sub> (second group of gases). This behavior of the diffusion coefficient  $D(\theta)$  can be satisfactorily described on the basis of the model proposed, which takes account of the pair interaction of particles with a very simple form of the interaction potential for hard spheres. It is obvious that this coefficient is different for different molecules.

The physical mechanism leading to an increase of the diffusion coefficient consists in a decrease of the activation barriers for diffusion, which is due to an interaction of the particles for high filling factors. Indeed, it follows from the relation (75) for the effective diffusion activation energy  $\tilde{E}(\theta_0)$  that in this case, when the filling factor is low,  $\theta_0 \ll 1$ , gas diffusion in the channel can be studied in the single-particle approximation neglecting the pair interaction of the gas particles with one another. As the filling factor increases, the diffusion activation energy decreases as a result of the effective attraction of the gas particles to one another. This can be interpreted as the formation of widely separated clusters. Diffusion in each cluster can be treated as a transfer of “excitation” along a chain of close gas particles. A further increase of the filling factor increases the cluster lifetime and decreases the average intercluster distance and, in consequence, increases the diffusion coefficient. For  $\theta_0 \sim 1$ , the diffusion process can be regarded as a motion of this “excitation” along the entire channel, when the arrival of a particle at the channel entrance results in the end-most particle leaving the channel.

Figure 5(a) shows the temperature dependences of the gas flux through a membrane for ethane and argon, calculated

using the formulas (5) and (81) and a relation following from (81):  $J \propto D(\theta_0(T, p))\theta_0(T, p)$ . These dependences were compared with the experimental values obtained in [42]. It is evident that the theoretical and experimental results agree satisfactorily with one another. The temperature dependence can also be understood on the basis of the model developed in the present work. Indeed, it follows from the relation (5) that at low temperatures ( $T \rightarrow 0$ ), the filling factor  $\theta_0 \sim 1$ .

The effective diffusion activation energy  $\tilde{E}(\theta_0)$  is  $E_0$  at zero temperature (56). The diffusion coefficient of the gas particles in the channel (81) approaches zero as a result of the “freezing out” of the thermal motion of the particles in the potential field of the channel surface. Increasing the temperature decreases  $\tilde{E}(\theta_0)$  without appreciably changing the filling factor. The value of  $\tilde{E}(\theta_0)$  reaches a minimum at a certain temperature  $T_0$ . It is obvious that the diffusion coefficient reaches its maximum value precisely at this temperature. It follows from (54) and (75) that a further increase of temperature decreases the filling factor  $\theta_0$ , and this is accompanied by an increase in the effective diffusion activation energy right up to the value  $E_0$  which is attained for  $\theta_0(p, T) \approx \theta_0 \ll 1$  at some temperature  $T = T_1(p)$ . The temperature  $T_1$  corresponds to a minimum in the function  $D(T)$ . A further increase of the diffusion coefficient with increasing temperature corresponds to the variation of the coefficient according to the Arrhenius law  $D \propto \exp(-E_0/T)$ . Figure 5(b) shows the temperature dependence of the flux for argon, calculated using (81) and the data from [57]. We note that the theory developed in the present paper predicts that the presence of a minimum at  $T \sim 400$  K should be accompanied by the appearance of a maximum at  $T \sim 200$  K. In this connection, for further elaboration of the theory, it is of interest to make an experimental search for a maximum in the temperature dependence of the flux for argon near  $T \sim 200$  K. Thus, two types of behavior of particles in a channel, which have different diffusion mechanisms, can be distinguished in the pressure and temperature ranges investigated. For the first group, this is the diffusion of single particles in a channel, and for the second group it is diffusion as a result of a collective interaction of particles in a completely filled channel. Such behavior of single-component gases is a direct consequence of the real one-dimensionality of subnanometer channels, where molecules cannot change places with one another. The proposed model is based on two basic assumptions: (1) the pair interaction between gas particles plays the decisive role in the description of the state and transport phenomena in a one-component gas in subnanometer channels, and (2) as a result of the fact that the channel diameter is comparable to the diameter of the gas molecules, such channels can be assumed to be one dimensional. The one-dimensionality of the system studied is actually due to the fact that the gas molecules do not have classical transverse degrees of freedom. This difference from the conventional systems plays a fundamental role in the analysis of all phenomena described above.

We note that (73) derived previously possesses, besides the solution described in the text, strongly nonuniform nonstationary soliton-like solutions. It should be expected

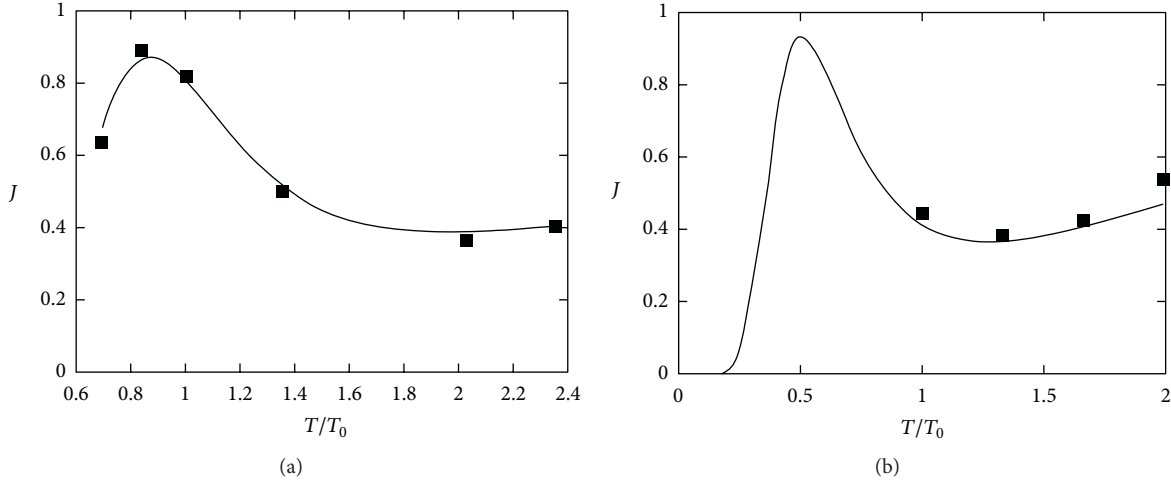


FIGURE 5: Relative flux versus the relative temperature  $T/T_0$ ,  $T_0 = 296$  K. Solid lines—theoretical curves calculated using (5), (34), and (81); dots—experimental data for ethane (a) [42] and argon (b) [58].

that an experimental consequence of the existence of such solutions will be the appearance of substantial fluctuations of the gas flux through a membrane. The proposed model satisfactorily describes the equilibrium properties of a gas in a channel (specifically, the filling factor) and the weakly nonequilibrium properties of the gas, such as the diffusion coefficient and flux. It should be noted that a satisfactory description of the equilibrium properties, for example, the adsorption isotherm, has been obtained previously on the basis of a number of phenomenological models [42]. A qualitative analysis of the maximum (but not minimum) in the temperature dependence of the relative diffusion coefficient is presented in [43]. A model describing the dependence of the diffusion coefficient on the filling factor on the basis of a one-particle approximation by introducing into the diffusion rate jumps of individual particles a phenomenological correction factor  $\chi = (1 - \theta_0)^{-1}$  has been proposed in [36]. However, even though each of the phenomena indicated previously can be described on the basis of individual models, the approximations used in so doing either are not physically substantiated or completely contradict one another.

**2.2. Particle Mobility and Diffusion in 1D System.** Although, in many cases, the parameters of 1D systems can be calculated exactly, their complete theoretical description has not yet been accomplished. 1D systems belong to the class of strongly fluctuating systems [59]; thus, in contrast to systems of higher dimensionalities, they cannot unambiguously be described only by mean values such as mean density and compressibility [59]. The transport properties of 1D systems can also be rather specific (see [43, 57, 60] and Section 2.1). Recent ab initio calculations [61] have shown that water flux through hydrophobic nanotubes is more than one order of magnitude higher than the estimated ordinary diffusion flux. The permeation experiments on zeolite membranes [57] have shown that for gases, whose particle diameter is larger than half the zeolite channel diameter, the increase of the diffusion coefficient with density is more than one order of

magnitude larger than would be expected for one-particle diffusion. On the other hand, there are also experimental results, for example, obtained using nuclear magnetic resonance (NMR) and quasi-elastic neutron scattering (QENS) techniques, indicating that the particle mobility in 1D systems can decrease and the mean square displacement (MSD) can become proportional not to time, as it is in the case of a normal (Einstein) diffusion, but to the square root of time,  $\langle x^2 \rangle \sim t^{1/2}$  (so-called single-file diffusion mode (SFD)) [43, 62–67]. Moreover, the experiments [64, 66] show that both the Einstein and SFD diffusion modes can exist for the same particles but at different densities and observation times. Furthermore, for certain investigated gases, a density increase leads to a transition from the Einstein diffusion to the SFD mode [64]. Thus some experiments suggest that the particle mobility in 1D systems must decrease with increasing density, whereas others show that diffusion accelerates as density becomes larger. An explanation for this contradiction is absent at present.

Diffusion in 1D systems has been studied in numerous theoretical works [36, 57, 67–73]. The dependence  $\langle x^2 \rangle \sim t^{1/2}$  has been obtained for a 1D system within the screened-gas model, which partly takes into account correlations between the particles [68–73]. It has been suggested [70–73] that the appearance of the two diffusion modes, characterized by the different time dependences of MSD, can be explained by a transition from the one-particle diffusion mode, occurring at short times, to SFD appearing at longer times when the particle mobility is limited by its neighbors. In this case at  $t \rightarrow \infty$  the dependence of MSD is always  $\langle x^2 \rangle \sim t^{1/2}$ . Although this approach can describe the experimentally observed dependences of MSD, corresponding to SFD, it fails to explain the increase of the diffusion coefficient and transport acceleration observed in dense 1D systems [43]. The physical reason for this failing is that the proposed model [60] considered the system of individual tagged particles, whereas in experiments one does not follow the diffusion of a particular particle but rather deals with the system

of many of identical particles. We propose a description for the particle diffusion [57] and mobility [43, 62–65] in 1D systems of identical particles with blocking effect (BE) when the motion of a particle is blocked by other particles or clusters. According to our model, different mobility and diffusion transport mechanisms can be realized in a 1D system depending on its density. At low densities, an ordinary diffusion of single particles takes place. As density increases, a formation of 1D clusters of a finite size and lifetime takes place. In this case, there are two competing mechanisms prevalent in the system: a barrier-free propagation of density perturbations (“collective diffusion” (CD)) [60] and a blocking effect. When BE dominates, the SFD mode is realized, whereas when the CD mechanism prevails, we predict an essential transport acceleration, as compared to the one-particle diffusion mode. In this case, MSD is Einstein-like with the diffusion coefficient increasing with density. The proposed model consequently takes into account all the time-space correlations occurring in a 1D system composed of identical particles with an arbitrary interaction potential. This model is able to describe the experimentally observed MSD dependencies at different densities as well as the transport acceleration with increasing density of a 1D system. To describe the transport properties of a 1D system, we apply the response function method (see Section 2.1 and [31, 32, 48]). This approach allows one to consistently take into account many-body correlations and obtain the diffusion coefficient and MSD for a 1D system of arbitrary density. Within response function method, we calculate the response function  $\beta(k, \omega)$ , which determines the Fourier image of the density fluctuation  $\delta n(k, \omega)$  occurring in the 1D system in the external field of frequency  $\omega$  and wave number  $k$ . The relaxation spectrum of a density fluctuation ( $\omega(k)$ ) can be calculated from the relation  $\beta^{-1}(k, \omega) = 0$ . Note that in response function method,  $\delta n(x, t)$  can be interpreted as a distribution function if  $t \gg a^2/D$ , where  $a$  is the particle diameter and  $D$  is the one-particle diffusion coefficient [48]. A density fluctuation  $\delta n(x, t)$  in a 1D system is determined by the relation (87), and the MSD can be expressed as

$$\langle x^2 \rangle = \frac{\int x^2 dx dk e^{-i\omega(k)t} e^{ikx}}{\int dx dk e^{-i\omega(k)t} e^{ikx}}. \quad (83)$$

It is evident from (87) and (83) that MSD is determined by the relaxation spectrum  $\omega(k)$ . The evaluation of  $\omega(k)$  is reduced to the solution of Dyson equation for the response function (55) and for the 1D system takes the form (70), where  $\nu(k, \theta)$  is the Fourier image of the pair correlation function of interacting particles. The function  $\nu(k, \theta)$  can be obtained for a 1D system with an arbitrary interaction potential  $\Phi(x)$  [45]:

$$\begin{aligned} \nu(k, \theta) &= \frac{2}{n_0} \left( \frac{\phi(p(\theta) - ika)}{\phi(p(\theta)) - \phi(p(\theta) - ika)} + \frac{\theta}{ika} \right), \\ \phi(z) &= \int_0^\infty e^{-zx} \exp\left(-\frac{\Phi(x)}{T}\right) dx, \\ \frac{1}{\theta} + (\ln \phi(z))'_{z=p(\theta)} &= 0. \end{aligned} \quad (84)$$

Here  $T$  is the temperature. The last expression in (84) helps us to obtain the dependence of pressure on the filling factor ( $p(\theta)$ ). It follows from (70) and (84) that at  $\theta \rightarrow 0$ , the relaxation spectrum  $\omega(k)$  describes the one-particle diffusion  $\omega(k) = -iD_0k^2$ . For  $ka \gg 1$ , the Fourier image of the pair correlation function  $\nu(k, \theta)$  approaches zero for any arbitrary short-range potential  $\Phi(x)$ . This corresponds to the absence of correlations between the particles at the length scale  $a < l_0$ , where  $l_0$  is the average particle path between two collisions. In this case, the relaxation spectrum  $\omega(k)$  also describes the one-particle diffusion mode  $\omega(k) = -iD_0k^2$ . The analysis of the relaxation spectrum performed in Section 2.1 for the hard-core potential has shown that due to collective effects and density fluctuations, the 1D system can transform into a nonhomogeneous state as density increases. This state is characterized by the formation of 1D clusters with a finite lifetime (Section 2.3) (Section 2.1). In this case at high density ( $\theta \rightarrow 1$ ), long distances ( $k \rightarrow 0$ ), and  $t \rightarrow \infty$  (see (70), (84)) the spectrum becomes diffusion-like with the diffusion coefficient increasing with density (72) that corresponds to the CD mode existing in a nonhomogeneous, clustered 1D system [62]. In order to describe the relaxation of density fluctuations at times  $t \gg a^2/D_0$  (that corresponds to the long-time limit  $t \rightarrow \infty$ ) for an arbitrary filling factor  $\theta$ , one should do series expansions of (70) and (84) with respect to the parameter  $ka \ll 1$  and keep the expansion terms following the first one. It is convenient to rewrite this expansion with respect to parameter  $kl_0$ . Having done this, the relaxation spectrum for  $k \ll 1/a$  can be written as

$$\omega(k) = -i \left( D(\theta) k^2 + F(\theta) k^2 (kl_0)^2 + iF_1(\theta) k^2 (kl_0) \right), \quad (85)$$

where the expansion coefficients are  $D(\theta) = D_0\zeta(0, \theta)$ ,  $F_1(\theta) = D\theta\nu'(0, \theta)\zeta^2(0, \theta)$ , and  $F(\theta) = D\theta^2((1/2)\nu''(0, \theta)\zeta^2(0, \theta) - \nu'^2(0, \theta)\zeta^3(0, \theta))$ . The values with apostrophes represent the corresponding derivatives of  $\nu(k, \theta)$  with respect to wave number  $k$ , calculated at  $k = 0$ . Equations (83) and (85) can be used to evaluate the time dependence of  $\langle x^2 \rangle$  at any length scale, starting from a diffusion path of just few particle jumps up to those comparable to the total length of the channel. Note that the real part of the spectrum  $\text{Re} \omega(k)$ , which at  $\theta \rightarrow 1$  corresponds to the sound mode, describes the collective effect of density perturbation propagation ( $\delta n(x, t) \sim \int dk e^{-i\omega(k)t} e^{ikx} = \int dk \delta n_1(k, t) \delta n_2(k, t) e^{ikx}$ ,  $\delta n_1 \sim e^{i \text{Re} \omega(k)t}$ ), and its imaginary part  $\text{Im} \omega(k)$  determines the diffusion mode for the relaxation of a density fluctuation taking into account the length-time correlations between the particles ( $\delta n_2 \sim e^{-\text{Im} \omega(k)t}$ ). Equations (87), (83), and (85) allow us to study the mobility and distribution function of the particles in a 1D system for different length/time scales, filling factors and interaction potentials  $\Phi(x)$ . Figure 6 presents the dependences of the distribution function on the dimensionless coordinate  $\bar{x} = x/l_0$ , calculated for different dimensionless times  $t' = t/\tau$  ( $\tau \sim l_0^2/D_0$ ) using the square-well interaction potential with the well depth  $V \sim T$  ( $u = V/T \sim 1$ ) and width  $R$ .

It is important to mention that the obtained results do not depend on the specific form of the pair interaction potential

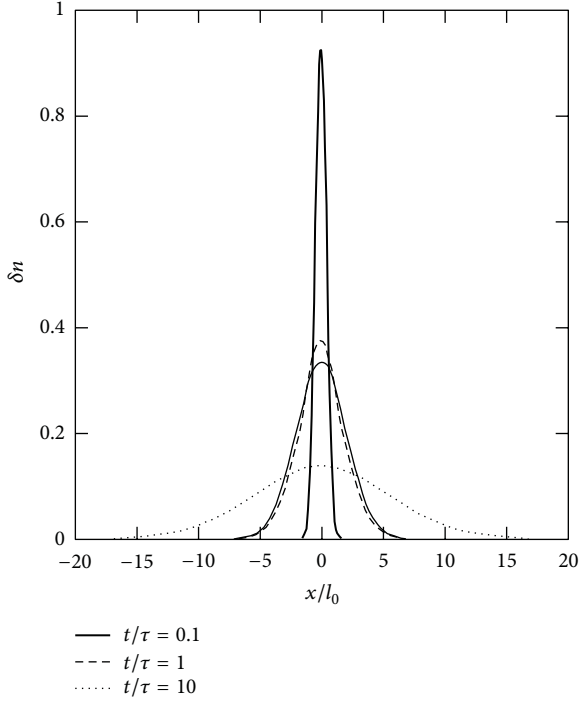


FIGURE 6: Typical distribution functions  $\delta n(x, t)$  versus dimensionless coordinate  $x/l_0$  (solid lines) at different times  $t/\tau$ , ( $\tau \sim l_0^2/D_0$ ) at  $\theta \sim 0.2$ ,  $u = 1$ , and  $R = a$ . Dashed lines show Gauss distributions for the corresponding times.

$\Phi(x)$ ; we have obtained similar results using rectangular potentials, the Lennard-Jones and Morse potentials. We also note that the shape of the distribution function is independent on density as both dimensionless coordinate and time are determined by the filling factor. The distribution functions at different time scales clearly differ from each other. The distribution is a Gauss-like function at short times ( $\theta^2 \ll t' < 1$ ,  $\theta \ll |\bar{x}| < 1$ ) that corresponds to the one-particle diffusion (Figure 6). At  $t' \sim 1$ ,  $|\bar{x}| \sim 1$ , the distribution function varies faster than the Gauss distribution (Figure 6) that corresponds to limited mobility of a particle due to its blocking by other particles. At longer times ( $t' \gg 1$ ,  $|\bar{x}| \gg 1$ ), the distribution function becomes Gauss-like again (Figure 6) as the transport in a dense 1D system is due to the CD mechanism [60]. In this case, the relaxation spectrum is diffusion-like with a density-dependent diffusion coefficient  $D_u(\theta) \approx D_0/(1 - \theta)^2$ .

MSDs calculated at different time and length scales (Figure 7) using the distribution functions (Figure 6) noticeably differ from each other confirming the existence of several diffusion modes in the system. At short length-time scales ( $t < \tau$ ,  $\langle x^2 \rangle \ll l_0^2$ ), one should observe the one-particle diffusion mode with  $\langle x^2 \rangle \sim t$  (Figure 7(a)). When  $\langle x^2 \rangle$  is comparable to  $l_0^2$  and time  $t \sim \tau$ , the correlations between the particles become essential that lead to the appearance of blocking effect. In this case, MSD has a non-Einstein character (Figure 7(b)). At longer times  $t \gg \tau$ ,  $\langle x^2 \rangle \gg l_0^2$ , the particle mobility is mostly determined by the second term

in (85). This leads to the reappearance of the Einstein-type 110 dependence of MSD,  $\langle x^2 \rangle = 2D(\theta)t$ , where  $D(\theta)$  is an effective diffusion coefficient. Notice that the characteristic times at which different diffusion modes can be observed depend on the density of the system. Indeed, the average distance between the particles and, consequently, the time  $\tau \sim 1/\theta^2$  decrease with increasing density.

Further we compare our results to those of the QENS, NMR [43, 62–65], and permeation [57] experiments as well as to the results of the molecular dynamics (MD) calculations [71] summarized in Table 1. Notice that such a system can be considered as one dimensional with the presence of BE as the diameters of the experimentally investigated molecules are less than the doubled diameter of the membrane channel. Our estimates for zeolite ZSM-48 obtained using the data from [71] show that for the low filling factor ( $\theta = 0.11$ ) and times  $\sim 10$  ns, the normal diffusion mode,  $\langle x^2 \rangle \sim t$ , should occur while at higher density ( $\theta = 0.48$ ) the dependence  $\langle x^2 \rangle \sim t^{1/2}$  should be observed, which is in a perfect agreement with the experimental data (Table 1). In Table 1, experimental and MD results are presented;  $a$  and  $d$  are the particle and membrane channel diameters, respectively,  $T$  is a temperature, and  $\theta$  is a degree of filling of the channel. The fifth column represents the data on the motion mode of a particle in a channel (“SFD” means  $x^2 \sim t^\alpha$ ,  $\alpha < 1$ , “normal” corresponds to  $x^2 \sim t$ ). The observation time of corresponding modes is represented in the sixth column.

The experimental results obtained for ethane molecules in zeolite  $\text{AlPO}_4\text{-5}$  and for methane molecules in zeolite ZSM-48 (Table 1) are successfully described by our model. Indeed, using (85), one can write MSD for the SFD mode at  $F(\theta) > 0$  as

$$\langle x^2 \rangle = (1 - \theta) l_0 \sqrt{32DtF(\theta)},$$

$$F(\theta) = D_0 \theta^2 \left( \frac{1}{2} \nu''(0, \theta) \zeta^2(0, \theta) - \nu'^2(0, \theta) \zeta^3(0, \theta) \right). \quad (86)$$

Equation (86) with  $F(\theta) = 1$  is identical to the relation derived in [62] with the accuracy of the numeric coefficient  $\sqrt{32}$ . Note that  $F(\theta)$  describes the correlations effects in a 1D system of interacting particles. Using (86) and the parameters for  $\text{AlPO}_4\text{-5}$  [62], we obtain  $\langle x^2 \rangle \sim 3 \mu\text{m}$  for times  $\sim 100$  ns that is in good agreement with the values reported in [62, 64]. At short times  $t \leq l_0^2/D \sim 10^{-8}$  s, the main contribution comes from the first term in (85), and, in this case, the normal diffusion mode is realized. Our results obtained using (83) and (85) at  $u = 1$  and the experimental data for ethane molecules in zeolite  $\text{AlPO}_4\text{-5}$  are compared in Figure 8.

The dependence of the diffusion coefficient on the filling factor was investigated for several gases ( $\text{CH}_4$ ,  $\text{C}_2\text{H}_6$ , and  $\text{C}_3\text{H}_8$ ) in silicalite-1 membrane at times  $t > 10$  s [57]. The diffusion coefficients for these gases were found to increase more than 20 times as the filling factor varied from 0 to 0.9. This observation can be explained by the collective effect of density perturbation propagation through a 1D clustered system. The calculated dependence of the relative diffusion coefficient  $D/D_0 = (\text{Im } \omega(k)/D_0 k^2)_{k=0}$  on the

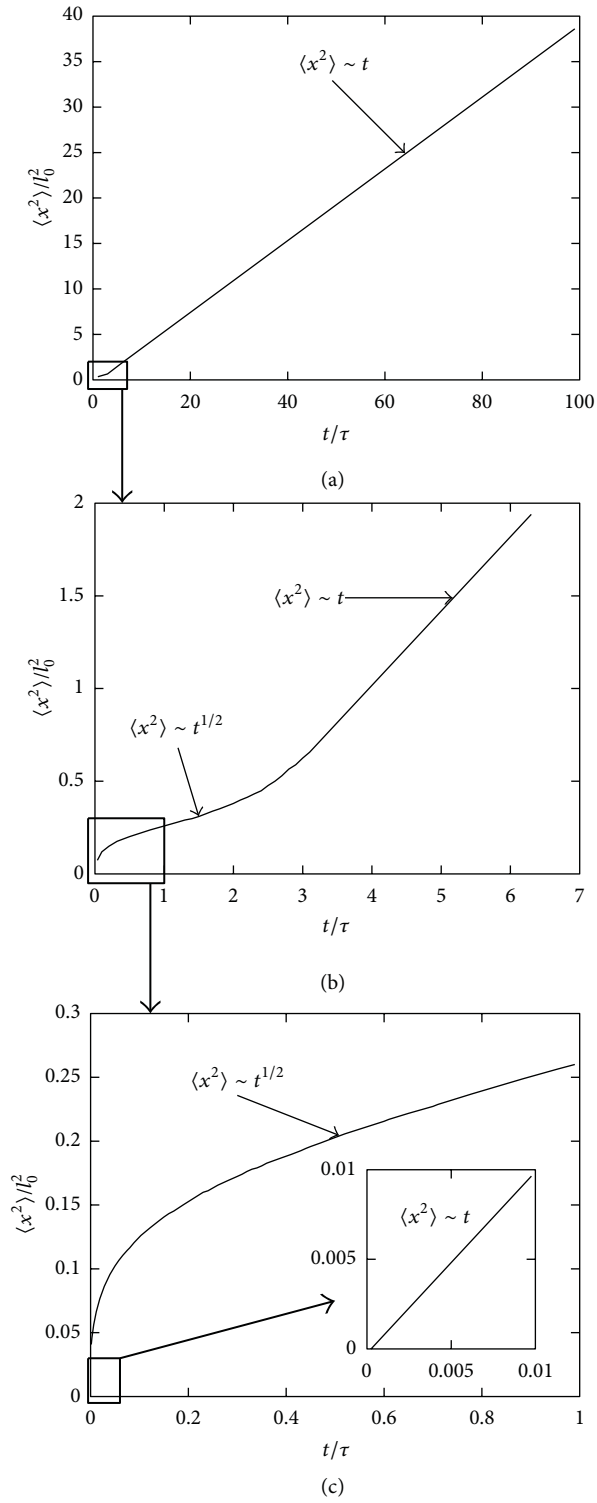


FIGURE 7: Typical  $\langle x^2 \rangle / l_0^2$  versus time ( $t/\tau$ ,  $\tau \sim l_0^2/D$ ) dependence calculated for  $\theta \sim 0.1$ ,  $u = 1$ , and  $R = a$  and shown at different time scales. (a) shows the curve up to  $100t/\tau$ ; its magnification is shown in (b) ( $0: 7t/\tau$ ) and (c) ( $0: 1t/\tau$ ). The insert in (c) shows very short times up to 0.01, when the normal diffusion mode is observed.

TABLE I: Experimental and MD results:  $a$  and  $d$  are the particle and membrane channel diameters, respectively.

| Method | Molecule, zeolite                                                | $T$ , K | $\theta$ | Diffusion mode | Observation time | Reference |
|--------|------------------------------------------------------------------|---------|----------|----------------|------------------|-----------|
| NMR    | $C_2H_6$ , $a = 3.8\text{\AA}$                                   | 300     | 0.15     | SFD            | 100 ms           | [62]      |
|        | $AlPO_4-5$ , $d = 7.3\text{\AA}$                                 |         |          |                |                  |           |
| NMR    | $CF_4$ , $a = 4.7\text{\AA}$<br>$AlPO_4-5$ , $d = 7.3\text{\AA}$ | 180     | 0.003    | SFD            | 2 ms             | [71]      |
|        |                                                                  |         | 0.03     | SFD            | 150 ms           |           |
|        |                                                                  |         | 0.11     | SFD            | 50 ms            |           |
|        |                                                                  |         | 0.22     | SFD            | 150 ms           |           |
| MD     | $CF_4$ , $a = 4.7\text{\AA}$                                     | 180     | 0.11     | SFD            | $10^{-8}$ s      | [64]      |
|        | $CH_4$ , $a = 3.8\text{\AA}$                                     |         | 155      | 0.3            | Normal           |           |
|        | $AlPO_4-5$ , $d = 7.3\text{\AA}$                                 | 250     | 0.45     | Normal         | $10^{-8}$ s      |           |
|        | $C_2H_6$ , $a = 3.8\text{\AA}$                                   |         | 0.36     | Normal         | $10^{-8}$ s      |           |
|        | $AlPO_4-5$ , $d = 7.3\text{\AA}$                                 |         | 0.6      | Normal         | $10^{-8}$ s      |           |
|        | $CH_4$ , $a = 3.8\text{\AA}$                                     | 155     | 0.72     | Normal         | $10^{-8}$ s      |           |
|        | $ZSM-48$ , $d = 5.6\text{\AA}$                                   |         | 0.48     | SFD            | $10^{-8}$ s      |           |

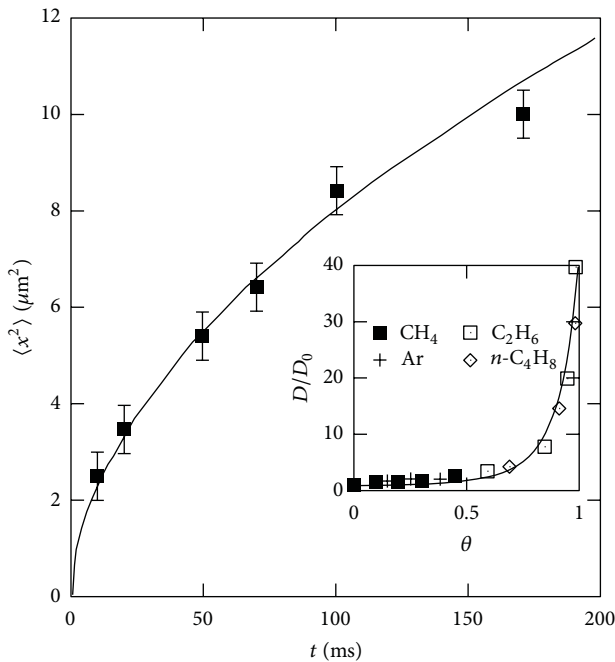


FIGURE 8: MSD versus time at  $u = 1$ ,  $R = a$ . The solid line shows the results calculated using (55), (70), (87), and (85); points represent the experimental data for the diffusion of ethane in zeolite  $AlPO_4-5$  [61]. The insert shows the dependence of the relative diffusion coefficient on the filling factor obtained for several gases (solid line) using (84) and (85) and  $V/T = 1$ . Points are the experimental data from [57].

filling factor  $\theta$  in comparison with experimental results is presented in Figure 8 (insert). The figure shows that the diffusion coefficient is only weakly dependent on the filling factor for  $\theta < 0.5$  (Figure 8 insert) but it rapidly increases when the filling factor becomes larger. This behavior of  $D(\theta)$  can be easily understood as at low filling factors, the particles inside the membrane channel do not interact with each other, no clusters are formed, and particle motion is purely diffusive.

The increase of the diffusion coefficient for  $\theta > 0.5$  is due to the cluster formation inside the channel and activation of the CD mode (Section 2.1).

**2.3. Formation of High- and Low-Density Clusters in a 1D System.** In recent experiments [74], the one-dimensional (1D) Au chains formed on the (110) NiAl surface have been investigated at low temperature ( $T = 12$  K). This surface exhibits 1D grooves made of the rows of Ni atoms, which suppress the transverse movements of Au adatoms allowing them to move only along the groove. The measured Au-Au distances in such chains were about  $2.9\text{\AA}$  that is very close to those in bulk gold [74]. The properties of 1D Au chains were also investigated in experiments [8, 12, 75–77] where they were either pulled out of a gold surface by an STM tip or created in a process of thin film etching. Such chains were stable during the observation time and consisted of several gold atoms. The Au-Au distances in some of them appeared to be strikingly large, up to  $3.5\text{--}4.0\text{\AA}$  [75–77], whereas in others much smaller Au-Au separations ( $\sim 2.5\text{--}2.9\text{\AA}$ ) were observed [8, 12, 78–80]. These results suggest that a 1D gold chain can exist in two different states characterized by different interatomic distances.

The ab initio calculations performed at zero temperature have shown that a 1D gold wire should break when the Au-Au separations exceed  $\sim 2.9\text{\AA}$  [81–84]. Being in agreement with the experiments reporting the Au-Au distances of  $2.5\text{--}2.9\text{\AA}$ , this result, however, does not explain the existence of large Au-Au separations. It has lately been demonstrated that the presence of hydrogen or other light atoms in the wire structure can stabilize gold chains and significantly alter their properties [3, 4, 82–88]. Assuming a somewhat ordered distribution of impurities within the wire, one can easily explain the experimentally observed large Au-Au separations [6, 82, 83, 87]. Although this finding offers an intriguing possibility to modify the wire properties by an intentional incorporation of impurities ( $Im$ ), a spontaneous formation

of locally ordered Au-Im-Au structures seems unlikely and remains to be proven experimentally. Another explanation has been proposed by Sun et al. [89] who suggested that the large Au-Au distances might result from chain melting. It is known, however, that phase transitions do not occur in 1D systems [34]; thus, the proposed model should be taken with precaution.

Monoatomic chains can disintegrate due to atomic movements in both longitudinal and transverse directions caused by thermal fluctuations. The probability of disintegration is determined by the characteristic frequencies of atomic vibrations in the chain, and the energy barrier atoms need to be overcome in order to leave the chain, which is comparable with the energy per atom in the chain. A change of interatomic distances due to transversal or longitudinal motion of one of the atoms leads to a transition to a nonequilibrium state, and the energy per atom increases. As the energy barriers in the longitudinal and transversal directions are comparable [90], the disintegration probabilities for these two mechanisms appear to be comparable as well. Therefore, further on we consider only one mechanism occurring due to longitudinal fluctuations.

The probability of disintegration of a chain due to longitudinal fluctuations is determined by the frequency spectrum of relaxation of density fluctuations (relaxation spectrum) of the quasi-1D system. To study the relaxation spectrum of a quasi-1D system, we apply the previously stated response functions for density functional method, which allows one to describe the equilibrium and dynamical properties of a system if its interaction potential is known. Within this method, one can find the response function  $\beta(x, t)$  that determines the relation between the density fluctuation  $\delta n(x, t)$  and the external field as well as all the space-time correlations in the system. Additionally, one can find the free energy of the quasi-1D system taking into account density fluctuations ([38] and Section 2.1). A density fluctuation appearing in the quasi-1D system can be determined as

$$\delta n(x, t) = \text{Re} \left( \int_0^\infty dk A(k) e^{-i\omega(k)t} e^{ikx} \right), \quad (87)$$

$$A(k) = \begin{cases} A = \text{const}, & k_{\min} \leq k \leq k_{\max} \\ \sim 0, & \text{otherwise.} \end{cases}$$

Here  $k$  is the modulus of the wave number, and  $A(k)$  is the amplitude of the density fluctuation, which in the analysis of cluster relaxation can be arbitrary and adequately considered to be a constant for  $k$  in the interval  $\{k_{\min} = 2\pi/L; k_{\max} = 2\pi/d\}$ . Clusters forming in the system are characterized by the parameter  $\delta n(x, t)$ , which is defined as a Fourier integral (87) in the interval  $\{k_{\min}; k_{\max}\}$ , where  $L$  is the cluster length, and  $d$  is the atomic diameter. The cluster lifetime ( $t$ ) is determined by the maximal magnitude of the imaginary part of the spectrum  $\omega(k)$  ( $\tau^{-1} = \text{Im} \omega(k)$ ) in the interval  $k_{\min} < k < k_{\max}$ .

The relaxation spectrum of the 1D system  $\omega(k)$  is determined by (70). If the relaxation of such a system is determined by diffusion with the coefficient  $D_0$ , then  $\omega_0(k) = -iD_0k^2$ .  $\theta = n_0d$  is a dimensionless density.  $n_0$  is the average number

of particles per length unit.  $\nu(k, \theta)$  is a Fourier image of the pair correlation function for interacting particles, which is related to the Fourier component of the pair distribution ( $g(k)$ ) as  $\nu(k) = g(k) - \delta(k)$ , where  $\delta(k)$  is the Dirac delta-function. Note that the divergence must be removed from  $g(k)$  before any analysis. Otherwise reverse Fourier transformation and the transition from wave numbers to coordinates are impossible due to the integral divergence. For a quasi-1D system, the pair distribution can be calculated exactly for an arbitrary short-range interaction potential  $\Phi(x)$  [44]:

$$g(x) = \frac{1}{2\pi} \int_0^\infty dk e^{ikx} g(k),$$

$$g(k) = \frac{1}{n_0} \frac{\phi(p_{1D}/T - ik)}{\phi(p_{1D}/T) - \phi(p_{1D}/T - ik)}, \quad (88)$$

$$\phi(p_{1D}) = \int_0^\infty \exp\left(-\frac{p_{1D}x + \Phi}{T}\right) dx.$$

Here  $p_{1D}$  and  $T$  are 1D pressure and temperature, respectively. Equation (88) allows one to evaluate the pair distribution and consequently the relaxation spectrum of the 1D system. We have performed an extensive analysis, which has shown that the properties of quasi-1D clusters are determined by the presence of the repulsive and attractive terms in the potential but not by the specific form of  $\Phi(x)$ . In particular, we have obtained similar results using rectangular potentials, and the Lennard-Jones as well as Morse potentials. We notice that this finding correlates well with the known results of the liquid state theory [45, 46, 91]. For the sake of simplicity, we present here the calculations of 1D pressure  $p_{1D}(\theta)$  ( $\theta = (Nd/L)$  is dimensionless density) and pair distribution done for the square-well potential with the well width  $R$  and depth  $U_0$ :

$$\Phi(x) = \begin{cases} \infty, & x \leq d \\ -U_0, & d < x \leq d + R \\ 0, & x > d + R. \end{cases} \quad (89)$$

The performed calculations give the  $p_{1D}(\theta)$  dependence:

$$p_{1D}d \left( \frac{1}{\theta} - 1 \right) = T - p_{1D}R \left[ \frac{\exp(p_{1D}R/T)}{(1 - \exp(U_0/T))} - 1 \right]^{-1}. \quad (90)$$

Equations (88) and (90) allow one to analyze the possible states of the quasi-1D system of the interacting particles of an arbitrary density. They also let us to estimate the relaxation time of a density fluctuation (cluster) as well as the interatomic distances in the clusters. We choose to perform this analysis using the parameters of the pair potential (89),  $U_0 = 1.1$  eV,  $d = 2.5$  Å, and  $R = 2.5$  Å, corresponding to the gold atoms [80]. For these parameters, we calculate the compressibility  $\eta = -(\partial\theta/\partial p_{1D})$  (Figure 9), pair distribution (Figure 10), and dimensionless spectrum  $\Omega \equiv \omega(k)/\omega_0(k)$  (Figure 11).

At low densities ( $\theta < 0.67$ ), the compressibility increases with increasing density and it approaches its first maximum at  $\theta = \theta_c = 0.18$  (Figure 9). The compressibility has a

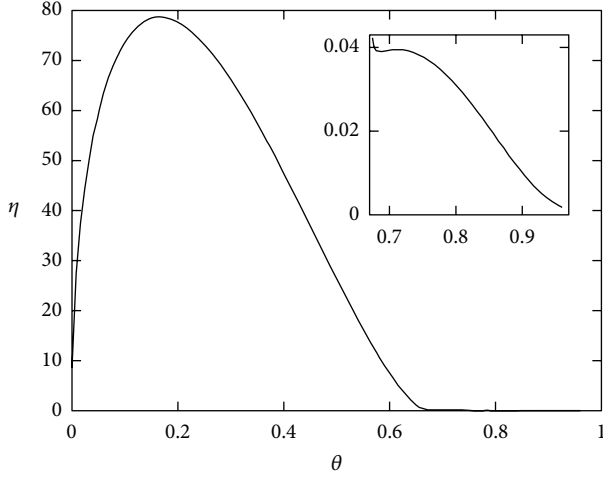


FIGURE 9: The compressibility versus density for Au atoms at room temperature.

second maximum at  $\theta = \theta_c^{(1)} = 0.71$ . The derivative of the compressibility equals 0 at extrema. Therefore, the presence of extrema can indicate changes in the system state. As we show in the following, the presence of maxima does not depend on the specific form of the pair interaction potential  $\Phi(x)$ , but it is determined by the  $U_0/T$  ratio ( $U_0$  is a characteristic depth of an arbitrary potential). The second maximum of the compressibility disappears if  $U_0/T \ll 1$ . When  $U_0/T \gg 1$ , the second maximum always exists if the condition  $R \geq d$  is satisfied regardless of the specific form of the potential  $\Phi(x)$ . Also we have to note that the ratio  $U_0/T$  provides the existence of the second maximum whereas the position of this maximum does not depend on the magnitude of this ratio. This allows us to conclude that in the limiting case  $U_0/T \gg 1$ , the variation of the temperature of a system does not lead to any qualitative changes in a state of a system.

To demonstrate how the physical state of the system changes at the compressibility maxima, let us analyze the pair distribution  $g(x)$  that determines the probability to find atoms at a certain distance from each other. It has been shown in Section 2.1 that the function  $g(x) \rightarrow 1$  when  $x \rightarrow \infty$ . The distances between the maxima of  $g(x)$  are equal to 1, 2, 3, and so forth, atomic diameters. Hence, the separation between these maxima corresponds to the interatomic distance in the clusters [45].

In the vicinity of the first compressibility maximum ( $\theta_c = 0.18$ ), the distance between the peaks of  $g(x)$  and, correspondingly, the interatomic distances in the clusters are  $\sim 3.6 \text{ \AA}$  (Figure 10(a)). At densities close to the second maximum, interatomic distance in the cluster  $\leq 3 \text{ \AA}$  (Figure 10(b)). As it was mentioned above in the limiting case  $U_0/T \gg 1$ , the variation of the temperature of a system does not lead to any changes in the state of this system. Therefore, at  $T = 300$  and 12 K, the magnitude of the gold cluster interatomic distance will be the same.

As it has been noticed previously the qualitative shape and the distance between the peaks of the pair distribution function are independent of the concrete form of the interaction potential. The pair distributions  $g(x)$  calculated for  $\theta = 0.15$

with square-well potential (solid line) and Morse potential for the Au atoms (dashed line) are compared in Figure 11.

Figure 11 demonstrates that the distances between the peaks are the same for both potentials, but the peaks for the Morse potential are higher compared to the ones obtained with the square-well potential. This difference is due to the different characteristic length scales of the Morse and square-well potentials. The characteristic length scale of the Morse potential is larger than that of the square-well potential that leads to a larger atomic attraction at long distances. Note that in the case of the Morse potential  $U_0$  in (89) is a potential well depth and  $d + R$  is the characteristic length scale of the potential.

Further, we analyze the stability of the 1D clusters. The change of the free energy of the 1D system ( $\Delta\Phi$ ) due to the cluster disintegration determines the probability of such a disintegration [34].  $\Delta\Phi$  can be divided into the following contributions:  $\Delta\Phi_0$  that is the change of the free energy due to the pair interactions in the cluster;  $\Delta\Phi_1$  that is the change of the free energy coming from changes in the cluster electronic states; and the fluctuation part  $\Delta\Phi_f$  that is an average fluctuation of the free energy of the 1D system caused by cluster disintegration calculated for the stationary state of the 1D system. Therefore, the probability of cluster disintegration can be written as

$$\begin{aligned} W &\propto W_f W_i, & W_f &\propto e^{\Delta F_f/T}, \\ W_i &\propto e^{\Delta F_i/T}, & \Delta F_i &= \Delta F_0 + \Delta F_1. \end{aligned} \quad (91)$$

To estimate the cluster lifetime  $\tau \sim W^{-1}$ , we analyze the contributions to  $\Delta\Phi$ . Since there are no phase transitions in 1D systems,  $\Delta\Phi_f$  is always positive and its magnitude is determined by the spectrum  $\Omega(k)$  [46] (Figure 12):

$$\Delta F_f \sim T \int_0^\infty dk \Omega(k) (\delta n(k))^2. \quad (92)$$

It follows from (92) that  $\Delta\Phi_f$ , which is related to the probability of cluster disintegration due to the loss of one or several atoms, is determined by the maximal magnitude of  $\Omega(k)$  in the interval ( $k_{\min} = 2\pi/L$ ;  $k_{\max} = 2\pi/d$ ). In the vicinity of the first maximum of the compressibility at  $\theta = 0.2$  (Figure 9),  $\Delta\Phi_f \sim TN\Omega(k')$ . Here  $k'$  is the wave number corresponding to the maximum of  $\Omega(k)$ ,  $k'd \sim 2$  (Figure 12(a)), and  $N$  is the number of particles in the cluster. It follows from (91) that in this case the magnitude of  $W_f$  is large for all the clusters with the length exceeding several atomic radii. In the vicinity of the second maximum of the compressibility at  $\theta = 0.7$  (Figure 9),  $\Delta\Phi_f$  becomes larger as the cluster length increases (Figure 12(b)). In this case for all clusters with the length exceeding  $L'$ , for which  $\Omega(2\pi/L') \gg 1$ ,  $\Delta\Phi_f \sim TN\Omega(2\pi/L')$  and the probability  $W_f$  is large. Thus at all densities, only clusters of a certain maximal length can exhibit a noticeable lifetime, and the formation of long clusters appears to be unfavorable.

$\Delta\Phi_i$  is the sum of the changes of the free energy of the pair interaction between atoms in the cluster  $\varepsilon_0$  and the free energy of the cluster electronic states  $\varepsilon_1$  ( $\Delta\Phi_i/N = \varepsilon_0 + \varepsilon_1$ ).

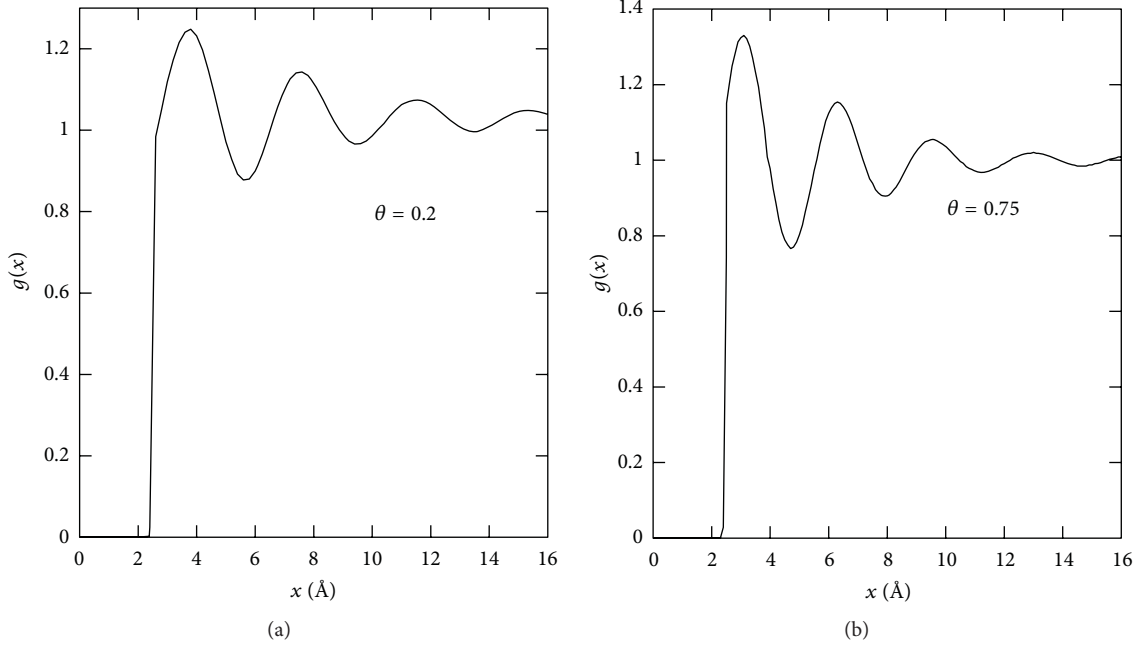


FIGURE 10: Pair distribution of gold atoms at room temperature.

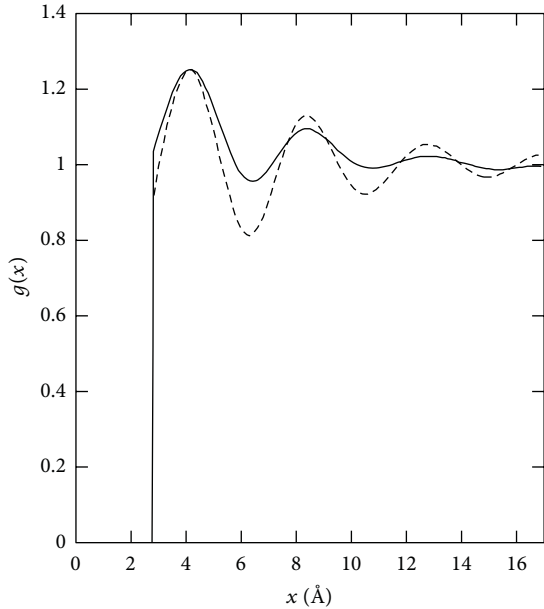
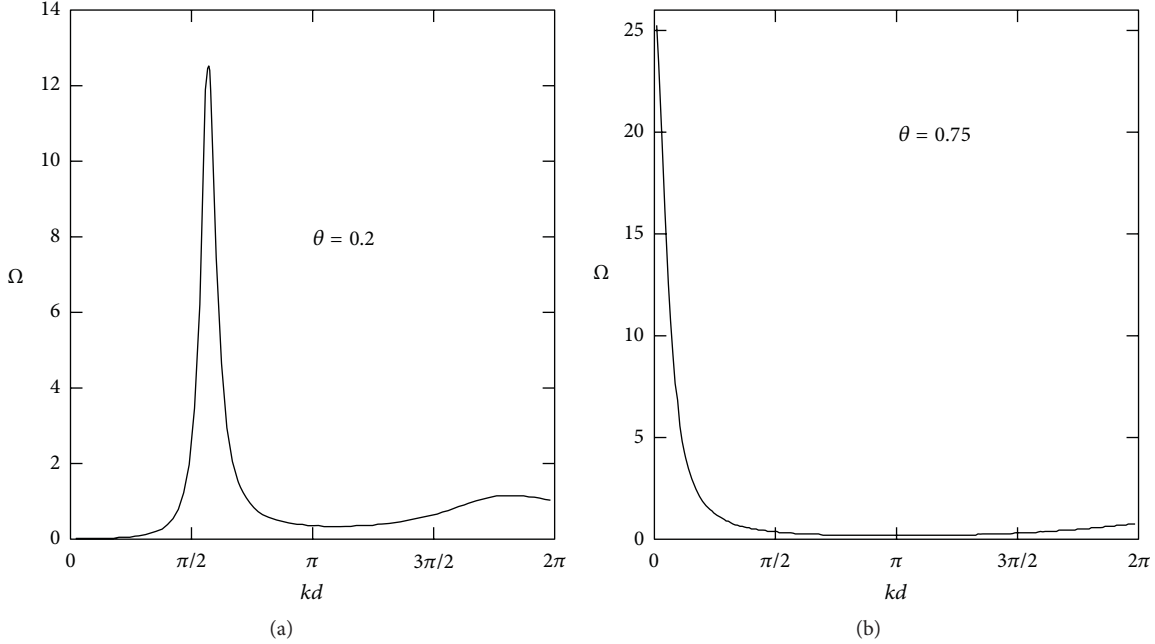


FIGURE 11: Pair distribution calculated with both square-well (solid) and Morse (dashed) potentials.

In the limiting case  $T \ll |\varepsilon_1|$ ,  $\varepsilon_1$ , is negative [92] and it is determined by the overlap of the atomic orbitals. This overlap is determined by the penetrability coefficient  $\Gamma$  of the potential barrier separating the electronic potential wells of the neighboring atoms (Section 2.4). In the quasi-classical approximation,  $\Gamma$  depends exponentially on the width and height of the potential barrier (Section 2.4). It has been shown [92] that due to collective effects, the penetrability coefficient

$\Gamma$  depends not only on the interatomic distances, but also on the difference between the maximum and minimum values ( $\Delta g$ ) of the pair distribution  $g(x)$  (Figure 10). The interatomic distances in the clusters formed at the densities about  $\theta \sim 0.2$  are larger than those for the clusters existing at  $\theta \sim 0.7$  (Figure 10), but  $\Delta g(\theta = 0.75) > \Delta g(\theta = 0.2)$ . Using the approach of [92], we find that in this case the magnitudes  $|\varepsilon_1|$  ( $|\varepsilon_1| \sim G$ ) for the clusters of both kinds appear to be similar. Thus, for our analysis of cluster stability, we can use the value  $|\varepsilon_1| \sim 0.5$  eV obtained from the measurements of the cluster conductivity in the scanning tunneling spectroscopy (STS) experiments for the Au chains on the NiAl surface [74]. The energy  $\varepsilon_0$  per atom can be written as  $\varepsilon_0 \sim (\theta/2) \int_0^\infty dx \Phi(x)g(x)$  [46]. Calculations show that  $\varepsilon_0$  is negative and  $|\varepsilon_0| \sim 1$  eV and  $|\varepsilon_0| \sim 0.7$  eV for the clusters at  $\theta \sim 0.7$  and  $\theta \sim 0.2$ , respectively.

Let us now compare the lifetime and interatomic distances calculated for the 1D clusters to the known properties of the 1D chains fabricated in experiments [74–80]. The results of the STS experiments [74] as well as the ab initio study of the electronic structure of gold wires on (110) NiAl [93] suggest that the main role of the substrate is to be a natural template insuring the one-dimensionality of the Au chains. This allows one to suggest that the observed Au-Au distances ( $\sim 2.9$  Å) in such chains to a large extent might be determined by the one-dimensionality of the system. Taking into account the minimal possible distance between Au atoms ( $\sim 2.5$  Å [81]), we can estimate the density in these chains:  $\theta = (2.5/2.9) = 0.87$ . Thus, the fabrication of Au chains on (110) NiAl can be understood as an artificial formation of 1D clusters with the density  $\theta$  fulfilling the condition  $\theta > \theta_c^{(1)}$  ( $\theta_c^{(1)} = 0.71$ ). As we have shown previously, the Au-Au separations in such 1D clusters should range from 3 Å

FIGURE 12: Dimensionless spectrum  $\Omega(k)$  versus the wave number  $k$ .

( $\theta = 0.74$ ) to  $2.7 \text{ \AA}$  ( $\theta = 0.9$ ) or  $2.5 \text{ \AA}$  ( $\theta = 1$ ). The lifetime of such clusters of the length  $L$  can be estimated as the characteristic time ( $\tau \sim \tau_f \exp(Q/T)$ ) during which an atom stays in the potential well of the depth  $Q = |\varepsilon_0| + |\varepsilon_1| - T\Omega(2\pi/L)$  (see (91)). Here  $\tau_f \sim \omega_0^{-1}(k = 2\pi/d) \sim 10^{-12} \text{ s}$ . The calculations of the spectrum  $\Omega(k)$  at  $\theta = 0.87$  show that, for example, for the cluster of the length  $L \sim 15 \text{ \AA}$ , containing  $\sim 5$  Au atoms  $\Omega(2\pi/L) \sim 10$ . In this case using the estimates obtained previously ( $|\varepsilon_1| \sim 0.5 \text{ eV}$ ,  $|\varepsilon_0| \sim 1 \text{ eV}$ ), one can estimate the lifetime of such chains to be  $t > 1000 \text{ s}$  ( $T = 300 \text{ K}$ ). Notice that in the absence of collective effects and attractive interaction between atoms in a quasi-1D system the lifetime of the chain of  $L \sim 15 \text{ \AA}$  would be very short,  $\tau \sim \omega^{-1}(k = 2\pi/L) \sim L^2/D \sim 10^{-9} \text{ s}$  (here  $D \sim 10^{-5} \text{ m}^2/\text{s}$  is the diffusion coefficient for Au atoms at the surface of NiAl [94] at  $T = 300 \text{ K}$ ).

The formation of suspended Au chains by pulling them out of the Au surface or by etching an Au film with an electron beam [2, 8, 12, 75–79] corresponds to conditions where considerable tensile stress is applied to the chain. The presence of an external force corresponds to the appearance of the one-dimensional pressure  $p_{1D} = -(\partial F/\partial L)$ , where  $F$  is a free energy of the 1D chain. One can see from (90) that 1D chains of finite length are affected by two types of forces: forces corresponding to the effective repulsion of the atoms from each other as a result of their movement (the first term in (90)) and forces corresponding to their mutual attraction that is determined by interaction potential of atoms with each other. The attractive force  $|p_{1D}^v|$  depends on depth of potential well and radius of the potential  $R$  and equals  $p_{1D}^v = -(N^2/L^2)\varepsilon R$  in the van der Waals approximation. Thus a cluster is in a compressed state. The value of compression is  $|p_{1D}^v| = (N^2/L^2)\varepsilon R$ . The presence of such a compression

can lead to loss of stability of the cluster in the transverse direction and formation of a zigzag configuration of a chain. Therefore, to form a stable linear chain, it is necessary to attach an external force to the end of a chain to compensate the compression  $|p_{1D}^v|$ . The presence of an external force corresponds to the appearance of one-dimensional pressure  $|p_{1D}^v| = -(\partial F/\partial L)$ , where  $F$  is the free energy of a one-dimensional chain. Let us estimate the lifetime of these chains.

The decrease of the tensile force corresponds to the decrease of the density  $\theta$  (90). The observation of Au chains [75–77] containing three or more atoms and exhibiting large Au-Au separations ( $\sim 3.6 \text{ \AA}$ ) can be considered as a formation of a 1D cluster at the pressure  $p_{1D}$  for which  $\gamma$  satisfies the condition  $\theta_c < \theta < \theta_c^{(1)}$  ( $\theta_c = 0.18$ ,  $\theta_c^{(1)} = 0.71$ ). The lifetime of such chains can be estimated as  $\tau \sim \tau_f \exp(Q/T)$ , where  $Q = |\varepsilon_0| + |\varepsilon_1| - T\Omega(k')$ ,  $k'd \sim 2$ . For  $|\varepsilon_1| \sim 0.7 \text{ eV}$ ,  $|\varepsilon_0| \sim 0.5 \text{ eV}$  and  $\Omega(k') \sim 10$  (Figure 12(a)), it turns out that  $\tau > 100 \text{ s}$  ( $T = 300 \text{ K}$ ). The experimentally obtained chains [1, 8, 12, 78–80] with the Au-Au separations of  $2.5\text{--}2.9 \text{ \AA}$  are formed at the pressure  $p$  for which  $\theta$  fulfills the condition  $\theta > \theta_c^{(1)}$ . According to our estimations, the Au-Au separations in such clusters should be  $< 3 \text{ \AA}$  (Figures 10(b) and 12(b)) and their lifetime is  $\tau > 1000 \text{ s}$  ( $T = 300 \text{ K}$ ,  $L \sim 25 \text{ \AA}$ ,  $\Omega(2\pi/L) \sim 20$ ) (Figure 11).

Within the framework of these assumptions, we can also estimate minimal lifetime of chains of other metals, such as Ag, Ni, and Pt. Due to the lack of experimental data on the characteristic values of  $\varepsilon_0$  for these materials let us assume  $|\varepsilon_1| + |\varepsilon_2| \sim |\varepsilon|$ , where  $\varepsilon$  is the binding energy per atom for dimer [95]. The calculated values of minimal lifetime of one-dimensional chains are presented in Table 2. As one can

TABLE 2: Minimal chain lifetime  $\tau$ , minimum number of atoms in a stable chain  $N_{\min}$ , and  $F_{0th}$ ,  $F_{0e}$  are the estimated and experimental values of the force required to break the cluster with a minimum number of atoms in it correspondingly.

|                           | Ag   | Au               | Ni               | Pt               |
|---------------------------|------|------------------|------------------|------------------|
| $ \varepsilon $ , eV [95] | 1.15 | 1.46             | 1.78             | 2.22             |
| $a$ , Å [95]              | 2.58 | 2.58             | 2.08             | 2.32             |
| $\tau$ , s                | >1   | >10 <sup>2</sup> | >10 <sup>5</sup> | >10 <sup>7</sup> |
| $N_{\min}$                | 2    | 3                | 4                | 5                |
| $F_{0th}$ , nN            | 1.4  | 2.03             | 1.5              | 2.2              |
| $F_{0e}$ , nN [13]        | 1.2  | 0.19             | 1.7              | 3.1              |

see, the material of a one-dimensional chain greatly affects its stability.

Let us estimate the minimal length of stable chains and the force that is necessary for their formation. Note that if we consider the chain as a rod of length  $L$  with a radius equal to the atomic radius  $\sigma$ , then such a rod loses its stability when it is compressed with a force greater than  $F_c = \pi^3 E \sigma^4 / L^2$  [96], where  $E$  is the Youngs modulus. So, if the compression pressure of the chain is  $|p_{1D}^v| > F_c$ , then the chain is unstable. Therefore, the minimum compressive force that ensures stability of the chain is  $|p_{1D}^v| = F_c$ . Chains of metal atoms have a conductivity comparable to the metal one [13], so the range of the interatomic potential is comparable to the length of the chain  $R = \kappa L$ , where  $\kappa \sim 1$  and varies from metal to metal. Relations  $|p_{1D}^v| = (N^2 / L^2) \varepsilon R$  and  $F_c = (\pi^3 E \sigma^4 / L^2)$  allow to estimate the minimum number of atoms in a cluster  $N_{\min} = \pi (E \sigma^4 / \kappa a)^{1/3}$ , where  $a$  is an interatomic distance in the cluster. The value  $|p_{1D}^v|$  is the force that compresses a stable cluster without external influences on it. In this case,  $|p_{1D}^v| = (N_{\min} / a) \varepsilon \kappa$  is a force  $F_0$  required to break the cluster with the minimum number of atoms in it. Table 2 shows the results of the estimations of the minimum number of particles in the chain  $N_{\min}$  and the corresponding force required to break the chains  $F_{0th}$  for chains of different material. It was assumed that  $\kappa_{Ag} = 1$  for the chains of Ag. For the rest of metal chains, this coefficient was estimated by using the relative conductivities  $\kappa_i = \kappa_{Ag} (\sigma_i / \sigma_{Ag})$ ,  $i = Au, Ni, Pt$ .

**2.4. Transport of a Two-Component Mixture in One-Dimensional Channels.** The dependence of transport selectivity on the pressure in a two-component system of atomic particles is nonmonotonic: the selectivity attains its maximal value and then decreases instead of increasing. Thus, the mechanism of diffusion enhancement in 1D channel, which was proposed in Section 2.1, is inapplicable for two-component mixtures.

The transport of a two-component mixture in subnanometer channels was considered earlier [51, 97] on the basis of the generalized phenomenological Stephan-Maxwell equation. The authors of these publications used the dependence of the chemical potential on the fill factor, taking into account the finite size of particles, but disregarding their interaction. The dependences obtained in [51, 97] also indicate a monotonous increase in the diffusion coefficients, fluxes, and selectivity upon an increase in  $\theta$  and, hence,

fail to describe the experimental data for two-component mixtures.

**2.4.1. Ground State of a System in 1D Channels.** Let us consider the surface of a porous body in contact with a two-component gas mixture at temperature  $T$  and pressure  $p$ . Suppose that  $N$  adsorption centers are located on the surface. We assume that the particles on the outer surface do not interact with one another. We also assume that the energy of a gas molecule on the surface is equal to  $\varepsilon_0^{(i)}$ ,  $i = 1, 2$ , depending on the species of the molecule. We also suppose that  $\kappa$  cylindrical channels ( $\kappa \gg 1$ ) of diameter  $d$  and length  $L$  emerge at the surface. We assume that the diameter of a cylinder is comparable to the maximal diameter of the gas molecule. Let us assume that  $\varepsilon_1^{(i)}$  is the binding energy of the  $i$ th particle at the mouth of a channel,  $N_1^{(i)}$  is the number of particles of the  $i$ th species above the membrane,  $q^{(i)}$  is the total number of particles of the  $i$ th species in the channel,  $n^{(i)}$  is the total number of  $i$ th particles in the channel and on the surface, and  $N_0$  is the number of ‘‘seats’’ in the channel. Then the partition function of the grand canonical ensemble taking into account the interaction of system of atomic particles in the channel has the form

$$\begin{aligned} \Theta = & \sum_{i=1}^2 \sum \frac{(N-k)! \exp[\beta \varepsilon_0^{(i)} (N_1^{(i)} - n^{(i)})]}{(N_1^{(i)} - n^{(i)})! [n-k - (N_1^{(i)} - n^{(i)})]} \\ & \times \frac{\kappa! \exp[\beta \varepsilon_1^{(i)} (n^{(1)} - q^{(1)})]}{(n^{(1)} - q^{(1)})! [\kappa - (n^{(1)} - q^{(1)})]} \\ & \times \frac{N_0! \exp(\beta \varepsilon_2^{(i)} q^{(i)})}{q^{(i)}! (N_0 - q^{(i)})!} \exp(\beta \mu N_1^{(i)}) Z_{\text{int}}(q^{(1)}, q^{(2)}), \\ & N_1^{(i)} + q^{(i)} = n^{(i)}. \end{aligned} \quad (93)$$

Here, the second sum corresponds to summation over configurations  $\beta = T^{-1}$ ,  $\varepsilon_2^{(i)}$  is the binding energy of particles of the  $i$ th component in the channel,  $\mu$  is the chemical potential, and  $Z_{\text{int}}(q^{(1)}, q^{(2)})$  is the partition function corresponding to the inclusion of particle interaction in the channel. Considering that the main contribution to the partition function comes from states with a large number of particles ( $q^{(i)} \gg 1$ ), we can replace partition function  $Z_{\text{int}}(q^{(1)}, q^{(2)})$  by the partition function for particles interacting in the channel, calculated for the mean value  $\bar{q}^{(i)}$  of the number of particles of each species in the channel. From the physics standpoint, this corresponds to ‘‘averaging over channels,’’ when a single channel (whose state is calculated by averaging the parameters of particles in  $\kappa$  channels) is considered instead of the large number of channels. It should be noted that this approximation is possible since the number of channels having a diameter of  $d < 1$  nm and emerging on a square centimeter of the zeolite membrane surface is large:  $\kappa \sim l_c^{-2} \sim 10^{14} \text{ cm}^{-2} \gg 1$ , where  $l_c$  is the characteristic distance between the channels on the membrane surface (Section 2.1). Using relation

(93) and following the method proposed in Section 2.1, we obtain for the adsorption isotherm

$$\begin{aligned} \frac{a}{\sigma_{av}} \theta &= c \frac{P}{p + p_0^{(1)}} + (1 - c) \frac{P}{p + p_0^{(2)}}, \\ \frac{a}{\sigma_{av}} c_1 \theta &= c \frac{P}{p + p_0^{(1)}}, \quad \frac{a}{\sigma_{av}} c_2 \theta = (1 - c) \frac{P}{p + p_0^{(2)}}, \\ p_0^{(i)} &= \frac{1}{1 - c} \left( \frac{1 - c}{c} \right)^c \left( \frac{\alpha^{(2)}}{\alpha^{(1)}} \right)^c \frac{1}{\alpha^{(2)}} \exp \left[ -\beta (\varepsilon_2^{(i)} + F_{int}) \right], \\ & \quad i = 1, \dots, 2, \\ \alpha^{(i)} &= \frac{1}{T} \left( \frac{2\pi\hbar^2}{m^{(i)}T} \right)^{3/2}, \quad i = 1, \dots, 2, \end{aligned} \quad (94)$$

where  $a = L/N_0$  is the mean distance between the seats in a channel,  $c$  is the concentration of the first component in the gas phase above the membrane,  $c_1$  and  $c_2$  are the concentrations of the components in a channel,  $\sigma_1$  and  $\sigma_2$  are the diameters of molecules of the first and second species,  $\sigma_{av} \equiv (\sigma_1 + \sigma_2)/2$  is the average diameter,  $\theta$  is the fill factor of the channel, and  $F_{int}$  has the meaning of the free energy of interaction per particle in the system of atomic particles in the channel. The concentrations of the components in the channel are chosen so that the following relation is satisfied:

$$c_1 + c_2 = 1. \quad (95)$$

In accordance with relations (94), the calculation of the adsorption isotherm is reduced to the calculation of the value of  $F_{int}$ :

$$F_{int} = -T \ln \left( \frac{Q_N}{L^N} \right), \quad (96)$$

where

$$\begin{aligned} Q_N &= \int \cdots \int \exp \left[ -\beta \sum_{i,m} U(x_i^w) \right] dx_1^w \cdots dx_N^w, \\ & \quad i = 1 \dots N, \quad w = 1, 2, \end{aligned} \quad (97)$$

$U(x)$  is the potential energy of interaction of particles of species  $w$  separated by distance  $x$  from each other. It is convenient for subsequent computations to introduce, instead of coordinates  $x_i$  of individual particles in a channel, "pair" coordinates  $\zeta_i^{lm}$ , where  $l = 1, m = 1$  corresponds to the location of two particles of the first species in the vicinity of point  $z_i$ ;  $l = 2, m = 2$  corresponds to the same for particles of the second species, and so on. Obviously, the coordinates are connected through the relation

$$\sum_1^{N_{11}} \zeta_i^{11} = L_1, \quad \sum_1^{N_{12}} \zeta_i^{12} = L_2, \quad \sum_1^{N_{22}} \zeta_i^{22} = L_2. \quad (98)$$

Here  $N_{ij}$  has the meaning of the total number of pairs of closely spaced particles of species  $i$  and  $j$  and  $L_1$  ( $L_2, L_3$ )

is the effective length "occupied" by all pairs  $N_{11}$  ( $N_{12}, N_{22}$ ) of particles. Considering that  $L_1 + L_2 + L_3 = L$  and, as a consequence, the impossibility of mutual penetration of particles through one another, we can reduce integration with respect to coordinates  $x_i$  to integration with respect to coordinates  $\zeta_{lm}$ , which corresponds to summation over all possible configurations of pairs of particles of the first and second species in the channel. Consequently, we obtain the following expression for  $Q_N$  from (97):

$$\begin{aligned} Q_N &= \int_0^\infty \cdots \int_0^\infty \delta \left( \sum_1^{N_{11}} \zeta_i^{11} - L_1 \right) \delta \left( \sum_1^{N_{12}} \zeta_i^{12} - L_2 \right) \\ & \quad \times \delta \left( \sum_1^{N_{22}} \zeta_i^{22} - L_3 \right) \\ & \quad \times \delta(L_1 + L_2 + L_3 - L) \exp \left[ -\beta \sum U(\zeta_i^{km}) \right] \\ & \quad \times \prod_i d\zeta_i^{11} d\zeta_i^{12} d\zeta_i^{22}. \end{aligned} \quad (99)$$

Using the delta function representation in the form of a line integral [45] and carrying out integration with respect to  $\zeta_i^{lm}$  independently for different values of indices  $l$  and  $m$ , we obtain

$$\begin{aligned} Q_N &= \frac{1}{16\pi^4} \oint \cdots \oint e^{S_1 L_1} \left[ \int_0^\infty \exp(\beta U(\zeta_i^{11}) - S_1 \zeta_i^{11}) \right. \\ & \quad \left. \times \prod_i d\zeta_i^{11} \right]^{N_{11}} \\ & \quad \times e^{S_2 L_2} \left[ \int_0^\infty \exp(\beta U(\zeta_i^{12}) - S_2 \zeta_i^{12}) \prod_i d\zeta_i^{12} \right]^{N_{12}} \\ & \quad \times e^{S_3 L_3} \left[ \int_0^\infty \exp(\beta U(\zeta_i^{22}) - S_3 \zeta_i^{22}) \prod_i d\zeta_i^{22} \right]^{N_{22}} \\ & \quad \times e^{S[L - (L_1 + L_2 + L_3)]} dS_1 dS_2 dS_3 dS. \end{aligned} \quad (100)$$

Integrating this relation with respect to  $\zeta_{lm}$  for the simplest form of the intermolecular interaction potential of the hard-sphere type

$$\begin{aligned} U(\xi_i^{11}) &= \begin{cases} 0, & \zeta_i^{11} > \sigma_1 \\ \infty, & \zeta_i^{11} \leq \sigma_1, \end{cases} \\ U(\xi_i^{12}) &= \begin{cases} 0, & \zeta_i^{12} > \sigma_{av} \\ \infty, & \zeta_i^{12} \leq \sigma_{av}, \end{cases} \\ U(\xi_i^{22}) &= \begin{cases} 0, & \zeta_i^{22} > \sigma_2 \\ \infty, & \zeta_i^{22} \leq \sigma_2, \end{cases} \end{aligned} \quad (101)$$

we obtain

$$Q_N = \frac{\Gamma(Nc_1^2 + 1) \Gamma(Nc_1c_2 + 1) \Gamma(Nc_2^2 + 1)}{4\pi} \frac{1}{N} \quad (102)$$

$$\times [L - N(\sigma_1c_1^2 + \sigma_2c_2^2 + 2\sigma_{av}c_1c_2)]^N.$$

Here we have used the definition  $N_{ij} = Nc_i c_j$  ( $N$  is the total number of particles in a channel) and the representation of a factorial in terms of the gamma function,  $N! = \Gamma(N + 1)$ . Eliminating the factor corresponding to an ideal system of atomic particles from relation (102) and substituting the result into (96), we obtain the following expression for  $F_{int}$ :

$$F_{int} = -T \ln(1 - C\theta), \quad C \equiv \frac{1}{\sigma} (\sigma_1c_1^2 + \sigma_2c_2^2 + 2\sigma_{av}c_1c_2). \quad (103)$$

As  $c_1 \rightarrow 0$  or  $c_2 \rightarrow 0$ , expression (103) is transformed into the corresponding expression for the free energy of a one-component system of atomic particles in a 1D channel (Section 2.1). From relations (103) and (94) for the adsorption isotherm of a two-component system of atomic particles, we finally derive the expressions

$$\frac{a}{\sigma_{av}} \theta = c \frac{p(1 - C\theta)}{p(1 - C\theta) + \tilde{p}_0^{(1)}} + (1 - c) \frac{p(1 - C\theta)}{p(1 - C\theta) + \tilde{p}_0^{(2)}},$$

$$\tilde{p}_0^{(i)} = \frac{1}{1 - c} \left( \frac{1 - c}{c} \right)^c \left( \frac{\alpha^{(2)}}{\alpha^{(1)}} \right)^c \frac{1}{\alpha^{(2)}} \exp[-\beta \varepsilon_2^{(i)}], \quad i = 1, \dots, 2. \quad (104)$$

Using these relations and specifying the external conditions, we can obtain the fill factor and the component concentration in the channel. For  $c = 0$  and  $c = 1$ , isotherm (104) transforms into the isotherm for a one-component system of atomic particles, which was obtained in Section 2.1. Let us now analyze the ground state of a mixture in 1D channels. It is known (Section 2.1) that short-lived clusters can be formed in 1D channels in the case of a one-component system of atomic particles. The formation of clusters can apparently be expected in the case of a two-component system of atomic particles also. In order to describe possible transition to an inhomogeneous clustered state, we must calculate and analyze the free energy of the system taking into account fluctuations and the equation determining the amplitude of these fluctuations in the system (equation for the order parameter), which follows from the free energy. Since molecular transport depends on the lifetime of clusters, the analysis of the equation for the order parameter aims at determining the characteristic lifetime of clusters as a function of the channel fill factor and, hence, as a function of pressure, temperature, and composition of the mixture above the membrane. In order to describe the ground state of the 1D system and relaxation process to the ground state, one is to know the free energy  $F$  of the 1D system and two-component functional  $\Delta[n_\alpha]$ ,  $\alpha = 1, 2$ , determined by the relations (39), (44). The functional  $\Delta[n_\alpha]$  can be written in the way of (49):

$$\Delta[n_\alpha] = \Delta_0[n_\alpha] + \Delta_{int}[n_\alpha]. \quad (105)$$

Here  $\Delta_0[n_\alpha]$  is the functional of the non-interacting system and  $\Delta_{int}[n_\alpha]$  corresponds to the particles interaction:

$$\Delta_0[n_\alpha] = \lim_{\tau \rightarrow \infty} \tau^{-1} \int_0^\tau F_0[n_\alpha(x, t)] dt, \quad (106)$$

$$\Delta_{int}[n_\alpha] = \lim_{\tau \rightarrow \infty} \tau^{-1} \int_0^\tau F_1[n_\alpha(x, t)] dt,$$

where  $F_0$  is the free energy per temperature unit of the ideal (non-interacting) system,  $F_1$  is the fluctuation part of the free energy due to interatomic interaction in the mixture. Quantity  $\Delta$  can be expressed in terms of the response function  $\beta_{\alpha\beta}(x, x', t, t')$  of the two-component system, which is defined as

$$\delta n_\alpha(x, t) = \int \beta_{\alpha\beta}(x, x', t, t') eV_\beta^{ext}(x', t') dx' dt', \quad (107)$$

where  $\delta n_\alpha(x, t)$  is the density fluctuation of particles of species  $\alpha$  and  $eV_{ext}(x', t')$  is a weak external field depending on time. Here and in the following, we assume summation over recurrent indices. Response function  $\delta n_\alpha(x, t)$  can be derived by varying directly the mean value of functional  $\Delta$  over  $\delta n(x, t)$  [38]:

$$\beta_{\alpha\beta}(x, x', t, t') = - \left( \frac{\delta^2 \Delta}{\delta n_\alpha(x, t) \delta n_\beta(x', t')} \right)^{-1}. \quad (108)$$

Using this relation, we can obtain the expansion of functional  $\Delta$  into a series in deviations  $\delta n$  of density from its mean value in the case of a multicomponent system. In the Fourier representation, the result has the form

$$\Delta = \frac{1}{2} \int dk d\omega \beta_{\alpha\beta}^{-1}(k, \omega) \delta n_\alpha(k, \omega) \delta n_\beta^*(k, \omega)$$

$$+ \frac{1}{3} \int dk d\omega dk' d\omega' \frac{\delta \beta_{\alpha\beta}^{-1}(k, \omega)}{\delta n_\gamma(k', \omega')}$$

$$\times \delta n_\alpha(k, \omega) \delta n_\beta^*(k, \omega) \delta n_\gamma(k', \omega')$$

$$+ \frac{1}{4} \int dk d\omega dk' d\omega' dk'' d\omega'' \frac{\delta^2 \beta_{\alpha\beta}^{-1}(k, \omega)}{\delta n_\gamma(k', \omega') \delta n_\delta^*(k'', \omega'')}$$

$$\times \delta n_\alpha(k, \omega) \delta n_\beta^*(k, \omega) \delta n_\gamma(k', \omega') \delta n_\delta^*(k, \omega) + \dots \quad (109)$$

Here  $\beta_{\alpha\beta}(k, \omega)$  is the response function of the multi-component system in the Fourier representation, and the asterisk indicates complex conjugation. It follows from the fluctuation-dissipative theorem [98] that response function  $\beta_{\alpha\beta}(k, \omega)$  is directly proportional to the pair distribution; this enables us to calculate  $\beta_{\alpha\beta}(k, \omega)$  for a 1D system with an arbitrary density, for which the pair distribution is known exactly [45]. To calculate  $\Delta$ , we use the local approximation that makes it possible to replace functional derivatives by ordinary derivatives [38]:

$$\frac{\delta^2 \varphi}{\delta \rho(x_1) \delta \rho(x_2)} \approx \delta(x - x_1) \delta(x - x_2) \frac{d^2 \varphi}{d\rho^2}. \quad (110)$$

Using this relation, we obtain from (109)

$$\begin{aligned} \Delta = & \frac{1}{2} \int dk d\omega \beta_{\alpha\beta}^{-1}(k, \omega) \delta n_{\alpha}(k, \omega) \delta n_{\beta}^*(k, \omega) \\ & + \frac{1}{3} \int dk d\omega dk' d\omega' \frac{\partial \beta_{\alpha\beta}^{-1}(k, \omega)}{\partial n_{\gamma}(k', \omega')} \\ & \quad \times \delta n_{\alpha}(k, \omega) \delta n_{\beta}^*(k, \omega) \delta n_{\gamma}(k', \omega') \\ & + \frac{1}{4} \int dk d\omega dk' d\omega' dk'' d\omega'' \frac{\partial^2 \beta_{\alpha\beta}^{-1}(k, \omega)}{\partial n_{\gamma}(k', \omega') \partial n_{\delta}^*(k'', \omega'')} \\ & \quad \times \delta n_{\alpha}(k, \omega) \delta n_{\beta}^*(k, \omega) \delta n_{\gamma}(k', \omega') \delta n_{\delta}^*(k'', \omega'') + \dots \end{aligned} \quad (111)$$

Thus, the evaluation of functional (111) in the one-dimensional case can be reduced to the calculation of response functions. In the case of two-component systems, the equations for determining partial response functions  $\beta$  have the form [38]

$$\begin{aligned} \widehat{\beta}(k, \omega) &= \widehat{\beta}^{(0)}(k, \omega) + \widehat{\beta}^{(0)}(k, \omega) \widehat{R}(k, \omega) \widehat{\beta}(k, \omega), \\ \widehat{\beta}(k, \omega) &\equiv \beta_{ik}(k, \omega) = \begin{pmatrix} \beta_{11}(k, \omega) & \beta_{12}(k, \omega) \\ \beta_{21}(k, \omega) & \beta_{22}(k, \omega) \end{pmatrix}, \\ \widehat{R}(k, \omega) &\equiv R_{ik}(k, \omega) = \begin{pmatrix} R_{11}(k, \omega) & R_{12}(k, \omega) \\ R_{21}(k, \omega) & R_{22}(k, \omega) \end{pmatrix}, \\ \widehat{\beta}^{(0)}(k, \omega) &\equiv \beta_{ik}^{(0)}(k, \omega) = \begin{pmatrix} \beta_{11}^{(0)}(k, \omega) & \beta_{12}^{(0)}(k, \omega) \\ \beta_{21}^{(0)}(k, \omega) & \beta_{22}^{(0)}(k, \omega) \end{pmatrix}. \end{aligned} \quad (112)$$

Here  $\beta_{ik}^{(0)}(k, \omega)$  and  $\beta_{ik}(k, \omega)$  are the partial response functions for noninteracting and interacting particles, respectively. The quantity  $R_{ik}(k, \omega)$  describes the effective dynamic interaction between particles and is defined as

$$R_{ik}(k, \omega) = \frac{\delta^2 \Delta_{\text{int}}}{\delta n_i(k, \omega) \delta n_k(k, \omega)}. \quad (113)$$

Premultiplying expression (112) by  $(\widehat{\beta}^{(0)}(k, \omega))^{-1}$  and postmultiplying it by  $\widehat{\beta}^{-1}(k, \omega)$ , we obtain

$$(\widehat{\beta}^{(0)}(k, \omega))^{-1} = \widehat{\beta}^{-1}(k, \omega) + \widehat{R}(k, \omega). \quad (114)$$

Over long time periods ( $t \gg \tau_{\text{mom}}$ ), function  $R_{ik}(k, \omega)$  can be represented in the form

$$\widehat{R}(k, 0) = (\widehat{\beta}^{(0)}(k, 0))^{-1} - \widehat{\beta}^{-1}(k, 0). \quad (115)$$

In view of homogeneity and the absence of correlations in a system of noninteracting particles, we have  $\widehat{\beta}^{(0)}(k, 0) = \widehat{\beta}^{(0)}(0, 0) = b_{ij}$ , where

$$b_{ij} \equiv -\frac{\partial^2 S}{\partial c_i \partial c_j}, \quad (116)$$

with  $S$  being the entropy of the two-component system of atomic particles divided by temperature in the absence of the intermolecular interaction. In this case, we obtain the following expression for the effective interaction from (115):

$$\widehat{R}(k, 0) = (\widehat{\beta}^{(0)}(0, 0))^{-1} - \widehat{\beta}^{-1}(k, 0). \quad (117)$$

Substituting this expression into (114), we obtain the following relation for response function  $\widehat{\beta}(k, \omega)$ :

$$\widehat{\beta}^{-1}(k, \omega) = (\widehat{\beta}^{(0)}(k, \omega))^{-1} + \widehat{\beta}^{-1}(k, 0) - (\widehat{\beta}^{(0)}(0, 0))^{-1}. \quad (118)$$

In order to calculate the response function  $\widehat{\beta}(k, 0)$  for a system of interacting particles, we can use the fluctuation-dissipative theorem connecting response function  $\widehat{\beta}(k, 0)$  with the pair correlation function for a system of interacting particles:

$$\beta_{ij}(k, 0) = -[b_{ij}^{-1} + c_i c_j \theta^2 \nu_{ij}(k)]. \quad (119)$$

Here  $\nu_{ij}(k)$  is the pair correlation function divided by temperature [46]. Relation (119) is a generalization of the relation (68) for one-component systems to two-component systems.

Thus, the calculation of the response function can be reduced to the calculation of the pair correlation function or function  $g_{ik}$  called a pair distribution [46] and connected with the pair correlation function through the relation

$$\nu_{ij}(k) = g_{ij}(k) - c_i c_j \delta(k). \quad (120)$$

We will calculate the pair distribution using the method described in [45] and determine  $g_{11}(k)$ . Functions  $g_{12}(k)$  and  $g_{22}(k)$  are calculated similarly. Pair distribution  $g_{11}(x)$  can be written in the form [45]

$$g_{11}(k) = \sum_{m=1}^{\infty} \Psi_m^{11}(k) - 1, \quad (121)$$

where the function  $\Psi_m^{11}(k)$  is the Fourier transform of the function  $\Psi_m^{11}(\zeta)$ , which is equal to the probability of finding two particles of the first species separated from each other by  $m$  other particles and by distance  $\zeta$ . Function  $\Psi_m^{11}(k)$  can be written in the form

$$\begin{aligned} \Psi_m^{11}(k) = & \int d\zeta e^{ik\zeta} \left( \left( \sum_{n=0}^{N_{12} N_{22}} \overline{Q}_{m-n-l, n, l}(\zeta) \right. \right. \\ & \left. \left. \cdot \overline{Q}_{N_{11}-(m-n-l), N_{12}-n, N_{22}-l}(L-\zeta) \right) \right. \\ & \left. \times (\overline{Q}_{N_{11}, N_{12}, N_{22}}(L))^{-1} \right), \end{aligned} \quad (122)$$

where  $\overline{Q}_{m,n,l}(\zeta)$  is the configuration integral corresponding to the presence of  $m$  pairs of particles of the first species,  $n$  pairs of particles of the first and second species, and  $l$  pairs of particles of the second species in a channel. For  $m = N_{11}$ ,  $n = N_{12}$ , and  $l = N_{22}$ , the expression for configuration integral  $\overline{Q}_{m,n,l}(\zeta)$  coincides with (98) [45]:

$$\begin{aligned} \overline{Q}_{m,n,l}(\zeta) &= \oint dS [\varphi_{11}(S)]^m [\phi_{12}(S)]^n [\phi_{22}(S)]^l e^{S\zeta}, \\ \phi_{ij}(S) &= \int_0^\infty e^{-Sx} e^{-U_{ij}(x)/T} dx. \end{aligned} \quad (123)$$

Here  $\zeta$  has the meaning of a coordinate and  $\phi_{ij}(S)$  is the Laplace mapping of function  $f_{ij}(x) \equiv \exp(-U_{ij}(x)/T)$ . In the case of an intermolecular interaction potential in the form of that in the hard-sphere model, we have

$$\begin{aligned} U_{11}(x) &= \begin{cases} 0, & x > \sigma_1 \\ \infty, & x \leq \sigma_1, \end{cases} \\ U_{12}(x) &= \begin{cases} 0, & x > \sigma_{av} \\ \infty, & x \leq \sigma_{av}, \end{cases} \\ U_{22}(x) &= \begin{cases} 0, & x > \sigma_2 \\ \infty, & x \leq \sigma_2. \end{cases} \end{aligned} \quad (124)$$

Substituting these relations into (123), we obtain the following expression for the configuration integral:

$$\begin{aligned} \overline{Q}_{m,n,l}(\xi) &= e^{p\xi/T} \left[ \phi_{11}\left(\frac{p}{T}\right) \right]^m \left[ \phi_{12}\left(\frac{p}{T}\right) \right]^n \left[ \phi_{22}\left(\frac{p}{T}\right) \right]^l, \\ \phi_{11}\left(\frac{p}{T}\right) &= \frac{T}{p} e^{-p\sigma_1/T}, \quad \phi_{12}\left(\frac{p}{T}\right) = \frac{T}{p} e^{-p\sigma_{av}/T}, \\ \phi_{22}\left(\frac{p}{T}\right) &= \frac{T}{p} e^{-p\sigma_2/T}. \end{aligned} \quad (125)$$

Here  $p$  has the meaning of one-dimensional ‘‘pressure.’’ Substituting relation (125) into (122), we obtain the following expression for pair distribution  $g_{11}(k)$ :

$$\begin{aligned} g_{11}(k) &= \frac{(p/T) e^{ik\sigma_1}}{(p/T) - ik - (p/T) e^{ik\sigma_1}} \cdot \frac{1}{1 - e^{ik(\sigma_{av} - \sigma_1)}} \\ &\cdot \frac{1}{1 - e^{ik(\sigma_2 - \sigma_1)}}. \end{aligned} \quad (126)$$

In the long-wave approximation ( $0 \leq k \leq 2\pi/\max\{\sigma_1, \sigma_2\}$ ), expression (126) contains no poles and we obtain

$$\begin{aligned} g_{11}(x) &= \frac{1}{\theta_{\text{eff}} \sum_{m,x-ma>0} \frac{(y-m(\sigma_1/a))^{m-1}}{(m-1)!(1/\theta_{\text{eff}} - 1)^m} \\ &\cdot \exp\left(-\frac{y-m}{1/\theta_{\text{eff}} - 1}\right), \end{aligned} \quad (127)$$

$$y = \frac{x}{a(c_1, c_2)}, \quad \theta_{\text{eff}} = \frac{N \cdot a(c_1, c_2)}{L},$$

$$a_{\text{eff}}(c_1, c_2) = \sigma_1 c_1^2 + \sigma_2 c_2^2 + 2\sigma_{av} c_1 c_2.$$

Functions  $g_{12}(x)$  and  $g_{22}(x)$  can be calculated similarly. Substituting expressions (127) and (119) into (118), we obtain the final expression for response function  $\hat{\beta}(k, 0)$ :

$$\begin{aligned} (\hat{\beta}(k, 0))^{-1} &= \begin{pmatrix} -\frac{a_{11}}{1 + a_{11}\theta^2 c_1^2 \Delta\nu_{11}(k)} & -\frac{a_{12}}{1 + a_{12}\theta^2 c_1 c_2 \Delta\nu_{12}(k)} \\ -\frac{a_{21}}{1 + a_{21}\theta^2 c_1 c_2 \Delta\nu_{21}(k)} & -\frac{a_{22}}{1 + a_{22}\theta^2 c_2^2 \Delta\nu_{22}(k)} \end{pmatrix}. \end{aligned} \quad (128)$$

Here

$$\Delta\nu_{ij}(k) \equiv \nu_{ij}(k) - \nu_{ij}(0), \quad a_{ij} \equiv -\frac{\partial^2 F}{\partial c_i \partial c_j}. \quad (129)$$

$F$  is the free energy of a two-component system of atomic particles with interaction, referred to temperature, which can be calculated by differentiating configuration integral  $\overline{Q}_N$  twice with respect to concentration. Function  $\hat{\beta}(k, \omega)$  can be obtained by generalizing the response function of the one-component system of atomic particles,

$$\beta_0^{-1}(k, \omega) = -\frac{1}{\theta} \left(1 + \frac{\omega}{\omega_0}\right) = \frac{\partial^2 F}{\partial \theta^2} \left(1 + \frac{\omega}{\omega_0}\right) \quad (130)$$

derived in Section 2.1, to the case of a two-component mixture:

$$\begin{aligned} (\hat{\beta}^{(0)}(k, \omega))^{-1} &= \begin{pmatrix} \left(1 + \frac{\omega}{\omega_1}\right) b_{11} & \left(1 + \frac{\omega}{\omega_1}\right) b_{12} \\ \left(1 + \frac{\omega}{\omega_2}\right) b_{21} & \left(1 + \frac{\omega}{\omega_2}\right) b_{22} \end{pmatrix}, \end{aligned} \quad (131)$$

$$\omega_1^{(p)} = -iD_1 k^2, \quad \omega_2^{(p)} = -iD_2 k^2.$$

Here  $D_1$ ,  $D_2$ ,  $\omega_1^{(p)}$ , and  $\omega_2^{(p)}$  are the diffusion coefficients and the relaxation frequency spectra for pure components. Substituting relations (128) and (131) into (118), we obtain the following expression for response function  $\beta(k, \omega)$ :

$$(\beta(k, \omega))^{-1} = \begin{pmatrix} \frac{\omega}{\omega_1^{(p)}} b_{11} - \frac{a_{11}}{1 + a_{11} \theta^2 c_1^2 \Delta \nu_{11}(k)} & \frac{\omega}{\omega_1^{(p)}} b_{12} - \frac{a_{12}}{1 + a_{12} \theta^2 c_1 c_2 \Delta \nu_{12}(k)} \\ \frac{\omega}{\omega_2^{(p)}} b_{21} - \frac{a_{21}}{1 + a_{21} \theta^2 c_1 c_2 \Delta \nu_{21}(k)} & \frac{\omega}{\omega_2^{(p)}} b_{22} - \frac{a_{22}}{1 + a_{22} \theta^2 c_2^2 \Delta \nu_{22}(k)} \end{pmatrix}. \quad (132)$$

It is convenient for subsequent analysis to pass to new variables. For a two-component system, the relation  $c_1 + c_2 = 1$  holds and quantity  $\delta n$  can be represented in the form

$$\delta \mathbf{n}(k, \omega) = \begin{pmatrix} 1 \\ -1 \end{pmatrix} \xi(k, \omega), \quad (133)$$

where  $\xi$  can be interpreted as an order parameter. Substituting (133) into (111), we obtain the expression for functional  $\Delta$ :

$$\Delta = \frac{1}{2} \int dk d\omega \Omega |\xi_{k,\omega}|^2 + \frac{2}{3} \int dk d\omega \frac{\partial \Omega}{\partial n} |\xi_{k,\omega}|^2 \xi_{k,\omega} + \int dk d\omega \frac{\partial^2 \Omega}{\partial n^2} |\xi_{k,\omega}|^4 + \dots, \quad (134)$$

where

$$\Omega \equiv (\beta_{11}(k, \omega))^{-1} - (\beta_{12}(k, \omega))^{-1} - (\beta_{21}(k, \omega))^{-1} + (\beta_{22}(k, \omega))^{-1}. \quad (135)$$

Series (134) can be summed and written in the form

$$\Delta = \frac{1}{2} \int dk d\omega |\xi_{k,\omega}|^2 \Omega(n, c + \xi_{k,\omega}, k, \omega). \quad (136)$$

The formal proof of the correctness of representing quantity  $\Delta$  in form (136) without analyzing the convergence of the corresponding series follows from the expansion of expression (136) into a power series of order parameter  $\xi$ . This expansion exactly reproduces series (134) (at least, to within terms on the order of  $\xi^5$ ). Using relations (132), (135), and (136), we can obtain the dependence of functional  $\Delta$  on the wave vector and order parameter of the system. The minimum of functional  $\Delta$  determines the ground state of the system. Substituting relation (132) into (136), evaluating the derivative of  $\Delta$  with respect to the order parameter, and applying the inverse Fourier transformation in frequency  $\omega$  to the resulting relation, we obtain

$$\frac{\partial \xi_k}{\partial t} = -\bar{D} k^2 \frac{\partial (F_1(\xi_k, k))}{\partial \xi_k}, \quad (137)$$

where

$$\bar{D} = \left( \frac{b_{11} - b_{12}}{D_1} + \frac{b_{22} - b_{21}}{D_2} \right)^{-1},$$

$$F_1(\xi_k, k) \equiv \frac{1}{2} \Omega(c + \xi_k, k) \xi_k^2,$$

$$\Omega(c, k) = -\frac{a_{11}}{1 + a_{11} \theta^2 c_1^2 \Delta \nu_{11}(k)} + \frac{2a_{12}}{1 + a_{12} \theta^2 c_1 c_2 \Delta \nu_{12}(k)} - \frac{a_{22}}{1 + a_{22} \theta^2 c_2^2 \Delta \nu_{22}(k)}. \quad (138)$$

Equation (137) has the same form as the equation usually used for the order parameter. The role of the order parameter is played in this case by the quantity defined by relation (133). It should be noted that the order parameter here could be either positive or negative. The cases when  $\xi > 0$  and  $\xi < 0$  correspond to the density fluctuation of the first and the second components, respectively. The role of the diffusion coefficient is played by quantity  $\bar{D}$  depending on the fill factor and the concentration of components in channels via coefficients  $a_{ij}$  and  $b_{ij}$  defined by relations (116) and (128). It should be noted that the concentration of the components in a channel (and its fill factor) could be determined unambiguously from isotherm (104) proceeding from the pressure, temperature, and composition of the system of atomic particles. Analysis of functional  $F_1$  as a function of order parameter  $\xi$  and wave vector  $k$  makes it possible to investigate the possibility for a transition of the system to an inhomogeneous state. For example, when the minimum of functional  $F_1$  is attained for  $\xi \neq 0$ ,  $k = 0$ , a conventional phase transition to a homogeneous state takes place [99]. The minimum at  $\xi = 0$ ,  $k \equiv k_c \neq 0$  corresponds to the propagation of a density wave over a distance of  $r \sim k_c^{-1}$ . In the case when the minimum is attained at  $\xi \neq 0$  and  $k \neq 0$ , a transition to an inhomogeneous state with clusters formed in the system is realized [99]. Local minima here determine metastable states. Figure 13 shows the graphs illustrating the dependence of  $F_1$  on order parameter  $\xi_k$  and wave vector  $k$  for a mixture in which one of the gases (first) is a strong sorbate, while the other gas is a weak sorbate. The chosen parameters ( $a = 3.8 \text{ \AA}$ ,  $\sigma_1 = 4.3 \text{ \AA}$ ,  $\sigma_2 = 3.6 \text{ \AA}$ ,  $\varepsilon_1 = 0.61 \text{ eV}$ ,  $\varepsilon_2 = 0.38 \text{ eV}$ ,  $p = 2000 \text{ kPa}$ , and  $T = 300 \text{ K}$ ) correspond to a methane-butane molecular mixture [51] and make it possible to describe adsorption and fluxes of these one-component gases in zeolite membranes. It should be noted that the choice of parameters  $p$ ,  $T$ , and  $c$  determines unambiguously the filling factor  $\theta$  and concentrations  $c_1$  and  $c_2$  of gases in a channel.

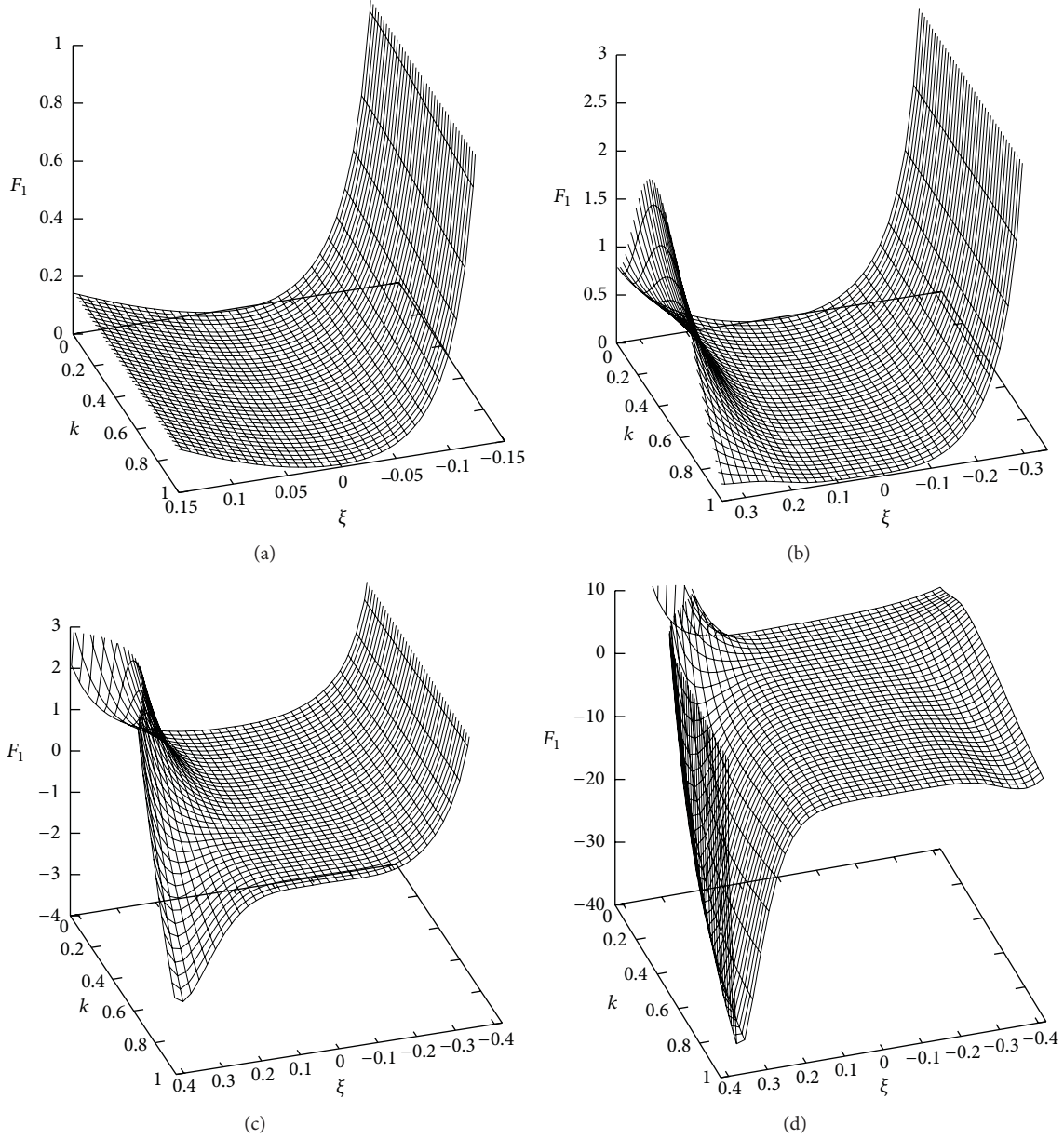


FIGURE 13: Dependence of free energy  $F_1$  on the order parameter and wave vector for various concentrations of the first component in the mixture: (a)  $c = 0.1$  ( $\theta = 0.67$ ), (b)  $c = 0.25$  ( $\theta = 0.71$ ), (c)  $c = 0.3$  ( $\theta = 0.74$ ), and (d)  $c = 0.45$  ( $\theta = 0.75$ ).

For low concentrations of the first component in a gas mixture and for fill factors  $\theta \leq 0.7$ , functional  $F_1$  has only one minimum at  $\xi = 0$ ,  $k = 0$  (Figures 13(a) and 13(b)). This corresponds to a homogeneous state of the system. An increase in the concentration of the first component leads to the emergence of local minima in functional  $F_1$ .

In this case, the global minimum is shifted to point  $\xi = \xi_c > 0$ ,  $k = k_c$ . In this case, the ground state of the system becomes spatially inhomogeneous, which corresponds to the formation of clusters in the system. This situation will be analyzed in greater detail later. Equation (137) for the order parameter also allows us to calculate the characteristic relaxation times for the emerging density fluctuation depending on external conditions. For this purpose, we expand

functional  $F_1(\xi_k, k)$  into a series in the vicinity of  $\xi_k = 0$  to within the first nonvanishing term:

$$F_1(\xi_k, k) \sim \lambda(k) \xi_k^2. \quad (139)$$

Substituting (139) into (137), we obtain

$$\frac{\partial \xi_k}{\partial t} = -\frac{\xi_k}{\tau}, \quad \tau = (2\lambda(k) \bar{D} k^2)^{-1}. \quad (140)$$

The quantity  $\tau$  is the lifetime of the  $k$ th mode of the density fluctuation emerging in the vicinity of  $\xi_k = 0$ . The curves describing the lifetime of the emerging fluctuation as a function of the wave vector for different mixture compositions are shown in Figure 14. It can be seen from Figure 14 that,

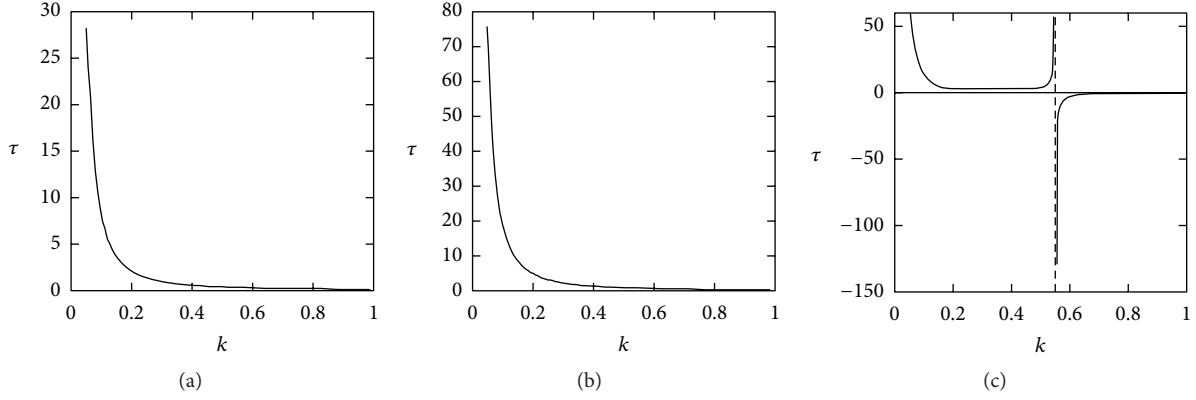


FIGURE 14: Dependence of lifetime  $\tau$  on wave vector  $k$  for  $c = 0.1$  (a), 0.3 (b), and 0.45 (c).

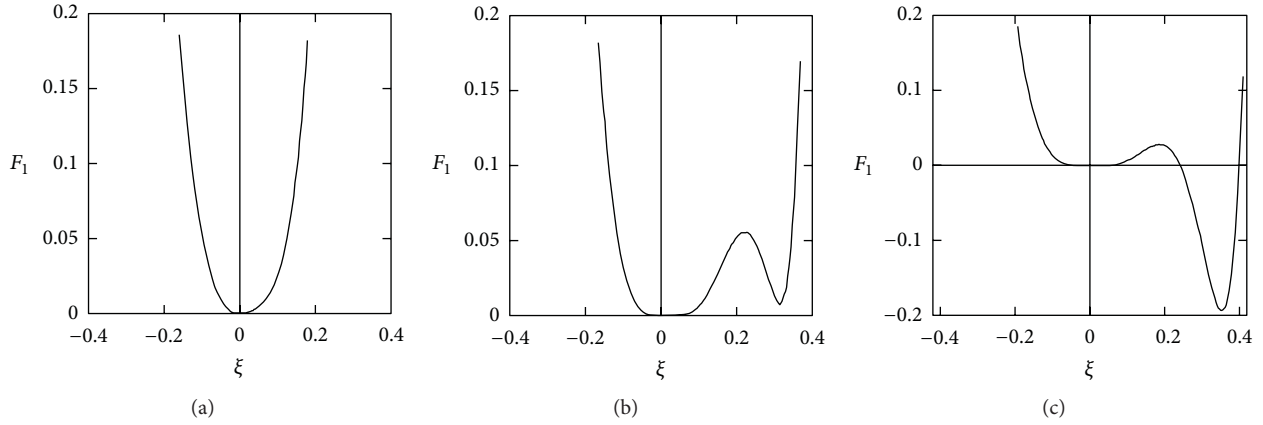


FIGURE 15: Dependence of free energy  $F_1$  on the order parameter for different values of the wave vector for  $c = 0.3$ :  $k = 0.1$  (a), 0.3 (b), and 0.5 (c).

for a low concentration of the highly adsorbed component, the lifetime decreases monotonically with increasing wave vector, while the free energy has a minimum at  $\xi = 0$ . From the physics standpoint, this means that the state of the system in a channel for a given composition of the mixture is homogeneous and the growth of clusters is energetically disadvantageous. It should be noted that the fill factor of the channel is small in this case, but short-lived clusters with the lifetime

$$\tau \sim \frac{r^2}{D} = \frac{r^2}{D_0} \exp\left(\frac{E_a}{T}\right) \quad (141)$$

can be formed due to density fluctuations. Here  $D = D_0 \exp(-E_a/T)$  is the diffusion coefficient of solitary particles,  $E_a$  is the diffusion activation energy, and  $r$  is the characteristic size of fluctuations. Characteristic size  $r$  is determined, as in Section 2.1, from the position of the extremum of the imaginary part of the spectrum divided by the square of the wave vector. It should be noted that the value of  $r$  increases with the fill factor of the channel Section 2.1. Expression (142) can be derived by expanding order parameter (137) into a series in the vicinity of  $\xi = 0$ .

For low concentrations, expression (141) coincides with the characteristic diffusion decay time for density fluctuations.

An increase in the concentration of the first component of the mixture to  $c = 0.3$  elevates the fill factor of the channel to  $\theta = 0.74$  (see Figure 13(c)), while  $F_1$  acquires two more minima for  $k \sim 1$ . Figure 15 shows the dependences of the free energy on the order parameter for different values of the wave vector at  $c = 0.3$ . It can be seen from the figure that the free energy minimum is attained at point  $\xi = 0$  for values of the wave vector  $0 < k < 0.4$ . For  $k \approx 0.5$ , functional  $F$  has two minima (at  $\xi_c^{(0)} = 0$  and  $\xi_c^{(1)} = 0.35$ ), and the state with  $\xi_c^{(1)}$  is separated from the state with  $\xi_c^{(0)}$  by a potential barrier. Since the global minimum is attained at  $\xi = \xi_c^{(1)}$ , the state with  $\xi_c^{(0)}$  is metastable. The ground state of the system is attained at  $\xi = \xi_c^{(1)}$  and is clustered. It should be noted that, in accordance with formula (133), clusters of the first component are formed in the channel since  $\xi_c^{(1)} > 0$ .

The lifetime of the clusters can be determined by passing from (137) for the order parameter to a stochastic differential equation (Langevin equation) and the corresponding Fokker-Planck equation via the introduction of additive noise. Steady-state solutions to the Fokker-Planck equation define

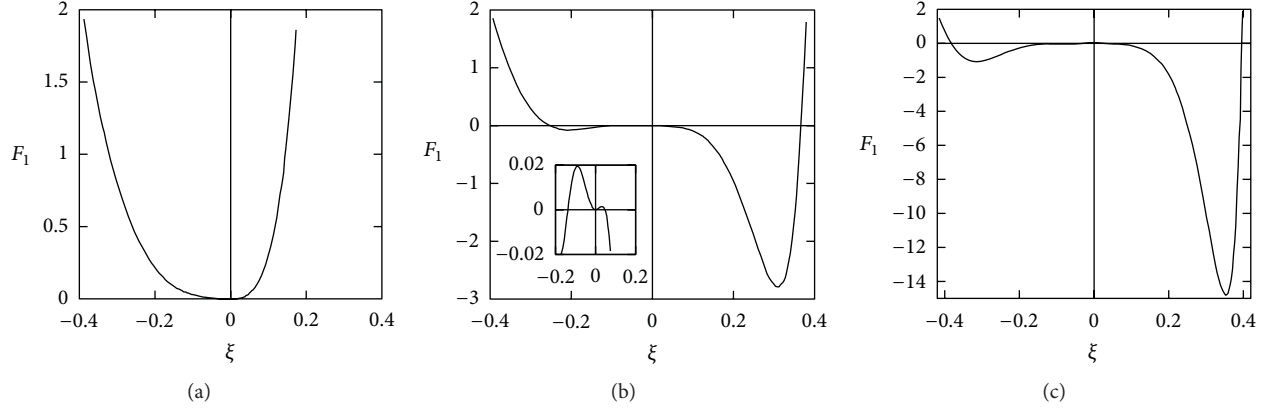


FIGURE 16: Dependence of free energy  $F_1$  on the order parameter for different values of the wave vector for  $c = 0.45$ :  $k = 0.1$  (a),  $0.3$  (b), and  $0.5$  (c).

the probability for the system being in the state described by order parameter  $\xi_c^{(1)}$ . For the lifetime, we have

$$\tau \sim \frac{r^2}{D_0} \exp\left(\frac{E_a}{T} - \delta F\right), \quad (142)$$

$$\delta F = F_1(c + \xi_c^{(1)}, k_c) \cdot T.$$

The decay of a cluster formed in the system occurs via overcoming an energy barrier of height  $\delta F$ . From the standpoint of physics, this can be interpreted as an effective increase in the diffusion activation energy for the particles in the cluster. However, for  $c = 0.3$ , the barrier height is small ( $\delta F \sim 0.2T$ ; see Figure 13(c)), and lifetime (142) is comparable to time (141). A further increase in the first component concentration in the mixture leads to negative values of the lifetime for a certain value of  $k = k_c < 1$  (see Figure 14(c)). In this case, clusters with a size of  $r \sim k_c^{-1}$  are formed in the channel; for  $k < k_c$ , fluctuations decay over a finite time, while for  $k > k_c$ , the emerging density fluctuations evolve. Such a situation is typical of transitions to an inhomogeneous condensate state [99].

The curves describing the dependence of the free energy on the order parameter for different values of the wave vector are shown in Figure 16. Since functional  $F_1$  has a single minimum at  $\xi = 0$  for  $k \sim 0$ , the state of particles in the channel is homogeneous. However, as the wave vector increases, curve  $F_1(\xi)$  acquires two more minima separated from the state with  $\xi = 0$  by potential barriers. A further increase in the wave vector leads to disappearance of the barriers between the state with  $\xi = 0$  and the states corresponding to two other minima of  $F_1$ , and the state with  $\xi = 0$  becomes unstable.

Thus, for a low concentration of the highly adsorbed component, the fill factor of the channel is small and the state of the system in the channel is homogeneous. As the concentration of the highly adsorbed component increases, the fill factor of the channel increases, and short-lived clusters of the highly adsorbed component can be formed in the channel. A further increase in the concentration (and the fill factor of the channel) leads to an increase in the lifetime of

the clusters formed in the channel. At a certain concentration of the highly adsorbed component, the clusters in the channel become long lived and the ground state of the system becomes clustered.

The formation of clusters of one of the components in a channel may strongly affect the transport of the gas through the membrane (see Section 2.1). In the next chapter, partial gas fluxes through the membrane will be calculated, and the effect of clusters on the mechanisms of transport will be analyzed.

**2.4.2. Transport in a Two-Component Gas in a High-Density 1D System.** In order to calculate partial fluxes and to analyze the transport, we will use the approach proposed in Section 2.1. It will be shown in the following that the evaluation of the flux can be reduced to the calculation of the relaxation frequency spectra  $\omega(\mathbf{k})$  for density fluctuations of the components. We can judge the mechanism of particle transport in a subnanometer channel from the type of the dependence of the spectrum on the wave vector of the system. We can write the expression determining the relaxation of the Fourier component  $n(k, t)$  of the number density of particles in a channel in the case of an arbitrary density  $n(k, t)$  under the conditions of slight deviation from equilibrium (see Section 2.1 and [100]):

$$\dot{n}(k, t) = i\omega(k) n(k, t). \quad (143)$$

It follows from this relation that the equation for fluctuation amplitude  $\delta n$  can be written in the form

$$\delta \dot{n}(k, t) = i\omega(k) \delta n(k, t), \quad (144)$$

where  $\omega(k)$  is the relaxation frequency spectrum for the system under study; in the case of diffusion of noninteracting particles, this spectrum has the form [98]

$$\omega = \omega_0(k) = -iDk^2. \quad (145)$$

Equation (144) describes relaxation of the  $k$ th component of density fluctuation for an arbitrary value of the wave vector. In

particular, this equation for  $k \neq 0$  makes it possible to describe the relaxation of density fluctuations and the propagation of a perturbation over a finite-size cluster in the case of its formation. For  $k \rightarrow 0$ , (144) describes the relaxation of density fluctuation on a large spatial scale. This quantity is associated with macroscopic fluxes. In order to calculate the fluxes, we write the continuity equation

$$\dot{n} + \frac{\partial j}{\partial x} = 0 \quad (146)$$

and apply the Fourier transformation to this equation:

$$ikj(k, t) = -\dot{n}(k, t). \quad (147)$$

Substituting (143) into (147), we obtain the following relation for flux  $j(k)$ :

$$j(k, t) = \frac{n(k, t) \omega(k)}{k}. \quad (148)$$

For partial fluxes, we have

$$j_i(k, t) = \frac{n_i(k, t)}{k} \omega_i(k), \quad (149)$$

where  $n_i$  is the density of the  $i$ th component and  $\omega_i$  is the corresponding spectrum. The total gas flux is defined as the sum of partial fluxes of the components:

$$\sum_{i=1}^2 j_i(k, t) = j(k, t). \quad (150)$$

It follows from (149) that partial fluxes are determined by relaxation frequency spectra  $\omega_i(k)$ . Thus, the problem is reduced to computing these spectra. The relaxation frequency spectra can be determined from the condition of the existence of nonzero density fluctuations for each component in an arbitrarily weak external field. Consequently, applying the Fourier transformation to (107), we find that the relaxation frequency spectrum can be determined by solving the following system of homogeneous equations:

$$\beta^{-1}(k, \omega) \begin{pmatrix} 1 \\ -1 \end{pmatrix} = 0. \quad (151)$$

Here matrix  $\beta^{-1}(k, \omega)$  of the response functions is defined by relation (132). In view of  $\delta$ -function singularities for  $k \rightarrow 0$  that emerge in pair correlation functions (120) appearing in (132), we must calculate spectra  $\omega_i(k)$  and the values of  $\omega_i(k=0)$ , after which the renormalization procedure must be carried out. Using (132) and passing to the limit  $k \rightarrow 0$  for spectra  $\omega_i(k=0)$ ,

$$\beta^{-1}(0, \omega) \begin{pmatrix} 1 \\ -1 \end{pmatrix} = \begin{pmatrix} \frac{\omega}{\omega_1^{(p)}} b_{11} - \frac{\omega}{\omega_1^{(p)}} b_{12} + a_{11} - a_{12} \\ \frac{\omega}{\omega_2^{(p)}} b_{22} - \frac{\omega}{\omega_2^{(p)}} b_{21} + a_{22} - a_{21} \end{pmatrix} = 0, \quad (152)$$

where  $a_{ij}$ ,  $b_{ij}$ ,  $\omega_1^{(0)}$ , and  $\omega_2^{(p)}$  are defined by relations (116), (129), and (131). For  $\omega^{(0)} \equiv \omega_i(k=0)$ , we obtain from relation (152)

$$\omega_1^{(0)} = -\frac{\omega_1^{(p)}(a_{11} - a_{12})}{b_{11} - b_{12}}, \quad (153)$$

$$\omega_2^{(0)} = -\frac{\omega_2^{(p)}(a_{22} - a_{21})}{b_{22} - b_{21}}.$$

On the other hand, substituting (132) into (152), we obtain the following expressions for relaxation frequency spectra  $\omega_i(k)$  of the system under investigation:

$$\tilde{\omega}_1(k) = \frac{iD_1 k^2}{b_{11} - b_{12}} \left[ \frac{1}{\theta^2 c_1^2 \nu_{11}(k) + b_{11}^{-1}} - \frac{1}{\theta^2 c_1 c_2 \nu_{12}(k) + b_{12}^{-1}} \right],$$

$$\tilde{\omega}_2(k) = \frac{iD_2 k^2}{b_{22} - b_{21}} \left[ \frac{1}{\theta^2 c_2^2 \nu_{22}(k) + b_{22}^{-1}} - \frac{1}{\theta^2 c_1 c_2 \nu_{21}(k) + b_{21}^{-1}} \right]. \quad (154)$$

Tildes indicate that  $\tilde{\omega}_i(k=0) \neq \omega_i^{(0)}$  ( $\omega_i^{(0)}$  are defined in relations (153)).

We will carry out the renormalization procedure for spectra (154) taking into account relations (153), that is, imposing the requirement

$$\tilde{\omega}_i = \omega_i^{(0)}(k=0). \quad (155)$$

Taking into account the value of  $\omega_i^{(0)}$ , we find from relations (153) and (154) that

$$a_{11} - a_{12} = \frac{b_{11}}{b_{11} \theta^2 c_1^2 \nu_{11}(k) + 1} - \frac{b_{12}}{b_{12} \theta^2 c_1 c_2 \nu_{12}(k) + 1} \quad (156)$$

or

$$a_{11} = \frac{b_{11}}{b_{11} \theta^2 c_1^2 \nu_{11}(k) + 1}, \quad a_{12} = \frac{b_{12}}{b_{12} \theta^2 c_1 c_2 \nu_{12}(k) + 1}. \quad (157)$$

Similarly, for  $a_{22}$ , we have

$$a_{22} = \frac{b_{22}}{b_{22} \theta^2 c_2^2 \nu_{22}(k) + 1}. \quad (158)$$

In order to separate singularities of pair correlation function  $\nu_{ij}(k)$  for  $k \rightarrow 0$ , we expand it into a series in the vicinity of  $k=0$  to within first-order terms. Using relations (154), we then obtain

$$\tilde{\omega}_1(k) = \frac{iD_1 k^2}{b_{11} - b_{12}} \left[ \frac{1}{\theta^2 c_1^2 (\nu_{11}(0) + k\nu'_{11}(k)) + b_{11}^{-1}} - \frac{1}{\theta^2 c_1 c_2 (\nu_{12}(0) + k\nu'_{12}(k)) + b_{12}^{-1}} \right],$$

$$= \frac{iD_1 k^2}{b_{11} - b_{12}} \left[ \frac{a_{11}}{1 + ka_{11} \theta^2 c_1^2 \nu'_{11}(k)} - \frac{a_{12}}{1 + ka_{12} \theta^2 c_1 c_2 \nu'_{12}(k)} \right]. \quad (159)$$

Taking into account the long-wave approximation and the smallness of  $k$ , replacing the derivative in the last expression by the difference  $kv'_{ik}(k) \approx v_{ij}(k) - v_{ij}(0)$ , omitting primes, and carrying out similar calculations for  $\omega_2$ , we finally obtain

$$\omega_1(k) = \frac{iD_1 k^2}{b_{11} - b_{12}} \left[ \frac{a_{11}}{1 + a_{11} \theta^2 c_1^2 (v_{11}(k) - v_{11}(0))} - \frac{a_{12}}{1 + a_{12} \theta^2 c_1 c_2 (v_{12}(k) - v_{12}(0))} \right],$$

$$\omega_2(k) = \frac{iD_2 k^2}{b_{22} - b_{21}} \left[ \frac{a_{22}}{1 + a_{22} \theta^2 c_2^2 (v_{22}(k) - v_{22}(0))} - \frac{a_{21}}{1 + a_{21} \theta^2 c_1 c_2 (v_{21}(k) - v_{21}(0))} \right]. \quad (160)$$

Using relations (104), (149), and (161) and passing to the limit for  $k \rightarrow 0$ , we can obtain the dependence of partial fluxes of the components on the pressure, temperature, and composition of the mixture. For  $k \neq 0$ , expressions (144) and (160) enable us to analyze the relaxation mechanism of the emerging density fluctuation with a characteristic size of  $r \approx 2\pi/k$ .

In order to analyze the experimentally observed partial fluxes, it is convenient to pass to the coordinate representation. Spectra (160) have the real and imaginary parts since pair correlation function  $v_{ij}(k)$  is a complex quantity in accordance with relations (120) and (125). Separating the real and imaginary parts of the spectra and applying the inverse Fourier transformation to expression (149), we obtain

$$j_i = n_i \Psi_i - D_i \frac{\partial n_i}{\partial x},$$

$$\Psi_i = \text{Re } \omega_i \left( k \rightarrow \frac{2\pi}{L} \right), \quad (161)$$

$$D_i = \text{Im } \frac{\omega_i(k)}{k^2} \Big|_{k \rightarrow 2\pi/L}.$$

Here  $D_i$  is the diffusion coefficient of a component,  $L$  is the channel length, and  $\Psi$  is the term emerging due to the mutual effect on the mixture components in a channel for large fill factors. It should be noted that, since  $L \gg r_c$ , where  $r_c$  is the characteristic size of clusters, passing to the limit for  $k \rightarrow 2\pi/L$  in relation (161) corresponds to averaging over characteristic scales of inhomogeneities in the case when the ground state of the system is clustered. Separating the terms linear in the wave vector from the real part of the spectrum, we obtain the following expression for  $\Psi$ :

$$\Psi_i = -D_i \frac{1}{T} \frac{\partial U_i}{\partial x} + V_i. \quad (162)$$

Here the first term describes the transport of molecules of the  $i$ th component, which is induced by the effective intermolecular interaction, while the second term has the meaning of the "drag" effect familiar in the kinetics of mixtures. Substituting

(162) into (161), we obtain the final expression for partial fluxes:

$$j_i = -D_i \frac{\partial n_i}{\partial x} - D_i \frac{n_i}{T} \frac{\partial U_i}{\partial x} + V_i n_i. \quad (163)$$

Thus, it follows from this equation that the partial flux is the sum of three terms. The first term corresponds to diffusion transport, while the second term emerges due to field diffusion. These two terms in the  $k$  representation can be combined into one by introducing the effective diffusion coefficient

$$D_i = D_i^{(0)} \left( 1 + \frac{n_i}{T} U(k) \right). \quad (164)$$

It was shown in the previous section that, for large filling factors, clusters are formed in the system. The mechanism of density relaxation may be different for the case of transport over the characteristic scale  $L$ , when  $2\pi\sigma_{av}/L \ll 1$  and  $k \rightarrow 0$  (which corresponds to macroscopic transport of gas components through the channel), and for the case when  $k \neq 0$ , which corresponds to relaxation over distances comparable to the size of clusters formed in the system. To prove this, we must analyze dependences  $\Delta v_{ij}(k)$ . In order to avoid cumbersome formulas, we consider this problem in greater detail in the limiting case of  $c_1 = 1$ , which corresponds to a one-component mixture.

Passing to the limit for  $c_1 \rightarrow 1$  in (160), we obtain the relaxation frequency spectrum for a one-component system; it is easy to obtain (70). It should be noted that, in accordance with the relation (70), the pair distribution and, hence, the pair correlation function associated with it depend not on the wave vector  $k$ , but on the product  $ik$ :

$$\theta v(k) \equiv \theta v(ik). \quad (165)$$

Let us now write relation (164) in the form

$$\omega(k) = -\frac{iD_0 k^2}{1 + \theta v(0) + \theta v(k) - \theta v(0)} = -\frac{iD_0 k^2}{1 + \theta v(0) + \theta \Delta v}$$

$$= -\frac{iD_0 k^2}{1 + \theta v(0) + \theta \text{Re } \Delta v + \theta i \text{Im } \Delta v}. \quad (166)$$

Separating the real and imaginary parts from relation (165), we obtain

$$\omega(k) = -\frac{iD_0 k^2 \left( (1 - \theta)^2 + \theta \text{Re } \Delta v \right)}{\left( (1 - \theta)^2 + \theta \text{Re } \Delta v \right)^2 + \left( \theta \text{Im } \Delta v \right)^2}$$

$$- \frac{D_0 k^2 \theta \text{Im } \Delta v}{\left( (1 - \theta)^2 + \theta \text{Re } \Delta v \right)^2 + \left( \theta \text{Im } \Delta v \right)^2}. \quad (167)$$

Here we have used the fact that

$$1 + \theta v(0) \approx (1 - \theta)^2. \quad (168)$$

This relation follows from the known relation [46]

$$\frac{\partial p}{\partial \theta} \approx \frac{1}{1 + \theta v(0)} \quad (169)$$

describing the increase in the compressibility with density. Using relation (165), we now expand  $\Delta\nu$  to within first-order terms:

$$\Delta\nu = \left. \frac{\partial\theta\nu(k)}{\partial(ik)} \right|_{k=0} ik \equiv i\theta\nu'(0)k. \quad (170)$$

The value of  $\nu'(0)$  is finite for  $\theta \neq 0$ . For example, using direct expansion into the Taylor series, we can obtain

$$\theta\nu'(0) = -\theta + \frac{4}{3}\theta^2 - \frac{1}{2}\theta^3. \quad (171)$$

Substituting relation (170) into (167), we get

$$\omega(k) \approx -\frac{iD_0k^2(1-\theta)^2}{(1-\theta)^4 + (\theta\nu'(0))^2k^2} - \frac{D_0k^3\theta\nu'(0)}{(1-\theta)^4 + (\theta\nu'(0))^2k^2}. \quad (172)$$

To calculate the fluxes for high densities ( $\theta \sim 1$ ), we must consider two limiting transitions in relation (172): for  $\theta \rightarrow 1$  and  $k \rightarrow 0$ . From the standpoint of physics, the transition for  $\theta \rightarrow 1$  and  $k \neq 0$  corresponds to the analysis of transport in a dense cluster. The transition for  $k \rightarrow 0$  and arbitrary  $\theta$  is equivalent to analysis of diffusion in a channel of length  $L \gg r_c$ , where  $r_c$  is the characteristic size of a cluster. For  $\theta \rightarrow 1$ , we obtain, instead of relation (172),

$$\omega(k) = -\frac{D_0k}{\theta\nu'(0)}. \quad (173)$$

This relation shows that spectrum  $\omega(k)$  corresponds to the hydrodynamic mode [46], for which quantity  $D_0/\nu'(0)$  is the effective velocity of sound.

Passing in relation (172) to the limit for  $k \rightarrow 0$  and retaining the lowest order in wave number  $k$ , we obtain

$$\omega(k) = -\frac{iD_0k^2}{(1-\theta)^2}. \quad (174)$$

This relation shows that the spectrum in this case is of the diffusion type with the diffusion coefficient

$$D \approx \frac{D_0}{(1-\theta)^2}, \quad (175)$$

which increases indefinitely as  $\theta \rightarrow 1$ .

It should be noted that, in accordance with (172), both relaxation mechanisms (hydrodynamic and diffusion) operate in the system when  $k \neq 0$  and  $\theta \neq 1$ . From the standpoint of physics, this corresponds to the diffusion transport between clusters (diffusion mode), over which density perturbations propagate (hydrodynamic mode). In spite of different interpretations of the sequence of limiting transitions, the calculated dependences of fluxes on external conditions are found to be equivalent from the physics standpoint. This is due to the fact that the hydrodynamic component is manifested in the second case in the increase in the effective diffusion coefficient  $D \approx D_0/(1-\theta)^2$  for high values of fill factor  $\theta$ .

In the two-component case, the transition for  $k \rightarrow 0$  corresponds to the transition from relation (160) to (153).

It can be seen from relation (153) that the obtained spectra are of the diffusion type since  $\omega_j^{(0)} = -iD_jk^2$ ,  $j = 1, 2$ , while quantities  $a_{ij}$  and  $b_{ij}$  are independent of  $k$ . The limiting transition for  $\theta \rightarrow 1$  in the two-component case involves considerable computational difficulties. However, the above analysis shows that the relaxation frequency spectra for the components also acquire a hydrodynamic mode in view of the dependence of pair correlation function (120) on factor  $ik$  for  $\theta \rightarrow 1$ .

Depending on the sequence of limiting transition, a decisive role in relation (163) is played either by the term corresponding to diffusion or the nongradient (hydrodynamic) part of the flux. Since the gas flux for arbitrary fill factors is measured in experiments on the penetrability of the membrane over large distance ( $L \gg r_c$ ,  $k \rightarrow 0$ ), the limiting transition for  $k \rightarrow 0$  should be performed first. In this case, the effects associated with the formation of clusters are taken into account in the dependence of the diffusion coefficient on the concentration and fill factor of the channel. Numerical calculations show that the last term in relation (160) is insignificant in the entire range of concentrations and fill factors of the channel. Thus, the relaxation frequency spectrum of a two-component system can be treated as a diffusion spectrum in the entire range of concentrations and fill factors, where the role of diffusion coefficient is played by a quantity taking into account clustering of the components in the channel.

It should be noted that for calculating response function (132), relaxation frequency spectra (160), and, as a consequence, partial fluxes (163), we used the fluctuation-dissipative theorem (119) presuming the homogeneous ground state of the system. In the case when the ground state of the system is clustered (see Figure 13(d)), the kinetic version of the fluctuation-dissipative theorem [98] should be used:

$$\begin{aligned} & \langle \delta n(x, t) \delta n(x', t) \rangle \\ & = -T \int_0^\infty \beta(x, x', t, \tau) (f(x, \tau) - f(x', \tau)) d\tau, \end{aligned} \quad (176)$$

where  $f(x, \tau)$  is the probability of a particle being located at point  $x$ . In accordance with the detailed balancing principle, in the case when states  $x$  and  $x'$  differ from the equilibrium state insignificantly, we have

$$f(x', t) \sim f(x, t) \exp\left(\frac{\Delta E}{T}\right), \quad (177)$$

where  $\Delta E$  is the energy difference between states  $x$  and  $x'$ . Using this relation, we obtain the following expression for the fluctuation-dissipative theorem:

$$\begin{aligned} & \langle \delta n(k, \omega) \delta n(k', \omega) \rangle \\ & = -T \int dx dx' dt \exp(ikx) \exp(ik'x') \exp(i\omega t) \\ & \quad \times \int_0^\infty \beta(x, x', t, \tau) \exp\left(\frac{\Delta E}{T}\right) d\tau. \end{aligned} \quad (178)$$

Applying the Fourier transformation to this relation and using (151), we obtain the relaxation frequency spectrum in the form

$$\omega^{(\text{new})}(k) = \omega(k) \exp\left(-\frac{\Delta E}{T}\right). \quad (179)$$

Thus, the application of relation (176) instead of (132) leads to the emergence of an additional exponential term in relation (163):

$$j_i(k, t) = \frac{n_i(k, t)}{k} \omega_i(k) \exp\left(-\frac{\Delta E}{T}\right), \quad (180)$$

where  $\Delta E$  is the depth of the potential well occupied by the system. In the case of small fill factors of the channel, the state of the system is homogeneous and  $\Delta E = 0$  (see Figure 13(a)). Then relation (180) transforms into (163). As the fill factor of the channel increases, the state of the system becomes clustered. For  $\Delta E \ll T$ , the exponential in relation (180) can be disregarded, and the flux virtually coincides with the flux calculated for a homogeneous state. This is due to the fact that expression (142) for the lifetime of clusters practically coincides with expression (141) for the lifetime of clusters in a homogeneous state. In this case, as noted previously, density excitation propagates via a cluster, leading to an increase in the effective diffusion coefficient. A further increase in the fill factor of the channel increases the value of  $\Delta E$ . The flux decreases thereby, which can be explained by an increase in the lifetime of the clusters formed in the channel. As a result, the mechanism of excitation transport via a cluster is not realized.

Thus, for small fill factors of the channel, the transport in the system follows the diffusion mode. This can be demonstrated by passing to the limit of small fill factors  $\theta$  in relation (160). Then the second term in the denominator becomes insignificant and the spectra are reduced to diffusion spectra (153). An increase in the fill factor results in the formation of clusters. It was shown in the previous section that, depending on the fill factor of the channel, the clusters formed may be either short lived or stable in the case when the ground state of the system is clustered. For short-lived clusters (see Figure 13(b)), the transport between clusters occurs through diffusion, while the transport over clusters occurs through a rapid barrier-free transfer of density excitation, and the arrival of a particle from one side of a cluster leads to the emergence of a particle from the other side [100]. In this case, the spectra contain both the diffusion and the hydrodynamic modes, and the effective diffusion coefficient increases in accordance with (175). An increase in the fill factor of the channel reduces the distance between clusters and increases their size. Since the transport over a cluster is faster than the diffusion transport, the effective diffusion coefficient and the partial flux increase. However, an increase in the fill factor also increases the lifetime of the clusters formed in the channel; as a result, the rate of excitation transfer over a cluster decreases. In the case when a cluster is stable (see Figure 13(d)), the transport of excitation over the cluster is ruled out, and the presence of such a cluster in the channel leads to blocking of transport in the system.

Using relations (160) and (180), we can calculate the partial gas fluxes proceeding from the data on the penetrability for pure components. Figures 17(a) and 17(b) show the dependence of partial fluxes on the mixture composition in the case when both gases are slightly adsorbed. The energies of interaction and the diameters of particles correspond to a methane-argon gas mixture ( $a = 3.8 \text{ \AA}$ ,  $\sigma_1 = 3.6 \text{ \AA}$ ,  $\sigma_2 = 3.0 \text{ \AA}$ ,  $\varepsilon_1 = 0.38 \text{ eV}$ ,  $\varepsilon_2 = 0.25 \text{ eV}$  [51],  $p = 100 \text{ kPa}$ , and  $T = 300 \text{ K}$ ).

It can be seen from Figure 17(a) that an increase in the concentration of the first component for fixed pressure and temperature reduces the filling factor with the second component, while the filling factor with the first component increases thereby. A decrease in the total fill factor of the channel in the concentration range  $0 < c < 0.4$  of first component takes place due to depletion of the channel in the second component (Figure 17(b)). An increase in the total fill factor of the channel for  $c > 0.4$  is associated with preferred enrichment of the channel in the first component (see Figure 17(b)). The partial flux of the first component in this case increases monotonically due to an increase in the filling factor with the first component (see Figure 17(a)), while the partial flux of the second component decreases due to a decrease in the filling factor with the second component. The transport is of the diffusion type, and clusters are not formed in the channel in view of small fill factors of the channel ( $\theta \leq 0.25$  for any composition of the mixture).

Figures 17(c) and 17(d) show the dependence of partial fluxes on the mixture composition in the case when one of the gases (the first) is a strong sorbate, while the other gas is a weak sorbate. The energy of interaction and the diameter of particles correspond to a butane-methane gas mixture ( $a = 3.8 \text{ \AA}$ ,  $\sigma_1 = 4.3 \text{ \AA}$ ,  $\sigma_2 = 3.6 \text{ \AA}$ ,  $\varepsilon_1 = 0.61 \text{ eV}$ ,  $\varepsilon_2 = 0.38 \text{ eV}$  [51],  $p = 2000 \text{ kPa}$ , and  $T = 300 \text{ K}$ ). The behavior of the total and partial fill factors of the channel upon an increase in the concentration of the first (highly adsorbed) component in this case coincides qualitatively with the case of slightly adsorbed gases described previously: the partial filling factor with the first (highly adsorbed) component increases monotonically against the background of a monotonic decrease in the filling factor with the second (slightly adsorbed) component (see Figure 17(c)).

The behavior of partial fluxes in this case is less trivial. It can be seen from the figure that the partial flux of the first component increases in the concentration interval  $0 < c < 0.2$ . This is due to the fact that, in accordance with relation (141), short-lived clusters (see Figure 13(a)) whose size increases with concentration are formed for such concentrations and fill factors of the channel. The transport over clusters occurs via a barrier-free transfer of density excitation, which increases the effective diffusion coefficient. This process is similar to the transport in one-component systems for high fill factors (see Section 2.1). It should be noted, however, that the formation of clusters and the mechanism of transfer of density excitation through a cluster in a two-component mixture can be realized for smaller fill factors ( $\theta = 0.71$ ; see Figures 13(b), 17(c), and 17(d)) as compared to the one-component case ( $\theta \geq 0.8$ ). An increase in the concentration of the first component increases the lifetime

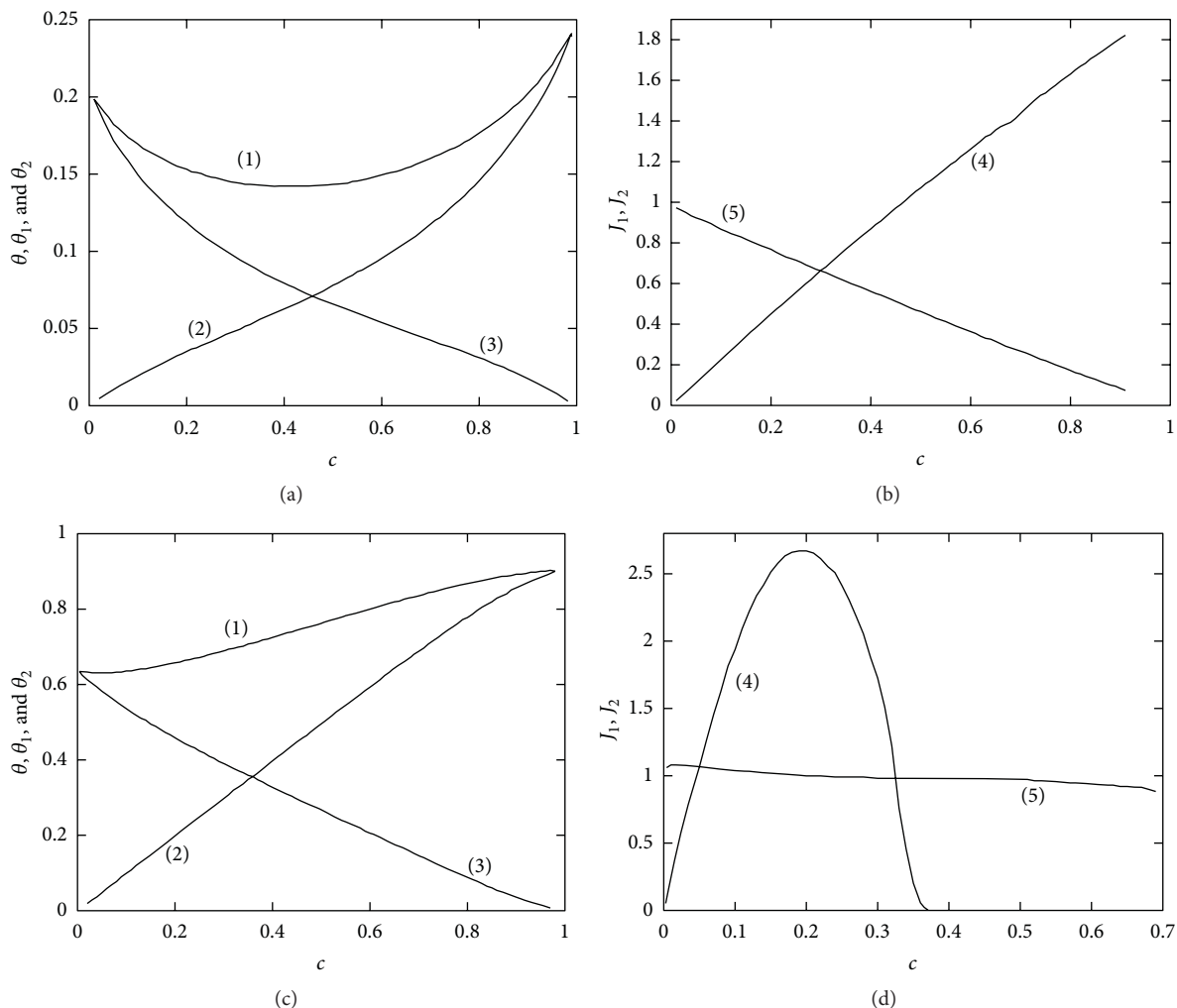


FIGURE 17: Dependence of the total and partial fill factors of a channel (a, c) and partial fluxes (b, d) on the composition of methane-argon (a, b) and butane-ethane mixtures (c, d): (1)—total fill factor of a channel; (2), (3)—filling factors with the first and second components, respectively; (4), (5)—partial fluxes of the first and second components, respectively;  $c$  is the concentration of the first component in the mixture.

of the clusters formed in the system (see Figures 14(b) and 15(c)). As a result of this increase, the transport over clusters becomes slower and the flux decreases. A further increase in the concentration leads to the formation of stable clusters in the channel (see Figures 14(c) and 16(c)); in accordance with relation (120), the lifetime of these clusters is much longer than the lifetime (141) of short-lived clusters since  $\delta F \gg T$ . In this case, the transfer of density excitation over clusters is ruled out and the partial flux vanishes.

Thus, three mechanisms of particle transport in a channel are possible in the two-component case. For small fill factors, the transport occurs through diffusion. An increase in the fill factor leads to the formation of short-lived clusters in a channel. As in the one-component case, this leads to an increase in the effective diffusion coefficient due to barrier-free transport of density excitation over a cluster. As the fill factor increases further, the characteristic lifetime of clusters increases, leading to a decrease in the flux. A further increase in the fill factor makes the clusters stable, and the so-called

blocking effect takes place, when the partial flux of one of the components vanishes. A decrease in pressure does not lead to a qualitative change in the behavior of the dependences of partial fluxes on the mixture composition.

**2.4.3. Comparison with Experiment.** The transport of two-component gas mixtures in zeolite membranes MFI (silicalite, ZSM-5) with a pore diameter of  $\sim 0.6$  nm has been studied by the technique widely used for one-component gases [51]. However, in contrast to the rich variety of experiments with one-component gases, a consistent analysis of a two-component mixture has not been reported in the literature. The most detailed information on penetrability for two-component mixtures is given in [51, 97].

The experiments [51, 97] on penetration of two-component mixtures were made in a chamber with a porous stainless steel substrate with a thickness of approximately 3 mm. A polycrystalline layer of zeolite ZSM-5 with a thickness of

$\sim 50 \mu\text{m}$  and a random orientation of crystals was deposited on the substrate. Zeolites have a complex crystalline structure based on silicon oxide with admixtures of sodium and aluminum [51]. The crystalline structure of zeolite ZSM-5 is formed by straight channels with an elliptical cross section ( $0.57 \times 0.52 \text{ nm}^2$ ) intersecting sinusoidal channels with a circular cross section of diameter  $0.54 \text{ nm}$  (Section 2.1). The measured adsorption capacity and the calculated fraction of molecules in the channel intersections make it possible to treat the channels as one dimensional for the molecular mixtures under study (Section 2.1). The experiments [51, 97] were carried out at temperatures from 300 to 700 K under pressures from 25 to 500 kPa on the external side of the membrane. The purity of the mixture components was higher than 99.95%. The mixture composition at the membrane exit was measured on a quadrupole mass spectrometer with a sensitivity of approximately 25 ppm when a Faraday cell was used for recording. The selectivity measured in the experiments was determined as the relative change in concentration  $c$  of *n*-butane molecules and concentration  $1 - c$  of methane molecules at the membrane entrance ( $F$ ) and exit ( $p$ ):

$$\alpha = \left( \frac{c}{1-c} \right)_F : \left( \frac{c}{1-c} \right)_p. \quad (181)$$

It should be noted that, for a constant composition of the mixture at the membrane entrance, the selectivity is proportional to the ratio of partial fluxes of the mixture components at the membrane exit:

$$\alpha \sim \frac{J_1}{J_2}. \quad (182)$$

It was found experimentally [51] that the partial flux of the highly adsorbed gas *n*-C<sub>4</sub>H<sub>10</sub> at  $T = 300 \text{ K}$  under a total pressure of  $p = 100 \text{ kPa}$  changes considerably (by a factor of several units) in the presence of the slightly adsorbed component CH<sub>4</sub> as compared to the flux of a pure gas, while the partial flux of the slightly adsorbed gas changes by two orders of magnitude in the presence of the strongly adsorbed component. Depending on the mixture composition, selectivity  $\alpha$  varies and attains its maximum value  $\alpha_{\text{max}} = 380$  for a concentration ratio of 5:95 at the membrane entrance. It was shown [97] that the dependences of partial fluxes on the mixture composition and external pressure for the mixtures studied (C<sub>2</sub>H<sub>6</sub>-CH<sub>4</sub> and C<sub>3</sub>H<sub>8</sub>-CH<sub>4</sub>) are monotonic in the range of experimental pressures. The partial flux of methane decreases in the presence of the second component (ethane or propane), while the partial flux of the second component increases with its concentration in the mixture. The selectivity of both mixtures increases monotonically with the concentration of the more highly adsorbed component in the mixture. The dependences of the partial fluxes on the total pressure of the mixture are also monotonic, but the pressure dependence of selectivity in ethane for the mixture C<sub>2</sub>H<sub>6</sub>-CH<sub>4</sub> has a peak at a pressure of  $p \approx 300 \text{ kPa}$  [97]. Similar dependences of partial fluxes were observed in experiments with another mixture of slightly adsorbed gases (CO<sub>2</sub>-N<sub>2</sub>) [53] (Figure 18).

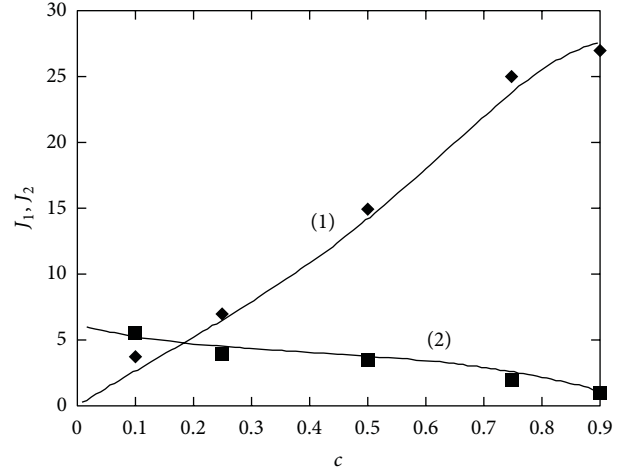


FIGURE 18: Dependence of partial fluxes on the mixture composition for slightly adsorbed gases: (1), (2)—theoretical dependences for CO<sub>2</sub> and N<sub>2</sub> fluxes, respectively;  $c$  is the CO<sub>2</sub> concentration above the membrane; squares correspond to experimental data from [53];  $a = 3.8 \text{ \AA}$ ,  $\sigma_1 = 3.8 \text{ \AA}$ , and  $\sigma_2 = 3.6 \text{ \AA}$  [51];  $p = 100 \text{ kPa}$ ,  $T = 300 \text{ K}$ .

The theory developed in the previous sections enables us to describe peculiarities in the transport of binary gas mixtures in zeolite membranes. In the case of a mixture of slightly adsorbed gases, when the fill factor of a channel is small ( $\theta \ll 1$ ) for any mixture composition, the system relaxes in accordance with the diffusion mechanism corresponding to diffusion of solitary particles without the formation of clusters in a channel. In this case, in accordance with (104), (160), and (180), the partial flux of the first component decreases monotonically upon an increase in the concentration of the second component, while the partial flux of the second component increases with its concentration in the mixture.

Figure 18 shows that the theoretical curves calculated by formulas (104), (160), and (180) are in good agreement with the experimental data borrowed from [53]. The mean distance  $a$  between the seats in a channel was estimated proceeding from the value corresponding to a close packing of a unit cell of a ZSM-5 membrane with nitrogen (Section 2.1).

The filling factor for mixtures with a strongly adsorbed component depends on the mixture composition; it is significant and can be as high as  $\theta \sim 1$ . In this case, in accordance with the arguments put forth in Section 2.4.1, the dependence of fluxes on the mixture composition is nonmonotonic due to the formation of clusters in a channel.

Figure 19 shows the dependence of the ratio of partial fluxes of gases for the mixture *n*-C<sub>4</sub>H<sub>10</sub>-CH<sub>4</sub> on the butane concentration in the mixture under a pressure of  $p = 100 \text{ kPa}$  at temperature  $T = 300 \text{ K}$ . It can be seen from the figure that the ratio of partial fluxes increases with the concentration of the highly adsorbed component (butane) in the concentration range  $0 < c < 0.35$ . Analysis of experimental data [51] and calculations based on formulas (104), (160), and (180) show that the methane flux for a butane concentration of  $c > 0.05$  changes insignificantly upon an

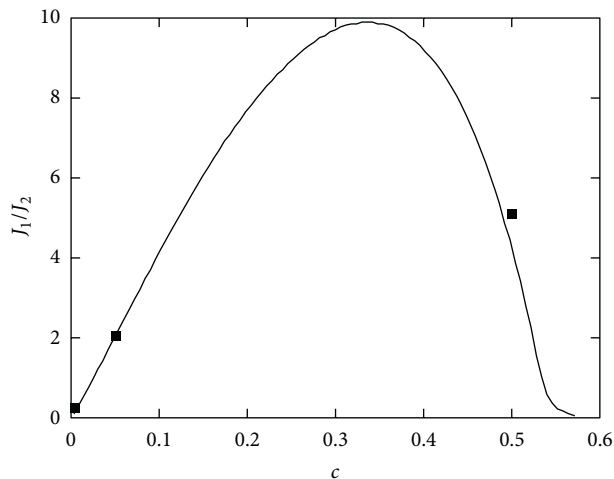


FIGURE 19: Ratio of the partial fluxes of butane and methane as a function of the butane concentration;  $c$  is the concentration of  $n$ - $C_4H_{10}$  above the membrane; squares correspond to experimental data obtained in [51];  $a = 3.8 \text{ \AA}$ ,  $\sigma_1 = 4.3 \text{ \AA}$ , and  $\sigma_2 = 3.6 \text{ \AA}$  [51];  $p = 100 \text{ kPa}$ ,  $T = 300 \text{ K}$ .

increase in the butane concentration in the mixture. In this case, the behavior of the flux ratio is completely determined by the behavior of the butane flux. The increase in the butane flux is due to the fact that, in accordance with formula (141), short-lived butane clusters are formed for concentrations  $0 < c < 0.35$  and for the fill factors corresponding to these concentrations (see Figure 13(a)); the size of these clusters increases with the concentration of the highly adsorbed component. The transport over clusters (see Figure 13(b)) occurs via barrier-free transfer of density excitation, leading to an increase in the effective diffusion coefficient for butane, which is observed for  $c < 0.35$ . The increase in the butane concentration in the mixture increases the lifetime of the clusters formed in the system (see Figures 14(b) and 15(c)). With increasing lifetime, the transport over the clusters slows down and the butane flux decreases for concentrations  $c > 0.35$ . A further increase in the concentration results in the formation of stable clusters in a channel (see Figures 14(c) and 16(c)), leading to a rapid (exponential) decrease in the butane flux upon an increase in its concentration in the mixture.

Thus, it follows from the theory that the butane flux becomes exponentially small for a butane concentration of  $c > 0.6$  in the mixture, and the transport of particles must be blocked. It should be noted that calculations based on formulas (104), (160), and (180) for butane concentrations in the interval  $0 < c < 0.05$  show that the methane flux decreases approximately by an order of magnitude upon an increase in the butane concentration, which is also in qualitative agreement with the experimental data [51]. The numerical difference between the predictions of the theory developed previously and the experimental data in this range of butane concentrations are due to the fact that relations (104), (160), and (180) were derived for the model potential of intermolecular interaction of the type of interaction (101) between hard spheres. It is well known that the potentials of hard spheres correctly describe the behavior of real systems

for high densities [46, 101]. In order to describe the behavior of the system in the entire range of fill factors, potentials of the Lennard-Jones type, which take into account the attraction between particles even in the zeroth order in density, should be used. However, although the application of this type of potentials of intermolecular interaction does not change the results qualitatively, it leads to the formation of butane clusters at lower filling factors and, hence, to a sharper decrease in the methane flux upon an increase in the butane concentration in the concentration range under investigation.

Relations (104), (160), (180), and (181) also make it possible to derive the dependence of the selectivity on the pressure, temperature and composition of the mixture. Figure 20(a) shows the dependence of the ethane selectivity for the  $C_2H_6$ - $CH_4$  mixture with a concentration ratio of 50:50 at the entrance on the total pressure of the mixture [97]. It can be seen that the dependence is nonmonotonic. This is due to the fact that the diffusion coefficient first increases due to an increase in the pressure and fill factor of the channel as a result of the formation of short-lived clusters, and the partial ethane flux increases (Figure 20(b)). The increase in the total fill factor of the channel is determined by the increase in the partial fill factors for both components. This process continues until the channel filling with ethane slows down. In this case, the fill factor of the channel increases mainly due to channel filling with methane. At such pressures, the increase in the ethane flux slows down (see Figure 20(b)), while the methane flux continues to increase (Figure 20(c)). The theoretical dependences plotted in the figures show that a further increase in pressure due to an increase in the lifetime of ethane clusters formed in the channel must lead to a decrease in the ethane flux (Figure 20(b)). Thus, the analysis of experimental data proves that the theory constructed here describes the experimental results satisfactorily.

One of the main results of the proposed theory is the prediction of nonmonotonic dependences of partial fluxes and selectivities on the mixture composition and pressure (see Figures 19 and 20), while conventional models [51, 53, 97] (in particular, the generalized Maxwell-Stefan equation [51, 97]) lead to monotonic dependences of these quantities on the same parameters (see Figure 20(a)). The qualitative discrepancy between the dependences in question is due to the fact that conventional models [51, 53, 97] take into account only the finite size of particles, in which the interaction between particles in a channel is disregarded. It is well known [46, 47, 101], however, that the interaction between particles in dense systems plays a decisive role both in the construction of the equations of state of the system and in the description of transport. For example, the inclusion of interaction between particles of the hard-sphere type leads to the emergence of peaks in the pair correlation function at distances equal to one, two, three, and so forth particle diameters [44, 46, 101]. This fact indicates the existence of "effective" attraction between particles and necessitates the inclusion of cluster formation in the description of the behavior of the system at high densities, when it passes to a spatially inhomogeneous state. It was demonstrated previously that this leads to the emergence of nonmonotonic dependences of fluxes and selectivities on external parameters.

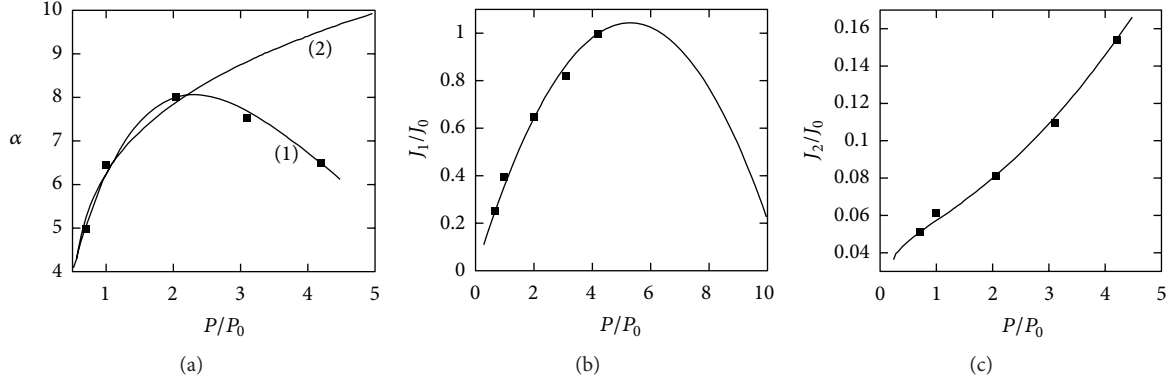


FIGURE 20: Dependence of the ethane selectivity (a) and of the partial fluxes of  $C_2H_6$  (b) and  $CH_4$  (c) for the  $C_2H_6$ - $CH_4$  mixture on the total pressure of the mixture: (1)—calculations based on formulas (104), (160), and (180) and (181); (2)—calculations based on the generalized Maxwell-Stefan equation [97]; squares correspond to experimental data obtained in [51];  $a = 3.8 \text{ \AA}$ ,  $\sigma_1 = 3.8 \text{ \AA}$ , and  $\sigma_2 = 3.6 \text{ \AA}$  [51];  $J_0 = 63 \text{ mmole}/(\text{m}^2 \text{ s})$ ,  $p_0 = 100 \text{ kPa}$ .

It should be noted that the stabilization of clusters in 1D systems by the second component at high fill factors, which has been investigated here, was obtained numerically in a recent work [83]. It should be borne in mind, however, that, in accordance with our previous results (Section 2.1), clusters with a large but finite lifetime can be formed even in a one-component system with high filling factors. It is 1D gold clusters of this type that were apparently observed in recent experiments under the ultrahigh vacuum conditions.

### 3. Results and Discussion

The analysis of the experimental data showed that for most gases investigated, the sorption and transport can be treated as a process in a one-dimensional (1D) system. In statistical physics, the theoretical models of 1D systems are classical examples of exactly solvable models [44]. It is well known [34, 46] that in 1D systems, a phase transition (condensation) does not occur as density increases. This means that, specifically, no critical nuclei are present in the system, and stable nuclei of a new phase with macroscopically long lifetimes do not appear in the system. At the same time, the system of 1D channels in zeolite membranes consists of channels of finite length, where for a sufficiently high filling factors, clusters with sizes comparable to the channel length can form. Thus, the description of molecular transport in zeolite membranes reduces to describing transport in a 1D system, where there are strong density fluctuations with a finite lifetime of clusters. The density functional method [38] makes it possible to calculate the spectrum of density fluctuations and the diffusion coefficient for particles with arbitrary density and arbitrary laws of interaction with one another and with the channel walls. Since the flux measured in the experiments performed in [41] is determined by the diffusion coefficient and the filling factor of the channels in the membrane, the sorption isotherm of a one-component molecular gas is calculated separately. For the one-dimensional channels considered in the present paper, this problem is solved exactly for an arbitrary intermolecular interaction potential. A new

feature here is an analysis of the dependence of the lifetime and size of the 1D clusters on the filling factor of the channel with particles. A description of molecular transport for an arbitrary filling factor ( $\theta$ ) of a channel is performed. It was found that as the filling factor approaches 1, so that blocking of the relative motion of the particles becomes substantial, the diffusion coefficient increases. Following [31], a new diffusion mechanism is observed. It makes it possible to explain the transition from activated diffusion of single particles in a channel with low filling factors to collective fast barrier-free diffusion, which consists of the propagation of density disturbances for large values of  $\varepsilon_0$ . In the hard-sphere approximation, as  $\bar{N}_1$  increases, the well-known [46] effective attraction of the molecules—hard spheres—results in vanishing of the energy barrier for diffusion along the channel axis. Another consequence of the effective attraction of molecules is the formation of molecular clusters in the channel, which have a finite lifetime because of the one-dimensionality of the system. The size and lifetime of the clusters increase as  $\theta$  increases. The diffusion of particles in clusters is described as a barrier-free process of propagation of density disturbances. The pressure, temperature, and filling factor dependences of the flux of molecules make it possible, even in the high-sphere model, to describe the experimental data currently known to the authors.

We have shown that contradictory experimental data, reporting the presence of the SFD mode and transport acceleration with the increasing density, can be described within the proposed model consistently accounting for correlation effects in a strongly fluctuating 1D system of identical particles. The molecular transport in a 1D system can change with time going from the Einstein diffusion mode to SFD mode and then again to a normal diffusion at large observation times. Whereas the sequence of these modes is general, their actual realization depends on the concrete characteristics of the system. For example, at very low densities one expects to observe only a normal diffusion mode. If we consider a system of weakly interacting particles ( $u \leq 1$ ), we can see that at low densities  $\theta \leq 0.2$  and time scale  $t < l_0^2/D_0$ , the particles

move independently and MSD obeys the Einstein law  $\langle x^2 \rangle \sim t$ . At times  $t > l_0^2/D_0$ , when a particle mobility is limited by other particles, the SFD diffusion mode ( $\langle x^2 \rangle \sim t^{1/2}$ ) should appear. As the density is increased, collective effects force the 1D system to transform into a nonhomogeneous state, characterized by a formation of clusters with a finite lifetime [31]. In such a clustered system, a particle moves in a limited space between the clusters and at collision, it transfers its momentum to a cluster. This transfer of momentum can cause the cluster to emit a particle from the opposite side to the impact. For a system of identical particles, such a process, which we call collective diffusion (CD), results in an increase of the diffusion coefficient with increasing density [31]. Therefore at long times ( $t \rightarrow \infty$ ) MSD again obeys the Einstein law  $\langle x^2 \rangle \sim t$  with an effective diffusion coefficient  $D_u(\theta) \sim D_0/(1 - \theta)^2$ . We suggest that further experimental investigations could confirm the reappearance of the Einstein-like diffusion mode at high densities, which is characterized by a diffusion coefficient increasing with density. When the interaction between the particles in the 1D system is strong ( $u \gg 1$ ), cluster formation occurs even at low filling factors ( $\theta \leq 0.2$ ); one has the same general physical picture but the transitions from one diffusion mode to the other take place at lower densities.

In this paper, we also analyse the transport of a two-component gas mixture in subnanometer channels theoretically for an arbitrary filling factor. The main problem in this case is to take into account consistently the density effects associated with both the interaction and the finite size of the particles. This is done in the hard-sphere model, in which the interaction is manifested as an effective (dynamic) attraction of particles, leading to their correlation [46]. It is well known [46, 101] that, applying this model to 3D system, one can describe the density effects qualitatively and even quantitatively in some cases. The comparison with experimental data with the obtained theoretical dependences demonstrates the possibility of a quantitative description of diffusion of a two-component mixture in a 1D system.

The adsorption isotherm of a mixture in 1D channels is calculated; this isotherm relates the fill factor and the concentration of particles in channels to the temperature, pressure, and composition of a mixture of gases whose diffusion is studied in experiments [51, 53, 97]. The ground state of a mixture of particles in 1D channels is analyzed by the density functional method [38] generalized to the case of a two-component mixture. However, in contrast to [38], the free energy is obtained by calculating directly the correlation function and the response function using the method developed for 1D systems [45]. The density functional method is used to derive, from microscopic considerations, the equation of motion for the order parameter of the system, which is the Fourier component of the deviation of the particle concentration from its mean value. Analysis of this equation shows that the two-component mixture in channels is transformed to a spatially inhomogeneous state upon an increase in  $\theta$ . As a result, short-lived clusters appear in channels, with the cluster size and lifetime increasing with  $\theta$ . A new and unexpected result obtained in this case is the

emergence of a minimum in the fluctuating part of the free energy as a function of the wave vector and the Fourier component of the order parameter. Thus, at high filling levels, the two-component mixture acquires a new property: clusters of a definite size are stabilized by a potential barrier due to the emergence of effective attraction between particles in the channels. Such a situation is typical of transitions of the system to an inhomogeneous state [99]. The lifetime of clusters formed increases exponentially in accordance with the Arrhenius law; at a low temperature, channels with such clusters might be blocked for the transportation of particles forming the mixture. It should be noted that the idea of stabilizing the clusters of one component by the other component in 1D systems was put forth in [83]. Thus, the description of transport in nanochannels is reduced to the description of diffusion in a spatially inhomogeneous high-density one-dimensional system.

For a weakly nonequilibrium system, the problem of computing fluxes in 1D channel is reduced to the calculation of relaxation frequency spectra for density fluctuations of mixture components. Spectra  $\omega_i(k)$  were determined by using the response functions derived in Section 2.4.1. Analysis of the dependences of  $\omega_i$  on  $k$  and on fill factor  $\theta$  proved that a hydrodynamic spectrum  $\omega_i(k) = c_i k$  is typical of clusters ( $\theta \sim 1$ , finite values of  $k$ ), while for transport of excitations over distances much longer than the characteristic size of clusters ( $k \ll 1$ ), the spectrum is of the diffusion type,  $\omega_i(k) \propto D_i k^2$ , for an arbitrary fill factor. In accordance with the dependences of spectra and fluxes on the fill factor obtained here, three regimes of particle transport can be singled out. For  $\theta \ll 1$ , we have diffusion of solitary particles. As the value of  $\theta$  increases, the flux and the diffusion coefficient increase due to the barrier-free (hydrodynamic) transport of particles along the increasing part of the length of a 1D channel filled with short-lived clusters formed in it. As the value of  $\theta$  increases further and the potential barrier ( $E_i$ ) stabilizing the clusters arises, particle fluxes decrease exponentially since the value of  $E_i$  increases with  $\theta$ . Thus, an increase in the fill factor gives rise to the new property of 1D two-component systems (transport blocking by the clusters formed). A comparison of the theory with experimental data and discussion of results was carried out (Section 2.4.3). The obtained dependences of the fluxes on the mixture composition (fill factor) and of the selectivity on pressure successfully describe the experimental data known to the authors.

We have also considered an infinite quasi-1D system and showed by means of statistical methods [102] that in spite of the absence of phase transitions in an infinite quasi-1D system it can be in two states due to collective effects [33]. These two states of a quasi-1D system are characterized by the formation of clusters with finite lifetimes but different structural properties [33]. Clusters in a quasi-1D system can be interpreted as density fluctuations that can exhibit macroscopic lifetimes. As a concrete example, we estimate the lifetime, interatomic distances for 1D gold clusters and compare them to the available experimental and theoretical data on monoatomic gold chains. Depending on the density of the quasi-1D gold system, clusters with either large

(3.5 ÷ 4.0 Å) or smaller Au-Au separations (2.5 ÷ 2.9 Å) can have an observable lifetime. Also we have estimated the minimal number of atoms in a 1D chain and a force required to break a chain with a minimal number of atoms in it for different metals (Au, Ag, Ni, and Pt). Thus we show that the methods of statistical mechanics, in some cases, can be used to investigate the properties of finite systems. In particular, these methods allow one to explain experimentally observed anomalously large interatomic distances in monoatomic Au chains and to predict its maximal length and to estimate its lifetime. The described approach was applied to analyze the interatomic distances and lifetimes of quasi-1D structures of different materials such as Ag, Ni, and Pt. The obtained results successfully describe the experimental data.

#### 4. Conclusions

The paper is devoted to the analysis of the correlation effects and manifestations of general properties of 1D systems (spatial heterogeneity that is associated with strong density fluctuations, the lack of phase transitions, the presence of frozen disorder, confinement, and blocked movement of nuclear particle by its neighbours) in nonequilibrium phenomena by considering the four examples. The anomalous transport in zeolite channels is considered. The mechanism of the transport in carbon nanotubes and MOF structures, relaxation, mechanical properties, and stability of nonequilibrium states of free chains of metal atoms, non-Einstein atomic mobility in 1D atomic systems is considered.

Description of molecular transport in zeolite membranes is reduced to the description of transport in 1D system in which strong density fluctuations with a finite lifetime of the clusters are presented. Response function method for density functional allows us to calculate the spectrum of density fluctuations and the diffusion coefficient of the particle with arbitrary density and arbitrary laws of interaction between particles and between a particle and a wall of the channel. Systematic account of correlation effects leads to the following physical picture of transport and mobility in strong fluctuating 1D confinement system.

Thus, if the interaction between particles in the 1D system is low ( $u \leq 1$ ), at low densities  $\theta \leq 0.1$  at times  $t < l_0^2/D_0$  particles move independently of each other, and, therefore, their mobility is of the Einstein type  $\langle x^2 \rangle \sim t$ . At the times  $t > l_0^2/D_0$ , the motion of the particles is limited due to blocking by other particles that results in the SFD regime  $\langle x^2 \rangle \sim t^{1/2}$ . 1D system becomes spatially inhomogeneous due to collective effects in it by increasing of density of system. This state is characterized by the presence of clusters with a finite lifetime. In such a system, the diffusion of a particle is the result of its moving in a confined space between clusters with subsequent transfer of momentum to a cluster. This effect results in a disintegration of a cluster and a disconnection of the particles from the other side of the cluster. For identical particles, this process is a result of diffusion due to the “excitation” transfer along the chain of closely spaced particles and leads to an increase of a diffusion coefficient with increasing density of particles in 1D clustered system.

A further increase of the filling factor leads to the increase of a cluster lifetime, to the simultaneous decrease in the average distance between these clusters, and to the increase of diffusion coefficient. In this case, the dependence of the mean square displacement of particles at the large times ( $t \rightarrow \infty$ ) is of the Einstein type with an increased diffusion coefficient  $D(\theta) \sim D_0/(1 - \theta)^2$ ,  $\theta \sim 1$ . If the pair interaction between particles is large, the cluster formation occurs at low densities, so that all the discussed above becomes true for small filling factors zeolite channels also.

Cluster of atomic particles that forms in 1D systems allows to describe and explain the phenomena observed in experiments, such as the formation of atomic chains with two different interatomic distances, mechanical properties, and stability of the nonequilibrium free chains, and allows to calculate the minimal number of atomic particles of different metals in free chains. In this case, it is not necessary to use impurity atoms, the presence of which requires experimental confirmation in the chain to explain the large interatomic distances in the 1D chains of gold.

The description of the practically important transport of two-component mixture in membranes with subnanometer channels by the response function method allowed to show that in 1D system of two types of particles at high filling factors, a phase transition in an inhomogeneous state with the formation of clusters of a finite size components may occur due to an effective particle attraction.

In the framework of the response function method, the equation of motion of the order parameter of the system is derived. The order parameter is the Fourier component of the density fluctuations. Analysis of this equation shows that two-component mixture in the channels passes into a spatially inhomogeneous state with the increase of  $\theta$  that results in formation of a short-lived clusters, the size and the lifetime of which increase with increasing of  $\theta$ .

A new result here was the occurrence of a minimum of a dependence of fluctuation part of the free energy on the wave vector and the Fourier component of the order parameter. Thus, at high filling factors in the two-component mixture, there is a new feature: the clusters of a certain size in the channels stabilizes by a potential barrier due to the effective attraction of particles.

Such a situation is typical for the transition to an inhomogeneous state. The lifetime of the clusters increases exponentially according to the Arrhenius law, and the clusters can be locked for transport of the particles of the mixture at sufficiently low temperature channels. The observed increase of the separation factor with conductivity of 1D channels in case of blocking a channel by stable clusters with a certain concentration is described. The dependence of the separation coefficient on the concentration, temperature, and density is defined.

A comparison of the theory with experimental data and results is discussed. The resulting fluxes depending on the composition of the mixture (the filling factor) and selectivity depending on pressure describe the experimental data presented in the literature.

## Acknowledgments

The study was supported by The Ministry of Education and Science of Russian Federation, Project no. 16.740.11.0536 and state Grants no. 2.6310.2011 and no. 2.5466.2011.

## References

- [1] A. Kumar, A. Kumar, and P. K. Ahluwalia, "Ab initio study of structural, electronic and dielectric properties of free standing ultrathin nanowires of noble metals," *Physica E*, vol. 46, pp. 259–269, 2012.
- [2] P. Makk, D. Tomaszewski, J. Martinek et al., "Correlation analysis of atomic and single-molecule junction conductance," *ACS Nano*, vol. 6, no. 4, pp. 3411–3423, 2012.
- [3] K. Tsysar, D. Bazhanov, A. Saletsky, O. Brovko, and V. Stepanyuk, "Influence of hydrogen impurities on atomic and electronic structure of palladium nanowires and nanocontacts," *Physical Review B*, vol. 84, no. 8, Article ID 085457, 8 pages, 2011.
- [4] D. Çakır and O. Gülseren, "Effect of impurities on the mechanical and electronic properties of Au, Ag, and Cu monatomic chain nanowires," *Physical Review B*, vol. 84, no. 8, Article ID 085450, 10 pages, 2011.
- [5] E. H. Huisman, M. L. Trouwborst, F. L. Bakker, B. J. van Wees, and S. J. van der Molen, "The mechanical response of lithographically defined break junctions," *Journal of Applied Physics*, vol. 109, no. 10, Article ID 104305, 7 pages, 2011.
- [6] P. Vélez, S. A. Dassie, and E. P. M. Leiva, "Kinetic model for the long term stability of contaminated monoatomic nanowires," *Physical Review B*, vol. 81, no. 12, Article ID 125440, 2010.
- [7] M. Zelený, M. Šob, and J. Hafner, "Ab initio density functional calculations of ferromagnetism in low-dimensional nanostructures: from nanowires to nanorods," *Physical Review B*, vol. 79, no. 13, Article ID 134421, 10 pages, 2009.
- [8] T. Kizuka and K. Monna, "Atomic configuration, conductance, and tensile force of platinum wires of single-atom width," *Physical Review B*, vol. 80, no. 20, Article ID 205406, 2009.
- [9] A. Hasmy, L. Rincón, R. Hernández, V. Mujica, M. Márquez, and C. González, "On the formation of suspended noble-metal monatomic chains," *Physical Review B*, vol. 78, no. 11, Article ID 115409, 5 pages, 2008.
- [10] A. Thiess, Y. Mokrousov, S. Blügel, and S. Heinze, "Theory and application of chain formation in break junctions," *Nano Letters*, vol. 8, no. 8, pp. 2144–2149, 2008.
- [11] T. Shiota, A. I. Mares, A. M. C. Valkering, T. H. Oosterkamp, and J. M. Van Ruitenbeek, "Mechanical properties of Pt monatomic chains," *Physical Review B*, vol. 77, no. 12, Article ID 125411, 2008.
- [12] T. Kizuka, "Atomic configuration and mechanical and electrical properties of stable gold wires of single-atom width," *Physical Review B*, vol. 77, no. 15, Article ID 155401, 2008.
- [13] F. Pauly, M. Dreher, J. K. Viljas, M. Häfner, J. C. Cuevas, and P. Nielaba, "Theoretical analysis of the conductance histograms and structural properties of Ag, Pt, and Ni nanocontacts," *Physical Review B*, vol. 74, no. 23, Article ID 235106, 2006.
- [14] S. López-Moreno, A. H. Romero, A. Muñoz, and U. Schwingenschlögl, "First-principles description of atomic gold chains on Ge(001)," *Physical Review B*, vol. 81, no. 4, Article ID 041415, 4 pages, 2010.
- [15] P. C. Snijders, "Colloquium: electronic instabilities in self-assembled atom wires," *Reviews of Modern Physics*, vol. 82, no. 1, pp. 307–329, 2010.
- [16] D. H. Wei, C. L. Gao, Kh. Zakeri, and M. Przybylski, "Pd atomic chain formation as a result of submonolayer deposition of 3d metals on Pd(110)," *Physical Review Letters*, vol. 103, no. 22, Article ID 225504, 2009.
- [17] H. Garbouj, M. Said, F. Picaud, C. Ramseyer, D. Spanjaard, and M. C. Desjonquères, "Growth of perfect and smooth Ag and Co monatomic wires on Pt vicinal surfaces: a kinetic Monte Carlo study," *Surface Science*, vol. 603, no. 1, pp. 22–26, 2009.
- [18] C. Liu, T. Uchihashi, and T. Nakayama, "Self-alignment of Co adatoms on in atomic wires by quasi-one-dimensional electron-gas-mediated interactions," *Physical Review Letters*, vol. 101, no. 14, Article ID 146104, 2008.
- [19] K. D. Ryang, P. G. Kang, H. W. Yeom, and S. Jeong, "Structures and defects of atomic wires on Si(553)-Au: an STM and theoretical study," *Physical Review B*, vol. 76, no. 20, Article ID 205325, 2007.
- [20] J. Gascon, F. Kapteijn, B. Zornoza, V. Sebastián, C. Casado, and J. Coronas, "Practical approach to zeolitic membranes and coatings: state of the art, opportunities, barriers, and future perspectives," *Chemistry of Materials*, vol. 24, no. 15, pp. 2829–2844, 2012.
- [21] D. A. Fedosov, A. V. Smirnov, E. E. Knyazeva, and I. I. Ivanova, "Zeolite membranes: synthesis, properties, and application," *Petroleum Chemistry*, vol. 51, no. 8, pp. 657–667, 2011.
- [22] A. García-Suárez, *Computational study of adsorption and diffusion in zeolites with cations [Ph.D. thesis]*, Universidad Pablo de Olavide, Seville, Spain, 2011.
- [23] J. A. Thomas and A. J. H. McGaughey, "Water flow in carbon nanotubes: transition to subcontinuum transport," *Physical Review Letters*, vol. 102, no. 18, Article ID 184502, 2009.
- [24] J. Su and H. Guo, "Effect of nanotube-length on the transport properties of single-file water molecules: transition from bidirectional to unidirectional," *Journal of Chemical Physics*, vol. 134, no. 24, Article ID 244513, 2011.
- [25] A. Berezhkovskii and G. Hummer, "Single-file transport of water molecules through a carbon nanotube," *Physical Review Letters*, vol. 89, no. 6, Article ID 064503, 4 pages, 2002.
- [26] H. Kumar, B. Mukherjee, S. T. Lin, C. Dasgupta, A. K. Sood, and P. K. Maiti, "Thermodynamics of water entry in hydrophobic channels of carbon nanotubes," *Journal of Chemical Physics*, vol. 134, no. 12, Article ID 124105, 2011.
- [27] J. K. Holt, H. G. Park, W. Yinmin et al., "Fast mass transport through sub-2-nanometer carbon nanotubes," *Science*, vol. 312, no. 5776, pp. 1034–1037, 2006.
- [28] M. Kac, G. E. Uhlenbeck, and P. C. Hemmer, "On the van der Waals theory of the vapor-liquid equilibrium. I. Discussion of a one-dimensional model," *Journal of Mathematical Physics*, vol. 4, no. 2, pp. 216–228, 1963.
- [29] M. Kac, G. E. Uhlenbeck, and P. C. Hemmer, "On the van der Waals theory of the vapor-liquid equilibrium. III. Discussion of the critical region," *Journal of Mathematical Physics*, vol. 5, no. 1, article 60, 10 pages, 1964.
- [30] V. D. Borman, I. V. Tronin, V. N. Tronin, V. I. Troyan, B. Johansson, and N. V. Skorodumova, "Formation of high- and low-density clusters in a 1D system," *Physica E*, vol. 40, no. 3, pp. 643–648, 2008.
- [31] V. D. Borman, V. V. Teplyakov, V. N. Tronin, I. V. Tronin, and V. I. Troyan, "Molecular transport in subnanometer channels," *Journal of Experimental and Theoretical Physics*, vol. 90, no. 6, pp. 950–963, 2000.

- [32] V. D. Borman, B. Johansson, N. V. Skorodumova, I. V. Tronin, V. N. Tronin, and V. I. Troyan, "Diffusion and particle mobility in 1D system," *Physics Letters A*, vol. 359, no. 5, pp. 504–508, 2006.
- [33] V. D. Borman, V. N. Tronin, I. V. Tronin, and V. I. Troyan, "Transport of a two-component mixture in one-dimensional channels," *Journal of Experimental and Theoretical Physics*, vol. 98, no. 1, pp. 102–122, 2004.
- [34] L. D. Landau and E. M. Lifshitz, *Statistical Physics*, part 1, Pergamon Press, Oxford, UK, 1980.
- [35] V. N. Bogomolov, "Capillary phenomena in extremely thin zeolite channels and metal-dielectric interaction," *Physical Review B*, vol. 51, no. 23, pp. 17040–17045, 1995.
- [36] S. Yu. Krylov, A. V. Prosyantov, and J. J. M. Beenakker, "One dimensional surface diffusion. II. Density dependence in a corrugated potential," *Journal of Chemical Physics*, vol. 107, no. 17, pp. 6970–6979, 1997.
- [37] J. J. M. Beenakker, V. D. Borman, and S. Y. Krylov, "Molecular transport in the nanometer regime," *Physical Review Letters*, vol. 72, no. 4, pp. 514–517, 1994.
- [38] Yu. N. Devyatko and V. N. Tronin, "Kinetics of the relaxation of gas-like systems to equilibrium," *Journal of Experimental and Theoretical Physics*, vol. 71, no. 5, pp. 880–887, 1990.
- [39] V. D. Borman, S. Yu. Krylov, and A. V. Prosyantov, "Theory of nonequilibrium phenomena at a gas-solid interface," *Journal of Experimental and Theoretical Physics*, vol. 70, pp. 1013–1022, 1990.
- [40] K. K. Sirkar, "Membrane separation technologies: current developments," *Chemical Engineering Communications*, vol. 157, pp. 145–184, 1997.
- [41] S. T. Hwang and K. Kammermeyer, *Membranes in Separations*, Wiley, New York, NY, USA, 1975.
- [42] J. M. Van de Graaf, "Permeation and Separation Properties of Supported Silicalite-1 Membranes," [Ph.D. thesis], University of Delft, Delft, The Netherlands, 1999.
- [43] F. Kapteijn, W. J. W. Bakker, G. Zheng, J. Poppe, and J. A. Moulijn, "Permeation and separation of light hydrocarbons through a silicalite-1 membrane. Application of the generalized Maxwell-Stefan equations," *The Chemical Engineering Journal and The Biochemical Engineering Journal*, vol. 57, no. 2, pp. 145–153, 1995.
- [44] J. M. Ziman, *Models of Disorder: The Theoretical Physics of Homogeneously Disordered Systems*, Cambridge University Press, Cambridge, UK, 1979.
- [45] I. Z. Fisher, *Statistical Theory of Liquids*, University of Chicago Press, Chicago, Ill, USA, 1964.
- [46] R. Balescu, *Equilibrium and Nonequilibrium Statistical Mechanics*, Wiley, New York, NY, USA, 1975.
- [47] P. Resibois and M. De Leener, *Classical Kinetic Theory of Fluids*, Wiley, New York, NY, USA, 1977.
- [48] Y. N. Devyatko and V. N. Tronin, "Kinetics of the relaxation of gas-like systems to equilibrium," *Soviet Physics. Journal of Experimental and Theoretical Physics*, vol. 98, pp. 1570–1584, 1990.
- [49] G. K. L. Chan and R. Finken, "Time-dependent density functional theory of classical fluids," *Physical Review Letters*, vol. 94, no. 18, Article ID 183001, 2005.
- [50] R. E. Richards and L. V. C. Rees, "Sorption and packing of n-alkane molecules in ZSM-5," *Langmuir*, vol. 3, no. 3, pp. 335–340, 1986.
- [51] W. J. W. Bakker, G. Zheng, F. Kapteijn, M. Makke, and J. A. Moulijn, *Precision Process Technology*, Kluwer, Amsterdam, The Netherlands, 1993.
- [52] H. Van Bekkam, E. M. Flanigen, J. C. Jansen et al., Eds., *Introduction to Zeolite Science and Practice*, vol. 58, Elsevier, Amsterdam, The Netherlands, 1991.
- [53] L. J. P. Van den Broeke, W. J. W. Bakker, F. Kapteijn, and J. A. Moulijn, "Binary permeation through a silicalite-1 membrane," *AIChE Journal*, vol. 45, no. 5, pp. 976–985, 1999.
- [54] G. T. Kokotailo, S. L. Lawton, D. H. Olson, and W. M. Meier, "Structure of synthetic zeolite ZSM-5," *Nature*, vol. 272, no. 5652, pp. 437–438, 1978.
- [55] D. H. Olson, W. O. Haag, and R. M. Lago, "Chemical and physical properties of the ZSM-5 substitutional series," *Journal of Catalysis*, vol. 61, no. 2, pp. 390–396, 1980.
- [56] R. Krishna, "A unified approach to the modelling of intraparticle diffusion in adsorption processes," *Gas Separation and Purification*, vol. 7, no. 2, pp. 91–104, 1993.
- [57] F. Kapteijn, W. J. W. Bakker, G. Zheng, and J. A. Moulijn, "Temperature- and occupancy-dependent diffusion of n-butane through a silicalite-1 membrane," *Microporous Materials*, vol. 3, no. 3, pp. 227–234, 1994.
- [58] W. J. W. Bakker, F. Kapteijn, J. C. Jansen, H. van Bekkam, and J. A. Moulijn, "Hoge permeabiliteit en selectiviteit bereikt. Doorbraak in ontwikkeling zeolietmembranen," *Procestechologie*, vol. 3, no. 12, pp. 7–16, 1993 (Dutch).
- [59] A. Tselik, *Quantum Field Theory in Condensed Matter Physics*, Cambridge, UK, 1998.
- [60] H. van Beijeren, K. W. Kehr, and R. Kutner, "Diffusion in concentrated lattice gases. III. Tracer diffusion on a one-dimensional lattice," *Physical Review B*, vol. 28, no. 10, pp. 5711–5723, 1983.
- [61] G. Hummer, J. C. Rasaiah, and J. P. Noworyta, "Water conduction through the hydrophobic channel of a carbon nanotube," *Nature*, vol. 414, no. 6860, pp. 188–190, 2001.
- [62] V. Gupta, S. S. Nivarthi, A. V. McCormick, and H. T. Davis, "Evidence for single file diffusion of ethane in the molecular sieve AlPO<sub>4</sub>-5," *Chemical Physics Letters*, vol. 247, no. 4–6, pp. 596–600, 1995.
- [63] V. Kukla, J. Kornatowski, D. Demuth et al., "NMR studies of single-file diffusion in unidimensional channel zeolites," *Science*, vol. 272, no. 5262, pp. 702–704, 1996.
- [64] H. Jobic, K. Hahn, J. Kärger et al., "Unidirectional and single-file diffusion of molecules in one-dimensional channel systems. A quasi-elastic neutron scattering study," *Journal of Physical Chemistry B*, vol. 101, no. 30, pp. 5834–5841, 1997.
- [65] S. Vasenkov and J. Kärger, "Different time regimes of tracer exchange in single-file systems," *Physical Review E*, vol. 66, no. 5, Article ID 052601, 4 pages, 2002.
- [66] J. B. Delfau, C. Coste, C. Even, and M. Saint Jean, "Single-file diffusion of interacting particles in a finite-sized channel," *Physical Review E*, vol. 82, no. 3, Article ID 031201, 2010.
- [67] J.-B. Delfau, "Christophe Coste, and Michel Saint Jean. Single-file diffusion of particles in a box: transient behaviors," *Physical Review E*, vol. 85, no. 6, Article ID 061111, 14 pages, 2012.
- [68] P. A. Fedders, "Two-point correlation functions for a distinguishable particle hopping on a uniform one-dimensional chain," *Physical Review B*, vol. 17, no. 1, pp. 40–46, 1978.
- [69] J. Kärger, "Straightforward derivation of the long-time limit of the mean-square displacement in one-dimensional diffusion," *Physical Review A*, vol. 45, no. 6, pp. 4173–4174, 1992.
- [70] M. Kollmann, "Single-file diffusion of atomic and colloidal systems: asymptotic laws," *Physical Review Letters*, vol. 90, no. 18, Article ID 180602, 2003.

- [71] K. Hahn, J. Kärger, and V. Kukla, "Single-file diffusion observation," *Physical Review Letters*, vol. 76, no. 15, pp. 2762–2765, 1996.
- [72] C. Rödenbeck, J. Kärger, and K. Hahn, "Exact analytical description of tracer exchange and particle conversion in single-file systems," *Physical Review E*, vol. 55, no. 5, pp. 5697–5712, 1997.
- [73] C. Rodenbeck, J. Kärger, and K. Hahn, "Calculating exact propagators in single-file systems via the reflection principle," *Physical Review E*, vol. 57, no. 4, pp. 4382–4397, 1998.
- [74] N. Nilius, T. M. Wallis, and W. Ho, "Localized molecular constraint on electron delocalization in a metallic chain," *Physical Review Letters*, vol. 90, no. 18, Article ID 186102, 4 pages, 2003.
- [75] N. Agraït, A. L. Yeyatib, and M. van Ruitenbeek, "Quantum properties of atomic-sized conductors," *Physics Reports*, vol. 377, no. 2-3, pp. 281–279, 2003.
- [76] H. Ohnishi, Y. Kondo, and K. Takayanagi, "Quantized conductance through individual rows of suspended gold atoms," *Nature*, vol. 395, no. 6704, pp. 780–783, 1998.
- [77] V. Rodrigues and D. Ugarte, "Real-time imaging of atomistic process in one-atom-thick metal junctions," *Physical Review B*, vol. 63, no. 7, Article ID 073405, 4 pages, 2001.
- [78] Y. Takai, T. Kawasaki, Y. Kimura, T. Ikuta, and R. Shimizu, "Dynamic observation of an atom-sized gold wire by phase electron microscopy," *Physical Review Letters*, vol. 87, no. 10, Article ID 106105, 4 pages, 2001.
- [79] T. Kizuka, S. Umehara, and S. Fujisawa, "Metal-insulator transition in stable one-dimensional arrangements of single gold atoms," *Japanese Journal of Applied Physics*, vol. 40, no. 1, pp. L71–L74, 2001.
- [80] C. Untiedt, A. Yanson, R. Grande et al., "Calibration of the length of a chain of single gold atoms," *Physical Review B*, vol. 66, no. 8, Article ID 085418, 6 pages, 2002.
- [81] N. V. Skorodumova and S. I. Simak, "Spatial configurations of monoatomic gold chains," *Computational Materials Science*, vol. 17, no. 2–4, pp. 178–181, 2000.
- [82] N. V. Skorodumova, S. I. Simak, A. E. Kochetov, and B. Johansson, "Ab initio study of electronic and structural properties of gold nanowires with light-element impurities," *Physical Review B*, vol. 75, no. 23, Article ID 235440, 2007.
- [83] N. V. Skorodumova and S. I. Simak, "Stability of gold nanowires at large Au-Au separations," *Physical Review B*, vol. 67, no. 12, Article ID 121404, 4 pages, 2003.
- [84] V. Rodrigues, T. Fuhrer, and D. Ugarte, "Signature of atomic structure in the quantum conductance of gold nanowires," *Physical Review Letters*, vol. 85, no. 19, pp. 4124–4127, 2000.
- [85] S. R. Bahn, N. Lopez, J. K. Nørskov, and K. W. Jacobsen, "Adsorption-induced restructuring of gold nanochains," *Physical Review B*, vol. 66, no. 8, Article ID 081405, 2002.
- [86] S. B. Legoas, D. S. Galvão, V. Rodrigues, and D. Ugarte, "Origin of anomalously long interatomic distances in suspended gold chains," *Physical Review Letters*, vol. 88, no. 7, pp. 761051–761054, 2002.
- [87] S. Di Napoli, A. Thiess, S. Blügel, and Y. Mokrousov, "Modeling impurity-assisted chain creation in noble-metal break junctions," *Journal of Physics*, vol. 24, no. 13, Article ID 135501, 2012.
- [88] M. Kiguchi, R. Stadler, I. S. Kristensen, D. Djukic, and J. M. van Ruitenbeek, "Evidence for a single hydrogen molecule connected by an atomic chain," *Physical Review Letters*, vol. 98, no. 14, Article ID 146802, 2007.
- [89] C. Q. Sun, C. M. Li, S. Li, and B. K. Tay, "Breaking limit of atomic distance in an impurity-free monatomic chain," *Physical Review B*, vol. 69, no. 24, Article ID 245402, 2004.
- [90] C. Kittel, *Introduction to Solid State Physics*, Wiley, New-York, NY, USA, 1995.
- [91] T. Hill, *Statistical Mechanics*, McGraw-Hill Book Company, New York, NY, USA, 1956.
- [92] E. M. Lifshitz and L. P. Pitaevskii, *Statistical Physics*, part 2, Pergamon Press, Oxford, UK, 1980.
- [93] A. Calzolari, C. Cavazzoni, and M. B. Nardelli, "Electronic and transport properties of artificial gold chains," *Physical Review Letters*, vol. 93, no. 9, pp. 1–96404, 2004.
- [94] G. M. Francis, L. Kuipers, J. R. A. Cleaver, and R. E. Palmer, "Diffusion controlled growth of metallic nanoclusters at selected surface sites," *Journal of Applied Physics*, vol. 79, no. 6, pp. 2942–2947, 1996.
- [95] E. Y. Zarechnaya, N. V. Skorodumova, S. I. Simak, B. Johansson, and E. I. Isaev, "Theoretical study of linear monoatomic nanowires, dimer and bulk of Cu, Ag, Au, Ni, Pd and Pt," *Computational Materials Science*, vol. 43, no. 3, pp. 522–530, 2008.
- [96] L. D. Landau, L. P. Pitaevskii, E. M. Lifshitz, and A. M. Kosevich, *Course of Theoretical Physics*, vol. 7 of *Theory of Elasticity*, Butterworth-Heinemann, 3 edition, 1986.
- [97] J. M. Van de Graaf, F. Kapteijn, and J. A. Moulijn, "Modeling permeation of binary mixtures through zeolite membranes," *AIChE Journal*, vol. 45, no. 3, pp. 497–511, 1999.
- [98] Yu. L. Klimontovich, *Statistical Physics*, Harwood Academic, New-York, NY, USA, 1986.
- [99] D. N. Voskresenskii, *Multiparticle Effects in Solids*, Energoatomizdat, Moscow, Russia, 1983.
- [100] O. G. Bakunin, "Mysteries of diffusion and labyrinths of destiny," *Physics-Uspekhi*, vol. 46, no. 3, pp. 309–313, 2003.
- [101] G. N. Sarkisov, "Approximate equations of the theory of liquids in the statistical thermodynamics of classical liquid systems," *Physics-Uspekhi*, vol. 42, no. 6, pp. 545–561, 1999.
- [102] F. Baletto and R. Ferrando, "Structural properties of nanoclusters: energetic, thermodynamic, and kinetic effects," *Reviews of Modern Physics*, vol. 77, no. 1, pp. 371–423, 2005.

## Research Article

# Electrical Resistivity of Pristine and Functional Single-Wall Carbon Nanotubes

Yijiang Lu,<sup>1</sup> Jing Li,<sup>1</sup> and Haiping Hong<sup>2</sup>

<sup>1</sup> Nanotechnology Branch, NASA Ames Research Center, Moffett Field, Sunnyvale, CA 94035, USA

<sup>2</sup> Department of Material and Metallurgical, South Dakota School of Mines and Technology, Rapid City, SD 57701, USA

Correspondence should be addressed to Haiping Hong; [haiping.hong@sdsmt.edu](mailto:haiping.hong@sdsmt.edu)

Received 6 January 2013; Accepted 16 February 2013

Academic Editor: Yun Zhao

Copyright © 2013 Yijiang Lu et al. This is an open access article distributed under the Creative Commons Attribution License, which permits unrestricted use, distribution, and reproduction in any medium, provided the original work is properly cited.

The resistance of several pristine and functional single-wall carbon nanotubes (SWNTs) deposited and dried on interdigitated electrode (IDE) chips was investigated to better understand how functional groups influence their resistivity. Without the external electrical field, the resistance was generally increased for the sulfonated and fluorinated SWNTs but not for COOH-SWNTs. With a 3 V electric field applied during depositing, while no change in resistance was found for the purified pristine SWNTs, fluorinated SWNTs, COOH SWNTs, and Ni-SWNTs, a significant decrease in resistance was observed in sulfonated SWNTs and unpurified pristine SWNTs, which could be due to the alignment of SWNTs in an electric field. The alignment of the sulfonated SWNTs is most likely due to the charge of the sulfate functional group. It is interesting to note that the alignment was found in the unpurified pristine SWNTs but not in the purified pristine ones which have lessened resistivity. The lower resistivity in the purified pristine SWNTs may be due to the smaller number (<5%) of impurities. The significance of this research is that hydrophilic COOH-SWNTs could be a better candidate than the hydrophobic pristine SWNTs for being used in many applications, especially in polymer nanocomposites.

## 1. Introduction

Carbon nanotubes have attracted extensive attention recently because of their extraordinary thermal, electrical, and mechanical properties [1–3]. Due to these unique properties, they have the potential to be used in electrical devices [4], nanofluids [5, 6], grease [7], and sensors [8–10].

Measuring the electrical properties of carbon nanotubes in solutions is not easy because it is difficult to get a homogeneous solution with carbon nanotubes. It is very hard to dissolve or disperse the carbon nanotubes in their pristine form in the hydrophilic fluids, such as water and ethylene glycol, simply because carbon nanotubes are inorganic solids (hydrophobic) [11]. Usually chemical surfactants are added to disperse the nanotubes. But the added chemical surfactant is always a concern in such measurements because it would complicate the interpretation of electrical conductivity results.

An alternative approach to improve the solubility of carbon nanotubes in water or organic solvents is by surface

modification, such as covalent, noncovalent, free-radical, and electrochemical modification or plasma treatments [12]. The most used and efficient method is chemical functionalization, through which carboxyl groups or other functional groups such as fluorinated groups and sulfonated groups are attached to the sidewall or the ends of the single-walled carbon nanotubes (SWNTs), leading to a reduction of the strong van der Waals interactions among carbon nanotubes and strongly facilitating the separation of SWNT bundles into individual tubes [12]. For example, recently, Dr. Billups' group at Rice University has synthesized highly exfoliated, water soluble, and single-walled carbon nanotubes with functional aryl sulfonated group [13]. Therefore, no chemical surfactant is necessary to disperse the nanotubes, thus eliminating the influence of chemical surfactants and simplifying the experimental procedure. The addition of the functional groups to the SWNTs causes a change of the electronic structure from a trigonal-planar local bonding geometry to a tetrahedral geometry, leading to the transformation of  $sp^2$ - into  $sp^3$ -hybridized carbon atoms [12], which may affect the intrinsic

electronic properties of SWNTs and their potential application in electronic devices and sensors. Therefore, it is interesting to investigate the effect of the added functional groups on electrical resistance to better understand how the chemical bonds and geometric/electronic configuration affect the electrical properties of the SWNTs.

In this paper, the electrical resistance of several pristine and functionalized SWNTs was investigated with and without an electric field to better understand the relationship between nanotube structure and physical properties (thermal, electrical, and mechanical).

## 2. Experimental and Procedure

The functional sulfonated SWNTs were obtained from Dr. Billups' group, Rice University. The details for the synthesis of these materials can be found in [13]. The COOH SWNTs were obtained from School of Mines and Nankai University respectively. (fluorinated single-wall carbon nanotubes) F-SWNTs were purchased from Carbon Nanotechnologies Incorporation (CNI, Houston, TX, USA). The surfaces have not been treated chemically or physically. Ni-coated SWNTs were prepared using the methodology as reported previously [14, 15]. A handheld sonic probe (Sonic Dismembrator, Model 100) was used to efficiently disperse the nanotubes into solvents. All flocculation of the nanotubes visible to the eye was removed by this process.

The nanotube coatings on the interdigitated electrode (IDE) chips were applied by a Nanoject II (Drummond Scientific Co.). The smallest drop distributed by this device is 2.3 nL. Ten drops of each sample were put to each IDE chip to ensure a uniform 23 nL SWNTs coating. When an electrical field was applied, 3 V or 5 V was added to the IDE chips before dropping the solution droplets on the electrodes. At the same time, the IDE sensor chip is heated up to 60°C. The electric field is removed once the SWNTs are dried. The IDE is made by a P-type boron-doped silicon (100) wafer with a resistivity of 0.006–0.01 ohm-cm and thickness of  $500 \pm 25 \mu\text{m}$ . A layer of 0.5  $\mu\text{m}$  silicon dioxide was thermally grown on top of the Si substrates. A layer of 200 nm platinum on top of 20 nm titanium was deposited on the SiO<sub>2</sub> layer with the designed finger patterns. These patterns consisted of 4, 8, 12, and 50  $\mu\text{m}$  finger gaps with 10  $\mu\text{m}$  finger width [16]. The IDE used for the conductivity measurement is shown in Figure 1 with a finger width of 10  $\mu\text{m}$  and a gap width of 12  $\mu\text{m}$ .

The electrical conductivities of various fillers (nanotubes) in solid phase were measured by Keithley 2002/7001 High performance DMM/Multiplexer and Agilent 34401 DMM (precisely calibrated). A Keithley 237 High voltage measure unit was used to measure the voltage of the electric field when the nanotube coating was applied.

## 3. Results and Discussion

In order to better understand the influence of functional groups on the conductivity (resistivity) of nanotubes, the electrical resistivity of various fillers (nanotubes) in solid phase was measured. Table 1 lists seven nanofillers (nanotubes) with different functional groups and chemical structures. All solutions were prepared to make SWNTs in the similar

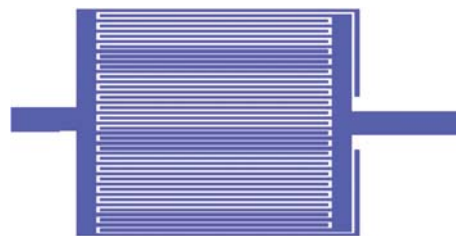


FIGURE 1: Interdigitated electrode (IDE) chip for measuring the resistance of different SWNTs.



FIGURE 2: Picture of five nanofiller (nanotube) solutions with different functional groups and chemical structures. (1) Unpurified pristine SWNT, (2) fluorinated SWNT, (3) COOH SWNT (school of mines), (4) COOH SWNT (outside campus), and (5) sulfonated SWNT.

TABLE 1: Types of nanofillers, concentrations, and solvents.

| No. | Type of nanofiller          | Concentration, wt% | Solvent type |
|-----|-----------------------------|--------------------|--------------|
| 1   | Unpurified pristine SWNT    | 0.0324%            | DMF          |
| 2   | Fluorinated SWNT            | 0.0364%            | DMF          |
| 3   | COOH SWNT (school of mines) | 0.0363%            | DMF          |
| 4   | COOH SWNT (outside campus)  | 0.0365%            | DMF          |
| 5   | Sulfonated SWNT             | 0.0366%            | DMF          |
| 6   | Ni-SWNT                     | 0.037%             | DMF          |
| 7   | Purified pristine SWNT      | 0.037%             | DMF          |

concentration by wt% in order to control the amount of nanotubes deposited on each IDE.

Pristine SWNTs were not distributed as well as the others in Dimethylformamide (DMF) even after being set in an ultrasonicator for 15 minutes, see Figure 2. The possible reason is that the pristine nanotube is hydrophobic. The other functional SWNTs dispersed better in DMF because they are hydrophilic.

Table 2 lists the conductivity (resistivity) data of the SWNTs with and without an applied electric field when depositing the nanotubes onto the electrodes.

TABLE 2: Resistance of SWNTs with and without an applied electric field.

| Coating sample            | Agilent<br>34401 DMM | Keithley<br>2002 DMM | Comments       |
|---------------------------|----------------------|----------------------|----------------|
| Unpurified pristine SWNT  | 256 K $\Omega$       | 270 K $\Omega$       |                |
| Unpurified pristine SWNT* | 29.9 $\Omega$        | 29.9 $\Omega$        | Applied<br>3 V |
| Fluorinated SWNT          | 41.2 K $\Omega$      | 40.5 K $\Omega$      |                |
| Fluorinated SWNT*         | 39.1 K $\Omega$      | 39.2 K $\Omega$      | Applied<br>3 V |
| COOH SWNT(S3)             | 12.0 $\Omega$        | 12.0 $\Omega$        |                |
| COOH SWNT(S3)*            | 16.1 $\Omega$        | 16.2 $\Omega$        | Applied<br>3 V |
| COOH SWNT(S4)             | 18.5 $\Omega$        | 18.2 $\Omega$        |                |
| COOH SWNT(S4)*            | 17.8 $\Omega$        | 17.8 $\Omega$        | Applied<br>3 V |
| Sulfonated SWNT           | 5.34 K $\Omega$      | 5.29 K $\Omega$      |                |
| Sulfonated SWNT*          | 25.6 $\Omega$        | 25.7 $\Omega$        | Applied<br>3 V |
| Ni-SWNT                   | 17.6 $\Omega$        |                      |                |
| Ni-SWNT*                  | 26.5 $\Omega$        |                      | Applied<br>3 V |
| Purified pristine SWNT    | 21.5 $\Omega$        |                      |                |
| Purified pristine SWNT*   | 34.1 $\Omega$        |                      | Applied<br>3 V |

\* An electric field of 3 V across the fingers with a gap size of 12 mm was applied while the SWNT samples were being coated on the IDE.

Instrument used for the resistance measurement: Keithley 2002 digital multimeter and Agilent 34401 DMM.

When no electric field is applied, the resistance of the sulfonated SWNTs and fluorinated SWNTs is 5.34 k $\Omega$  and 41.5 k $\Omega$ , respectively, which are about two to three orders of magnitude higher than that of purified pristine ones with a value of 21.5  $\Omega$ , indicating that functionalization generally increases the resistance except for COOH-SWNTs and Ni-SWNTs, with a resistance range from 12.0  $\Omega$  to 17.8  $\Omega$ , close to or even lower than 21.5  $\Omega$  of purified pristine ones. It is reported that coating nickel on the SWNT aids in exfoliation of SWNTs agglomerates and enables good dispersions [17]. The enhanced dispersions and formation of continuous interconnections between SWNTs lead to the low electrical resistance of Ni-SWNTs. In addition, coating the SWNTs with nickel will not diminish the sidewall properties and affect the electrical properties as in sulfonated SWNTs and fluorinated SWNTs [17], resulting in a much lower electric resistance in Ni-SWNTs than that of other functional SWNTs.

When a 3 V electric field was applied during coating the SWNTs onto IDE chips, the resistance decreased from 5.34 k $\Omega$  to 25.6  $\Omega$  for sulfonated SWNTs and from 256 k $\Omega$  to 29.9  $\Omega$  for unpurified pristine SWNTs, respectively. The decrease in resistance is most likely caused by the nanotubes alignment. In our previous study [15, 18], a significantly increase in thermal conductivity was observed in the nanofluids containing magnetic-metal-coated carbon nanotubes when a magnetic field was applied. Real images showed that

the initial randomly dispersed Ni-coated SWNTs gradually stretched and finally aligned to form chains and clusters which are longer than the real length of individual nanotubes [18]. The contact between the individual nanotubes in these chains and clusters leads to the increase in thermal conductivity of the nanofluids. Similarly, since the sulfated SWNTs have charged sulfate functional groups, these charges could make SWNTs align in an electric field, leading to the contact enhancements among the nanotubes, thus decreasing the electrical resistance. No change in resistance was found in the purified pristine SWNTs when they were applied in an electric field, which indicates that there is no alignment for the purified pristine SWNTs in an electric field because there is no charged functional group. The same thing (no alignment) should also be expected for the unpurified pristine SWNTs because they are the same except that there are more impurities (e.g., metal catalysts and their oxides and graphite) in the unpurified ones. Therefore, these impurities in the unpurified pristine SWNTs could be the reason for the unexpected alignment.

The resistance of the Ni-SWNTs does not change in a 3 V electric field but change in a 5 V electric field (data is not listed) because Ni-SWNTs are slightly polarized in nature due to the addition of Ni. These slightly polarized Ni-SWNTs will align along the electric field when the field is strong enough (5 V in this study) and leads to the decrease in electric resistance. It was reported that Cu and Ti atoms adsorbed on SWNTs are positively charged and the two nearest carbon atoms carry a little negative charge based on the model using pseudo-potential plane wave method [19]. Such charge transfer increased several times when an electric field was applied. The binding energy of Ni to SWNT is very close to that of Ti but larger than that of Cu [20]. Therefore, similar charge transfer would be expected in Ni-SWNTs, and it would increase with the strength of an electric field, leading to the polarization of the Ni-SWNTs and their alignment.

No significant change was observed for the resistance of the fluorinated SWNTs and COOH SWNTs after an electric field was applied to the IDE during SWNTs deposition. This is due to that the COOH and fluorine functional groups have no charges, and, therefore, they were not aligned under an electric field. It is also worth noting that the resistance of COOH SWNTs is three magnitudes lower than that of fluorinated SWNTs. The much lower resistance of COOH-SWNTs is because that, during the well-controlled carboxyl functionalization, the chemical modification is limited mostly to the opening of the tube caps at the ends and the formation of functional groups at defect sites along the sidewall. SWNTs functionalized in this manner basically retain their pristine electronic properties [12]. Therefore, the resistance of the COOH-SWNTs is very similar to that of the purified pristine ones. It was found using the density functional theory that vacancy-COOH pairs with a strong covalent bond are energetically favorable on the zigzag nanotube sidewall after acid treatment, and the electrical conductivity would be enhanced [21]. This is the case in the present study as seen from Table 2, the resistance of the COOH-SWNTs is pretty close to and even lower than that of the pristine ones with an applied electric field or not. By comparison, addition

reactions enable the direct coupling of functional groups such as fluorine onto the  $\pi$ -conjugated carbon framework of the tubes. It is known that the formation of carbon-heteroatom bonds will transform a  $sp^2$ -hybridized configuration to that of a  $sp^3$ -hybridized structure, leading to the disruption of the pseudo-one-dimensional lattice of the SWNTs and increase in resistance [12]. This is consistent with the results in the present study that the resistance of the fluorinated SWNTs is three magnitudes higher than that of the pristine SWNTs and COOH-SWNTs.

Previous study showed that the tensile strength of the cross-link membrane with 5 wt% of sulfonated SWNTs and sulfonated polystyrene is only 35 MPa, which is much lower than the expected value by considering the extremely high tensile strength of SWNTs (around 60 GPa) [22]. Assuming that nanotubes disperse very well in the polymer matrix, ideally, a 5 wt% nanotube loading in a film would have a tensile strength of around  $\approx 3$  GPa. One possible explanation of the lower than expected values is that the inserted functional groups interfere with the conjugate structure of the nanotube, thereby reducing its macromechanical strength. The effective electrical conductivity measurement of sulfonated SWNTs solution [11] provides strong evidence and support to this. No percolation threshold phenomenon is observed in the experiments. The linear conductivity increase versus the weight percentage indicates that the dominant conduction mechanism might be the ionic conduction, which is in agreement with the chemical structure of sulfonated SWNTs (anion  $SO_3^-$  group).

The existence of anion  $SO_3^-$  group in sulfonated SWNTs is also proved in the present study. The resistivity of the SWNTs is 5.34 k $\Omega$ , which are about two orders of magnitude higher than that of purified pristine ones with a value of 21.5  $\Omega$ . It decreased from 5.34 k $\Omega$  to 25.6  $\Omega$  under the external electrical field, probably caused by the nanotubes alignment due to the existence of the anion  $SO_3^-$  groups.

The motivation of the resistivity measurement of pristine and functionalized SWNTs is to better understand the relationship between nanotube structure and physical properties (thermal, electrical, and mechanical). Our study indicated that macrophysical strength is damaged by addition (insertion) of functional group [22]. Electrical conductivity measurement could provide additional information of structure of SWNTs. COOH-SWNTs have a resistance around 12.0  $\Omega$ , even lower than that of purified pristine ones with a value of 21.5  $\Omega$ , indicating that COOH group would maximally reduce the interfacial influence and keep the unbroken nanotube conjugate structure.

Changing the SWNTs from hydrophobic to hydrophilic with COOH group, while keeping its excellent electrical conductivity, makes it a better choice than pristine one to be used as nanofillers for various applications, especially in polymer composites [23].

#### 4. Conclusions

The electrical resistivity of several pristine and functional SWNTs in solid phase was investigated with and without an applied electric field.

Without an applied electric field, the resistance generally increased for the sulfonated and fluorinated SWNTs but not for COOH-SWNTs. With an applied electric field, no change was observed in resistance for purified pristine SWNTs, COOH-SWNTs, and fluorinated SWNTs. A significant decrease in resistance was observed from sulfonated SWNTs and unpurified pristine SWNTs when an electric field was applied, indicating that they both align within an electric field. The alignment of the sulfonated SWNTs is most likely due to the charged sulfonate groups. Alignment was found in the unpurified pristine SWNT but not the purified pristine SWNTs, which indicates that the alignment of unpurified pristine SWNTs is probably due to the impurities within its structure. The lower resistivity in the purified pristine SWNTs may be due to the smaller number (<5%) of impurities.

The results in this study show that the resistance of pristine and functional singlewall nanotubes is correlated to the type of functional groups and the alignment of the nanotubes. The significance of this research is that the hydrophilic COOH-SWNTs show relative low resistivity, which indicates that conjugated  $\pi$  structure of nanotubes (sidewall properties) is alive. These results demonstrate that hydrophilic COOH-SWNTs could be a better candidate than the hydrophobic pristine SWNTs for being used in many applications, especially in polymer nanocomposites.

#### Acknowledgments

H. Hong would like to thank NASA EPSCoR (award no. NNX09AU83A) for financial support. Jing Li would like to thank for DHS HSARPAR (IAA no. HSHQDC-08-x-00870) for financial support. Thanks are due to Mianliang Huang for his useful comments and corrections.

#### References

- [1] S. Berber, Y. K. Kwon, and D. Tomanek, "Unusually high thermal conductivity of carbon nanotubes," *Physical Review Letters*, vol. 84, no. 20, pp. 4613–4616, 2000.
- [2] C. Zhou, J. Kong, and H. Dai, "Intrinsic electrical properties of individual single-walled carbon nanotubes with small band gaps," *Physical Review Letters*, vol. 84, no. 24, pp. 5604–5607, 2000.
- [3] M. S. Dresselhaus, G. Dresselhaus, J. C. Charlier, and E. Hernández, "Electronic, thermal and mechanical properties of carbon nanotubes," *Philosophical Transactions of the Royal Society A*, vol. 362, no. 1823, pp. 2065–2098, 2004.
- [4] A. Javey, R. Tu, D. B. Farmer, J. Guo, R. G. Gordon, and H. Dai, "High performance n-type carbon nanotube field-effect transistors with chemically doped contacts," *Nano Letters*, vol. 5, no. 2, pp. 345–348, 2005.
- [5] H. Hong, X. Luan, M. Horton, C. Li, and G. P. Peterson, "Alignment of carbon nanotubes comprising magnetically sensitive metal oxides in heat transfer nanofluids," *Thermochimica Acta*, vol. 525, no. 1–2, pp. 87–92, 2011.
- [6] J. Wensel, B. Wright, D. Thomas et al., "Enhanced thermal conductivity by aggregation in heat transfer nanofluids containing metal oxide nanoparticles and carbon nanotubes," *Applied Physics Letters*, vol. 92, no. 2, Article ID 023110, 3 pages, 2008.
- [7] H. Hong, D. Thomas, A. Waynick, W. Yu, P. Smith, and W. Roy, "Carbon nanotube grease with enhanced thermal and electrical

- conductivities,” *Journal of Nanoparticle Research*, vol. 12, no. 2, pp. 529–535, 2010.
- [8] Y. Lu, J. Li, J. Han et al., “Room temperature methane detection using palladium loaded single-walled carbon nanotube sensors,” *Chemical Physics Letters*, vol. 391, no. 4–6, pp. 344–348, 2004.
- [9] J. Li, Y. Lu, Q. Ye, M. Cinke, J. Han, and M. Meyyappan, “Carbon nanotube sensors for gas and organic vapor detection,” *Nano Letters*, vol. 3, no. 7, pp. 929–933, 2003.
- [10] J. Li and Y. Lu, “Carbon nanotube based chemical sensors for space and terrestrial applications,” *ECS Transactions*, vol. 19, no. 6, pp. 7–15, 2009.
- [11] B. Glover, K. W. Whites, H. Hong, A. Mukherjee, and W. E. Billups, “Effective electrical conductivity of functional single-wall carbon nanotubes in aqueous fluids,” *Synthetic Metals*, vol. 158, no. 12, pp. 506–508, 2008.
- [12] K. Balasubramanian and M. Burghard, “Chemically functionalized carbon nanotubes,” *Small*, vol. 1, no. 2, pp. 180–192, 2005.
- [13] F. Liang, J. M. Beach, P. K. Rai et al., “Highly exfoliated water-soluble single-walled carbon nanotubes,” *Chemistry of Materials*, vol. 18, no. 6, pp. 1520–1524, 2006.
- [14] Y. Zhang, N. W. Franklin, R. J. Chen, and H. Dai, “Metal coating on suspended carbon nanotubes and its implication to metal–tube interaction,” *Chemical Physics Letters*, vol. 331, no. 1, pp. 35–41, 2000.
- [15] B. Wright, D. Thomas, H. Hong et al., “Magnetic field enhanced thermal conductivity in heat transfer nanofluids containing Ni coated single wall carbon nanotubes,” *Applied Physics Letters*, vol. 91, no. 17, Article ID 173116, 3 pages, 2007.
- [16] J. Li, Y. Lu, Q. Ye, L. Delzeit, and M. Meyyappan, “A gas sensor array using carbon nanotubes and microfabrication technology,” *Electrochemical and Solid-State Letters*, vol. 8, no. 11, pp. H100–H102, 2005.
- [17] D. K. Chakravarthi, V. N. Khabashesku, R. Vaidyanathan et al., “Carbon fiber-bismaleimide composites filled with nickel-coated single-walled carbon nanotubes for lightning-strike protection,” *Advanced Functional Materials*, vol. 21, no. 13, pp. 2527–2533, 2011.
- [18] M. Horton, H. Hong, C. Li, B. Shi, G. P. Peterson, and S. Jin, “Magnetic alignment of Ni-coated single wall carbon nanotubes in heat transfer nanofluids,” *Journal of Applied Physics*, vol. 107, no. 10, Article ID 104320, 4 pages, 2010.
- [19] L. Wang and Y. Zhang, “Electronic and magnetic properties of metal atom adsorption on SWNT,” *Physica E: Low-Dimensional Systems and Nanostructures*, vol. 43, no. 4, pp. 889–892, 2011.
- [20] E. Durgun, S. Dag, V. M. K. Bagci, O. Gülseren, T. Yildirim, and S. Ciraci, “Systematic study of adsorption of single atoms on a carbon nanotube,” *Physical Review B*, vol. 67, no. 20, Article ID 201401, 4 pages, 2003.
- [21] C. Wang, G. Zhou, J. Wu, B. L. Gu, and W. Duan, “Effects of vacancy-carboxyl pair functionalization on electronic properties of carbon nanotubes,” *Applied Physics Letters*, vol. 89, no. 17, Article ID 173130, 3 pages, 2006.
- [22] Y. Dai, H. Hong, M. Guiver, and J. S. Welsh, “Reinforced films based on cross-linked water-soluble Sulfonated carbon nanotubes with Sulfonated Polystyrene,” *Journal of Nanoscience and Nanotechnology*, vol. 9, no. 9, pp. 5150–5156, 2009.
- [23] Z. Han and A. Fina, “Thermal conductivity of carbon nanotubes and their polymer nanocomposites: a review,” *Progress in Polymer Science*, vol. 36, no. 7, pp. 914–944, 2011.

## Research Article

# Synthesis and Characterisation of Calcium Carbonate Aragonite Nanocrystals from Cockle Shell Powder (*Anadara granosa*)

Abdullahi Shafiu Kamba,<sup>1</sup> Maznah Ismail,<sup>1</sup>  
Tengku Azmi Tengku Ibrahim,<sup>2</sup> and Zuki Abu Bakar Zakaria<sup>1</sup>

<sup>1</sup> Laboratory of Molecular Biomedicine, Institute of Bioscience, Universiti Putra Malaysia, 43400 Serdang, Malaysia

<sup>2</sup> Faculty of Veterinary Medicine, Universiti Putra Malaysia, 43400 Serdang, Malaysia

Correspondence should be addressed to Zuki Abu Bakar Zakaria; mdzukiabubakar@gmail.com

Received 24 November 2012; Accepted 24 March 2013

Academic Editor: Yun Zhao

Copyright © 2013 Abdullahi Shafiu Kamba et al. This is an open access article distributed under the Creative Commons Attribution License, which permits unrestricted use, distribution, and reproduction in any medium, provided the original work is properly cited.

The synthesis of pure calcium carbonate nanocrystals using a high pressure homogeniser (HPH) via a microemulsion system produced uniform nanosized particles, which were characterised using transmission electron microscopy (TEM), field-emission scanning electron microscopy (FESEM), X-ray diffraction (XRD), Fourier transform infrared spectroscopy (FTIR), and thermogravimetric analysis (TGA). The identified particles were aragonite polymorphs with a rod shape and were approximately 50 nm in size. The aragonite polymorph of calcium carbonate was prepared from biogenic materials, cockle shells, and exhibited unique characteristics (i.e., a higher density than that of calcite), which makes it biocompatible and potentially suitable for applications in the medical, pharmaceutical, cosmetic, and paint industries. The methods adopted and the nonionic surfactant used in the synthesis of calcium carbonate nanocrystalline aragonite polymorphs were environmentally friendly and can be scaled up for industrial production. The sources are naturally available materials that are by-products of the seafood industry, which offers an opportunity for exploitation in numerous industrial applications.

## 1. Introduction

Calcium carbonate nanoparticles are abundant inorganic biomaterials with different morphological structures that have attracted the interest of researchers in different fields. This interest is due to the wider application of these nanoparticles in many industries, such as the paint, rubber, and plastics industries. With the present focus of interest in nanotechnology, calcium carbonate nanoparticles have been observed to be biocompatible for use in medicine, pharmaceutical industries, and drug delivery systems [1, 2]. The most important aspect with respect to the synthesis of nanoparticles is control of the particle size, polymorphism, and morphology of the desired material. Control of this parameter has led to the development of new materials with unique properties that differ from those in the bulk material [3]. Many studies have been conducted to mimic nature in the synthesis of nanomaterial with the aim of analysing the biogenic materials

and identifying how nature controls the morphology, size, and polymorphism in organisms.

Biomineralization is the process by which a living organism secretes inorganic material in the form of a skeleton, a shell, teeth, or bone [1]. These processes are natural, are often performed with a high level of spatial control, and usually occur in a confined reaction environment. The organic matter or biopolymers observed in the hard tissue, such as the bones, teeth, and shells of living organisms, have the unique capacity to control the morphology, crystal size, polymorphism, and structure of the inorganic material. These biopolymers are usually soluble and are referred to as a functional matrix [1–3]. Biomaterials are highly optimised materials with remarkable properties, and they serve as natural archetypes for future materials [1]. These unusual properties have recently attracted the attention of numerous researchers, including both materials chemists and researchers in the medical and pharmaceutical sciences because of the biogenic origin and

potential biocompatibilities of these materials [3]. Biomaterials with an optimised structure exhibit better performance, durability, and appearance, which offers valuable opportunities for the development of new techniques for the synthesis and control of nanostructures materials with potential applications in pharmaceuticals, cosmetics, drug delivery, medicine, microelectronics, and energy technology [3].

Biological systems are capable of producing inorganic materials such as calcium carbonate with different structures, morphologies, and polymorphs. Such biological systems are observed in numerous marine organisms such as oyster shells, coral, ivory sea urchin, and mollusc shell bivalve nacre, whereby the main components of the shells are calcium carbonate and other organic components, such as anionic protein and glycoprotein [4].

Currently, research with respect to cockle shells, in which the primary component is approximately 98-99% calcium carbonate, is in its infancy [5, 6]. Calcium carbonate has three anhydrous crystalline phases: calcite, which is thermodynamically stable under ambient conditions; aragonite, which is a high-pressure polymorph that is less stable than calcite; and vaterite, which is the least stable among the three polymorphs and has the ability to transform into one of the other two polymorphs [7]. Different techniques for the preparation of calcium carbonate nanoparticles have been reported, including the precipitation of homogeneous solutions [8], water-in-oil-in-water emulsions [9], mechanochemical and sonochemical syntheses [10] and water-in-oil (W/O) microemulsions [11]. Other preparation methods include the high-pressure homogeniser (HPH) technique and high-gravity precipitation. For precipitation methods, two different routes have been reported with the only difference being the chemicals used. The first method is based on the carbonation process, whereby carbon dioxide gas is bubbled through aqueous slurry of calcium hydroxide at specific temperature in present of organic additive such as surfactant thereby inducing precipitation of calcium carbonate. The second method is known as double decomposition and involves the combination of salt of calcium ions with salt of carbonate ions, such as the reaction of calcium chloride or calcium nitrate with sodium carbonate or ammonium carbonate [12].

Most researchers are now diverting their attention to the microemulsion route for the synthesis of different types of nanoparticles. Microemulsions are a thermodynamically stable, optically transparent, isotropic dispersion of two immiscible liquids, such as water and oil, stabilised by an interfacial film of a surfactant molecule [13]. The system is a single optical dispersion of thermodynamically stable liquids that typically consists of small particle droplets with diameters in the range of less than from 10 nm to 100 nm [14]. A microemulsion serves as a special microreactor that inhibits the growth of nanosized particles [15]. The advantage of this method is that it increases the homogeneity of the chemical decomposition at the nanolevel and allows the easy preparation of nanocrystals of comparatively equal sizes [16].

The research in this paper was focused on the synthesis of calcium carbonate nanocrystals from cockle shells by the microemulsion route using a HPH. The process is a top-down

technique that occurs in a special homogenising valve at the heart of homogenising equipment. The fluid passes through a minute gap in the homogenising valve [17], which creates conditions of high turbulence and shear, combined with compression, acceleration, and a pressure drop. The impact causes disintegration of particles and dispersion throughout the sample [17]. After homogenisation, the particles are uniform in size, and their sizes depend on the number of cycles, the processing, and the operating pressure. The homogeniser is the most efficient device for the reduction of particle and droplet sizes.

To the best of our knowledge, no research related to the synthesis of calcium carbonate nanocrystals from biogenic origins or its reservoir using calcium carbonate as the main source of calcium and carbonate ions has been reported. Most research has focused on the use of chemical reactions, whereby the salts of calcium and carbonate ions act as the precursors for the synthesis of calcium carbonate nanocrystals.

## 2. Experimental

*2.1. Synthesis of Calcium Carbonate Powder.* Cockle shells were obtained from market. The calcium carbonate powders were prepared from the cockle shells according to the procedure described by Islam et al. [18]. Samples of the cockle shells were dried in an oven at 50°C for 7 days, and the shells were then crushed and blended into a fine powder, which was sieved through a 90- $\mu\text{m}$  laboratory stainless steel sieve (Endecott, London, England). The calcium carbonate powders were finally packed into a polyethylene plastic bag for further analyses.

*2.2. Synthesis of Calcium Carbonate Nanocrystals.* The synthesis of calcium carbonate nanocrystals was performed through oil-in-water (O/W) microemulsions using a HPH. In this technique, the particles sizes are reduced after leaving the homogenising gap by cavitations, particle collisions, and shear forces [19, 20].

The calcium carbonate nanocrystals were prepared by the dissolution of 2 g of dry cockle shell powder in a formulated oil-in-water (O/W) microemulsion, which was moderately stirred by a magnetic stirrer for 5 min at 100 rpm to form a calcium carbonate suspension. The formulated suspension was passed through the liquid inlet of a HPH for premilling at a moderate pressure of 300 and 500 bars for three cycles each. The premilled suspension was collected at the HPH outlet and was again passed through the HPH liquid inlet at a high pressure of 1500 bars for 25 homogenising cycles to obtain the desired product. The product of the crystal suspension was filtered and dried in an oven at 105°C for 24 hours.

*2.3. Characterisation of Calcium Carbonate Nanocrystals.* The following instruments were employed for the observation and characterisation of the calcium carbonate nanocrystals. The morphology and particle size of the nanocrystals were analysed using a transmission electron microscope (TEM, Hitachi H-7100) and a field-emission scanning electron microscope (FESEM, JOEL 7600F) operated at a voltage of

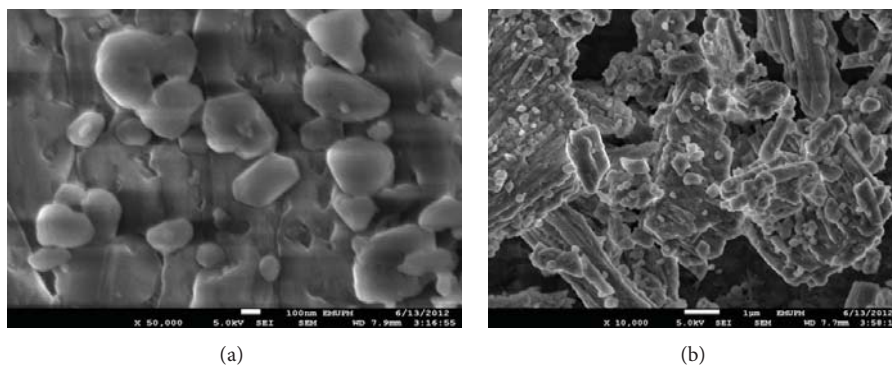


FIGURE 1: FESEM micrographs of (a) cockle shell calcium carbonate nanocrystals and (b) cockle shell powder.

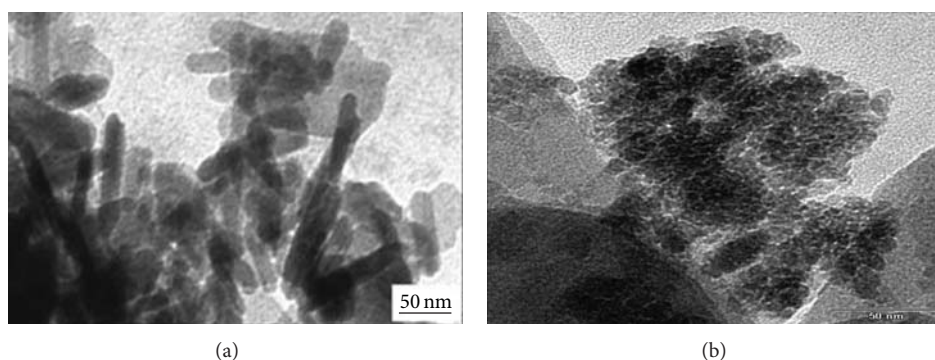


FIGURE 2: TEM images of (a) rod-shaped nanocrystals synthesised via microemulsion routes and (b) cockle shell powder without organic additive added.

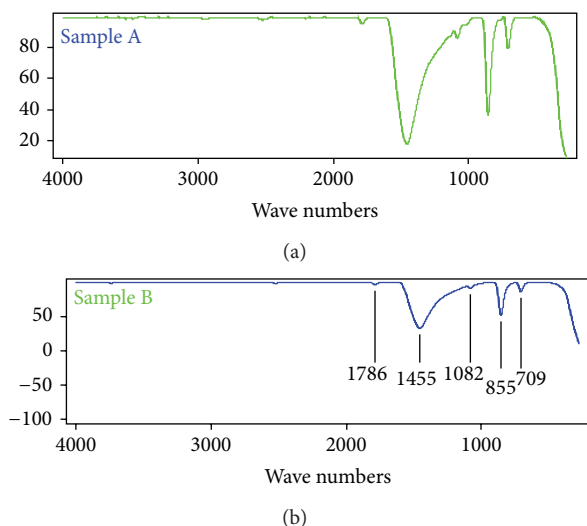


FIGURE 3: FTIR spectra of calcium carbonate nanocrystals (a) and cockle shell powder (b).

5 kV and equipped with an energy-dispersive X-ray spectroscopy (EDX) unit. The crystal powder was characterised by X-ray powder diffraction (XRD) using a Rigaku X-ray diffractometer equipped with a Cu  $K\alpha$  ( $\lambda = 0.15406$  nm) radiation source; samples were scanned at a rate of 40/min.

Pellets of the calcium carbonate nanocrystals were calibrated in a weight proportion of 1 wt% in Ker, and analyses were performed with a Fourier-transform infrared spectrometer (FTIR, model 100, Perkin Elmer, 710 Bridgeport Avenue, Shelton, CT, USA) in the range of 400–4000  $\text{cm}^{-1}$ . Thermogravimetric analysis of the calcium carbonate nanocrystals was performed using a TG-DTA instrument (Netzsch STA449C) with an air flow of 100 mL/min and a heating rate of 10 K/min from room temperature to 1000°C.

### 3. Results and Discussion

**3.1. FESEM and TEM Characterisation of Calcium Carbonate Nanocrystals.** The morphological characteristics of the calcium carbonate nanocrystals presented in Figures 1(a) and 1(b) are typical FESEM micrographs of the samples under study. The nanometre-sized and rod-shaped particles in Figure 1(a) were synthesised in the confined microemulsion system, whereas Figure 1(b) shows micrographs of a cockle shell powder without any organic additives. These results indicate a natural ability of the biological system to control specific size and morphology, which is very difficult to achieve using classical methods or colloid-chemistry routes [21]. A living organism has the ability to secrete macromolecules, such as in oyster shells, coral, mollusc shells and bivalve nacre. Living organisms achieve this natural

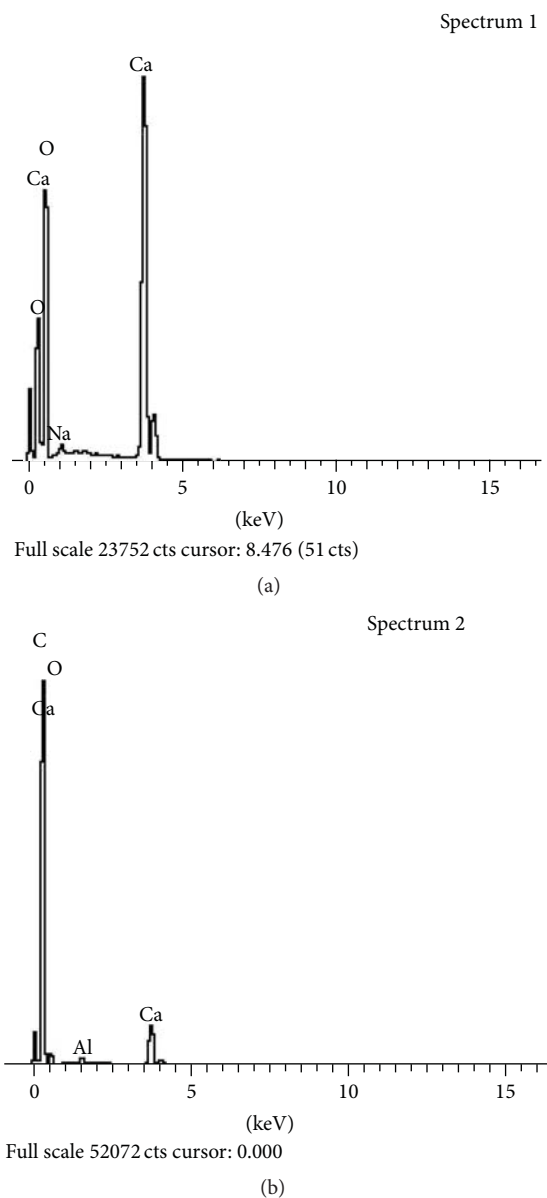


FIGURE 4: EDX spectral data for calcium carbonate nanocrystals and cockle shell powder.

phenomenon by utilising the secreted macromolecules (proteins, polysaccharides, and acidic macromolecules) as the nucleators (usually in the form of phospholipid membranes) to modulate the formation of a unique inorganic-organic material with a special morphology and function [21].

TEM was also used to study the calcium carbonate crystal particles. The images of the crystal presented in both Figures 2(a) and 2(b) reveal a rod shape of calcium carbonate aragonite polymorphs. The particles in Figure 2(a) are uniformly distributed at the nanometre scale and were formed in the microemulsion system; this system is considered an ideal medium for the preparation of inorganic nanoparticles [22]. The nanocrystal particles synthesised in the microemulsion

system presented in Figure 2(a) differ in size, being approximately 50 nm with individual particles measuring 12–30 nm; in addition, the shape of the particles is clear, and the difference in the particle size may result from the presence of Tween 80 used in the prepared microemulsion. In contrast, the particles shown in Figure 2(b) agglomerated, and the rod shape was not clear compared with the shape in Figure 2(a), which may be due to the differences in the preparation conditions and the additional surfactant (Tween 80) used. Surfactants, both ionic and nonionic, have been reported to strongly affect the size and morphology of calcium carbonate nanoparticles during synthesis [23]. However, nonionic surfactants have a weaker effect on the morphology than do ionic surfactants [23]. This result is most likely due to the weak interactions between a nonionic surfactant and  $\text{Ca}^{2+}$  and  $\text{CO}_3^{2-}$  ions [24]; in addition, the microemulsion route, when used for the synthesis of nanoparticles, enables control of the size and morphology of the obtained materials [23].

**3.2. FTIR Spectra of Calcium Carbonate Nanocrystals.** FTIR spectra of the calcium carbonate nanocrystals are presented in Figures 3(a) and 3(b). FTIR spectroscopy is an important instrument used to identify different phases of organic and inorganic compounds and, specifically, calcium carbonate phases due to the differences in their carbonate ions,  $\text{CO}_3^{2-}$ . Carbonate ions and similar molecules have four normal modes of vibration peaks:  $\nu_1$ , symmetric stretching;  $\nu_2$ , out-of-plane bending;  $\nu_3$ , doubly degenerate planar asymmetric stretching; and  $\nu_4$ , doubly degenerate planar bending [25]. The spectral data obtained for the samples reveal a broad absorption peak of  $\text{CO}_3^{2-}$  at  $\sim 1455\text{ cm}^{-1}$ ,  $\sim 1082\text{ cm}^{-1}$ ,  $\sim 1786\text{ cm}^{-1}$ ,  $\sim 855\text{ cm}^{-1}$ , and  $\sim 709\text{ cm}^{-1}$ , which have been reported to be the common characteristic features of the carbonate ions in calcium carbonate and are the fundamental modes of vibration for this molecule [26]. However, the observed bands at  $\sim 1082\text{ cm}^{-1}$  and  $\sim 855\text{ cm}^{-1}$  were carefully assigned as  $\nu_1$  symmetric stretching and  $\nu_2$  out-of-plane bending modes of  $\text{CO}_3^{2-}$ , respectively. The peak at  $\sim 1082\text{ cm}^{-1}$  was only observed in the spectrum of aragonite-phase calcium carbonate, whose  $\text{CO}_3^{2-}$  ions are inactive in the infrared region. This observation was verified by other reports in the literature on characteristic infrared bands, which are experimentally not observed in the spectrum of calcite [26]. In contrast, the doubly degenerate peak that appears at  $\sim 709\text{ cm}^{-1}$  can be attributed to the  $\nu_4$  in-plane bending mode of  $\text{CO}_3^{2-}$  ions, which indicates a structural change in the calcium ions from the symmetry of the calcite phase. This degeneracy can only be removed by splitting the band into two; thus, the band is attributed to the aragonite phase only, which has been confirmed in the literature [26]. This assertion was also supported by a very broad doubly degenerate band  $\nu_3$  at  $\sim 1452\text{ cm}^{-1}$ , which confirms the structural changes in the symmetry of the  $\text{CO}_3^{2-}$  molecular ions that correspond to the asymmetric stretching mode of  $\text{CO}_3^{2-}$ . A similar result was also reported by Cheng et al. [27]. The fundamental changes in the positions of the vibration mode of a molecule are caused by a modification of the electrostatic valence of the Ca–O bond due to changes in

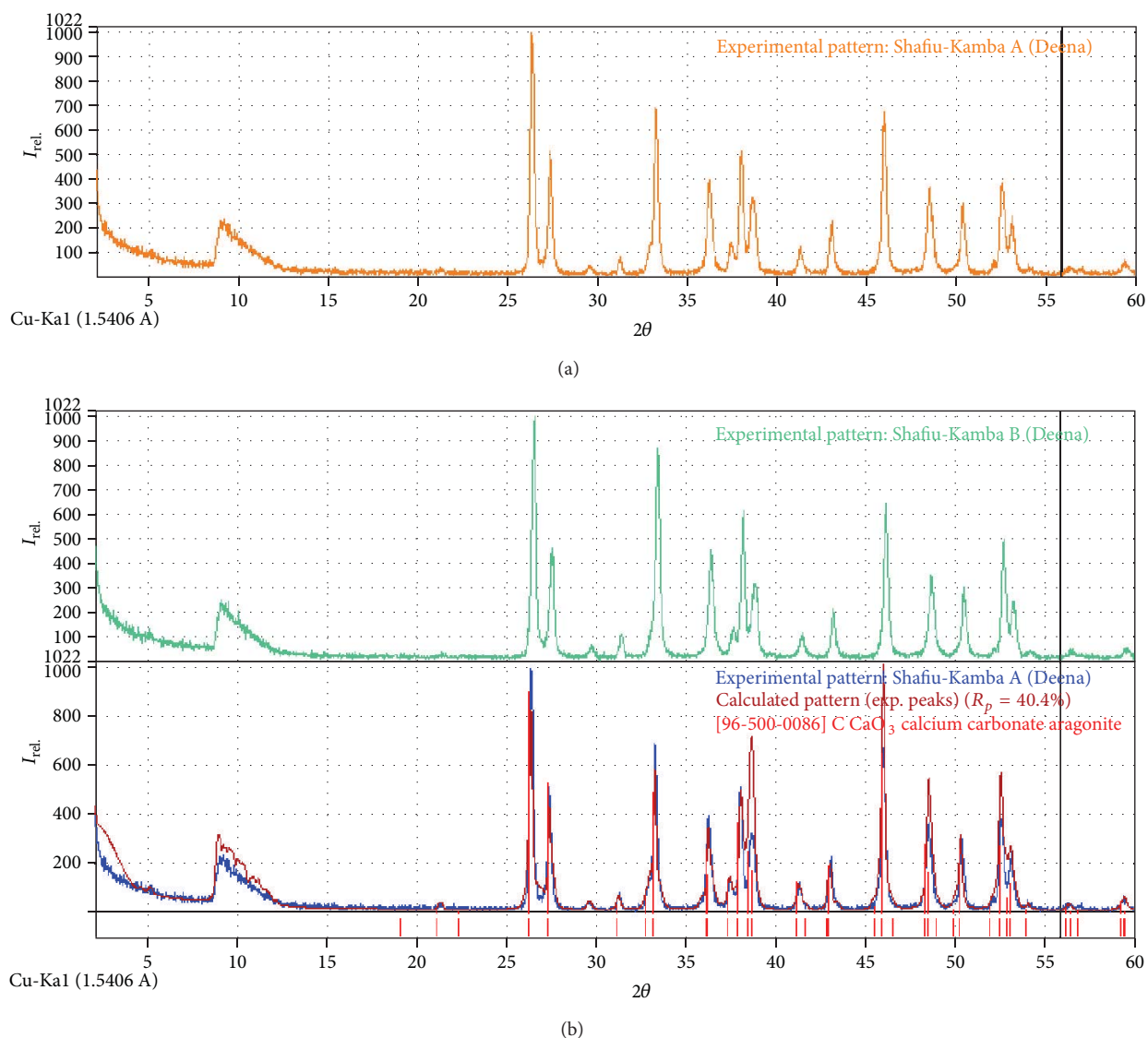


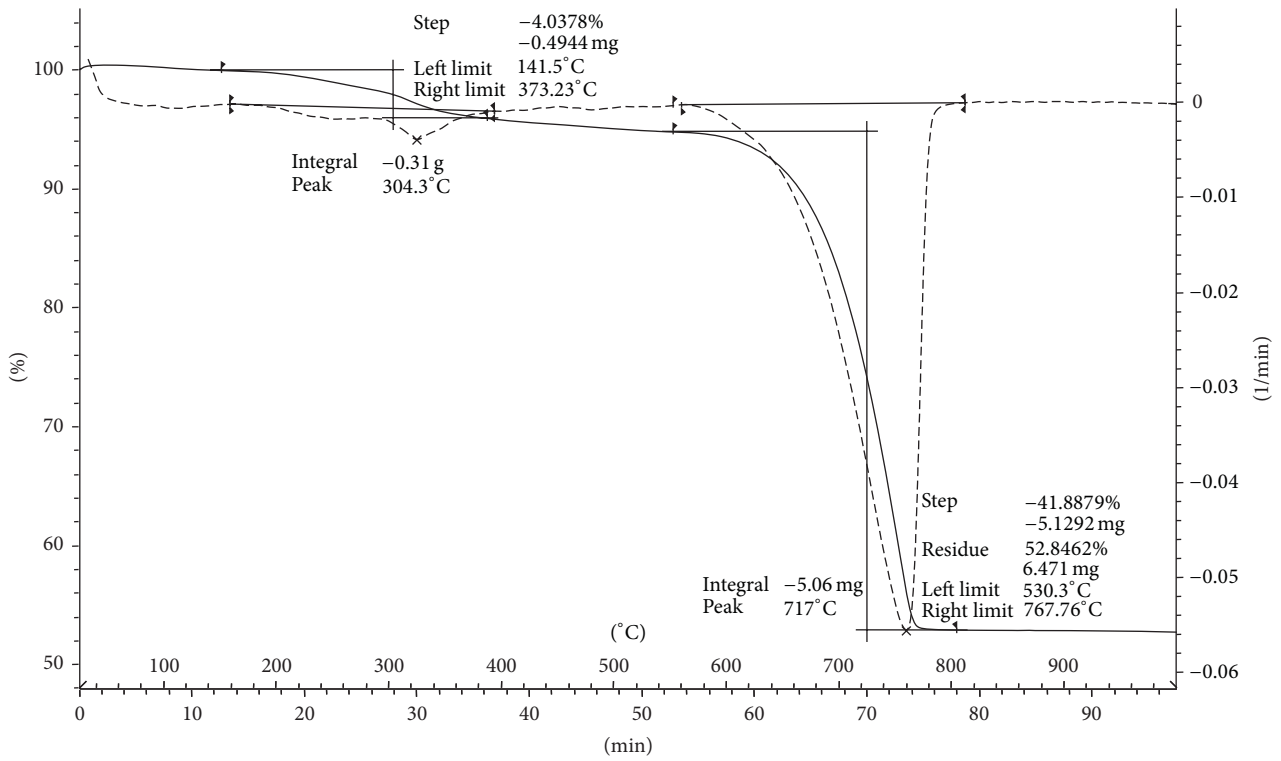
FIGURE 5: X-ray diffraction patterns of calcium carbonate nanocrystals (a) and cockle shell powder (b).

the coordination; the Ca–O bond alteration occurs because the displacement of the carbonate vibration mode changes in the environment of oxygen atoms [26–28]. This evidence further demonstrates that the synthesis involves a single phase of calcium carbonate aragonite crystals. The observed IR frequencies at  $\sim 1786\text{ cm}^{-1}$  and  $\sim 252\text{ cm}^{-1}$  are due to the combination of the fundamental vibration frequencies of the carbonate ions assigned between ( $\nu_1$  and  $\nu_4$ ) and ( $\nu_1$  and  $\nu_3$ ), respectively, as reported in the literature [26–28].

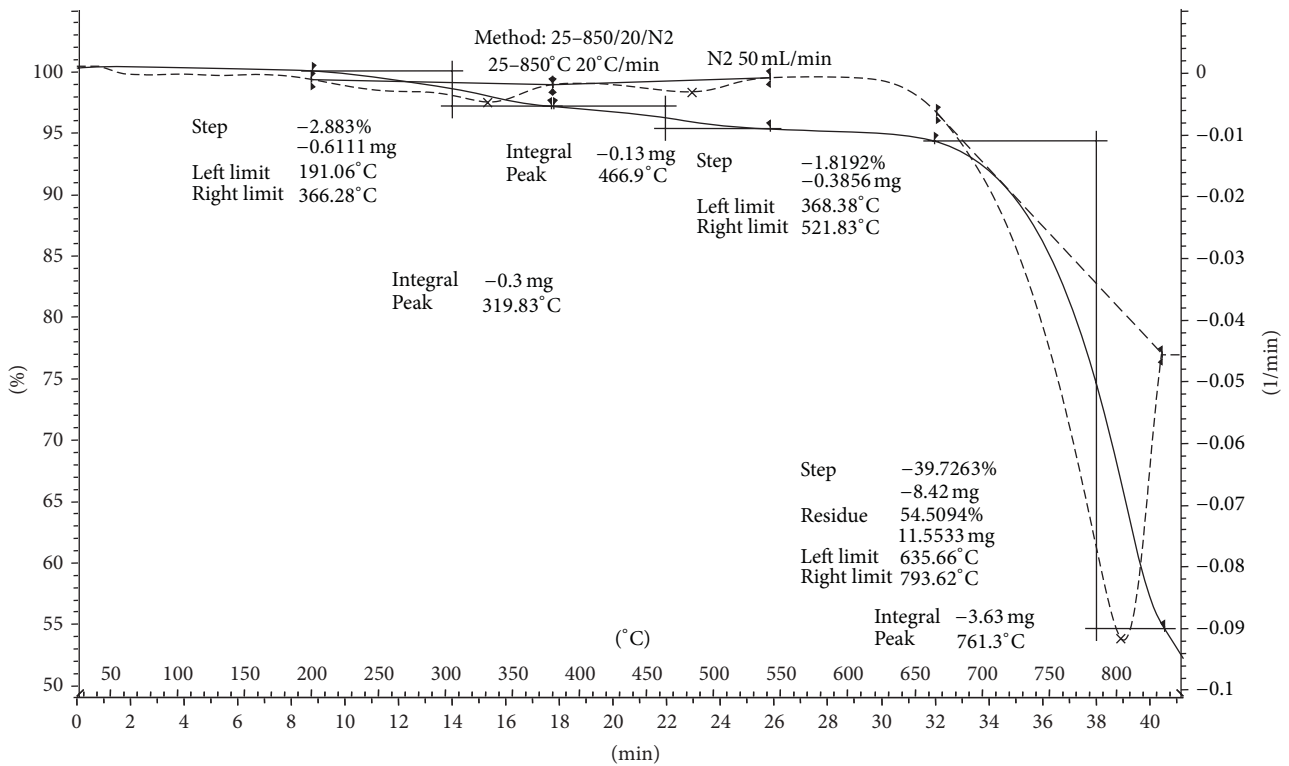
Both the cockle shell powder and the synthesised calcium carbonate nanocrystals possess the same vibration frequencies as observed in the FTIR data obtained in Figure 3(a). The results demonstrate that the nonionic surfactant (Tween 80) used in the preparation of the microemulsion does not affect the vibration frequencies because no additional peaks were observed when the spectrum of the calcium carbonate nanocrystals was compared with that of the cockle shell

powder in Figure 3(b). The cockle shell powder was prepared in distilled water only and without the use of additional organic additives or surfactants. This result may be due to the presence of a natural or organic matrix composed of an elastic biopolymer, such as the silk-like protein chitin; this organic matrix secreted by marine shell plays an important role in controlling the inorganic structure, morphology, size, and polymorphism [28, 29].

**3.3. Elemental Compositions of Synthesised Nanocrystals and Cockle Shell Powder.** The chemical compositions of the samples were analysed using EDX, which revealed the presence of individual elements in the samples. As indicated in Tables 1(a) and 1(b), the samples contained almost identical elements, with no significant differences observed between the elements detected in the two samples analysed. Both



(a)



(b)

FIGURE 6: (a) Graphical representation of nanocrystal TGA results. (b) Graphical representation of cockle shells powder TGA data.

TABLE 1: (a) Elemental compositions of calcium carbonate nanocrystals and (b) elemental compositions of cockle shell powder.

| (a)                |        |        |        |         |  |           |
|--------------------|--------|--------|--------|---------|--|-----------|
| Spectrum           | Carbon | Oxygen | Sodium | Calcium |  | Total (%) |
| Spectrum 1         | 20.18  | 59.51  | 0.53   | 19.78   |  | 100.00    |
| Spectrum 2         | 14.44  | 46.73  | 0.30   | 38.53   |  | 100.00    |
| Spectrum 3         | 13.57  | 28.14  | 0.18   | 58.11   |  | 100.00    |
| Mean               | 16.06  | 44.79  | 0.34   | 38.81   |  | 100.00    |
| Standard deviation | 3.59   | 15.78  | 0.17   | 19.17   |  |           |
| Max.               | 20.18  | 59.51  | 0.53   | 58.11   |  |           |
| Min.               | 12.65  | 28.14  | 0.18   | 19.78   |  |           |

| (b)                |        |        |        |         |           |           |
|--------------------|--------|--------|--------|---------|-----------|-----------|
| Spectrum           | Carbon | Oxygen | Sodium | Calcium | Aluminium | Total (%) |
| Spectrum 1         | 22.18  | 50.51  | 0.53   | 27.60   | 0.17      | 100.00    |
| Spectrum 2         | 12.44  | 46.32  | 0.30   | 30.53   | 0.41      | 100.00    |
| Spectrum 3         | 13.57  | 37.14  | 0.18   | 58.11   |           | 100.00    |
| Mean               | 16.06  | 44.79  | 0.34   | 38.81   |           | 100.00    |
| Standard deviation | 3.59   | 15.78  | 0.17   | 19.17   |           |           |
| Max.               | 19.82  | 69.52  | 0.36   | 58.11   |           |           |
| Min.               | 13.57  | 26.42  | 0.16   | 23.87   |           |           |

samples contained negligible traces of elemental sodium, and a minute percentage of aluminium was recorded only in the cockle shell powder (Figure 4(b)). This analysis proves that the composition of the calcium carbonate in the cockle shell powder is not 100% pure due to the presence of other elements such as aluminium and sodium.

**3.4. X-Ray Diffraction Pattern of Calcium Carbonate Nanocrystals.** X-ray diffraction is a sensitive instrument used for the identification of crystalline phases of inorganic compounds. The data obtained from the X-ray diffraction patterns in Figures 5(a) and 5(b) demonstrate the crystalline nature and phase composition of both samples under analysis. The X-ray diffraction pattern of the synthesised calcium carbonate nanocrystals and cockle shell powder in Figures 3(a) and of 3(b) exhibits characteristics peaks of aragonite at  $2\theta$  values of  $26.34^\circ$ ,  $33.24^\circ$ ,  $45.98^\circ$  and  $26.31^\circ$ ,  $33.24^\circ$ ,  $45.98^\circ$ , and respectively, which correlate with (hkl) indices of (111), (012), (221), and (021), (012), and (221), respectively. These are the strongest peaks observed in the X-ray diffraction patterns of the analysed samples. However, peaks are also observed at  $26.71^\circ$ ,  $26.87^\circ$ ,  $27.02^\circ$ ,  $27.38^\circ$ ,  $27.57^\circ$ ,  $27.72^\circ$ ,  $41.28^\circ$ ,  $45.62^\circ$ ,  $46.54^\circ$ ,  $48.84^\circ$ , and  $52.53^\circ$ . These values also correspond with calcium carbonate aragonite polymorphs reported in the PDF-4+ data bank of the International Centre for Diffraction Data [30]. All the reflections can be attributed to the pure aragonite phase of calcium carbonate, which validates the FTIR results of the aragonite polymorph of calcium carbonate.

**3.5. Thermal Decomposition of Calcium Carbonate Nanocrystals.** Thermogravimetric analyses of the cockle shell powder and the nanocrystals synthesised from the powder were

performed using the shrinking core model (SCM), whereby the reaction usually begins from the outer layer of the particles and moves toward the solid, which yields an ash solid as the converted material [5]. Therefore, Figures 6(a) and 6(b) illustrate the weight losses of the samples analysed during the process. Both samples were stable until  $300^\circ\text{C}$  and then decomposed in two steps. The first step was the initial process, which started with a very small weight loss of 4.0% due to the moisture content in the samples [31]; a similar result has been reported by Yu et al. [32] for bulk or microcalcium carbonate, and this value would also be the loss for nanoparticles of the same material, as reported as by Mohamed et al. [5]. Endothermic behaviour was also observed in the temperature range from  $304$  to  $373^\circ\text{C}$ , which may be due to the removal of water molecules from the carbonate lattice and the phase transformation of aragonite to calcite due to its unstable nature, as described previously. The phase transition of aragonite to calcite in coral and other marine shells occurs at a lower temperature than that of the phase transition in aragonite of mineral origin [26]. Second, a rapid weight loss of 41.88% and endothermic behaviour from  $600$  to  $800^\circ\text{C}$  were observed in both samples; in this temperature range, volatile minerals in the sample began to decompose, thereby releasing  $\text{CO}_2$ . For the cockle shell powder, the rate of decomposition was slower compared with that of the nanocrystals, as shown in Figure 6(a); this result has been reported in the literature, whereby particles of smaller size decompose faster than larger particles [5] because smaller-sized particles have a greater surface area than larger particles. However, both samples remained unchanged when the temperature reached  $900^\circ\text{C}$ . This result indicates the total decomposition of calcium carbonate to  $\text{CaO}$  and signifies the release of  $\text{CO}_2$  from calcium carbonate, leaving only the product, that is, "ash" [5]. This assumption

derived from the TGA analysis is also supported by the XRD data shown in Figure 5.

#### 4. Conclusions

Cockle shells consist of a higher percentage of calcium carbonate aragonite polymorphs, as described in the introduction of this paper. On the basis of the analysis of calcium carbonate nanocrystals from the cockle shell powder and that of the powder itself, the shells are composed of the aragonite form of calcium carbonate, which is less stable and denser than calcite. These properties make it a potential biomaterial for medical applications. The thermogravimetric analyses of the two samples revealed the solid-state phase transformation of aragonite to calcite. The transformation of aragonite began at approximately at 300–373°C and at 600–700°C; the complete removal of volatile substances occurred, and the phase transformation of aragonite to calcite was completed with a loss of 41% of the initial weight of the sample. These results also demonstrate that smaller particles decompose faster than larger particles within a short time at low temperatures.

The methods adopted and the nonionic surfactant used in the synthesis of aragonite nanocrystals are environmentally friendly and could be scaled up for industrial production, thereby permitting a greener synthesis from naturally available materials and utilising the waste shells that are a by-product of the seafood industry. This method thus offers a great opportunity for exploitation in numerous industrial applications.

#### Conflict of Interests

The authors would like to confirm that there is no conflicts of interests associated with this paper submitted for publication, and there has been no significant financial support for this work that could have affected its outcome. The authors confirm that the paper has been read and approved by all named authors and that there are no other persons who satisfy the criteria for authorship but who are not listed. The authors further confirm that the order of authors listed in the paper has been approved by all of the authors. The authors confirm that they have given due consideration to the protection of intellectual property associated with this work and that there are no impediments to publication, including the timing of publication, with respect to intellectual property. In so doing, The authors confirm that they have followed the regulations of their institutions concerning intellectual property.

#### References

- [1] A. Xu, Y. Ma, and H. Colfen, "Biomimetic mineralization," *Journal of Material Chemistry*, vol. 17, pp. 415–449, 2006.
- [2] Y. Fukui and K. Fujimoto, "Bioinspired nanoreactor based on miniemulsion system to create organic-inorganic hybrid nanoparticle and nanofilm," *Journal of Material Chemistry*, vol. 22, no. 8, pp. 3493–3499, 2012.
- [3] Q. L. Feng, G. Pu, Y. Pei, F. Z. Cui, H. D. Li, and T. N. Kim, "Polymorph and morphology of calcium carbonate crystals induced by proteins extracted from mollusk shell," *Journal of Crystal Growth*, vol. 216, no. 1, pp. 459–465, 2000.
- [4] R. Velázquez-Castillo, V. Reyes-Gasga, D. I. García-Gutierrez, and M. Jose-Yacaman, "Nanoscale characterization of nautilus shell structure: an example of natural self-assembly," *Journal of Materials Research*, vol. 21, no. 6, pp. 1484–1489, 2006.
- [5] M. Mohamed, S. Yusup, and S. Maitra, "Decomposition study of calcium carbonate in cockle shells," *Journal of Engineering Science and Technology*, vol. 7, no. 1, pp. 1–10, 2012.
- [6] A. J. Awang-Hazmi, A. B. Z. Zuki, M. M. Nordin, A. Jalila, and Y. Norimah, "Mineral composition of the cockle (*Anadara Granosa*) shells of west coast of peninsular Malaysia and its potential as biomaterial for use in bone repair," *Journal of Animal and Veterinary Advances*, vol. 6, no. 5, pp. 591–594, 2007.
- [7] Y. Guowei., L. Wang, and H. Jianhua, "The crystallization behavior of calcium carbonate in ethanol/water solution containing mixed nonionic/anionic surfactants," *Powder Technology*, vol. 192, no. 1, pp. 58–64, 2009.
- [8] R. Gupter, *Synthesis of Precipitated Calcium Carbonate Nanoparticles Using Modified Emulsion Membranes [M.S. thesis]*, Georgia Institute of Technology, Atlanta, Ga, USA, 2004.
- [9] G. X. Wu, J. Ding, and J. M. Xue, "Synthesis of calcium carbonate capsules in water-in-oil-in-water double emulsions," *Journal of Materials Research*, vol. 23, no. 1, pp. 140–149, 2008.
- [10] T. A. Hassan, V. K. Rangari, V. Fallon, Y. Farooq, and S. Jeelani, "Mechanochemical and sonochemical synthesis of bio-based nanoparticles," in *Proceedings of the Nanotechnology Conference*, pp. 278–281, June 2010.
- [11] A. Georgieva, B. Georgieva, Z. Bogdanov, and D. K. Stefanov, "Microemulsion water-in-oil (W/O)—microreactor for synthesis of ultrafine carbonate nanostructures," *University of Ruse Union of Scientists-Ruse*, vol. 50, no. 9, pp. 34–38, 2011.
- [12] R. Babou-Kammoe, S. Hamoudi, F. Larachi, and K. Belkacemi, "Synthesis of calcium carbonate nanoparticles by controlled precipitation of saturated carbonated and calcium Nitrate aqueous solution," *The Canadian Journal of Chemical Engineering*, vol. 90, pp. 26–33, 2012.
- [13] Y. H. Cho, S. Kim, E. K. Bae, C. K. Mok, and J. Park, "Formulation of a cosurfactant-free O/W microemulsion using nonionic surfactant mixtures," *Journal of Food Science*, vol. 73, no. 3, pp. E115–E121, 2008.
- [14] S. Talegaonkar, A. Azeem, F. J. Ahmad, R. K. Khar, S. A. Pathan, and Z. I. Khan, "Microemulsions: a novel approach to enhanced drug delivery," *Recent Patents on Drug Delivery and Formulation*, vol. 2, no. 3, pp. 238–257, 2008.
- [15] K. C. Song and J. H. Kim, "Synthesis of high surface area tin oxide powders via water-in-oil microemulsions," *Powder Technology*, vol. 107, no. 3, pp. 268–272, 2000.
- [16] C. Karagiozov and D. Momchilova, "Synthesis of nano-sized particles from metal carbonates by the method of reversed mycelles," *Chemical Engineering and Processing*, vol. 44, no. 1, pp. 115–119, 2005.
- [17] GEA.Niro-Soavi, "Laboratory Manual for Higher pressure Homogenizer," 2011, <http://www.nirosoavi.com/index.asp>.
- [18] N. Islam, Z. B. A. Bakar, M. M. Noordin, M. Z. B. Hussain, N. S. B. A. Rahman, and E. Ali, "Characterisation of calcium carbonate and its polymorphs from cockle shells (*Anadara granosa*)," *Powder Technology*, vol. 213, no. 1–3, pp. 188–191, 2011.
- [19] K. Mitri, R. Shegokar, S. Gohla, C. Anselmi, and R. H. Müller, "Lutein nanocrystal as antioxidant formulation for oral and

- dermal delivery," *International Journal of Pharmaceutics*, vol. 420, pp. 141–146, 2011.
- [20] R. Shegokar and R. H. Müller, "Nanocrystals: industrially feasible multifunctional formulation technology for poorly soluble actives," *International Journal of Pharmaceutics*, vol. 399, no. 1-2, pp. 129–139, 2010.
- [21] B. Cheng, M. Lei, J. Yu, and X. Zhao, "Preparation of monodispersed cubic calcium carbonate particles via precipitation reaction," *Materials Letters*, vol. 58, no. 10, pp. 1565–1570, 2004.
- [22] Y. Dong, Y. Chu, L. Dong, and Z. Yu-jiang, "Controllable synthesis of CaCO<sub>3</sub> micro/nanocrystals with different morphologies in microemulsion," *Chemical Journal of Chinese Universities*, vol. 26, no. 5, pp. 678–682, 2010.
- [23] A. Szcześ, "Influence of the surfactant nature on the calcium carbonate synthesis in water-in-oil emulsion," *Journal of Crystal Growth*, vol. 311, no. 4, pp. 1129–1135, 2009.
- [24] Y. Tang, B. Du, L. Li, J. Yang, and Y. Zhang, "Effects of Tx-100-SDS on crystal growth of calcium carbonate in reverse microemulsion solution," *Chinese Science Bulletin*, vol. 52, no. 1, pp. 78–83, 2007.
- [25] Y. Wang, Y. X. Moo, C. Chen, P. Gunawan, and R. Xu, "Fast precipitation of uniform CaCO<sub>3</sub> nanospheres and their transformation to hollow hydroxyapatite nanospheres," *Journal of Colloid and Interface Science*, vol. 352, no. 2, pp. 393–400, 2010.
- [26] C. Linga Raju, K. V. Narasimhulu, N. O. Gopal, J. L. Rao, and B. C. V. Reddy, "Electron paramagnetic resonance, optical and infrared spectral studies on the marine mussel *Arca burnesi* shells," *Journal of Molecular Structure*, vol. 608, no. 2-3, pp. 201–211, 2002.
- [27] B. Cheng, W. Cai, and J. Yu, "DNA-mediated morphosynthesis of calcium carbonate particles," *Journal of Colloid and Interface Science*, vol. 352, no. 1, pp. 43–49, 2010.
- [28] V. Vongsavat, P. Winotai, and S. Meejoo, "Phase transitions of natural corals monitored by ESR spectroscopy," *Nuclear Instruments and Methods in Physics Research B*, vol. 243, no. 1, pp. 167–173, 2006.
- [29] Y. Hu, Y. Ma, Y. Zhou, F. Nie, X. Duan, and C. Pei, "Hen eggwhite-mediated stack crystallization of calcium carbonate," *Journal of Crystal Growth*, vol. 312, no. 6, pp. 831–836, 2010.
- [30] C. A. Korash, "Mechanical properties of a Nanostructure Poly (KAMPS)/Aragonite composite," in *Mechanic of Biological System and Materials. Volume 2*, Conference proceedings of the society for experimental mechanic series, pp. 131–136, 2011.
- [31] *Powder Diffraction File-4 Release*, International Centre for Diffraction Data (ICDD), Newton square, Pa, USA, 2012.
- [32] J. Yu, H. Guo, S. A. Davis, and S. Mann, "Fabrication of hollow inorganic microspheres by chemically induced self-transformation," *Advanced Functional Materials*, vol. 16, no. 15, pp. 2035–2041, 2006.

## Research Article

# Improved Processing of Carbon Nanotube Yarn

Chaminda Jayasinghe,<sup>1</sup> Trent Amstutz,<sup>1</sup> Mark J. Schulz,<sup>2</sup> and Vesselin Shanov<sup>1</sup>

<sup>1</sup> Department of Chemical and Material Science Engineering, University of Cincinnati, Cincinnati, OH 45221-0012, USA

<sup>2</sup> Department of Mechanical Engineering, University of Cincinnati, Cincinnati, OH 45221-0072, USA

Correspondence should be addressed to Vesselin Shanov; [Vesselin.Shanov@uc.edu](mailto:Vesselin.Shanov@uc.edu)

Received 22 October 2012; Accepted 10 March 2013

Academic Editor: Qian-Ming Gong

Copyright © 2013 Chaminda Jayasinghe et al. This is an open access article distributed under the Creative Commons Attribution License, which permits unrestricted use, distribution, and reproduction in any medium, provided the original work is properly cited.

We compared mechanical and electrical properties of carbon nanotube (CNT) yarns formed from four different spinning methods. In these methods, a yarn was spun from two aligned CNT arrays. CNT yarns fabricated from each method were tested quantitatively through the mechanical and electrical properties and reported. This improvement is considered to be caused by multiple factors, such as reduction of the yarn diameter, densification, water evaporation, and CNT orientation. The best electrical and mechanical property of CNT yarn was observed from the fourth spinning method where heating and tension during spinning were applied. The introduced yarn spinning methods are appropriate for continuous mass production of high strength carbon nanotube yarns with controlled diameter, strength, and electrical conductivity.

## 1. Introduction

Carbon nanotubes (CNTs) are considered one of the strongest and stiffest materials known. They have unique atomic structure with interesting related properties such as high tensile strength and Young's modulus, high aspect ratio, and good electrical and thermal conductivities. These unique properties open up various applications in different areas, for example, in advance electronics, biotechnology, and nanomechanics.

Research efforts have been carried out to fabricate macroscopic threads and yarn structures to make the use of the CNTs unique properties. However there are technical challenges to transfer individual CNT properties into spun yarn structures because CNT bundles tend to slide in yarn microstructures. Therefore may be promising techniques have been implemented to improve the strength of the CNT yarn. One practical application is polymer dip coating which will improve the mechanical properties of CNT yarns structures but it will not help to improve the electrical properties of the yarn. Other is high temperature annealing which will help to improve the electrical and thermal properties of the CNT yarn. However, the disadvantage of thermal annealing is high cost and brittle behavior of the yarn structures.

There are mainly two methods of CNT yarn production: liquid-state spinning and solid-state spinning. Most synthetic fibers are created from a concentrated, viscous liquid. In liquid based spinning, CNTs are dispersed into fluids and either extruded or coagulation spun into fibers [1–3]. The major issue with applying this approach to CNTs is that there is a relatively high fraction of remaining polymer and using of short CNTs, which limits the overall strength and electrical and thermal conductivity of the produced fiber [4]. The solid-state spinning can be done in two methods. One is spinning CNT yarns directly from a furnace using floating catalyst [5]. The second method is substrate base spinning. Spinning directly from a furnace is a very efficient approach for continuous production of yarn that has good properties [6, 7]. Limitations of this method are the nanotubes used relatively short and there are catalyst impurities deposited in the final product.

Cotton and wool are naturally made fibers that are made by solid-state spinning. In solid state spinning, CNTs are assembled into either yarns or sheets without the use of any chemical additives. This process is practiced by a handful of research groups [2, 5, 8–11]. The posttreatment methods play an important role to improve the properties of CNTs. Zhang et al. showed substantial increase in the strength of

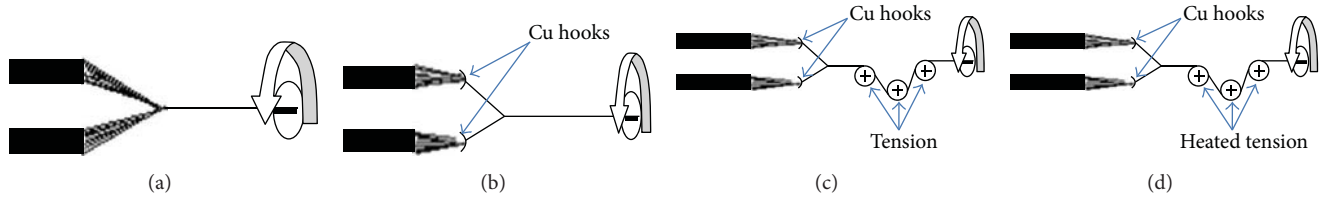


FIGURE 1: Schematic of the four different spinning methods (Methods 1 to 4) illustrated in the schematic corresponding to figures (a) to (d).

the CNT threads after infiltration with a polymer [10]. Zhu et al. reported that CNT yarn load capacity can be improved by postspun twisting which is affected by two factors: bringing the CNTs into closer contact with one another and therefore enhancing the van der Waals forces and higher radial compressive stress [5]. Other posttreatments involve densification with organic solvents such as ethanol and acetone, or heating the thread at high temperatures by applying an electric current [12]. Those posttreatment techniques require extra processing time [13–15]. In this paper, four improved methods for spinning CNT yarns are presented. The mechanical and electrical properties of CNT yarns made by each method are compared.

## 2. Experimental Procedure

We introduce four comparative methods of CNT yarn spinning. Spinnable carbon nanotube arrays were grown on silicon wafers using Chemical Vapor Deposition (CVD) at 750°C for 30 minutes [16]. CNT arrays about 325 μm in height were spun into yarns at about a 2000 rpm twisting rate and a 324 mm/minute pulling speed.

Based on Method 1 (spinning yarn from two CNT arrays), two CNT forests were drawn out forming two ribbons which were directly spun into a two-ply thread without any further treatment (Figure 1(a)). This spinning technique has been used by several other groups [2, 5, 8–11] and served in our experiments as a reference (baseline) to which all the other techniques were compared in the present work. Method 2 (two arrays with copper hooks) was designed to employ two copper hooks which applied small tension force to the ribbons prior to spinning (Figure 1(b)). This arrangement forced the ribbons to condense and spin into low tension threads before they were combined into the final thread. Method 3 (two arrays with copper hooks and tension rods) improves the second method by using the same hook system but also implementing several tensioning rods along the spun yarn (Figure 1(c)). The rods applied tension to the thread in order to increase the interactions between the CNTs and to enhance the van der Waals forces between the individual carbon nanotubes. The intention of this arrangement was to increase the strength and decrease the resistivity of the thread. Method 4 (two arrays with copper hooks and heated tension rods) is a modification of the third one, where the tensioning rods were modified to heat the thread simultaneously while applying tension (Figure 1(d)). This the method we call heating and tension spinning (HTS).

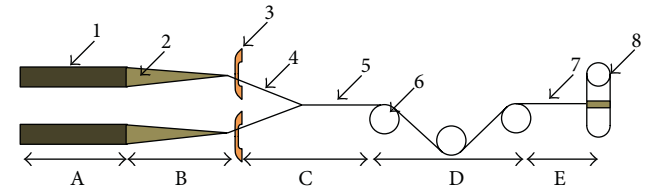


FIGURE 2: Schematic of the setup used in the proposed improved spinning process: A: CNT forest; B: web formation zone; C: partially twisted thread and yarn formation zone; D: tension and heat zone; E: twisting zone; (1) spinnable CNT forest; (2) CNT web; (3) copper hook; (4) partially twisted thread; (5) low twisted yarn; (6) heated rod for applying tension; (7) high twisted yarn; (8) spool.

The produced yarns were collected on spools. The samples were tested to determine their electrical resistivity and ultimate tensile strengths. Scanning electron microscopy (SEM) was used to measure the diameters of the tested yarns. The tensile strength measurement was conducted with a 3345-Instron stress-strain instrument. A four-probe setup was employed to determine the electrical properties of the yarn using a Keithley 6220 current source and a 2182A nanovoltmeter. All the tests were conducted multiple times to verify consistency of the acquired data.

## 3. Results and Discussion

**3.1. Production of Carbon Nanotube Yarn.** Currently, dry spinning of CNTs is conducted by twisting the formed web while pulling CNTs from a single substrate [2, 5, 8–11]. This process can be improved by introducing different spinning techniques. Recently, Hu et al. tested a modified spinning process attempting to improve the mechanical properties of CNT yarns [17]. They formed CNT threads under tension spinning in a high volume heated environment. Here we introduced resistive heating tension rods which can be used as tension rods as well as heat sources. Therefore the process is really simple and cost effective. This paper also provides a detailed characterization and explanation of the improved spinning process. Figure 2 shows the main components of the improved spinning setup. The main steps in the process for spinning thread are described next.

**3.1.1. Web Formation.** CNTs initially pulled from the forest form a web. As the CNT bundles are pulled away from the forest they form a long “line” in which all the CNT centerlines are

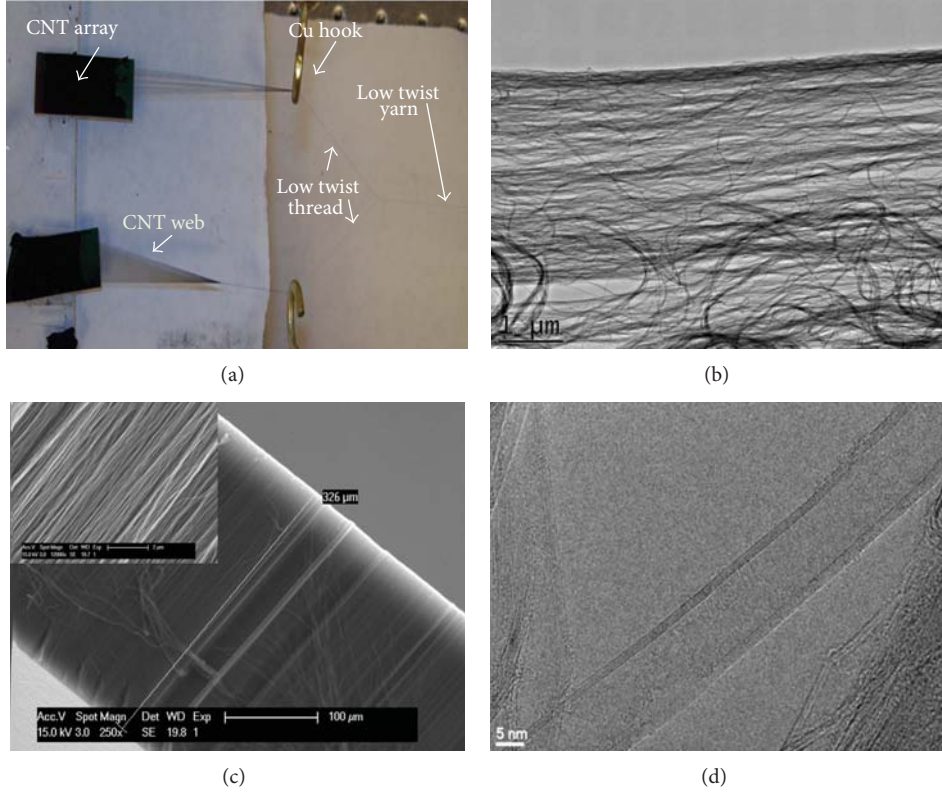


FIGURE 3: (a) Two CNT arrays spun into a yarn using the improved spinning method, (b) TEM image of CNT web, (c) SEM image of aligned CNT array (inset shows the forest cross-section at high magnification) and (d) HRTEM image of individual CNT with diameter  $\sim 15$  nm.

aligned and parallel. The CNT web is orthogonal to the initial nanotube direction in the array and parallel to the substrate surface. The web must be kept stable during the spinning process in order to yield well-formed yarn. As shown in Figure 3(a), smooth copper hooks are placed between the first tension rod and the substrates. This improves the contact between the loosely attached CNT bundles within the web. The portion between the CNT forest and the copper hooks is the CNT web, and just after the copper hook it is transformed into a low twist thread. During the spinning process, those low twisted threads are combined to form one yarn. The joining point is called the convergence point. The convergence point is located before the first tension rod. The portion of the yarn shown in Figure 2 at position 5 is called low twisted yarn. In general, the web is “fluffy” and for this reason it needs to be compacted before spinning. Transmission electron microscopy (TEM) images show that the CNT web consists of poorly aligned and randomly orientated CNT bundles (Figure 3(b)). The thickness of the web ranges from 50 nm to 100 nm. According to the capstan equation from the rope theory, when yarn passes through a pulley, the change in tension and the corresponding radial pressure on the yarn can be written as follows [17, 18]:

$$\frac{T_2}{T_1} = e^{\mu\varphi}, \quad (1)$$

$$N_1 = \frac{T_2}{\mu} (e^{\mu\varphi} - 1), \quad (2)$$

where  $T_1$ ,  $T_2$ ,  $\mu$ ,  $\varphi$ , and  $N_1$  are the low incoming tension and high outgoing tension, the frictional coefficient, the contact angle, and the radial pressure on the yarn, respectively.

**3.1.2. Thread Formed under Tension.** Figure 4 illustrates the arrangement of two copper hooks which apply a small initial tension force to the ribbons prior to the spinning. This force helps the ribbons to condense and spin together slightly before they combine into partially twisted yarn. This part of the fiber is called “low twisted yarn.” When the CNT web passes through the copper hooks, tension increases according to the capstan equation (1). This tension causes convergence of the web which is observed at a point close to the copper hooks. Further, Figure 4 displays the system using spinning under tension, where  $T_w$ ,  $T_1$ ,  $T_5$ ,  $\Omega_1$ , and  $\Omega_5$  are the web tension (incoming and outgoing after copper hook), final tension (near the CNT yarn winding spool), twisting of pre-formed thread, and twisting of final yarn, respectively. As the yarn passes through different stages, it is subjected to gradually increasing tension. The magnitude of the tension for a 3-tension rod arrangement increases accordingly:  $T_w < T_1 < T_2 < T_3 < T_4 < T_5 < T_3 < T_4 < T_5$ . Thus, for the tested spinning system, the change in tension after the last tension rod ( $T_5$ ) and the corresponding final radial pressure ( $N_5$ ) on the yarn is given by the following two equations, respectively:

$$\begin{aligned} T_5 &= 2 \cos \theta T_1 e^{\mu \sum_{i=1}^n \theta_i}, \\ N_5 &= \frac{T_5}{\mu} (e^{\mu\varphi_i} - 1), \end{aligned} \quad (3)$$

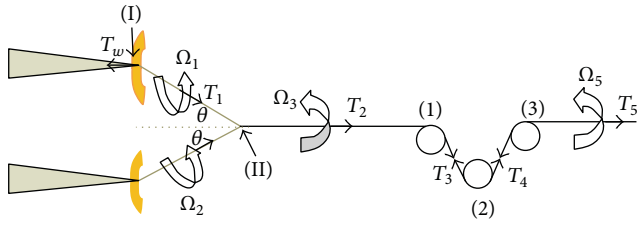


FIGURE 4: Schematic of heating and tension spinning system (HTS) with incorporated tension rods showing related process parameters:  $T_w$ ,  $T_1$ ,  $T_5$ ,  $\Omega_1$ , and  $\Omega_5$  denoted as the web tension (incoming and outgoing after copper hook), final tension (near the CNT yarn winding spool), twisting of pre-formed thread and twisting of final yarn respectively.

where  $\theta$  is the angle between partially twisted thread and the initially formed yarn at the convergent point (near II). Lastly, Figure 4 illustrates various stages in yarn formation leading to the final tension. Alignment and slip occur at the copper hooks, where tension is first applied to the thread. This causes increased CNT interaction in the bundles and yarn. Higher alignment of the CNTs and bundles results in more compact yarn. Therefore, the net effect of the multistage system is to increase the mechanical and electrical properties of the CNT yarn. However, we have observed after a certain maximum tension, further increase in this parameter leads to decreased yarn strength.

**3.2. Twisting and Heating Effect on Yarn Formation.** For short bundles of CNT drawn from the forest, in the absence of twisting action applied to the yarn, the strength of yarn is limited because of absence of significant transverse forces to bind the CNT assembly together [5]. In order to achieve higher mechanical and electrical properties, the CNTs and bundles need to have maximum contact with one another. This makes twisting a very important part in spinning CNT yarns. At low twist, there is considerable cohesion between the CNTs that can provide reasonable strength to the web. As twisting increases, cohesion also increases, and at a very high level of twisting, brittle behavior is observed [19]. The variation in diameter of CNT yarn is shown in Figures 5(a) to 5(d) at different stages (I to IV) of the HTS process. The SEM images indicate that the diameter of the yarn suddenly decreased as it passed through stage I to stage II (from  $14.2 \mu\text{m}$  to  $12.1 \mu\text{m}$ ) and then stage II to stage III ( $12.1 \mu\text{m}$  to  $10.9 \mu\text{m}$ ) and remained relatively unchanged afterwards. It was observed from the SEM images (Figures 5(a) to 5(c)) that the twisting angle of the fibers gradually increased with the yarn passing through the stages. We have observed when both heating and tension are applied the diameters of the CNT yarn decreased by about 23% from  $14$  to  $10.3 \mu\text{m}$  (see Figures 5(a) and 5(d)). SEM images demonstrated that the HTS technique improved the uniformity along the CNT yarn (Figure 5(d)). This technique provides two benefits. First, it increases the alignment of the carbon nanotubes in the thread and also the interbundle lateral cohesion. Second, it reduces the intertube distance and increases the van der Waals force interaction between all the CNTs. Figure 5(e) illustrated the schematic of different

positions of heating and tension spinning (HTS) stages are illustrated in Figure 5(f). Raman spectroscopy performed on both CNT yarn formed from treatment 1 and treatment 4 (see Figure 5(f)) do not show important differences that can be readily related to morphological differences in the CNTs for different treatments.

Figure 6(a) shows the resistivity (left  $y$ -axis) and strength (right  $y$ -axis) as a function of the tested four different methods of spinning. Substantial improvements in both the electrical and mechanical properties of the threads occurred when applying these methods. Method 4 was carried out using an HTS system temperature of about  $225^\circ\text{C}$ . Figure 6(b) shows that the strength and electrical conductivity of CNT yarn improve 61% and 71%, respectively, when employing Method 4 as opposed to the Method 1. Method 1 is state of art of spinning yarn which is practiced by most of the research groups [8] and is used in this study as a baseline for comparison. Spinning under tension brings the CNTs in closer contact to each other and therefore enhances the van der Waal interactions. The later causes increased friction between the CNTs, which improves the load transfer between the tubes.

The experimental results showed that treatments 2–4 brought improvement in the mechanical and electrical properties of the CNT yarns relative to treatment 1. The highest percentage improvement compared to the baseline treatment 1 was observed for treatments 3 and 4. This effect is obviously due to applying tension during spinning. However we also noticed that there is a considerable improvement of CNT yarn in treatment 4 compared to treatment 3. Figures 5(c) and 5(d) display SEM images of CNT yarns formed from treatment 3 and Method 4. Treatment 4 utilized three tension rods preheated up to  $225^\circ\text{C}$ . It shows that the diameter of the CNT yarn formed from treatment 4 decreases from  $10.9$  to  $10.2 \mu\text{m}$ . We assume that the applied simultaneous heating and tension during spinning improve the thread structure by stretching the CNT bundles and enabling more effective thread compactions.

Another interpretation of the results is based on the hypothesis of collapsing the CNTs under tension, which may be enhanced by the applied heating. It was observed by Motta et al. that double walled tubes in yarn corresponding to diameters larger than  $\sim 5 \text{ nm}$  collapse into structures with dog-bone cross-sections thus forming stacks of parallel graphene layers [7]. The applied tension and radial force change the microscopic structure of the CNTs which tend to polygonize from circular to hexagonal shape.

In the experiments, the mechanical and electrical properties of the CNT yarns substantially improved. This could be due to two reasons. The first reason is the applied heat may have caused evaporation of the absorbed water molecules within the CNT bundles thus increasing the friction and decreasing the air gaps between them. The second is associated with the possible CNT collapse due to the radial pressure incurred from the HTS action. In this scenario stacks of flattened nanotubes can share maximum contact area which will cause increased yarn cohesion. The nanotubes used in this study are double walled with diameters in the range of  $8$  to  $12 \text{ nm}$  which qualifies them for collapsing according to

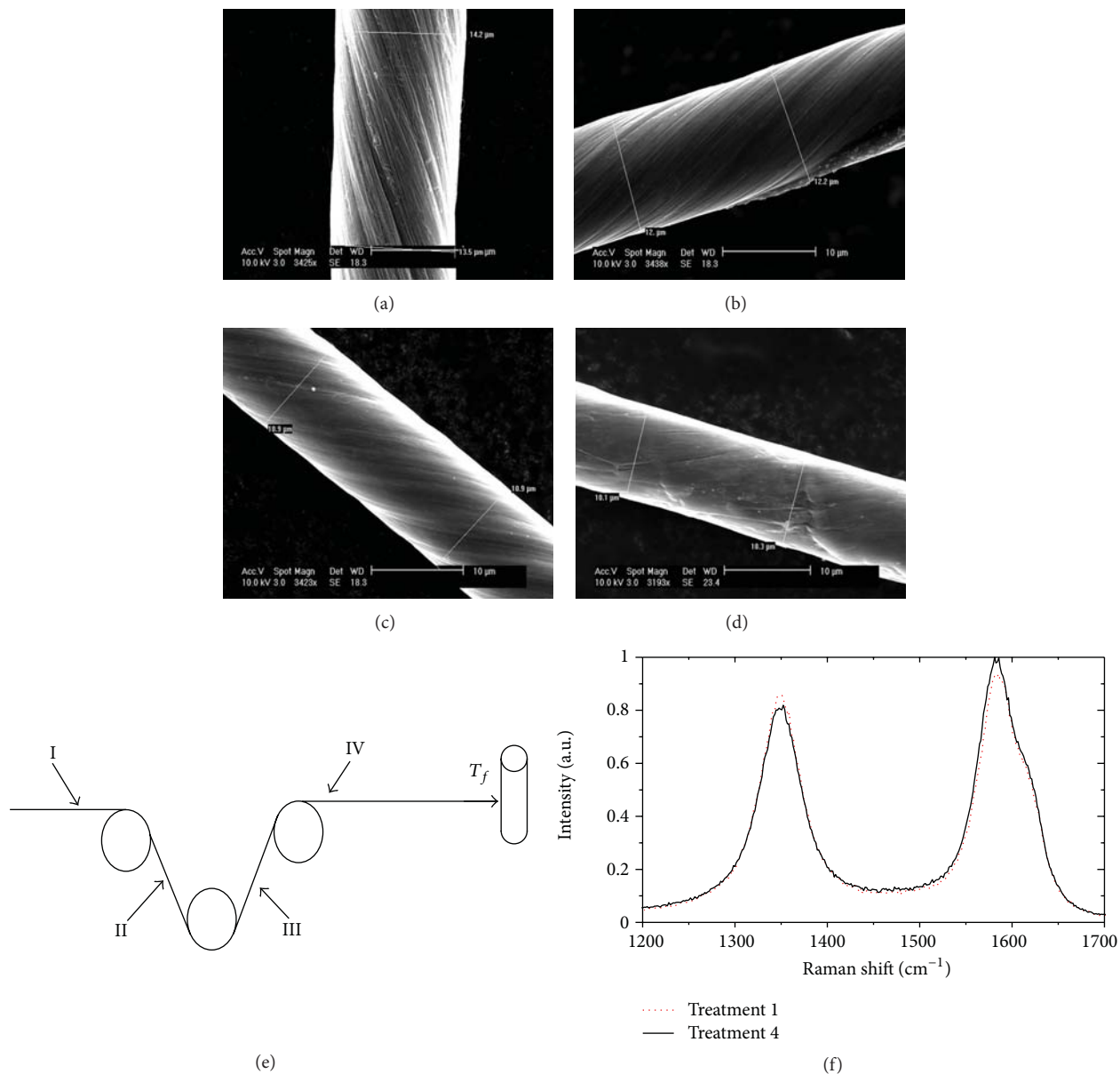


FIGURE 5: SEM images of CNT yarn at different stages of the spinning process. Stage I (a), Stage II (b), Stage III (c), and Stage IV (d), schematic of the applied heating and tension spinning (HTS) stages (e). I-denotes the position before 1st applied tension; II before 2nd tension; III before 3rd tension; IV before winding on the spool; Raman spectra of CNT yarn formed from treatment 1 and treatment 4(f).

[17]. Thorough High Resolution TEM studies of the CNT yarn may be able to confirm such a phenomenon.

#### 4. Conclusions

This work introduced new and improved methods for dry spinning of CNT yarns, which helped to positively affect the yarn structure by stretching the CNT bundles and enabling more effective yarn compaction. The preliminary results for spinning CNT yarn under tension showed an improvement of the fiber mechanical and electrical properties with respect to a standard spinning method used as a baseline. Further

enhancement of the CNT yarn quality was observed by introducing a heating and tension spinning (HTS) technique. The tensile strength of the spun yarn when employing HTS improved about 61% and the electrical conductivity increased by ~71%. Optimization of the new spinning techniques has not been fully achieved and will require further studies to understand the entire temperature and tension effect on the quality of HTS spun yarns. Further optimization of the spinning parameters employing the HTS environment is required, since the results obtained are promising for manufacturing high performance CNT-based yarns. Such experiments are in progress and will be reported in the near future.

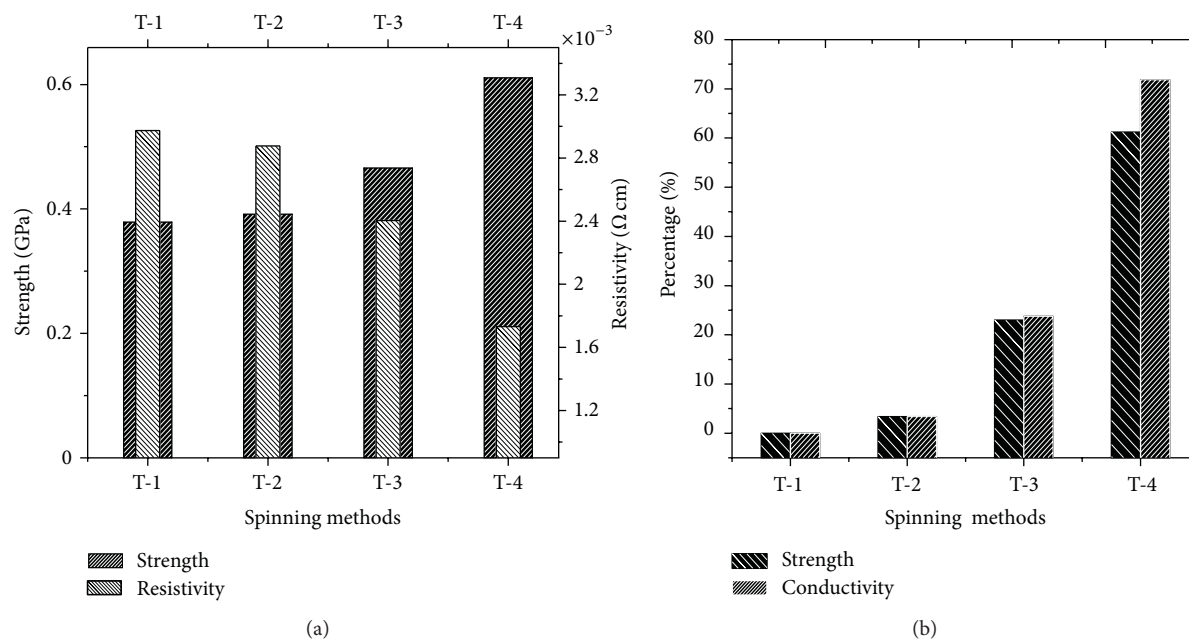


FIGURE 6: (a) Stress (left  $y$ -axis) and resistivity (right  $y$ -axis) versus spinning methods, (b) strength and electrical conductivity improvement in percentage versus spinning methods.

## Supporting Data

See Movie 1 in supplementary material available online at <http://dx.doi.org/10.1155/2013/309617>.

## Acknowledgments

The authors would like to acknowledge Dr. Sergey Yarmolenko and Svetlana Fialkova from North Carolina A&T State University for providing instrumentation to test the mechanical properties of the CNT threads and Mr. Doug Hurd for helping to design and manufacture the spinning machine. The financial support from NSF through Grant CMMI-07272500 program officer Dr. Haris Domanidis and from NCA&T through the ONR is highly appreciated.

## References

- [1] L. M. Ericson, H. Fan, H. Peng et al., "Macroscopic, neat, single-walled carbon nanotube fibers," *Science*, vol. 305, no. 5689, pp. 1447–1450, 2004.
- [2] M. E. Kozlov, R. C. Capps, W. M. Sampson, H. Von Ebron, J. P. Ferraris, and R. H. Baughman, "Spinning solid and hollow polymer-free carbon nanotube fibers," *Advanced Materials*, vol. 17, no. 5, pp. 614–617, 2005.
- [3] B. Vigolo, A. Penicaud, C. Coulon et al., "Macroscopic fibers and ribbons of oriented carbon nanotubes," *Science*, vol. 290, no. 5495, pp. 1331–1334, 2000.
- [4] X. Zhang, Q. Li, Y. Tu et al., "Strong carbon-nanotube fibers spun from long carbon-nanotube arrays," *Small*, vol. 3, no. 2, pp. 244–248, 2007.
- [5] H. W. Zhu, C. L. Xu, D. H. Wu, B. Q. Wei, R. Vajtai, and P. M. Ajayan, "Direct synthesis of long single-walled carbon nanotube strands," *Science*, vol. 296, no. 5569, pp. 884–886, 2002.
- [6] M. Motta, A. Moiala, I. A. Kinloch, and A. H. Windle, "High performance fibres from "dog bone" carbon nanotubes," *Advanced Materials*, vol. 19, no. 21, pp. 3721–3726, 2007.
- [7] M. Motta, Y. L. Li, I. Kinloch, and A. Windle, "Mechanical properties of continuously spun fibers of carbon nanotubes," *Nano Letters*, vol. 5, no. 8, pp. 1529–1533, 2005.
- [8] R. H. Baughman, A. A. Zakhidov, and W. A. De Heer, "Carbon nanotubes—the route toward applications," *Science*, vol. 297, no. 5582, pp. 787–792, 2002.
- [9] K. Koziol, J. Vilatela, A. Moiala et al., "High-performance carbon nanotube fiber," *Science*, vol. 318, no. 5858, pp. 1892–1895, 2007.
- [10] M. Zhang, K. R. Atkinson, and R. H. Baughman, "Multi-functional carbon nanotube yarns by downsizing an ancient technology," *Science*, vol. 306, no. 5700, pp. 1358–1361, 2004.
- [11] Q. Li, X. Zhang, R. F. DePaula et al., "Sustained growth of ultralong carbon nanotube arrays for fiber spinning," *Advanced Materials*, vol. 18, no. 23, pp. 3160–3163, 2006.
- [12] X. Zhang, Q. Li, T. G. Holesinger et al., "Ultrastrong, stiff, and lightweight carbon-nanotube fibers," *Advanced Materials*, vol. 19, no. 23, pp. 4198–4201, 2007.
- [13] C. Feng, K. Liu, J. S. Wu et al., "Flexible, stretchable, transparent conducting films made from superaligned carbon nanotubes," *Advanced Functional Materials*, vol. 20, no. 6, pp. 885–891, 2010.
- [14] M. Naraghi, T. Filleter, A. Moravsky, M. Locascio, R. O. Loutfy, and H. D. Espinosa, "A multiscale study of high performance double-walled nanotube-polymer fibers," *ACS Nano*, vol. 4, no. 11, pp. 6463–6476, 2010.
- [15] S. Fang, M. Zhang, A. A. Zakhidov, and R. H. Baughman, "Structure and process-dependent properties of solid-state spun carbon nanotube yarns," *Journal of Physics Condensed Matter*, vol. 22, no. 33, Article ID 334221, 2010.
- [16] C. Jayasinghe, S. Chakrabarti, M. J. Schulz, and V. Shanov, "Spinning yarn from long carbon nanotube arrays," *Journal of Materials Research*, vol. 26, pp. 1–7, 2011.

- [17] L. Hu, D. S. Hecht, and G. Grüner, "Infrared transparent carbon nanotube thin films," *Applied Physics Letters*, vol. 94, no. 8, Article ID 081103, 2009.
- [18] J. H. Jung, T. J. Kang, and J. R. Youn, "Effect of bending rigidity on the capstan equation," *Textile Research Journal*, vol. 74, no. 12, pp. 1085–1096, 2004.
- [19] S. Hutton, C. Skourtis, and K. Atkinson, "Tensile and electrical properties of carbon nanotube yarns and knitted tubes in pure or composite form," *International Journal of Technology Transfer and Commercialisation*, vol. 7, no. 2-3, pp. 258–264, 2008.

## Research Article

# A Comparative Study of Three Different Chemical Vapor Deposition Techniques of Carbon Nanotube Growth on Diamond Films

Betty T. Quinton,<sup>1,2</sup> Paul N. Barnes,<sup>3</sup> Chakrapani V. Varanasi,<sup>4</sup> Jack Burke,<sup>5</sup>  
Bang-Hung Tsao,<sup>5</sup> Kevin J. Yost,<sup>1</sup> and Sharmila M. Mukhopadhyay<sup>2</sup>

<sup>1</sup> Air Force Research Laboratory (AFRL), Wright-Patterson, Air Force Base, OH 45433, USA

<sup>2</sup> Wright State University, Dayton, OH 45420, USA

<sup>3</sup> Army Research Laboratory, Adelphi, MD 20783, USA

<sup>4</sup> Army Research Office, Research Triangle Park, NC 27709, USA

<sup>5</sup> University of Dayton Research Institute (UDRI), Dayton, OH 45469, USA

Correspondence should be addressed to Betty T. Quinton; [bettyyanguic@gmail.com](mailto:bettyyanguic@gmail.com)

Received 28 November 2012; Accepted 17 February 2013

Academic Editor: Lijun Ji

Copyright © 2013 Betty T. Quinton et al. This is an open access article distributed under the Creative Commons Attribution License, which permits unrestricted use, distribution, and reproduction in any medium, provided the original work is properly cited.

This paper compares between the methods of growing carbon nanotubes (CNTs) on diamond substrates and evaluates the quality of the CNTs and the interfacial strength. One potential application for these materials is a heat sink/spreader for high-power electronic devices. The CNTs and diamond substrates have a significantly higher specific thermal conductivity than traditional heat sink/spreader materials making them good replacement candidates. Only limited research has been performed on these CNT/diamond structures and their suitability of different growth methods. This study investigates three potential chemical vapor deposition (CVD) techniques for growing CNTs on diamond: thermal CVD (T-CVD), microwave plasma-enhanced CVD (MPE-CVD), and floating catalyst thermal CVD (FCT-CVD). Scanning electron microscopy (SEM) and high-resolution transmission electron microscopy (TEM) were used to analyze the morphology and topology of the CNTs. Raman spectroscopy was used to assess the quality of the CNTs by determining the  $I_D/I_G$  peak intensity ratios. Additionally, the CNT/diamond samples were sonicated for qualitative comparisons of the durability of the CNT forests. T-CVD provided the largest diameter tubes, with catalysts residing mainly at the CNT/diamond interface. The MPE-CVD process yielded non uniform defective CNTs, and FCT-CVD resulted in the smallest diameter CNTs with catalyst particles imbedded throughout the length of the nanotubes.

## 1. Introduction

Carbon nanotubes (CNTs) are lightweight materials that express superior mechanical, electrical, and thermal properties [1–4]. Diamond films are well known for their hardness and scratch resistance combined with excellent thermal conductivity [5, 6]. Successful CNT growth on a diamond substrate creates a unique all-carbon structure that can be beneficial for advanced power and electronic applications. Various methods such as chemical vapor deposition (CVD), laser ablation, thermal evaporation, arc discharge, and glow discharge have been used to grow CNTs on different surfaces [7–9] including diamond substrates and nanoparticles [9–11].

Among these methods, CVD is perhaps the most promising and scalable approach for future power and electronic devices.

There are many different varieties of CVD used to grow CNTs. The variations depend on power sources, type of catalyst deposition, gas composition, and operating temperatures. In addition to variations of the CVD process, CNT growth is expected to depend significantly on the chemistry, morphology, and activity of the substrate. Catalyst and substrate interactions can create differences in root growth or tip growth mechanisms, size distribution, and defects in CNTs growth [12–14].

Several CVD approaches have been investigated and documented on common electronic substrates such as silicon, but no work seems to have been reported on specialty substrates such as CVD diamond. It is desirable to test the applicability of these techniques on diamond substrates and compare the CNTs obtained from different CVD growth techniques. This would enable future device manufacturers to select the most appropriate technique for a specific application. This study compares three types of CVD techniques believed to be the most probable candidate techniques to be scaled up and utilized for future power devices. They all utilize transition metal catalysts that can readily form metastable carbides needed for CNT growth on any substrate [15–17]. The three CVD approaches selected were thermal CVD (T-CVD) with presputtered metal catalyst, microwave plasma-enhanced CVD (MPE-CVD) with presputtered metal catalyst, and floating catalyst thermal CVD (FCT-CVD) with xylene and ferrocene liquid mixture without any prior catalyst deposition. T-CVD is a low-cost system that can easily be set up to grow CNTs. In comparison to arc discharge, T-CVD operates at a lower temperature which increases the range of substrate material selections. However, the resulting CNTs' structure may be defective compared to arc discharge or laser ablation [18]. MPE-CVD is very suitable for large surface CNT production and can grow CNTs at even lower temperatures than T-CVD [19]. Both these techniques involve predeposition of catalyst on the substrate. The FCT-CVD introduces the carbon and catalyst simultaneously on the substrate via a gas mixture. This approach cuts out the first step of catalyst deposition giving it a potential economic advantage for future scale-up. However, it coats everything in the growth chamber and may be problematic when selective area growth is required [20].

The CNT forests grown have been investigated in detail, and each sample has been analyzed using a scanning electron microscope (SEM), transmission electron microscope (TEM), Raman spectroscopy, and energy dispersive X-ray spectroscopy (EDS) to fully characterize the structures.

## 2. Experimental Methods

**2.1. Sample Preparation.** Polished free-standing diamond substrates grown by a CVD technique were purchased from SP<sup>3</sup> Diamond Technologies Inc. The substrate measurements were  $5 \times 5 \text{ mm}^2$ , with a  $400 \mu\text{m}$  thickness. The surface roughness was determined to be 5 nm as measured by an atomic force microscope. Three CVD-based CNT growth techniques have been investigated: (i) T-CVD, (ii) MPE-CVD, and (iii) FCT-CVD. The first two techniques involved predeposition of seed catalysts prior to CNT growth and were optimized first on an electronic grade silicon substrate with a layer of thermal silicon dioxide layer on the surface. The last one had the catalyst source combined with the carbon source in the feeder gas and had been optimized earlier on graphitic carbon substrates.

Due to limited quantities of CVD diamond substrates, each -of the growth methods described below were first tested and optimized using other standard substrates before

deposition on the diamond. While it is recognized that optimization of parameters on identical diamond substrates would be ideal, the large number of diamond substrates necessary for such an undertaking was not available. It was, however, verified that the growth conditions on standard substrates were repeatable on other available substrates. As for growth parameters of CNTs on the diamond available in the literature the values reported for T-CVD and MPE-CVD were found to be very comparable to ones derived in house on standard substrates [10, 21]. There is no reported growth on CNTs on diamond substrate using the FCT-CVD method. However, this technique involves precoating the substrate with a plasma-enhanced oxide layer, which is expected to make the CNT growth more independent of the underlying substrate. Additional optimization and refinement on specific diamond substrates may be performed in the future as more varieties of diamond substrates become available in larger quantities. At the current time, Raman spectroscopy was used as an indicator of CNT quality, and the *D*-peak to *G*-peak intensity ratios from CNTs obtained on all samples were more than satisfactory. Successful and repeatable experiments from earlier research indicated that the best CNT forests were obtained by using T-CVD and MPE-CVD growth processes with nickel and iron catalysts, respectively. For the FCT-CVD approach, ferrocene is used as an iron source to promote CNT growth. Based on these repeatable results, the CNT growth parameters were used to grow CNTs on the diamond films.

**2.2. T-CVD Method.** Polished free-standing CVD diamond substrates were cleaned in an ultrasonic acetone bath for 5 minutes followed by 5 minutes in an ultrasonic isopropanol bath. After cleaning, the samples were placed into a radio frequency (RF) sputtering system loaded with a 99.999% pure nickel target. The sputtering system uses RF power to create a plasma plume that deposits material from the target to the substrate surface. The substrate was first sputtered with a 10 nm thin film of nickel in a sputter chamber. Then, the nickel-sputtered sample then placed into a T-CVD furnace. The furnace was heated from room temperature to the growth temperature of  $800^\circ\text{C}$  in 20 minutes with an argon/5% hydrogen (Ar/5% H<sub>2</sub>) gas mixture at a flow rate of 300 standard cubic centimeters per minute (sccm). Upon reaching the growth temperature, the sample was held for 10 minutes to allow the thin nickel film to break up into nanoscale islands. Then 400 sccm of argon/10% methane (Ar/10% C<sub>2</sub>H<sub>2</sub>) was introduced as the carbon feedstock source at the end of the 10-minute heat treatment. The growth process continued for 2 hours followed by a slow cool to room temperature again using a flow of 300 sccm of a (Ar/5% H<sub>2</sub>) gas mixture. The entire growth process was performed at a pressure of 90 torr.

**2.3. MPE-CVD Method.** The same sample cleaning procedures discussed above were followed here. The sputtering process was used again, but with a 99.999% pure iron target to form a 10 nm thin film of iron on the CVD diamond samples. The sample was loaded into the MPE-CVD chamber. The furnace was heated from room temperature to  $400^\circ\text{C}$  with pure hydrogen gas flowing at 150 sccm. Once the

temperature reached 400°C, a microwave frequency was used on the hydrogen gas to induce a hydrogen plasma within the chamber. The sample was held for 5 minutes with the hydrogen plasma at 400°C to allow iron island formation. After 5 minutes of annealing in plasma, the temperature was increased to the 650°C growth temperature, followed by the introduction of 15 sccm of methane gas as a carbon source. Methane gas was allowed to flow for 5 minutes for growth to take place. After that, the methane gas was shut off. With hydrogen gas still flowing into the chamber, the current source for the plasma was also shut off. Finally, the heating unit was turned off to allow the system to cool naturally.

**2.4. FCT-CVD Method.** The free-standing CVD diamond samples were treated with microwave plasma containing dimethyl sulfoxide (DMSO) to deposit a thin film of silica, 100 nm in thickness, onto the CVD diamond substrate. Note that there is a correlation between the silica thickness and the quality of CNTs and that this silica layer is required in order for CNTs to grow using FCT-CVD methods [22, 23]. The FCT-CVD system is a two-stage furnace with Ar gas flowing at 600 sccm and hydrogen gas flowing at 45 sccm. The low-temperature furnace is kept at 250°C, while the high-temperature furnace is ramped up to the growth temperature of 750°C. Ferrocene was dissolved into a xylene solvent in a 0.008 : 1 molar volume ratio. The xylene/ferrocene liquid mixture serves as a carbon feed stock as well as an iron catalytic particle source carrier. During growth, xylene/ferrocene was introduced at a flow rate of 3 mL/hr via a syringe pump. The growth time was 20 minutes followed by a cooldown with 600 sccm of Ar gas. Details of silica treatment as well as the CNT growth parameters can be found in earlier publications [24].

**2.5. Characterization.** The resulting samples were characterized using a FEI Sirion high-resolution SEM for analysis of carpet surface and nanotube morphology. Cross-sectional views of the interfaces are needed to understand how catalyst particles play a role during CNT growth. A thin TEM foil of the cross section of interest was made using a DB235 FEI focused ion beam. To protect CNTs from the gallium ion etching, a layer of platinum cap was sputtered on top of the CNT before the trenching process began for a lift out sample. The resulting foil was attached to a molybdenum TEM grid for final thinning until a transparent foil was formed. The TEM foil was first analyzed using a Philips CM200 TEM for general appearances and identified the different layers that it contains. The foils containing CNTs with both catalyst and substrate intact were then analyzed for elemental compositions by energy dispersive X-ray spectroscopy (EDS) using the FEI Titan 80–300 TEM. In addition to the imaging analysis, Raman spectroscopy analysis was used to provide a qualitative value for the growth structures of CNTs. It uses the intensity ratio of the disorder peak (*D*-peak) over the graphite peak (*G*-peak) to determine this qualitative value [25]. In order to monitor the durability and strength of bonding between CNTs and the diamond substrate, a sonication test was performed on samples made from each growth method.

This test uses Branson 3210, an ultrasonic cleaner with 40 kHz frequency. The samples were sonicated for 15 minutes while submerged in deionized water. The results from the previous analyses are discussed in the next section.

### 3. Results and Discussions

**3.1. Initial Catalyst Distribution in Preseeded Samples.** It is well established that the underlying catalysts play a big role in the structure and properties of the resulting CNTs. The three different techniques compared here have two different approaches of introducing the catalyst: T-CVD and MPE-CVD involve predeposition of nickel and iron catalysts, respectively, while FCT-CVD technique introduces catalyst with the feeder gas during CNT growth. In the first two cases, the morphology of the starting catalyst film could be analyzed prior to CNT growth. For the last case, there is no precursor catalyst film, and catalyst morphology can only be seen after the CNT layer is formed, as discussed later.

Figure 1(a) shows that thermal treatment of the 10 nm nickel film covering the polished diamond surface resulted in nanoislands with average diameters of 53 nm distributed uniformly across the substrate surface. According to Homma et al. [26], the resulting particle size can be modified and is dependent on the film thickness. A thinner film thickness using the procedure mentioned above provided a low CNTs growth yield. Because of this, the study uses 10 nm film thicknesses as the testing film thickness.

Figure 1(b) shows the SEM surface analysis of a sample treated at 400°C with hydrogen plasma inside the MPE-CVD system for 5 minutes. The image shows that the iron catalyst agglomerated into a continuous uneven film rather than solidified as isolated nanoparticles.

**3.2. Nanotube Morphology.** Figure 2 shows SEM images of the CNT layer formed on diamond film using the three different techniques. Figure 2(a) is the image of T-CVD grown CNTs which have an average tube diameter of 61 nm ± 12 nm, with smooth and uniform tubular structure. This correlates well with the uniform size distribution of nickel islands of similar sizes seen in Figure 1(a).

Figure 2(b) is an SEM image of MPE-CVD-grown CNTs that indicates that the CNTs are not uniform and contain various defects as well as variation in diameters. This may be the result of the seed catalyst layer consisting of irregular-shaped particles. The nonuniformity of individual tubes may also be influenced by defects developed during formation. The MPE-CVD method uses a hydrogen plasma that forms a reducing environment within the chamber. The SEM image taken can be compared to the study done by Behr which indicates that hydrogen can etch CNTs during the growth process. This can create surface defects throughout the growth process [27]. Some studies suggest that exposing growing CNTs to hydrogen-rich environments convert them into diamonds [28, 29]. Figure 2(b) shows the MPE-CVD CNTs tubes with defects similar to the ones reported by Behr after exposure to the hydrogen-rich environment.

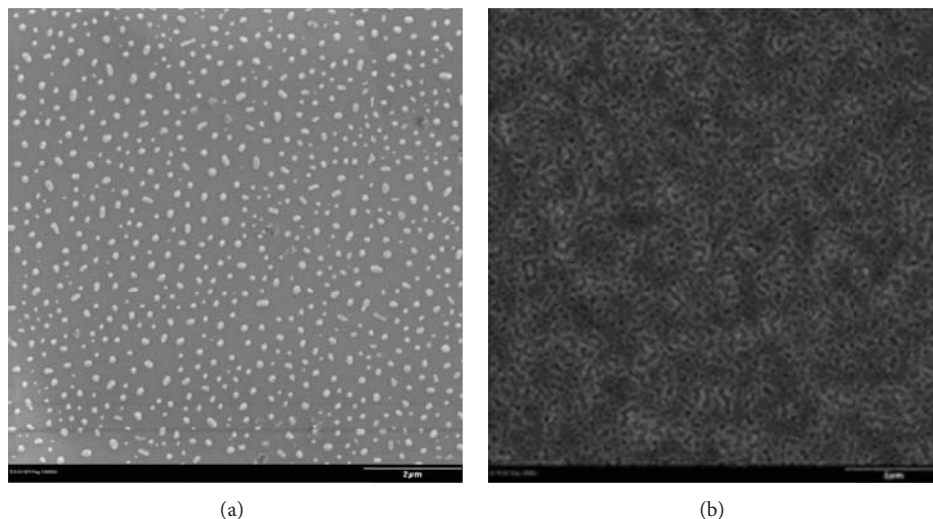


FIGURE 1: (a) Ni catalyst after thermal treatment in T-CVD. (b) Fe catalyst after thermal treatment in MPE-CVD with hydrogen plasma.

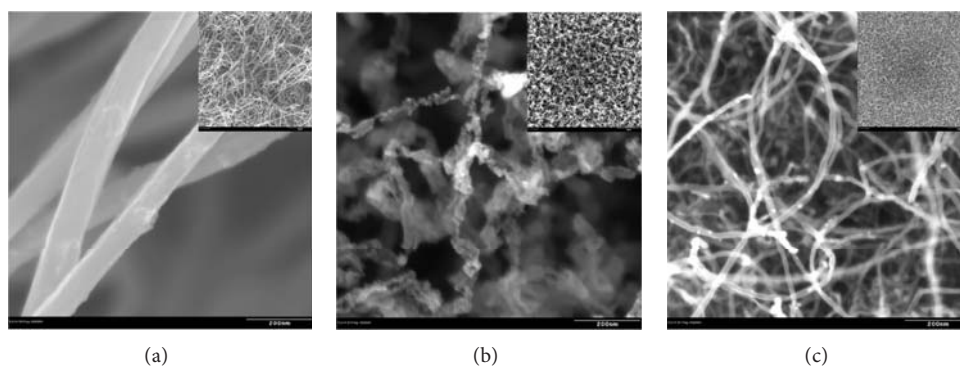


FIGURE 2: (a) T-CVD-grown CNTs. (b) MPE-CVD-grown CNTs. (c) FCT-CVD-grown CNTs.

Figure 2(c) shows an image of FCT-CVD-grown CNTs. This figure indicates that the CNTs are uniform in diameter and grow as densely entangled forests. These CNTs have average diameters of  $12 \text{ nm} \pm 1.8 \text{ nm}$ , making them the smallest of the three growth methods. The image also suggests that there are particles residing on the outer surface of the CNTs. This is expected because the xylene/ferrocene mixture provides continuous source of iron particles throughout the entire process, some of which are expected to attach to the growing CNT surface. The diameter of the outer particles can provide an estimate of iron catalyst size, and they have an averaging diameter size of  $12 \text{ nm} \pm 2.2 \text{ nm}$ .

**3.3. Catalyst Distribution in the Final CNT-Covered Diamond Structure.** Figures 3–5 show high-resolution TEM images with EDS elemental mapping. Figure 3 indicates that in T-CVD, nickel particles are encapsulated with a layer of carbon, and CNT growth originates from the outer carbon layer. This explains why the average CNT diameter is slightly higher than the average nickel catalyst diameter as shown later. The encapsulated catalyst particle remains anchored at the diamond-CNT interface implying the predominant growth

mechanism is root growth. There are a few instances where the catalyst particle moved several nanometers into the CNT length, away from the interface. Growth patterns similar to this indicate a small probability of catalyst lift-off.

Figure 4 shows an energy-filtered transmission electron microscope (EF-TEM) image of an MPE-CVD film. It can be seen that iron particles in this case do not reside along the interface, but rather move easily into the CNT, away from the interface. The mobility of nonanchored catalytic particles at the interface may also contribute to disordered CNT growth.

As seen in Figure 5, EF-TEM analysis of the FCT-CVD sample indicates a high distribution of iron particles residing at the diamond CNT interface which has the silica functional layer. There are additional iron particles found further away in the CNT forest. This is expected due to the continuous iron particle introduction throughout the CNT growth phase. The large number of iron catalysts at the interface suggests that the silica nanolayer keeps them anchored and prevents them from migrating during CNT growth.

Figure 6 shows the average particle size distribution taken with Image J software. This software provides qualitative values for the catalyst particle size and tube diameter comparison taken from the resulting TEM images. For T-CVD, the

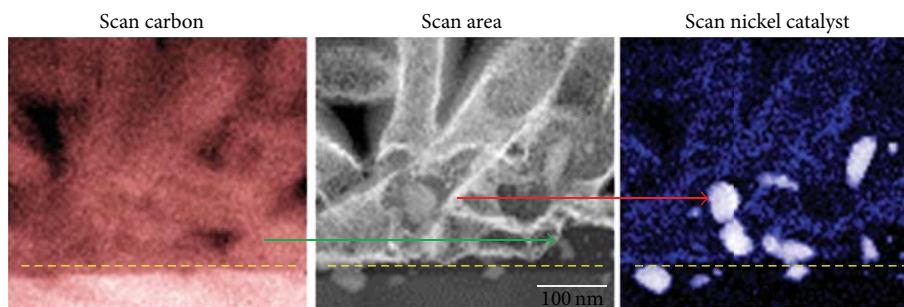


FIGURE 3: Cross-sectional TEM image of T-CVD-grown CNTs, the scale bar is 100 nm.

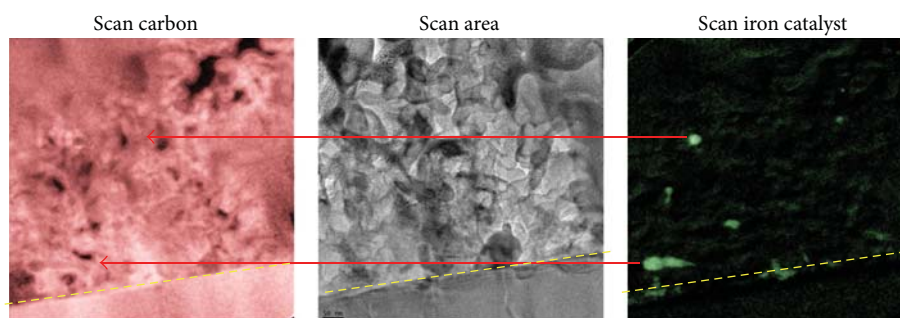


FIGURE 4: Cross-sectional TEM image of MPE-CVD-grown CNTs, the scale bar is 50 nm.

average catalyst particle diameter was measured to be  $53 \text{ nm} \pm 16 \text{ nm}$ , and the average tube diameter was  $61 \text{ nm} \pm 12 \text{ nm}$ . Thus, the catalyst diameters measured using TEM images are within the margin of error with the top view images seen by SEM. For MPE-CVD, the average catalyst particle diameter was  $21 \text{ nm} \pm 7 \text{ nm}$ , and the average tube diameter was  $40 \text{ nm} \pm 18 \text{ nm}$ . For the FCT-CVD method, the average catalyst particle size was  $12 \text{ nm} \pm 2 \text{ nm}$ , and the average tube diameter was  $12 \text{ nm} \pm 2 \text{ nm}$ . Cross-sectional TEM images provided additional information about particle location and concentration relative to the interface. For T-CVD, the image indicated that catalyst particles are the largest of all growth methods and reside close to the interface. For MPE-CVD, the catalyst particles are distributed away from the interface. This migration may be due to either the fact that they are smaller in size compared to T-CVD samples, the excess energy provided by the hydrogen plasma, or both. For FCT-CVD, the image indicates that the majority of the iron particles used as catalysts are anchored along the  $\text{SiO}_2$  layer and the iron particles that arrived later reside outside the growing CNTs. The anchoring of smaller nanoparticles may be caused by the silica functional layer and may assist in uniform CNT growth. It can be seen that the nanocatalyst particle size in each case correlates with the CNT diameters observed by SEM and TEM and further validates the hypothesis that the CNT size is largely governed by catalyst particles.

**3.4. Raman Spectrograph Results.** Raman spectroscopy was performed on samples produced by the different growth methods. The results are presented in Figure 7. According to the Handbook of Raman Spectroscopy and Dresselhaus

et al., Raman spectroscopy can be used as a guide to describe different carbon structures, such as diamond-like carbon which has C–C  $\text{sp}^3$  bonding, graphitic carbon which has  $\text{sp}^2$  bonding, and glassy/amorphous carbon which has C–H and disordered mixed bonds [25, 30, 31]. The peaks found around  $1350\text{--}1365 \text{ cm}^{-1}$  are called *D*-peaks, resulting from the disorderly network of  $\text{sp}^2$  and  $\text{sp}^3$  carbon clusters, whereas the peaks found around  $1580\text{--}1620 \text{ cm}^{-1}$  are called *G*-peaks as a result of graphite, and finally the peak found at  $1332 \text{ cm}^{-1}$  is the diamond peak [30–32]. The most interesting finding from our experiment concerned the calculated intensity of the *D*-peak to *G*-peak ratios ( $I_D/I_G$ ). This ratio matched the CNT morphology in terms of defect appearance in the SEM. The  $I_D/I_G$  ratios are given as follows: T-CVD = 0.30; MPE-CVD = 1.94; FCT-CVD = 0.84. Note that the T-CVD has the lowest  $I_D/I_G$  ratio; its SEM images indicated that this tube structure looks the smoothest. In contrast, the  $I_D/I_G$  for MPE-CVD is the highest and its SEM images indicated that the tube structure appears damaged and full of defects. Earlier, we stated that hydrogen may etch the CNT and introduce defect sites that can raise the intensity of the *D*-peak. Another possibility that causes high *D*-peak is when CNT is introduced to a hydrogen rich environment; the hydrogen alters CNT's C–H bonding and transforms them into diamond or disordered carbon [27, 33]. If this is the case, it explains why the disordered bonding peak, the *D*-peak, is much higher in the MPE-CVD sample.

Since the CNTs were grown on diamond substrates, one might suggest that the high intensity of *D*-peak resulted from signals coming from the diamond substrate underneath. However, the recorded *D*-peak intensity lies around

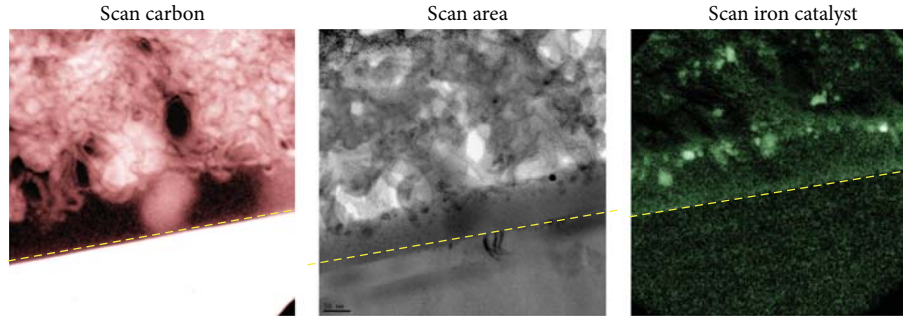


FIGURE 5: Cross-sectional TEM image of FCT-CVD-grown CNTs, the scale bar is 50 nm.

Average catalytic particle size and CNTs diameter distribution

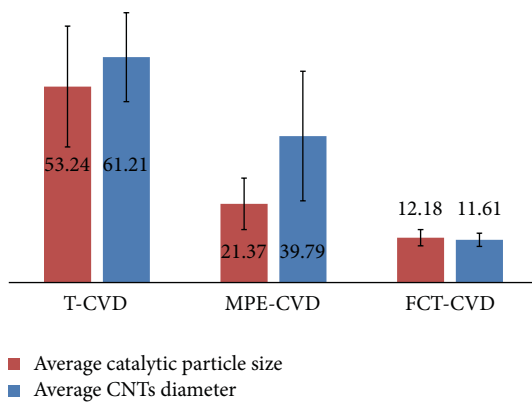


FIGURE 6: Particle size and CNTs tube diameter distribution chart.

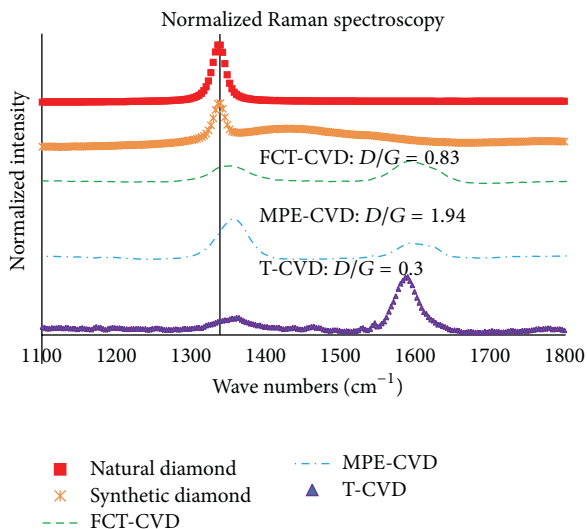


FIGURE 7: Raman spectroscopy signals for natural diamond, synthetic diamond, and CNTs from the three CVD methods.

(1354  $\text{cm}^{-1}$ ), whereas known diamond  $D$ -peaks are detected at (1332  $\text{cm}^{-1}$ ), indicating that the peak signal did not result from the diamond substrate. For confirmation, a razor blade was used to scrape away the CNTs from a sample and expose

the diamond substrate underneath. The Raman spectra taken from the exposed diamond surface has a peak intensity at (1338  $\text{cm}^{-1}$ ), which closely matches the published Raman peak for diamond (1332  $\text{cm}^{-1}$ ). This additional test further indicates that the (1354  $\text{cm}^{-1}$ ) peak is indeed the  $D$ -peak from the disordered CNT and not from the diamond substrate.

**3.5. Sonication Results.** If the sample was used in a commercial device, it would be important to know if the CNTs had the strength to stay intact within the substrate. The sonication test was used as a qualitative comparison of the forces needed to detach CNT from the substrate [34–36]. SEM images were taken before and after the sonication tests as shown in Figure 8. The images in the top row of Figure 8 were taken prior to sonication, and the bottom row images were taken after the test. Figures 8(a) were from the T-CVD, Figures 8(b) were from the MPE-CVD, Figures 8(c) were from FCT-CVD, and Figures 8(d) were optical images taken from MPE-CVD sample. The before sonication image seen in Figure 8(d) can also be used to represent T-CVD and FCT-CVD, because there were no visual differences observed after the sonication test. It can be seen that the nanotubes were intact even after sonication and that there were no noticeable differences seen in the before and after images from SEM. The low-magnification optical images show a difference for the MPE-CVD sample. Before sonication, all samples look identical at this magnification as seen in Figure 8(d) top image. The optical images after the sonication test were unchanged for T-CVD and FCT-CVD which are also represented by Figure 8(d) top image. The MPE-CVD after sonication sample was different as shown in Figure 8(d) bottom image. While postsonication SEM images of MPE-CVD sample show that CNTs were present on the scanned regions, the low-magnification optical images show exposed diamond substrate on the corners of the sample. This indicates detachment of CNTs at the corners of this sample, implying that the bonding between CNTs and substrate may be the weakest in this fabrication method. It must be noted that because of the extremely high length/diameter ratio of the nanotubes, agitation in an ultrasonic bath produces concentrated stresses at the root of the CNT. Survival under these conditions indicates that these materials will be robust in many service conditions. Among the three samples, MPE-CVD specimen may be the weakest, and detachment begins

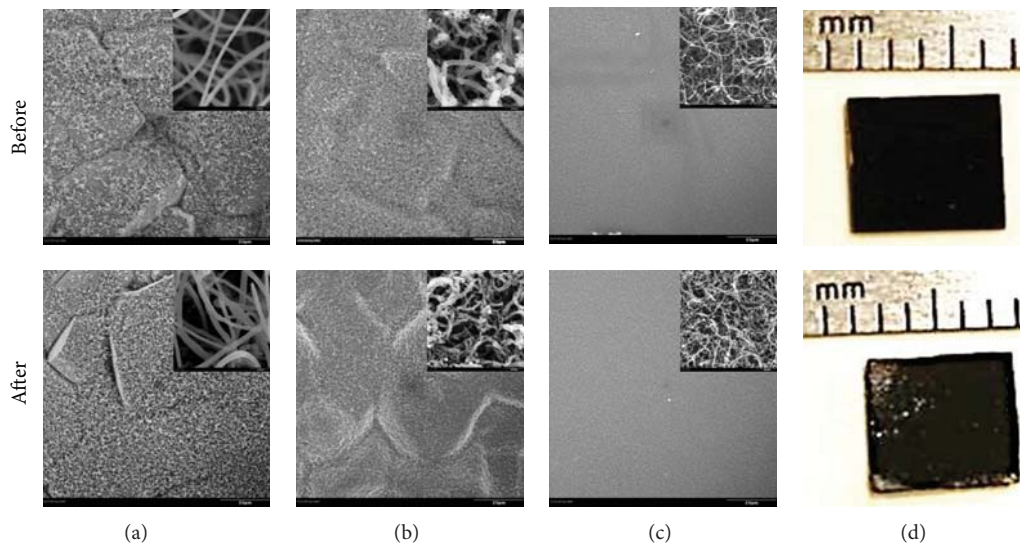


FIGURE 8: (a), (b), and (c) are SEM images, and (d) is the optical image. The images in the top row were taken prior to sonication, and those in the bottom row were taken after the test. (a) is the T-CVD sample. (b) is the MPE-CVD sample. (c) is the FCT-CVD sample, and (d) is taken from MPE-CVD Sample. There were no visual changes seen after the sonication test for the T-CVD and the FCT-CVD sample. Therefore, the before image from (d), can also be used to represent before and after sonication test for T-CVD and FCT-CVD sample.

to occur at the corners, which are the most vulnerable regions of the sample.

**3.6. Overall Comparison.** It is seen that very different types of CNT layers can be grown on diamond film by different techniques. It must be noted that T-CVD and MPE-CVD are multistep processes that separate the catalyst deposition step from the CNT growth step. The catalytic particles in the T-CVD growth are found to be the largest of the three types of growth for the conditions used. These particles were found to reside at the interface with minimal migration into the CNT layer. The resulting CNT structures were found to be the smoothest with the largest tube diameters of all three growth types. This smooth structure may be useful for electronic and thermal applications that require minimal defects.

The SEM images show the CNTs that resulted from the MPE-CVD method contains kinks and defects on the individual tubes. The defects may be the result of hydrogen plasma and excess hydrogen in the chamber. The excess hydrogen can etch the surface of CNTs as it grows, which results in a defected surface. The hydrogen plasma may also provide excess energy that inadvertently promotes catalyst migration. If this migration occurs during CNT growth, it may be another underlying reason as to why those CNT structures are kinked. It can be proposed that as the CNTs are growing with the migrating catalytic particles, a straight path for growth was not provided, which resulted in a kinked-type growth. Therefore, this approach which is suitable for large area growth will be useful only in situations where defective and kinked CNTs are acceptable. It would be interesting to determine if the defective CNTs grown under energetic conditions are more reactive than their smoother counterparts. Another noticeable difference provided by the MPE-CVD method is that it has the weakest bonding with the

substrate compared to the other two methods. Images from the three growth methods were compared after the sonication test. The images from the sonication test show the corners of the diamond substrate were exposed after the test, which is not seen in the other samples. The benefit of using FCT-CVD is that it is a one step process where catalyst and carbon source are introduced together. The resulting CNTs grown by this process had the smallest diameter, averaging 12 nm, with uniform and dense growth patterns. While this may be a very suitable approach in many applications, the disadvantage is the possibility of excess iron particles arising from continuous catalyst deposition. This may be mitigated by modifying the process to cut off ferrocene during the latter part of CNT growth.

Since each method has its unique advantages and disadvantages, these studies indicate that the selection of the CNT growth method is heavily influenced by the intended application.

## 4. Conclusions

In this paper, we have compared the growth of CNTs forests on synthetic diamond substrates using three different CVD growth methods. The CNTs were characterized using electron microscope imaging (SEM and TEM), elemental analysis (EDS), Raman spectroscopy, and the sonication test. The SEM and TEM images indicated each method produces CNTs with a distinctly different diameter and morphology. Raman spectroscopic analysis suggested that T-CVD had the lowest disordered carbon to graphite intensity ratio of 0.3 followed by FCT-CVD of 0.83 and the highest by MPE-CVD of 1.94. T-CVD also produces large diameter CNTs that are otherwise clean, with minimal tubular defects or additional catalytic contaminants. MPE-CVD is sometimes

the preferred method for larger scaled applications; however, the excess hydrogen plasma energy during growth may cause migrations of catalytic particles, surface etching, and defective CNTs that may be detrimental to precision applications. MPE-CVD has the highest probability for catalytic mobility, the most defective CNTs structure morphology, and the weakest interfacial bonding strength. It may be possible to improve this situation through extensive processing parameter changes, but not certain. FCT-CVD has the advantage of being a one-step CNT growth method that does not need a separate catalyst deposition step, yet produces dense uniform CNTs. This technique provided the finest CNT diameter, and intermediate diamond/graphite ratio in the Raman signal. This method does produce some excess metal particles due to continuous catalyst nucleation. However, this issue can be easily addressed in the future if needed, by stopping the catalytic source after a certain growth time. Finally, this study indicates that there is a clear correlation between the size of catalyst particle and the CNT diameters.

### Conflict of Interests

B. Quinton, as the author of this paper, does not have a direct financial relation with the incorporation and software mentioned in this paper and that might lead to a conflict of interests for any of the authors.

### Acknowledgments

The authors of the paper would like to thank the funding support of Air Force Office of Scientific Research, Air Force Research Laboratory Propulsion Directorate, Wright State University, and Ohio Board of Regents. The authors would like to acknowledge Dr. Robert Wheeler for his guidance on TEM and EDS.

### References

- [1] M. Meyyappan, *Carbon Nanotubes: Science and Applications*, CRC Press, Boca Raton, Fla, USA, 2004.
- [2] S. Iijima, "Helical microtubules of graphitic carbon," *Nature*, vol. 354, no. 6348, pp. 56–58, 1991.
- [3] R. Saito, M. Fujita, G. Dresselhaus, and M. S. Dresselhaus, "Electronic structure of chiral graphene tubules," *Applied Physics Letters*, vol. 60, no. 18, pp. 2204–2206, 1992.
- [4] P. Calvert, "Strength in disunity," *Nature*, vol. 357, no. 6377, pp. 365–366, 1992.
- [5] N. V. Novikov and S. N. Dub, "Hardness and fracture toughness of CVD diamond film," *Diamond and Related Materials*, vol. 5, no. 9, pp. 1026–1030, 1996.
- [6] S. V. Kidalov and F. M. Shakhov, "Thermal conductivity of diamond composites," *Materials*, vol. 2, pp. 2467–2495, 2009.
- [7] C. J. Lee, S. C. Lyu, Y. R. Cho, J. H. Lee, and K. I. Cho, "Diameter-controlled growth of carbon nanotubes using thermal chemical vapor deposition," *Chemical Physics Letters*, vol. 341, no. 3–4, pp. 245–249, 2001.
- [8] E. T. Thostenson, Z. Ren, and T. W. Chou, "Advances in the science and technology of carbon nanotubes and their composites: a review," *Composites Science and Technology*, vol. 61, no. 13, pp. 1899–1912, 2001.
- [9] N. Tumilty, L. Kasharina, T. Prokhoda, B. Sinelnikov, and R. B. Jackman, "Synthesis of carbon nanotubes on single crystal diamond," *Carbon*, vol. 48, no. 11, pp. 3027–3032, 2010.
- [10] C. Varanasi, J. Petry, L. Brunke et al., "Growth of high-quality carbon nanotubes on free-standing diamond substrates," *Carbon*, vol. 48, no. 9, pp. 2442–2446, 2010.
- [11] D. Takagi, Y. Kobayashi, and Y. Homma, "Carbon nanotube growth from diamond," *Journal of the American Chemical Society*, vol. 131, no. 20, pp. 6922–6923, 2009.
- [12] Y. Li, W. Kim, Y. Zhang, M. Rolandi, D. Wang, and H. Dai, "Growth of single-walled carbon nanotubes from discrete catalytic nanoparticles of various sizes," *Journal of Physical Chemistry B*, vol. 105, no. 46, pp. 11424–11431, 2001.
- [13] S. Helveg, C. López-Cartes, J. Sehested et al., "Atomic-scale imaging of carbon nanofibre growth," *Nature*, vol. 427, no. 6973, pp. 426–429, 2004.
- [14] R. T. K. Baker, M. A. Barber, P. S. Harris, F. S. Feates, and R. J. Waite, "Nucleation and growth of carbon deposits from the nickel catalyzed decomposition of acetylene," *Journal of Catalysis*, vol. 26, no. 1, pp. 51–62, 1972.
- [15] C. T. Wirth, S. Hofmann, and J. Robertson, "State of the catalyst during carbon nanotube growth," *Diamond and Related Materials*, vol. 18, pp. 940–945, 2009.
- [16] J. Y. Raty, F. Gygi, and G. Galli, "Growth of carbon nanotubes on metal nanoparticles: a microscopic mechanism from ab initio molecular dynamics simulations," *Physical Review Letters*, vol. 95, no. 9, Article ID 096103, 4 pages, 2005.
- [17] S. Hofmann, G. Csányi, A. Ferrari, M. Payne, and J. Robertson, "Surface diffusion: the low activation energy path for nanotube growth," *Physical Review Letters*, vol. 95, Article ID 036101, 4 pages, 2005.
- [18] K. Kozioł, B. O. Boskovic, and N. Yahya, *Carbon and Oxide Nanostructures: Synthesis, Characterisation and Applications*, Henry Dickens, Columbia, SC, USA, 2011.
- [19] Y. C. Choi, D. J. Bae, Y. H. Lee et al., "Growth of carbon nanotubes by microwave plasma-enhanced chemical vapor deposition at low temperature," *Journal of Vacuum Science and Technology A*, vol. 18, no. 4, pp. 1864–1868, 2000.
- [20] Teo, B. K. Kenneth, C. Singh, M. Chhowalla, and W. Milne, *Encyclopedia of Nanoscience and Nanotechnology*, 2003.
- [21] A. J. S. Fernandes, M. Pinto, M. A. Neto, F. J. Oliveira, R. F. Silva, and F. M. Costa, "Nano carbon hybrids from the simultaneous synthesis of CNT/NCD by MPCVD," *Diamond and Related Materials*, vol. 18, no. 2–3, pp. 160–163, 2009.
- [22] A. Cao, P. M. Ajayan, G. Ramanath, R. Baskaran, and K. Turner, "Silicon oxide thickness-dependent growth of carbon nanotubes," *Applied Physics Letters*, vol. 84, no. 1, pp. 109–111, 2004.
- [23] S. M. Mukhopadhyay, A. Karumuri, and I. T. Barney, "Hierarchical nanostructures by nanotube grafting on porous cellular surfaces," *Journal of Physics D*, vol. 42, no. 19, Article ID 195503, 2009.
- [24] S. M. Mukhopadhyay, P. Joshi, and R. V. Pulikollu, "Thin films for coating nanomaterials," *Tsinghua Science & Technology*, vol. 10, no. 6, pp. 709–717, 2005.
- [25] J. L. Lauer, *Handbook of Raman Spectroscopy from the Research Laboratory to the Process Line*, Marcel Dekker, West Yorkshire, UK, 1st edition, 2001.

- [26] Y. Homma, Y. Kobayashi, T. Ogino et al., "Role of transition metal catalysts in single-walled carbon nanotube growth in chemical vapor deposition," *Journal of Physical Chemistry B*, vol. 107, no. 44, pp. 12161–12164, 2003.
- [27] M. J. Behr, E. A. Gaulding, K. A. Mkhoyan, and E. S. Aydil, "Hydrogen etching and cutting of multiwall carbon nanotubes," *Journal of Vacuum Science & Technology B*, vol. 28, no. 6, pp. 1187–1194, 2010.
- [28] L. T. Sun, J. L. Gong, Z. Y. Zhu et al., "Nanocrystalline diamond from carbon nanotubes," *Applied Physics Letters*, vol. 84, no. 15, pp. 2901–2903, 2004.
- [29] Q. Yang, S. Yang, C. Xiao, and A. Hirose, "Transformation of carbon nanotubes to diamond in microwave hydrogen plasma," *Materials Letters*, vol. 61, no. 11-12, pp. 2208–2211, 2007.
- [30] M. S. Dresselhaus, G. Dresselhaus, R. Saito, and A. Jorio, "Raman spectroscopy of carbon nanotubes," *Physics Reports*, vol. 409, no. 2, pp. 47–99, 2005.
- [31] M. S. Dresselhaus, A. Jorio, A. G. Souza Filho, and R. Saito, "Defect characterization in graphene and carbon nanotubes using Raman spectroscopy," *Philosophical Transactions of the Royal Society A*, vol. 368, no. 1932, pp. 5355–5377, 2010.
- [32] L. C. O'Brien, R. L. Kubicek, and J. J. O'Brien, "Laser raman spectroscopy of diamond," *Journal of Chemical Education*, vol. 71, no. 9, pp. 759–760, 1994.
- [33] G. Zhang, P. Qi, X. Wang et al., "Hydrogenation and hydrocarbonation and etching of single-walled carbon nanotubes," *Journal of the American Chemical Society*, vol. 128, no. 18, pp. 6026–6027, 2006.
- [34] Q. Zhang, J. Liu, R. Sager, L. Dai, and J. Baur, "Hierarchical composites of carbon nanotubes on carbon fiber: influence of growth condition on fiber tensile properties," *Composites Science and Technology*, vol. 69, no. 5, pp. 594–601, 2009.
- [35] M. F. De Riccardis, D. Carbone, T. D. Makris, R. Giorgi, N. Lisi, and E. Salernitano, "Anchorage of carbon nanotubes grown on carbon fibres," *Carbon*, vol. 44, no. 4, pp. 671–674, 2006.
- [36] I. T. Barney, *Fabrication and Testing of Hierarchical Carbon Nanostructures For Multifunctional Applications*, Wright State University, 2012.

## Research Article

# Photoluminescence of Hexagonal ZnO Nanorods Hydrothermally Grown on Zn Foils in KOH Solutions with Different Values of Basicity

Nuengruethai Ekthammathat,<sup>1</sup> Titipun Thongtem,<sup>1,2</sup>  
Anukorn Phuruangrat,<sup>3</sup> and Somchai Thongtem<sup>2,4</sup>

<sup>1</sup> Department of Chemistry, Faculty of Science, Chiang Mai University, Chiang Mai 50200, Thailand

<sup>2</sup> Materials Science Research Center, Faculty of Science, Chiang Mai University, Chiang Mai 50200, Thailand

<sup>3</sup> Department of Materials Science and Technology, Faculty of Science, Prince of Songkla University, Hat Yai, Songkhla 90112, Thailand

<sup>4</sup> Department of Physics and Materials Science, Faculty of Science, Chiang Mai University, Chiang Mai 50200, Thailand

Correspondence should be addressed to Titipun Thongtem; [ttphongtem@yahoo.com](mailto:ttphongtem@yahoo.com) and Anukorn Phuruangrat; [phuruangrat@hotmail.com](mailto:phuruangrat@hotmail.com)

Received 18 November 2012; Revised 19 February 2013; Accepted 25 February 2013

Academic Editor: Yun Zhao

Copyright © 2013 Nuengruethai Ekthammathat et al. This is an open access article distributed under the Creative Commons Attribution License, which permits unrestricted use, distribution, and reproduction in any medium, provided the original work is properly cited.

Aligned hexagonal ZnO nanorods on pure Zn foils were hydrothermally synthesized in 30 mL solutions containing 0.05–0.50 g KOH. The products were characterized by X-ray diffraction (XRD), scanning electron microscopy (SEM), transmission electron microscopy (TEM), and photoluminescence (PL) spectroscopy. In this research, wurtzite hexagonal ZnO nanorods grown along the [002] direction with green light emission at 541 nm caused by singly ionized oxygen vacancies inside were detected.

## 1. Introduction

One-dimensional (1D) semiconducting materials are able to be used for a number of potential applications in short wavelength optical, nanoelectronic, and optoelectronic devices due to their tunable electronic and optoelectronic properties controlled by morphologies and dimensions [1–3]. Compared to two-dimensional (2D), three-dimensional (3D), and zero-dimensional (0D) nanostructures, the 1D nanostructure has unique characteristic: large aspect ratio, single crystalline structure, and oriented growth [3]. Zinc oxide is an important low-cost II–VI basic semiconductor with 3.37 eV wide band gap and strong exciton binding energy of 60 meV at room temperature [4–7]. It possesses unique catalytic, electrical, optoelectronic, and photochemical properties—very interesting for a number of potential applications as room-temperature UV lasers, sensors, light-emitting diodes, optical switches, solar cells, and photocatalysis due to its low dielectric constant, high chemical stability, good photoelectric, and piezoelectric behaviors [4, 6, 8].

In the paper, hexagonal ZnO nanorods on Zn foils were hydrothermally synthesized in solutions containing 0.05–0.50 g KOH at 120°C. Their phase, morphology, and photoluminescence were investigated and discussed in more details.

## 2. Experimental Procedure

Reagents of the research were of analytical grade and used without further purification. The hexagonal prism ZnO nanorods were grown on Zn foils by the following. Several 10 × 10 mm square Zn foils with 0.25 mm thick were cleaned with deionized water and absolute alcohol in an ultrasound bath and put in 30 mL of 0.05, 0.10, 0.20, 0.30, 0.40, and 0.50 g KOH aqueous solutions, containing 1, 2, 4, 6, 8, and 10 times of KOH in sequence. All of the solutions and zinc foils were transferred into 50 mL Teflon-lined stainless steel autoclaves, which were tightly closed, heated at 120°C in a laboratory electric oven for 24 h, and naturally cooled to room temperature. In the end, the zinc foils were thoroughly rinsed by

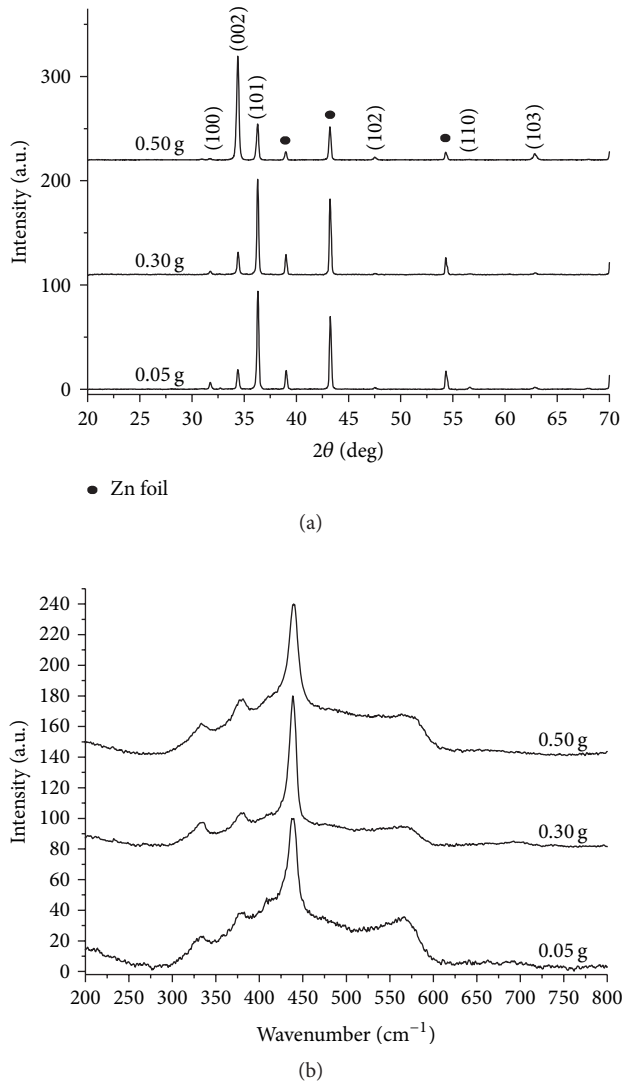


FIGURE 1: (a) XRD patterns and (b) Raman spectra of the as-synthesized ZnO in 30 mL solutions containing 1 (0.05 g), 6 (0.30 g) and 10 times (0.50 g) of KOH.

deionized water several times and alcohol, and dried at 70°C in an electric oven for 12 h for further characterization.

X-ray diffraction (XRD) operated on Philips X'Pert MPD X-ray diffractometer with Cu  $K_{\alpha}$  radiation in the  $2\theta$  of 20–70 deg with a scanning rate of 0.02 deg per step and Raman spectroscopy on T64000 HORIBA Jobin Yvon at 50 mW Ar Laser with 514.5 nm wavelength were used to determine phase, crystalline degree, purity, and vibration modes. Their morphologies were characterized by scanning electron microscopy (SEM, JEOL JSM-6335F) with an accelerating voltage of 15 kV across the LaB<sub>6</sub> cathode. Their nanostructures and growth direction were further investigated by transmission electronic microscopy (TEM) and selected area electronic diffraction (SAED) on a JEOL JEM-2010 TEM at 200 kV with LaB<sub>6</sub> gun. At the end, optical properties of the products were analyzed by a LS50B Perkin Elmer fluorescence spectrometer in the wavelength range of 450–700 nm.

### 3. Results and Discussion

Figure 1(a) exhibits typical XRD patterns of the as-grown ZnO on Zn foils, revealing that all diffraction peaks were explicable in term of wurtzite ZnO structure with  $a = b = 3.251 \text{ \AA}$  and  $c = 5.208 \text{ \AA}$  (JCPDS No. 36-1451) [9]. Sharp diffraction peaks indicate good crystalline degree of the as-synthesized crystals without other impurities detection.

Degree of  $c$  orientation of the as-synthesized ZnO samples was explained by the relative texture coefficient (TC) [10, 11] of the (002) peak calculated using the formula

$$TC_{002} = \frac{(I_{002}/I_{002}^0)}{[I_{002}/I_{002}^0 + I_{100}/I_{100}^0]} \quad (1)$$

$TC_{002}$  is the relative texture coefficient of the (002) over (100) diffraction peaks.  $I_{002}$  and  $I_{100}$  are the measured diffraction intensities of the (002) and (100) peaks, including the corresponding  $I_{002}^0$  and  $I_{100}^0$  values of the randomly oriented standard powder, respectively. For randomly crystallographic orientation, the texture coefficient of ZnO is 0.5. In the solution containing 0.50 g KOH, calculated  $TC_{002}$  was 0.86, which supported the preferential orientation of the as-synthesized ZnO nanorods grown along the [002] direction on the Zn foil.

Wurtzite ZnO structure belongs to  $C_{6v}^4$  (P6<sub>3</sub>mc) space group with two formula units per primitive cell, and all atoms occupy the  $C^{3v}$  sites. Group theory of wurtzite ZnO structure predicts eight sets of phonon modes:  $A_1 + E_1 + 2E_2$  (Raman active),  $2B_2$  (Raman silent), and  $A_1 + E_1$  (IR active). Moreover, the  $A_1$  and  $E_1$  symmetry are split into longitudinal (L) and transverse (T) optical (O) components due to the macroscopic electric fields associated with the LO phonons. Figure 1(b) shows Raman spectra of the as-synthesized ZnO nanorods. They show a dominant peak of typical characteristic of the wurtzite ZnO structure at 439  $\text{cm}^{-1}$ , assigned to be the optical phonon  $E_{2H}$  mode. The weak peak at 332  $\text{cm}^{-1}$  was assigned to be the second-order Raman scattering arising from the zone/zero boundary phonons  $E_{2H}-E_{2L}$  of multiphonon process, while the Raman peak at 379  $\text{cm}^{-1}$  is attributed to  $A_1$  symmetry with the TO mode. Furthermore, Raman spectra of ZnO samples at 567  $\text{cm}^{-1}$  are a contribution of the  $E_1$  (LO) mode which is directly associated with oxygen vacancies. The stronger  $E_1$  (LO) mode indicates the presence of higher oxygen vacancies inside [5, 12–14].

SEM images as shown in Figure 2 were investigated on surfaces of Zn foils after hydrothermal treatment in 30 mL solutions containing 1 (0.05 g), 2 (0.10 g), 4 (0.20 g), 6 (0.30 g), 8 (0.40 g), and 10 times (0.50 g) of KOH. An interesting feature of the nanostructures grown on the bottom surfaces exhibited the presence of aligned nanorods of ZnO with the diameter ranging from 400 nm to 700 nm without the detection of other nanostructures. The lengths of the ZnO nanorods are in the range of several micrometers to even longer than 5–7  $\mu\text{m}$ . These nanorods were enlarged and lengthened in sequence with an increase in the degree of basicity. The inset of Figure 2(f) demonstrates the hexagonal

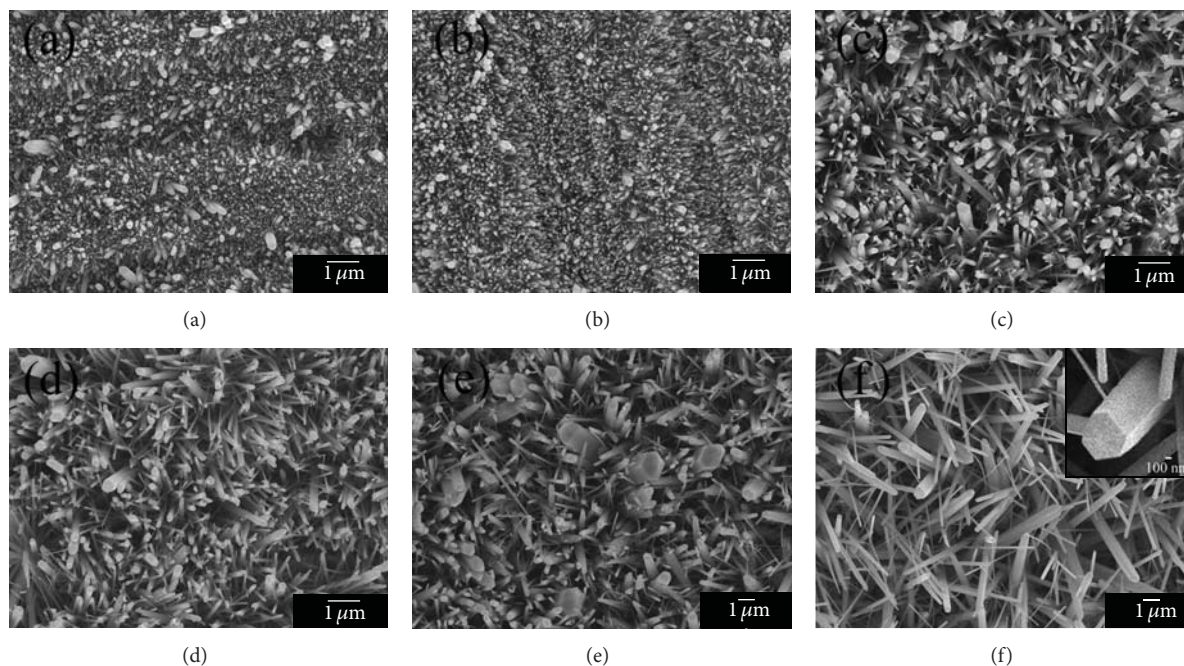


FIGURE 2: SEM images of the as-synthesized ZnO samples in 30 mL solutions containing (a) 1 (0.05 g), (b) 2 (0.10 g), (c) 4 (0.20 g), (d) 6 (0.30 g), (e) 8 (0.40 g), and (f) 10 times (0.50 g) of KOH.

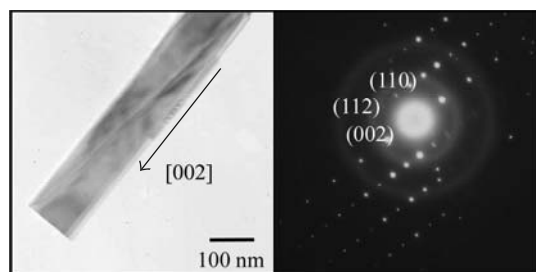
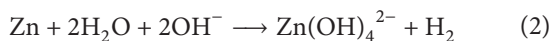


FIGURE 3: TEM image and SAED pattern of hexagonal ZnO nanorod in 30 mL solution containing 10 times (0.50 g) of KOH.

ZnO nanorod which was fully grown on Zn foil in the solution containing 0.50 g KOH.

The hexagonal ZnO nanorods were also characterized through TEM and SAED (Figure 3). TEM image reveals a single hexagonal ZnO nanorod with smooth surface and the preferred growth in the [002] direction. It shows the SAED pattern of bright spots corresponding to hexagonal wurtzite ZnO [9].

Based on the previous discussion, mechanism of the growth and morphology of ZnO nanostructure can be proposed as follows:



The formation of  $\text{Zn}(\text{OH})_4^{2-}$  ions from  $\text{Zn}^{2+}$  and  $\text{OH}^-$  ions by a hydrothermal reaction is a key role in the formation of hexagonal wurtzite ZnO nanorods. The primary ZnO

nanoparticles began to nucleate on Zn foil by the dissolution of Zn atoms into the solution and the cause of concentration gradient of  $\text{Zn}^{2+}$ . The intrinsic electric fields of the polar ZnO lattice could be responsible for further growth of ZnO crystals, described as alternating planes of  $\text{Zn}^{2+}$  and  $\text{O}^{2-}$ , stacked along the  $c$ -axis. The oppositely charged ions produced positively charged and negatively charged surfaces, resulting in polarization along the  $c$ -axis. The preferred  $c$ -axis orientation of ZnO nanostructure is driven by electrostatic interaction between the polar charges to minimize surface energy. Finally, ZnO nanorods grew on Zn foil as substrate [15].

The main emission of ZnO nanorods can be assigned as the recombination of free excitons. Other peaks probably originated from position of band-edge emission of ZnO of relatively large dimensions with different concentration of native defects [16]. It is well known that visible photoluminescence mainly originates from defect states of Zn interstitials, zinc vacancies, and oxygen vacancies [17]. Photoluminescence (PL) of ZnO nanorods grown on Zn foils was investigated using excitation wavelength of 214 nm at room temperature as shown in Figure 4. PL spectrum of hexagonal ZnO nanorods using 0.50 g KOH shows the highest strong green light emission at 541 nm, due to the singly ionized oxygen vacancies of ZnO, in accordance with other reports [16–18].

#### 4. Conclusions

In summary, densely aligned hexagonal ZnO nanorods on Zn foils were synthesized by a 120°C and 24 h hydrothermal reaction. The XRD, SEM, and TEM analyses showed that the

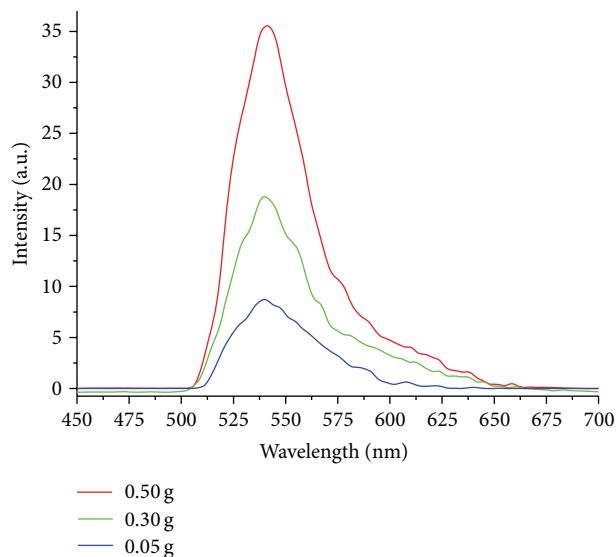


FIGURE 4: PL spectra of the as-synthesized ZnO in 30 mL solutions containing 1 (0.05 g), 6 (0.30 g), and 10 times (0.50 g) of KOH.

as-synthesized products were pure wurtzite ZnO nanorods with uniform hexagonal structure of 400–700 nm diameter and 5–7  $\mu\text{m}$  long. Room temperature PL spectrum of the ZnO nanorods exhibited one strong green light emission at 541 nm due to the singly ionized oxygen vacancies inside.

## Acknowledgments

The authors wish to thank the Thailand's Office of the Higher Education Commission for providing financial support through the National Research University (NRU) Project for Chiang Mai University (CMU) and the Human Resource Development Project in Science Achievement Scholarship of Thailand (SAST) and the Thailand Research Fund (TRF) for providing financial support through the TRF Research Grant BRG5380020, including the Graduate School of CMU through a general support.

## References

- [1] L. Z. Pei, H. S. Zhao, W. Tan, H. Y. Yu, Y. W. Chen, and Q. F. Zhang, "Single crystalline ZnO nanorods grown by a simple hydrothermal process," *Materials Characterization*, vol. 60, no. 9, pp. 1063–1067, 2009.
- [2] Z. Li, X. Huang, J. Liu, Y. Li, and G. Li, "Morphology control and transition of ZnO nanorod arrays by a simple hydrothermal method," *Materials Letters*, vol. 62, no. 10–11, pp. 1503–1506, 2008.
- [3] X. Wu, H. Chen, L. Gong, F. Qu, and Y. Zheng, "Low temperature growth and properties of ZnO nanorod arrays," *Advances in Natural Sciences*, vol. 2, Article ID 035006, 2011.
- [4] H. Zhang, J. Feng, J. Wang, and M. Zhang, "Preparation of ZnO nanorods through wet chemical method," *Materials Letters*, vol. 61, no. 30, pp. 5202–5205, 2007.
- [5] J. H. Yang, J. H. Zheng, H. J. Zhai, L. L. Yang, J. H. Lang, and M. Gao, "Growth mechanism and optical properties of ZnO nanosheets by the hydrothermal method on Si substrates," *Journal of Alloys and Compounds*, vol. 481, no. 1–2, pp. 628–631, 2009.
- [6] X. Ren, D. Han, D. Chen, and F. Tang, "Large-scale synthesis of hexagonal cone-shaped ZnO nanoparticles with a simple route and their application to photocatalytic degradation," *Materials Research Bulletin*, vol. 42, no. 5, pp. 807–813, 2007.
- [7] S. Suwanboon, R. Tanattha, and R. Tanakorn, "Fabrication and properties of nanocrystalline zinc oxide thin film prepared by sol-gel method," *Songklanakarinn Journal of Science and Technology*, vol. 30, no. 1, pp. 65–69, 2008.
- [8] D. Wang, C. Song, Z. Hu, W. Chen, and X. Fu, "Growth of ZnO prisms on self-source substrate," *Materials Letters*, vol. 61, no. 1, pp. 205–208, 2007.
- [9] Powder Diffract. File, JCPDS Internat. Centre Diffract. Data, PA, 19073–3273, U.S.A, 2001.
- [10] J. H. Park, P. Muralidharan, and D. K. Kim, "Solvothermally grown ZnO nanorod arrays on (101) and (002) single- and polycrystalline Zn metal substrates," *Materials Letters*, vol. 63, no. 12, pp. 1019–1022, 2009.
- [11] F. Li, Z. Li, and F. J. Jin, "Structural and luminescent properties of ZnO nanorods," *Materials Letters*, vol. 61, no. 8–9, pp. 1876–1880, 2007.
- [12] L. I. Yang, J. H. Yang, D. D. Wang et al., "Photoluminescence and Raman analysis of ZnO nanowires deposited on Si(100) via vapor-liquid-solid process," *Physica E*, vol. 40, no. 4, pp. 920–923, 2008.
- [13] O. Lupan, L. Chow, L. K. Ono et al., "Synthesis and characterization of Ag- or Sb-doped ZnO nanorods by a facile hydrothermal route," *Journal of Physical Chemistry C*, vol. 114, no. 29, pp. 12401–12408, 2010.
- [14] S. J. Chen, Y. C. Liu, Y. M. Lu, J. Y. Zhang, D. Z. Shen, and X. W. Fan, "Photoluminescence and Raman behaviors of ZnO nanostructures with different morphologies," *Journal of Crystal Growth*, vol. 289, no. 1, pp. 55–58, 2006.
- [15] J. Y. Kim, H. Jeong, and D. J. Jang, "Hydrothermal fabrication of well-ordered ZnO nanowire arrays on Zn foil: room temperature ultraviolet nanolasers," *Journal of Nanoparticles Research*, vol. 13, no. 12, pp. 6699–6706, 2011.
- [16] W. Li, Y. Sun, and J. Xu, "Controllable hydrothermal synthesis and properties of ZnO hierarchical micro/nanostructures," *Nano-Micro Letters*, vol. 4, no. 2, pp. 98–102, 2012.
- [17] Y. J. Gao, W. C. Zhang, X. L. Wu et al., "Hydrothermal self-assembly of ZnO nanorods into sphere-like superstructures and their optical characteristics," *Applied Surface Science*, vol. 255, no. 5, pp. 1982–1987, 2008.
- [18] G. Z. Wang, N. G. Ma, C. J. Deng et al., "Large-scale synthesis of aligned hexagonal ZnO nanorods using chemical vapor deposition," *Materials Letters*, vol. 58, no. 16, pp. 2195–2198, 2004.

## Research Article

# Growth and Physical Property Study of Single Nanowire (Diameter $\sim 45$ nm) of Half Doped Manganite

Subarna Datta,<sup>1</sup> Sayan Chandra,<sup>2</sup> Sudeshna Samanta,<sup>1</sup> K. Das,<sup>1</sup>  
H. Srikanth,<sup>2</sup> and Barnali Ghosh<sup>1</sup>

<sup>1</sup> Unit for Nanoscience, Department of Condensed Matter Physics and Material Sciences, S.N. Bose National Centre for Basic Sciences, Salt Lake, Kolkata 700098, India

<sup>2</sup> Department of Physics, University of South Florida, Tampa, FL 33620, USA

Correspondence should be addressed to Barnali Ghosh; barnali@bose.res.in

Received 11 December 2012; Accepted 17 February 2013

Academic Editor: Lijun Ji

Copyright © 2013 Subarna Datta et al. This is an open access article distributed under the Creative Commons Attribution License, which permits unrestricted use, distribution, and reproduction in any medium, provided the original work is properly cited.

We report here the growth and characterization of functional oxide nanowire of hole doped manganite of  $\text{La}_{0.5}\text{Sr}_{0.5}\text{MnO}_3$  (LSMO). We also report four-probe electrical resistance measurement of a single nanowire of LSMO (diameter  $\sim 45$  nm) using focused ion beam (FIB) fabricated electrodes. The wires are fabricated by hydrothermal method using autoclave at a temperature of  $270^\circ\text{C}$ . The elemental analysis and physical property like electrical resistivity are studied at an individual nanowire level. The quantitative determination of Mn valency and elemental mapping of constituent elements are done by using Electron Energy Loss Spectroscopy (EELS) in the Transmission Electron Microscopy (TEM) mode. We address the important issue of whether as a result of size reduction the nanowires can retain the desired composition, structure, and physical properties. The nanowires used are found to have a ferromagnetic transition ( $T_C$ ) at around 325 K which is very close to the bulk value of around 330 K found in single crystal of the same composition. It is confirmed that the functional behavior is likely to be retained even after size reduction of the nanowires to a diameter of 45 nm. The electrical resistivity shows insulating behavior within the measured temperature range which is similar to the bulk system.

## 1. Introduction

Nanowires of functional oxide materials because of their unique one-dimensional-like structural characteristics and size effects exhibit many novel physical properties that are different from their bulk counterparts. It had been shown before that down to size range of 40 nm the ferromagnetic  $T_C$  is enhanced in nanowires of  $\text{La}_{0.67}\text{Ca}_{0.33}\text{MnO}_3$  [1]. In past studies nanowires of  $\text{La}_{0.67}\text{Ca}_{0.33}\text{MnO}_3$  were grown within templates [1, 2]. The enhancement in  $T_C$  of nanowires corroborates the enhancement in  $T_C$  of nanoparticles of same materials [3]. Our motivation is to investigate to what extent nanowires of complex oxides such as manganites retain their functionality and physical properties on size reduction when the wires are grown by hydrothermal method. The 1D nanostructures with well-controlled size, phase purity, crystallinity, and chemical composition are synthesized by

hydrothermal method in this paper. As a result, the retention of the composition and structural and physical properties on size reduction are important issues that need to be established. Often such structural characterizations are done at average level on an ensemble of nanowires. However, characterizations at the level of a single nanowire using spatially resolved tools are needed. In the present work we have used spatially resolved technique like TEM-based EELS to investigate the chemical composition along with other structural and microscopic tools. Importantly we are able to carry out four-probe electrical measurement using FIB grown contacts on a single nanowire of diameter  $\sim 45$  nm.

The nanowires of functional oxides can be fabricated by different methods like template-assisted growth along with chemical solution processing [4], laser-assisted vapor-liquid-solid phase growth [5], lithography, solvothermal method [6], hydrothermal process [7], and so forth. All the

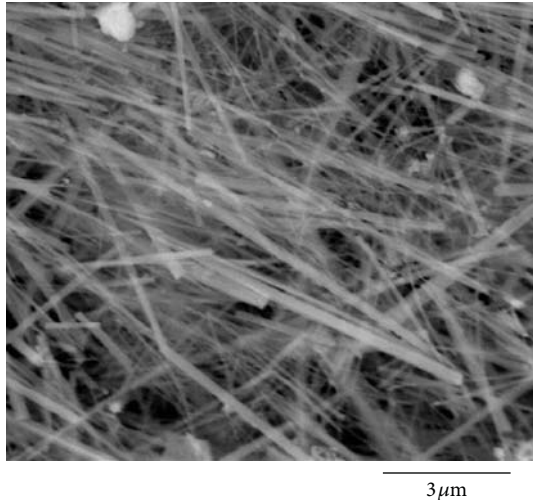


FIGURE 1: SEM image of collection of nanowires.

above-mentioned methods have their own advantages and disadvantages. We have already reported template-assisted growth of functional oxide nanowires by sol-gel synthesis method and magnetic properties of such nanowires [3, 8]. We report here template free fabrication of single-crystalline nanowires ( $\sim 50$  nm, length  $\sim 1\text{--}10$   $\mu\text{m}$ ) of hole doped manganite of  $\text{La}_{0.5}\text{Sr}_{0.5}\text{MnO}_3$  (LSMO) using hydrothermal method. Though this method is suffering from size (diameter) dispersion, it has the advantage of high throughput.

## 2. Experimental Details

Functional oxide nanowires of hole doped manganite  $\text{La}_{0.5}\text{Sr}_{0.5}\text{MnO}_3$  (LSMO) were fabricated by hydrothermal synthesis using autoclave.  $\text{MnCl}_2$ ,  $4\text{H}_2\text{O}$ ,  $\text{La}(\text{NO}_3)_3$ ,  $6\text{H}_2\text{O}$ , and  $\text{Sr}(\text{NO}_3)_2$  were used as precursor materials;  $\text{KOH}$  served as mineralizer, while  $\text{KMnO}_4$  was used as oxidizer. The precursor materials were dissolved in deionized water, and  $\text{KOH}$  was added while stirring to adjust the alkalinity of the solution [7]. The initial mole ratios of the input species were  $0.6\text{KMnO}_4 : 1.4\text{MnCl}_2 \cdot 4\text{H}_2\text{O} : 1.0\text{La}(\text{NO}_3)_3 \cdot 6\text{H}_2\text{O} : 1.0\text{Sr}(\text{NO}_3)_2 : 400\text{H}_2\text{O} : 70\text{KOH}$ . The reaction mixture was vigorously stirred and poured into an autoclave. The main reaction was done in a Teflon vessel which has to be placed in a stainless steel autoclave for higher temperature hydrothermal treatment. The Teflon vessel was filled till 80% of its volume, and then this vessel was placed in the stainless steel container. The crystallization reaction was performed at  $270^\circ\text{C}$  for 30 hours. After the reaction, the autoclave was cooled and depressurized; the products were washed with deionized water and dried in an oven at  $120^\circ\text{C}$  for overnight. A black powder that contains the nanowires was finally obtained.

Nanowires were characterized by using different characterization tools like X-ray diffraction, Scanning Electron Microscope (SEM), Energy Dispersive Analysis of X-ray (EDAX), and High Resolution Transmission Electron Microscopy (HRTEM). The phase formation and phase purity were confirmed by powder diffraction X-ray. The data was taken by PANalytical X'Pert PRO Laboratory powder

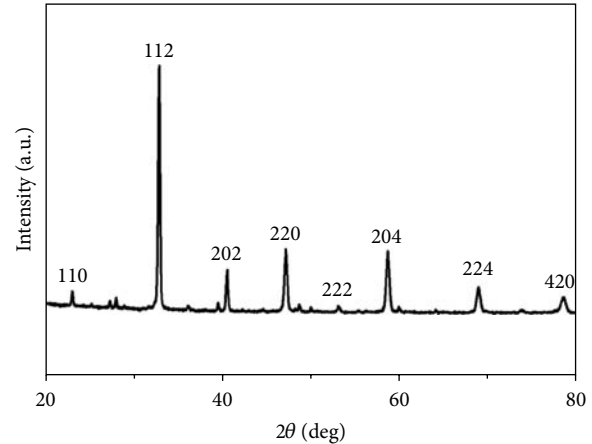


FIGURE 2: XRD pattern of  $\text{La}_{0.5}\text{Sr}_{0.5}\text{MnO}_3$  nanowires confirms the phase formation and phase purity.

X-ray diffractometer with  $\text{Cu K}\alpha$  radiation. The diameter and length of the wires are around  $20\text{--}50$  nm and  $1\text{--}10$  micron, respectively, confirmed by Quanta FEI 200 Scanning Electron Microscope (SEM) and 200 KV Tecnai G2 TF-20 Transmission Electron Microscope. The stoichiometry of the compound LSMO was determined using TEM-EDAX.

To establish the retention of composition on size reduction, we have used TEM-based Electron Energy Loss Spectroscopy (EELS) to investigate the chemical composition at a single nanowire level [9]. 200 kV Tecnai G2-TF-20 TEM with a Gatan parallel detection EELS spectrometer was used for this study. The unknown Mn valency of LSMO nanowire is estimated from EELS. Energy Filtered Transmission Electron Microscopy (EFTEM) mode was done to image the distribution of constituent elements within the nanowire. In addition to the basic characterizations the magnetic nature of the nanowires was determined by a commercial Physical Property Measurement System (PPMS).

To make the four-wire electrical contacts on a single nanowire, we have dispersed the nanowires on  $\text{SiO}_2$  substrate. A single nanowire of LSMO of diameter  $\sim 45$  nm was connected to Cr/Au contact pads by interconnectors made of Pt deposited by FIB (FEI-HELIOS 600) using Ga ions at a voltage of 30 keV and beam current of 80 pA. The temperature variation of resistivity of a single nanowire down to liquid helium temperature (5 K) was done by using cryogenic cryocooler model SRDK 305.

## 3. Results and Discussions

**3.1. Structural and Elemental Characterization.** A typical collection of nanowires obtained from autoclave is given in Figure 1. Phase formation and phase purity were checked with X-ray diffraction measurement shown in Figure 2. It is the tetragonal structure of the space group  $I4/mcm$ , it compares well with bulk values [10], and it matches well with the data reported in ICSD pattern (ref. code: 01-089-0786). The lattice parameters are  $a = 0.545$  nm,  $b = 0.545$  nm, and  $c = 0.770$  nm. From the structural characterization (shown

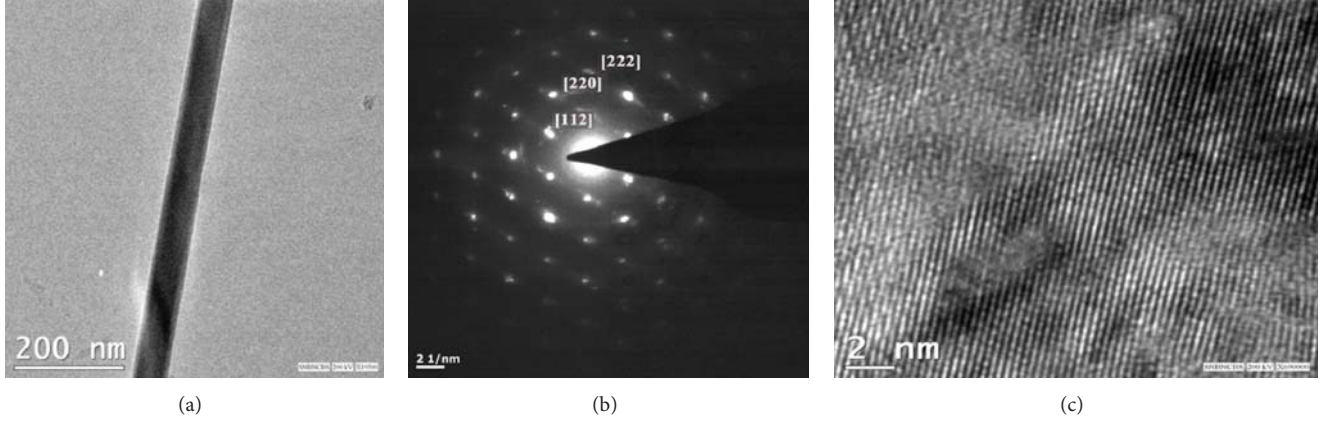


FIGURE 3: (a) Single nanowire of diameter around 45 nm, (b) the selected area diffraction pattern taken with a Transmission Electron Microscope, and (c) HRTEM image shows the single crystalline nature of LSMO nanowires.

in Figure 2) of hydrothermally grown nanowires, it has been observed that we could form single tetragonal phase of LSMO ( $x = 0.5$ ) nanowires which has no impurity.

**3.2. Transmission Electron Microscopy.** The wires were grown of different diameters and lengths ranging 20–50 nm and 1–10 micron, respectively. The TEM image of a single nanowire is shown in Figure 3(a). The single crystalline nature of the nanowires was confirmed from the diffraction pattern and HRTEM images shown in Figures 3(b) and 3(c). The lattice spacing is around 3.11 Å, and (hkl) values are estimated from diffraction pattern data. Nanowires fabricated are of pure phase and single crystalline in nature. It has been observed from the TEM-EDAX data that the atomic percentage ratio (La : Sr) : Mn : O is approximately 1 : 1 : 3 which is the desired composition. We have done the TEM analysis on many single nanowires across the length of the nanowires, and it shows single crystallinity throughout the length.

**3.3. Elemental Analysis Using EELS.** The elemental analysis of these nanowires was done by EELS on different single nanowires repeatedly and estimated the valency of Mn from the calibration curve shown in Figure 4(a). We have determined Mn valency using the white lines ( $L_2$ ,  $L_3$  ionization edges of Mn) and the intensity ratio of  $L_3$  and  $L_2$  lines [11]. The intensities of  $L_3$  and  $L_2$  lines are related to the unoccupied states in the 3d bands. Transition from Mn 2p shell is actually split into two components separated by spin orbit splitting of the ionized 2p core level. Transitions from  $2p^{3/2}$  to  $3d^{3/2}$   $3d^{5/2}$  and from  $2p^{1/2}$  to  $3d^{1/2}$  are  $L_3$  and  $L_2$  lines, respectively. Comparing the intensity  $L_3/L_2$  ratio of Mn of LSMO nanowire and that of Mn with known valency of some compounds, quantitative determination of Mn valency of our sample was evaluated [9]. The intensity ratios of  $L_3$  and  $L_2$  lines of different Mn oxide compounds as a function of their known valency are plotted in Figure 4(a). This curve serves as the calibration curve from which the valence state of unknown materials can be obtained by using the observed intensity ratios. From the calibration curve, we have estimated the valency of Mn of LSMO nanowire. The Mn

TABLE 1: Comparison of  $T_C$  and valency of LSMO nanowires with the bulk.

| Sample        | $T_C$ (K) | Mn valency |
|---------------|-----------|------------|
| LSMO bulk     | 330       | 3.5        |
| LSMO nanowire | 325       | 3.5        |

valency is of the order of  $\sim 3.5$ , and it is very close to its bulk value as shown in Table 1. Energy Filtered TEM image was taken to check the homogeneity of the elemental distribution in each nanowire. Figure 4(b) shows the EFTEM image of LSMO nanowire, where red, green, blue, and yellow colors are used for elements O, Mn, La, and Sr, respectively. The EFTEM analysis shows that all the constituent elements La, Sr, Mn, and O are homogeneously distributed within the nanowire.

**3.4. Magnetic Measurements.** The results of magnetic measurements are shown in Figure 5. It has been observed from the temperature variation of magnetization data that the LSMO nanowires undergo a transition from ferromagnetic (FM) to paramagnetic (PM) phase around 325 K shown in Figure 5(a). The observed  $T_C$  was compared with the phase diagram of bulk LSMO [12], shown in Table 1. Field variations of magnetization ( $M$  versus  $H$ ) were done at 300 K and 5 K in Figure 5(b). The nanowires show ferromagnetic behavior with large coercivity  $\sim 645$  Oe at 5 K shown in the inset of Figure 5(b).

Based on the magnetic data and the work on magnetocaloric study on these LSMO ( $x = 0.5$ ) nanowires [13], we have observed the signatures of three distinct magnetic transitions from the change in magnetic entropy  $-\Delta S_M(T)$ : two maxima at 290 K and 45 K and a minimum at 175 K. The maximum at 290 K arises due to PM-FM transition, and around 175 K the transition is due to antiferromagnetic (AFM) transition. The above two transitions are also observed in bulk LSMO ( $x = 0.5$ ) sample [14–16]. Around 45 K there is one maximum in the magnetization curve; this behavior is not seen in bulk. We have explained this transition as

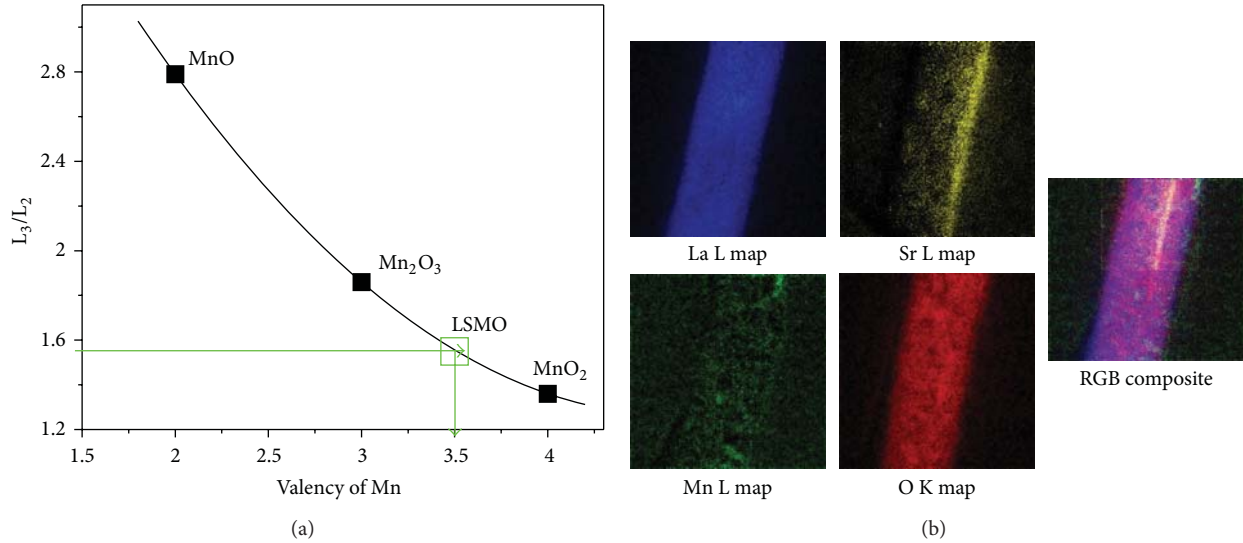


FIGURE 4: (a) Intensity ratios of  $L_3$  and  $L_2$  lines of different Mn oxide compounds as a function of their known valency in the energy range 600–1000 eV and (b) Energy Filtered Transmission Electron Microscope (EFTEM) image of each constituent element: L map of La, Sr, and Mn and K map of O in LSMO nanowire. The red, green, blue, and yellow colors represent the distribution of elements O, Mn, La, and Sr, respectively in the nanowire in the RGB composite map.

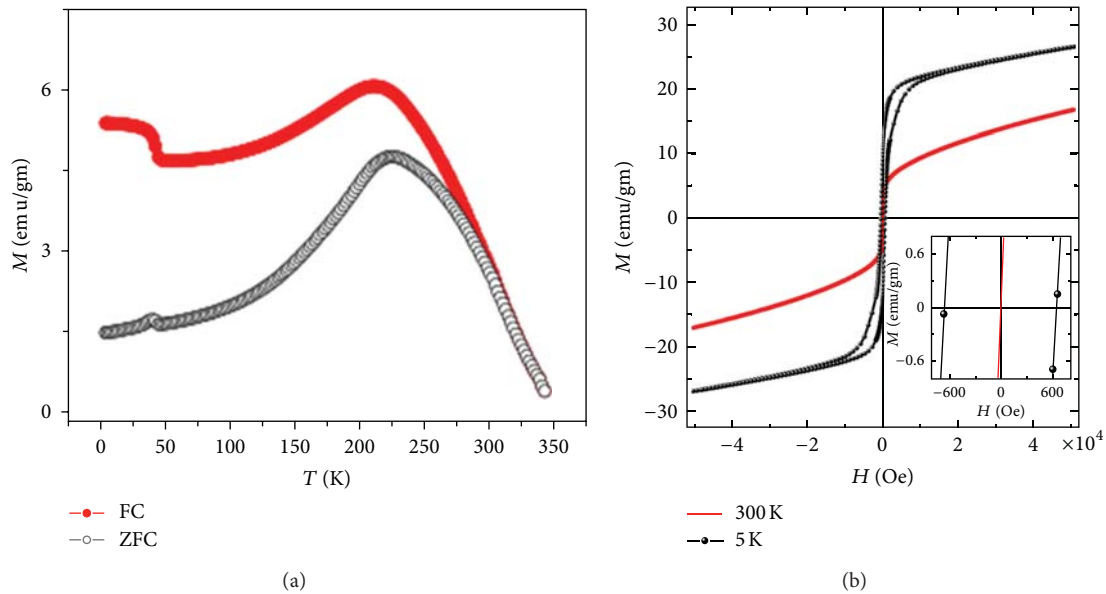


FIGURE 5: (a) Temperature variation of magnetization data of LSMO at 100 Oe and (b) plot of field variation magnetization of LSMO at 5 K and 300 K.

FM transition as observed in the magnetic entropy change plot [13]. From the magnetic measurements and from our previous magnetocaloric study [13], we can infer that the hydrothermally grown nanowires show the basic ferromagnetic property as seen in bulk.

### 3.5. Electrical Resistivity Measurement

**3.5.1. Fabrication of Contact Pads Using FIB.** For resistivity measurement Cr/Au contact pads are deposited on  $SiO_2$

substrate by thermal evaporation using hard mask as shown in Figure 6(a). Using Helios Dual Beam System consisting of an FEG source and an ion beam source, we have located one single nanowire of diameter  $\sim 45$  nm as shown in Figure 6(b). The electrical contact pads were deposited by using a Pt source by Focused Electron Beam (FEB), and then these four pads were finally connected to the prefabricated gold contact pads by FIB, shown in Figure 6(c). The separation between two consecutive probes is around  $\sim 300$  nm. Each contact pad has width of  $\sim 300$  nm.

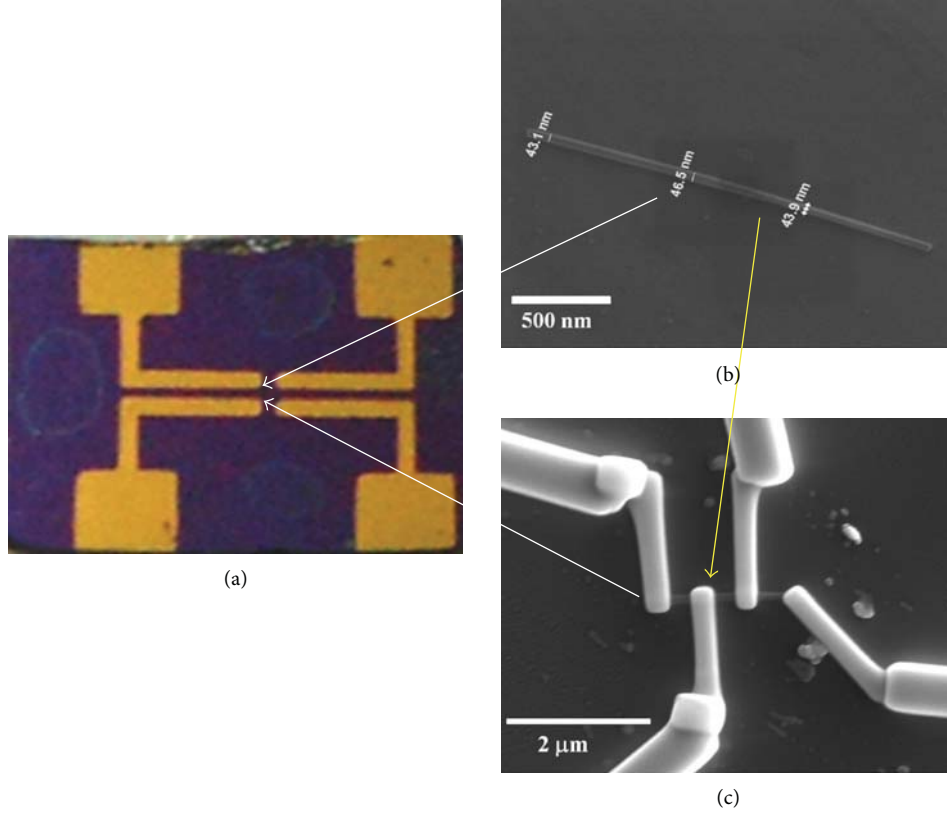


FIGURE 6: (a) Cr/Au contact pads deposited on  $\text{SiO}_2$  substrate by thermal evaporation using hard mask, (b) SEM image of single nanowire of diameter  $\sim 45$  nm, and (c) SEM image of four-wire electrical contact made of Pt by using FIB. The white lined arrows in (a) indicate the area where the nanowires are dispersed and made contact with FIB. The yellow lined arrow indicates that nanowire is connected to four contact pads by Focused Electron Beam (FEB), and after that these are connected to gold contact pads by FIB.

**3.5.2. Transport Measurement on Single Nanowire.** The resistivity data are plotted in Figure 7(a) as a function of temperature which were taken at a current of  $1 \mu\text{A}$ .

We are able to make proper electrical contact and have measured the resistivity of single nanowire of LSMO ( $x = 0.5$ ). Variation of resistivity as a function of temperature plotted in Figure 7(a) shows insulating behaviour within the measured temperature range. The behaviour is similar to that seen in the bulk LSMO ( $x = 0.5$ ) system [14]. The comparison of the resistivity of nanowire compared to the bulk ceramic sample is depicted quantitatively in Figure 7(b). The bulk sample was prepared by ceramic method which shows quite higher resistivity than the nanowire. The  $\rho$  at 5 K is around  $2.7 \times 10^{-3} \Omega\text{-m}$  measured at  $1 \mu\text{A}$  current, and the resistivity at the highest temperature (310 K) is  $4 \times 10^{-5} \Omega\text{-m}$ . We have fitted our conductivity data with variable range hopping model ( $\sigma = \sigma_0 \exp(-(T_0/T))^{1/4}$ ) appropriate for whole temperature ranges ( $\sim 10$  K–310 K) as shown in inset of Figure 7(a) [17]. We have found the characteristic temperature ( $T_0$ ) and density of states (DOS) at Fermi level ( $N(E_F)$ ) from the fitted equation. From the slope of the fitted curve the estimated  $T_0$  is  $\sim 2.4 \times 10^4$  K.  $N(E_F)$  is related to  $T_0$  by the relation  $N(E_F) = (24/\pi a^3 K_B T_0)$ , where  $a$  is localization length ( $\sim 0.39$  nm) which is around one unit cell. From measured  $T_0$ , we obtain  $N(E_F) \sim 6.22 \times 10^{22} \text{ eV}^{-1} \text{ cm}^{-3}$

or  $1.55 \times 10^{43} \text{ J}^{-1} \text{ mole}^{-1}$ . From heat capacity data for a similar compound (LSMO  $x = 0.3$ ) we obtain  $N(E_F) \sim 0.96 \times 10^{43} \text{ J}^{-1} \text{ mole}^{-1}$  [18]. The two DOS values are quite comparable, and this validates the use of VRH model for the electrical conduction in the nanowire.

## 4. Conclusions

We have demonstrated the fabrication of functional oxide nanowires of Sr doped lanthanum manganite system using autoclave and have used EELS as a tool to study the elemental composition of LSMO nanowires of diameter  $\sim 45$  nm. From the EELS and magnetic measurements it has been observed that the nanowires retain the desired composition as well as basic ferromagnetic property, though  $H_C$  increases even after the size reduction down to  $\sim 45$  nm. Finally we are able to make four-probe contacts to a single nanowire and perform the electrical transport measurements on a single nanowire down to 5 K. The resistivity from 310 K down to 10 K shows variable range hopping.

## Acknowledgments

B. Ghosh wants to thank DST, Government of India, under UNANST Phase II for financial support. S. Datta would like to thank DST for financial support. The work has been done

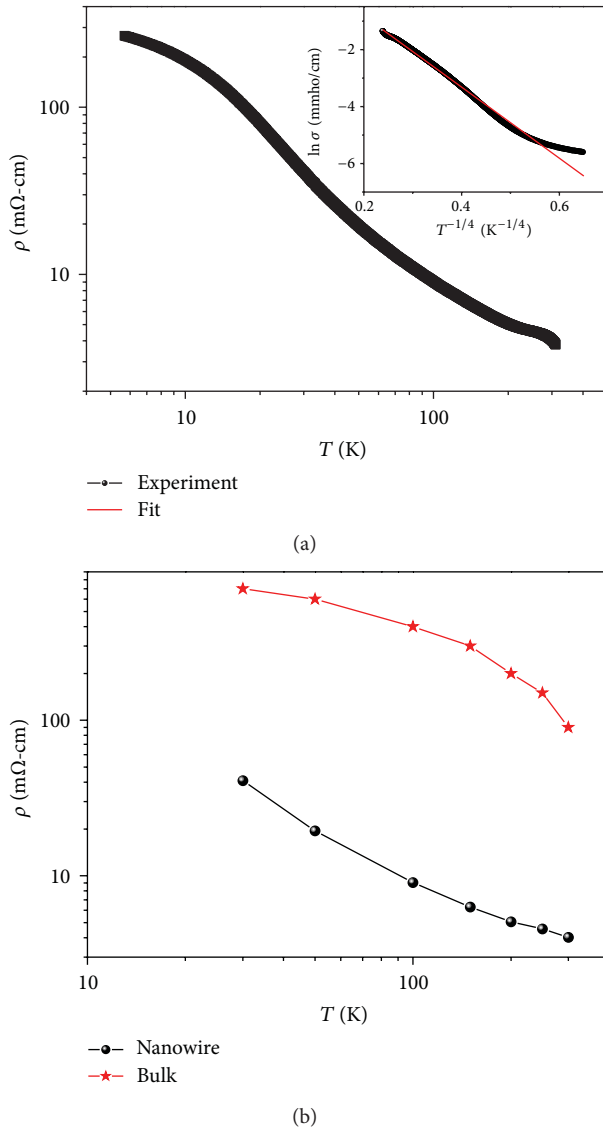


FIGURE 7: (a) Temperature variation of resistivity of single nanowire of  $\text{La}_{0.5}\text{Sr}_{0.5}\text{MnO}_3$  measured in the temperature range from 5 K to 310 K. Inset curve ( $\ln \sigma$  versus  $T^{-1/4}$ ) shows that conductivity data fitted with variable range hopping model for the whole temperature ranges and (b) quantitative comparison of resistivity of LSMO nanowires and bulk [14].

in the DST supported Unit for Nanoscience. S. Chandra and H. Srikanth would like to thank US Department of Energy (Grant no. DE-FG02-07ER46438), for the work at USF.

## References

- [1] B. Ghosh and A. K. Raychaudhuri, "Synthesis and physical properties of ordered arrays of nanowires of complex functional oxides," *Journal of Nanoscience and Nanotechnology*, vol. 9, no. 9, pp. 5533–5536, 2009.
- [2] K. S. Shankar, S. Kar, A. K. Raychaudhuri, and G. N. Subbanna, "Fabrication of ordered array of nanowires of  $\text{La}_{0.67}\text{Ca}_{0.33}\text{MnO}_3$  ( $x=0.33$ ) in alumina templates with enhanced ferromagnetic transition temperature," *Applied Physics Letters*, vol. 84, no. 6, pp. 993–995, 2004.
- [3] T. Sarkar, A. K. Raychaudhuri, A. K. Bera, and S. M. Yusuf, "Effect of size reduction on the ferromagnetism of the manganite  $\text{La}_{1-x}\text{Ca}_x\text{MnO}_3$  ( $x=0.33$ )," *New Journal of Physics*, vol. 12, Article ID 123026, 2010.
- [4] A. K. Raychaudhuri, *Nanolithography and Nanomanipulation, the Chemistry of Nanomaterials Synthesis Properties and Applications*, vol. 2 of edited by C. N. R. Rao, A. Muller, and A. K. Cheetham, Wiley-VCH, Berlin, Germany, 2004.
- [5] Y. Chen, J. Li, Y. Han, X. Yang, and J. Dai, "The effect of Mg vapor source on the formation of MgO whiskers and sheets," *Journal of Crystal Growth*, vol. 245, no. 1-2, pp. 163–170, 2002.
- [6] J. R. Heath and F. K. LeGoues, "A liquid solution synthesis of single crystal germanium quantum wires," *Chemical Physics Letters*, vol. 208, no. 3-4, pp. 263–268, 1993.
- [7] D. Zhu, H. Zhu, and Y. H. Zhang, "Hydrothermal synthesis of single-crystal  $\text{La}_{0.5}\text{Sr}_{0.5}\text{MnO}_3$  nanowire under mild conditions," *Journal of Physics: Condensed Matter*, vol. 14, no. 27, pp. L519–L524, 2002.
- [8] S. Chandra, A. I. Figueroa, B. Ghosh et al., "Fabrication and magnetic response probed by RF transverse susceptibility in  $\text{La}_{0.67}\text{Ca}_{0.33}\text{MnO}_3$  nanowires," *Physica B: Condensed Matter*, vol. 407, no. 1, pp. 175–178, 2012.
- [9] R. F. Egerton, "Electron energy-loss spectroscopy in the TEM," *Reports on Progress in Physics*, vol. 72, no. 1, Article ID 016502, 2009.
- [10] P. M. Woodward, T. Vogt, D. E. Cox et al., "Influence of cation size on the structural features of  $\text{Ln}_{1/2}\text{A}_{1/2}\text{MnO}_3$  Perovskites at room temperature," *Chemistry of Materials*, vol. 10, no. 11, pp. 3652–3665, 1998.
- [11] Z. L. Wang, J. S. Yin, and Y. D. Jiang, "EELS analysis of cation valence states and oxygen vacancies in magnetic oxides," *Micron*, vol. 31, no. 5, pp. 571–580, 2000.
- [12] A. Urushibara, Y. Moritomo, T. Arima, A. Asamitsu, G. Kido, and Y. Tokura, "Insulator-metal transition and giant magnetoresistance in  $\text{La}_{1-x}\text{Sr}_x\text{MnO}_3$ ," *Physical Review B*, vol. 51, no. 20, pp. 14103–14109, 1995.
- [13] S. Chandra, A. Biswas, S. Datta et al., "Multiple magnetic transitions and magnetocaloric effect in hydrothermally synthesized single crystalline  $\text{La}_{0.5}\text{Sr}_{0.5}\text{MnO}_3$  nanowires," *Materials Research Society Symposium Proceedings*, vol. 1454, 2012.
- [14] Z. Jirak, J. Hejtmanek, K. Knmzek, M. Marysk, V. Smma, and R. Sonntag, "Ferromagnetic-antiferromagnetic transition in tetragonal  $\text{La}_{0.50}\text{Sr}_{0.50}\text{MnO}_3$ ," *Journal of Magnetism and Magnetic Materials*, vol. 217, no. 1–3, pp. 113–119, 2000.
- [15] I. Dhiman, A. Das, P. K. Mishra, and L. Panicker, "Influence of A-site ionic radii on the magnetic structure of charge-ordered  $\text{La}_{0.5}\text{Ca}_{0.5-x}\text{Sr}_x\text{MnO}_3$  manganites," *Physical Review B*, vol. 77, no. 9, Article ID 094440, 11 pages, 2008.
- [16] J. Spooren, R. I. Walton, and F. Millange, "A study of the manganites  $\text{La}_{0.5}\text{M}_{0.5}\text{MnO}_3$  ( $M = \text{Ca}, \text{Sr}, \text{Ba}$ ) prepared by hydrothermal synthesis," *Journal of Materials Chemistry*, vol. 15, no. 15, pp. 1542–1551, 2005.
- [17] N. F. Mott and E. A. Davis, Eds., *Electronic Processes in Non-Crystalline Materials*, Clarendon Press: Oxford University Press, Oxford, UK, 2nd edition.
- [18] J. M. D. Coey, M. Viret, L. Ranno, and K. Ounadjela, "Electron localization in mixed-valence manganites," *Physical Review Letters*, vol. 75, no. 21, pp. 3910–3913, 1995.

## Research Article

# Spin-Filtering Effects in Würtzite and Graphite-Like AlN Nanowires with Mn Impurities

G. A. Nemnes

Faculty of Physics, “Materials and Devices for Electronics and Optoelectronics” Research Center, University of Bucharest, P.O. Box MG-II, Ilfov 077125 Magurele, Romania

Correspondence should be addressed to G. A. Nemnes; [nemnes@solid.fizica.unibuc.ro](mailto:nemnes@solid.fizica.unibuc.ro)

Received 14 December 2012; Accepted 28 February 2013

Academic Editor: Yun Zhao

Copyright © 2013 G. A. Nemnes. This is an open access article distributed under the Creative Commons Attribution License, which permits unrestricted use, distribution, and reproduction in any medium, provided the original work is properly cited.

Spin transport properties of magnetic nanowire systems—atomic-sized AlN nanowires with additional Mn impurities—are investigated employing *ab initio* constrained spin density functional theory calculations and nonequilibrium Green's functions formalism. The analyzed nanowire structures exhibit a stress-induced phase transition, between würtzite and graphite-like configurations. In these quasi-one dimensional systems, the surface states ensure the basic prerequisite in establishing spin and charge transfer, by reducing the relatively large bandgap of the group III nitride semiconductor. The results show in how far this phase transition affects the surface states, focusing on the consequences which appear in the spin-filtering processes.

## 1. Introduction

Group-III nitride nanowires provide nowadays a vast number of applications, ranging from chemical [1, 2] and temperature sensors to nanomechanical resonators, thermoelectrical [3] and field emitter [4] applications. In particular, since AlN is a wide bandgap (~6.2 eV) semiconductor, it has become a strong candidate for optoelectronic devices in the UV regime. AlN nanowires are currently produced by a number of techniques, such as self-patterning [5], direct arc discharge [6], or from Al powder [7]. Moreover, inserting transitional metal (TM) impurities (e.g., Mn), attempts have been made in order to produce ferromagnetic quasi-one dimensional diluted magnetic semiconductors [8].

Although the native structure of bulk AlN is würtzite (WZ, space group  $P6_3mc$ ), it was established that ultrathin nanowires occur naturally in a graphite-like (GL, space group  $P6_3/mmc$ ) phase [9–11]. However, upon applying pulling stress, the structures may retain the WZ configuration. Switching between these two configurations can occur due to thermal fluctuations or mechanically induced stress and this has a large impact in both charge and thermal transport.

The surface states play a significant role in the conduction properties of the nanowires, as they reduce the wide bandgap, which is found in the bulk semiconductor. In contrast to

bulk AlN, which has rather good insulating properties, the atomic sized nanowires can achieve reasonable conduction. Therefore, the structures can be regarded as viable solutions for the active region in field effect applications. It is also important to emphasize that it is essential for the nanowire systems to retain a small band gap (up to ~1-2 eV), that is, semiconducting behavior, in order to have an efficient field effect control exerted by an external gate.

The AlN nanowires may also provide the low dimensional building blocks for the future spintronic devices, since ferromagnetic ordering has been observed in the bulk semiconductor, doped with Mn impurities [12]. Specific studies on nanowire systems report experimental observation of ferromagnetic ordering [8], as well as the influence of the wire passivation on the stability of the ferromagnetic ground state using *ab initio* investigations [13]. Nonmagnetic dopants, for example, Mg, can produce unconventional magnetism in AlN nanowire systems, due to the interplay between the low dimensional effects generated by confinement and surface states [14].

In this paper the spin filtering effects are investigated in AlN atomic-sized nanowires with additional Mn impurities, with the main focus on the differences which arise by switching between the two structural configurations, WZ and GL. The GL phase corresponds to the freestanding nanowire,

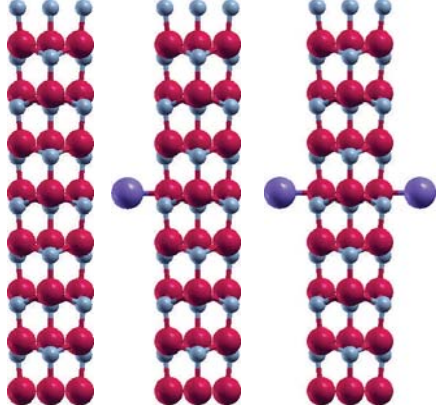


FIGURE 1: Pristine WZ nanowire and structures with one or two Mn impurities.

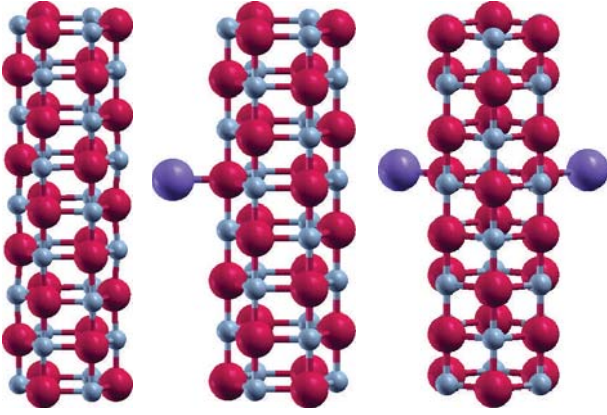


FIGURE 2: Pristine GL nanowire and structures with one or two Mn impurities.

while the WZ phase is obtained by tuning the applied axial stress. The contribution of the surface states to the spin transport is comparatively analyzed. The results convey the possibility of using AlN nanowires as nanomechanical spintronic devices, where the spin detection can indicate the magnetic and structural state of the system.

## 2. Structures and Methods

The structures considered are AlN nanowires with one or two additional impurities, depicted in Figures 1 and 2. The GL configurations correspond to free-standing wires, while the WZ structures are obtained by applying an external pulling stress. The nanowires are functionalized by introducing additional Mn impurities on the surface. Depending on the magnetic moments of the impurities the two components of spin current are scattered differently. For the systems considered here it is expected that the transmission is less affected compared to structures with substitutional TM impurities. However, one needs to assess in how far the adatoms can still produce a reasonable spin current polarization and, furthermore, evaluate the potential differences introduced by switching between the two structural configurations.

The *ab initio* calculations are performed in the framework of density functional theory (DFT), using the SIESTA package [15]. The magnetic structures are investigated using constrained spin-DFT calculations, in the local spin density approximation (LSDA), with the parametrization proposed by Ceperley and Alder. In the supercell approach implemented by SIESTA, the real space grid was set by a cutoff energy of 300 Ry, and a Monkhorst-Pack scheme to  $1 \times 1 \times 5$   $k$ -points was considered. In order to obtain the atomic coordinates, structural relaxations are performed. The starting point is the pristine AlN nanowire in the WZ phase, which is the native configuration of the bulk material. The initial lattice parameters correspond to the bulk system, that is,  $a_0^{\text{WZ}} = 3.112 \text{ \AA}$ ,  $c_0^{\text{WZ}} = 4.982 \text{ \AA}$ . The system is relaxed using a maximum displacement of  $0.1 \text{ \AA}$  until the forces are less than  $0.04 \text{ eV/\AA}$ . The final configuration obtained for the free-standing wire is the hexagonal GL phase. In the GL structure the Al and N atoms are placed in alternating positions in hexagonal layers, with the lattice constant  $a^{\text{GL}} = 1.97 \text{ \AA}$ , that is, the in-plane distance between two successive Al and N atoms. The distance between the hexagonal layers, which are equally spaced, is  $c^{\text{GL}} = 1.87 \text{ \AA}$ . The lattice constant along the wire direction is therefore reduced from  $4.982 \text{ \AA}$  to  $2c^{\text{GL}} = 3.74 \text{ \AA}$ . However, by applying a pulling force of  $0.40 \text{ nN}$ , the wire retains the original WZ configuration, with slightly modified lattice parameters,  $a^{\text{WZ}} = 2.79 \text{ \AA}$ ,  $c^{\text{WZ}} = 4.86 \text{ \AA}$ . The lattice parameters generally depend on the applied axial stress.

The spin dependent transmission functions are extracted using the non-equilibrium Green's functions (NEGF) formalism, which is implemented in TRANSIESTA [16]. The scattering region consists of four unit cells, with a total of 48 atoms and it is coupled to the left/right semi-infinite electrodes. The effects introduced by the additional Mn impurities, which are present on the nanowire surface, can be observed in the calculated transmission functions corresponding to the two spin channels,  $T_{\uparrow}$  and  $T_{\downarrow}$ . The total transmission function can be found for a total energy  $E$  using the relation

$$T(E) = \text{Tr} [\Gamma_L G^r \Gamma_R G^a], \quad (1)$$

where  $G^{r/a}$  are the retarded/advanced Green's functions and  $\Gamma_{L/R}$  are the self-energies corresponding to the couplings with the two contacts. In linear regime, the efficiency of a spin-filter device can be defined using the transmission of each spin component [17]:

$$p^s = \frac{T_{\uparrow} - T_{\downarrow}}{T_{\uparrow} + T_{\downarrow}}, \quad (2)$$

where  $s$  indicates the structural configuration,  $s = \text{WZ, GL}$ .

## 3. Results and Discussion

As it was already pointed out in the introduction, the surface states which appear in the considered quasi-one-dimensional structures effectively reduce the bandgap of the aluminium nitride. Figure 3 shows the total and partial densities of

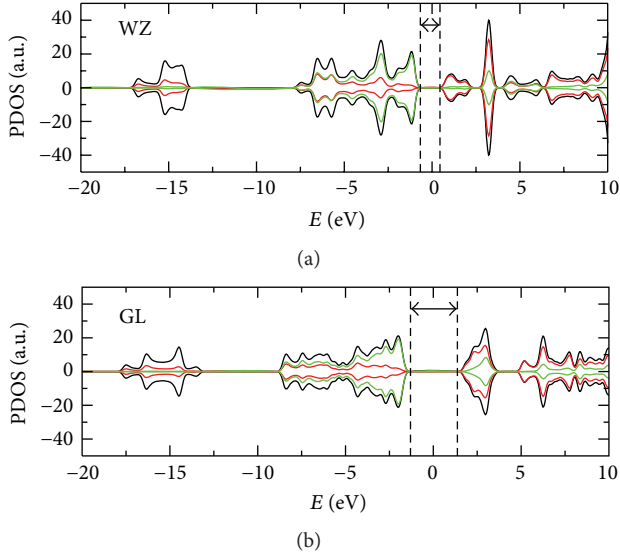


FIGURE 3: Total (black) and partial density of states for WZ and GL structural configurations. The contribution of the  $p$  orbitals of nitrogen (green) and  $s, p$  orbitals of aluminium (red) are represented. The arrows mark the minibandgaps between the valence band and the first group of surface states.

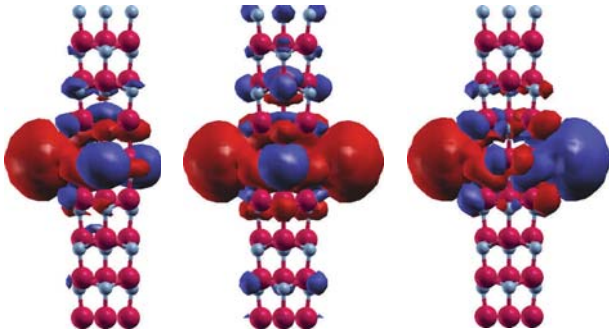


FIGURE 4: Spin densities for nanowires in the WZ configuration, with one and two Mn impurities. Both ferro- and antiferromagnetic configurations are indicated.

states (DOS) of the ideal nanowires, for the two structural configurations. One can see that the mini-bandgaps which appear,  $E_g^{WZ} \approx 1.2$  eV and  $E_g^{GL} \approx 2.5$  eV, are significantly smaller than the bandgap of bulk AlN. In both WZ and GL phases, the valence band is formed by  $p$  orbitals of nitrogen. For the WZ nanowire the first group of surface states is formed by both  $s$  and  $p$  orbitals of aluminium, while for the GL configuration there is also a noticeable contribution from the  $p$  orbitals of nitrogen. It is important to note that in the case of WZ nanowire there is an effective bandgap comparable with the one of bulk silicon, which suggests the atomic sized structure is suitable for spin and charge transfer applications.

Next, by introducing the Mn adatoms, the spin densities are comparatively analyzed for WZ and GL structures and a clear qualitative difference can be observed in Figures 4 and

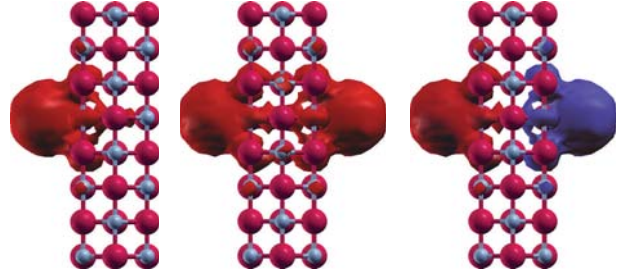


FIGURE 5: Spin densities for nanowires in the GL configuration, with one and two Mn impurities. Both ferro- and antiferro-magnetic configurations are indicated.

5. For the two impurity cases, both ferro- (FM) and antiferromagnetic (AFM) configurations of the magnetic moments are investigated. As expected, the spin polarization is maximum at the location of the magnetic impurities. In the case of WZ nanowire, there is also a large polarization of neighboring Al and N atoms, which are otherwise nonmagnetic. Opposite spin polarizations can be observed at the first and second order neighbors. This is in contrast with the case of the GL structure, which has better insulating properties and the net spin density remains confined at the magnetic adatoms. In the case of two impurities, placed symmetrically to one of the planes which bisect the structures in two identical halves, a mirrored symmetry in the spin density can be noticed. This has consequences in the spin transport, where both components of spin current are equally transmitted, that is, the net spin current is zero. Thermal excitations as well as small magnetic fields can switch the magnetic state of the impurities from FM to AFM, turning on and off the spin current. This suggests the possibility of using the considered magnetic nanowires as building blocks for high sensitivity temperature and magnetic field sensors.

The spin resolved transmission is depicted in Figures 6 and 7, for systems with one and two magnetic impurities, respectively. The pristine non-magnetic nanowires are first analyzed in both WZ and GL configurations. In this case each propagating mode adds one unit plateau to the total transmission. The ideal transmission follows closely the density of states plotted in Figure 3. The adatoms placed on the nanowire surface introduce a selective scattering on the two spin components, depending on the preset magnetic configuration. Contrary to the situation where the magnetic impurities are placed substitutional, in this case the transmission is rather close to ideal. More significant scattering is visible in the energy range corresponding to the first group of surface states. The mini-gaps are consistent with the previously obtained values from the DOS analysis. For the systems with the pair of magnetic impurities in the AFM configuration, there is a rather similar transmission function with the one indicated in Figures 6 and 7, with major qualitative difference that in this case one has  $T_{\uparrow} = T_{\downarrow}$ .

The spin polarization depends on the intricate scattering processes, which follow from the addition of magnetic impurities and which are also dependent on the magnetic configuration. Due to the sharp variations present in the transmission

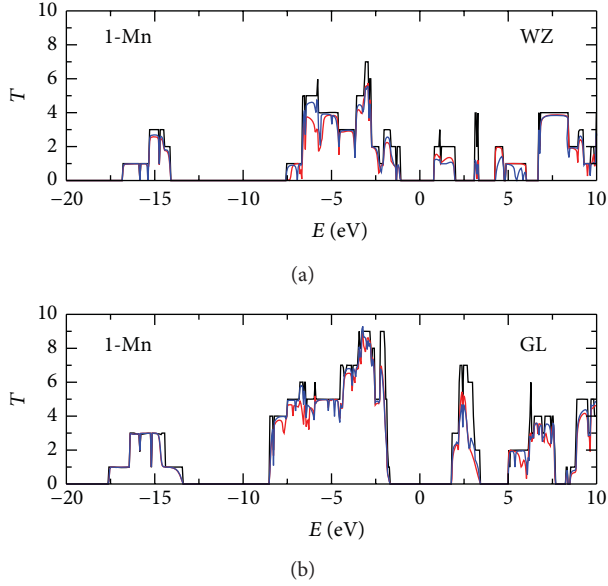


FIGURE 6: Transmission versus energy for nanowires in the WZ and GL configurations: pristine nanowire (black) and nanowires with one Mn impurity;  $T_{\uparrow}$  (red) and  $T_{\downarrow}$  (blue) are represented. The Fermi level is located at  $E = 0$ .

functions, polarizations close to unity are possible. However, they occur on small energy ranges. Therefore the data indicated in Figure 8 was averaged on energy intervals of  $\sim 25$  meV, consistent with realistic thermal fluctuations. By this procedure, spin polarizations above 20% can still be achieved for the GL structures. Focusing on the first group of surface states, one can notice that the differences between the one- and two-impurity cases are smaller for the GL structure, when compared to its WZ counterpart. This indicates the potential robustness of the spin characteristics with respect to adding one extra impurity.

To conclude, both WZ and GL structures with Mn adatoms exhibit reasonable transmission and are able to produce detectable spin polarization. The reduced bandgaps offer the possibility of using the magnetic AlN nanowires in spintronic field effect applications.

#### 4. Conclusions

AlN nanowires with Mn adatoms are investigated using constrained spin-DFT calculations. The phase transition between the wurtzite and graphite-like configurations is discussed in the context of exploring the spin transport properties. A general feature of the analyzed quasi-one dimensional structures is the reduction of the band gap, down to  $\sim 1.2$  eV for the WZ nanowire. Consequently, although bulk AlN is a wide bandgap semiconductor, it is suitable for atomic sized devices which employ the field effect. With the additional impurities placed on the surface of the nanowires, the scattering is reduced and the transmission is at a significant ratio, when compared with the ideal case. However, one or two Mn impurities in the ferromagnetic configuration still provide a reasonable spin separation and the net current may be further

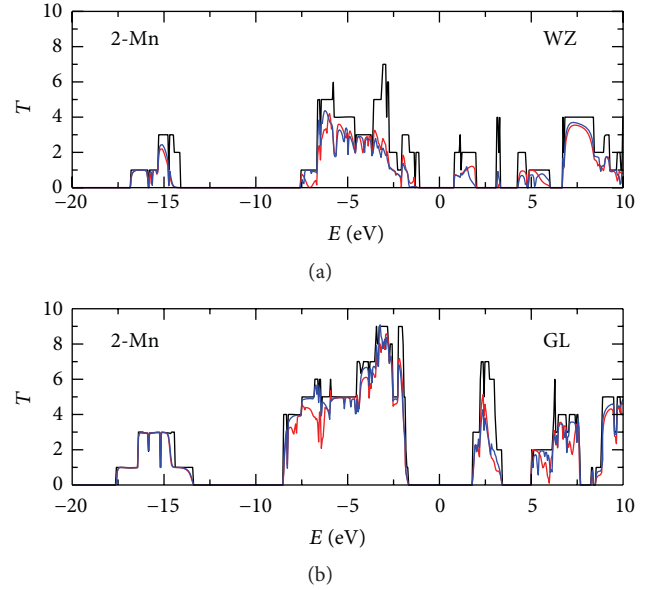


FIGURE 7: Similar data as in Figure 6 for nanowires with two Mn impurities, in the ferromagnetic configuration.

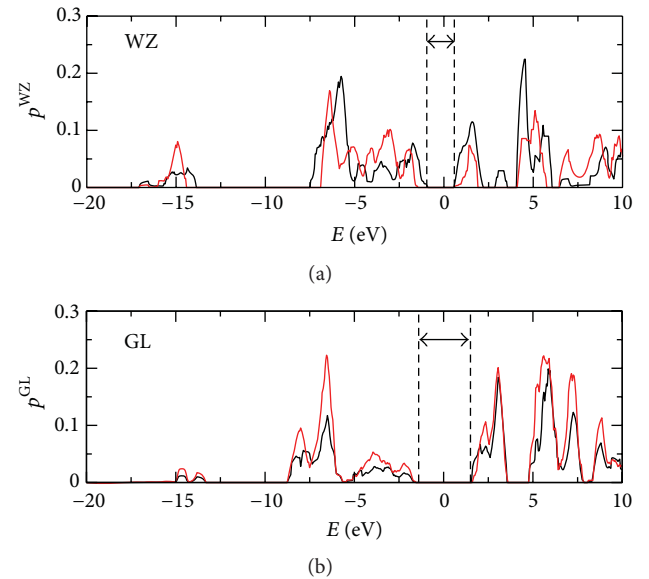


FIGURE 8: Spin polarization (absolute value) for WZ and GL nanowires with one (black) or two (red) impurities. The arrows indicate the mini-bandgaps.

manipulated in a spintronic device. Taking advantage of the symmetries, it was shown that the considered structures in the antiferro magnetic configurations provide zero net spin current. By switching the magnetic states of the impurities, a detection mechanism is provided. Applying axial stress, the changes in the spin transfer characteristics can be pointed out. The analyzed nanowire systems can therefore provide the building blocks for integrating both nanomechanical and spintronic devices.

## Acknowledgments

This work was supported by the Romanian National Authority for Scientific Research, CNCS-UEFISCDI, Projects nos. PN-II-RU-PD-2011-3-0044 and PN-II-ID-PCE-2011-3-0960 and in part by the European Commission under EU FP7 Project HP-SEE (under Contract no. 261499).

## References

- [1] S. Chattopadhyay, C. S. Shih, H. L. Zon, F. C. Chia, K. H. Chen, and L. C. Chen, "Molecular sensing with ultrafine silver crystals on hexagonal aluminum nitride nanorod templates," *Journal of the American Chemical Society*, vol. 127, no. 9, pp. 2820–2821, 2005.
- [2] Z. Zhou, J. Zhao, Y. Chen, P. von Ragu Schleyer, and Z. Chen, "Energetics and electronic structures of AlN nanotubes/wires and their potential application as ammonia sensors," *Nanotechnology*, vol. 18, Article ID 424023, 2007.
- [3] G. A. Nemnes, C. Visan, and S. Antohe, "Thermopower of atomized wurtzite AlN wires," *Physica E*, vol. 44, p. 1092, 2012.
- [4] C. Xu, L. Xue, C. Yin, and G. Wang, "Formation and photoluminescence properties of AlN nanowires," *Physica Status Solidi (A)*, vol. 198, no. 2, pp. 329–335, 2003.
- [5] G. R. Yazdi, M. Syvajarvi, and R. Yakimova, "Aligned AlN nanowires and microrods by self-patterning," *Applied Physics Letters*, vol. 90, Article ID 123103, 2007.
- [6] L. H. Shen, X. F. Li, J. Zhang et al., "Synthesis of single-crystalline wurtzite aluminum nitride nanowires by direct arc discharge," *Applied Physics A*, vol. 84, pp. 73–75, 2006.
- [7] R. K. Paul, K. H. Lee, B. T. Lee, and H. Y. Song, "Formation of AlN nanowires using Al powder," *Materials Chemistry and Physics*, vol. 112, no. 2, pp. 562–565, 2008.
- [8] Y. Yang, Q. Zhao, X. Z. Zhang et al., "Mn-doped AlN nanowires with room temperature ferromagnetic ordering," *Applied Physics Letters*, vol. 90, Article ID 092118, 2007.
- [9] L. H. Shen, X. F. Li, Y. M. Ma et al., "Pressure-induced structural transition in AlN nanowires," *Applied Physics Letters*, vol. 89, Article ID 141903, 2006.
- [10] Y. Wu, G. Chen, H. Ye, Y. Zhu, and S. H. Wei, "Origin of the phase transition of AlN, GaN, and ZnO nanowires," *Applied Physics Letters*, vol. 94, Article ID 253101, 2009.
- [11] T. L. Mitran, A. Nicolaev, G. A. Nemnes, L. Ion, and S. Antohe, "Ab initio vibrational and thermal properties of AlN nanowires under axial stress," *Computational Materials Science*, vol. 50, no. 10, pp. 2955–2959, 2011.
- [12] H. Li, H. Q. Bao, B. Song et al., "Ferromagnetic properties of Mn-doped AlN," *Physica B*, vol. 403, pp. 4096–4099, 2008.
- [13] Y. Zhang, H. Shi, R. Li, and P. Zhang, "Magnetic coupling properties of Mn-doped AlN nanowires: first-principles calculations," *Physics Letters A*, vol. 375, no. 15, pp. 1686–1689, 2011.
- [14] Z.-K. Tang, L. Wang, L.-M. Tang et al., "Ferromagnetic coupling in Mg-doped passivated AlN nanowires: a first-principles study," *Physica Status Solidi B*, vol. 249, pp. 185–189, 2012.
- [15] J. M. Soler, E. Artacho, J. D. Gale et al., "The SIESTA method for ab initio order-N materials simulation," *Journal of Physics Condensed Matter*, vol. 14, no. 11, pp. 2745–2779, 2002.
- [16] M. Brandbyge, J. L. Mozos, P. Ordejon, J. Taylor, and K. Stokbro, "Density-functional method for nonequilibrium electron transport," *Physical Review B*, vol. 65, Article ID 165401, 17 pages, 2002.
- [17] G. A. Nemnes, "Spin current switching and spin-filtering effects in Mn-doped boron nitride nanoribbons," *Journal of Nanomaterials*, vol. 2012, Article ID 748639, 5 pages, 2012.

## Research Article

# Investigation and Estimation of Structure of Web from Electrospun Nanofibres

**Jolanta Malašauskienė and Rimvydas Milašius**

*Department of Textile Technology, Kaunas University of Technology, Studentu 56, 51424 Kaunas, Lithuania*

Correspondence should be addressed to Jolanta Malašauskienė; [jolanta.malasauskiene@stud.ktu.lt](mailto:jolanta.malasauskiene@stud.ktu.lt)

Received 12 December 2012; Accepted 17 February 2013

Academic Editor: Lijun Ji

Copyright © 2013 J. Malašauskienė and R. Milašius. This is an open access article distributed under the Creative Commons Attribution License, which permits unrestricted use, distribution, and reproduction in any medium, provided the original work is properly cited.

During the electrospinning process the web of nanofibres is manufactured by means of electrostatic forces between two electrodes. The diameters of nanofibres usually differ and they depend on various parameters. The different fineness of fibres influences the structure of the web and herewith the end-use properties of such kind of nanomaterial. Analysis of nanofibres diameters distribution also shows big differences; even more, the distributions are not spread along the normal distribution. Understanding the influence of electrospinning parameters and the reason why the shapes of distributions are so sophisticated is very important. The goal of this paper is to analyse the distribution of diameter and to propose the new criterion for nanofibres diameter comparison and web of nanofibres estimation. In this paper the influence of covering time of support material on structure of PA6.6 nanofibre web has been investigated. It was estimated that this parameter does not have a significant influence on the average diameter of nanofibres, and only the structure of web has been influenced by the changes in covering time. According to the results provided the phenomena of nanofibres sticking on the support material at the time of electrospinning can be proved and explained.

## 1. Introduction

Electrospinning is one of the most common processes used for nonwovens production. The diameters of electrospun fibres diameter may range from 10 nm to 1500 nm [1]. It has been discovered that the diameter of nanofibres and the final properties of the produced nonwovens depend on type of polymer, solution properties (viscosity, conductivity, surface tension, etc.), applied voltage, distance between electrodes, coating time of support material, air humidity, and temperature [2–5]. The diameter of the fibre is arguably the most important factor for determining the quality of nonwoven structure. So, it is very important to understand how the diameter of fibre and its distribution is affected by various parameters [6].

There are a lot of studies analyzing the influence of various parameters on nonwoven structure. The analysis of such studies shows that in some cases the different researches, analyzing the influence of the same factor on the structure of nanofibres, obtain different results. The reasons of different conclusions can be explained in several ways. According to

one of them, in some cases the authors do not analyze the dispersions of nanofibres diameter. The other reason—quite often the authors skip the description of the main parameters which may have a significant influence on nonwoven structure. It is possible that the mismatches of the results occur because of the lack of common methodology for nanofiber diameter characterization.

While analyzing the literature sources we noticed that the measurements of nanofibres diameter are distributed in unclear distribution and the shapes of all distributions always differ. Ellison et al., Tsimliaraki et al., and Gu et al. [7–9] state that the measurements of nanofibres diameter are distributed by log normal distribution. Dosunmu et al. [10] states that distribution of electrospun nanofibres could be well fitted as normal distribution in log normal scale. But log normal distribution does not have the theoretical background in electrospinning process, because this process does not depend on the time and all nanofibers in the web are being manufactured simultaneously. Usually the values of fibres diameter of various textile materials are distributed by normal distribution [11]. But sometimes the

shapes of the distributions of nanofibres diameter are not similar to this one.

It is impossible to compare the average values when dispersions of diameter are different, so it is absolutely wrong way to estimate the web of nanofibres, in order to compare parameters having different kinds of distribution. According to mathematical statistic point the average value of nanofibres diameter (if they are distributed in not normal distribution) cannot characterize the nanofibres precisely, because changes in average values do not suppose changes in modal value and other characteristics. It means that in order to compare the diameter of nanofibres with an average value it is necessary to use the other characteristics too.

In our previous study [12] the similarity of empirical distribution of nanofibres diameters to the compound distribution, consisting of several normal distributions, has been noticed. The compound distribution is a characteristic of blended spun yarns, received from several kinds of fibres. It means that the web of nanofibres consists from nanofibres of different diameter. There is no single opinion about the reasons of this phenomenon. It is possible that the web of nanofibres forms when nanofibres in the distance from Taylor cone to the other electrode do not separate completely. Although the possibility also exists that the web of several kinds of fibres forms depending on the sticking of nanofibres at the time when they are moved to other electrode. The goal of this paper is to analyse the dispersion of nanofibres diameter and to check the hypothesis about the possibility of the sticking of several nanofibres.

## 2. Method of Distribution Calculation

In our previous study [12] the method of dividing the compound distribution into several normal distributions had been presented. The first normal distribution was calculated using the following method: empirical values up to the modal value of the total distribution were set as the points of the left part of the first normal distribution. It has been considered that the diameter of nanofibres had been distributed in normal distribution, so the right part of the first normal distribution was marked as symmetrical points of the left side. The first normal distribution has been calculated according to the probability density. The left part of the second normal distribution has been calculated as a difference between empirical measurements and measurements calculated by the first normal distribution. The right part of empirical values and the second normal distribution have been calculated similarly as in the previous case. All normal distributions have been calculated using this method. Finally the compound distribution has been calculating by summarising the values of all normal distributions. The coefficient of determination confirmed the correlation of empirical curve with the compound distribution. This method can be used for dividing a compound distribution into several normal distributions.

The main disadvantage of this method is sophistication of compound distribution calculation. For this reason the short-cut method of the quality of nonwoven structure

estimation has been presented [13]. The short-cut method is more straightforward and is based on the modal value of empirical values. The points of the modal value of the empirical distribution are called the points of left part of the first normal distribution. It has been considered that diameter of nanofibres is distributed by normal distribution, and in the other side of modal value the symmetrical points were marked. The results calculated by both methods were identical.

The obtaining of compound distribution confirms that the web of nanofibres at the electrospinning process consists of different kinds of nanofibres.

## 3. Material and Methods

An 8% solution of PA6.6 in 85% formic acid was gently stirred at ambient temperature for 12 hours until the polymer granules dissolved completely. The nonwoven web from PA6.6 nanofibres had been formed using the electrospinning equipment "Nanospider" (Figure 1). The principle of this equipment includes the rotating roller which is submerged in a bath filled with polymer solution. The Taylor cones with increasing electrostatic forces are formed on the rotating roller. When electrostatic forces overcome the surface tension, a jet of polymer solution is ejected from the Taylor cone and it is directed up to the support material [14]. During this experiment the electrode with narrower tines has been selected as it is easier to form PA6.6 nanofibres. The sufficiently powerful electric field is not formed by means of the cylindrical electrode; consequently the continuous flow of Taylor cones cannot be formed. According to the electric field theory, the major supply of electric charge has been collected on the top of tines, where the surface curvature is greater and the surface electric field density in these places is higher. As a result, the continuous flow of Taylor cones can be formed on the tines [15].

During all experiments, the ambient temperature was  $T = 24 \pm 2^\circ\text{C}$ , the humidity was  $\phi = 50 \pm 2\%$ . The distance between electrodes was 13 cm. The applied voltage was 70 kV. Experiment has been carried out by changing the duration of support material covering. The speed of support material was  $v = 0.010$  m/s, the time of covering  $t = 25$  s (indicate I);  $v = 0.006$  m/s,  $t = 41$  s (II);  $v = 0.002$  m/s,  $t = 125$  s (III).

The structure of received nanofibres web has been analyzed by Scanning Electron Microscopy (SEM)—SEM-FEI Quanta 200 (Netherlands). The value of diameter of PA6.6 nanofibres was measured from SEM images by LUCIA Image 5.0 programme, with an accuracy  $\pm 0.01$  nm. Nanofibres have been measured using the 5 different SEM images.

## 4. Results

Nanofibres have been manufactured from PA6.6 solution of 8% concentration. The first series of experiments were carried out at the speed of support material 0.010 m/s, the second 0.006 m/s, and the third 0.002 m/s. With decreasing in speed the covering time of support material increased from 25 s to 125 s. The influence of the speed (and herewith the

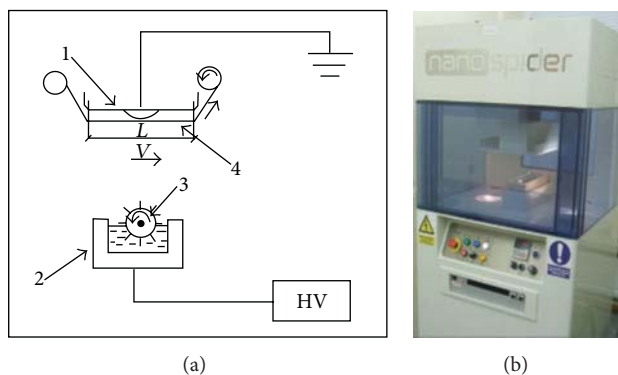


FIGURE 1: Principal scheme and photo of electrospinning technique “Nanospider”: 1: upper electrode, 2: bath with polymer solution, 3: rotating roller with tines, 4: support material,  $L$ : the distance of support material, which is covered with a layer of nanofibres (250 mm).

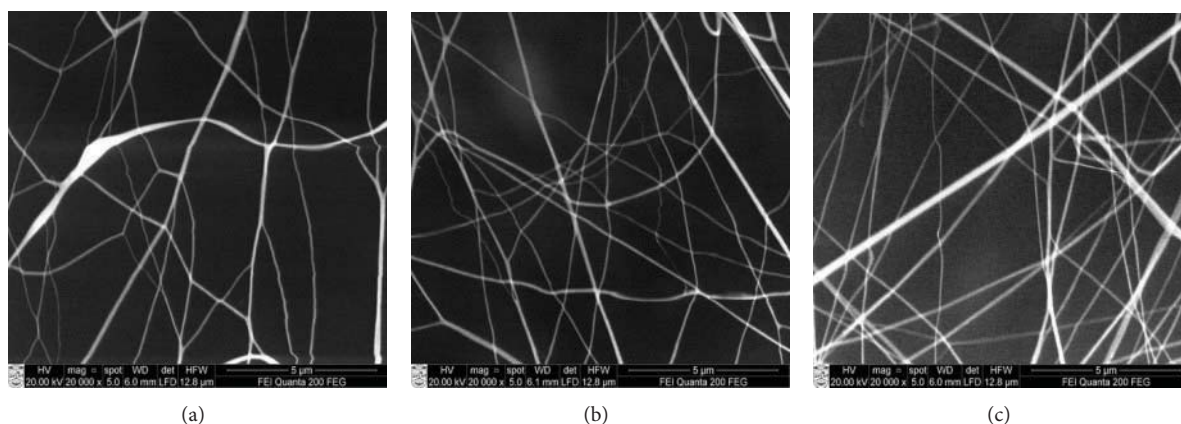


FIGURE 2: SEM images of electrospun PA6.6 mats when the speed of support material was (a)  $v = 0.010$  m/s,  $t = 25$  s (I); (b)  $v = 0.006$  m/s,  $t = 42$  s (II); (c)  $v = 0.002$  m/s,  $t = 125$  s (III).

covering time) of support material on PA6.6 nanofibres web morphology is presented in Figure 2.

As is seen from Figure 2, at the higher speed of support material fewer nanofibres cover it. During the tests the 5 SEM images for each variant of speed have been analysed. The 165 diameters of PA6.6 nanofibres for the I variant, 200 diameters of nanofibres for II variant, and 288 nanofibres for III variant were found and measured. The density of nanofibres was calculated by number of nanofibres in SEM images. The following density has been established—23 nanofibres for I variant, 29 nanofibres for II variant, and 42 nanofibres for III variant in  $100 \mu\text{m}^2$ . The results showed that the speed (also the covering time) of support material does not have significant influence on the average value of PA6.6 nanofibres diameter, as the difference is less than  $\pm 3.5\%$  (I  $d_{\text{average}} = 357$  nm; II  $d_{\text{average}} = 373$  nm; III  $d_{\text{average}} = 382$  nm), while the density of fibres depends on the speed. That means that the structure of web needs a deeper analysis. In the next step of investigations the dispersions of PA6.6 nanofibres have been studied. The frequency distributions of all series of experiment are presented in Figure 3.

First of all Figure 3 demonstrates that the diameter of nanofibres in all cases is distributed in different distributions.

In histogram which is presented in Figure 3(c) only one peak of distribution when the diameter of nanofibres is around 350 nm is observed. It is evident that this value is the modal value of this distribution too. Therefore we can make the assumption that this distribution is very close to normal distribution, because the average value is 382 nm. In the histogram presented in Figure 3(a) two peaks are observed: the first peak is around 200 nm, while the second peak is around 300 nm. A similar view, the distribution with several peaks, may be observed in Figure 3(b): first peak is around 200 nm, the second around 300 nm, and the third 400 nm. In Figure 4 more comprehensive analysis of measurements dispersion of I variant is presented—the interval of nanofibre diameter is distributed not by 50 nm as in Figure 3, but by 25 nm. As is seen from Figure 4 it is evident that the histogram really has not one peak—the first peak is around 212.5 nm, the second—around 312.5 nm. So, values are distributed not by normal but by compound distribution from several normal distributions.

According to the results it is possible to assume that at the lowest speed of support material, the thicker nanofibres were formed and at the higher speed the thinner nanofibres were formed.

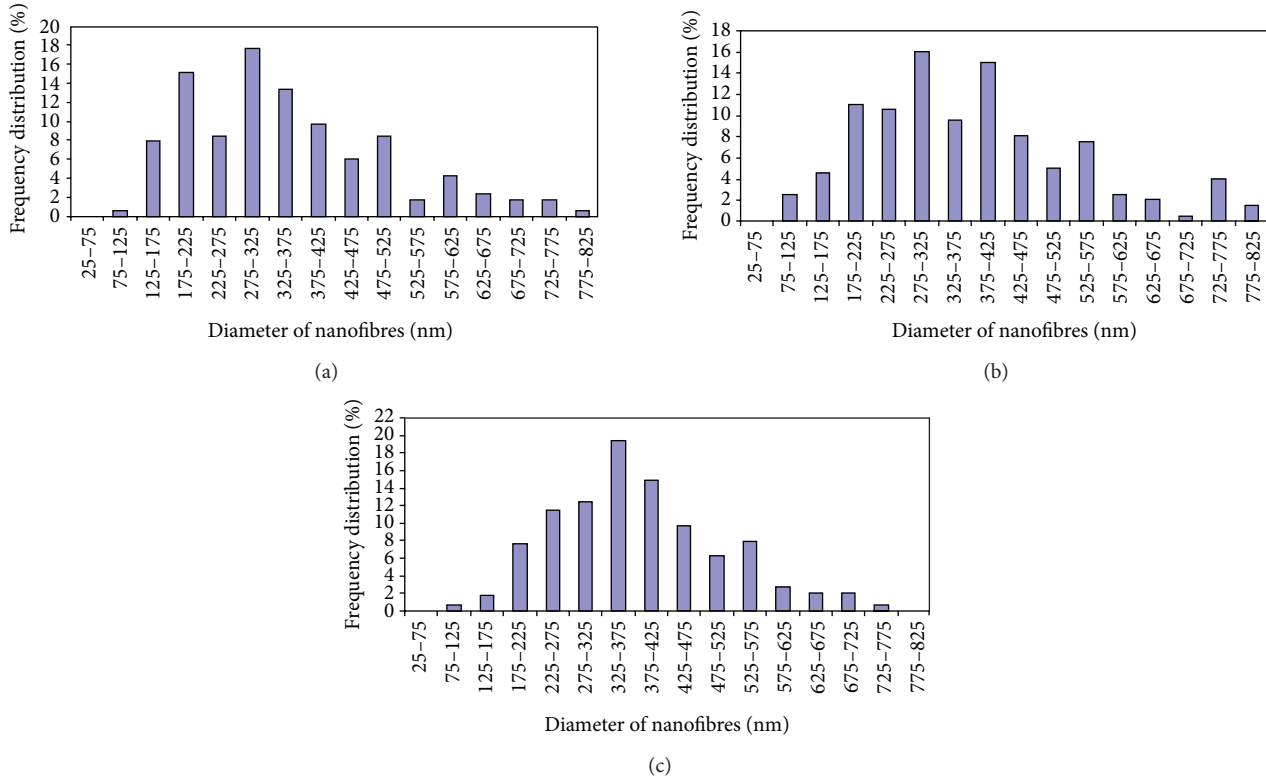


FIGURE 3: Distributions of PA6.6 nanofibres during the experiment: (a)  $v = 0.010$  m/s,  $t = 25$  s (I); (b)  $v = 0.006$  m/s,  $t = 42$  s (II); (c)  $v = 0.002$  m/s,  $t = 125$  s (III).

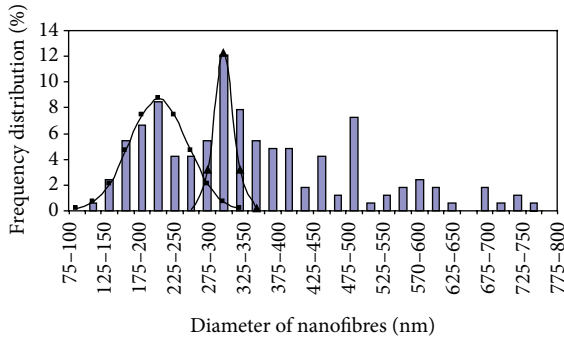


FIGURE 4: Detailed distributions of the results of the I variant.

In previous work [12] it was proved that in the case when the diameter of nanofibres is distributed in compound distribution from several normal distributions, the modal value of the first distribution and the percentage quantity of measurements of the first distribution can be used as a criterion of nanofibres diameter and measurement dispersion estimation. The more the percentage increases, the more unique the structure of the web obtained as well. Using this method we can determine the influence of covering speed (the covering time too) on the structure of manufactured web.

The following results have been received using the histograms presented in Figure 3. As is seen, in the variant I mostly single and no stucked nanofibres had been formed. The percentage quantity of nanofibres distributed in the first

distribution is 32.2%. As in the II variant the quantity of nanofibres distributed in the first distribution has been just 24.04%. It means that in this case less single nanofibres were formed. The modal value of the first distribution in both cases is 200 nm. In this work the new criterion is proposed for estimation of web structure. This criterion may conclude the average of two values—modal values and value of the second highest peak, and it can be calculated using the formula:  $d' = (d_{\text{modal}} + d_{2\text{modal}})/2$  (where  $d_{\text{modal}}$  is the modal value of all distribution;  $d_{2\text{modal}}$  is the second value, close to modal value of this distribution). During the analysis of the results, we noticed that the diameter  $d'$  decreased along with a speed of support material increase. Using the histograms in Figure 3 the following data has been calculated: (III)  $d' = 375$  nm; (II)  $d' = 350$  nm; (I)  $d' = 250$  nm. It means that thinner fibres are formed at a higher speed (lower time).

The next stage of our investigation has been aimed to check the hypothesis that the web from different diameter of nanofibres forms from single nanofibres which stick together on the support material. It is known that the surface area of cross-section of single nanofibre may be calculated using formula:  $S_1 = (\pi d_1^2)/4$ . A surface area of cross-section of stucked nanofibres makes  $S_n = nS_1$ . As a result, the diameter of stucked nanofibres is calculated using  $d_n = d_1 \sqrt{n}$ . So, if the modal value of the diameter of a single fibre is  $d_{\text{modal}} = 200$  nm (see Figures 3(a) and 3(b)), the diameter of a double fibre would be about  $d_2 = 283$  nm. As is seen from Figure 3(a), the second peak is when diameter of nanofibres is about  $d_{2\text{emp}} = 300$  nm. The relative error in both

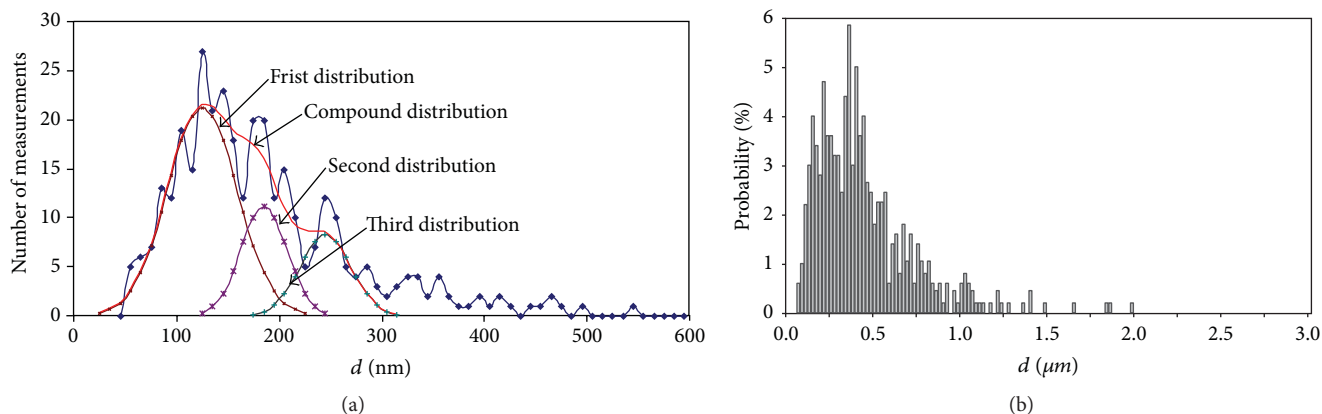


FIGURE 5: Fibre diameter distributions (a) from PVA [12]; (b) from PP [10].

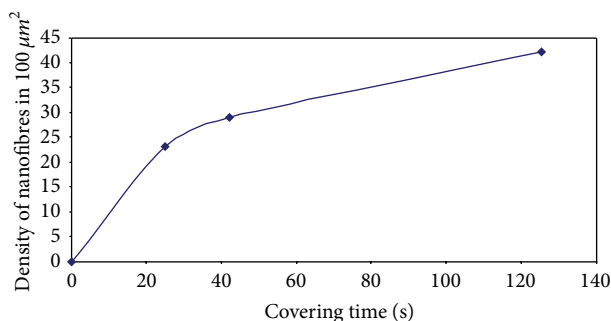


FIGURE 6: Dependence of the density of nanofibres (in  $100 \mu\text{m}^2$ ) on the covering time.

cases is  $\delta = 6\%$ . The recurrent values of nanofibres diameter confirm the hypothesis about the sticking of nanofibres on the web. The similar conclusions about the sticking were approved in our previous work, when the structure of PVA web was analysed [12]. The histograms of this article (especially of Figures 3(a) and 3(b)) can be compared with histogram from literature sources as well [10] (Figure 5).

In this figure few peaks can be noticed as well. According to this data one can guess that these peaks appeared for the sticking of PP nanofibres on the web. It means that this problem is typical for the whole electrospinning process regardless of the type of polymer—the similar results can be observed with PA6.6, PVA, and PP nanofibres.

At the last step of this study, the dependence of the density of nanofibres (in  $100 \mu\text{m}^2$ ) on the covering time is presented in Figure 6.

During the analysis of the data presented in Figure 6, it has been stated that during 1 second of the electrospinning process the support material is covered approximately by 1 nanofibre. According to this, we can state that as the covering time increases, the density of nanofibres should increase linearly. At the same time it is obvious that the curve in Figure 6 is not linear. It is very well visible that at the highest covering time there were not 120 nanofibres, just 42. That also confirms the phenomenon of fibres sticking on the support material. Such data make us sure that the covering time is a

very important parameter for the structure of nanofibre web, and, using the higher covering time, more stucked fibres are forming.

## 5. Conclusions

- (i) The distributions of electrospun nanofibres diameter are always different and the shapes of such distributions usually do not differ from the compound distribution, which consists of several normal distributions.
- (ii) The speed of support material from 0.002 m/s till 0.010 m/s does not have a significant influence on the average value of PA6.6 nanofibres diameter. It only influences the structure of nanofibre web; that is, as the speed of the support material decreases, the more stucked nanofibres are formed.
- (iii) For the web structure estimation the modal value of the first distribution, the percentage quantity of the first distribution, and the average diameter of two peaks of distribution—modal value and the value of the second highest peak—may be used.
- (iv) The results of the tests confirm that the web of nanofibres consists of various nanofibres due to the sticking of several nanofibres during the process of their manufacturing.

## Conflict of Interests

The authors declare no possible conflict of interests.

## References

- [1] M. Chowdhury and G. Stylios, "Effect of experimental parameters on the morphology of electrospun Nylon 6 fibres," *International Journal of Basic and Applied Sciences*, vol. 10, no. 6, pp. 116–131, 2010.
- [2] W. Sambaer, M. Zatloukal, and D. Kimmer, "The use of novel digital image analysis technique and rheological tools to characterize nanofiber nonwovens," *Polymer Testing*, vol. 29, no. 1, pp. 82–94, 2010.

- [3] X. M. Mo, C. Y. Xu, M. Kotaki, and S. Ramakrishna, "Electrospun P(LLA-CL) nanofiber: a biomimetic extracellular matrix for smooth muscle cell and endothelial cell proliferation," *Biomaterials*, vol. 25, no. 10, pp. 1883–1890, 2004.
- [4] E. Adomavičiūtė and R. Milašius, "The influence of applied voltage on poly(vinyl alcohol) (PVA) nanofibre diameter," *Fibres and Textiles in Eastern Europe*, vol. 15, no. 5-6, pp. 69–72, 2007.
- [5] E. Adomavičiūtė, R. Milašius, and A. Žemaitaitis, "The influence of main technological parameters on the diameter of poly(vinyl alcohol) (PVA) nanofibre and morphology of manufactured mat," *Materials Science (Medziagotyra)*, vol. 13, no. 2, pp. 152–155, 2007.
- [6] M. Ziabari, V. Mottaghitalab, and A. K. Haghi, "Simulated image of electrospun nonwoven web of PVA and corresponding nanofiber diameter distribution," *Korean Journal of Chemical Engineering*, vol. 25, no. 4, pp. 919–922, 2008.
- [7] C. J. Ellison, A. Phatak, D. W. Giles, C. W. Macosko, and F. S. Bates, "Melt blown nanofibers: fiber diameter distributions and onset of fiber breakup," *Polymer*, vol. 48, no. 11, pp. 3306–3316, 2007.
- [8] A. Tsimliaraki, I. Zuburtikudis, S. I. Marras, and C. Panayiotou, "Optimizing the nanofibrous structure of non-woven mats of electrospun bio-degradable polymer nanocomposites," in *Proceeding of the Latest Advances in High Tech Textiles and Textile-Based Materials*, pp. 128–133, Ghent, Belgium, September 2009.
- [9] S. Gu, Q. Wu, and J. Ren, "Preparation and surface structures of carbon nanofibers produced from electrospun PAN precursors," *Carbon Materials*, vol. 23, no. 2, pp. 171–176, 2008.
- [10] O. O. Dosunmu, G. G. Chase, W. Kataphinan, and D. H. Reneker, "Electrospinning of polymer nanofibres from multiple jets on a porous tubular surface," *Nanotechnology*, vol. 17, no. 4, pp. 1123–1127, 2006.
- [11] G. A. V. Leaf, *Practical Statistics for the Textile Industry: Part I*, The Textile Institute, Manchester, UK, 1984.
- [12] J. Malašauskienė and R. Milašius, "Mathematical analysis of the diameter distribution of electrospun nanofibres," *Fibres and Textiles in Eastern Europe*, vol. 18, no. 6, pp. 45–48, 2010.
- [13] J. Malašauskienė and R. Milašius, "Short-cut method of electrospun nanofibres diameter distribution estimation," in *Book of Proceedings of Magic World of Textiles: 6th International Textile Clothing & Design Conference*, Dubrovnik, Croatia, pp. 522–525, 2012.
- [14] J. Šukytė, E. Adomavičiūtė, and R. Milašius, "Investigation of the possibility of forming nanofibres with potato starch," *Fibres and Textiles in Eastern Europe*, vol. 18, no. 5, pp. 24–27, 2010.
- [15] A. Banuškevičiūtė, E. Adomavičiūtė, R. Milašius, and S. Stanys, "Formation of thermoplastic polyurethane (TPU) nano/micro fibers by electrospinning process using electrode with tines," *Materials Science (Medziagotyra)*, vol. 17, no. 3, pp. 287–292, 2011.



---

# **1D Nanomaterials: Synthesis, Properties, and Applications**



# **1D Nanomaterials: Synthesis, Properties, and Applications**

Guest Editors: Yun Zhao, Haiping Hong, Qianming Gong,  
and Lijun Ji



---

Copyright © 2013 Hindawi Publishing Corporation. All rights reserved.

This is a special issue published in "Journal of Nanomaterials." All articles are open access articles distributed under the Creative Commons Attribution License, which permits unrestricted use, distribution, and reproduction in any medium, provided the original work is properly cited.

## Editorial Board

- Katerina E. Aifantis, Greece  
Nageh K. Allam, USA  
Margarida Amaral, Portugal  
Xuedong Bai, China  
Lavinia Balan, France  
Enrico Bergamaschi, Italy  
Theodorian Borca-Tasciuc, USA  
C. Jeffrey Brinker, USA  
Christian Brosseau, France  
Xuebo Cao, China  
Shafiq Chowdhury, USA  
Kwang-Leong Choy, UK  
Cui ChunXiang, China  
Miguel A. Correa-Duarte, Spain  
Shadi A. Dayeh, USA  
Claude Estourns, France  
Alan Fuchs, USA  
Lian Gao, China  
Russell E. Gorga, USA  
Hongchen Chen Gu, China  
Mustafa O. Guler, Turkey  
John Zhanhu Guo, USA  
Smrati Gupta, Germany  
Michael Harris, USA  
Zhongkui Hong, China  
Michael Z. Hu, USA  
David Hui, USA  
Y.-K. Jeong, Republic of Korea  
Sheng-Rui Jian, Taiwan  
Wanqin Jin, China  
Rakesh K. Joshi, UK  
Zhenhui Kang, China  
Fathallah Karimzadeh, Iran  
Alireza Khataee, Iran
- Do Kyung Kim, Republic of Korea  
Alan K. T. Lau, Hong Kong  
Burtrand Lee, USA  
Jun Li, Singapore  
Benxia Li, China  
Xing-Jie Liang, China  
Shijun Liao, China  
Gong Ru Lin, Taiwan  
J.-Y. Liu, USA  
Tianxi Liu, China  
Jue Lu, USA  
Songwei Lu, USA  
Daniel Lu, China  
Ed Ma, USA  
Gaurav Mago, USA  
Santanu K. Maiti, India  
Sanjay R. Mathur, Germany  
Vikas Mittal, UAE  
Weihai Ni, Germany  
Sherine Obare, USA  
Atsuto Okamoto, Japan  
Abdelwahab Omri, Canada  
Edward Andrew Payzant, USA  
Kui-Qing Peng, China  
Anukorn Phuruangrat, Thailand  
Suprakas Sinha Ray, South Africa  
Ugur Serincan, Turkey  
Huaiyu Shao, Japan  
Donglu Shi, USA  
Vladimir Sivakov, Germany  
Marinella Striccoli, Italy  
Bohua Sun, South Africa  
Saikat Talapatra, USA  
Nairong Tao, China
- Titipun Thongtem, Thailand  
Somchai Thongtem, Thailand  
Alexander Tolmachev, Ukraine  
Valeri P. Tolstoy, Russia  
Tsung-Yen Tsai, Taiwan  
Takuya Tsuzuki, Australia  
Raquel Verdejo, Spain  
Mat U. Wahit, Malaysia  
Zhenbo Wang, China  
Ruiping Wang, Canada  
Shiren Wang, USA  
Cheng Wang, China  
Yong Wang, USA  
Jinquan Wei, China  
Ching-Ping Wong, Hong Kong  
Xingcai Wu, China  
Guodong Xia, Hong Kong  
Zhi Li Xiao, USA  
Ping Xiao, UK  
Yangchuan Xing, USA  
Shuangxi Xing, China  
N. Xu, China  
Doron Yadlovker, Israel  
Yingkui Yang,  
Khaled Youssef, USA  
Kui Yu, Canada  
William W. Yu, USA  
Haibo Zeng, China  
Tianyou Zhai, Japan  
Renyun Zhang, Sweden  
Bin Zhang, China  
Yanbao Zhao, China  
Lianxi Zheng, Singapore  
Chunyi Zhi, Hong Kong



# Contents

**ID Nanomaterials: Synthesis, Properties, and Applications**, Yun Zhao, Haiping Hong, Qianming Gong, and Lijun Ji

Volume 2013, Article ID 101836, 1 page

**Effect of Wrapped Carbon Nanotubes on Optical Properties, Morphology, and Thermal Stability of Electrospun Poly(vinyl alcohol) Composite Nanofibers**, Naoual Diouri, Mimouna Baitoul, and Malik Maaza

Volume 2013, Article ID 949108, 6 pages

**Shape Effects of Iron Nanowires on Hyperthermia Treatment**, Wei-Syuan Lin, Hong-Ming Lin, Hsiang-Hsin Chen, Yeu-Kuang Hwu, and Yuh-Jing Chiou

Volume 2013, Article ID 237439, 6 pages

**Correlation Effects in Kinetics of One-Dimensional Atomic Systems**, V. D. Borman, I. V. Tronin, V. N. Tronin, V. I. Troyan, and O. S. Vasiliev

Volume 2013, Article ID 682832, 43 pages

**Electrical Resistivity of Pristine and Functional Single-Wall Carbon Nanotubes**, Yijiang Lu, Jing Li, and Haiping Hong

Volume 2013, Article ID 635673, 5 pages

**Synthesis and Characterisation of Calcium Carbonate Aragonite Nanocrystals from Cockle Shell Powder (*Anadara granosa*)**, Abdullahi Shafiu Kamba, Maznah Ismail, Tengku Azmi Tengku Ibrahim, and Zuki Abu Bakar Zakaria

Volume 2013, Article ID 398357, 9 pages

**Improved Processing of Carbon Nanotube Yarn**, Chaminda Jayasinghe, Trent Amstutz, Mark J. Schulz, and Vesselin Shanov

Volume 2013, Article ID 309617, 7 pages

**A Comparative Study of Three Different Chemical Vapor Deposition Techniques of Carbon Nanotube Growth on Diamond Films**, Betty T. Quinton, Paul N. Barnes, Chakrapani V. Varanasi, Jack Burke, Bang-Hung Tsao, Kevin J. Yost, and Sharmila M. Mukhopadhyay

Volume 2013, Article ID 356259, 9 pages

**Photoluminescence of Hexagonal ZnO Nanorods Hydrothermally Grown on Zn Foils in KOH Solutions with Different Values of Basicity**, Nuengruethai Ekthammathat, Titipun Thongtem, Anukorn Phuruangrat, and Somchai Thongtem

Volume 2013, Article ID 208230, 4 pages

**Growth and Physical Property Study of Single Nanowire (Diameter ~45 nm) of Half Doped Manganite**, Subarna Datta, Sayan Chandra, Sudeshna Samanta, K. Das, H. Srikanth, and Barnali Ghosh

Volume 2013, Article ID 162315, 6 pages

**Spin-Filtering Effects in Würtzite and Graphite-Like AlN Nanowires with Mn Impurities**, G. A. Nemnes

Volume 2013, Article ID 408475, 5 pages



---

**Investigation and Estimation of Structure of Web from Electrospun Nanofibres**, Jolanta Malašauskiene.  
and Rimvydas Milašius  
Volume 2013, Article ID 416961, 6 pages

## Editorial

# 1D Nanomaterials: Synthesis, Properties, and Applications

**Yun Zhao,<sup>1</sup> Haiping Hong,<sup>2</sup> Qianming Gong,<sup>3</sup> and Lijun Ji<sup>4</sup>**

<sup>1</sup> School of Chemical Engineering and Environment, Beijing Institute of Technology, Beijing 100081, China

<sup>2</sup> Department of Materials and Metallurgical Engineering, South Dakota School of Mines and Technology, Rapid City, SD 57701, USA

<sup>3</sup> Department of Mechanical Engineering, Tsinghua University, Beijing 100084, China

<sup>4</sup> College of Chemistry and Chemical Engineering, Yangzhou University, Yangzhou, Jiangsu 225009, China

Correspondence should be addressed to Yun Zhao; zhaoyun@bit.edu.cn

Received 12 June 2013; Accepted 12 June 2013

Copyright © 2013 Yun Zhao et al. This is an open access article distributed under the Creative Commons Attribution License, which permits unrestricted use, distribution, and reproduction in any medium, provided the original work is properly cited.

One-dimensional (1D) nanostructured materials, including nanotubes, nanofibers, and nanowires, have attracted much attention due to their interesting properties and wide range of potential applications. Considerable research has been conducted on new routes to controllable synthesis of 1D nanomaterials. The unique properties of as-obtained 1D nanomaterials can lead to applications in various fields such as electronics, magnetism, optics, and catalysis. Therefore, researchers working in the 1D nanomaterials are constantly striving to develop new fundamental science as well as potential applications. The importance of a platform that allows active researchers in this field to present their new development in a timely and efficient manner is, therefore, necessary.

This special issue focuses on the recent progress in production techniques, novel properties, and applications of various 1D nanomaterials including oxides/metals/nitrides with 1D nanostructures, carbon nanotubes, and nanofibers.

A total of 11 articles are presented in the current issue and they are all research papers. They involve spin transport properties of AlN nanowires, photoluminescence of ZnO nanorods, heating efficiency of iron nanowires, optical properties and thermal stability of poly(vinyl alcohol) composite nanofibers, electrical properties of half-doped manganite single nanowire, carbon nanotube yarns, and pristine and functional single-wall carbon nanotubes. Production techniques include a hydrothermal reaction, reducing method, chemical vapor deposition, spinning method, and microemulsion system. Carbon nanotubes have attracted most research interest, maintaining their comfortable leading positions.

We are pleased to see the progress in synthesis and properties of 1D nanomaterials. We hope that this special issue will promote further development of large-scale economically feasible 1D nanomaterial-making technologies and also contribute to their wide use.

## Acknowledgments

The editors gratefully thank the authors for their contributions to this special issue and the reviewers for their constructive comments and dedication.

Yun Zhao  
Haiping Hong  
Qianming Gong  
Lijun Ji

## Research Article

# Effect of Wrapped Carbon Nanotubes on Optical Properties, Morphology, and Thermal Stability of Electrospun Poly(vinyl alcohol) Composite Nanofibers

Naoual Diouri,<sup>1</sup> Mimouna Baitoul,<sup>1</sup> and Malik Maaza<sup>2,3</sup>

<sup>1</sup> University USMBA, Faculty of Sciences Dhar El Mahraz, Laboratory of Solid State Physics, Group Polymers and Nanomaterials, Regional University Center of the Interface (CURI), P.O. Box 1796 Atlas, 30000 Fez, Morocco

<sup>2</sup> iThemba LABS, National Research Foundation, NANOAFNET, 1 Old Faure Road, Somerset West 7129, P.O. Box 722, Somerset, Western Cape Province, South Africa

<sup>3</sup> UNESCO, UNISA Africa Chair in Nanosciences/Nanotechnology, College of Graduate Studies, University of South Africa (UNISA), Muckleneuk Ridge, P.O. Box 392, Pretoria, South Africa

Correspondence should be addressed to Mimouna Baitoul; [baitoul@yahoo.fr](mailto:baitoul@yahoo.fr)

Received 29 October 2012; Accepted 19 May 2013

Academic Editor: Haiping Hong

Copyright © 2013 Naoual Diouri et al. This is an open access article distributed under the Creative Commons Attribution License, which permits unrestricted use, distribution, and reproduction in any medium, provided the original work is properly cited.

Electrospinning was used to elaborate poly(vinyl alcohol) (PVA) nanofibers in the presence of embedded multiwall carbon nanotubes (MWCNTs) in surfactant and polymer. MWCNTs were dispersed in aqueous solution using both sodium dodecyl sulfate (SDS) as surfactant and Poly(vinyl pyrrolidone) (PVP). Changing the surfactant and polymer concentration reveals that the maximum dispersion achievable is corresponding to the mass ratios MWCNTs:SDS=1:5 and MWCNTs:SDS:PVP=1:5:0.6 in the presence of the PVP. After the optimization of the dispersion process, the SEM image of the PVA/PVP/SDS/MWCNTs electrospun fibers presents high stability of the fibers with diameter around 224 nm. Infrared spectroscopy and thermal gravimetric analysis elucidate the type of interaction between the PVA and the coated carbon nanotube. The presence of PVP wrapped carbon nanotubes reduced slightly the onset of the degradation temperature of the electrospun nanofibers.

## 1. Introduction

Electrospun nanofibers present an exciting avenue for development of novel nanomaterials with well-defined functionalities which have attracted researchers' interest. Because of their unique physical, chemical properties and a specific surface approximately two order larger than flat films, nanofibers have great potential use in sensors [1–3], filtration for bacteria, medical applications, tissue scaffolding [4–8], textile fabric [9], and other applications in nanoscience and nanotechnology. Due to their electronic, mechanical, and thermal properties, CNTs enjoy an incomparable status in the panoply of nanomaterials finding large range of applications in composites. However, the fabrication of high quality polymer-CNTs nanocomposites with predictable and optimal performance requires homogenous dispersion of the CNTs in polymer matrix. This is a challenging task for their

utilization due to the highly nonwetting character of CNTs surface and strong tendency to form bundles by van der Waals attractive forces. Currently, different approaches are used to disperse CNTs, such as covalent or noncovalent functionalization. From the nondestructive point of view, in situ polymerization, polymers, and also surfactants are used to obtain homogenous CNTs dispersion in various solvents or matrices [10–12]. A series of cationic, anionic, and nonionic surfactants and polymers have been studied for their ability to suspend individual CNTs [13, 14]. The present work confronts the dispersion assisted by surfactant as well as polymer. In the first step, we investigate the dispersion of MWCNTs in aqueous solution using SDS as an anionic surfactant. Different concentrations of SDS compared to those of MWCNTs were used, and the second step consisted in improving the dispersion and it is stabilization while using the PVP. After the optimization of the dispersion of MWCNTs, we elaborated

the nanocomposite fibers via electrospinning process. The optical properties and thermal stability of the electrospun nanofibers will be presented.

## 2. Experimental

**2.1. Materials.** Poly(vinyl alcohol) (Mw: 70000, 99% hydrolyzed), poly(vinyl pyrrolidone), and sodium dodecyl sulfate were purchased from Sigma Aldrich. Multiwall carbon nanotubes (CCVD method, purity >95%, outer mean diameter 10–15 nm, and length 0.1–10  $\mu\text{m}$ ) were purchased from Arkema France.

**2.2. Dispersion of MWCNTs.** In a typical dispersion procedure, two steps were realized in order to achieve better dispersion in the one hand and for preparing three suspensions of MWCNTs. The anionic surfactant SDS,  $\text{NaC}_{12}\text{H}_{25}\text{SO}_4$ , is first used for the exfoliation of the CNTs by varying the concentration to 10 wt% of MWCNTs aqueous solution. It can penetrate easily inside the aggregates of MWCNTs, and it was useful for improving the dispensability. After the characterization with the UV-Vis spectroscopy, the solution with the ratio 1:5 of MWCNTs:SDS was chosen. However, this surfactant does not prevent individual nanotubes from agglomeration after sonication process. In order to achieve better stabilization of the dispersion, different amounts of the nonionic PVP ( $\text{C}_6\text{H}_9\text{ON}$ )<sub>n</sub>, which possesses both hydrophilic and hydrophobic groups have been added to this solution to further improve the dispersion. The temperature was around room temperature, and all solutions were ultrasonicated for 60 min. Moreover, rings in PVP contain a proton accepting carbonyl moiety, while PVA presents hydroxyl groups as side groups. Indeed, interactions by hydrogen bonding can be expected between hydroxyl groups of PVA and carboxyl groups of PVP.

**2.3. Preparation of PVA/MWCNTs/SDS/PVP Nanofibers.** PVA was dissolved in warm water by heating at 80°C under a continuous slight stirring for 2 h to prepare PVA solution with the desired concentration. The PVP/SDS/MWCNTs suspension was added to an aqueous solution of PVA to obtain a final solution of 12 wt% PVA and 0.3 wt% of MWCNTs. The solution of PVA/MWCNTs/SDS/PVP was briefly sonicated and stirred to remove trapped air bubbles and for effective mixing prior to electrospinning. After the complete homogenization of the nanocomposite, the solution was poured into the syringe. A voltage of 15 Kv was applied to the solution, and the solution jet emerging from the needle was collected on the stationary electrode (Figure 1).

**2.4. Characterization.** The dispersions of MWCNTs in the surfactant and polymer were characterized using UV-visible spectrophotometer—Cecil 2000 series which cover the full 190–1000 nm wavelength range with a narrow 1.8 nm optical bandwidth. The baseline correction was carried out using a quartz cuvette.

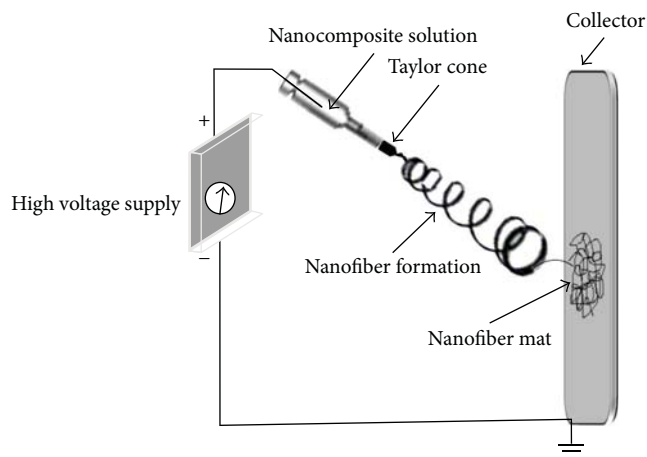


FIGURE 1: Scheme of the electrospinning process.

The morphology of electrospun nanofibers and their average diameter were characterized using environmental scanning electronic microscopy (ESEM) equipped with sonde EDAX for the surface microanalysis.

An analysis was carried out by ATR using PerkinElmer, Spotlight 400 FTIR Imaging system, while thermal analysis was accomplished using SETSYS Evolution.

## 3. Results and Discussion

**3.1. Ultraviolet-Visible Spectroscopy.** It has been demonstrated that carrier dynamics in carbon nanotubes bundles are dominated by the tunnel coupling between carbon nanotubes. These bundled carbon nanotubes are not active in the UV-Vis region and only individual carbon nanotubes absorb in the UV-Vis region [15]. Here, we describe combination of two concepts for dispersing MWCNTs by using SDS as surfactant and PVP.

To disperse MWCNTs, both maintaining stabilization and intrinsic properties of carbon nanotubes are required. We used the ionic surfactant to disperse MWCNTs because it is known to disperse them in aqueous solution via noncovalent method without affecting MWCNTs properties [16]. Since SDS molecules have featureless absorbance in the region, we were interested in this work. The mechanism of MWCNTs dispersion according to the duration and power of sonication has been studied by other researchers [15].

To obtain better dispersion, the solutions were resounded after the variation of the mass of SDS compared to that of the MWCNTs using the same conditions of sonication during all experiments.

The UV-Vis absorbance spectra (Figure 2(A)) show the prepared MWCNTs dispersion with different amounts of SDS. The MWCNTs have characteristic absorption peak around the wavelength of 290 nm corresponding to the intrinsic optical properties of graphite [17] and will thus be present in MWCNTs. Unlike optical transitions in a particle, the carbon nanotubes present different collective excitations of electrons, called  $\pi$ -plasmon, which involve the electron orbitals  $\sigma$  and exist at much higher energy. Since the size of carbon nanotubes is less than the wavelength of excitation in

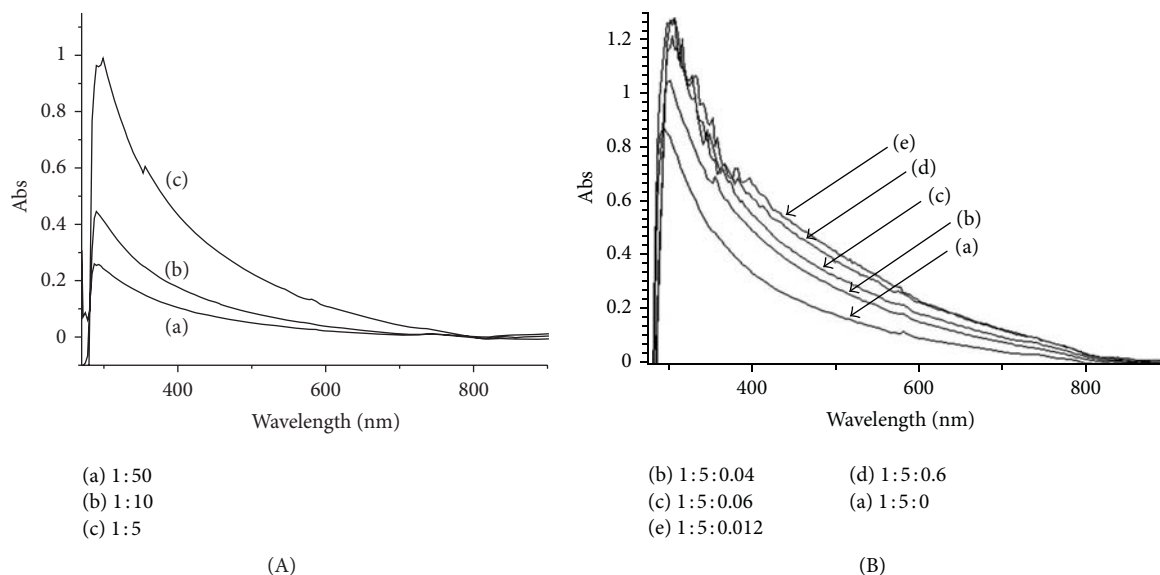


FIGURE 2: (A) UV-Vis optical absorbance spectra of aqueous solution of MWCNTs with different concentrations of SDS. (B) UV-Vis optical absorbance spectra of aqueous solution of MWCNTs-SDS with different concentrations of PVP.

the UV-Vis, there is a movement phase of the charge density and charge accumulation at the surface, and therefore  $\pi$ -plasmon carbon nanotubes can be coupled with light. But the distribution of charges at the surface of carbon nanotubes is not in mechanical equilibrium and oscillates around the equilibrium position. The plasmon resonance corresponds to a strong increase in absorption at the resonant frequency. Indeed, when we reduced the mass of SDS compared to that of MWCNTs which was fixed at 1 mg, from 50 mg to 5 mg of SDS, the intensity of absorbance was significantly increased, and the best absorbance was achieved for the mass ratio of MWCNTs : SDS—1 : 5.

To study the effect of the PVP on the dispersion of MWCNTs in the presence of SDS, we have taken the same quantities used for the MWCNTs : SDS, 1 : 5, which gave the best dispersion, and different amounts of PVP were added. All suspensions of MWCNTs-SDS-PVP were prepared in the same conditions as the previous suspensions.

The UV-Vis spectra of all suspensions (Figure 2(B)) show that when the mass of PVP increased from 0.04 mg to 0.6 mg compared to the mass of MWCNTs : SDS—1 : 5 the solutions absorbance has improved considerably and the characteristic absorbance band of the MWCNTs is shifted to higher wavelengths. This redshift can be explained by the improvement of the density fluctuations of  $\pi$ -plasmon of internal and external surfaces of MWCNTs [18]. So, we can deduce that the dispersion of MWCNTs is enhanced with the addition of the PVP until a certain threshold. For the mass increasing from 0.6 mg to 1.2 mg, the absorbance is found to saturate with even a slight drop. These optimized concentrations were used for the solutions used in electrospinning process.

**3.2. SEM Analysis.** The characteristics of the fibrous structures produced via the electrospinning process were observed by SEM micrograph.

Nanofibers diameter and morphology can be controlled by several processing parameters including solution viscosity (as controlled by changing the polymer concentration), voltage, feed solution conductivity, and capillary-to-collector distance. In addition, the spinning process is expected to align CNTs or their bundles along the fiber direction due to combination of dielectrophoretic forces caused by dielectric or conductivity mismatch between the CNTs and the polymer solution and high shear forces induced by spinning.

The selected SEM representative images (Figure 3) show the as-spun PVA (Figure 3(a)), PVA/SDS/MWCNTs (Figure 3(b)), and PVA/SDS/PVP/MWCNTs (Figure 3(c)) fibers deposited on the glass substrate at 20 000x magnification. The treatment of the images with Image J software shows that the diameter average was varying from 230 nm for the pure PVA to 210 nm for PVA/SDS/MWCNTs. The decrease of the fibers diameter indicates that the incorporation of the MWCNTs into the fibers increases the conductivity of the matrix solution, which favors the stretching of the solution under electric field during the electrospinning. Furthermore, for PVA/SDS/PVP/MWCNTs composite nanofibers, the fibers diameter decreases to be 224 nm due to the increase of solution viscosity. It should be noted that the fibers structures were completely stabilized and any beads were observed.

**3.3. FTIR Spectroscopy.** To determine the interaction between PVA, MWCNTs, and PVP, FTIR measurements of pure PVA, PVA/SDS/MWCNTs, and PVA/SDS/PVP/MWCNTs fibers were conducted.

The FTIR spectrum of pure PVA fibers (Figure 4(a)) shows the main characteristic bonds as follows.

The C–H stretching vibration is observed at  $3283\text{ cm}^{-1}$ . The symmetric and antisymmetric  $-\text{CH}_2$  vibrations appear at, respectively,  $2940\text{ cm}^{-1}$  and  $2912\text{ cm}^{-1}$ . The peaks located

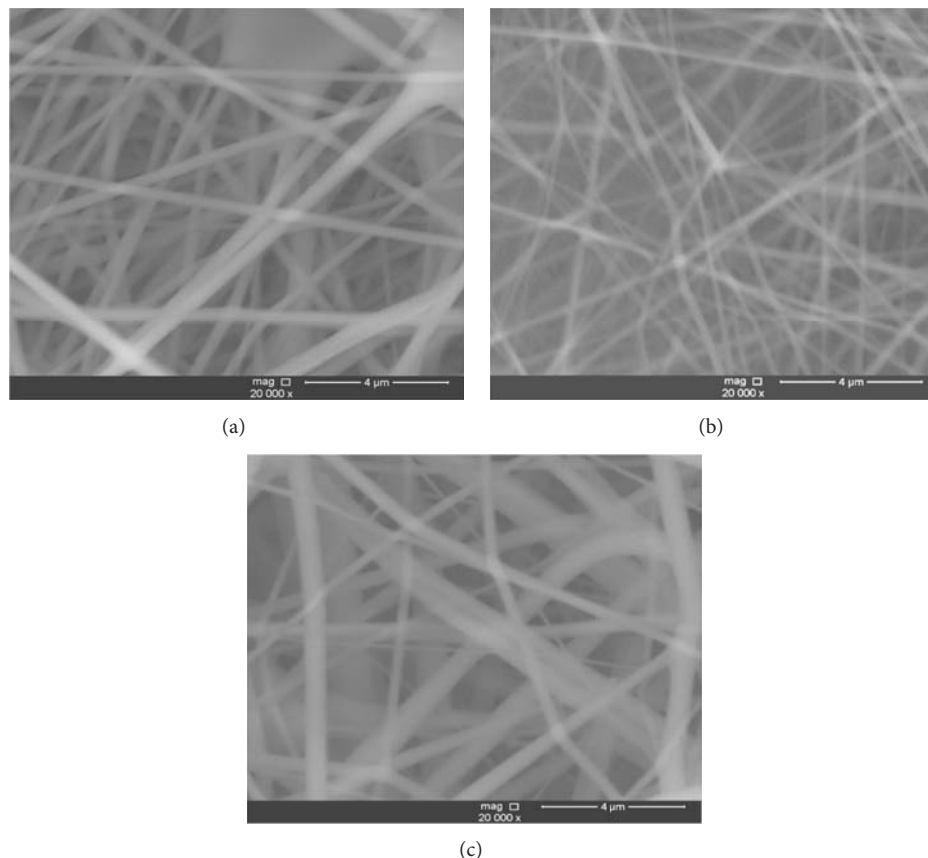


FIGURE 3: SEM images of PVA fibers (a), PVA/SDS/MWCNTs (b), and PVA/SDS/PVP/MWCNTs (c).

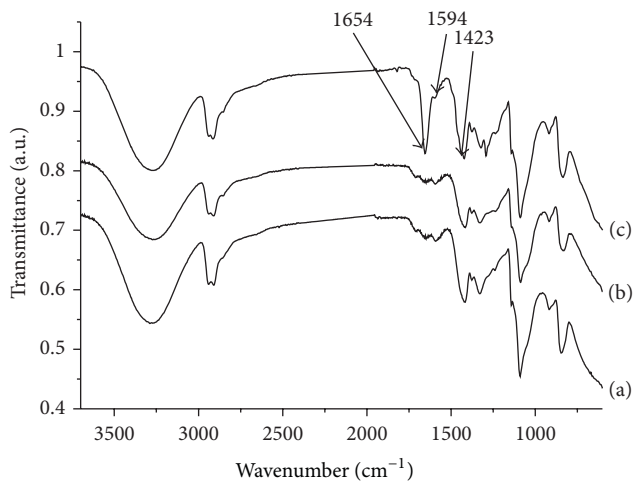


FIGURE 4: FTIR spectra of PVA (a), PVA/SDS/MWCNTs (b), and PVA/SDS/PVP/MWCNTs (c).

at 1417 cm<sup>-1</sup> and 1330 cm<sup>-1</sup> are attributed to the -CH deformation vibration. At 1089 cm<sup>-1</sup>, we observe a characteristic peak of C-O stretching vibration. In addition, the peak of O-H stretching vibration appears at 919 cm<sup>-1</sup> [19, 20].

Compared to the PVA spectrum (Figure 4(a)), it could be observed that any additional band was observed in the PVA/SDS/MWCNTs spectra (Figure 4(b)). This indicates

that any covalent bond was created between PVA and MWCNTs coated with SDS. Consequently, we confirmed that MWCNTs were dispersed in the PVA via noncovalent functionalization.

Concerning the PVA/SDS/PVP/MWCNTs nanocomposite fibers, the FTIR spectra of the fibers (Figure 4(c)) showed a characteristic peak of PVP at 1423 cm<sup>-1</sup> which is assigned to the deformation of CH<sub>2</sub> in PVP. The shoulder at 1594 cm<sup>-1</sup> is characteristic of C=C (aromatic) and C-N stretching. The additional peak located at 1654 cm<sup>-1</sup> is assigned to the C=O vibration [21–23]. The appearance of this band is due to the interaction of MWCNTs with PVP.

**3.4. Thermal Analysis.** Thermal gravimetric analysis (TGA) was carried out at a heating rate of 10°C·min<sup>-1</sup> in nitrogen atmosphere.

The thermal decomposition of the three samples was multistage processes; it exhibits two degradation steps. In the first region, as can be seen, the three samples displayed a similar behavior with degradation temperature close to 240°C. In fact, the degradation of isobutyl groups [24, 25] was located at about 246°C for the neat PVA fibers (Figure 5(a)). This temperature was decreased slightly for the PVA/SDS/MWCNTs fibers (Figure 5(b)) to be 239°C, and the shift is due to the presence of SDS in the bulk PVA polymer matrix [26], while the PVA/SDS/PVP/MWCNTs fibers (Figure 5(c)) degradation temperature was decreased

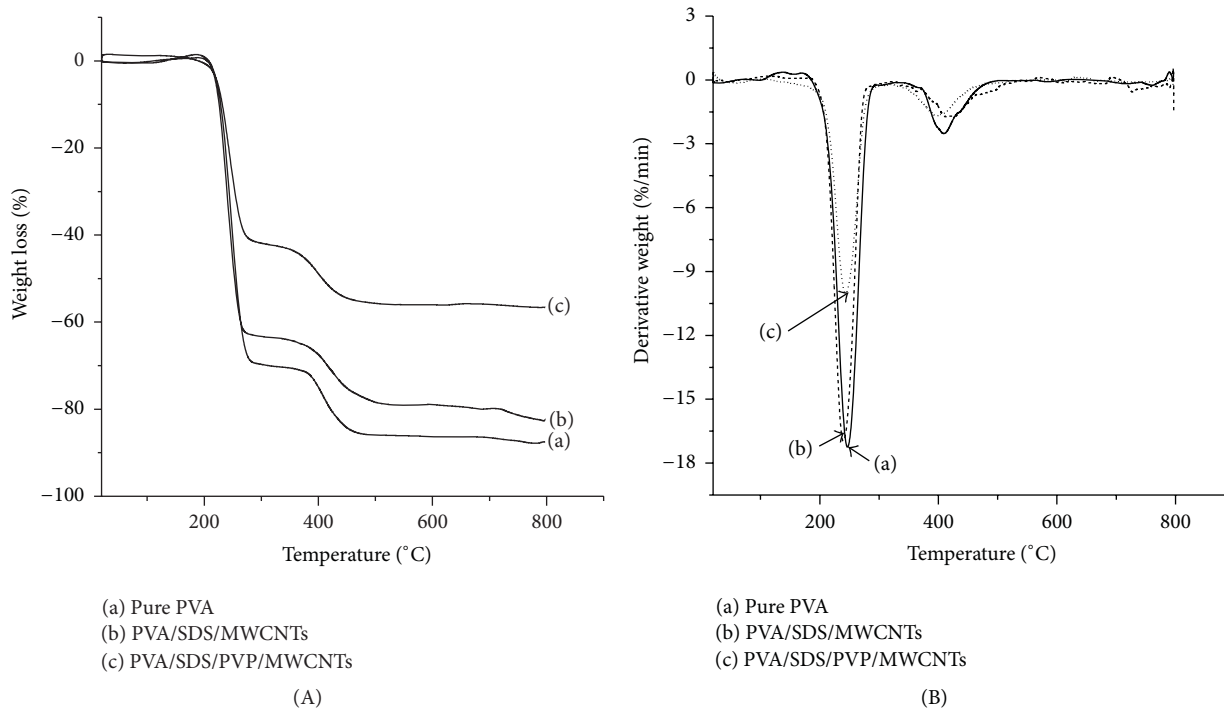


FIGURE 5: TGA and derivative TGA curves of (a) pure PVA, (b) PVA/SDS/MWCNTs and (c) PVA/SDS/PVP/MWCNTs.

TABLE 1: TGA results of weight loss of pure PVA, PVA/SDS/MWCNTs, and PVA/SDS/PVP/MWCNTs fibers.

|                  | Pure PVA fibers |       | PVA/SDS/MWCNTs fibers |      | PVA/SDS/PVP/MWCNTs fibers |     |
|------------------|-----------------|-------|-----------------------|------|---------------------------|-----|
| Temperature (°C) | 246.5           | 408.9 | 239.8                 | 413  | 242.7                     | 396 |
| Weight loss (%)  | 70              | 17    | 63.5                  | 18.7 | 43.7                      | 14  |

from 246°C to 242°C compared to the pure PVA fibers. This change reflects the specific multiple hydrogen bonding interaction between PVA and PVP [27].

The second stage appearing around 400°C is corresponding to the cleavage of C–C backbone of side and main chains of PVA [25]. According to Figure 4, all these transitions were accompanied with a weight loss as listed in Table 1.

All samples show a small loss in weight at around 100°C which is assigned to the detachment of residual water (from fibers preparation). For the neat PVA, the major weight loss (70 wt%) is at 193°C, and this continued to increase rapidly with temperature, until a stable plateau region appeared between 351 and 477°C, while the difference between the weight loss of pure PVA and PVA/SDS/MWCNTs fibers indicated the interfacial interaction between the matrix and MWCNTs. When the PVP was incorporated into the composite, the weight loss decreased considerably due to the interaction of PVA with the MWCNTs coated by the PVP through hydrogen bonding interaction between PVA and PVP.

#### 4. Conclusion

PVA electrospun nanofibers containing SDS/PVP/MWCNTs were fabricated, using different concentrations of the SDS

and PVP in order to achieve a stable dispersion lasting for several months. Our results showed clearly that the absorption of the wrapped MWCNTs in aqueous solution increased with the concentration of SDS and PVP and the best absorption was achieved for MWCNTs : SDS : PVP = 1 : 5 : 0.6. SEM images of PVA/SDS/PVP/MWCNTs nanofibers showed that the diameter was decreasing to around 224 nm and the interaction between the PVA and the coated carbon nanotubes with PVP was elucidated by FTIR and TGA.

#### Conflict of Interests

The authors declare no conflict of interests.

#### References

- [1] B. Ding, M. Wang, J. Yu, and G. Sun, "Gas sensors based on electrospun nanofibers," *Sensors*, vol. 9, no. 3, pp. 1609–1624, 2009.
- [2] R. Dersch, M. Steinhart, U. Boudriot, A. Greiner, and J. H. Wendorff, "Nanoprocessing of polymers: applications in medicine, sensors, catalysis, photonics," *Polymers for Advanced Technologies*, vol. 16, no. 2-3, pp. 276–282, 2005.
- [3] M. Bognitzki, T. Frese, M. Steinhart et al., "Preparation of fibers with nanoscaled morphologies: electrospinning of polymer

- blends," *Polymer Engineering and Science*, vol. 41, no. 6, pp. 982–989, 2001.
- [4] Q. Li, S. Mahendra, D. Y. Lyon et al., "Antimicrobial nanomaterials for water disinfection and microbial control: potential applications and implications," *Water Research*, vol. 42, no. 18, pp. 4591–4602, 2008.
  - [5] K. H. Hong, J. L. Park, I. N. Hwan Sul, J. H. Youk, and T. J. Kang, "Preparation of antimicrobial poly(vinyl alcohol) nanofibers containing silver nanoparticles," *Journal of Polymer Science B*, vol. 44, no. 17, pp. 2468–2474, 2006.
  - [6] K. Yoon, K. Kim, X. Wang, D. Fang, B. S. Hsiao, and B. Chu, "High flux ultrafiltration membranes based on electrospun nanofibrous PAN scaffolds and chitosan coating," *Polymer*, vol. 47, no. 7, pp. 2434–2441, 2006.
  - [7] J. Jagur-Grodzinski, "Polymers for tissue engineering, medical devices, and regenerative medicine. Concise general review of recent studies," *Polymers for Advanced Technologies*, vol. 17, no. 6, pp. 395–418, 2006.
  - [8] Z. Rožek, W. Kaczorowski, D. Lukáš, P. Louda, and S. Mitura, "Potential applications of nanofiber textile covered by carbon coatings," *Journal of Achievements in Materials and Manufacturing Engineering*, vol. 27, pp. 35–38, 2008.
  - [9] J. Nader, C. Bhuvanesh, M. Apparao et al., "Functional fabric with embedded nanotube actuators/sensors," Tech. Rep., National Textile Center Annual Report, 2004.
  - [10] A. Martinez, S. Uchida, Y.-W. Song, T. Ishigure, and S. Yamashita, "Fabrication of Carbon nanotube-poly-methylmethacrylate composites for nonlinear photonic devices," *Optics Express*, vol. 16, no. 15, pp. 11337–11343, 2008.
  - [11] B. Vigolo, A. Penicaud, C. Coulon et al., "Macroscopic fibers and ribbons of oriented carbon nanotubes," *Science*, vol. 290, no. 5495, pp. 1331–1334, 2000.
  - [12] H. Aarab, M. Baitoul, J. Wéry et al., "Electrical and optical properties of PPV and single-walled carbon nanotubes composite films," *Synthetic Metals*, vol. 155, no. 1, pp. 63–67, 2005.
  - [13] O. Matarredona, H. Rhoads, Z. Li, J. H. Harwell, L. Balzano, and D. E. Resasco, "Dispersion of single-walled carbon nanotubes in aqueous solutions of the anionic surfactant NaDDBS," *Journal of Physical Chemistry B*, vol. 107, no. 48, pp. 13357–13367, 2003.
  - [14] L. Liu, F. Zhao, F. Xiao, and B. Zeng, "Improved voltammetric response of malachite green at a multi-walled carbon nanotubes coated glassy carbon electrode in the presence of surfactant," *International Journal of Electrochemical Science*, vol. 4, no. 4, pp. 525–534, 2009.
  - [15] J. Yu, N. Grossiord, C. E. Koning, and J. Loos, "Controlling the dispersion of multi-wall carbon nanotubes in aqueous surfactant solution," *Carbon*, vol. 45, no. 3, pp. 618–623, 2007.
  - [16] N. Diouri and M. Baitoul, "Studies of multiwall carbon nanotubes dispersion in poly vinyl alcohol," *Mediterranean Journal of Electronics and Communications*, vol. 6, pp. 127–131, 2010.
  - [17] M. E. Hughes, E. Brandin, and J. A. Golovchenko, "Optical absorption of DNA-carbon nanotube structures," *Nano Letters*, vol. 7, no. 5, pp. 1191–1194, 2007.
  - [18] L. Zeng, W. Wang, J. Liang et al., "The changes of morphology, structure and optical properties from carbon nanotubes treated by hydrogen plasma," *Materials Chemistry and Physics*, vol. 108, no. 1, pp. 82–87, 2008.
  - [19] X. M. Sui, C. L. Shao, and Y. C. Liu, "White-light emission of polyvinyl alcohol/ZnO hybrid nanofibers prepared by electrospinning," *Applied Physics Letters*, vol. 87, no. 11, Article ID 113115, 2005.
  - [20] L. Zhang, P. Yu, and Y. Luo, "Dehydration of caprolactam-water mixtures through cross-linked PVA composite pervaporation membranes," *Journal of Membrane Science*, vol. 306, no. 1-2, pp. 93–102, 2007.
  - [21] R. F. Bhajantri, V. Ravindrachary, B. Poojary, I. Ismayil, A. Harisha, and V. Crasta, "Studies on fluorescent PVA + PVP + MPDMAPP composite films," *Polymer Engineering and Science*, vol. 49, no. 5, pp. 903–909, 2009.
  - [22] S. F. Wei, J. S. Lian, and Q. Jiang, "Controlling growth of ZnO rods by polyvinylpyrrolidone (PVP) and their optical properties," *Applied Surface Science*, vol. 255, no. 15, pp. 6978–6984, 2009.
  - [23] S. Sethia and E. Squillante, "Solid dispersion of carbamazepine in PVP K30 by conventional solvent evaporation and supercritical methods," *International Journal of Pharmaceutics*, vol. 272, no. 1-2, pp. 1–10, 2004.
  - [24] Y.-W. Chang, E. Wang, G. Shin, J.-E. Han, and P. T. Mather, "Poly(vinyl alcohol) (PVA)/sulfonated polyhedral oligosilsesquioxane (sPOSS) hybrid membranes for direct methanol fuel cell applications," *Polymers for Advanced Technologies*, vol. 18, no. 7, pp. 535–543, 2007.
  - [25] E. D. Wang, T. S. Zhao, and W. W. Yang, "Poly (vinyl alcohol)/3-(trimethylammonium) propyl-functionalized silica hybrid membranes for alkaline direct ethanol fuel cells," *International Journal of Hydrogen Energy*, vol. 35, no. 5, pp. 2183–2189, 2010.
  - [26] C. Bartholome, P. Miaudet, A. Derré et al., "Influence of surface functionalization on the thermal and electrical properties of nanotube-PVA composites," *Composites Science and Technology*, vol. 68, no. 12, pp. 2568–2573, 2008.
  - [27] A. B. Seabra and M. G. De Oliveira, "Poly(vinyl alcohol) and poly(vinyl pyrrolidone) blended films for local nitric oxide release," *Biomaterials*, vol. 25, no. 17, pp. 3773–3782, 2004.

## Research Article

# Shape Effects of Iron Nanowires on Hyperthermia Treatment

Wei-Syuan Lin,<sup>1</sup> Hong-Ming Lin,<sup>1</sup> Hsiang-Hsin Chen,<sup>2</sup>  
Yeu-Kuang Hwu,<sup>2</sup> and Yuh-Jing Chiou<sup>3</sup>

<sup>1</sup> Department of Materials Engineering, Tatung University, Taipei 104, Taiwan

<sup>2</sup> Institute of Physics, Academia Sinica, Nankang, Taipei 115, Taiwan

<sup>3</sup> Department of Chemical Engineering, Tatung University, Taipei 104, Taiwan

Correspondence should be addressed to Hong-Ming Lin; [hmlin@ttu.edu.tw](mailto:hmlin@ttu.edu.tw)

Received 7 October 2012; Accepted 12 May 2013

Academic Editor: Haiping Hong

Copyright © 2013 Wei-Syuan Lin et al. This is an open access article distributed under the Creative Commons Attribution License, which permits unrestricted use, distribution, and reproduction in any medium, provided the original work is properly cited.

This research discusses the influence of morphology of nanomagnetic materials (one-dimensional iron nanowires and zero-dimensional iron nanoparticles) on heating efficiency of the hyperthermia treatment. One-dimensional iron nanowires, synthesized by reducing method in external magnetic field, are explored in terms of their material properties, magnetic anisotropy, and cytotoxicity of EMT-6 cells. The magnetic anisotropy of an array of nanowires is examined in parallel and perpendicular magnetic fields by VSM. For the magnetic hyperthermia treatment tests, iron nanowires and nanoparticles with different concentrations are heated in alternating magnetic field to measure their actual heating efficiency and SLP heating properties. The shape effects of iron nanomaterials can be revealed from their heating properties. The cytotoxicity of nanowires with different concentrations is measured by its survival rate in EMT-6 with the cells cultivated for 6 and 24 hours.

## 1. Introduction

According to the World Health Organization (WHO), cancers were the top causes of death all over the world. In 2008 alone, 7.6 million victims died from cancers, accounting for 13% of the total death toll [1]. Currently, cancer can be treated by chemotherapy, radiation therapy, surgery, gene therapy, and immunotherapy, and so forth. Conventional hyperthermia treatments include ultrasound, radiofrequency, microwaves, infrared radiation, and tubes with hot water. Some of them will cause side effect all over the patients' bodies during the treatment [2–4].

This research is focused on the magnetic targeted hyperthermia treatments. This treatment can directly eliminate the cancer cells without damaging the normal ones. Most importantly, the medication applied on the surfaces of magnetic materials can directly perform the treatment [5, 6]. Magnetic targeted hyperthermia treatments are conducted by placing magnetic targeted medicines on the tumor and imposing the alternating magnetic field (~kHz–~MHz) on it [7, 8].

To generate heat in an alternating field, magnetic materials activate more than four different known mechanisms, which are generation of eddy currents, hysteresis losses,

relaxation losses, and frictional losses, and so forth. There are two modes, rotational (Brownian) and Neel, in which the relaxation losses in single-domain MNPs occur. The magnetic moment fixed along the crystal easy axis revolves away towards the external field in the Neel mode. Similar to the hysteresis loss in multidomain magnetic particles, the Neel mechanism can also generate heat by means of “internal friction” caused by the movement of the magnetic moment in an external field. In the Brownian mode, however, the interaction between a thermal force and viscous drag in the suspending medium will influence the particle movement significantly. The whole particle moves towards the external field with the moment locked along the crystal axis instead. This phenomenon serves to account for the mechanical friction component in a given suspending medium. Applying the mechanism mentioned above, the local temperature of the tumor can rise up to 42–50°C, with that the cancer cells will be killed [9–11].

The important factor for magnetic heating is the specific loss power (SLP) (also called the specific absorption rate (SAR)). SLP is equal to  $C \times m_{\text{sample}}/m_{\text{metal}} \times \Delta T/\Delta t$ , where  $C$  is the specific heat capacity of sample ( $C_{\text{water}} = 4.185 \text{ J/g}^\circ\text{C}$ ),

$m_{\text{sample}}$  is the mass of sample,  $m_{\text{metal}}$  is the mass of the magnetic material in sample, and  $\Delta T/\Delta t$  is the slope of the heating curve. And SLP is very sensitive to the material properties [7, 12, 13].

The factors that affect the biodistribution of polymeric iron nanoparticles (NPs) include the size, shape, hydrophobic/hydrophilic balance of the surface, and surface charge [14]. Thus, this experiment explores the characteristic differences of heating effectiveness between 1D iron nanowires (NWs) and commercial iron nanoparticles (NPs) in hyperthermia treatments. Iron NWs reveal a special property that may easily destroy the cancer cells by its 1D spinning radius. The cellular toxic tests of the nanoiron are also conducted for the iron NWs in further studies.

## 2. Experimental

Iron (III) chloride hexahydrate ( $\text{FeCl}_3 \cdot 6\text{H}_2\text{O}$ , 98%, assay) and sodium borohydride (98%, assay) are purchased from Sigma-Aldrich Company and Acros Organics Company, respectively. Ethanol (99.5%, assay) was obtained from Shimakyu Pure Chemicals Company. Iron NWs are fabricated by the reduction of iron (III) chloride under high magnetic field. The aqueous iron (III) chloride hexahydrate (0.5 M, 0.2 mL) is diluted with 5 mL of aqueous dextran (40 ppm) and the iron (III) precursor is kept in an external magnetic field of about 2000 gauss. The argon gas is bubbling through the solution to purge the dissolved oxygen. The reducing agent,  $\text{NaBH}_4$ , is added dropwisely under Ar. After 5 minutes, the products are washed with ethanol for several times and dried at  $95^\circ\text{C}$  [15]. The iron nanoparticles are obtained from Yong-Zhen Technomaterial Co., Ltd. with 10–60 nm in diameter for comparison.

X-ray powder diffraction (XRD) analysis of samples is carried out at NSRRIC beam line. High-resolution images of samples are examined by field emission transmission electron microscope (FE-TEM), JEOL 2100F. Magnetic hysteresis loop is measured by using vibration sample magnetization (VSM, Lakeshore) at room temperature.

The hyperthermia device (Power cube 64/900) used in this study is produced by AREZZO, President Honor Ind. Co., Ltd., Taiwan. The experimental samples are placed in the inductive coil heater of 3 cm diameter with an optic fiber (Luxtron One, Lambda Photometrics, UK) to measure the raise of temperature.

The biocompatibility of iron NWs is evaluated by murine breast cancer cells, EMT-6 cells. EMT-6 cells are cultured in DMEM/F12 medium with 10% of the fetal bovine serum (FBS) and 1% of penicillin-streptomycin in 5% of  $\text{CO}_2$  humidified chamber at  $37^\circ\text{C}$ . After the cells are seeded on multiple plates for overnight, iron NWs dispersed in culture medium are applied to each well of culture plates. The cells are treated with different concentrations of nanoiron for 6 and 24 hours. The control cell is treated in the normal culture medium without adding iron nanowires. After incubation, the cells are directly counted by trypan blue exclusion assay for assaying cellular viability.

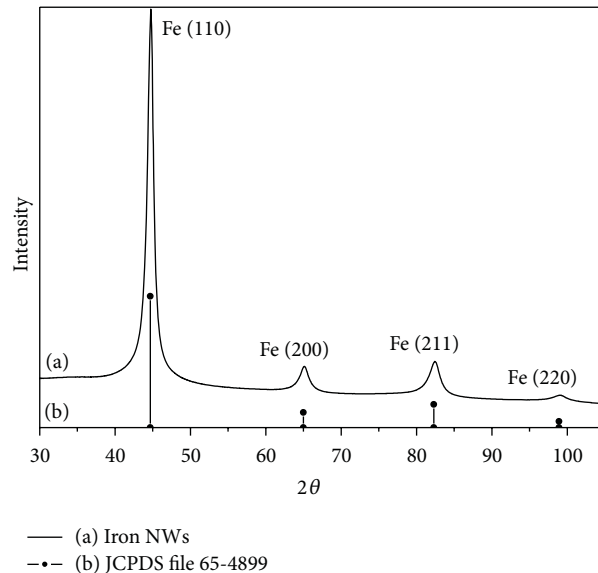


FIGURE 1: X-ray diffraction patterns of (a) iron NWs; (b) JCPDS file 65-4899.

## 3. Results and Discussion

XRD pattern of iron NWs and JCPDS file 65-4899 are shown in Figure 1. The diffraction angles of JCPDS file 65-4899 at  $2\theta = 44.662^\circ$ ,  $65.006^\circ$ , and  $82.311^\circ$  are related to (110), (200), and (211) planes of pure iron, respectively. This pattern shows clearly that a strong diffraction peak corresponds to the (110) plane. The growth orientation of iron NWs is highly dependent on applied magnetic field. According to these results, preferred crystal orientation of the iron NWs is in (110) direction. The lattice parameters of iron NWs are less than theoretical lattice constants. This may be due to lattice defects.

Figures 2(a)–2(d) show HR-TEM images of iron NWs. The diameter of iron NWs is around 60 nm with length of about 2–6  $\mu\text{m}$  as indicated in Figure 2(a). The selective area diffraction (SAD) of circle area in Figure 2(a) is shown in Figure 2(d). It indicates that iron NWs exhibit bcc crystal structure. The diffraction planes are assigned to (110), (200), (220), (310), and (222) from inside to outside diffraction rings. Figure 2(c) indicates an oxide layer of about 4 nm is passivated on the surface of iron NWs. The oxide layer on iron NWs results from magnetite formation during the reduction process. TEM images show that the iron NWs are synthesized by pearl-linking of iron NPs due to external magnetic field. Figures 2(c)-2.1 to 2(c)-5.1 are the atoms resolution related to c1, c2, c3, c4, and c5 positions in Figure 2(c), respectively. The d-spacing of Figures 2(c)-1.1, 2(c)-2.1, 2(c)-3.1, 2(c)-4.1, and 2(c)-5.1 are 1.889 Å, 1.879 Å, 1.888 Å, 2.022 Å, and 1.884 Å, respectively.

The magnetic hysteresis curve of iron NWs at room temperature is shown in Figure 3. The results indicate that the saturation magnetization and coercive force of iron NWs are 157.93 emu/g and 9.74 Oe, respectively. The saturation magnetization of iron NWs is lower than that of bulk iron (220 emu/g) due to the existence of a high surface/volume

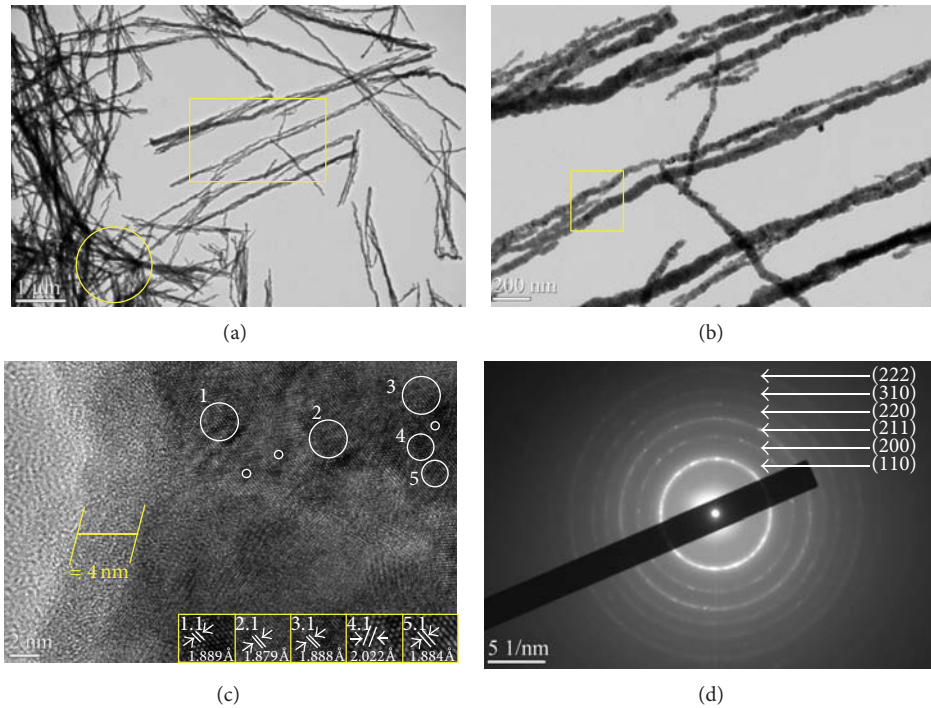


FIGURE 2: HR-TEM images of iron NWs: (a) low-magnification image; (b) high-magnification image at square area of (a); (c) HR-TEM images of iron NWs, 1.1, 2.1, 3.1, 4.1, and 5.1 are atomic resolution related to 1, 2, 3, 4, and 5 positions in (c), respectively; and (d) electron diffraction pattern at circle area of (a).

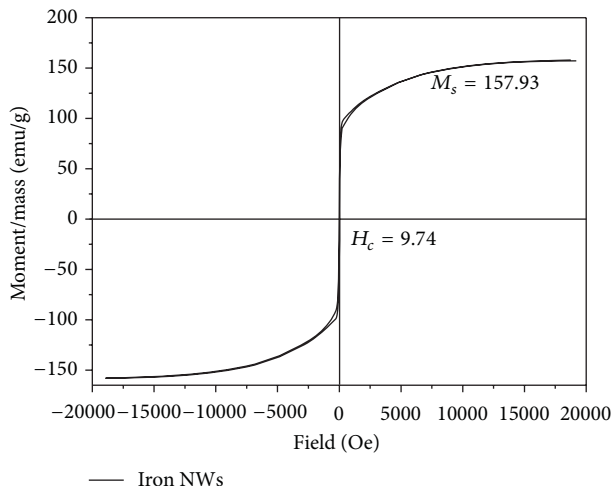


FIGURE 3: The hysteresis loops of iron NWs at 300 K.

ratio. And structural defects may be one of the possible causes for decreasing magnetization of iron NWs.

As shown in Figure 4, the formations of an array of nanowires under (a) parallel and (b) perpendicular magnetic fields at room temperature are measured for their magnetic properties such as coercive force and squareness ratio (remnant magnetization/saturation magnetization). In Table 1, the arrayed nanowires under the parallel magnetic field have greater squareness ratio (about 64.20%), while those under the perpendicular magnetic field have less squareness ratio

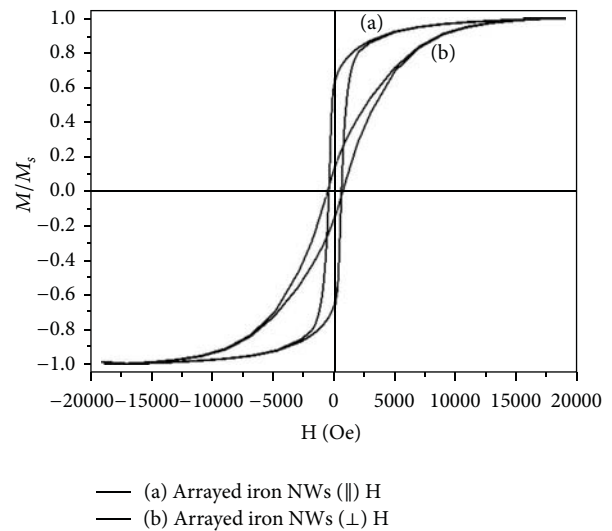


FIGURE 4: The hysteresis loops of an array of nanowires under parallel and perpendicular magnetic fields at room temperature are shown in (a) and (b), respectively.

(about 14.20%). The former's coercive force is 100 Oe less than the latter one.

Two sets of different amounts of iron NWs (0.1 mg, 0.25 mg, and 0.5 mg) and commercial iron nanoparticles (0.5 mg) are dispersed in 1 mL of deionized water. SEM image of commercial iron nanoparticles produced by Yong-Zhen Technomaterial Co., Ltd. is shown in Figure 5.

TABLE 1: The Hc (coercive force) and Mr/Ms (squareness ratio) of an array of nanowires under parallel and perpendicular magnetic fields.

|                                    | Hc (Oe) | Mr/Ms  |
|------------------------------------|---------|--------|
| Arrayed iron NWs ( $\parallel$ ) H | 520.3   | 64.20% |
| Arrayed iron NWs ( $\perp$ ) H     | 628     | 14.20% |

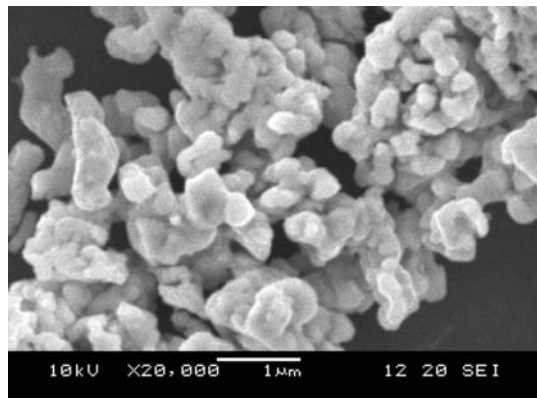


FIGURE 5: The SEM image of commercial iron nanoparticles.

Three different concentrations (100, 250, and 500 ppm) of iron NWs or commercial iron nanoparticles (500 ppm) solution in centrifuge tube is placed in the coil of inductive heater for an hour. The rising temperature of solution with time is shown in Figure 6. The maximal temperatures of iron NWs of 500, 250, and 100 ppm can be 73.8°C, 49.6°C, and 36.0°C, respectively. The heating rates of commercial iron nanoparticles of 500 ppm are 0.006°C/sec and are listed in Table 2. When the iron nanowires and commercial iron nanoparticles have the same concentration of 500 ppm, the heating rates of iron NWs are much higher than those of the commercial iron nanoparticles. The average of SLP values for different concentrations of iron NWs and commercial iron nanoparticles are also listed in Table 2. For iron NWs, the SLP values are 619.7 W/g, 535.8 W/g, and 920.8 W/g; and for commercial iron nanoparticles (500 ppm), the SLP values are 50.2 W/g. The highest SLP value (920.8 W/g) is obtained at 100 ppm of iron NWs. From the heating results of the iron nanowires and commercial iron nanoparticles with the same concentration of 500 ppm, the former have higher saturated temperature and efficiency than the latter one.

As mentioned above, this study presents the hypothesis in Figure 7 as an imaginary rundown. Because the iron nanowires, as compared to iron nanoparticles, have more spinning radii, the materials which are heated and stirred in the alternating magnetic field have larger reactive areas. This fact leads iron NWs to better heating efficiency than that of the iron nanoparticles.

When one-dimensional iron nanowires are applied to the tumor hyperthermia treatment, they can provide larger frictional reactive areas than zero-dimensional iron nanoparticles. This enables one-dimensional iron nanowires to have a better heating efficiency, which reduces the treatment time of the cancer patients.

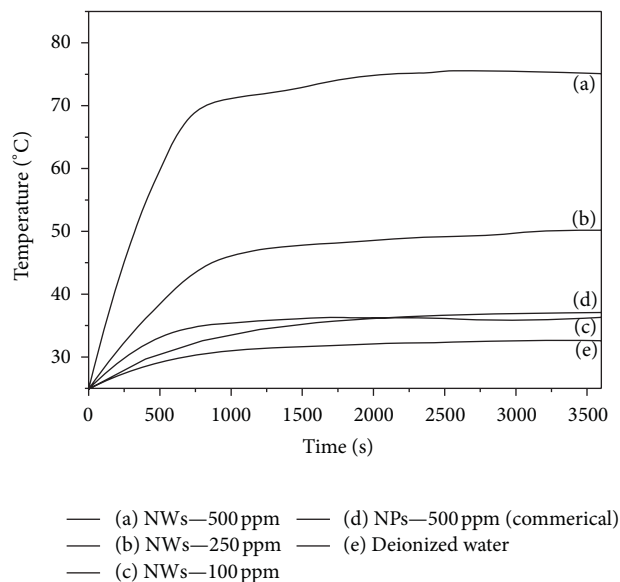


FIGURE 6: The heating effectiveness of the iron NWs in different concentrations, (a) 500 ppm of iron NWs (0.5 mg/mL), (b) 250 ppm of iron NWs (0.25 mg/mL), (c) 100 ppm of iron NWs (0.1 mg/mL), (d) 250 ppm of commercial iron NPs (0.5 mg/mL), and (e) deionized water is shown for reference.

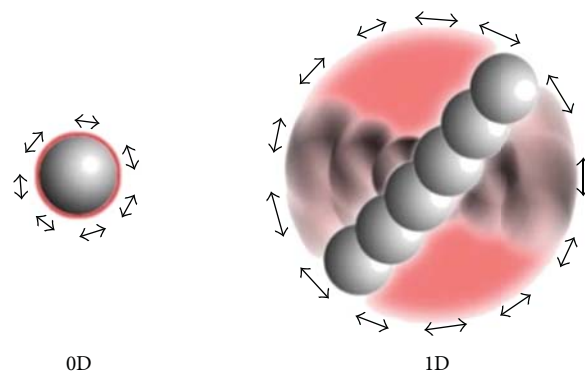


FIGURE 7: One-dimensional materials have large spinning radii.

TABLE 2: Heating effectiveness of iron NWs and commercial iron NPs.

| Samples (ppm) | Max. Temp. (°C) | Heating rate (°C/sec) | SLP (W/g) |
|---------------|-----------------|-----------------------|-----------|
| NWs—500       | 73.8            | 0.074                 | 619.7     |
| NWs—250       | 49.6            | 0.032                 | 535.8     |
| NWs—100       | 36.0            | 0.022                 | 920.8     |
| NPs—500*      | 37.1            | 0.006                 | 50.2      |

\* NPs—500: commercial iron nanoparticles.

The cytotoxicity in response to iron NWs in different concentrations (1, 10, 250, and 500 ppm) is performed by directly counting the number of live cells after incubation. Figure 8 shows the results of cytotoxicity of iron NWs in EMT-6 cells. The number of cellular vesicles appearing in the cytoplasm increases due to being exposed to iron NWs

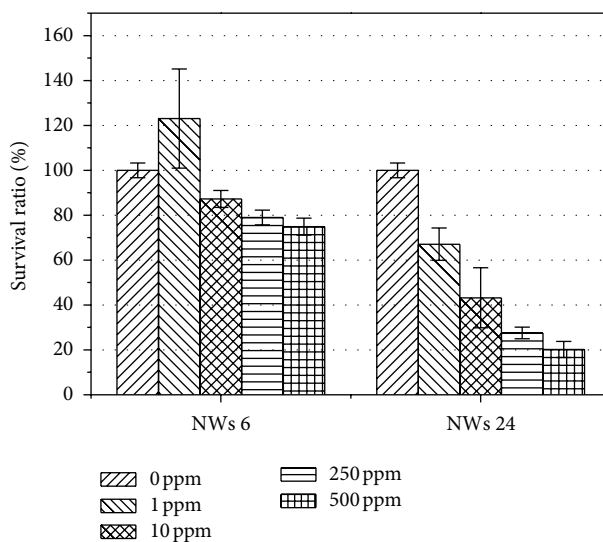


FIGURE 8: Survival ratio of iron NWs and NPs coculture with EMT-6 cells in concentrations of 0, 1, 10, 250, and 500 ppm for 6 and 24 hours.

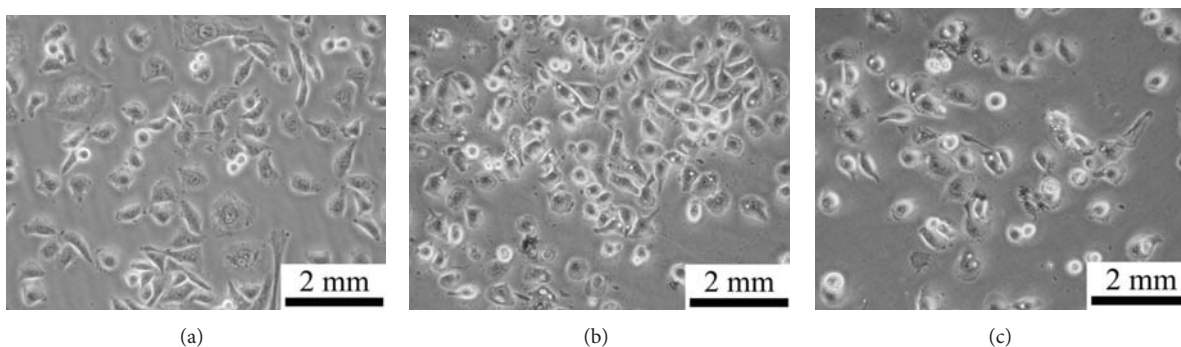


FIGURE 9: The optical images of (a) untreated EMT-6 cells; (b) and (c) cocultured iron NWs (10 ppm) and EMT-6 cells in 6 and 24 hours, respectively.

at lower concentrations in shorter time. After 6 hours of incubation, iron NWs shows cell survivability of more than 80%. Figures 9(b) and 9(c) show the optical images of EMT-6 cocultured with iron NWs for 6 and 24 hours, respectively. The untreated cells are shown in Figure 9(a). It is also noted that the cell morphology is transformed into spherical shape.

#### 4. Conclusions

This study synthesizes the iron nanowires with diameter of about 60 nm and length of approximately 2–6  $\mu\text{m}$ . Their saturation magnetization is about 157.9 emu/g while their coercive force is about 9.7 Oe. They have greater squareness ratio of about 64.2% under the parallel external magnetic field, whereas it is only about 14.20% under the perpendicular magnetic field. With regard to heating efficiency, one-dimensional iron nanowires have a better heating efficiency at the external alternating magnetic field than that of zero-dimensional ones at the same concentration of 500 ppm. The one-dimensional

iron nanowires have the saturated heating temperature at about 73.8°C (that of the nanoparticles is only 40°C) and their heating efficiency is about 0.074 (that of the nanoparticles is about 0.006). These results indicate the strong shape effects of nanomaterials on its heating efficiency. The cytotoxicity of the iron nanowires (10 ppm) in EMT-6 cells undergoing 6 hours of toxic test has the mortality rate of about 80%. These results indicate that with further study the iron nanowires are feasible to be used in hyperthermia therapy.

#### Conflict of Interests

The authors declare that they have no conflict of interests with the chemical companies (Sigma-Aldrich Company, Acros Organics Company, Shimakyu Pure Chemicals Company, and Yung-Zhen Technomaterial Co., Ltd.), instrument providers (Lakeshore, AREZZO President Honor Ind. Co., Ltd., Taiwan, Luxtron one, Lambda Photometrics, UK, NSRRC, NISP Lab in Maryland University, and Composites Lab in NTU), and research funding (NSC of Taiwan).

## Acknowledgments

The authors acknowledge the Grant from NSC of Taiwan, the support from SRRC, Taiwan, TEM/SEM from NISP Lab in Maryland University, and hyperthermia test from Bioceramics and Composites Lab in NTU, Taiwan.

## References

- [1] Globocan 2008, IARC, 2010, <http://www.iarc.fr/>.
- [2] B. E. Billard, K. Hynynen, and R. B. Roemer, "Effects of physical parameters on high temperature ultrasound hyperthermia," *Ultrasound in Medicine and Biology*, vol. 16, no. 4, pp. 409–420, 1990.
- [3] P. Wust, B. Hildebrandt, G. Sreenivasa et al., "Hyperthermia in combined treatment of cancer," *The Lancet Oncology*, vol. 3, no. 8, pp. 487–497, 2002.
- [4] C. J. Diederich and K. Hynynen, "Ultrasound technology for hyperthermia," *Ultrasound in Medicine and Biology*, vol. 25, no. 6, pp. 871–887, 1999.
- [5] P. Cherukuri, E. S. Glazer, and S. A. Curley, "Targeted hyperthermia using metal nanoparticles," *Advanced Drug Delivery Reviews*, vol. 62, no. 3, pp. 339–345, 2010.
- [6] D. L. Zhao, X. X. Wang, X. W. Zeng, Q. S. Xia, and J. T. Tang, "Preparation and inductive heating property of Fe<sub>3</sub>O<sub>4</sub>-chitosan composite nanoparticles in an AC magnetic field for localized hyperthermia," *Journal of Alloys and Compounds*, vol. 477, no. 1–2, pp. 739–743, 2009.
- [7] C. S. S. R. Kumar and F. Mohammad, "Magnetic nanomaterials for hyperthermia-based therapy and controlled drug delivery," *Advanced Drug Delivery Reviews*, vol. 63, no. 9, pp. 789–808, 2011.
- [8] G. Zhang, Y. Liao, and I. Baker, "Surface engineering of core/shell iron/iron oxide nanoparticles from microemulsions for hyperthermia," *Materials Science and Engineering C*, vol. 30, no. 1, pp. 92–97, 2010.
- [9] R. Kötz, W. Weitschies, L. Trahms, and W. Semmler, "Investigation of Brownian and Néel relaxation in magnetic fluids," *Journal of Magnetism and Magnetic Materials*, vol. 201, no. 1–3, pp. 102–104, 1999.
- [10] G. Nedelcu, "Magnetic nanoparticles impact on tumoral cells in the treatment by magnetic fluid hyperthermia," *Digest Journal of Nanomaterials and Biostructures*, vol. 3, no. 3, pp. 103–107, 2008.
- [11] G. Nedelcu, "The heating study of two types of colloids with magnetite nanoparticles for tumours therapy," *Digest Journal of Nanomaterials and Biostructures*, vol. 3, no. 2, pp. 99–102, 2008.
- [12] R. Hergt, S. Dutz, R. Müller, and M. Zeisberger, "Magnetic particle hyperthermia: nanoparticle magnetism and materials development for cancer therapy," *Journal of Physics Condensed Matter*, vol. 18, no. 38, pp. S2919–S2934, 2006.
- [13] F. Mohammad, G. Balaji, A. Weber, R. M. Uppu, and C. S. S. R. Kumar, "Influence of gold nanoshell on hyperthermia of superparamagnetic iron oxide nanoparticles," *Journal of Physical Chemistry C*, vol. 114, no. 45, pp. 19194–19201, 2010.
- [14] F. Sonvico, S. Mornet, S. Vasseur et al., "Folate-conjugated iron oxide nanoparticles for solid tumor targeting as potential specific magnetic hyperthermia mediators: synthesis, physico-chemical characterization, and in vitro experiments," *Bioconjugate Chemistry*, vol. 16, no. 5, pp. 1181–1188, 2005.
- [15] W. S. Lin, Z. J. Jian, H. M. Lin et al., "Synthesis and characterization of iron nanowires," *Journal of the Chinese Chemical Society*, vol. 60, pp. 85–91, 2013.

## Research Article

# Correlation Effects in Kinetics of One-Dimensional Atomic Systems

**V. D. Borman, I. V. Tronin, V. N. Tronin,  
V. I. Troyan, and O. S. Vasiliev**

*National Research Nuclear University, MEPhI, Kashirskoye Sh. 31, Moscow 115409, Russia*

Correspondence should be addressed to V. D. Borman; [vdborman@mephi.ru](mailto:vdborman@mephi.ru)

Received 10 January 2013; Accepted 7 March 2013

Academic Editor: Yun Zhao

Copyright © 2013 V. D. Borman et al. This is an open access article distributed under the Creative Commons Attribution License, which permits unrestricted use, distribution, and reproduction in any medium, provided the original work is properly cited.

The paper is devoted to the analysis of the correlation effects and manifestations of general properties of 1D systems (such as spatial heterogeneity that is associated with strong density fluctuations, the lack of phase transitions, the presence of frozen disorder, confinement, and blocked movement of nuclear particle by its neighbours) in nonequilibrium phenomena by considering the four examples. The anomalous transport in zeolite channels is considered. The mechanism of the transport may appear in carbon nanotubes and MOF structures, relaxation, mechanical properties, and stability of nonequilibrium states of free chains of metal atoms, non-Einstein atomic mobility in 1D atomic systems. Also we discuss atomic transport and separation of two-component mixture of atoms in a 1D system—a zeolite membrane with subnanometer channels. We discuss the atomic transport and separation of two-component mixture of atoms in a 1D system—zeolite membrane with subnanometer channels. These phenomena are described by the response function method for nonequilibrium systems of arbitrary density that allows us to calculate the dynamic response function and the spectrum of relaxation of density fluctuations 1D atomic system.

## 1. Introduction

In recent years, one-dimensional objects became available and actively investigated due to their unique properties. They are free chains of metals just one atom thick (Au, Ag, Pt, In, Mn, Li, and Ni) [1–13], chains on specially prepared surfaces of crystals with high crystalline indices [14–19], the molecules (atoms) in subnanometer channels of complex oxides, zeolites [20–22], carbon nanotubes [23–27], and in some metal organic frameworks (MOF).

According to modern concepts, the common feature of one-dimensional objects as statistical systems is spatially inhomogeneous state and density fluctuations. These fluctuations are caused by the crucial role of many-particle correlations in 1D systems. This feature is connected with the absence of phase transitions in 1D systems of particles of one kind with short-range potential of the interparticle interaction (see van Hove Theorem [28, 29]). In this case, for certain values of the density the susceptibility of 1D system has a maximum but stays finite in contrast to 3D systems,

where susceptibility becomes infinite in vapour-liquid and liquid-solid phase transitions [30].

The absence of phase transition means that stable nuclei of a new phase are not formed, and the one-dimensional clusters nuclei that are formed in a system have a finite lifetime and are the density fluctuations. 1D systems are characterized by frozen disorder because the atomic particles cannot be exchanged with their neighbours and block the movement of each particle neighbors. For kinetic phenomena in atomic 1D confinement system, the role of confinement is not only to preserve the geometry of the system, but also the system relaxation by phonons. Relaxation of the system in confinement due to strong interparticle correlations depends on the ratio of the energy of particle interaction with confinement and interparticle interaction [31].

This paper is devoted to the analysis of correlation effects and manifestations of these general properties of nonequilibrium phenomena in the four examples. The anomalous transport in zeolite channels is considered. The mechanism

of the transport may appear in carbon nanotubes and MOF structures, relaxation, mechanical properties, and stability of nonequilibrium states of free chains of metal atoms, non-Einstein atomic mobility in 1D atomic systems. Also we discuss atomic transport and separation of two-component mixture of atoms in a 1D system—a zeolite membrane with subnanometer channels.

These phenomena are described below using the response function method for nonequilibrium systems of arbitrary density [31]. This method allows us to calculate the dynamic response function and the spectrum of relaxation of density fluctuations of 1D atomic system. The spectrum contains diffusion and hydrodynamic modes. In the latter case, the relaxation of the system and the nuclear transport occurs through the distribution of density waves and not by the diffusion of particles. This relaxation mechanism becomes the determining by increasing the density that allows one to explain the abnormally high rate of atomic transport in subnanometer channels. The change of relaxation mechanism by increase of the density is associated with the observed non-Einstein character of mobility of atomic particles (the law for the mean square displacement  $x^2 = 2Dt$  is violated ( $D$  is the diffusion coefficient, and  $t$  is the time of observation) [32]). The found spectrum of relaxation allows to calculate the probability of decay of 1D free clusters of various lengths [30] and to explain the dependence of the stability of clusters of metal atoms on the chain atoms properties, the mechanical state of a cluster under the influence of an external force, and the number of particles in a stable cluster. These values were measured simultaneously in experiments [13].

The response function method was used to describe the practically important transport of two-component mixture in membranes with subnanometer channels.

It was shown that a phase transition in an inhomogeneous state may occur in 1D system of particles of two kinds with the increase of filling factor. Such a phase transition occurs due to an effective particle attraction and is characterised by the formation of clusters of a finite size [33]. The amplitude of the fluctuations in the density corresponding to the formation of such a state is the order parameter. An equation for the order parameter for a mixture of particles in the channels is derived. In contrast to the well-known phenomenological Landau-Ginzburg equation [34], the coefficients of the equation are calculated for a known interparticle interaction potential depending on the density and temperature. The analysis of this equation allows us to describe the observed increase in the separation factor with increasing flux through 1D channels at their closing by a stable clusters with a certain concentration of the components and determine the dependence of the separation on the concentration, temperature, and density.

## 2. Materials and Methods

**2.1. Molecular Transport in Subnanometer Channels.** Molecular transport in nanometer and subnanometer channels in porous bodies is currently drawing a great deal of interest

from the standpoint of fundamental science [35–39] and because of the many applications of membrane and nanotechnologies in various fields ranging from nuclear power to ecology [40, 41]. Polycrystalline ceramic membranes consisting of complex oxides (zeolites), possessing subnanometer channels ranging in diameter from 0.3 to 1.4 nm, have been synthesized recently [40]. On account of the high selectivity of molecular transport in zeolite membranes, as compared with the well-known polymeric membranes [41–43], new technologies for separation, reprocessing, and utilization of materials are being intensively developed on the basis of zeolite membranes [41–43].

When the channel diameters in membranes decrease to the nanometer scale, molecular transport is determined by the Knudsen flow in the central zone of the channel, free of interaction of molecules with walls, and particle diffusion in the surface force field [39]. In subnanometer channels, the interaction potentials between molecules and the opposite walls overlap, and molecular transport occurs under conditions of a constant interaction of molecules with a solid. Consequently, the diffusion coefficient in the limit of small filling numbers of a channel is determined by the relaxation of particles on phonons and surface defects [37]. For molecules, with the exception of light particles (H, He), the channel walls are impenetrable, and consequently molecular transport is possible only along the channel axes. In this sense, it is different from diffusion in solids and may be assumed to be one-dimensional. In contrast to surface diffusion in channels with diameter  $d > 1$  nm, a fundamentally new property of molecular transport should appear in subnanometer channels. As the filling factor of a channel or the diameter ( $\sigma$ ) of molecules increases, so that  $d < 2\sigma$ , each molecule can block the motion of two molecules. Consequently, it can be expected that as the diameter of the molecules or the external gas pressure increases, the molecular flux in membranes with subnanometer channels should decrease. However, experiments have shown that the diffusion flux of a number of molecules ( $\text{CH}_4$ ,  $\text{C}_2\text{H}_6$ , and others) in a ZSM-5 zeolite membrane with channel diameters 0.54–0.57 nm does not decrease but rather increases as the external gas pressure increases [43]. It has also been established that the diffusion coefficient for these gases increases by more than an order of magnitude as the filling factor of the channels with molecules increases. It has been found that for a number of gases, the temperature dependence of the flux possesses a maximum and a minimum.

In this section, the transport of a single-component molecular gas (system of atomic particles) in subnanometer-diameter channels is investigated theoretically.

**2.1.1. Sorption Isotherm in a 1D Channel.** Let us consider a surface in contact with an ideal single-component gas with temperature  $T$  and pressure  $p$ . Let us assume that particles located on the surface do not interact with one another. We will also assume that the energy of the gas molecules on the surface is  $\epsilon_0$ . Let there be  $N$  adsorption centers on the surface. Then the average number  $\bar{N}_1$  of particles adsorbed on

the surface as a function of the gas pressure and temperature has the form (Langmuir isotherm)

$$\begin{aligned} \frac{\bar{N}_1}{N} &= \frac{p}{p + p_0(T)}, \\ p_0(T) &\equiv T \left( \frac{\hbar^2}{2m\pi T} \right)^{-3/2} \exp(-\beta\epsilon_0), \end{aligned} \quad (1)$$

where  $m$  is the mass of a gas molecule,  $\hbar$  is Planck's constant, and  $\beta = T^{-1}$  is the reciprocal of the temperature. The method used to derive the Langmuir isotherms (1) admits wide extensions. Specifically, this method can be used to solve the problem of the filling factor of a cylindrical channel with diameter  $d$  taking into account the interparticle interaction in the channel. Let the channel diameter be comparable to the maximum diameter of a gas molecule. Let us consider the equilibrium of the gas with the surface on which  $k$  of the channels described previously emerge. Let  $\epsilon_1$  be the binding energy of a particle at the entrance to the channel. If the energy  $\epsilon_1$  is negative, then it is energetically favorable for the gas molecule to enter the channel. Let  $q$  be the total number of particles in a channel of length  $L$ ,  $n$  the total number of particles in the channel and on the surface, and  $N_0$  the number of settling locations in the channel. Then the partition function for the grand canonical ensemble, taking into account the interaction of the gas particles in the channel, is

$$\begin{aligned} \Theta &= \sum \frac{(N-k)! \exp[\beta\epsilon_0(N_1-n)]}{(N_1-n)!(N-k-(N_1-n))!} \\ &\times \frac{k! \exp[\beta\epsilon_1(n-q)]}{(n-q)!(k-(n-q))!} \\ &\times \frac{N_0! \exp(\beta\epsilon_2 q)}{q!(N_0-q)!} \exp(\beta\mu N_1) Z_{\text{int}}(q), \\ N_1 + q &= n. \end{aligned} \quad (2)$$

Here  $\epsilon_2$  is the binding energy of the particles in the channel and  $Z_{\text{int}}(q)$  is the partition function, corresponding to taking account of the interaction of the gas particles in the channel. Since  $Z_{\text{int}}$  depends on the number  $q$  of particles in the channel, it is impossible to calculate the partition function (2) in the grand canonical ensemble in the general case. However, in the problem of filling of a channel, the states for which the number of particles in the channel  $q \gg 1$  should make the main contribution to the partition function (2). Then the quantity  $Z_{\text{int}}(q)$  can be replaced by the partition function of interacting particles in the channel, calculated with the average number  $\bar{q}$  of particles in the channel:

$$Z_{\text{int}}(q) \approx Z_{\text{int}}(\bar{q}). \quad (3)$$

The approximation (3) corresponds to the thermodynamic limit ( $q \gg 1$ ) for gas (system of atomic particles) molecules located in the channel. Using the relation (3), the partition function (2) can be easily calculated. Using the condition for

equilibrium between the gas and the surface, we obtain for the average number  $\bar{q}$  of particles in the channel

$$\begin{aligned} \frac{\bar{q}}{N_0} &= \frac{p}{p + \bar{p}(T, \bar{q})}, \quad \bar{p}(\bar{q}, T) = \frac{\exp[-\beta\epsilon(\bar{q}, T)]}{\alpha(T)}, \\ (\alpha(T))^{-1} &= T \left( \frac{\hbar^2}{2m\pi T} \right)^{-3/2}, \quad \epsilon = \epsilon_1 - F_{\text{int}}(\bar{q}, T), \\ F_{\text{int}}(\bar{q}, T) &\equiv -T \ln Z_{\text{int}}(\bar{q}, T). \end{aligned} \quad (4)$$

Here  $F_{\text{int}}(\bar{q}, T)$  is the free energy of interaction per atomic particle in the channel. Instead of the number  $N_0$  of settling locations in the channel, it is convenient to introduce the average distance between settling locations in the channel ( $\eta = L/N_0$ ) and to replace  $\bar{q}$  by the filling factor  $\theta \equiv \bar{q}\sigma/L$  of particles in the channel. Then, we obtain from (4) an equation determining the pressure and temperature dependences of the filling factor  $\theta$  of the channel:

$$\frac{\eta\theta}{\sigma} = \frac{p}{p + \bar{p}(T, \theta)}. \quad (5)$$

The relations (4) show that the problem of obtaining the equation for the adsorption  $\theta(p, T)$ , determining the filling factor at various pressures and temperatures of the gas above the surface, reduces to calculating the quantity  $F_{\text{int}}(\theta, T) \equiv -T \ln Z_{\text{int}}(\theta, T)$ , determining the "correction" to the pressure as a result of the interaction of the particles in the channel. Thus, to obtain the adsorption isotherms in the system under study, it is necessary to calculate the total free energy of the particles in a subnanometer channel taking into account their interaction with the channel wall and with one another. For this, we will consider  $N$  particles in a channel whose size is comparable to the average particle diameter. In the general case, the total potential energy of such a system can be written as

$$E(\mathbf{r}_1, \dots, \mathbf{r}_N) = \sum_{i,j=1}^N V(\mathbf{r}_i - \mathbf{r}_j) + \sum_{i=1}^N U(\mathbf{r}_i). \quad (6)$$

Here  $V(\mathbf{r}_i - \mathbf{r}_j)$  is the potential energy of the pair interaction of the particles located at points with coordinates  $\mathbf{r}_i$  and  $\mathbf{r}_j$ ;  $U(\mathbf{r}_i)$  is the interaction energy between a particle located at the point  $\mathbf{r}_i$  and the channel walls. We will transform the expression for the pair interaction potential of the particles using the fact that the channel diameter is comparable to the particle diameter. Then the interaction potential depends only on the particle coordinates along the channel  $r$ . We write the expression for  $V(\mathbf{r}_i - \mathbf{r}_j)$  in the form

$$\begin{aligned} V(\mathbf{r}_i - \mathbf{r}_j) &\equiv V(x_i - x_j, y_i - y_j, r_i - r_j) \\ &\approx V(r_i - r_j, 0, 0) \equiv \Phi(r_i - r_j). \end{aligned} \quad (7)$$

This relation holds when the channel diameter is comparable to the particle diameter, and the pair interaction potential  $V(\mathbf{r}_i - \mathbf{r}_j)$  of the particles is not a long-range potential.

It is convenient to represent the interaction energy between a particle and the channel walls in the form

$$U(\mathbf{r}_i) = U(\mathbf{r}'_i, r_i). \quad (8)$$

Here  $\mathbf{r}'_i$  is a dimensionless two-dimensional radius vector in a plane perpendicular to the channel. It is convenient to write the partition function of such a system in the form

$$Z_N \propto \int d\mathbf{r}'_1 \cdots d\mathbf{r}'_N dz_1 \cdots dz_N \exp(-\beta U_N) \times \exp\left[-\beta \sum_{i=1}^N U(\mathbf{r}'_i, r_i)\right]. \quad (9)$$

Here

$$U_N = \sum_{1 \leq i, j \leq N} \Phi(r_i - r_j). \quad (10)$$

The integration over the particle coordinates in a plane perpendicular to the channel can be performed exactly:

$$\begin{aligned} & \int d\mathbf{r}'_1 \cdots d\mathbf{r}'_N \exp\left[-\beta \sum_{i=1}^N U(\mathbf{r}'_i, r_i)\right] \\ &= \int d\mathbf{r}'_1 \exp[-\beta U(\mathbf{r}'_1, r_1)] \int d\mathbf{r}'_2 \exp[-\beta U(\mathbf{r}'_2, r_2)] \\ & \quad \times \cdots \times \int d\mathbf{r}'_N \exp[-\beta U(\mathbf{r}'_N, r_N)] \\ &\equiv \exp\left[-\beta \sum_{i=1}^N \Psi(r_i)\right]. \end{aligned} \quad (11)$$

Here  $\Psi(r_i)$  is the effective potential in which a particle moves in the channel as a result of the interaction of the particle with the walls:

$$\exp[-\beta \Psi(r)] \equiv \int \exp[-\beta U(\mathbf{r}', r)] d\mathbf{r}'. \quad (12)$$

Let us assume that the energy of a gas molecule interacting with the channel surface is constant and equal to  $\varepsilon_1 = \Psi(r_{\min}) = \Psi(0)$ . Then

$$Z'_N \propto \exp(-\beta N \varepsilon_2) \int dr_1 \cdots dr_N \exp(-\beta U_N). \quad (13)$$

The energy  $\varepsilon_1$  physically corresponds to the binding energy of a particle in the surface potential  $\Psi(r)$ . Thus, under the assumptions made previously, the gas in the channel can be assumed to be one-dimensional (the channel diameter is comparable to the maximum diameter of an atomic particle). It is well known [44, 45] that the partition function of a one-dimensional gas with an arbitrary interaction potential can be calculated exactly under certain assumptions, which are formulated in the following. Indeed, let us consider an equilibrium system of  $N$  particles in a channel which possesses only one degree of freedom per particle that are

located in the segment  $[0, L]$  of the  $r$  axis. The total partition function of the system has the form

$$\tilde{Z}_N = \left(\frac{mT}{2\pi\hbar^2}\right) \frac{Q_N}{N!} \exp(-\beta N \varepsilon_1), \quad (14)$$

where

$$\begin{aligned} Q_N &= \int_0^L \cdots \int_0^L \exp(-\beta U_N) dr_1 \cdots dr_N \\ U_N &= \sum_{1 \leq y \leq N-1} \Phi(r_{y+1} - r_y). \end{aligned} \quad (15)$$

Here  $\Phi(r)$  is the pair interaction potential of the particles in the channel. To calculate  $F_{\text{int}}$ , the cofactor responsible for the partition function of an ideal gas must be eliminated from the partition function (14). In our problem, the cofactor corresponding to a gas of particles in a channel without a pair interaction potential between the particles is already included in the expression (2). Thus, since the partition function of a one-dimensional gas without an interaction has the form

$$Z_{\text{int}} = \left(\frac{mT}{2\pi\hbar^2}\right)^{N/2} \frac{L^N}{N!} \exp(-\beta N \varepsilon_2), \quad (16)$$

we obtain from (2)

$$F_{\text{int}} = -T \frac{\ln \tilde{Z}_N(\theta, T)}{Z_{\text{id}}} = -T \ln \left(\frac{Q_N}{L^N}\right). \quad (17)$$

Thus, the problem has been reduced to calculating the configuration integral

$$\begin{aligned} Q_N &= \int \cdots \int \exp[-\beta \{\Phi(\xi_1) + \Phi(\xi_2) \\ & \quad + \cdots + \Phi(\xi_N)\}] d\xi_1 \cdots d\xi_N, \quad (18) \\ \xi_i &\equiv r_{i+1} - r_i. \end{aligned}$$

In studying the configuration space of a system of particles in a one-dimensional channel, it should be kept in mind that the quantities  $\xi_i$  are not independent. They are related as

$$\sum_{j=1}^N \xi_j = L, \quad (19)$$

where  $L$  is the total length of the channel. Physically, this relation corresponds to the impossibility of particles penetrating one another and the condition of "blocking" of particles with diameter  $\sigma$  in a channel whose diameter  $d < 2\sigma$ . An explicit expression for the configuration integral can be obtained if the explicit form of the pair interaction potential of the particles is known. We will consider a simple but nontrivial case: a system of hard spheres with diameter  $\sigma$ . The expression for the interatomic interaction energy in this case is

$$\Phi_i(\xi) = \begin{cases} \infty & \text{for } \xi < \sigma, \\ 0 & \text{for } \xi \geq \sigma. \end{cases} \quad (20)$$

We obtain for  $F_{\text{int}}$  in the hard-sphere approximation

$$F_{\text{int}}(\theta, T) = -T \ln(1 - \theta). \quad (21)$$

Thus, in the hard-sphere approximation, the adsorption isotherm for a gas in a subnanometer channel has the form

$$\frac{\eta\theta}{\sigma} = \frac{(1 - \theta)p}{(1 - \theta)p + \tilde{p}_0(T)}, \quad (22)$$

$$\tilde{p}_0(T) \equiv T \left( \frac{\hbar^2}{2\pi m T} \right)^{-3/2} \exp(-\beta\epsilon_1).$$

The relation (22) makes it possible to construct the dependence of the filling factor on the gas pressure for various molecules. It should be kept in mind that the sign of the energy  $\epsilon_1$  determines the possibility or impossibility of a particle entering a channel: for  $\epsilon_1 > 0$ , it is energetically favorable for a gas particle to enter the channel for any external pressure greater than  $p_0$ . For  $\epsilon_1 < 0$ , the particles must overcome a potential barrier to enter the channel. The configuration integral can be calculated exactly for an arbitrary interaction between the particles in the channels [45]. This makes it possible to obtain an equation of state of a 1D gas for an arbitrary interaction. Thus, for an interparticle interaction potential of the form

$$\Phi(z) = \begin{cases} +\infty & \text{for } r \leq \sigma, \\ -\epsilon & \text{for } \sigma < r \leq \sigma + R, \\ 0 & \text{for } r < R + \sigma, \end{cases} \quad (23)$$

where  $r$  is the effective radius of attraction, the equation of state of a one-dimensional gas is

$$p_{1D}\sigma \left( \frac{1}{\theta} - 1 \right) = T - p_{1D}R \left[ \frac{\exp(\beta p_{1D}R)}{1 - \exp(-\beta\epsilon)} - 1 \right]^{-1}. \quad (24)$$

In the limits  $\epsilon \rightarrow 0$  and  $R \rightarrow 0$ , this equation becomes the equation of state of a system of hard spheres. The isotherms calculated numerically starting from (24) are presented in Figure 1. It is also evident in this figure that at high temperatures the gas behaves almost as an ideal gas ( $p_{1D} \propto \theta$ ). At low temperatures the isotherms seem to consist of two parts. For high density  $\theta \approx \text{const}$ , which is typical for a condensed phase, whereas at pressure less than a characteristic value a gas-like phase for which  $p_{1D} \propto \theta$  appears.

It can be shown that at a transition from one regime to another, the free energy of the system has no singularities. For this reason, there is no exact analogy with phase transitions. This assertion agrees completely with the Landau-van Hove Theorem [44], according to which any one-dimensional model of a gas with a finite interaction radius does not undergo phase transitions. On the other hand, it should be expected that for sufficiently low temperatures, as the filling factor  $\theta$  increases, the gas in the channel tends to form clusters whose size increases with the filling factor. The number and size of the clusters grow with the total number of particles in the system in a manner so as to ensure the existence

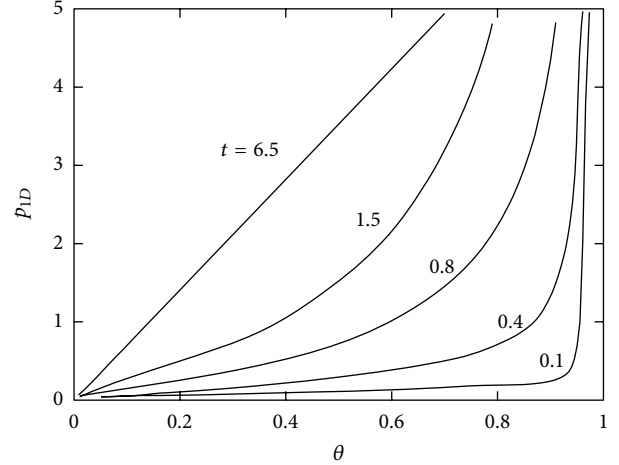


FIGURE 1: Reduced “pressure” ( $p_{1D}$ ) (24) of a one-dimensional gas in a channel versus the filling factor ( $\theta$ ) of the channel at various temperatures  $t = T/T_0$ .

of such clusters in the thermodynamic limit, where  $N \rightarrow \infty$ ,  $L \rightarrow \infty$ , and  $N/L = \text{const}$ . This agrees completely with the formation of nuclei of a new phase in three-dimensional systems with first-order phase transitions [34, 46]. On the other hand, in our one-dimensional system, in contrast to three-dimensional systems, a continuous behavior of thermodynamic quantities determined as derivatives of the free energy of the system with respect to the temperature, pressure, and filling factor should be expected in the entire range of variation of the thermodynamic parameters. For example, the specific heat calculated using the relation (24) will possess a maximum at the “critical” point. This fact has been observed experimentally [35], which attests to the applicability of the one-dimensional model employed previously.

**2.1.2. Transport in a Dense 1D System.** The gas flux through a membrane is the main experimentally measurable parameter (Section 2.1.3). Particle transport is usually described using a relation between the outgoing particle flux and the parameters of the problem, such as, for example, the difference of the gas pressures on different sides of the membrane. This description is based on Fick’s relation between the gas flux density  $\mathbf{J}$ , the gradient of the gas concentration, and the diffusion coefficient  $\tilde{D}$ , using the conservation law for the number of particles:

$$\mathbf{J} = -\tilde{D}\nabla n, \quad (25)$$

$$\frac{\partial n}{\partial t} + \text{div } \mathbf{J} = 0. \quad (26)$$

In the relations (25) and (26),  $\mathbf{J}$  is the flux,  $\tilde{D}$  is the diffusion coefficient, and  $\nabla n$  is the gradient of the particle concentration. The relation (25) is actually a definition of the diffusion coefficient  $\tilde{D}$ . Thus, the problem of determining the particle flux through a channel reduces to calculating the diffusion coefficient. A more general method of describing

transport is to calculate the characteristic relaxation time of density fluctuations arising or specially created in the system under study [47]. Formally, the problem of determining this time reduces to calculating the characteristic frequency or spectrum  $\omega(\mathbf{k})$  for the system under study. Thus, when the particle density is low and there is no interparticle interaction, an explicit expression for the spectrum  $\omega(\mathbf{k})$  can be easily obtained from the relation (25). Indeed, let  $n_0$  be the average particle concentration in the system. From (25), we obtain an equation determining the dynamics of the density fluctuations  $\delta n(\mathbf{r}, t) = n - n_0$ :

$$\frac{\partial (\delta n)}{\partial t} = \bar{D} \Delta (\delta n). \quad (27)$$

Switching to a Fourier representation of the density fluctuations

$$\delta n(\mathbf{r}, t) = \frac{1}{(2\pi)^4} \int d\mathbf{k} d\omega \exp(-i\mathbf{k} \cdot \mathbf{r} - i\omega t) \delta n(\mathbf{k}, \omega), \quad (28)$$

we obtain an expression determining the reciprocal of the relaxation time of the density fluctuations  $\delta n$  in the case at hand:

$$\omega_0(\mathbf{k}) = -i \bar{D} k^2. \quad (29)$$

It is obvious that a spectrum of this type is characteristic for systems where relaxation to equilibrium occurs by diffusion. Let us consider a system of interacting particles with arbitrary density. Assume that we have been able to calculate the characteristic relaxation time  $\omega^{-1}$  of density fluctuations in the system. If the spectrum of relaxation times in such a system has the form

$$\omega(\mathbf{k}) = -iD(\mathbf{k}, n_0) k^2, \quad (30)$$

then it is natural to consider the quantity  $D(\mathbf{k}, n_0)$  to be the diffusion coefficient in the system, provided that in the limit of low densities  $n_0$  the quantity  $D(\mathbf{k}, n_0)$  becomes the diffusion coefficient for a low-density system of particles:

$$\lim_{n_0 \rightarrow 0} D(\mathbf{k}, n_0) = \bar{D}. \quad (31)$$

This definition of the diffusion coefficient means that the system possesses a diffusion characteristic mode. Proceeding from the definition (30), to calculate the diffusion coefficient  $D(\mathbf{k}, n_0)$ , it is necessary to know the characteristic modes of a weakly nonequilibrium system. If these characteristic modes have the form (30), then  $D(\mathbf{k}, n_0)$  will be the diffusion coefficient of the system. It is obvious that the diffusion coefficient in the general case is nonlocal and is a functional of the density of the diffusing particles. The expression for the flux of diffusing particles will have a form generalizing equation (25):

$$\mathbf{J} = - \int d\mathbf{r}' D(\mathbf{r}, \mathbf{r}', n(\mathbf{r}', t)) \nabla n(\mathbf{r}', t). \quad (32)$$

The equation, obtained using this relation, for the particle number density in the system is in general a nonlinear

integrodifferential equation. When studying the diffusion of a single-component gas in subnanometer channels, it should be kept in mind that the pair interaction potential between the particles is of short range, and no phase transitions occur in the system of particles in the channel (see the preceding section). In this case, it can be assumed that the diffusion coefficient  $D(\mathbf{r}, \mathbf{r}', n(\mathbf{r}, t))$  is local:

$$D(\mathbf{r}, \mathbf{r}', n(\mathbf{r}, t)) = D(n(\mathbf{r}, t)) \delta(\mathbf{r} - \mathbf{r}'). \quad (33)$$

The corresponding expression for the flux of diffusing particles and the equation for their density become

$$\begin{aligned} \mathbf{J} &= -D(n) \nabla n, \\ \frac{\partial n}{\partial t} &= \nabla (D(n) \nabla n). \end{aligned} \quad (34)$$

For low densities, the relation (34) becomes (25), which is the first term in the expansion of the flux in odd powers of the density gradient. Thus, for systems where the relaxation spectrum of the fluctuations is of the form (30), the diffusion coefficient can be determined starting from the explicit form of this spectrum. The expression obtained for the diffusion coefficient in this case is a generalization of the expressions obtained for the diffusion coefficient in various models, specifically, in the Maxwell-Stefan model [43].

It is convenient to calculate the relaxation spectrum using the response functions [31, 48, 49]. Let us formulate the basis of this formalism. Consider the system of the atomic particles, which can interact with each other as well as the environment such as liquid, solid, or surface. Let us show, following [49], that many-particles distribution functions of such a system are the density functionals. Assume that each particle at the coordinate  $\mathbf{r}$  interacts with time-dependent external field  $v(\mathbf{r}, t)$ . In order to describe such a system, one can use Liouville equation for many-particle distribution function  $F(x_1, x_2, \dots, x_N, t)$ , where  $x_i = (\mathbf{r}_i, \mathbf{p}_i)$  are the coordinates and th momentum of the particles. Solving the Liouville equation with the fixed initial distribution function and for the different external potentials  $V(\mathbf{r}_1, \mathbf{r}_2, \dots, t) = \sum_i v(\mathbf{r}_i, t)$ , one can obtain one-to-one conformance between  $F(x_1, x_2, \dots, x_N, t)$  and  $V(\mathbf{r}_1, \mathbf{r}_2, \dots, t)$ . On the other hand, introducing the density of the particles

$$n(\mathbf{r}, t) = \int d\Gamma \hat{n} F(x_1, x_2, \dots, x_N, t), \quad (35)$$

where  $d\Gamma$  is the phase space element, and  $\hat{n}$  is the density operator, one can obtain one-to-one conformance between the external field  $V(\mathbf{r}_1, \mathbf{r}_2, \dots, t)$  and the density  $n(\mathbf{r}, t)$ . From this it directly follows that many-particles distribution functions are density functionals:

$$F(x_1, x_2, \dots, x_N, t) = F(x_1, x_2, \dots, x_N, t, [n]). \quad (36)$$

Following [49], let us write the action for the Liouville equation in the form

$$S = \frac{1}{t_2 - t_1} \int_{t_1}^{t_2} dt \int d\Gamma L F, \quad (37)$$

where  $L$  is the Lagrangian of the system, which is equal to the difference between the kinetic and potential energy of the particles. It follows from (36) and (37) that the action  $S$  is the density functional:

$$S = \Delta[n] = \frac{1}{t_2 - t_1} \int_{t_1}^{t_2} dt \int d\Gamma LF(x_1, x_2, \dots, x_N, t, [n]). \quad (38)$$

Functional  $\Delta[n]$  has an extrema for the equilibrium state of the system [48, 49]. Due to the linearity of the (38) by the potential energy, system of the particles interacting with the external field  $v(\mathbf{r}, t)$  corresponds to the functional  $\Delta[n, v]$ , which can be expressed as

$$\Delta[n, v] = \Delta[n] + \frac{1}{t_2 - t_1} \int_{t_1}^{t_2} v(\mathbf{r}, t) n(\mathbf{r}, t) d\mathbf{r} dt. \quad (39)$$

Functional (39) has an extrema for the stationary or quasi-stationary  $n(\mathbf{r}, t) = n_0(\mathbf{r}, t) \equiv n^{(0)}$  state of the system [48, 49]

$$\left. \frac{\delta \Delta[n]}{\delta n} \right|_{n=n^{(0)}} = 0 \quad (40)$$

and represents the time average of the free energy functional  $F[n(\mathbf{r}, t), t]$ :

$$\Delta[n] = \tau^{-1} \int_0^\tau F[n(\mathbf{r}, t), t] dt. \quad (41)$$

The functional  $\Delta[n]$  was for the first time introduced in such a form in the papers [31, 48]. Equation (40) determines the density of the atomic particles  $n(\mathbf{r}, t)$ . Let us express the free energy using the response functions defined as follows. Consider the system in the external field  $ev_{\text{ext}}(\mathbf{r}, t)$  ( $e$  - external field amplitude). The response function  $\beta(\mathbf{r}, \mathbf{r}', t, t')$  of such a system couples the density fluctuation  $\delta n(\mathbf{r}, t)$  with the external field  $ev_{\text{ext}}(\mathbf{r}, t)$ , which generate this fluctuation [31, 48] at  $e \rightarrow 0$ :

$$\delta n(\mathbf{r}, t) = \int d\mathbf{r}' dt' \beta(\mathbf{r}, \mathbf{r}', t, t') ev_{\text{ext}}(\mathbf{r}', t') \Big|_{e \rightarrow 0}. \quad (42)$$

It is obvious that in the case of the linear response and  $e \rightarrow 0$ , the response function  $\beta(\mathbf{r}, \mathbf{r}', t, t')$  is independent on  $e$ . Let us rewrite the definition (42) in the operator form

$$\delta n = ev_{\text{ext}} \beta. \quad (43)$$

Such a form (43) will be used further in the paper. In the presence of the external field, the functional  $\Delta[n, v]$  at  $e \rightarrow 0$  is determined by the relation (39):

$$\Delta[n, ev_{\text{ext}}] = \Delta[n] + \frac{1}{t_2 - t_1} \int_{t_1}^{t_2} ev_{\text{ext}}(\mathbf{r}, t) n(\mathbf{r}, t) d\mathbf{r} dt. \quad (44)$$

Here  $\Delta[n]$  is the functional at  $e = 0$ , determined by the formula (38). In order to obtain linear response function, let us use the relation (39). One can rewrite the solution of the (39) at  $e \rightarrow 0$  with the sum  $n(\mathbf{r}, t) = n^{(0)}(\mathbf{r}, t) + \delta n(\mathbf{r}, t)$ . In

this case, one can obtain, in the first order and with respect to (39),

$$\left. \frac{\delta \Delta[n]}{\delta n} \right|_{n=n^{(0)}} + \left. \frac{\delta^2 \Delta[n]}{\delta n^2} \right|_{n=n^{(0)}} \delta n + ev_{\text{ext}} = 0 \quad (45)$$

or

$$-\left( \left. \frac{\delta^2 \Delta[n]}{\delta n^2} \right|_{n=n^{(0)}} \right)^{-1} ev_{\text{ext}} = \delta n. \quad (46)$$

At  $e \rightarrow 0$ , the quantity

$$\left. \frac{\delta^2 \Delta[n]}{\delta n^2} \right|_{n=n^{(0)}} \equiv \frac{\delta^2 \Delta}{\delta n(\mathbf{r}, t) \delta n(\mathbf{r}', t')} \quad (47)$$

is independent on  $e$ . Comparison of the relations (43) and (46) gives the following form of the response function  $\beta(\mathbf{r}, \mathbf{r}', t, t')$ :

$$\begin{aligned} \beta(\mathbf{r}, \mathbf{r}', t, t') &= -\left( \left. \frac{\delta^2 \Delta[n]}{\delta n^2} \right|_{n=n^{(0)}} \right)^{-1} \\ &= -\left( \frac{\delta^2 \Delta}{\delta n(\mathbf{r}, t) \delta n(\mathbf{r}', t')} \right)^{-1}. \end{aligned} \quad (48)$$

It follows from the functional  $\Delta[n]$  definition that it can be expressed as

$$\Delta[n] = \Delta_0[n] + \Delta_{\text{int}}[n]. \quad (49)$$

Here  $\Delta_0[n]$  corresponds to the functional of the particles without their interaction with each other, and  $\Delta_{\text{int}}[n]$  corresponds to the functional (38), which represents particle-particle interactions. Two times variation of the (49), with respect to (48), gives the following:

$$-\beta^{-1} = -\beta_0^{-1} + R, \quad (50)$$

where

$$\beta_0^{-1}(\mathbf{r}, \mathbf{r}', t, t') = -\left. \frac{\delta^2 \Delta_0[n]}{\delta n^2} \right|_{n=n^{(0)}} = -\frac{\delta^2 \Delta_0}{\delta n(\mathbf{r}, t) \delta n(\mathbf{r}', t')} \quad (51)$$

is the response function of the noninteracting particles

$$R(\mathbf{r}, \mathbf{r}', t, t') = -\left. \frac{\delta^2 \Delta_{\text{int}}[n]}{\delta n^2} \right|_{n=n^{(0)}} = -\frac{\delta^2 \Delta_{\text{int}}}{\delta n(\mathbf{r}, t) \delta n(\mathbf{r}', t')}. \quad (52)$$

It is shown in the paper [31, 48] that the function  $R(\mathbf{r}, \mathbf{r}', t, t')$  is connected to the effective lagged interaction between the particles. Multiplying the relation (45) on the  $\beta$  in the left and on the  $\beta_0$  in the right, one can obtain the equation on the response function. In the case of the homogeneous quasi-stationary state of the atomic system, the functions  $\beta_0(\mathbf{r}, \mathbf{r}', t, t')$ ,  $\beta(\mathbf{r}, \mathbf{r}', t, t')$  и  $R(\mathbf{r}, \mathbf{r}', t, t')$  depend only on the differences  $\mathbf{r} - \mathbf{r}'$  и  $t - t'$ , so (50) can be rewritten as

$$\beta(\mathbf{k}, \omega) = \beta_0(\mathbf{k}, \omega) + \beta_0(\mathbf{k}, \omega) R(\mathbf{k}, \omega) \beta(\mathbf{k}, \omega), \quad (53)$$

where  $\beta(\mathbf{k}, \omega)$ ,  $\beta_0(\mathbf{k}, \omega)$  и  $R(\mathbf{k}, \omega)$  are the Fourier transform of the response functions  $\beta(\mathbf{r} - \mathbf{r}', t - t')$ ,  $\beta_0(\mathbf{r} - \mathbf{r}', t - t')$ , and  $R(\mathbf{r} - \mathbf{r}', t - t')$ , respectively; for example,

$$\beta_0(\mathbf{r} - \mathbf{r}', t - t') = \int d\mathbf{k} d\omega e^{-i\omega(t-t') + i\mathbf{k}(\mathbf{r}-\mathbf{r}')} \beta_0(\mathbf{k}, \omega). \quad (54)$$

Equation (53) allows us (when the  $R$  function is known) to determine the response function of the system of interacting particles and relaxation spectrum of the system [31, 48].

In order to determine the relaxation spectrum, let us note, that the expression  $\beta^{-1}\delta n = ev_{\text{ext}}$  follows directly from (43). Due to the response function definition (as the response of the system on the arbitrary small external field), one can write  $\beta^{-1}\delta n = 0$ . This equation has the nontrivial solutions  $\delta n \neq 0$  only if  $\beta^{-1} = 0$ . So, we can write that the relaxation spectrum of the system  $\omega(\mathbf{k})$  is determined by the relation [31, 48]

$$\beta^{-1}(\mathbf{k}, \omega) = 0. \quad (55)$$

We will use the response function formalism to calculate the response function and the diffusion coefficient of a dense system of atomic particles in a subnanometer channel. We will calculate first the response function  $\beta_0(k, \omega)$  and the relaxation spectrum of such a gas when there is no interaction between the particles. We write the diffusion equation for the filling factor  $\theta$  of the channel with molecules in the presence of a weak perturbing external field  $ev_{\text{ext}}(x, t)$  in the form

$$\frac{\partial \theta}{\partial t} = D_0 \nabla \left( \nabla \theta + \frac{\theta}{T} \nabla ev_{\text{ext}} \right), \quad \nabla \equiv \frac{\partial}{\partial x}. \quad (56)$$

Here  $D_0$  is the diffusion coefficient for noninteracting particles. Let  $\theta_0$  be the equilibrium filling factor of the channel. We will seek the solution of (56) in the form

$$\theta = \theta_0 + \delta\theta(x, t). \quad (57)$$

Then, we obtain from (56), assuming the external field  $e_{\text{ext}}$  to be weak, an equation for  $\delta\theta(r, t)$ :

$$\frac{\partial \delta\theta}{\partial t} = D_0 \Delta \delta\theta + \frac{D_0 \theta_0 \Delta ev_{\text{ext}}}{T}. \quad (58)$$

In deriving (58), only first-order infinitesimals in  $\delta\theta$  and  $ev_{\text{ext}}$  were retained in all terms. We will seek the solution of (58) in the form of a Fourier integral

$$\begin{aligned} \delta\theta(x, t) &= \frac{1}{(2\pi)^2} \int e^{ikx} e^{i\omega t} \delta\theta(k, \omega) dk d\omega, \\ ev_{\text{ext}}(x, t) &= \frac{1}{(2\pi)^2} \int e^{ikx} e^{i\omega t} ev_{\text{ext}}(k, \omega) dk d\omega. \end{aligned} \quad (59)$$

Substituting the expressions (59) into (58) and solving the resulting linear equation for  $\delta\theta(k, \omega)$ , we obtain

$$\delta\theta(k, \omega) = \beta_0(k, \omega) ev_{\text{ext}}(k, \omega). \quad (60)$$

Here

$$\beta_0(k, \omega) = -\frac{\theta_0 k^2 D}{T(i\omega + k^2 D_0)} \quad (61)$$

is the response function of a gas of noninteracting diffusing particles. Indeed, as  $\omega \rightarrow 0$ , the function  $\beta_0(k, \omega)$  reduces to the well-known response function of an ideal equilibrium gas with density  $\theta_0$  at temperature  $T$  [38, 47]:

$$\beta_0(k, 0) = -\frac{\theta_0}{T}. \quad (62)$$

The relaxation spectrum of such a gas is determined from the relation (55) and has the form

$$\omega_0(k) = -iD_0 k^2. \quad (63)$$

In accordance with the definition (26), the quantity  $D_0$  is the diffusion coefficient. The relations obtained make it possible to calculate the relaxation spectrum  $\omega(k)$  by solving (54). Thus, we find for the response function of a one-dimensional system

$$\beta(k, \omega) = \frac{\beta_0(k, \omega)}{1 - \beta_0(k, \omega) R(k, \omega)}. \quad (64)$$

Using the relations (61) and (64), we obtain an equation determining the relaxation spectrum of the system under study:

$$1 + \frac{\theta_0}{T} \frac{\omega_0}{\omega + \omega_0} R(k, \omega) = 0. \quad (65)$$

Equation (65) can be solved in a general form in the quasistatic case  $\omega \rightarrow 0$ . Indeed, in this case, we find from (65)

$$\omega(k) = -iD(\theta_0, k) k^2, \quad (66)$$

$$D(\theta_0, k) = D_0 \left[ 1 + \frac{\theta_0}{T} R(k, 0) \right]. \quad (67)$$

It is convenient to rewrite the relation (67), introducing the pair distribution function  $n_2(x - x') = \theta_0^2 [1 + \nu(x - x')]$ :

$$T\beta(k, 0) = -\theta_0 (1 + \theta_0 \nu(k)). \quad (68)$$

Then we obtain from relations (53) and (61)

$$R(k, 0) = -\frac{T\nu(k)}{1 + \theta_0 \nu(k)}. \quad (69)$$

Substituting the expression (69) into (67) gives a relation determining the relaxation spectrum of a dense gas in a one-dimensional channel:

$$\omega(k) = -\frac{iD_0 k^2}{1 + \theta_0 \nu(k)}. \quad (70)$$

We will now calculate the diffusion coefficient of a gas in a one-dimensional channel taking into account the interaction between hard-sphere particles. In this case, the correlation function  $n_2(x) = \theta_0^2 [1 + \nu(x)]$  has been calculated exactly [45] with an arbitrary filling factor of the channel:

$$\begin{aligned} n_2(x) &= \begin{cases} 0, & r < \sigma, \\ \frac{1}{\theta_0} \sum_m \frac{(x\sigma^{-1} - m)^{m-1}}{(m-1)!(\theta_0^{-1} - 1)^m} \exp\left(-\frac{x\sigma^{-1} - m}{\theta_0^{-1} - 1}\right), & x > \sigma. \end{cases} \end{aligned} \quad (71)$$

Using the relations (70) and (71), we find

$$\begin{aligned}\omega(k) &= -iD(\theta_0)k^2, \\ D(\theta_0) &= D_0 \left( \frac{1}{(1-\theta_0)^2} \right).\end{aligned}\quad (72)$$

It follows from (72) that the general equation describing particle transport in a dense 1D system, in accordance with (34), has the form

$$\frac{\partial \theta}{\partial t} = \frac{\partial}{\partial x} \left[ D_0 \left( \frac{1}{(1-\theta_0)^2} \right) \frac{\partial \theta}{\partial x} \right]. \quad (73)$$

This equation can be obtained from (72) if the characteristic local equilibration times in a dense system of particles in a channel are short compared with the characteristic propagation times of disturbances along such a system. For the cases considered in the following, this assumption obviously holds. We will consider solutions of (73) in the case where complete equilibrium has been established in the channel and the filling factor  $\theta = \theta_0(p, T)$ , with the function  $\theta_0(p, T)$  being determined by the relation (23). Transport in a channel in this case will be determined by the dynamics of the motion of disturbances of the filling factor. The solution of (73) in this case should be sought in the form  $\theta = \theta_0(p, T) + \delta\theta(x, t)$ . It follows from (73) that the relaxation spectrum of disturbances in this case has the form (72), where  $\theta = \theta_0(p, T)$ . Thus, taking account of the interaction of hard-sphere particles in a channel does not change the character of the relaxation of its weakly nonequilibrium state: the relaxation spectrum (72) remains a diffusion spectrum with diffusion coefficient  $D(\theta_0)$ . However, it is important to underscore that transport in the channel in this case is a collective effect and proceeds via transport of disturbances of the equilibrium density  $\theta_0(p, T)$ . The diffusion coefficient  $D(\theta_0)$  in this case is the diffusion coefficient of disturbances of the equilibrium density. It is convenient to rewrite the relation (72) for the diffusion coefficient in a different form. Using the Arrhenius character of the diffusion coefficient for noninteracting particles

$$D_0 = \tilde{D}_0 \exp\left(-\frac{E}{T}\right) \quad (74)$$

( $\tilde{D}_0$  is proportional to the product of the squared lattice constant of the wall material of the channel and the relaxation frequency of particles in a channel on defects and lattice phonons and is calculated in [37], and  $E \approx \Psi(r_{\max})$  (13) is the activation energy of diffusing of noninteracting particles in the channel), we will rewrite (72) in the form

$$\begin{aligned}D(\theta_0) &= \tilde{D}_0 \exp\left(-\frac{\tilde{E}(\theta_0)}{T}\right), \\ \tilde{E}(\theta_0) &\equiv E - T \ln\left(\frac{1}{(1-\theta_0)^2}\right).\end{aligned}\quad (75)$$

This way of writing the diffusion coefficient for a gas of interacting particles in a channel makes it possible to give

a physical interpretation for the change in the diffusion coefficient accompanying a change in the filling factor  $\theta_0$ . The relation (75) shows that the interaction of particles in a channel decreases the activation energy  $E$  of the motion of particles, even in the hard-sphere model. For an interaction between hard-sphere particles such that there is no direct attraction between the particles, the diffusion activation energy decreases with increasing filling factor  $\theta_0$  as a result of the effective interaction (see the following). Physically, this corresponds to a change because of the presence of another particle in a neighboring potential well, in the parameters of the potential in which a gas particle moves. Since the gas particles are assumed to be indistinguishable, diffusion with the filling factor  $\theta_0 \sim 1$  (when the effective diffusion activation energy  $\tilde{E}(\theta_0)$  becomes comparable to the temperature of the system) can be interpreted as a transfer of “excitation” of the density along a chain of close gas particles. It is obvious that the motion of such an “excitation” will occur with substantial velocities. This leads to a large increase in the diffusion coefficient when  $\theta_0 \sim 1$ . For  $E = 0$ , the possibility of such a diffusion mechanism is played out in [36]. We note that for all gases investigated, the barrier  $E$  is different from 0. This is indicated by the presence of a maximum in the temperature dependence of the flux in a zeolite membrane [43]. It can be assumed that the increase in the diffusion coefficient in a channel observed with filling factors  $\theta_0 \geq 0.5$  is related to the formation of clusters in the channel whose sizes increase with the filling factor. The transport of gas in the channel containing such clusters is determined by the motion of “excitation” in a finite-size cluster. The formation of clusters in a gas consisting of particles with a hard-sphere pair interaction potential is related to the well-known [46] appearance of an effective attraction between such particles. This effect is manifested in the appearance of a maximum in the correlation function  $n_2(x)$ , describing the probability of finding the “first” particle at a distance  $x$  from the “second” particle.

The relaxation spectra of the system for an arbitrary wave vector  $k$  can be found from (70) and (71). It is found that the spectrum  $\omega(k)$  contains a real part, which corresponds to transport of an “excitation” in the system. The imaginary part of the spectrum obtained has a minimum at a definite value of the wave vector  $k = k_{\min}$ , which depends on the filling factor  $\theta_0$ . It is natural to interpret the value  $R = 2\pi/k_{\min}(\theta_0)$  as the characteristic size of a cluster with a given filling factor and the value  $\tau = \text{Im} \omega^{-1}(k_{\min}(\theta_0))$  as its characteristic lifetime. As the filling factor increases, the value of the effective attraction between the particles increases [46]; this could lead to the appearance of clusters consisting of two or more particles. However, it is found that as a result of the one-dimensionality of the channel, the lifetime of the clusters that are formed is finite, which corresponds to the absence, as noted previously, of a phase transition in such systems. The dependences of the lifetime and size of the clusters formed on the filling factor  $\theta_0$  are presented in Figure 2.

It is evident in the figure that increasing the filling factor increases the lifetime and the size of the clusters formed. In finite-size channels, for a definite value of the filling factor

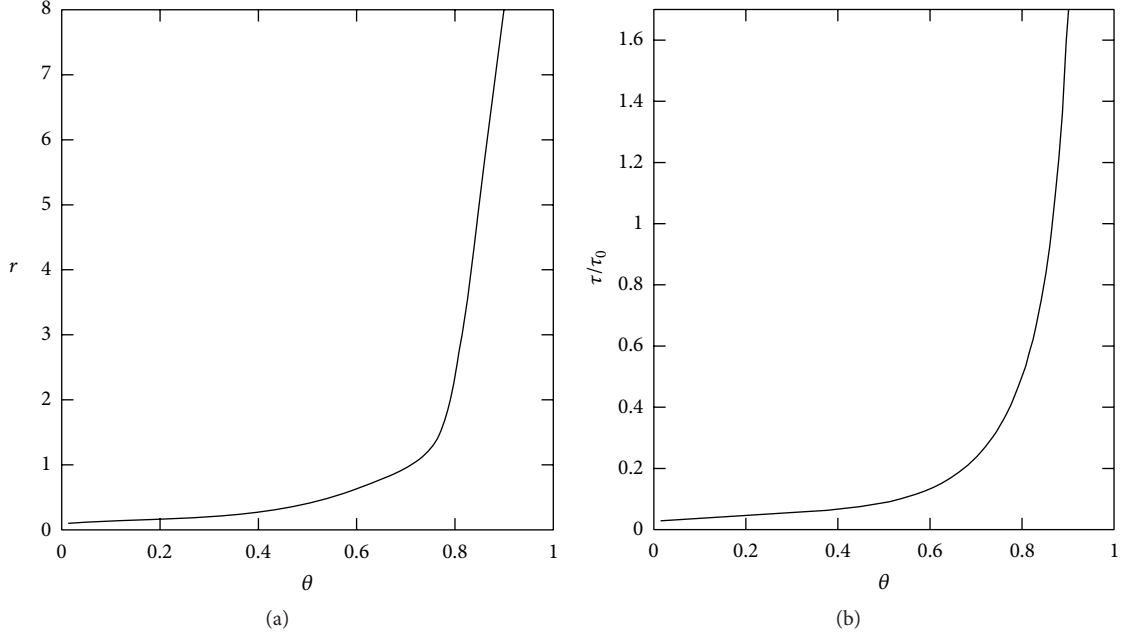


FIGURE 2: Size ( $r = R/\sigma$ ) (a) and lifetime ( $\tau/\tau_0, \tau_0 = \sigma^2/D_0$ ) (b) of clusters versus the filling factor.

$\theta_0 = \theta_c$ , a cluster equal in size to the length of the channel is formed. It is obvious that the diffusion coefficient in such a channel increases without bound as  $\theta_0 \rightarrow \theta_c$ , even though the lifetime of such a cluster is finite. If the range of relaxation frequencies  $\omega(k)$  is known, then an expression that defines the relaxation of the Fourier components of the particle density in the channel  $n(k, t)$  in the case of arbitrary density  $n(k, t)$  is given by

$$\dot{n}(k, t) = i\omega(k) n(k, t). \quad (76)$$

From (76), we can get that the equation for the amplitude of the fluctuations can be written as

$$\delta \dot{n}(k, t) = i\omega(k) \delta n(k, t). \quad (77)$$

Equation (77) describes the relaxation of  $k$  component of the density fluctuation at arbitrary wave vector. In particular, at  $k \neq 0$ , this equation allows to describe the relaxation of density fluctuations and propagation of disturbances on the cluster of finite size in the case of the formation of the cluster. At  $k \rightarrow 0$ , the equation describes the relaxation of density fluctuations on large spatial scales. This value is related to the macroscopic flux. Let us write the equation of continuity to calculate the flux  $j$ :

$$\dot{n} + \frac{\partial j}{\partial x} = 0. \quad (78)$$

After applying the Fourier transform, (78) takes the form

$$ikj(k, t) = -\dot{n}(k, t). \quad (79)$$

Using (76) and (79), one can get for  $j(k)$

$$j(k, t) = \frac{n(k, t) \omega(k)}{k}. \quad (80)$$

Using the relation (70) we find that  $\nu(k)$  and therefore the spectrum contains both real and imaginary parts, corresponding to the “hydrodynamic” (real part of  $\omega(k)$ ) and diffusive (imaginary part of  $\omega(k)$ ) transport of particles. Therefore, (80) for the flux  $j(k, t)$  contains terms relating to hydrodynamic transport of particles in a cluster and diffusive transport of particles in the space between clusters. We note that the response function method can be used to take into account the interaction of particles in a channel for a potential that is different from a hard-spheres interaction, similarly to the way this was done previously.

Analysis of the experimental data showed that for high filling factors  $\theta_0 \sim 1$ , the dependence of the diffusion coefficient  $D(\theta_0)$ , calculated from the relation (72), leads to a discrepancy between theory and experiment (Section 2.1.3). This discrepancy could be due, in our opinion, to the above-described influence of a finite channel length, the asphericity of the gas molecules, and the possible breakdown of one dimensionality of the problem. These effects lead to the following dependence of the diffusion coefficient on the filling factor:

$$D(\theta_0) = D_0 \left( \frac{1}{(1 - \zeta\theta_0)^2} \right). \quad (81)$$

Here  $\zeta$  is a coefficient that takes into account the finite size of the channel, the possible deviation of the channel from one-dimensionality, and the asphericity of the molecules. The relations (72), (81), and (52) make it possible to describe transport in a subnanometer channel for different values of parameters such as the gas pressure and the pressure difference outside the membrane, the temperature of the membrane, and the type of gas molecules. As an example, we present the dependence, calculated according

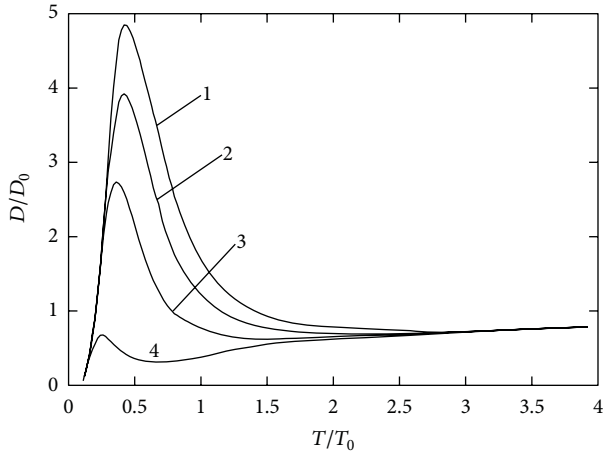


FIGURE 3: Theoretical curves of the relative diffusion coefficient  $D/D_0$  versus the relative temperature  $T/T_0$  for various values of the relative pressure  $p/p_0$ : (1)  $p/p_0 = 3$ , (2)  $p/p_0 = 2$ , (3)  $p/p_0 = 1$ , and (4)  $p/p_0 = 0.1$ .

to (72), (81), and (23), of the diffusion coefficient in a subnanometer channel on the relative temperature  $T/T_0$  for various relative pressures  $p/p_0$  (Figure 3).

It is evident in the figure that the character of the temperature dependence of the relative diffusion coefficient in subnanometer channels is substantially different at different pressures  $p$ . For example, if the pressure is high ( $p/p_0 > 1$ ), the dependence of  $D/D_0$  on  $T/T_0$  has a pronounced maximum at temperatures  $T \sim 0.5T_0$  (curve 1). As pressure decreases, the magnitude of this maximum decreases and the maximum itself shifts into the region of lower temperatures (curves 2, 3). A further decrease of pressure to values  $p/p_0 < 1$  results in the appearance of a minimum in the dependence of  $D/D_0$  on  $T/T_0$  in the temperature range  $T \sim 0.5T_0$ . The maximum occurs at  $T \sim 0.3T_0$ . Since for  $p/p_0 < 1$ , the flux depends on  $p$  and the average distance between particles in the channel is much greater than the diameter of the particles, the increase in the diffusion coefficient for  $T \sim 0.5T_0$  is due to the temperature dependence of the diffusion coefficient  $D_0$  on individual molecules in the channel. At high temperatures, all curves saturate at a value corresponding to  $D/D_0 = 1$ . In the next section, the theoretical laws obtained previously will be compared with the experimental data.

**2.1.3. Analysis of the Experimental Data: Comparison of Theory with Experiment.** Quite extensive experimental investigations of the sorption and transport properties of a series of organic molecules ( $\text{CH}_4$ ,  $\text{C}_2\text{H}_6$ ,  $n\text{-C}_4\text{H}_{10}$ ,  $i\text{-C}_4\text{H}_{10}$ , and others) and the inert gases Ar, Ne, and Kr in ZSM-5 zeolite membranes (MFI, silicate-1) have now been performed. The results are presented in [42, 50, 51]. According to [52], ZSM-5 zeolite membranes have a complicated chemical and crystalline structure. The chemical structure of zeolite membranes is given by the formula



For small values of  $n$ , zeolite membranes of this type are called silicate-1 membranes. The crystalline structure of ZSM-5 membranes has been studied quite well. It consists of a 3D structure, consisting of sinusoidal channels with a circular cross section ( $0.54 \pm 0.02 \text{ nm}$ ) parallel to the  $a$  axis [53], which intersect straight channels with an elliptical cross section ( $0.57\text{-}0.58$ )  $\times$  ( $0.51\text{-}0.52$ )  $\text{nm}^2$  parallel to the  $b$  axis [010] [50, 54]. Cavities  $\sim 0.9 \text{ nm}$  in size form at the intersection of the channels. The sorption capacity of ZSM-5 zeolite is determined by the number of sorbed (entering the channels) molecules per cell of a crystal. According to [50, 55], the cell parameters are  $a = 2.007 \text{ nm}$ ,  $b = 1.992 \text{ nm}$ , and  $c = 1.342 \text{ nm}$ . A single cell is a structure consisting of four segments of  $0.46 \text{ nm}$  linear channels, four segments of  $0.66 \text{ nm}$  sinusoidal channels, and four  $0.54 \text{ nm}$  intersections. Depending on the structure of a molecule, sorption of one or two molecules per intersection is possible. In [50], the sorption capacity of ZSM-5 was measured for a number of molecules. It was concluded that the molecules  $\text{CH}_4$ ,  $\text{C}_3\text{H}_8$ , and  $n\text{-C}_4\text{H}_{10}$  are sorbed with one molecule per intersection, while nitrogen,  $n$ -hexane, and  $p$ -xylene are sorbed with two molecules per intersection. Thus, for gases of the type  $\text{CH}_4$ ,  $n\text{-C}_3\text{H}_8$ , and  $\text{C}_4\text{H}_{10}$ , channels in the crystal structure of ZSM-8 can be treated as one dimensional. For nitrogen-type molecules, two molecules can be arranged at an intersection, and therefore molecules can change places at an intersection (absence of blocking). Nonetheless, since there are significantly more nitrogen molecules in a channel (24 molecules per unit cell [50]), the one-dimensional model can also be used for this gas. Analysis of the experimental data presented [43, 55–58] shows that all gases investigated can be conditionally divided into two groups. The first group of gases, containing, specifically, Ar, Kr, Ne, and  $\text{CH}_4$ , is characterized by a linear pressure dependence of the filling factor  $\theta$ ; that is, Henry's law holds for them [43]. For these gases, the pressure dependence of the flux is nearly linear, and the diffusion coefficient is essentially independent of the filling factor [55]. The temperature dependence of the flux is characterized by the presence of a minimum at temperatures  $T \sim 400 \text{ K}$  (e.g., for Ar and Kr), while a maximum is not observed in the diffusion coefficient [57, 58]. Here neon, whose diffusion coefficient increases with temperature [58], is an exception. The second group of gases, containing, specifically,  $i\text{-C}_4\text{H}_{10}$ ,  $\text{C}_2\text{H}_4$ ,  $\text{C}_2\text{H}_6$ , and  $\text{C}_4\text{H}_8$ , is characterized by a dependence of the filling factor  $\theta$  on the pressure  $p$  in the form of a curve that saturates [43]. For these gases, the pressure dependence of the flux is likewise characterized by a curve that emerges at a value that is pressure independent [55]. For this group of gases, the diffusion coefficient depends strongly on the filling factor [56]. The temperature dependence of the flux is characterized by the existence of a maximum and minimum at high ( $T > 500 \text{ K}$ ) temperature [57]. The model, constructed in this paper, of the sorption and transport properties makes it possible to describe these dependences of transport in one-dimensional channels on the basis of general assumptions. Figure 4 shows the dependence of the diffusion coefficient  $D$  on the filling factor  $\theta$  (solid line), calculated using (81) and the experimental data obtained in [57] for various gases.

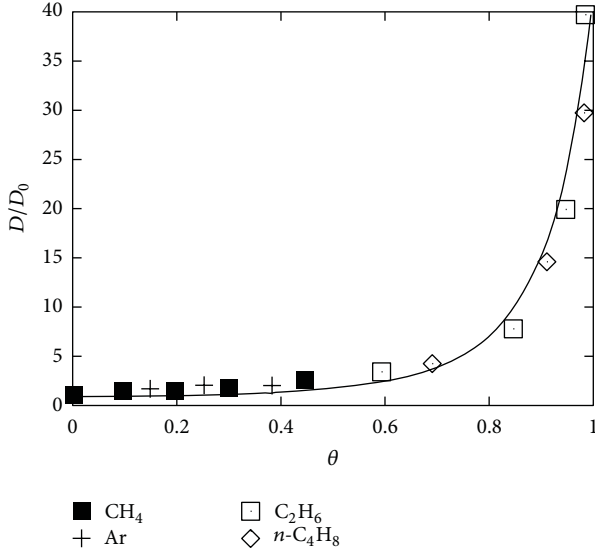


FIGURE 4: Relative diffusion coefficient versus the filling factor. Solid curve—theoretical dependence (81) with  $\zeta = 0.86$ ; dots—experimental data from [57].

We note that the dependence (81) presented in Figure 4 takes into account the asphericity of the molecules, equal to  $\zeta = 0.86$ . For inert gases and methane (first group of gases), the diffusion coefficient measured in the range of filling factors  $\theta_0 < 0.5$  depends weakly on  $\theta_0$ . A large increase in the diffusion coefficient at  $\theta_0 \sim 1$  is observed for gases of the type C<sub>2</sub>H<sub>6</sub> and n-C<sub>4</sub>H<sub>8</sub> (second group of gases). This behavior of the diffusion coefficient  $D(\theta)$  can be satisfactorily described on the basis of the model proposed, which takes account of the pair interaction of particles with a very simple form of the interaction potential for hard spheres. It is obvious that this coefficient is different for different molecules.

The physical mechanism leading to an increase of the diffusion coefficient consists in a decrease of the activation barriers for diffusion, which is due to an interaction of the particles for high filling factors. Indeed, it follows from the relation (75) for the effective diffusion activation energy  $\tilde{E}(\theta_0)$  that in this case, when the filling factor is low,  $\theta_0 \ll 1$ , gas diffusion in the channel can be studied in the single-particle approximation neglecting the pair interaction of the gas particles with one another. As the filling factor increases, the diffusion activation energy decreases as a result of the effective attraction of the gas particles to one another. This can be interpreted as the formation of widely separated clusters. Diffusion in each cluster can be treated as a transfer of “excitation” along a chain of close gas particles. A further increase of the filling factor increases the cluster lifetime and decreases the average intercluster distance and, in consequence, increases the diffusion coefficient. For  $\theta_0 \sim 1$ , the diffusion process can be regarded as a motion of this “excitation” along the entire channel, when the arrival of a particle at the channel entrance results in the end-most particle leaving the channel.

Figure 5(a) shows the temperature dependences of the gas flux through a membrane for ethane and argon, calculated

using the formulas (5) and (81) and a relation following from (81):  $J \propto D(\theta_0(T, p))\theta_0(T, p)$ . These dependences were compared with the experimental values obtained in [42]. It is evident that the theoretical and experimental results agree satisfactorily with one another. The temperature dependence can also be understood on the basis of the model developed in the present work. Indeed, it follows from the relation (5) that at low temperatures ( $T \rightarrow 0$ ), the filling factor  $\theta_0 \sim 1$ .

The effective diffusion activation energy  $\tilde{E}(\theta_0)$  is  $E_0$  at zero temperature (56). The diffusion coefficient of the gas particles in the channel (81) approaches zero as a result of the “freezing out” of the thermal motion of the particles in the potential field of the channel surface. Increasing the temperature decreases  $\tilde{E}(\theta_0)$  without appreciably changing the filling factor. The value of  $\tilde{E}(\theta_0)$  reaches a minimum at a certain temperature  $T_0$ . It is obvious that the diffusion coefficient reaches its maximum value precisely at this temperature. It follows from (54) and (75) that a further increase of temperature decreases the filling factor  $\theta_0$ , and this is accompanied by an increase in the effective diffusion activation energy right up to the value  $E_0$  which is attained for  $\theta_0(p, T) \approx \theta_0 \ll 1$  at some temperature  $T = T_1(p)$ . The temperature  $T_1$  corresponds to a minimum in the function  $D(T)$ . A further increase of the diffusion coefficient with increasing temperature corresponds to the variation of the coefficient according to the Arrhenius law  $D \propto \exp(-E_0/T)$ . Figure 5(b) shows the temperature dependence of the flux for argon, calculated using (81) and the data from [57]. We note that the theory developed in the present paper predicts that the presence of a minimum at  $T \sim 400$  K should be accompanied by the appearance of a maximum at  $T \sim 200$  K. In this connection, for further elaboration of the theory, it is of interest to make an experimental search for a maximum in the temperature dependence of the flux for argon near  $T \sim 200$  K. Thus, two types of behavior of particles in a channel, which have different diffusion mechanisms, can be distinguished in the pressure and temperature ranges investigated. For the first group, this is the diffusion of single particles in a channel, and for the second group it is diffusion as a result of a collective interaction of particles in a completely filled channel. Such behavior of single-component gases is a direct consequence of the real one-dimensionality of subnanometer channels, where molecules cannot change places with one another. The proposed model is based on two basic assumptions: (1) the pair interaction between gas particles plays the decisive role in the description of the state and transport phenomena in a one-component gas in subnanometer channels, and (2) as a result of the fact that the channel diameter is comparable to the diameter of the gas molecules, such channels can be assumed to be one dimensional. The one-dimensionality of the system studied is actually due to the fact that the gas molecules do not have classical transverse degrees of freedom. This difference from the conventional systems plays a fundamental role in the analysis of all phenomena described above.

We note that (73) derived previously possesses, besides the solution described in the text, strongly nonuniform nonstationary soliton-like solutions. It should be expected

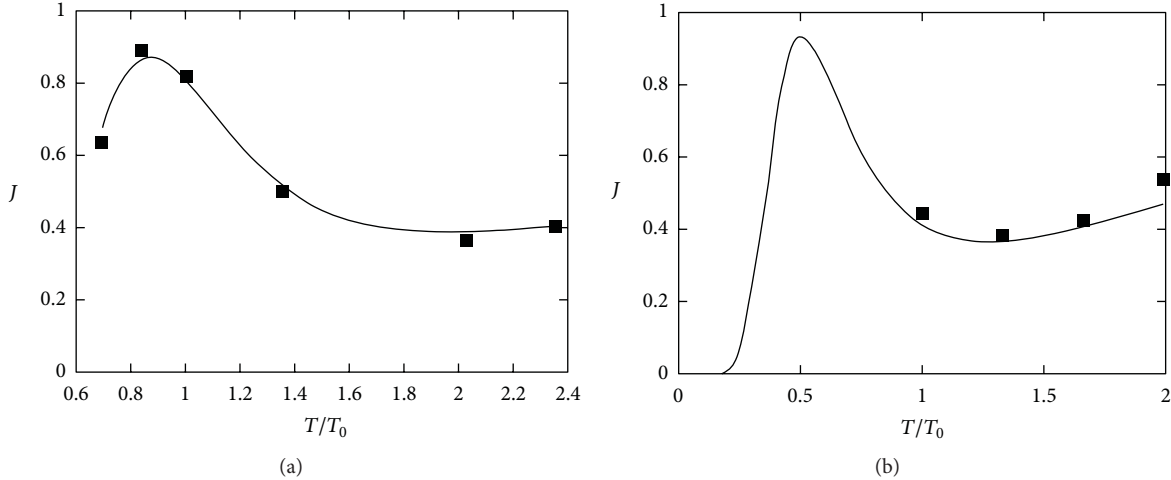


FIGURE 5: Relative flux versus the relative temperature  $T/T_0$ ,  $T_0 = 296$  K. Solid lines—theoretical curves calculated using (5), (34), and (81); dots—experimental data for ethane (a) [42] and argon (b) [58].

that an experimental consequence of the existence of such solutions will be the appearance of substantial fluctuations of the gas flux through a membrane. The proposed model satisfactorily describes the equilibrium properties of a gas in a channel (specifically, the filling factor) and the weakly nonequilibrium properties of the gas, such as the diffusion coefficient and flux. It should be noted that a satisfactory description of the equilibrium properties, for example, the adsorption isotherm, has been obtained previously on the basis of a number of phenomenological models [42]. A qualitative analysis of the maximum (but not minimum) in the temperature dependence of the relative diffusion coefficient is presented in [43]. A model describing the dependence of the diffusion coefficient on the filling factor on the basis of a one-particle approximation by introducing into the diffusion rate jumps of individual particles a phenomenological correction factor  $\chi = (1 - \theta_0)^{-1}$  has been proposed in [36]. However, even though each of the phenomena indicated previously can be described on the basis of individual models, the approximations used in so doing either are not physically substantiated or completely contradict one another.

**2.2. Particle Mobility and Diffusion in 1D System.** Although, in many cases, the parameters of 1D systems can be calculated exactly, their complete theoretical description has not yet been accomplished. 1D systems belong to the class of strongly fluctuating systems [59]; thus, in contrast to systems of higher dimensionalities, they cannot unambiguously be described only by mean values such as mean density and compressibility [59]. The transport properties of 1D systems can also be rather specific (see [43, 57, 60] and Section 2.1). Recent ab initio calculations [61] have shown that water flux through hydrophobic nanotubes is more than one order of magnitude higher than the estimated ordinary diffusion flux. The permeation experiments on zeolite membranes [57] have shown that for gases, whose particle diameter is larger than half the zeolite channel diameter, the increase of the diffusion coefficient with density is more than one order of

magnitude larger than would be expected for one-particle diffusion. On the other hand, there are also experimental results, for example, obtained using nuclear magnetic resonance (NMR) and quasi-elastic neutron scattering (QENS) techniques, indicating that the particle mobility in 1D systems can decrease and the mean square displacement (MSD) can become proportional not to time, as it is in the case of a normal (Einstein) diffusion, but to the square root of time,  $\langle x^2 \rangle \sim t^{1/2}$  (so-called single-file diffusion mode (SFD)) [43, 62–67]. Moreover, the experiments [64, 66] show that both the Einstein and SFD diffusion modes can exist for the same particles but at different densities and observation times. Furthermore, for certain investigated gases, a density increase leads to a transition from the Einstein diffusion to the SFD mode [64]. Thus some experiments suggest that the particle mobility in 1D systems must decrease with increasing density, whereas others show that diffusion accelerates as density becomes larger. An explanation for this contradiction is absent at present.

Diffusion in 1D systems has been studied in numerous theoretical works [36, 57, 67–73]. The dependence  $\langle x^2 \rangle \sim t^{1/2}$  has been obtained for a 1D system within the screened-gas model, which partly takes into account correlations between the particles [68–73]. It has been suggested [70–73] that the appearance of the two diffusion modes, characterized by the different time dependences of MSD, can be explained by a transition from the one-particle diffusion mode, occurring at short times, to SFD appearing at longer times when the particle mobility is limited by its neighbors. In this case at  $t \rightarrow \infty$  the dependence of MSD is always  $\langle x^2 \rangle \sim t^{1/2}$ . Although this approach can describe the experimentally observed dependences of MSD, corresponding to SFD, it fails to explain the increase of the diffusion coefficient and transport acceleration observed in dense 1D systems [43]. The physical reason for this failing is that the proposed model [60] considered the system of individual tagged particles, whereas in experiments one does not follow the diffusion of a particular particle but rather deals with the system

of many of identical particles. We propose a description for the particle diffusion [57] and mobility [43, 62–65] in 1D systems of identical particles with blocking effect (BE) when the motion of a particle is blocked by other particles or clusters. According to our model, different mobility and diffusion transport mechanisms can be realized in a 1D system depending on its density. At low densities, an ordinary diffusion of single particles takes place. As density increases, a formation of 1D clusters of a finite size and lifetime takes place. In this case, there are two competing mechanisms prevalent in the system: a barrier-free propagation of density perturbations (“collective diffusion” (CD)) [60] and a blocking effect. When BE dominates, the SFD mode is realized, whereas when the CD mechanism prevails, we predict an essential transport acceleration, as compared to the one-particle diffusion mode. In this case, MSD is Einstein-like with the diffusion coefficient increasing with density. The proposed model consequently takes into account all the time-space correlations occurring in a 1D system composed of identical particles with an arbitrary interaction potential. This model is able to describe the experimentally observed MSD dependencies at different densities as well as the transport acceleration with increasing density of a 1D system. To describe the transport properties of a 1D system, we apply the response function method (see Section 2.1 and [31, 32, 48]). This approach allows one to consistently take into account many-body correlations and obtain the diffusion coefficient and MSD for a 1D system of arbitrary density. Within response function method, we calculate the response function  $\beta(k, \omega)$ , which determines the Fourier image of the density fluctuation  $\delta n(k, \omega)$  occurring in the 1D system in the external field of frequency  $\omega$  and wave number  $k$ . The relaxation spectrum of a density fluctuation ( $\omega(k)$ ) can be calculated from the relation  $\beta^{-1}(k, \omega) = 0$ . Note that in response function method,  $\delta n(x, t)$  can be interpreted as a distribution function if  $t \gg a^2/D$ , where  $a$  is the particle diameter and  $D$  is the one-particle diffusion coefficient [48]. A density fluctuation  $\delta n(x, t)$  in a 1D system is determined by the relation (87), and the MSD can be expressed as

$$\langle x^2 \rangle = \frac{\int x^2 dx dk e^{-i\omega(k)t} e^{ikx}}{\int dx dk e^{-i\omega(k)t} e^{ikx}}. \quad (83)$$

It is evident from (87) and (83) that MSD is determined by the relaxation spectrum  $\omega(k)$ . The evaluation of  $\omega(k)$  is reduced to the solution of Dyson equation for the response function (55) and for the 1D system takes the form (70), where  $\nu(k, \theta)$  is the Fourier image of the pair correlation function of interacting particles. The function  $\nu(k, \theta)$  can be obtained for a 1D system with an arbitrary interaction potential  $\Phi(x)$  [45]:

$$\begin{aligned} \nu(k, \theta) &= \frac{2}{n_0} \left( \frac{\phi(p(\theta) - ika)}{\phi(p(\theta)) - \phi(p(\theta) - ika)} + \frac{\theta}{ika} \right), \\ \phi(z) &= \int_0^\infty e^{-zx} \exp\left(-\frac{\Phi(x)}{T}\right) dx, \\ \frac{1}{\theta} + (\ln \phi(z))'_{z=p(\theta)} &= 0. \end{aligned} \quad (84)$$

Here  $T$  is the temperature. The last expression in (84) helps us to obtain the dependence of pressure on the filling factor ( $p(\theta)$ ). It follows from (70) and (84) that at  $\theta \rightarrow 0$ , the relaxation spectrum  $\omega(k)$  describes the one-particle diffusion  $\omega(k) = -iD_0k^2$ . For  $ka \gg 1$ , the Fourier image of the pair correlation function  $\nu(k, \theta)$  approaches zero for any arbitrary short-range potential  $\Phi(x)$ . This corresponds to the absence of correlations between the particles at the length scale  $a < l_0$ , where  $l_0$  is the average particle path between two collisions. In this case, the relaxation spectrum  $\omega(k)$  also describes the one-particle diffusion mode  $\omega(k) = -iD_0k^2$ . The analysis of the relaxation spectrum performed in Section 2.1 for the hard-core potential has shown that due to collective effects and density fluctuations, the 1D system can transform into a nonhomogeneous state as density increases. This state is characterized by the formation of 1D clusters with a finite lifetime (Section 2.3) (Section 2.1). In this case at high density ( $\theta \rightarrow 1$ ), long distances ( $k \rightarrow 0$ ), and  $t \rightarrow \infty$  (see (70), (84)) the spectrum becomes diffusion-like with the diffusion coefficient increasing with density (72) that corresponds to the CD mode existing in a nonhomogeneous, clustered 1D system [62]. In order to describe the relaxation of density fluctuations at times  $t \gg a^2/D_0$  (that corresponds to the long-time limit  $t \rightarrow \infty$ ) for an arbitrary filling factor  $\theta$ , one should do series expansions of (70) and (84) with respect to the parameter  $ka \ll 1$  and keep the expansion terms following the first one. It is convenient to rewrite this expansion with respect to parameter  $kl_0$ . Having done this, the relaxation spectrum for  $k \ll 1/a$  can be written as

$$\omega(k) = -i \left( D(\theta) k^2 + F(\theta) k^2 (kl_0)^2 + iF_1(\theta) k^2 (kl_0) \right), \quad (85)$$

where the expansion coefficients are  $D(\theta) = D_0\zeta(0, \theta)$ ,  $F_1(\theta) = D\theta\nu'(0, \theta)\zeta^2(0, \theta)$ , and  $F(\theta) = D\theta^2((1/2)\nu''(0, \theta)\zeta^2(0, \theta) - \nu'^2(0, \theta)\zeta^3(0, \theta))$ . The values with apostrophes represent the corresponding derivatives of  $\nu(k, \theta)$  with respect to wave number  $k$ , calculated at  $k = 0$ . Equations (83) and (85) can be used to evaluate the time dependence of  $\langle x^2 \rangle$  at any length scale, starting from a diffusion path of just few particle jumps up to those comparable to the total length of the channel. Note that the real part of the spectrum  $\text{Re } \omega(k)$ , which at  $\theta \rightarrow 1$  corresponds to the sound mode, describes the collective effect of density perturbation propagation ( $\delta n(x, t) \sim \int dk e^{-i\omega(k)t} e^{ikx} = \int dk \delta n_1(k, t) \delta n_2(k, t) e^{ikx}$ ,  $\delta n_1 \sim e^{i \text{Re } \omega(k)t}$ ), and its imaginary part  $\text{Im } \omega(k)$  determines the diffusion mode for the relaxation of a density fluctuation taking into account the length-time correlations between the particles ( $\delta n_2 \sim e^{-\text{Im } \omega(k)t}$ ). Equations (87), (83), and (85) allow us to study the mobility and distribution function of the particles in a 1D system for different length/time scales, filling factors and interaction potentials  $\Phi(x)$ . Figure 6 presents the dependences of the distribution function on the dimensionless coordinate  $\bar{x} = x/l_0$ , calculated for different dimensionless times  $t' = t/\tau$  ( $\tau \sim l_0^2/D_0$ ) using the square-well interaction potential with the well depth  $V \sim T$  ( $u = V/T \sim 1$ ) and width  $R$ .

It is important to mention that the obtained results do not depend on the specific form of the pair interaction potential

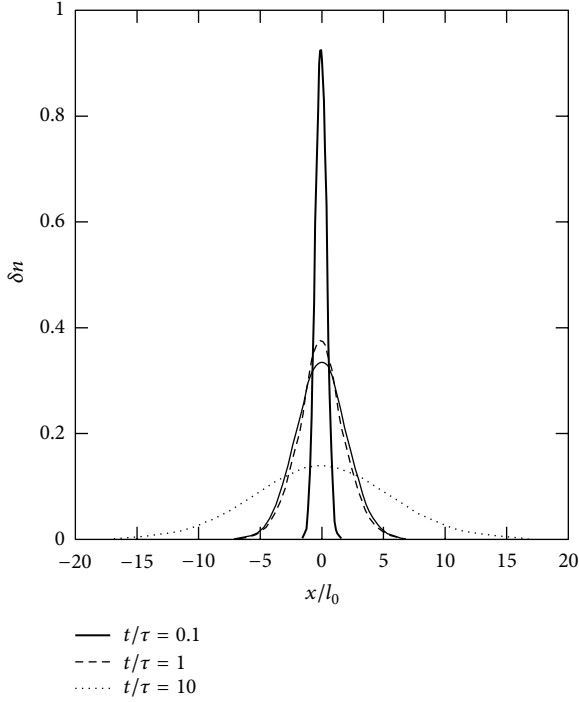


FIGURE 6: Typical distribution functions  $\delta n(x, t)$  versus dimensionless coordinate  $x/l_0$  (solid lines) at different times  $t/\tau$ , ( $\tau \sim l_0^2/D_0$ ) at  $\theta \sim 0.2$ ,  $u = 1$ , and  $R = a$ . Dashed lines show Gauss distributions for the corresponding times.

$\Phi(x)$ ; we have obtained similar results using rectangular potentials, the Lennard-Jones and Morse potentials. We also note that the shape of the distribution function is independent on density as both dimensionless coordinate and time are determined by the filling factor. The distribution functions at different time scales clearly differ from each other. The distribution is a Gauss-like function at short times ( $\theta^2 \ll t' < 1$ ,  $\theta \ll |\bar{x}| < 1$ ) that corresponds to the one-particle diffusion (Figure 6). At  $t' \sim 1$ ,  $|\bar{x}| \sim 1$ , the distribution function varies faster than the Gauss distribution (Figure 6) that corresponds to limited mobility of a particle due to its blocking by other particles. At longer times ( $t' \gg 1$ ,  $|\bar{x}| \gg 1$ ), the distribution function becomes Gauss-like again (Figure 6) as the transport in a dense 1D system is due to the CD mechanism [60]. In this case, the relaxation spectrum is diffusion-like with a density-dependent diffusion coefficient  $D_u(\theta) \approx D_0/(1 - \theta)^2$ .

MSDs calculated at different time and length scales (Figure 7) using the distribution functions (Figure 6) noticeably differ from each other confirming the existence of several diffusion modes in the system. At short length-time scales ( $t < \tau$ ,  $\langle x^2 \rangle \ll l_0^2$ ), one should observe the one-particle diffusion mode with  $\langle x^2 \rangle \sim t$  (Figure 7(a)). When  $\langle x^2 \rangle$  is comparable to  $l_0^2$  and time  $t \sim \tau$ , the correlations between the particles become essential that lead to the appearance of blocking effect. In this case, MSD has a non-Einstein character (Figure 7(b)). At longer times  $t \gg \tau$ ,  $\langle x^2 \rangle \gg l_0^2$ , the particle mobility is mostly determined by the second term

in (85). This leads to the reappearance of the Einstein-type 110 dependence of MSD,  $\langle x^2 \rangle = 2D(\theta)t$ , where  $D(\theta)$  is an effective diffusion coefficient. Notice that the characteristic times at which different diffusion modes can be observed depend on the density of the system. Indeed, the average distance between the particles and, consequently, the time  $\tau \sim 1/\theta^2$  decrease with increasing density.

Further we compare our results to those of the QENS, NMR [43, 62–65], and permeation [57] experiments as well as to the results of the molecular dynamics (MD) calculations [71] summarized in Table 1. Notice that such a system can be considered as one dimensional with the presence of BE as the diameters of the experimentally investigated molecules are less than the doubled diameter of the membrane channel. Our estimates for zeolite ZSM-48 obtained using the data from [71] show that for the low filling factor ( $\theta = 0.11$ ) and times  $\sim 10$  ns, the normal diffusion mode,  $\langle x^2 \rangle \sim t$ , should occur while at higher density ( $\theta = 0.48$ ) the dependence  $\langle x^2 \rangle \sim t^{1/2}$  should be observed, which is in a perfect agreement with the experimental data (Table 1). In Table 1, experimental and MD results are presented;  $a$  and  $d$  are the particle and membrane channel diameters, respectively,  $T$  is a temperature, and  $\theta$  is a degree of filling of the channel. The fifth column represents the data on the motion mode of a particle in a channel (“SFD” means  $x^2 \sim t^\alpha$ ,  $\alpha < 1$ , “normal” corresponds to  $x^2 \sim t$ ). The observation time of corresponding modes is represented in the sixth column.

The experimental results obtained for ethane molecules in zeolite  $\text{AlPO}_4\text{-5}$  and for methane molecules in zeolite ZSM-48 (Table 1) are successfully described by our model. Indeed, using (85), one can write MSD for the SFD mode at  $F(\theta) > 0$  as

$$\langle x^2 \rangle = (1 - \theta) l_0 \sqrt{32DtF(\theta)},$$

$$F(\theta) = D_0 \theta^2 \left( \frac{1}{2} \nu''(0, \theta) \zeta^2(0, \theta) - \nu'^2(0, \theta) \zeta^3(0, \theta) \right). \quad (86)$$

Equation (86) with  $F(\theta) = 1$  is identical to the relation derived in [62] with the accuracy of the numeric coefficient  $\sqrt{32}$ . Note that  $F(\theta)$  describes the correlations effects in a 1D system of interacting particles. Using (86) and the parameters for  $\text{AlPO}_4\text{-5}$  [62], we obtain  $\langle x^2 \rangle \sim 3 \mu\text{m}$  for times  $\sim 100$  ms that is in good agreement with the values reported in [62, 64]. At short times  $t \leq l_0^2/D \sim 10^{-8}$  s, the main contribution comes from the first term in (85), and, in this case, the normal diffusion mode is realized. Our results obtained using (83) and (85) at  $u = 1$  and the experimental data for ethane molecules in zeolite  $\text{AlPO}_4\text{-5}$  are compared in Figure 8.

The dependence of the diffusion coefficient on the filling factor was investigated for several gases ( $\text{CH}_4$ ,  $\text{C}_2\text{H}_6$ , and  $\text{C}_3\text{H}_8$ ) in silicalite-1 membrane at times  $t > 10$  s [57]. The diffusion coefficients for these gases were found to increase more than 20 times as the filling factor varied from 0 to 0.9. This observation can be explained by the collective effect of density perturbation propagation through a 1D clustered system. The calculated dependence of the relative diffusion coefficient  $D/D_0 = (\text{Im } \omega(k)/D_0 k^2)_{k=0}$  on the

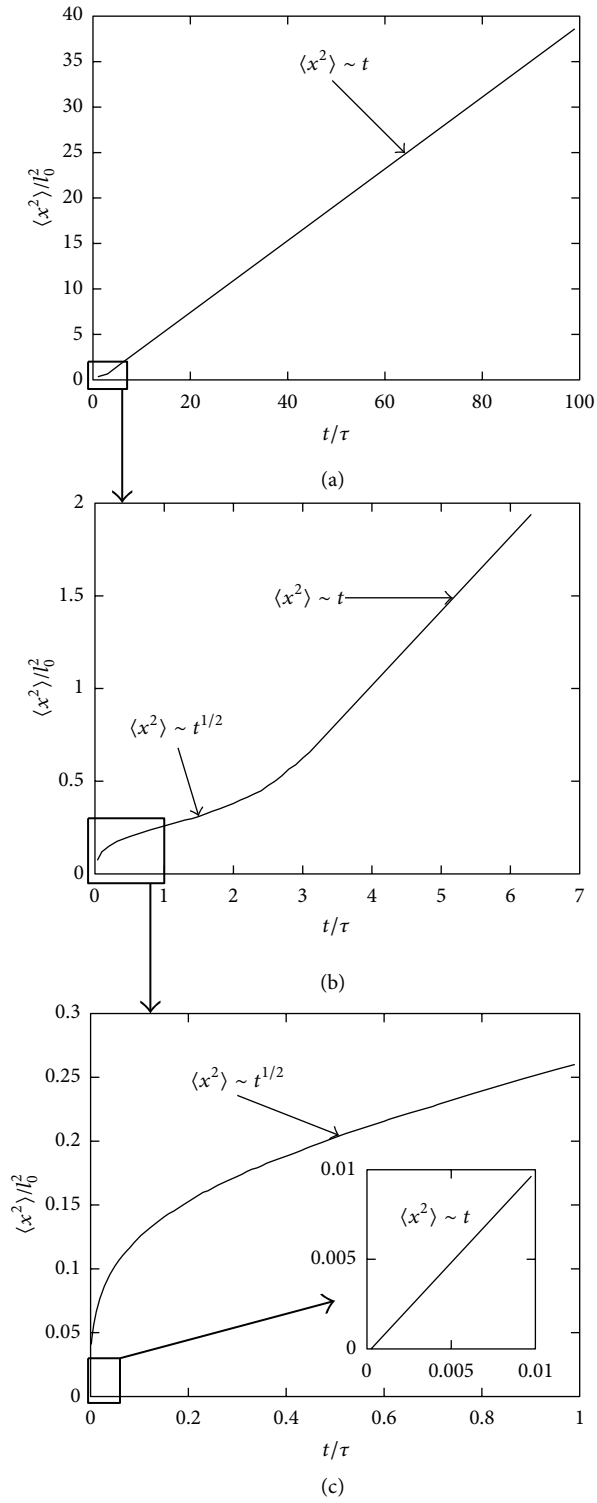


FIGURE 7: Typical  $\langle x^2 \rangle / l_0^2$  versus time ( $t/\tau$ ,  $\tau \sim l_0^2/D$ ) dependence calculated for  $\theta \sim 0.1$ ,  $u = 1$ , and  $R = a$  and shown at different time scales. (a) shows the curve up to  $100t/\tau$ ; its magnification is shown in (b) ( $0: 7t/\tau$ ) and (c) ( $0: 1t/\tau$ ). The insert in (c) shows very short times up to 0.01, when the normal diffusion mode is observed.

TABLE I: Experimental and MD results:  $a$  and  $d$  are the particle and membrane channel diameters, respectively.

| Method | Molecule, zeolite                                                | $T$ , K | $\theta$ | Diffusion mode | Observation time | Reference |
|--------|------------------------------------------------------------------|---------|----------|----------------|------------------|-----------|
| NMR    | $C_2H_6$ , $a = 3.8\text{\AA}$                                   | 300     | 0.15     | SFD            | 100 ms           | [62]      |
|        | $AlPO_4-5$ , $d = 7.3\text{\AA}$                                 |         |          |                |                  |           |
| NMR    | $CF_4$ , $a = 4.7\text{\AA}$<br>$AlPO_4-5$ , $d = 7.3\text{\AA}$ | 180     | 0.003    | SFD            | 2 ms             | [71]      |
|        |                                                                  |         | 0.03     | SFD            | 150 ms           |           |
|        |                                                                  |         | 0.11     | SFD            | 50 ms            |           |
|        |                                                                  |         | 0.22     | SFD            | 150 ms           |           |
| MD     | $CF_4$ , $a = 4.7\text{\AA}$                                     | 180     | 0.11     | SFD            | $10^{-8}$ s      | [64]      |
|        | $CH_4$ , $a = 3.8\text{\AA}$                                     |         | 155      | 0.3            | Normal           |           |
|        | $AlPO_4-5$ , $d = 7.3\text{\AA}$                                 | 250     | 0.45     | Normal         | $10^{-8}$ s      |           |
|        | $C_2H_6$ , $a = 3.8\text{\AA}$                                   |         | 0.36     | Normal         | $10^{-8}$ s      |           |
|        | $AlPO_4-5$ , $d = 7.3\text{\AA}$                                 |         | 0.6      | Normal         | $10^{-8}$ s      |           |
|        | $CH_4$ , $a = 3.8\text{\AA}$                                     | 155     | 0.72     | Normal         | $10^{-8}$ s      |           |
|        | $ZSM-48$ , $d = 5.6\text{\AA}$                                   |         | 0.48     | SFD            | $10^{-8}$ s      |           |

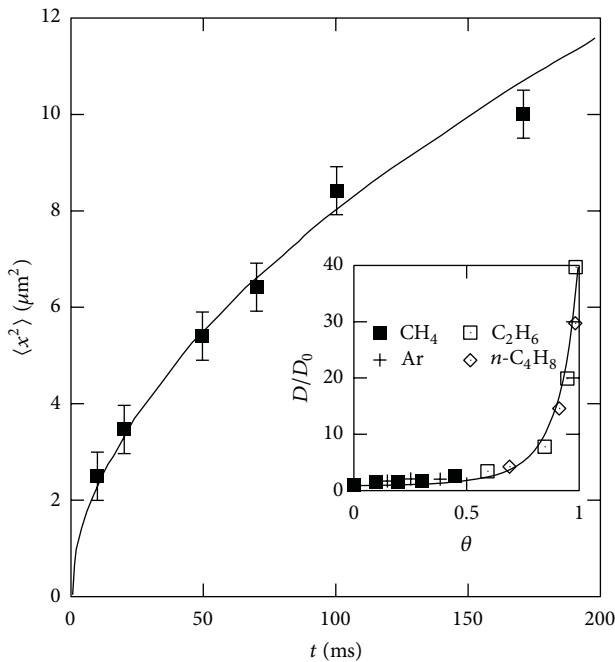


FIGURE 8: MSD versus time at  $u = 1$ ,  $R = a$ . The solid line shows the results calculated using (55), (70), (87), and (85); points represent the experimental data for the diffusion of ethane in zeolite  $AlPO_4-5$  [61]. The insert shows the dependence of the relative diffusion coefficient on the filling factor obtained for several gases (solid line) using (84) and (85) and  $V/T = 1$ . Points are the experimental data from [57].

filling factor  $\theta$  in comparison with experimental results is presented in Figure 8 (insert). The figure shows that the diffusion coefficient is only weakly dependent on the filling factor for  $\theta < 0.5$  (Figure 8 insert) but it rapidly increases when the filling factor becomes larger. This behavior of  $D(\theta)$  can be easily understood as at low filling factors, the particles inside the membrane channel do not interact with each other, no clusters are formed, and particle motion is purely diffusive.

The increase of the diffusion coefficient for  $\theta > 0.5$  is due to the cluster formation inside the channel and activation of the CD mode (Section 2.1).

**2.3. Formation of High- and Low-Density Clusters in a 1D System.** In recent experiments [74], the one-dimensional (1D) Au chains formed on the (110) NiAl surface have been investigated at low temperature ( $T = 12$  K). This surface exhibits 1D grooves made of the rows of Ni atoms, which suppress the transverse movements of Au adatoms allowing them to move only along the groove. The measured Au-Au distances in such chains were about  $2.9\text{\AA}$  that is very close to those in bulk gold [74]. The properties of 1D Au chains were also investigated in experiments [8, 12, 75–77] where they were either pulled out of a gold surface by an STM tip or created in a process of thin film etching. Such chains were stable during the observation time and consisted of several gold atoms. The Au-Au distances in some of them appeared to be strikingly large, up to  $3.5\text{--}4.0\text{\AA}$  [75–77], whereas in others much smaller Au-Au separations ( $\sim 2.5\text{--}2.9\text{\AA}$ ) were observed [8, 12, 78–80]. These results suggest that a 1D gold chain can exist in two different states characterized by different interatomic distances.

The ab initio calculations performed at zero temperature have shown that a 1D gold wire should break when the Au-Au separations exceed  $\sim 2.9\text{\AA}$  [81–84]. Being in agreement with the experiments reporting the Au-Au distances of  $2.5\text{--}2.9\text{\AA}$ , this result, however, does not explain the existence of large Au-Au separations. It has lately been demonstrated that the presence of hydrogen or other light atoms in the wire structure can stabilize gold chains and significantly alter their properties [3, 4, 82–88]. Assuming a somewhat ordered distribution of impurities within the wire, one can easily explain the experimentally observed large Au-Au separations [6, 82, 83, 87]. Although this finding offers an intriguing possibility to modify the wire properties by an intentional incorporation of impurities ( $Im$ ), a spontaneous formation

of locally ordered Au-Im-Au structures seems unlikely and remains to be proven experimentally. Another explanation has been proposed by Sun et al. [89] who suggested that the large Au-Au distances might result from chain melting. It is known, however, that phase transitions do not occur in 1D systems [34]; thus, the proposed model should be taken with precaution.

Monoatomic chains can disintegrate due to atomic movements in both longitudinal and transverse directions caused by thermal fluctuations. The probability of disintegration is determined by the characteristic frequencies of atomic vibrations in the chain, and the energy barrier atoms need to be overcome in order to leave the chain, which is comparable with the energy per atom in the chain. A change of interatomic distances due to transversal or longitudinal motion of one of the atoms leads to a transition to a nonequilibrium state, and the energy per atom increases. As the energy barriers in the longitudinal and transversal directions are comparable [90], the disintegration probabilities for these two mechanisms appear to be comparable as well. Therefore, further on we consider only one mechanism occurring due to longitudinal fluctuations.

The probability of disintegration of a chain due to longitudinal fluctuations is determined by the frequency spectrum of relaxation of density fluctuations (relaxation spectrum) of the quasi-1D system. To study the relaxation spectrum of a quasi-1D system, we apply the previously stated response functions for density functional method, which allows one to describe the equilibrium and dynamical properties of a system if its interaction potential is known. Within this method, one can find the response function  $\beta(x, t)$  that determines the relation between the density fluctuation  $\delta n(x, t)$  and the external field as well as all the space-time correlations in the system. Additionally, one can find the free energy of the quasi-1D system taking into account density fluctuations ([38] and Section 2.1). A density fluctuation appearing in the quasi-1D system can be determined as

$$\delta n(x, t) = \text{Re} \left( \int_0^\infty dk A(k) e^{-i\omega(k)t} e^{ikx} \right), \quad (87)$$

$$A(k) = \begin{cases} A = \text{const}, & k_{\min} \leq k \leq k_{\max} \\ \sim 0, & \text{otherwise.} \end{cases}$$

Here  $k$  is the modulus of the wave number, and  $A(k)$  is the amplitude of the density fluctuation, which in the analysis of cluster relaxation can be arbitrary and adequately considered to be a constant for  $k$  in the interval  $\{k_{\min} = 2\pi/L; k_{\max} = 2\pi/d\}$ . Clusters forming in the system are characterized by the parameter  $\delta n(x, t)$ , which is defined as a Fourier integral (87) in the interval  $\{k_{\min}; k_{\max}\}$ , where  $L$  is the cluster length, and  $d$  is the atomic diameter. The cluster lifetime ( $t$ ) is determined by the maximal magnitude of the imaginary part of the spectrum  $\omega(k)$  ( $\tau^{-1} = \text{Im} \omega(k)$ ) in the interval  $k_{\min} < k < k_{\max}$ .

The relaxation spectrum of the 1D system  $\omega(k)$  is determined by (70). If the relaxation of such a system is determined by diffusion with the coefficient  $D_0$ , then  $\omega_0(k) = -iD_0k^2$ .  $\theta = n_0d$  is a dimensionless density.  $n_0$  is the average number

of particles per length unit.  $\nu(k, \theta)$  is a Fourier image of the pair correlation function for interacting particles, which is related to the Fourier component of the pair distribution ( $g(k)$ ) as  $\nu(k) = g(k) - \delta(k)$ , where  $\delta(k)$  is the Dirac delta-function. Note that the divergence must be removed from  $g(k)$  before any analysis. Otherwise reverse Fourier transformation and the transition from wave numbers to coordinates are impossible due to the integral divergence. For a quasi-1D system, the pair distribution can be calculated exactly for an arbitrary short-range interaction potential  $\Phi(x)$  [44]:

$$g(x) = \frac{1}{2\pi} \int_0^\infty dk e^{ikx} g(k),$$

$$g(k) = \frac{1}{n_0} \frac{\phi(p_{1D}/T - ik)}{\phi(p_{1D}/T) - \phi(p_{1D}/T - ik)}, \quad (88)$$

$$\phi(p_{1D}) = \int_0^\infty \exp\left(-\frac{p_{1D}x + \Phi}{T}\right) dx.$$

Here  $p_{1D}$  and  $T$  are 1D pressure and temperature, respectively. Equation (88) allows one to evaluate the pair distribution and consequently the relaxation spectrum of the 1D system. We have performed an extensive analysis, which has shown that the properties of quasi-1D clusters are determined by the presence of the repulsive and attractive terms in the potential but not by the specific form of  $\Phi(x)$ . In particular, we have obtained similar results using rectangular potentials, and the Lennard-Jones as well as Morse potentials. We notice that this finding correlates well with the known results of the liquid state theory [45, 46, 91]. For the sake of simplicity, we present here the calculations of 1D pressure  $p_{1D}(\theta)$  ( $\theta = (Nd/L)$  is dimensionless density) and pair distribution done for the square-well potential with the well width  $R$  and depth  $U_0$ :

$$\Phi(x) = \begin{cases} \infty, & x \leq d \\ -U_0, & d < x \leq d + R \\ 0, & x > d + R. \end{cases} \quad (89)$$

The performed calculations give the  $p_{1D}(\theta)$  dependence:

$$p_{1D}d \left( \frac{1}{\theta} - 1 \right) = T - p_{1D}R \left[ \frac{\exp(p_{1D}R/T)}{(1 - \exp(U_0/T))} - 1 \right]^{-1}. \quad (90)$$

Equations (88) and (90) allow one to analyze the possible states of the quasi-1D system of the interacting particles of an arbitrary density. They also let us to estimate the relaxation time of a density fluctuation (cluster) as well as the interatomic distances in the clusters. We choose to perform this analysis using the parameters of the pair potential (89),  $U_0 = 1.1$  eV,  $d = 2.5$  Å, and  $R = 2.5$  Å, corresponding to the gold atoms [80]. For these parameters, we calculate the compressibility  $\eta = -(\partial\theta/\partial p_{1D})$  (Figure 9), pair distribution (Figure 10), and dimensionless spectrum  $\Omega \equiv \omega(k)/\omega_0(k)$  (Figure 11).

At low densities ( $\theta < 0.67$ ), the compressibility increases with increasing density and it approaches its first maximum at  $\theta = \theta_c = 0.18$  (Figure 9). The compressibility has a

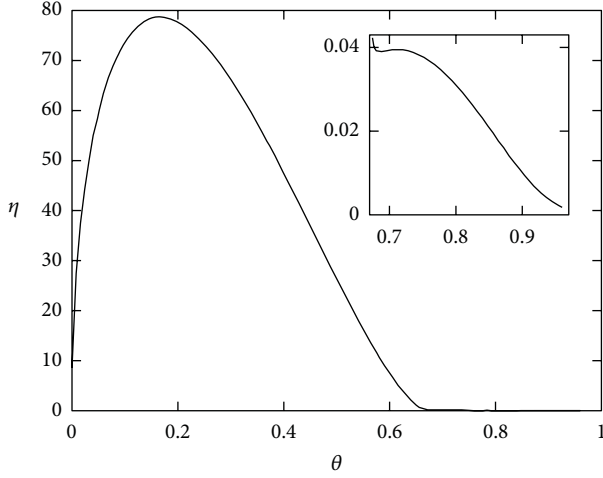


FIGURE 9: The compressibility versus density for Au atoms at room temperature.

second maximum at  $\theta = \theta_c^{(1)} = 0.71$ . The derivative of the compressibility equals 0 at extrema. Therefore, the presence of extrema can indicate changes in the system state. As we show in the following, the presence of maxima does not depend on the specific form of the pair interaction potential  $\Phi(x)$ , but it is determined by the  $U_0/T$  ratio ( $U_0$  is a characteristic depth of an arbitrary potential). The second maximum of the compressibility disappears if  $U_0/T \ll 1$ . When  $U_0/T \gg 1$ , the second maximum always exists if the condition  $R \geq d$  is satisfied regardless of the specific form of the potential  $\Phi(x)$ . Also we have to note that the ratio  $U_0/T$  provides the existence of the second maximum whereas the position of this maximum does not depend on the magnitude of this ratio. This allows us to conclude that in the limiting case  $U_0/T \gg 1$ , the variation of the temperature of a system does not lead to any qualitative changes in a state of a system.

To demonstrate how the physical state of the system changes at the compressibility maxima, let us analyze the pair distribution  $g(x)$  that determines the probability to find atoms at a certain distance from each other. It has been shown in Section 2.1 that the function  $g(x) \rightarrow 1$  when  $x \rightarrow \infty$ . The distances between the maxima of  $g(x)$  are equal to 1, 2, 3, and so forth, atomic diameters. Hence, the separation between these maxima corresponds to the interatomic distance in the clusters [45].

In the vicinity of the first compressibility maximum ( $\theta_c = 0.18$ ), the distance between the peaks of  $g(x)$  and, correspondingly, the interatomic distances in the clusters are  $\sim 3.6 \text{ \AA}$  (Figure 10(a)). At densities close to the second maximum, interatomic distance in the cluster  $\leq 3 \text{ \AA}$  (Figure 10(b)). As it was mentioned above in the limiting case  $U_0/T \gg 1$ , the variation of the temperature of a system does not lead to any changes in the state of this system. Therefore, at  $T = 300$  and 12 K, the magnitude of the gold cluster interatomic distance will be the same.

As it has been noticed previously the qualitative shape and the distance between the peaks of the pair distribution function are independent of the concrete form of the interaction potential. The pair distributions  $g(x)$  calculated for  $\theta = 0.15$

with square-well potential (solid line) and Morse potential for the Au atoms (dashed line) are compared in Figure 11.

Figure 11 demonstrates that the distances between the peaks are the same for both potentials, but the peaks for the Morse potential are higher compared to the ones obtained with the square-well potential. This difference is due to the different characteristic length scales of the Morse and square-well potentials. The characteristic length scale of the Morse potential is larger than that of the square-well potential that leads to a larger atomic attraction at long distances. Note that in the case of the Morse potential  $U_0$  in (89) is a potential well depth and  $d + R$  is the characteristic length scale of the potential.

Further, we analyze the stability of the 1D clusters. The change of the free energy of the 1D system ( $\Delta\Phi$ ) due to the cluster disintegration determines the probability of such a disintegration [34].  $\Delta\Phi$  can be divided into the following contributions:  $\Delta\Phi_0$  that is the change of the free energy due to the pair interactions in the cluster;  $\Delta\Phi_1$  that is the change of the free energy coming from changes in the cluster electronic states; and the fluctuation part  $\Delta\Phi_f$  that is an average fluctuation of the free energy of the 1D system caused by cluster disintegration calculated for the stationary state of the 1D system. Therefore, the probability of cluster disintegration can be written as

$$\begin{aligned} W &\propto W_f W_i, & W_f &\propto e^{\Delta F_f/T}, \\ W_i &\propto e^{\Delta F_i/T}, & \Delta F_i &= \Delta F_0 + \Delta F_1. \end{aligned} \quad (91)$$

To estimate the cluster lifetime  $\tau \sim W^{-1}$ , we analyze the contributions to  $\Delta\Phi$ . Since there are no phase transitions in 1D systems,  $\Delta\Phi_f$  is always positive and its magnitude is determined by the spectrum  $\Omega(k)$  [46] (Figure 12):

$$\Delta F_f \sim T \int_0^\infty dk \Omega(k) (\delta n(k))^2. \quad (92)$$

It follows from (92) that  $\Delta\Phi_f$ , which is related to the probability of cluster disintegration due to the loss of one or several atoms, is determined by the maximal magnitude of  $\Omega(k)$  in the interval ( $k_{\min} = 2\pi/L$ ;  $k_{\max} = 2\pi/d$ ). In the vicinity of the first maximum of the compressibility at  $\theta = 0.2$  (Figure 9),  $\Delta\Phi_f \sim TN\Omega(k')$ . Here  $k'$  is the wave number corresponding to the maximum of  $\Omega(k)$ ,  $k'd \sim 2$  (Figure 12(a)), and  $N$  is the number of particles in the cluster. It follows from (91) that in this case the magnitude of  $W_f$  is large for all the clusters with the length exceeding several atomic radii. In the vicinity of the second maximum of the compressibility at  $\theta = 0.7$  (Figure 9),  $\Delta\Phi_f$  becomes larger as the cluster length increases (Figure 12(b)). In this case for all clusters with the length exceeding  $L'$ , for which  $\Omega(2\pi/L') \gg 1$ ,  $\Delta\Phi_f \sim TN\Omega(2\pi/L')$  and the probability  $W_f$  is large. Thus at all densities, only clusters of a certain maximal length can exhibit a noticeable lifetime, and the formation of long clusters appears to be unfavorable.

$\Delta\Phi_i$  is the sum of the changes of the free energy of the pair interaction between atoms in the cluster  $\varepsilon_0$  and the free energy of the cluster electronic states  $\varepsilon_1$  ( $\Delta\Phi_i/N = \varepsilon_0 + \varepsilon_1$ ).

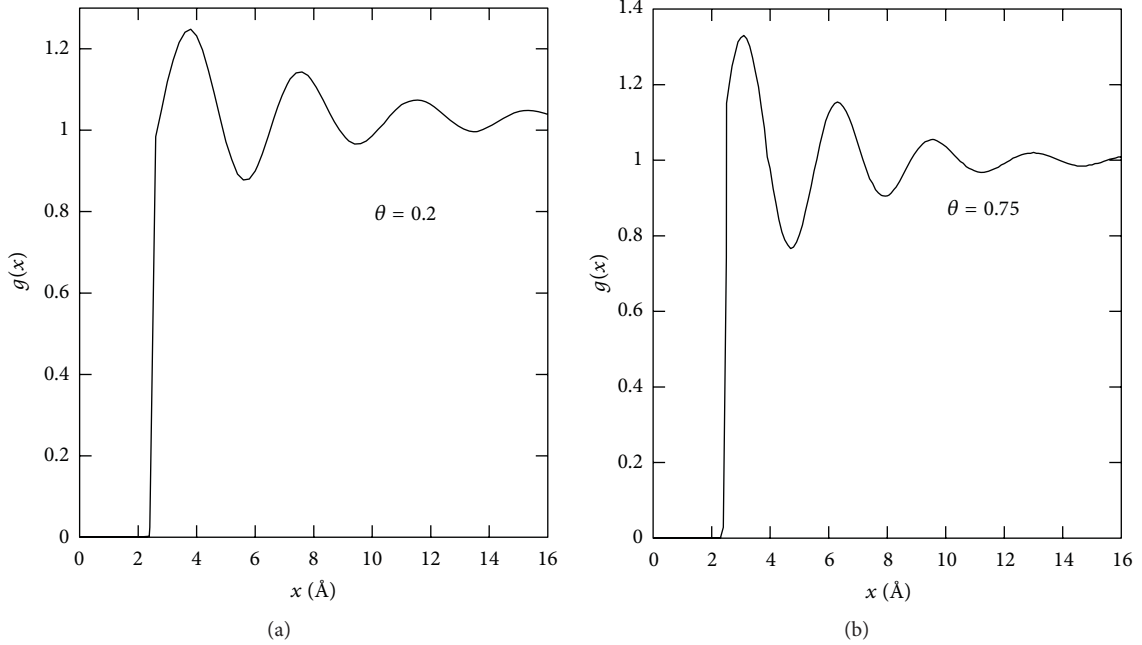


FIGURE 10: Pair distribution of gold atoms at room temperature.

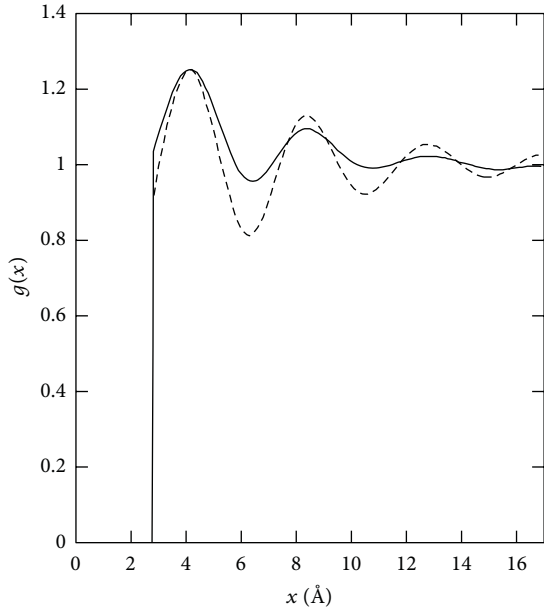
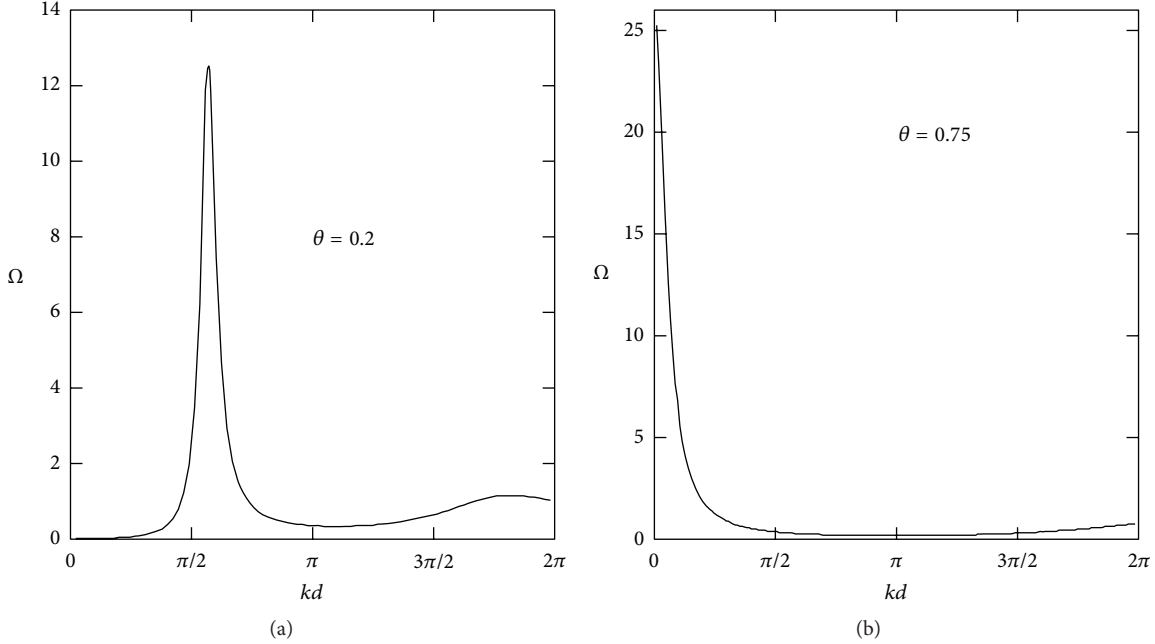


FIGURE 11: Pair distribution calculated with both square-well (solid) and Morse (dashed) potentials.

In the limiting case  $T \ll |\varepsilon_1|$ ,  $\varepsilon_1$ , is negative [92] and it is determined by the overlap of the atomic orbitals. This overlap is determined by the penetrability coefficient  $\Gamma$  of the potential barrier separating the electronic potential wells of the neighboring atoms (Section 2.4). In the quasi-classical approximation,  $\Gamma$  depends exponentially on the width and height of the potential barrier (Section 2.4). It has been shown [92] that due to collective effects, the penetrability coefficient

$\Gamma$  depends not only on the interatomic distances, but also on the difference between the maximum and minimum values ( $\Delta g$ ) of the pair distribution  $g(x)$  (Figure 10). The interatomic distances in the clusters formed at the densities about  $\theta \sim 0.2$  are larger than those for the clusters existing at  $\theta \sim 0.7$  (Figure 10), but  $\Delta g(\theta = 0.75) > \Delta g(\theta = 0.2)$ . Using the approach of [92], we find that in this case the magnitudes  $|\varepsilon_1|$  ( $|\varepsilon_1| \sim G$ ) for the clusters of both kinds appear to be similar. Thus, for our analysis of cluster stability, we can use the value  $|\varepsilon_1| \sim 0.5$  eV obtained from the measurements of the cluster conductivity in the scanning tunneling spectroscopy (STS) experiments for the Au chains on the NiAl surface [74]. The energy  $\varepsilon_0$  per atom can be written as  $\varepsilon_0 \sim (\theta/2) \int_0^\infty dx \Phi(x)g(x)$  [46]. Calculations show that  $\varepsilon_0$  is negative and  $|\varepsilon_0| \sim 1$  eV and  $|\varepsilon_0| \sim 0.7$  eV for the clusters at  $\theta \sim 0.7$  and  $\theta \sim 0.2$ , respectively.

Let us now compare the lifetime and interatomic distances calculated for the 1D clusters to the known properties of the 1D chains fabricated in experiments [74–80]. The results of the STS experiments [74] as well as the ab initio study of the electronic structure of gold wires on (110) NiAl [93] suggest that the main role of the substrate is to be a natural template insuring the one-dimensionality of the Au chains. This allows one to suggest that the observed Au-Au distances ( $\sim 2.9$  Å) in such chains to a large extent might be determined by the one-dimensionality of the system. Taking into account the minimal possible distance between Au atoms ( $\sim 2.5$  Å [81]), we can estimate the density in these chains:  $\theta = (2.5/2.9) = 0.87$ . Thus, the fabrication of Au chains on (110) NiAl can be understood as an artificial formation of 1D clusters with the density  $\theta$  fulfilling the condition  $\theta > \theta_c^{(1)}$  ( $\theta_c^{(1)} = 0.71$ ). As we have shown previously, the Au-Au separations in such 1D clusters should range from 3 Å

FIGURE 12: Dimensionless spectrum  $\Omega(k)$  versus the wave number  $k$ .

( $\theta = 0.74$ ) to  $2.7 \text{ \AA}$  ( $\theta = 0.9$ ) or  $2.5 \text{ \AA}$  ( $\theta = 1$ ). The lifetime of such clusters of the length  $L$  can be estimated as the characteristic time ( $\tau \sim \tau_f \exp(Q/T)$ ) during which an atom stays in the potential well of the depth  $Q = |\varepsilon_0| + |\varepsilon_1| - T\Omega(2\pi/L)$  (see (91)). Here  $\tau_f \sim \omega_0^{-1}(k = 2\pi/d) \sim 10^{-12} \text{ s}$ . The calculations of the spectrum  $\Omega(k)$  at  $\theta = 0.87$  show that, for example, for the cluster of the length  $L \sim 15 \text{ \AA}$ , containing  $\sim 5$  Au atoms  $\Omega(2\pi/L) \sim 10$ . In this case using the estimates obtained previously ( $|\varepsilon_1| \sim 0.5 \text{ eV}$ ,  $|\varepsilon_0| \sim 1 \text{ eV}$ ), one can estimate the lifetime of such chains to be  $t > 1000 \text{ s}$  ( $T = 300 \text{ K}$ ). Notice that in the absence of collective effects and attractive interaction between atoms in a quasi-1D system the lifetime of the chain of  $L \sim 15 \text{ \AA}$  would be very short,  $\tau \sim \omega^{-1}(k = 2\pi/L) \sim L^2/D \sim 10^{-9} \text{ s}$  (here  $D \sim 10^{-5} \text{ m}^2/\text{s}$  is the diffusion coefficient for Au atoms at the surface of NiAl [94] at  $T = 300 \text{ K}$ ).

The formation of suspended Au chains by pulling them out of the Au surface or by etching an Au film with an electron beam [2, 8, 12, 75–79] corresponds to conditions where considerable tensile stress is applied to the chain. The presence of an external force corresponds to the appearance of the one-dimensional pressure  $p_{1D} = -(\partial F/\partial L)$ , where  $F$  is a free energy of the 1D chain. One can see from (90) that 1D chains of finite length are affected by two types of forces: forces corresponding to the effective repulsion of the atoms from each other as a result of their movement (the first term in (90)) and forces corresponding to their mutual attraction that is determined by interaction potential of atoms with each other. The attractive force  $|p_{1D}^v|$  depends on depth of potential well and radius of the potential  $R$  and equals  $p_{1D}^v = -(N^2/L^2)\varepsilon R$  in the van der Waals approximation. Thus a cluster is in a compressed state. The value of compression is  $|p_{1D}^v| = (N^2/L^2)\varepsilon R$ . The presence of such a compression

can lead to loss of stability of the cluster in the transverse direction and formation of a zigzag configuration of a chain. Therefore, to form a stable linear chain, it is necessary to attach an external force to the end of a chain to compensate the compression  $|p_{1D}^v|$ . The presence of an external force corresponds to the appearance of one-dimensional pressure  $|p_{1D}^v| = -(\partial F/\partial L)$ , where  $F$  is the free energy of a one-dimensional chain. Let us estimate the lifetime of these chains.

The decrease of the tensile force corresponds to the decrease of the density  $\theta$  (90). The observation of Au chains [75–77] containing three or more atoms and exhibiting large Au-Au separations ( $\sim 3.6 \text{ \AA}$ ) can be considered as a formation of a 1D cluster at the pressure  $p_{1D}$  for which  $\gamma$  satisfies the condition  $\theta_c < \theta < \theta_c^{(1)}$  ( $\theta_c = 0.18$ ,  $\theta_c^{(1)} = 0.71$ ). The lifetime of such chains can be estimated as  $\tau \sim \tau_f \exp(Q/T)$ , where  $Q = |\varepsilon_0| + |\varepsilon_1| - T\Omega(k')$ ,  $k'd \sim 2$ . For  $|\varepsilon_1| \sim 0.7 \text{ eV}$ ,  $|\varepsilon_0| \sim 0.5 \text{ eV}$  and  $\Omega(k') \sim 10$  (Figure 12(a)), it turns out that  $\tau > 100 \text{ s}$  ( $T = 300 \text{ K}$ ). The experimentally obtained chains [1, 8, 12, 78–80] with the Au-Au separations of  $2.5\text{--}2.9 \text{ \AA}$  are formed at the pressure  $p$  for which  $\theta$  fulfills the condition  $\theta > \theta_c^{(1)}$ . According to our estimations, the Au-Au separations in such clusters should be  $< 3 \text{ \AA}$  (Figures 10(b) and 12(b)) and their lifetime is  $\tau > 1000 \text{ s}$  ( $T = 300 \text{ K}$ ,  $L \sim 25 \text{ \AA}$ ,  $\Omega(2\pi/L) \sim 20$ ) (Figure 11).

Within the framework of these assumptions, we can also estimate minimal lifetime of chains of other metals, such as Ag, Ni, and Pt. Due to the lack of experimental data on the characteristic values of  $\varepsilon_0$  for these materials let us assume  $|\varepsilon_1| + |\varepsilon_2| \sim |\varepsilon|$ , where  $\varepsilon$  is the binding energy per atom for dimer [95]. The calculated values of minimal lifetime of one-dimensional chains are presented in Table 2. As one can

TABLE 2: Minimal chain lifetime  $\tau$ , minimum number of atoms in a stable chain  $N_{\min}$ , and  $F_{0th}$ ,  $F_{0e}$  are the estimated and experimental values of the force required to break the cluster with a minimum number of atoms in it correspondingly.

|                           | Ag   | Au               | Ni               | Pt               |
|---------------------------|------|------------------|------------------|------------------|
| $ \varepsilon $ , eV [95] | 1.15 | 1.46             | 1.78             | 2.22             |
| $a$ , Å [95]              | 2.58 | 2.58             | 2.08             | 2.32             |
| $\tau$ , s                | >1   | >10 <sup>2</sup> | >10 <sup>5</sup> | >10 <sup>7</sup> |
| $N_{\min}$                | 2    | 3                | 4                | 5                |
| $F_{0th}$ , nN            | 1.4  | 2.03             | 1.5              | 2.2              |
| $F_{0e}$ , nN [13]        | 1.2  | 0.19             | 1.7              | 3.1              |

see, the material of a one-dimensional chain greatly affects its stability.

Let us estimate the minimal length of stable chains and the force that is necessary for their formation. Note that if we consider the chain as a rod of length  $L$  with a radius equal to the atomic radius  $\sigma$ , then such a rod loses its stability when it is compressed with a force greater than  $F_c = \pi^3 E \sigma^4 / L^2$  [96], where  $E$  is the Youngs modulus. So, if the compression pressure of the chain is  $|p_{1D}^v| > F_c$ , then the chain is unstable. Therefore, the minimum compressive force that ensures stability of the chain is  $|p_{1D}^v| = F_c$ . Chains of metal atoms have a conductivity comparable to the metal one [13], so the range of the interatomic potential is comparable to the length of the chain  $R = \kappa L$ , where  $\kappa \sim 1$  and varies from metal to metal. Relations  $|p_{1D}^v| = (N^2 / L^2) \varepsilon R$  and  $F_c = (\pi^3 E \sigma^4 / L^2)$  allow to estimate the minimum number of atoms in a cluster  $N_{\min} = \pi (E \sigma^4 / \kappa a)^{1/3}$ , where  $a$  is an interatomic distance in the cluster. The value  $|p_{1D}^v|$  is the force that compresses a stable cluster without external influences on it. In this case,  $|p_{1D}^v| = (N_{\min} / a) \varepsilon \kappa$  is a force  $F_0$  required to break the cluster with the minimum number of atoms in it. Table 2 shows the results of the estimations of the minimum number of particles in the chain  $N_{\min}$  and the corresponding force required to break the chains  $F_{0th}$  for chains of different material. It was assumed that  $\kappa_{Ag} = 1$  for the chains of Ag. For the rest of metal chains, this coefficient was estimated by using the relative conductivities  $\kappa_i = \kappa_{Ag} (\sigma_i / \sigma_{Ag})$ ,  $i = Au, Ni, Pt$ .

**2.4. Transport of a Two-Component Mixture in One-Dimensional Channels.** The dependence of transport selectivity on the pressure in a two-component system of atomic particles is nonmonotonic: the selectivity attains its maximal value and then decreases instead of increasing. Thus, the mechanism of diffusion enhancement in 1D channel, which was proposed in Section 2.1, is inapplicable for two-component mixtures.

The transport of a two-component mixture in subnanometer channels was considered earlier [51, 97] on the basis of the generalized phenomenological Stephan-Maxwell equation. The authors of these publications used the dependence of the chemical potential on the fill factor, taking into account the finite size of particles, but disregarding their interaction. The dependences obtained in [51, 97] also indicate a monotonous increase in the diffusion coefficients, fluxes, and selectivity upon an increase in  $\theta$  and, hence,

fail to describe the experimental data for two-component mixtures.

**2.4.1. Ground State of a System in 1D Channels.** Let us consider the surface of a porous body in contact with a two-component gas mixture at temperature  $T$  and pressure  $p$ . Suppose that  $N$  adsorption centers are located on the surface. We assume that the particles on the outer surface do not interact with one another. We also assume that the energy of a gas molecule on the surface is equal to  $\varepsilon_0^{(i)}$ ,  $i = 1, 2$ , depending on the species of the molecule. We also suppose that  $\kappa$  cylindrical channels ( $\kappa \gg 1$ ) of diameter  $d$  and length  $L$  emerge at the surface. We assume that the diameter of a cylinder is comparable to the maximal diameter of the gas molecule. Let us assume that  $\varepsilon_1^{(i)}$  is the binding energy of the  $i$ th particle at the mouth of a channel,  $N_1^{(i)}$  is the number of particles of the  $i$ th species above the membrane,  $q^{(i)}$  is the total number of particles of the  $i$ th species in the channel,  $n^{(i)}$  is the total number of  $i$ th particles in the channel and on the surface, and  $N_0$  is the number of ‘‘seats’’ in the channel. Then the partition function of the grand canonical ensemble taking into account the interaction of system of atomic particles in the channel has the form

$$\begin{aligned} \Theta = & \sum_{i=1}^2 \sum \frac{(N-k)! \exp[\beta \varepsilon_0^{(i)} (N_1^{(i)} - n^{(i)})]}{(N_1^{(i)} - n^{(i)})! [n-k - (N_1^{(i)} - n^{(i)})]} \\ & \times \frac{\kappa! \exp[\beta \varepsilon_1^{(i)} (n^{(1)} - q^{(1)})]}{(n^{(1)} - q^{(1)})! [\kappa - (n^{(1)} - q^{(1)})]} \\ & \times \frac{N_0! \exp(\beta \varepsilon_2^{(i)} q^{(i)})}{q^{(i)}! (N_0 - q^{(i)})!} \exp(\beta \mu N_1^{(i)}) Z_{\text{int}}(q^{(1)}, q^{(2)}), \\ & N_1^{(i)} + q^{(i)} = n^{(i)}. \end{aligned} \quad (93)$$

Here, the second sum corresponds to summation over configurations  $\beta = T^{-1}$ ,  $\varepsilon_2^{(i)}$  is the binding energy of particles of the  $i$ th component in the channel,  $\mu$  is the chemical potential, and  $Z_{\text{int}}(q^{(1)}, q^{(2)})$  is the partition function corresponding to the inclusion of particle interaction in the channel. Considering that the main contribution to the partition function comes from states with a large number of particles ( $q^{(i)} \gg 1$ ), we can replace partition function  $Z_{\text{int}}(q^{(1)}, q^{(2)})$  by the partition function for particles interacting in the channel, calculated for the mean value  $\bar{q}^{(i)}$  of the number of particles of each species in the channel. From the physics standpoint, this corresponds to ‘‘averaging over channels,’’ when a single channel (whose state is calculated by averaging the parameters of particles in  $\kappa$  channels) is considered instead of the large number of channels. It should be noted that this approximation is possible since the number of channels having a diameter of  $d < 1$  nm and emerging on a square centimeter of the zeolite membrane surface is large:  $\kappa \sim l_c^{-2} \sim 10^{14} \text{ cm}^{-2} \gg 1$ , where  $l_c$  is the characteristic distance between the channels on the membrane surface (Section 2.1). Using relation

(93) and following the method proposed in Section 2.1, we obtain for the adsorption isotherm

$$\begin{aligned} \frac{a}{\sigma_{av}} \theta &= c \frac{P}{p + p_0^{(1)}} + (1 - c) \frac{P}{p + p_0^{(2)}}, \\ \frac{a}{\sigma_{av}} c_1 \theta &= c \frac{P}{p + p_0^{(1)}}, \quad \frac{a}{\sigma_{av}} c_2 \theta = (1 - c) \frac{P}{p + p_0^{(2)}}, \\ p_0^{(i)} &= \frac{1}{1 - c} \left( \frac{1 - c}{c} \right)^c \left( \frac{\alpha^{(2)}}{\alpha^{(1)}} \right)^c \frac{1}{\alpha^{(2)}} \exp \left[ -\beta (\varepsilon_2^{(i)} + F_{int}) \right], \\ & \quad i = 1, \dots, 2, \\ \alpha^{(i)} &= \frac{1}{T} \left( \frac{2\pi\hbar^2}{m^{(i)}T} \right)^{3/2}, \quad i = 1, \dots, 2, \end{aligned} \quad (94)$$

where  $a = L/N_0$  is the mean distance between the seats in a channel,  $c$  is the concentration of the first component in the gas phase above the membrane,  $c_1$  and  $c_2$  are the concentrations of the components in a channel,  $\sigma_1$  and  $\sigma_2$  are the diameters of molecules of the first and second species,  $\sigma_{av} \equiv (\sigma_1 + \sigma_2)/2$  is the average diameter,  $\theta$  is the fill factor of the channel, and  $F_{int}$  has the meaning of the free energy of interaction per particle in the system of atomic particles in the channel. The concentrations of the components in the channel are chosen so that the following relation is satisfied:

$$c_1 + c_2 = 1. \quad (95)$$

In accordance with relations (94), the calculation of the adsorption isotherm is reduced to the calculation of the value of  $F_{int}$ :

$$F_{int} = -T \ln \left( \frac{Q_N}{L^N} \right), \quad (96)$$

where

$$\begin{aligned} Q_N &= \int \cdots \int \exp \left[ -\beta \sum_{i,m} U(x_i^w) \right] dx_1^w \cdots dx_N^w, \\ & \quad i = 1 \dots N, \quad w = 1, 2, \end{aligned} \quad (97)$$

$U(x)$  is the potential energy of interaction of particles of species  $w$  separated by distance  $x$  from each other. It is convenient for subsequent computations to introduce, instead of coordinates  $x_i$  of individual particles in a channel, "pair" coordinates  $\zeta_i^{lm}$ , where  $l = 1, m = 1$  corresponds to the location of two particles of the first species in the vicinity of point  $z_i$ ;  $l = 2, m = 2$  corresponds to the same for particles of the second species, and so on. Obviously, the coordinates are connected through the relation

$$\sum_1^{N_{11}} \zeta_i^{11} = L_1, \quad \sum_1^{N_{12}} \zeta_i^{12} = L_2, \quad \sum_1^{N_{22}} \zeta_i^{22} = L_2. \quad (98)$$

Here  $N_{ij}$  has the meaning of the total number of pairs of closely spaced particles of species  $i$  and  $j$  and  $L_1$  ( $L_2, L_3$ )

is the effective length "occupied" by all pairs  $N_{11}$  ( $N_{12}, N_{22}$ ) of particles. Considering that  $L_1 + L_2 + L_3 = L$  and, as a consequence, the impossibility of mutual penetration of particles through one another, we can reduce integration with respect to coordinates  $x_i$  to integration with respect to coordinates  $\zeta_{lm}$ , which corresponds to summation over all possible configurations of pairs of particles of the first and second species in the channel. Consequently, we obtain the following expression for  $Q_N$  from (97):

$$\begin{aligned} Q_N &= \int_0^\infty \cdots \int_0^\infty \delta \left( \sum_1^{N_{11}} \zeta_i^{11} - L_1 \right) \delta \left( \sum_1^{N_{12}} \zeta_i^{12} - L_2 \right) \\ & \quad \times \delta \left( \sum_1^{N_{22}} \zeta_i^{22} - L_3 \right) \\ & \quad \times \delta(L_1 + L_2 + L_3 - L) \exp \left[ -\beta \sum U(\zeta_i^{km}) \right] \\ & \quad \times \prod_i d\zeta_i^{11} d\zeta_i^{12} d\zeta_i^{22}. \end{aligned} \quad (99)$$

Using the delta function representation in the form of a line integral [45] and carrying out integration with respect to  $\zeta_i^{lm}$  independently for different values of indices  $l$  and  $m$ , we obtain

$$\begin{aligned} Q_N &= \frac{1}{16\pi^4} \oint \cdots \oint e^{S_1 L_1} \left[ \int_0^\infty \exp(\beta U(\zeta_i^{11}) - S_1 \zeta_i^{11}) \right. \\ & \quad \left. \times \prod_i d\zeta_i^{11} \right]^{N_{11}} \\ & \quad \times e^{S_2 L_2} \left[ \int_0^\infty \exp(\beta U(\zeta_i^{12}) - S_2 \zeta_i^{12}) \prod_i d\zeta_i^{12} \right]^{N_{12}} \\ & \quad \times e^{S_3 L_3} \left[ \int_0^\infty \exp(\beta U(\zeta_i^{22}) - S_3 \zeta_i^{22}) \prod_i d\zeta_i^{22} \right]^{N_{22}} \\ & \quad \times e^{S[L - (L_1 + L_2 + L_3)]} dS_1 dS_2 dS_3 dS. \end{aligned} \quad (100)$$

Integrating this relation with respect to  $\zeta_{lm}$  for the simplest form of the intermolecular interaction potential of the hard-sphere type

$$\begin{aligned} U(\xi_i^{11}) &= \begin{cases} 0, & \zeta_i^{11} > \sigma_1 \\ \infty, & \zeta_i^{11} \leq \sigma_1, \end{cases} \\ U(\xi_i^{12}) &= \begin{cases} 0, & \zeta_i^{12} > \sigma_{av} \\ \infty, & \zeta_i^{12} \leq \sigma_{av}, \end{cases} \\ U(\xi_i^{22}) &= \begin{cases} 0, & \zeta_i^{22} > \sigma_2 \\ \infty, & \zeta_i^{22} \leq \sigma_2, \end{cases} \end{aligned} \quad (101)$$

we obtain

$$Q_N = \frac{\Gamma(Nc_1^2 + 1) \Gamma(Nc_1c_2 + 1) \Gamma(Nc_2^2 + 1)}{4\pi} \frac{1}{N} \quad (102)$$

$$\times [L - N(\sigma_1c_1^2 + \sigma_2c_2^2 + 2\sigma_{av}c_1c_2)]^N.$$

Here we have used the definition  $N_{ij} = Nc_i c_j$  ( $N$  is the total number of particles in a channel) and the representation of a factorial in terms of the gamma function,  $N! = \Gamma(N + 1)$ . Eliminating the factor corresponding to an ideal system of atomic particles from relation (102) and substituting the result into (96), we obtain the following expression for  $F_{int}$ :

$$F_{int} = -T \ln(1 - C\theta), \quad C \equiv \frac{1}{\sigma} (\sigma_1c_1^2 + \sigma_2c_2^2 + 2\sigma_{av}c_1c_2). \quad (103)$$

As  $c_1 \rightarrow 0$  or  $c_2 \rightarrow 0$ , expression (103) is transformed into the corresponding expression for the free energy of a one-component system of atomic particles in a 1D channel (Section 2.1). From relations (103) and (94) for the adsorption isotherm of a two-component system of atomic particles, we finally derive the expressions

$$\frac{a}{\sigma_{av}} \theta = c \frac{p(1 - C\theta)}{p(1 - C\theta) + \tilde{p}_0^{(1)}} + (1 - c) \frac{p(1 - C\theta)}{p(1 - C\theta) + \tilde{p}_0^{(2)}},$$

$$\tilde{p}_0^{(i)} = \frac{1}{1 - c} \left( \frac{1 - c}{c} \right)^c \left( \frac{\alpha^{(2)}}{\alpha^{(1)}} \right)^c \frac{1}{\alpha^{(2)}} \exp[-\beta \varepsilon_2^{(i)}], \quad i = 1, \dots, 2. \quad (104)$$

Using these relations and specifying the external conditions, we can obtain the fill factor and the component concentration in the channel. For  $c = 0$  and  $c = 1$ , isotherm (104) transforms into the isotherm for a one-component system of atomic particles, which was obtained in Section 2.1. Let us now analyze the ground state of a mixture in 1D channels. It is known (Section 2.1) that short-lived clusters can be formed in 1D channels in the case of a one-component system of atomic particles. The formation of clusters can apparently be expected in the case of a two-component system of atomic particles also. In order to describe possible transition to an inhomogeneous clustered state, we must calculate and analyze the free energy of the system taking into account fluctuations and the equation determining the amplitude of these fluctuations in the system (equation for the order parameter), which follows from the free energy. Since molecular transport depends on the lifetime of clusters, the analysis of the equation for the order parameter aims at determining the characteristic lifetime of clusters as a function of the channel fill factor and, hence, as a function of pressure, temperature, and composition of the mixture above the membrane. In order to describe the ground state of the 1D system and relaxation process to the ground state, one is to know the free energy  $F$  of the 1D system and two-component functional  $\Delta[n_\alpha]$ ,  $\alpha = 1, 2$ , determined by the relations (39), (44). The functional  $\Delta[n_\alpha]$  can be written in the way of (49):

$$\Delta[n_\alpha] = \Delta_0[n_\alpha] + \Delta_{int}[n_\alpha]. \quad (105)$$

Here  $\Delta_0[n_\alpha]$  is the functional of the non-interacting system and  $\Delta_{int}[n_\alpha]$  corresponds to the particles interaction:

$$\Delta_0[n_\alpha] = \lim_{\tau \rightarrow \infty} \tau^{-1} \int_0^\tau F_0[n_\alpha(x, t)] dt, \quad (106)$$

$$\Delta_{int}[n_\alpha] = \lim_{\tau \rightarrow \infty} \tau^{-1} \int_0^\tau F_1[n_\alpha(x, t)] dt,$$

where  $F_0$  is the free energy per temperature unit of the ideal (non-interacting) system,  $F_1$  is the fluctuation part of the free energy due to interatomic interaction in the mixture. Quantity  $\Delta$  can be expressed in terms of the response function  $\beta_{\alpha\beta}(x, x', t, t')$  of the two-component system, which is defined as

$$\delta n_\alpha(x, t) = \int \beta_{\alpha\beta}(x, x', t, t') eV_\beta^{ext}(x', t') dx' dt', \quad (107)$$

where  $\delta n_\alpha(x, t)$  is the density fluctuation of particles of species  $\alpha$  and  $eV_{ext}(x', t')$  is a weak external field depending on time. Here and in the following, we assume summation over recurrent indices. Response function  $\delta n_\alpha(x, t)$  can be derived by varying directly the mean value of functional  $\Delta$  over  $\delta n(x, t)$  [38]:

$$\beta_{\alpha\beta}(x, x', t, t') = - \left( \frac{\delta^2 \Delta}{\delta n_\alpha(x, t) \delta n_\beta(x', t')} \right)^{-1}. \quad (108)$$

Using this relation, we can obtain the expansion of functional  $\Delta$  into a series in deviations  $\delta n$  of density from its mean value in the case of a multicomponent system. In the Fourier representation, the result has the form

$$\Delta = \frac{1}{2} \int dk d\omega \beta_{\alpha\beta}^{-1}(k, \omega) \delta n_\alpha(k, \omega) \delta n_\beta^*(k, \omega)$$

$$+ \frac{1}{3} \int dk d\omega dk' d\omega' \frac{\delta \beta_{\alpha\beta}^{-1}(k, \omega)}{\delta n_\gamma(k', \omega')}$$

$$\times \delta n_\alpha(k, \omega) \delta n_\beta^*(k, \omega) \delta n_\gamma(k', \omega')$$

$$+ \frac{1}{4} \int dk d\omega dk' d\omega' dk'' d\omega'' \frac{\delta^2 \beta_{\alpha\beta}^{-1}(k, \omega)}{\delta n_\gamma(k', \omega') \delta n_\delta^*(k'', \omega'')}$$

$$\times \delta n_\alpha(k, \omega) \delta n_\beta^*(k, \omega) \delta n_\gamma(k', \omega') \delta n_\delta^*(k, \omega) + \dots \quad (109)$$

Here  $\beta_{\alpha\beta}(k, \omega)$  is the response function of the multi-component system in the Fourier representation, and the asterisk indicates complex conjugation. It follows from the fluctuation-dissipative theorem [98] that response function  $\beta_{\alpha\beta}(k, \omega)$  is directly proportional to the pair distribution; this enables us to calculate  $\beta_{\alpha\beta}(k, \omega)$  for a 1D system with an arbitrary density, for which the pair distribution is known exactly [45]. To calculate  $\Delta$ , we use the local approximation that makes it possible to replace functional derivatives by ordinary derivatives [38]:

$$\frac{\delta^2 \varphi}{\delta \rho(x_1) \delta \rho(x_2)} \approx \delta(x - x_1) \delta(x - x_2) \frac{d^2 \varphi}{d\rho^2}. \quad (110)$$

Using this relation, we obtain from (109)

$$\begin{aligned} \Delta = & \frac{1}{2} \int dk d\omega \beta_{\alpha\beta}^{-1}(k, \omega) \delta n_{\alpha}(k, \omega) \delta n_{\beta}^*(k, \omega) \\ & + \frac{1}{3} \int dk d\omega dk' d\omega' \frac{\partial \beta_{\alpha\beta}^{-1}(k, \omega)}{\partial n_{\gamma}(k', \omega')} \\ & \quad \times \delta n_{\alpha}(k, \omega) \delta n_{\beta}^*(k, \omega) \delta n_{\gamma}(k', \omega') \\ & + \frac{1}{4} \int dk d\omega dk' d\omega' dk'' d\omega'' \frac{\partial^2 \beta_{\alpha\beta}^{-1}(k, \omega)}{\partial n_{\gamma}(k', \omega') \partial n_{\delta}^*(k'', \omega'')} \\ & \quad \times \delta n_{\alpha}(k, \omega) \delta n_{\beta}^*(k, \omega) \delta n_{\gamma}(k', \omega') \delta n_{\delta}^*(k'', \omega'') + \dots \end{aligned} \quad (111)$$

Thus, the evaluation of functional (111) in the one-dimensional case can be reduced to the calculation of response functions. In the case of two-component systems, the equations for determining partial response functions  $\beta$  have the form [38]

$$\begin{aligned} \widehat{\beta}(k, \omega) &= \widehat{\beta}^{(0)}(k, \omega) + \widehat{\beta}^{(0)}(k, \omega) \widehat{R}(k, \omega) \widehat{\beta}(k, \omega), \\ \widehat{\beta}(k, \omega) &\equiv \beta_{ik}(k, \omega) = \begin{pmatrix} \beta_{11}(k, \omega) & \beta_{12}(k, \omega) \\ \beta_{21}(k, \omega) & \beta_{22}(k, \omega) \end{pmatrix}, \\ \widehat{R}(k, \omega) &\equiv R_{ik}(k, \omega) = \begin{pmatrix} R_{11}(k, \omega) & R_{12}(k, \omega) \\ R_{21}(k, \omega) & R_{22}(k, \omega) \end{pmatrix}, \\ \widehat{\beta}^{(0)}(k, \omega) &\equiv \beta_{ik}^{(0)}(k, \omega) = \begin{pmatrix} \beta_{11}^{(0)}(k, \omega) & \beta_{12}^{(0)}(k, \omega) \\ \beta_{21}^{(0)}(k, \omega) & \beta_{22}^{(0)}(k, \omega) \end{pmatrix}. \end{aligned} \quad (112)$$

Here  $\beta_{ik}^{(0)}(k, \omega)$  and  $\beta_{ik}(k, \omega)$  are the partial response functions for noninteracting and interacting particles, respectively. The quantity  $R_{ik}(k, \omega)$  describes the effective dynamic interaction between particles and is defined as

$$R_{ik}(k, \omega) = \frac{\delta^2 \Delta_{\text{int}}}{\delta n_i(k, \omega) \delta n_k(k, \omega)}. \quad (113)$$

Premultiplying expression (112) by  $(\widehat{\beta}^{(0)}(k, \omega))^{-1}$  and postmultiplying it by  $\widehat{\beta}^{-1}(k, \omega)$ , we obtain

$$(\widehat{\beta}^{(0)}(k, \omega))^{-1} = \widehat{\beta}^{-1}(k, \omega) + \widehat{R}(k, \omega). \quad (114)$$

Over long time periods ( $t \gg \tau_{\text{mom}}$ ), function  $R_{ik}(k, \omega)$  can be represented in the form

$$\widehat{R}(k, 0) = (\widehat{\beta}^{(0)}(k, 0))^{-1} - \widehat{\beta}^{-1}(k, 0). \quad (115)$$

In view of homogeneity and the absence of correlations in a system of noninteracting particles, we have  $\widehat{\beta}^{(0)}(k, 0) = \widehat{\beta}^{(0)}(0, 0) = b_{ij}$ , where

$$b_{ij} \equiv -\frac{\partial^2 S}{\partial c_i \partial c_j}, \quad (116)$$

with  $S$  being the entropy of the two-component system of atomic particles divided by temperature in the absence of the intermolecular interaction. In this case, we obtain the following expression for the effective interaction from (115):

$$\widehat{R}(k, 0) = (\widehat{\beta}^{(0)}(0, 0))^{-1} - \widehat{\beta}^{-1}(k, 0). \quad (117)$$

Substituting this expression into (114), we obtain the following relation for response function  $\widehat{\beta}(k, \omega)$ :

$$\widehat{\beta}^{-1}(k, \omega) = (\widehat{\beta}^{(0)}(k, \omega))^{-1} + \widehat{\beta}^{-1}(k, 0) - (\widehat{\beta}^{(0)}(0, 0))^{-1}. \quad (118)$$

In order to calculate the response function  $\widehat{\beta}(k, 0)$  for a system of interacting particles, we can use the fluctuation-dissipative theorem connecting response function  $\widehat{\beta}(k, 0)$  with the pair correlation function for a system of interacting particles:

$$\beta_{ij}(k, 0) = -[b_{ij}^{-1} + c_i c_j \theta^2 \nu_{ij}(k)]. \quad (119)$$

Here  $\nu_{ij}(k)$  is the pair correlation function divided by temperature [46]. Relation (119) is a generalization of the relation (68) for one-component systems to two-component systems.

Thus, the calculation of the response function can be reduced to the calculation of the pair correlation function or function  $g_{ik}$  called a pair distribution [46] and connected with the pair correlation function through the relation

$$\nu_{ij}(k) = g_{ij}(k) - c_i c_j \delta(k). \quad (120)$$

We will calculate the pair distribution using the method described in [45] and determine  $g_{11}(k)$ . Functions  $g_{12}(k)$  and  $g_{22}(k)$  are calculated similarly. Pair distribution  $g_{11}(x)$  can be written in the form [45]

$$g_{11}(k) = \sum_{m=1}^{\infty} \Psi_m^{11}(k) - 1, \quad (121)$$

where the function  $\Psi_m^{11}(k)$  is the Fourier transform of the function  $\Psi_m^{11}(\zeta)$ , which is equal to the probability of finding two particles of the first species separated from each other by  $m$  other particles and by distance  $\zeta$ . Function  $\Psi_m^{11}(k)$  can be written in the form

$$\begin{aligned} \Psi_m^{11}(k) = & \int d\zeta e^{ik\zeta} \left( \left( \sum_{n=0}^{N_{12} N_{22}} \overline{Q}_{m-n-l, n, l}(\zeta) \right. \right. \\ & \cdot \overline{Q}_{N_{11}-(m-n-l), N_{12}-n, N_{22}-l}(L-\zeta) \left. \left. \right) \right. \\ & \left. \times (\overline{Q}_{N_{11}, N_{12}, N_{22}}(L))^{-1} \right), \end{aligned} \quad (122)$$

where  $\overline{Q}_{m,n,l}(\zeta)$  is the configuration integral corresponding to the presence of  $m$  pairs of particles of the first species,  $n$  pairs of particles of the first and second species, and  $l$  pairs of particles of the second species in a channel. For  $m = N_{11}$ ,  $n = N_{12}$ , and  $l = N_{22}$ , the expression for configuration integral  $\overline{Q}_{m,n,l}(\zeta)$  coincides with (98) [45]:

$$\begin{aligned} \overline{Q}_{m,n,l}(\zeta) &= \oint dS [\varphi_{11}(S)]^m [\phi_{12}(S)]^n [\phi_{22}(S)]^l e^{S\zeta}, \\ \phi_{ij}(S) &= \int_0^\infty e^{-Sx} e^{-U_{ij}(x)/T} dx. \end{aligned} \quad (123)$$

Here  $\zeta$  has the meaning of a coordinate and  $\phi_{ij}(S)$  is the Laplace mapping of function  $f_{ij}(x) \equiv \exp(-U_{ij}(x)/T)$ . In the case of an intermolecular interaction potential in the form of that in the hard-sphere model, we have

$$\begin{aligned} U_{11}(x) &= \begin{cases} 0, & x > \sigma_1 \\ \infty, & x \leq \sigma_1, \end{cases} \\ U_{12}(x) &= \begin{cases} 0, & x > \sigma_{av} \\ \infty, & x \leq \sigma_{av}, \end{cases} \\ U_{22}(x) &= \begin{cases} 0, & x > \sigma_2 \\ \infty, & x \leq \sigma_2. \end{cases} \end{aligned} \quad (124)$$

Substituting these relations into (123), we obtain the following expression for the configuration integral:

$$\begin{aligned} \overline{Q}_{m,n,l}(\xi) &= e^{p\xi/T} \left[ \phi_{11}\left(\frac{p}{T}\right) \right]^m \left[ \phi_{12}\left(\frac{p}{T}\right) \right]^n \left[ \phi_{22}\left(\frac{p}{T}\right) \right]^l, \\ \phi_{11}\left(\frac{p}{T}\right) &= \frac{T}{p} e^{-p\sigma_1/T}, \quad \phi_{12}\left(\frac{p}{T}\right) = \frac{T}{p} e^{-p\sigma_{av}/T}, \\ \phi_{22}\left(\frac{p}{T}\right) &= \frac{T}{p} e^{-p\sigma_2/T}. \end{aligned} \quad (125)$$

Here  $p$  has the meaning of one-dimensional ‘‘pressure.’’ Substituting relation (125) into (122), we obtain the following expression for pair distribution  $g_{11}(k)$ :

$$\begin{aligned} g_{11}(k) &= \frac{(p/T) e^{ik\sigma_1}}{(p/T) - ik - (p/T) e^{ik\sigma_1}} \cdot \frac{1}{1 - e^{ik(\sigma_{av} - \sigma_1)}} \\ &\cdot \frac{1}{1 - e^{ik(\sigma_2 - \sigma_1)}}. \end{aligned} \quad (126)$$

In the long-wave approximation ( $0 \leq k \leq 2\pi/\max\{\sigma_1, \sigma_2\}$ ), expression (126) contains no poles and we obtain

$$\begin{aligned} g_{11}(x) &= \frac{1}{\theta_{\text{eff}} \sum_{m,x-ma>0} \frac{(y-m(\sigma_1/a))^{m-1}}{(m-1)!(1/\theta_{\text{eff}} - 1)^m} \\ &\cdot \exp\left(-\frac{y-m}{1/\theta_{\text{eff}} - 1}\right), \end{aligned} \quad (127)$$

$$y = \frac{x}{a(c_1, c_2)}, \quad \theta_{\text{eff}} = \frac{N \cdot a(c_1, c_2)}{L},$$

$$a_{\text{eff}}(c_1, c_2) = \sigma_1 c_1^2 + \sigma_2 c_2^2 + 2\sigma_{av} c_1 c_2.$$

Functions  $g_{12}(x)$  and  $g_{22}(x)$  can be calculated similarly. Substituting expressions (127) and (119) into (118), we obtain the final expression for response function  $\hat{\beta}(k, 0)$ :

$$\begin{aligned} (\hat{\beta}(k, 0))^{-1} &= \begin{pmatrix} -\frac{a_{11}}{1 + a_{11}\theta^2 c_1^2 \Delta\nu_{11}(k)} & -\frac{a_{12}}{1 + a_{12}\theta^2 c_1 c_2 \Delta\nu_{12}(k)} \\ -\frac{a_{21}}{1 + a_{21}\theta^2 c_1 c_2 \Delta\nu_{21}(k)} & -\frac{a_{22}}{1 + a_{22}\theta^2 c_2^2 \Delta\nu_{22}(k)} \end{pmatrix}. \end{aligned} \quad (128)$$

Here

$$\Delta\nu_{ij}(k) \equiv \nu_{ij}(k) - \nu_{ij}(0), \quad a_{ij} \equiv -\frac{\partial^2 F}{\partial c_i \partial c_j}. \quad (129)$$

$F$  is the free energy of a two-component system of atomic particles with interaction, referred to temperature, which can be calculated by differentiating configuration integral  $\overline{Q}_N$  twice with respect to concentration. Function  $\hat{\beta}(k, \omega)$  can be obtained by generalizing the response function of the one-component system of atomic particles,

$$\beta_0^{-1}(k, \omega) = -\frac{1}{\theta} \left(1 + \frac{\omega}{\omega_0}\right) = \frac{\partial^2 F}{\partial \theta^2} \left(1 + \frac{\omega}{\omega_0}\right) \quad (130)$$

derived in Section 2.1, to the case of a two-component mixture:

$$\begin{aligned} (\hat{\beta}^{(0)}(k, \omega))^{-1} &= \begin{pmatrix} \left(1 + \frac{\omega}{\omega_1}\right) b_{11} & \left(1 + \frac{\omega}{\omega_1}\right) b_{12} \\ \left(1 + \frac{\omega}{\omega_2}\right) b_{21} & \left(1 + \frac{\omega}{\omega_2}\right) b_{22} \end{pmatrix}, \end{aligned} \quad (131)$$

$$\omega_1^{(p)} = -iD_1 k^2, \quad \omega_2^{(p)} = -iD_2 k^2.$$

Here  $D_1$ ,  $D_2$ ,  $\omega_1^{(p)}$ , and  $\omega_2^{(p)}$  are the diffusion coefficients and the relaxation frequency spectra for pure components. Substituting relations (128) and (131) into (118), we obtain the following expression for response function  $\beta(k, \omega)$ :

$$(\beta(k, \omega))^{-1} = \begin{pmatrix} \frac{\omega}{\omega_1^{(p)}} b_{11} - \frac{a_{11}}{1 + a_{11} \theta^2 c_1^2 \Delta \nu_{11}(k)} & \frac{\omega}{\omega_1^{(p)}} b_{12} - \frac{a_{12}}{1 + a_{12} \theta^2 c_1 c_2 \Delta \nu_{12}(k)} \\ \frac{\omega}{\omega_2^{(p)}} b_{21} - \frac{a_{21}}{1 + a_{21} \theta^2 c_1 c_2 \Delta \nu_{21}(k)} & \frac{\omega}{\omega_2^{(p)}} b_{22} - \frac{a_{22}}{1 + a_{22} \theta^2 c_2^2 \Delta \nu_{22}(k)} \end{pmatrix}. \quad (132)$$

It is convenient for subsequent analysis to pass to new variables. For a two-component system, the relation  $c_1 + c_2 = 1$  holds and quantity  $\delta n$  can be represented in the form

$$\delta \mathbf{n}(k, \omega) = \begin{pmatrix} 1 \\ -1 \end{pmatrix} \xi(k, \omega), \quad (133)$$

where  $\xi$  can be interpreted as an order parameter. Substituting (133) into (111), we obtain the expression for functional  $\Delta$ :

$$\begin{aligned} \Delta = & \frac{1}{2} \int dk d\omega \Omega |\xi_{k,\omega}|^2 + \frac{2}{3} \int dk d\omega \frac{\partial \Omega}{\partial n} |\xi_{k,\omega}|^2 \xi_{k,\omega} \\ & + \int dk d\omega \frac{\partial^2 \Omega}{\partial n^2} |\xi_{k,\omega}|^4 + \dots, \end{aligned} \quad (134)$$

where

$$\begin{aligned} \Omega \equiv & (\beta_{11}(k, \omega))^{-1} - (\beta_{12}(k, \omega))^{-1} \\ & - (\beta_{21}(k, \omega))^{-1} + (\beta_{22}(k, \omega))^{-1}. \end{aligned} \quad (135)$$

Series (134) can be summed and written in the form

$$\Delta = \frac{1}{2} \int dk d\omega |\xi_{k,\omega}|^2 \Omega(n, c + \xi_{k,\omega}, k, \omega). \quad (136)$$

The formal proof of the correctness of representing quantity  $\Delta$  in form (136) without analyzing the convergence of the corresponding series follows from the expansion of expression (136) into a power series of order parameter  $\xi$ . This expansion exactly reproduces series (134) (at least, to within terms on the order of  $\xi^5$ ). Using relations (132), (135), and (136), we can obtain the dependence of functional  $\Delta$  on the wave vector and order parameter of the system. The minimum of functional  $\Delta$  determines the ground state of the system. Substituting relation (132) into (136), evaluating the derivative of  $\Delta$  with respect to the order parameter, and applying the inverse Fourier transformation in frequency  $\omega$  to the resulting relation, we obtain

$$\frac{\partial \xi_k}{\partial t} = -\bar{D} k^2 \frac{\partial (F_1(\xi_k, k))}{\partial \xi_k}, \quad (137)$$

where

$$\bar{D} = \left( \frac{b_{11} - b_{12}}{D_1} + \frac{b_{22} - b_{21}}{D_2} \right)^{-1},$$

$$F_1(\xi_k, k) \equiv \frac{1}{2} \Omega(c + \xi_k, k) \xi_k^2,$$

$$\begin{aligned} \Omega(c, k) = & -\frac{a_{11}}{1 + a_{11} \theta^2 c_1^2 \Delta \nu_{11}(k)} + \frac{2a_{12}}{1 + a_{12} \theta^2 c_1 c_2 \Delta \nu_{12}(k)} \\ & - \frac{a_{22}}{1 + a_{22} \theta^2 c_2^2 \Delta \nu_{22}(k)}. \end{aligned} \quad (138)$$

Equation (137) has the same form as the equation usually used for the order parameter. The role of the order parameter is played in this case by the quantity defined by relation (133). It should be noted that the order parameter here could be either positive or negative. The cases when  $\xi > 0$  and  $\xi < 0$  correspond to the density fluctuation of the first and the second components, respectively. The role of the diffusion coefficient is played by quantity  $\bar{D}$  depending on the fill factor and the concentration of components in channels via coefficients  $a_{ij}$  and  $b_{ij}$  defined by relations (116) and (128). It should be noted that the concentration of the components in a channel (and its fill factor) could be determined unambiguously from isotherm (104) proceeding from the pressure, temperature, and composition of the system of atomic particles. Analysis of functional  $F_1$  as a function of order parameter  $\xi$  and wave vector  $k$  makes it possible to investigate the possibility for a transition of the system to an inhomogeneous state. For example, when the minimum of functional  $F_1$  is attained for  $\xi \neq 0$ ,  $k = 0$ , a conventional phase transition to a homogeneous state takes place [99]. The minimum at  $\xi = 0$ ,  $k \equiv k_c \neq 0$  corresponds to the propagation of a density wave over a distance of  $r \sim k_c^{-1}$ . In the case when the minimum is attained at  $\xi \neq 0$  and  $k \neq 0$ , a transition to an inhomogeneous state with clusters formed in the system is realized [99]. Local minima here determine metastable states. Figure 13 shows the graphs illustrating the dependence of  $F_1$  on order parameter  $\xi_k$  and wave vector  $k$  for a mixture in which one of the gases (first) is a strong sorbate, while the other gas is a weak sorbate. The chosen parameters ( $a = 3.8 \text{ \AA}$ ,  $\sigma_1 = 4.3 \text{ \AA}$ ,  $\sigma_2 = 3.6 \text{ \AA}$ ,  $\varepsilon_1 = 0.61 \text{ eV}$ ,  $\varepsilon_2 = 0.38 \text{ eV}$ ,  $p = 2000 \text{ kPa}$ , and  $T = 300 \text{ K}$ ) correspond to a methane-butane molecular mixture [51] and make it possible to describe adsorption and fluxes of these one-component gases in zeolite membranes. It should be noted that the choice of parameters  $p$ ,  $T$ , and  $c$  determines unambiguously the filling factor  $\theta$  and concentrations  $c_1$  and  $c_2$  of gases in a channel.

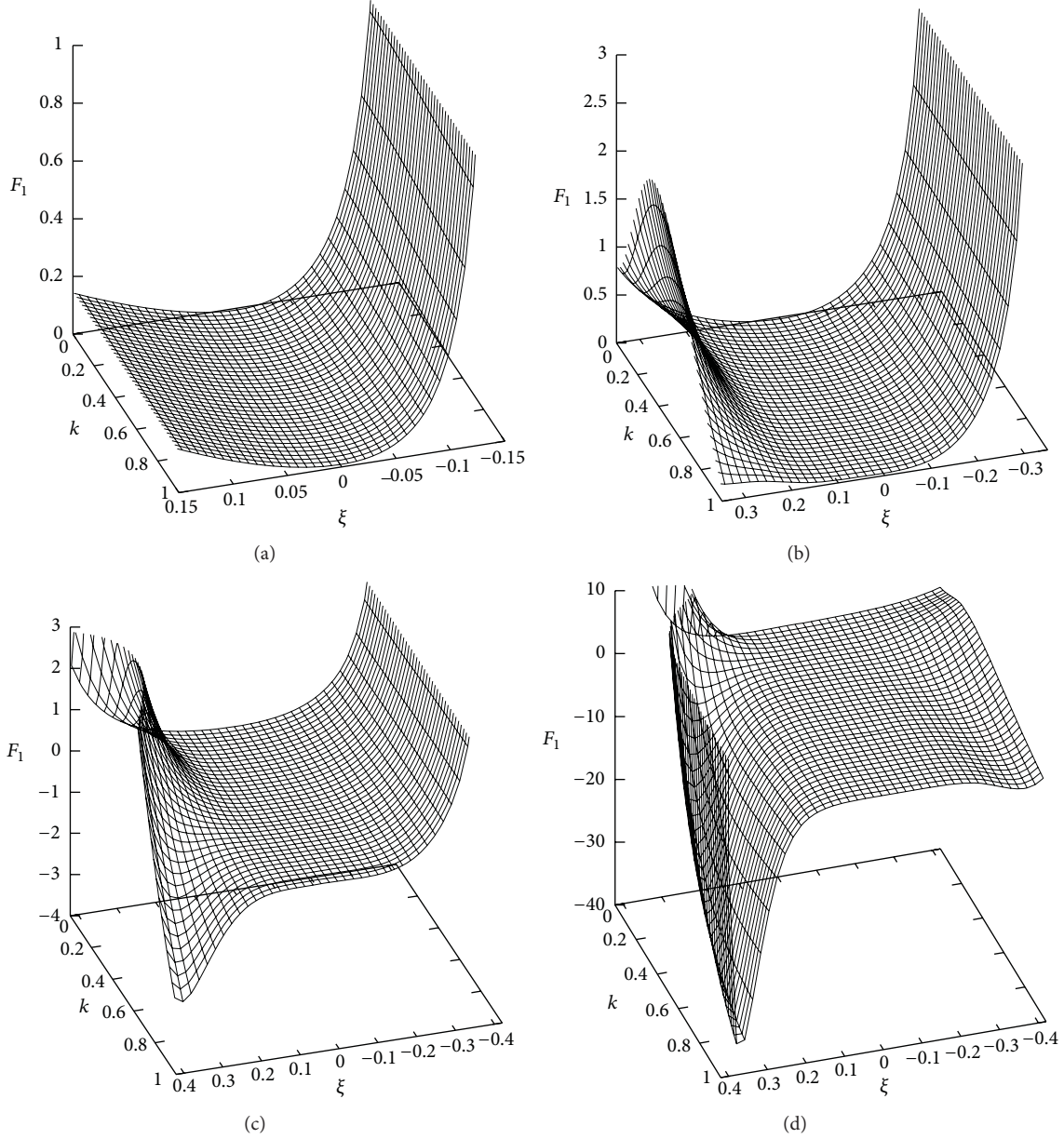


FIGURE 13: Dependence of free energy  $F_1$  on the order parameter and wave vector for various concentrations of the first component in the mixture: (a)  $c = 0.1$  ( $\theta = 0.67$ ), (b)  $c = 0.25$  ( $\theta = 0.71$ ), (c)  $c = 0.3$  ( $\theta = 0.74$ ), and (d)  $c = 0.45$  ( $\theta = 0.75$ ).

For low concentrations of the first component in a gas mixture and for fill factors  $\theta \leq 0.7$ , functional  $F_1$  has only one minimum at  $\xi = 0$ ,  $k = 0$  (Figures 13(a) and 13(b)). This corresponds to a homogeneous state of the system. An increase in the concentration of the first component leads to the emergence of local minima in functional  $F_1$ .

In this case, the global minimum is shifted to point  $\xi = \xi_c > 0$ ,  $k = k_c$ . In this case, the ground state of the system becomes spatially inhomogeneous, which corresponds to the formation of clusters in the system. This situation will be analyzed in greater detail later. Equation (137) for the order parameter also allows us to calculate the characteristic relaxation times for the emerging density fluctuation depending on external conditions. For this purpose, we expand

functional  $F_1(\xi_k, k)$  into a series in the vicinity of  $\xi_k = 0$  to within the first nonvanishing term:

$$F_1(\xi_k, k) \sim \lambda(k) \xi_k^2. \quad (139)$$

Substituting (139) into (137), we obtain

$$\frac{\partial \xi_k}{\partial t} = -\frac{\xi_k}{\tau}, \quad \tau = (2\lambda(k) \bar{D} k^2)^{-1}. \quad (140)$$

The quantity  $\tau$  is the lifetime of the  $k$ th mode of the density fluctuation emerging in the vicinity of  $\xi_k = 0$ . The curves describing the lifetime of the emerging fluctuation as a function of the wave vector for different mixture compositions are shown in Figure 14. It can be seen from Figure 14 that,

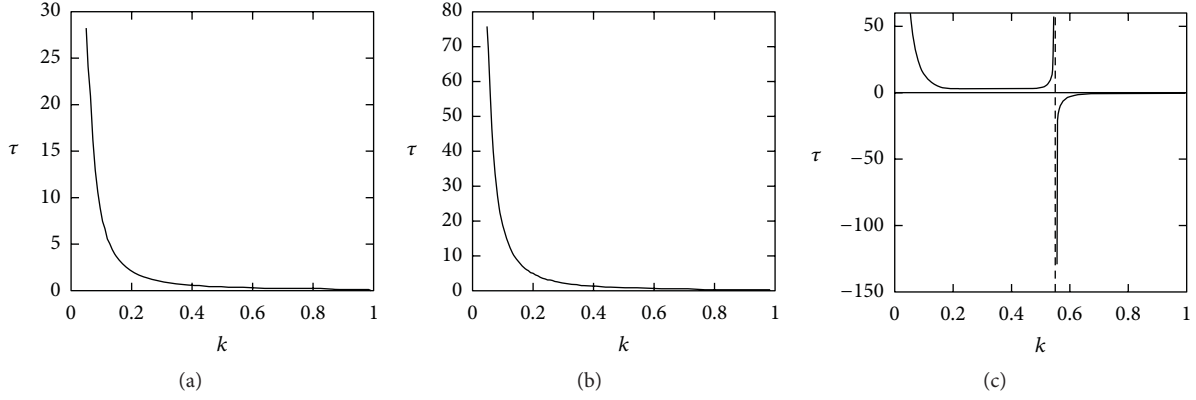


FIGURE 14: Dependence of lifetime  $\tau$  on wave vector  $k$  for  $c = 0.1$  (a), 0.3 (b), and 0.45 (c).

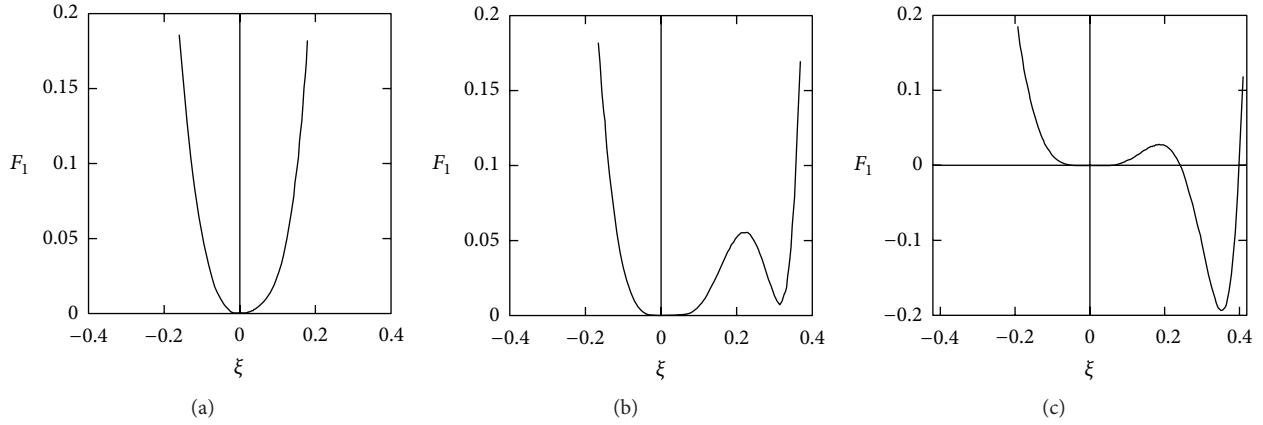


FIGURE 15: Dependence of free energy  $F_1$  on the order parameter for different values of the wave vector for  $c = 0.3$ :  $k = 0.1$  (a), 0.3 (b), and 0.5 (c).

for a low concentration of the highly adsorbed component, the lifetime decreases monotonically with increasing wave vector, while the free energy has a minimum at  $\xi = 0$ . From the physics standpoint, this means that the state of the system in a channel for a given composition of the mixture is homogeneous and the growth of clusters is energetically disadvantageous. It should be noted that the fill factor of the channel is small in this case, but short-lived clusters with the lifetime

$$\tau \sim \frac{r^2}{D} = \frac{r^2}{D_0} \exp\left(\frac{E_a}{T}\right) \quad (141)$$

can be formed due to density fluctuations. Here  $D = D_0 \exp(-E_a/T)$  is the diffusion coefficient of solitary particles,  $E_a$  is the diffusion activation energy, and  $r$  is the characteristic size of fluctuations. Characteristic size  $r$  is determined, as in Section 2.1, from the position of the extremum of the imaginary part of the spectrum divided by the square of the wave vector. It should be noted that the value of  $r$  increases with the fill factor of the channel Section 2.1. Expression (142) can be derived by expanding order parameter (137) into a series in the vicinity of  $\xi = 0$ .

For low concentrations, expression (141) coincides with the characteristic diffusion decay time for density fluctuations.

An increase in the concentration of the first component of the mixture to  $c = 0.3$  elevates the fill factor of the channel to  $\theta = 0.74$  (see Figure 13(c)), while  $F_1$  acquires two more minima for  $k \sim 1$ . Figure 15 shows the dependences of the free energy on the order parameter for different values of the wave vector at  $c = 0.3$ . It can be seen from the figure that the free energy minimum is attained at point  $\xi = 0$  for values of the wave vector  $0 < k < 0.4$ . For  $k \approx 0.5$ , functional  $F$  has two minima (at  $\xi_c^{(0)} = 0$  and  $\xi_c^{(1)} = 0.35$ ), and the state with  $\xi_c^{(1)}$  is separated from the state with  $\xi_c^{(0)}$  by a potential barrier. Since the global minimum is attained at  $\xi = \xi_c^{(1)}$ , the state with  $\xi_c^{(0)}$  is metastable. The ground state of the system is attained at  $\xi = \xi_c^{(1)}$  and is clustered. It should be noted that, in accordance with formula (133), clusters of the first component are formed in the channel since  $\xi_c^{(1)} > 0$ .

The lifetime of the clusters can be determined by passing from (137) for the order parameter to a stochastic differential equation (Langevin equation) and the corresponding Fokker-Planck equation via the introduction of additive noise. Steady-state solutions to the Fokker-Planck equation define

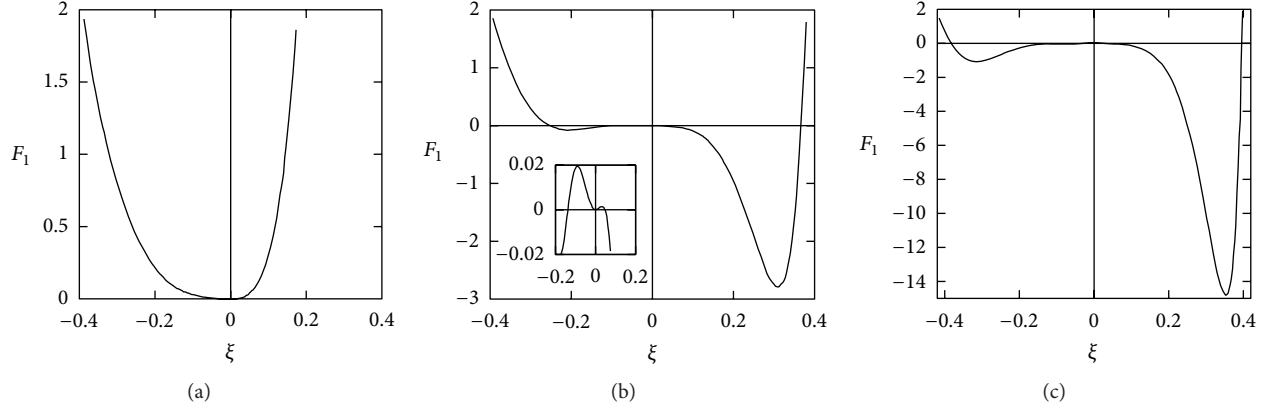


FIGURE 16: Dependence of free energy  $F_1$  on the order parameter for different values of the wave vector for  $c = 0.45$ :  $k = 0.1$  (a),  $0.3$  (b), and  $0.5$  (c).

the probability for the system being in the state described by order parameter  $\xi_c^{(1)}$ . For the lifetime, we have

$$\tau \sim \frac{r^2}{D_0} \exp\left(\frac{E_a}{T} - \delta F\right), \quad (142)$$

$$\delta F = F_1(c + \xi_c^{(1)}, k_c) \cdot T.$$

The decay of a cluster formed in the system occurs via overcoming an energy barrier of height  $\delta F$ . From the standpoint of physics, this can be interpreted as an effective increase in the diffusion activation energy for the particles in the cluster. However, for  $c = 0.3$ , the barrier height is small ( $\delta F \sim 0.2T$ ; see Figure 13(c)), and lifetime (142) is comparable to time (141). A further increase in the first component concentration in the mixture leads to negative values of the lifetime for a certain value of  $k = k_c < 1$  (see Figure 14(c)). In this case, clusters with a size of  $r \sim k_c^{-1}$  are formed in the channel; for  $k < k_c$ , fluctuations decay over a finite time, while for  $k > k_c$ , the emerging density fluctuations evolve. Such a situation is typical of transitions to an inhomogeneous condensate state [99].

The curves describing the dependence of the free energy on the order parameter for different values of the wave vector are shown in Figure 16. Since functional  $F_1$  has a single minimum at  $\xi = 0$  for  $k \sim 0$ , the state of particles in the channel is homogeneous. However, as the wave vector increases, curve  $F_1(\xi)$  acquires two more minima separated from the state with  $\xi = 0$  by potential barriers. A further increase in the wave vector leads to disappearance of the barriers between the state with  $\xi = 0$  and the states corresponding to two other minima of  $F_1$ , and the state with  $\xi = 0$  becomes unstable.

Thus, for a low concentration of the highly adsorbed component, the fill factor of the channel is small and the state of the system in the channel is homogeneous. As the concentration of the highly adsorbed component increases, the fill factor of the channel increases, and short-lived clusters of the highly adsorbed component can be formed in the channel. A further increase in the concentration (and the fill factor of the channel) leads to an increase in the lifetime of

the clusters formed in the channel. At a certain concentration of the highly adsorbed component, the clusters in the channel become long lived and the ground state of the system becomes clustered.

The formation of clusters of one of the components in a channel may strongly affect the transport of the gas through the membrane (see Section 2.1). In the next chapter, partial gas fluxes through the membrane will be calculated, and the effect of clusters on the mechanisms of transport will be analyzed.

**2.4.2. Transport in a Two-Component Gas in a High-Density 1D System.** In order to calculate partial fluxes and to analyze the transport, we will use the approach proposed in Section 2.1. It will be shown in the following that the evaluation of the flux can be reduced to the calculation of the relaxation frequency spectra  $\omega(\mathbf{k})$  for density fluctuations of the components. We can judge the mechanism of particle transport in a subnanometer channel from the type of the dependence of the spectrum on the wave vector of the system. We can write the expression determining the relaxation of the Fourier component  $n(k, t)$  of the number density of particles in a channel in the case of an arbitrary density  $n(k, t)$  under the conditions of slight deviation from equilibrium (see Section 2.1 and [100]):

$$\dot{n}(k, t) = i\omega(k) n(k, t). \quad (143)$$

It follows from this relation that the equation for fluctuation amplitude  $\delta n$  can be written in the form

$$\delta \dot{n}(k, t) = i\omega(k) \delta n(k, t), \quad (144)$$

where  $\omega(k)$  is the relaxation frequency spectrum for the system under study; in the case of diffusion of noninteracting particles, this spectrum has the form [98]

$$\omega = \omega_0(k) = -iDk^2. \quad (145)$$

Equation (144) describes relaxation of the  $k$ th component of density fluctuation for an arbitrary value of the wave vector. In

particular, this equation for  $k \neq 0$  makes it possible to describe the relaxation of density fluctuations and the propagation of a perturbation over a finite-size cluster in the case of its formation. For  $k \rightarrow 0$ , (144) describes the relaxation of density fluctuation on a large spatial scale. This quantity is associated with macroscopic fluxes. In order to calculate the fluxes, we write the continuity equation

$$\dot{n} + \frac{\partial j}{\partial x} = 0 \quad (146)$$

and apply the Fourier transformation to this equation:

$$ikj(k, t) = -\dot{n}(k, t). \quad (147)$$

Substituting (143) into (147), we obtain the following relation for flux  $j(k)$ :

$$j(k, t) = \frac{n(k, t) \omega(k)}{k}. \quad (148)$$

For partial fluxes, we have

$$j_i(k, t) = \frac{n_i(k, t)}{k} \omega_i(k), \quad (149)$$

where  $n_i$  is the density of the  $i$ th component and  $\omega_i$  is the corresponding spectrum. The total gas flux is defined as the sum of partial fluxes of the components:

$$\sum_{i=1}^2 j_i(k, t) = j(k, t). \quad (150)$$

It follows from (149) that partial fluxes are determined by relaxation frequency spectra  $\omega_i(k)$ . Thus, the problem is reduced to computing these spectra. The relaxation frequency spectra can be determined from the condition of the existence of nonzero density fluctuations for each component in an arbitrarily weak external field. Consequently, applying the Fourier transformation to (107), we find that the relaxation frequency spectrum can be determined by solving the following system of homogeneous equations:

$$\beta^{-1}(k, \omega) \begin{pmatrix} 1 \\ -1 \end{pmatrix} = 0. \quad (151)$$

Here matrix  $\beta^{-1}(k, \omega)$  of the response functions is defined by relation (132). In view of  $\delta$ -function singularities for  $k \rightarrow 0$  that emerge in pair correlation functions (120) appearing in (132), we must calculate spectra  $\omega_i(k)$  and the values of  $\omega_i(k=0)$ , after which the renormalization procedure must be carried out. Using (132) and passing to the limit  $k \rightarrow 0$  for spectra  $\omega_i(k=0)$ ,

$$\beta^{-1}(0, \omega) \begin{pmatrix} 1 \\ -1 \end{pmatrix} = \begin{pmatrix} \frac{\omega}{\omega_1^{(p)}} b_{11} - \frac{\omega}{\omega_1^{(p)}} b_{12} + a_{11} - a_{12} \\ \frac{\omega}{\omega_2^{(p)}} b_{22} - \frac{\omega}{\omega_2^{(p)}} b_{21} + a_{22} - a_{21} \end{pmatrix} = 0, \quad (152)$$

where  $a_{ij}$ ,  $b_{ij}$ ,  $\omega_1^{(0)}$ , and  $\omega_2^{(p)}$  are defined by relations (116), (129), and (131). For  $\omega^{(0)} \equiv \omega_i(k=0)$ , we obtain from relation (152)

$$\omega_1^{(0)} = -\frac{\omega_1^{(p)}(a_{11} - a_{12})}{b_{11} - b_{12}}, \quad (153)$$

$$\omega_2^{(0)} = -\frac{\omega_2^{(p)}(a_{22} - a_{21})}{b_{22} - b_{21}}.$$

On the other hand, substituting (132) into (152), we obtain the following expressions for relaxation frequency spectra  $\omega_i(k)$  of the system under investigation:

$$\tilde{\omega}_1(k) = \frac{iD_1 k^2}{b_{11} - b_{12}} \left[ \frac{1}{\theta^2 c_1^2 \nu_{11}(k) + b_{11}^{-1}} - \frac{1}{\theta^2 c_1 c_2 \nu_{12}(k) + b_{12}^{-1}} \right],$$

$$\tilde{\omega}_2(k) = \frac{iD_2 k^2}{b_{22} - b_{21}} \left[ \frac{1}{\theta^2 c_2^2 \nu_{22}(k) + b_{22}^{-1}} - \frac{1}{\theta^2 c_1 c_2 \nu_{21}(k) + b_{21}^{-1}} \right]. \quad (154)$$

Tildes indicate that  $\tilde{\omega}_i(k=0) \neq \omega_i^{(0)}$  ( $\omega_i^{(0)}$  are defined in relations (153)).

We will carry out the renormalization procedure for spectra (154) taking into account relations (153), that is, imposing the requirement

$$\tilde{\omega}_i = \omega_i^{(0)}(k=0). \quad (155)$$

Taking into account the value of  $\omega_i^{(0)}$ , we find from relations (153) and (154) that

$$a_{11} - a_{12} = \frac{b_{11}}{b_{11} \theta^2 c_1^2 \nu_{11}(k) + 1} - \frac{b_{12}}{b_{12} \theta^2 c_1 c_2 \nu_{12}(k) + 1} \quad (156)$$

or

$$a_{11} = \frac{b_{11}}{b_{11} \theta^2 c_1^2 \nu_{11}(k) + 1}, \quad a_{12} = \frac{b_{12}}{b_{12} \theta^2 c_1 c_2 \nu_{12}(k) + 1}. \quad (157)$$

Similarly, for  $a_{22}$ , we have

$$a_{22} = \frac{b_{22}}{b_{22} \theta^2 c_2^2 \nu_{22}(k) + 1}. \quad (158)$$

In order to separate singularities of pair correlation function  $\nu_{ij}(k)$  for  $k \rightarrow 0$ , we expand it into a series in the vicinity of  $k=0$  to within first-order terms. Using relations (154), we then obtain

$$\tilde{\omega}_1(k) = \frac{iD_1 k^2}{b_{11} - b_{12}} \left[ \frac{1}{\theta^2 c_1^2 (\nu_{11}(0) + k\nu'_{11}(k)) + b_{11}^{-1}} - \frac{1}{\theta^2 c_1 c_2 (\nu_{12}(0) + k\nu'_{12}(k)) + b_{12}^{-1}} \right],$$

$$= \frac{iD_1 k^2}{b_{11} - b_{12}} \left[ \frac{a_{11}}{1 + ka_{11} \theta^2 c_1^2 \nu'_{11}(k)} - \frac{a_{12}}{1 + ka_{12} \theta^2 c_1 c_2 \nu'_{12}(k)} \right]. \quad (159)$$

Taking into account the long-wave approximation and the smallness of  $k$ , replacing the derivative in the last expression by the difference  $kv'_{ik}(k) \approx v_{ij}(k) - v_{ij}(0)$ , omitting primes, and carrying out similar calculations for  $\omega_2$ , we finally obtain

$$\omega_1(k) = \frac{iD_1 k^2}{b_{11} - b_{12}} \left[ \frac{a_{11}}{1 + a_{11} \theta^2 c_1^2 (v_{11}(k) - v_{11}(0))} - \frac{a_{12}}{1 + a_{12} \theta^2 c_1 c_2 (v_{12}(k) - v_{12}(0))} \right],$$

$$\omega_2(k) = \frac{iD_2 k^2}{b_{22} - b_{21}} \left[ \frac{a_{22}}{1 + a_{22} \theta^2 c_2^2 (v_{22}(k) - v_{22}(0))} - \frac{a_{21}}{1 + a_{21} \theta^2 c_1 c_2 (v_{21}(k) - v_{21}(0))} \right]. \quad (160)$$

Using relations (104), (149), and (161) and passing to the limit for  $k \rightarrow 0$ , we can obtain the dependence of partial fluxes of the components on the pressure, temperature, and composition of the mixture. For  $k \neq 0$ , expressions (144) and (160) enable us to analyze the relaxation mechanism of the emerging density fluctuation with a characteristic size of  $r \approx 2\pi/k$ .

In order to analyze the experimentally observed partial fluxes, it is convenient to pass to the coordinate representation. Spectra (160) have the real and imaginary parts since pair correlation function  $v_{ij}(k)$  is a complex quantity in accordance with relations (120) and (125). Separating the real and imaginary parts of the spectra and applying the inverse Fourier transformation to expression (149), we obtain

$$j_i = n_i \Psi_i - D_i \frac{\partial n_i}{\partial x},$$

$$\Psi_i = \text{Re } \omega_i \left( k \rightarrow \frac{2\pi}{L} \right), \quad (161)$$

$$D_i = \text{Im } \frac{\omega_i(k)}{k^2} \Big|_{k \rightarrow 2\pi/L}.$$

Here  $D_i$  is the diffusion coefficient of a component,  $L$  is the channel length, and  $\Psi$  is the term emerging due to the mutual effect on the mixture components in a channel for large fill factors. It should be noted that, since  $L \gg r_c$ , where  $r_c$  is the characteristic size of clusters, passing to the limit for  $k \rightarrow 2\pi/L$  in relation (161) corresponds to averaging over characteristic scales of inhomogeneities in the case when the ground state of the system is clustered. Separating the terms linear in the wave vector from the real part of the spectrum, we obtain the following expression for  $\Psi$ :

$$\Psi_i = -D_i \frac{1}{T} \frac{\partial U_i}{\partial x} + V_i. \quad (162)$$

Here the first term describes the transport of molecules of the  $i$ th component, which is induced by the effective intermolecular interaction, while the second term has the meaning of the "drag" effect familiar in the kinetics of mixtures. Substituting

(162) into (161), we obtain the final expression for partial fluxes:

$$j_i = -D_i \frac{\partial n_i}{\partial x} - D_i \frac{n_i}{T} \frac{\partial U_i}{\partial x} + V_i n_i. \quad (163)$$

Thus, it follows from this equation that the partial flux is the sum of three terms. The first term corresponds to diffusion transport, while the second term emerges due to field diffusion. These two terms in the  $k$  representation can be combined into one by introducing the effective diffusion coefficient

$$D_i = D_i^{(0)} \left( 1 + \frac{n_i}{T} U(k) \right). \quad (164)$$

It was shown in the previous section that, for large filling factors, clusters are formed in the system. The mechanism of density relaxation may be different for the case of transport over the characteristic scale  $L$ , when  $2\pi\sigma_{av}/L \ll 1$  and  $k \rightarrow 0$  (which corresponds to macroscopic transport of gas components through the channel), and for the case when  $k \neq 0$ , which corresponds to relaxation over distances comparable to the size of clusters formed in the system. To prove this, we must analyze dependences  $\Delta v_{ij}(k)$ . In order to avoid cumbersome formulas, we consider this problem in greater detail in the limiting case of  $c_1 = 1$ , which corresponds to a one-component mixture.

Passing to the limit for  $c_1 \rightarrow 1$  in (160), we obtain the relaxation frequency spectrum for a one-component system; it is easy to obtain (70). It should be noted that, in accordance with the relation (70), the pair distribution and, hence, the pair correlation function associated with it depend not on the wave vector  $k$ , but on the product  $ik$ :

$$\theta v(k) \equiv \theta v(ik). \quad (165)$$

Let us now write relation (164) in the form

$$\omega(k) = -\frac{iD_0 k^2}{1 + \theta v(0) + \theta v(k) - \theta v(0)} = -\frac{iD_0 k^2}{1 + \theta v(0) + \theta \Delta v}$$

$$= -\frac{iD_0 k^2}{1 + \theta v(0) + \theta \text{Re } \Delta v + \theta i \text{Im } \Delta v}. \quad (166)$$

Separating the real and imaginary parts from relation (165), we obtain

$$\omega(k) = -\frac{iD_0 k^2 \left( (1 - \theta)^2 + \theta \text{Re } \Delta v \right)}{\left( (1 - \theta)^2 + \theta \text{Re } \Delta v \right)^2 + \left( \theta \text{Im } \Delta v \right)^2}$$

$$- \frac{D_0 k^2 \theta \text{Im } \Delta v}{\left( (1 - \theta)^2 + \theta \text{Re } \Delta v \right)^2 + \left( \theta \text{Im } \Delta v \right)^2}. \quad (167)$$

Here we have used the fact that

$$1 + \theta v(0) \approx (1 - \theta)^2. \quad (168)$$

This relation follows from the known relation [46]

$$\frac{\partial p}{\partial \theta} \approx \frac{1}{1 + \theta v(0)} \quad (169)$$

describing the increase in the compressibility with density. Using relation (165), we now expand  $\Delta\nu$  to within first-order terms:

$$\Delta\nu = \left. \frac{\partial\theta\nu(k)}{\partial(ik)} \right|_{k=0} ik \equiv i\theta\nu'(0)k. \quad (170)$$

The value of  $\nu'(0)$  is finite for  $\theta \neq 0$ . For example, using direct expansion into the Taylor series, we can obtain

$$\theta\nu'(0) = -\theta + \frac{4}{3}\theta^2 - \frac{1}{2}\theta^3. \quad (171)$$

Substituting relation (170) into (167), we get

$$\omega(k) \approx -\frac{iD_0k^2(1-\theta)^2}{(1-\theta)^4 + (\theta\nu'(0))^2k^2} - \frac{D_0k^3\theta\nu'(0)}{(1-\theta)^4 + (\theta\nu'(0))^2k^2}. \quad (172)$$

To calculate the fluxes for high densities ( $\theta \sim 1$ ), we must consider two limiting transitions in relation (172): for  $\theta \rightarrow 1$  and  $k \rightarrow 0$ . From the standpoint of physics, the transition for  $\theta \rightarrow 1$  and  $k \neq 0$  corresponds to the analysis of transport in a dense cluster. The transition for  $k \rightarrow 0$  and arbitrary  $\theta$  is equivalent to analysis of diffusion in a channel of length  $L \gg r_c$ , where  $r_c$  is the characteristic size of a cluster. For  $\theta \rightarrow 1$ , we obtain, instead of relation (172),

$$\omega(k) = -\frac{D_0k}{\theta\nu'(0)}. \quad (173)$$

This relation shows that spectrum  $\omega(k)$  corresponds to the hydrodynamic mode [46], for which quantity  $D_0/\nu'(0)$  is the effective velocity of sound.

Passing in relation (172) to the limit for  $k \rightarrow 0$  and retaining the lowest order in wave number  $k$ , we obtain

$$\omega(k) = -\frac{iD_0k^2}{(1-\theta)^2}. \quad (174)$$

This relation shows that the spectrum in this case is of the diffusion type with the diffusion coefficient

$$D \approx \frac{D_0}{(1-\theta)^2}, \quad (175)$$

which increases indefinitely as  $\theta \rightarrow 1$ .

It should be noted that, in accordance with (172), both relaxation mechanisms (hydrodynamic and diffusion) operate in the system when  $k \neq 0$  and  $\theta \neq 1$ . From the standpoint of physics, this corresponds to the diffusion transport between clusters (diffusion mode), over which density perturbations propagate (hydrodynamic mode). In spite of different interpretations of the sequence of limiting transitions, the calculated dependences of fluxes on external conditions are found to be equivalent from the physics standpoint. This is due to the fact that the hydrodynamic component is manifested in the second case in the increase in the effective diffusion coefficient  $D \approx D_0/(1-\theta)^2$  for high values of fill factor  $\theta$ .

In the two-component case, the transition for  $k \rightarrow 0$  corresponds to the transition from relation (160) to (153).

It can be seen from relation (153) that the obtained spectra are of the diffusion type since  $\omega_j^{(0)} = -iD_jk^2$ ,  $j = 1, 2$ , while quantities  $a_{ij}$  and  $b_{ij}$  are independent of  $k$ . The limiting transition for  $\theta \rightarrow 1$  in the two-component case involves considerable computational difficulties. However, the above analysis shows that the relaxation frequency spectra for the components also acquire a hydrodynamic mode in view of the dependence of pair correlation function (120) on factor  $ik$  for  $\theta \rightarrow 1$ .

Depending on the sequence of limiting transition, a decisive role in relation (163) is played either by the term corresponding to diffusion or the nongradient (hydrodynamic) part of the flux. Since the gas flux for arbitrary fill factors is measured in experiments on the penetrability of the membrane over large distance ( $L \gg r_c$ ,  $k \rightarrow 0$ ), the limiting transition for  $k \rightarrow 0$  should be performed first. In this case, the effects associated with the formation of clusters are taken into account in the dependence of the diffusion coefficient on the concentration and fill factor of the channel. Numerical calculations show that the last term in relation (160) is insignificant in the entire range of concentrations and fill factors of the channel. Thus, the relaxation frequency spectrum of a two-component system can be treated as a diffusion spectrum in the entire range of concentrations and fill factors, where the role of diffusion coefficient is played by a quantity taking into account clustering of the components in the channel.

It should be noted that for calculating response function (132), relaxation frequency spectra (160), and, as a consequence, partial fluxes (163), we used the fluctuation-dissipative theorem (119) presuming the homogeneous ground state of the system. In the case when the ground state of the system is clustered (see Figure 13(d)), the kinetic version of the fluctuation-dissipative theorem [98] should be used:

$$\begin{aligned} & \langle \delta n(x, t) \delta n(x', t) \rangle \\ & = -T \int_0^\infty \beta(x, x', t, \tau) (f(x, \tau) - f(x', \tau)) d\tau, \end{aligned} \quad (176)$$

where  $f(x, \tau)$  is the probability of a particle being located at point  $x$ . In accordance with the detailed balancing principle, in the case when states  $x$  and  $x'$  differ from the equilibrium state insignificantly, we have

$$f(x', t) \sim f(x, t) \exp\left(\frac{\Delta E}{T}\right), \quad (177)$$

where  $\Delta E$  is the energy difference between states  $x$  and  $x'$ . Using this relation, we obtain the following expression for the fluctuation-dissipative theorem:

$$\begin{aligned} & \langle \delta n(k, \omega) \delta n(k', \omega) \rangle \\ & = -T \int dx dx' dt \exp(ikx) \exp(ik'x') \exp(i\omega t) \\ & \quad \times \int_0^\infty \beta(x, x', t, \tau) \exp\left(\frac{\Delta E}{T}\right) d\tau. \end{aligned} \quad (178)$$

Applying the Fourier transformation to this relation and using (151), we obtain the relaxation frequency spectrum in the form

$$\omega^{(\text{new})}(k) = \omega(k) \exp\left(-\frac{\Delta E}{T}\right). \quad (179)$$

Thus, the application of relation (176) instead of (132) leads to the emergence of an additional exponential term in relation (163):

$$j_i(k, t) = \frac{n_i(k, t)}{k} \omega_i(k) \exp\left(-\frac{\Delta E}{T}\right), \quad (180)$$

where  $\Delta E$  is the depth of the potential well occupied by the system. In the case of small fill factors of the channel, the state of the system is homogeneous and  $\Delta E = 0$  (see Figure 13(a)). Then relation (180) transforms into (163). As the fill factor of the channel increases, the state of the system becomes clustered. For  $\Delta E \ll T$ , the exponential in relation (180) can be disregarded, and the flux virtually coincides with the flux calculated for a homogeneous state. This is due to the fact that expression (142) for the lifetime of clusters practically coincides with expression (141) for the lifetime of clusters in a homogeneous state. In this case, as noted previously, density excitation propagates via a cluster, leading to an increase in the effective diffusion coefficient. A further increase in the fill factor of the channel increases the value of  $\Delta E$ . The flux decreases thereby, which can be explained by an increase in the lifetime of the clusters formed in the channel. As a result, the mechanism of excitation transport via a cluster is not realized.

Thus, for small fill factors of the channel, the transport in the system follows the diffusion mode. This can be demonstrated by passing to the limit of small fill factors  $\theta$  in relation (160). Then the second term in the denominator becomes insignificant and the spectra are reduced to diffusion spectra (153). An increase in the fill factor results in the formation of clusters. It was shown in the previous section that, depending on the fill factor of the channel, the clusters formed may be either short lived or stable in the case when the ground state of the system is clustered. For short-lived clusters (see Figure 13(b)), the transport between clusters occurs through diffusion, while the transport over clusters occurs through a rapid barrier-free transfer of density excitation, and the arrival of a particle from one side of a cluster leads to the emergence of a particle from the other side [100]. In this case, the spectra contain both the diffusion and the hydrodynamic modes, and the effective diffusion coefficient increases in accordance with (175). An increase in the fill factor of the channel reduces the distance between clusters and increases their size. Since the transport over a cluster is faster than the diffusion transport, the effective diffusion coefficient and the partial flux increase. However, an increase in the fill factor also increases the lifetime of the clusters formed in the channel; as a result, the rate of excitation transfer over a cluster decreases. In the case when a cluster is stable (see Figure 13(d)), the transport of excitation over the cluster is ruled out, and the presence of such a cluster in the channel leads to blocking of transport in the system.

Using relations (160) and (180), we can calculate the partial gas fluxes proceeding from the data on the penetrability for pure components. Figures 17(a) and 17(b) show the dependence of partial fluxes on the mixture composition in the case when both gases are slightly adsorbed. The energies of interaction and the diameters of particles correspond to a methane-argon gas mixture ( $a = 3.8 \text{ \AA}$ ,  $\sigma_1 = 3.6 \text{ \AA}$ ,  $\sigma_2 = 3.0 \text{ \AA}$ ,  $\varepsilon_1 = 0.38 \text{ eV}$ ,  $\varepsilon_2 = 0.25 \text{ eV}$  [51],  $p = 100 \text{ kPa}$ , and  $T = 300 \text{ K}$ ).

It can be seen from Figure 17(a) that an increase in the concentration of the first component for fixed pressure and temperature reduces the filling factor with the second component, while the filling factor with the first component increases thereby. A decrease in the total fill factor of the channel in the concentration range  $0 < c < 0.4$  of first component takes place due to depletion of the channel in the second component (Figure 17(b)). An increase in the total fill factor of the channel for  $c > 0.4$  is associated with preferred enrichment of the channel in the first component (see Figure 17(b)). The partial flux of the first component in this case increases monotonically due to an increase in the filling factor with the first component (see Figure 17(a)), while the partial flux of the second component decreases due to a decrease in the filling factor with the second component. The transport is of the diffusion type, and clusters are not formed in the channel in view of small fill factors of the channel ( $\theta \leq 0.25$  for any composition of the mixture).

Figures 17(c) and 17(d) show the dependence of partial fluxes on the mixture composition in the case when one of the gases (the first) is a strong sorbate, while the other gas is a weak sorbate. The energy of interaction and the diameter of particles correspond to a butane-methane gas mixture ( $a = 3.8 \text{ \AA}$ ,  $\sigma_1 = 4.3 \text{ \AA}$ ,  $\sigma_2 = 3.6 \text{ \AA}$ ,  $\varepsilon_1 = 0.61 \text{ eV}$ ,  $\varepsilon_2 = 0.38 \text{ eV}$  [51],  $p = 2000 \text{ kPa}$ , and  $T = 300 \text{ K}$ ). The behavior of the total and partial fill factors of the channel upon an increase in the concentration of the first (highly adsorbed) component in this case coincides qualitatively with the case of slightly adsorbed gases described previously: the partial filling factor with the first (highly adsorbed) component increases monotonically against the background of a monotonic decrease in the filling factor with the second (slightly adsorbed) component (see Figure 17(c)).

The behavior of partial fluxes in this case is less trivial. It can be seen from the figure that the partial flux of the first component increases in the concentration interval  $0 < c < 0.2$ . This is due to the fact that, in accordance with relation (141), short-lived clusters (see Figure 13(a)) whose size increases with concentration are formed for such concentrations and fill factors of the channel. The transport over clusters occurs via a barrier-free transfer of density excitation, which increases the effective diffusion coefficient. This process is similar to the transport in one-component systems for high fill factors (see Section 2.1). It should be noted, however, that the formation of clusters and the mechanism of transfer of density excitation through a cluster in a two-component mixture can be realized for smaller fill factors ( $\theta = 0.71$ ; see Figures 13(b), 17(c), and 17(d)) as compared to the one-component case ( $\theta \geq 0.8$ ). An increase in the concentration of the first component increases the lifetime

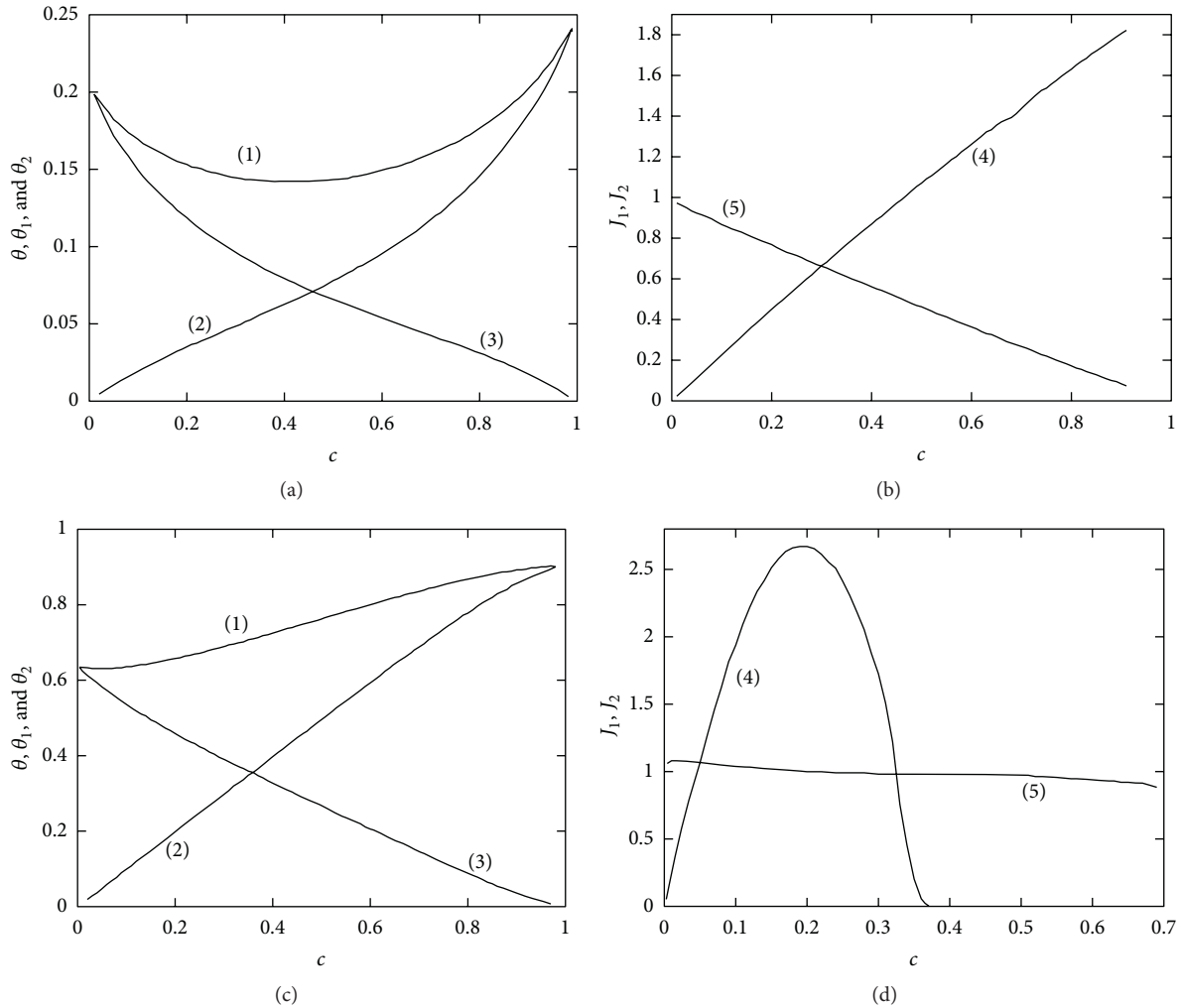


FIGURE 17: Dependence of the total and partial fill factors of a channel (a, c) and partial fluxes (b, d) on the composition of methane-argon (a, b) and butane-ethane mixtures (c, d): (1)—total fill factor of a channel; (2), (3)—filling factors with the first and second components, respectively; (4), (5)—partial fluxes of the first and second components, respectively;  $c$  is the concentration of the first component in the mixture.

of the clusters formed in the system (see Figures 14(b) and 15(c)). As a result of this increase, the transport over clusters becomes slower and the flux decreases. A further increase in the concentration leads to the formation of stable clusters in the channel (see Figures 14(c) and 16(c)); in accordance with relation (120), the lifetime of these clusters is much longer than the lifetime (141) of short-lived clusters since  $\delta F \gg T$ . In this case, the transfer of density excitation over clusters is ruled out and the partial flux vanishes.

Thus, three mechanisms of particle transport in a channel are possible in the two-component case. For small fill factors, the transport occurs through diffusion. An increase in the fill factor leads to the formation of short-lived clusters in a channel. As in the one-component case, this leads to an increase in the effective diffusion coefficient due to barrier-free transport of density excitation over a cluster. As the fill factor increases further, the characteristic lifetime of clusters increases, leading to a decrease in the flux. A further increase in the fill factor makes the clusters stable, and the so-called

blocking effect takes place, when the partial flux of one of the components vanishes. A decrease in pressure does not lead to a qualitative change in the behavior of the dependences of partial fluxes on the mixture composition.

**2.4.3. Comparison with Experiment.** The transport of two-component gas mixtures in zeolite membranes MFI (silicalite, ZSM-5) with a pore diameter of  $\sim 0.6$  nm has been studied by the technique widely used for one-component gases [51]. However, in contrast to the rich variety of experiments with one-component gases, a consistent analysis of a two-component mixture has not been reported in the literature. The most detailed information on penetrability for two-component mixtures is given in [51, 97].

The experiments [51, 97] on penetration of two-component mixtures were made in a chamber with a porous stainless steel substrate with a thickness of approximately 3 mm. A polycrystalline layer of zeolite ZSM-5 with a thickness of

$\sim 50 \mu\text{m}$  and a random orientation of crystals was deposited on the substrate. Zeolites have a complex crystalline structure based on silicon oxide with admixtures of sodium and aluminum [51]. The crystalline structure of zeolite ZSM-5 is formed by straight channels with an elliptical cross section ( $0.57 \times 0.52 \text{ nm}^2$ ) intersecting sinusoidal channels with a circular cross section of diameter  $0.54 \text{ nm}$  (Section 2.1). The measured adsorption capacity and the calculated fraction of molecules in the channel intersections make it possible to treat the channels as one dimensional for the molecular mixtures under study (Section 2.1). The experiments [51, 97] were carried out at temperatures from 300 to 700 K under pressures from 25 to 500 kPa on the external side of the membrane. The purity of the mixture components was higher than 99.95%. The mixture composition at the membrane exit was measured on a quadrupole mass spectrometer with a sensitivity of approximately 25 ppm when a Faraday cell was used for recording. The selectivity measured in the experiments was determined as the relative change in concentration  $c$  of *n*-butane molecules and concentration  $1 - c$  of methane molecules at the membrane entrance ( $F$ ) and exit ( $p$ ):

$$\alpha = \left( \frac{c}{1-c} \right)_F : \left( \frac{c}{1-c} \right)_p. \quad (181)$$

It should be noted that, for a constant composition of the mixture at the membrane entrance, the selectivity is proportional to the ratio of partial fluxes of the mixture components at the membrane exit:

$$\alpha \sim \frac{J_1}{J_2}. \quad (182)$$

It was found experimentally [51] that the partial flux of the highly adsorbed gas *n*-C<sub>4</sub>H<sub>10</sub> at  $T = 300 \text{ K}$  under a total pressure of  $p = 100 \text{ kPa}$  changes considerably (by a factor of several units) in the presence of the slightly adsorbed component CH<sub>4</sub> as compared to the flux of a pure gas, while the partial flux of the slightly adsorbed gas changes by two orders of magnitude in the presence of the strongly adsorbed component. Depending on the mixture composition, selectivity  $\alpha$  varies and attains its maximum value  $\alpha_{\text{max}} = 380$  for a concentration ratio of 5:95 at the membrane entrance. It was shown [97] that the dependences of partial fluxes on the mixture composition and external pressure for the mixtures studied (C<sub>2</sub>H<sub>6</sub>-CH<sub>4</sub> and C<sub>3</sub>H<sub>8</sub>-CH<sub>4</sub>) are monotonic in the range of experimental pressures. The partial flux of methane decreases in the presence of the second component (ethane or propane), while the partial flux of the second component increases with its concentration in the mixture. The selectivity of both mixtures increases monotonically with the concentration of the more highly adsorbed component in the mixture. The dependences of the partial fluxes on the total pressure of the mixture are also monotonic, but the pressure dependence of selectivity in ethane for the mixture C<sub>2</sub>H<sub>6</sub>-CH<sub>4</sub> has a peak at a pressure of  $p \approx 300 \text{ kPa}$  [97]. Similar dependences of partial fluxes were observed in experiments with another mixture of slightly adsorbed gases (CO<sub>2</sub>-N<sub>2</sub>) [53] (Figure 18).

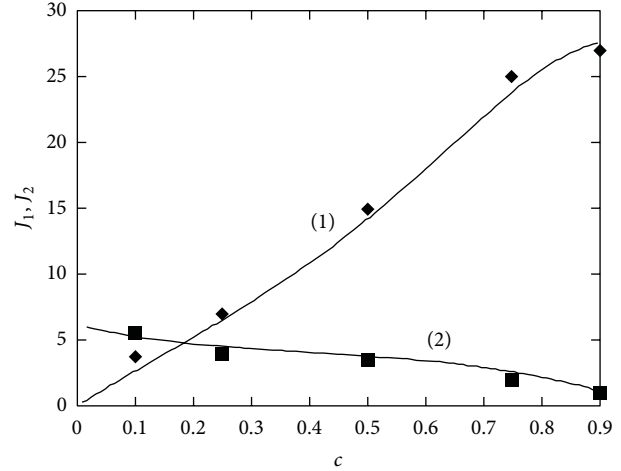


FIGURE 18: Dependence of partial fluxes on the mixture composition for slightly adsorbed gases: (1), (2)—theoretical dependences for CO<sub>2</sub> and N<sub>2</sub> fluxes, respectively;  $c$  is the CO<sub>2</sub> concentration above the membrane; squares correspond to experimental data from [53];  $a = 3.8 \text{ \AA}$ ,  $\sigma_1 = 3.8 \text{ \AA}$ , and  $\sigma_2 = 3.6 \text{ \AA}$  [51];  $p = 100 \text{ kPa}$ ,  $T = 300 \text{ K}$ .

The theory developed in the previous sections enables us to describe peculiarities in the transport of binary gas mixtures in zeolite membranes. In the case of a mixture of slightly adsorbed gases, when the fill factor of a channel is small ( $\theta \ll 1$ ) for any mixture composition, the system relaxes in accordance with the diffusion mechanism corresponding to diffusion of solitary particles without the formation of clusters in a channel. In this case, in accordance with (104), (160), and (180), the partial flux of the first component decreases monotonically upon an increase in the concentration of the second component, while the partial flux of the second component increases with its concentration in the mixture.

Figure 18 shows that the theoretical curves calculated by formulas (104), (160), and (180) are in good agreement with the experimental data borrowed from [53]. The mean distance  $a$  between the seats in a channel was estimated proceeding from the value corresponding to a close packing of a unit cell of a ZSM-5 membrane with nitrogen (Section 2.1).

The filling factor for mixtures with a strongly adsorbed component depends on the mixture composition; it is significant and can be as high as  $\theta \sim 1$ . In this case, in accordance with the arguments put forth in Section 2.4.1, the dependence of fluxes on the mixture composition is nonmonotonic due to the formation of clusters in a channel.

Figure 19 shows the dependence of the ratio of partial fluxes of gases for the mixture *n*-C<sub>4</sub>H<sub>10</sub>-CH<sub>4</sub> on the butane concentration in the mixture under a pressure of  $p = 100 \text{ kPa}$  at temperature  $T = 300 \text{ K}$ . It can be seen from the figure that the ratio of partial fluxes increases with the concentration of the highly adsorbed component (butane) in the concentration range  $0 < c < 0.35$ . Analysis of experimental data [51] and calculations based on formulas (104), (160), and (180) show that the methane flux for a butane concentration of  $c > 0.05$  changes insignificantly upon an

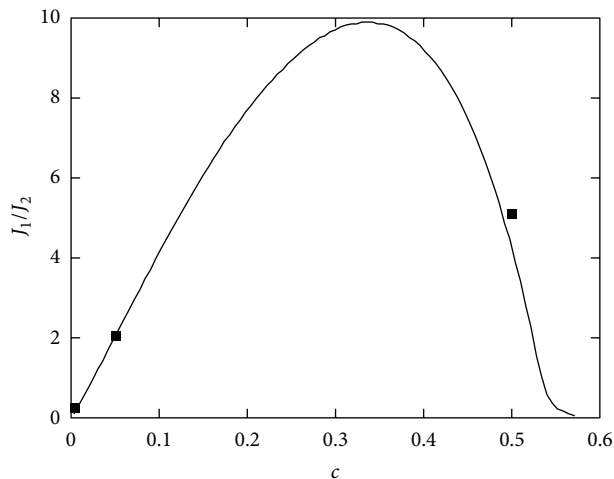


FIGURE 19: Ratio of the partial fluxes of butane and methane as a function of the butane concentration;  $c$  is the concentration of  $n$ - $C_4H_{10}$  above the membrane; squares correspond to experimental data obtained in [51];  $a = 3.8 \text{ \AA}$ ,  $\sigma_1 = 4.3 \text{ \AA}$ , and  $\sigma_2 = 3.6 \text{ \AA}$  [51];  $p = 100 \text{ kPa}$ ,  $T = 300 \text{ K}$ .

increase in the butane concentration in the mixture. In this case, the behavior of the flux ratio is completely determined by the behavior of the butane flux. The increase in the butane flux is due to the fact that, in accordance with formula (141), short-lived butane clusters are formed for concentrations  $0 < c < 0.35$  and for the fill factors corresponding to these concentrations (see Figure 13(a)); the size of these clusters increases with the concentration of the highly adsorbed component. The transport over clusters (see Figure 13(b)) occurs via barrier-free transfer of density excitation, leading to an increase in the effective diffusion coefficient for butane, which is observed for  $c < 0.35$ . The increase in the butane concentration in the mixture increases the lifetime of the clusters formed in the system (see Figures 14(b) and 15(c)). With increasing lifetime, the transport over the clusters slows down and the butane flux decreases for concentrations  $c > 0.35$ . A further increase in the concentration results in the formation of stable clusters in a channel (see Figures 14(c) and 16(c)), leading to a rapid (exponential) decrease in the butane flux upon an increase in its concentration in the mixture.

Thus, it follows from the theory that the butane flux becomes exponentially small for a butane concentration of  $c > 0.6$  in the mixture, and the transport of particles must be blocked. It should be noted that calculations based on formulas (104), (160), and (180) for butane concentrations in the interval  $0 < c < 0.05$  show that the methane flux decreases approximately by an order of magnitude upon an increase in the butane concentration, which is also in qualitative agreement with the experimental data [51]. The numerical difference between the predictions of the theory developed previously and the experimental data in this range of butane concentrations are due to the fact that relations (104), (160), and (180) were derived for the model potential of intermolecular interaction of the type of interaction (101) between hard spheres. It is well known that the potentials of hard spheres correctly describe the behavior of real systems

for high densities [46, 101]. In order to describe the behavior of the system in the entire range of fill factors, potentials of the Lennard-Jones type, which take into account the attraction between particles even in the zeroth order in density, should be used. However, although the application of this type of potentials of intermolecular interaction does not change the results qualitatively, it leads to the formation of butane clusters at lower filling factors and, hence, to a sharper decrease in the methane flux upon an increase in the butane concentration in the concentration range under investigation.

Relations (104), (160), (180), and (181) also make it possible to derive the dependence of the selectivity on the pressure, temperature and composition of the mixture. Figure 20(a) shows the dependence of the ethane selectivity for the  $C_2H_6$ - $CH_4$  mixture with a concentration ratio of 50:50 at the entrance on the total pressure of the mixture [97]. It can be seen that the dependence is nonmonotonic. This is due to the fact that the diffusion coefficient first increases due to an increase in the pressure and fill factor of the channel as a result of the formation of short-lived clusters, and the partial ethane flux increases (Figure 20(b)). The increase in the total fill factor of the channel is determined by the increase in the partial fill factors for both components. This process continues until the channel filling with ethane slows down. In this case, the fill factor of the channel increases mainly due to channel filling with methane. At such pressures, the increase in the ethane flux slows down (see Figure 20(b)), while the methane flux continues to increase (Figure 20(c)). The theoretical dependences plotted in the figures show that a further increase in pressure due to an increase in the lifetime of ethane clusters formed in the channel must lead to a decrease in the ethane flux (Figure 20(b)). Thus, the analysis of experimental data proves that the theory constructed here describes the experimental results satisfactorily.

One of the main results of the proposed theory is the prediction of nonmonotonic dependences of partial fluxes and selectivities on the mixture composition and pressure (see Figures 19 and 20), while conventional models [51, 53, 97] (in particular, the generalized Maxwell-Stefan equation [51, 97]) lead to monotonic dependences of these quantities on the same parameters (see Figure 20(a)). The qualitative discrepancy between the dependences in question is due to the fact that conventional models [51, 53, 97] take into account only the finite size of particles, in which the interaction between particles in a channel is disregarded. It is well known [46, 47, 101], however, that the interaction between particles in dense systems plays a decisive role both in the construction of the equations of state of the system and in the description of transport. For example, the inclusion of interaction between particles of the hard-sphere type leads to the emergence of peaks in the pair correlation function at distances equal to one, two, three, and so forth particle diameters [44, 46, 101]. This fact indicates the existence of "effective" attraction between particles and necessitates the inclusion of cluster formation in the description of the behavior of the system at high densities, when it passes to a spatially inhomogeneous state. It was demonstrated previously that this leads to the emergence of nonmonotonic dependences of fluxes and selectivities on external parameters.

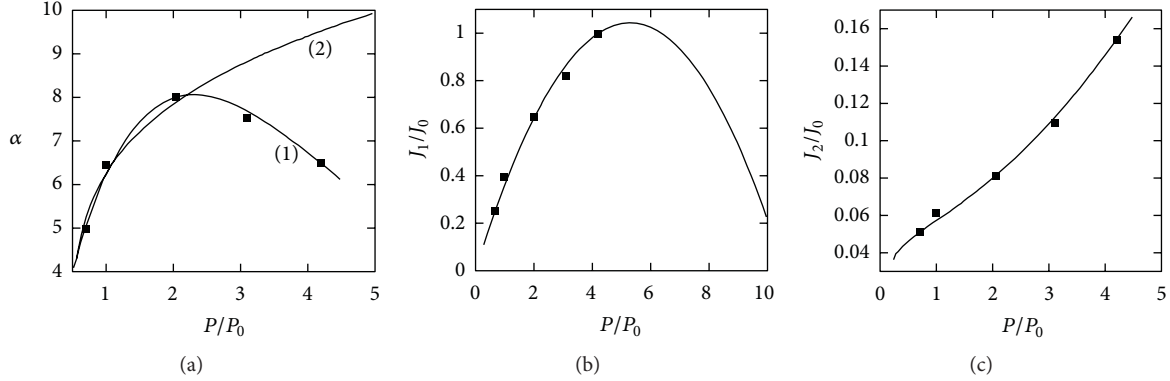


FIGURE 20: Dependence of the ethane selectivity (a) and of the partial fluxes of  $C_2H_6$  (b) and  $CH_4$  (c) for the  $C_2H_6$ - $CH_4$  mixture on the total pressure of the mixture: (1)—calculations based on formulas (104), (160), and (180) and (181); (2)—calculations based on the generalized Maxwell-Stefan equation [97]; squares correspond to experimental data obtained in [51];  $a = 3.8 \text{ \AA}$ ,  $\sigma_1 = 3.8 \text{ \AA}$ , and  $\sigma_2 = 3.6 \text{ \AA}$  [51];  $J_0 = 63 \text{ mmole}/(\text{m}^2 \text{ s})$ ,  $p_0 = 100 \text{ kPa}$ .

It should be noted that the stabilization of clusters in 1D systems by the second component at high fill factors, which has been investigated here, was obtained numerically in a recent work [83]. It should be borne in mind, however, that, in accordance with our previous results (Section 2.1), clusters with a large but finite lifetime can be formed even in a one-component system with high filling factors. It is 1D gold clusters of this type that were apparently observed in recent experiments under the ultrahigh vacuum conditions.

### 3. Results and Discussion

The analysis of the experimental data showed that for most gases investigated, the sorption and transport can be treated as a process in a one-dimensional (1D) system. In statistical physics, the theoretical models of 1D systems are classical examples of exactly solvable models [44]. It is well known [34, 46] that in 1D systems, a phase transition (condensation) does not occur as density increases. This means that, specifically, no critical nuclei are present in the system, and stable nuclei of a new phase with macroscopically long lifetimes do not appear in the system. At the same time, the system of 1D channels in zeolite membranes consists of channels of finite length, where for a sufficiently high filling factors, clusters with sizes comparable to the channel length can form. Thus, the description of molecular transport in zeolite membranes reduces to describing transport in a 1D system, where there are strong density fluctuations with a finite lifetime of clusters. The density functional method [38] makes it possible to calculate the spectrum of density fluctuations and the diffusion coefficient for particles with arbitrary density and arbitrary laws of interaction with one another and with the channel walls. Since the flux measured in the experiments performed in [41] is determined by the diffusion coefficient and the filling factor of the channels in the membrane, the sorption isotherm of a one-component molecular gas is calculated separately. For the one-dimensional channels considered in the present paper, this problem is solved exactly for an arbitrary intermolecular interaction potential. A new

feature here is an analysis of the dependence of the lifetime and size of the 1D clusters on the filling factor of the channel with particles. A description of molecular transport for an arbitrary filling factor ( $\theta$ ) of a channel is performed. It was found that as the filling factor approaches 1, so that blocking of the relative motion of the particles becomes substantial, the diffusion coefficient increases. Following [31], a new diffusion mechanism is observed. It makes it possible to explain the transition from activated diffusion of single particles in a channel with low filling factors to collective fast barrier-free diffusion, which consists of the propagation of density disturbances for large values of  $\varepsilon_0$ . In the hard-sphere approximation, as  $\bar{N}_1$  increases, the well-known [46] effective attraction of the molecules—hard spheres—results in vanishing of the energy barrier for diffusion along the channel axis. Another consequence of the effective attraction of molecules is the formation of molecular clusters in the channel, which have a finite lifetime because of the one-dimensionality of the system. The size and lifetime of the clusters increase as  $\theta$  increases. The diffusion of particles in clusters is described as a barrier-free process of propagation of density disturbances. The pressure, temperature, and filling factor dependences of the flux of molecules make it possible, even in the high-sphere model, to describe the experimental data currently known to the authors.

We have shown that contradictory experimental data, reporting the presence of the SFD mode and transport acceleration with the increasing density, can be described within the proposed model consistently accounting for correlation effects in a strongly fluctuating 1D system of identical particles. The molecular transport in a 1D system can change with time going from the Einstein diffusion mode to SFD mode and then again to a normal diffusion at large observation times. Whereas the sequence of these modes is general, their actual realization depends on the concrete characteristics of the system. For example, at very low densities one expects to observe only a normal diffusion mode. If we consider a system of weakly interacting particles ( $u \leq 1$ ), we can see that at low densities  $\theta \leq 0.2$  and time scale  $t < l_0^2/D_0$ , the particles

move independently and MSD obeys the Einstein law  $\langle x^2 \rangle \sim t$ . At times  $t > l_0^2/D_0$ , when a particle mobility is limited by other particles, the SFD diffusion mode ( $\langle x^2 \rangle \sim t^{1/2}$ ) should appear. As the density is increased, collective effects force the 1D system to transform into a nonhomogeneous state, characterized by a formation of clusters with a finite lifetime [31]. In such a clustered system, a particle moves in a limited space between the clusters and at collision, it transfers its momentum to a cluster. This transfer of momentum can cause the cluster to emit a particle from the opposite side to the impact. For a system of identical particles, such a process, which we call collective diffusion (CD), results in an increase of the diffusion coefficient with increasing density [31]. Therefore at long times ( $t \rightarrow \infty$ ) MSD again obeys the Einstein law  $\langle x^2 \rangle \sim t$  with an effective diffusion coefficient  $D_u(\theta) \sim D_0/(1 - \theta)^2$ . We suggest that further experimental investigations could confirm the reappearance of the Einstein-like diffusion mode at high densities, which is characterized by a diffusion coefficient increasing with density. When the interaction between the particles in the 1D system is strong ( $u \gg 1$ ), cluster formation occurs even at low filling factors ( $\theta \leq 0.2$ ); one has the same general physical picture but the transitions from one diffusion mode to the other take place at lower densities.

In this paper, we also analyse the transport of a two-component gas mixture in subnanometer channels theoretically for an arbitrary filling factor. The main problem in this case is to take into account consistently the density effects associated with both the interaction and the finite size of the particles. This is done in the hard-sphere model, in which the interaction is manifested as an effective (dynamic) attraction of particles, leading to their correlation [46]. It is well known [46, 101] that, applying this model to 3D system, one can describe the density effects qualitatively and even quantitatively in some cases. The comparison with experimental data with the obtained theoretical dependences demonstrates the possibility of a quantitative description of diffusion of a two-component mixture in a 1D system.

The adsorption isotherm of a mixture in 1D channels is calculated; this isotherm relates the fill factor and the concentration of particles in channels to the temperature, pressure, and composition of a mixture of gases whose diffusion is studied in experiments [51, 53, 97]. The ground state of a mixture of particles in 1D channels is analyzed by the density functional method [38] generalized to the case of a two-component mixture. However, in contrast to [38], the free energy is obtained by calculating directly the correlation function and the response function using the method developed for 1D systems [45]. The density functional method is used to derive, from microscopic considerations, the equation of motion for the order parameter of the system, which is the Fourier component of the deviation of the particle concentration from its mean value. Analysis of this equation shows that the two-component mixture in channels is transformed to a spatially inhomogeneous state upon an increase in  $\theta$ . As a result, short-lived clusters appear in channels, with the cluster size and lifetime increasing with  $\theta$ . A new and unexpected result obtained in this case is the

emergence of a minimum in the fluctuating part of the free energy as a function of the wave vector and the Fourier component of the order parameter. Thus, at high filling levels, the two-component mixture acquires a new property: clusters of a definite size are stabilized by a potential barrier due to the emergence of effective attraction between particles in the channels. Such a situation is typical of transitions of the system to an inhomogeneous state [99]. The lifetime of clusters formed increases exponentially in accordance with the Arrhenius law; at a low temperature, channels with such clusters might be blocked for the transportation of particles forming the mixture. It should be noted that the idea of stabilizing the clusters of one component by the other component in 1D systems was put forth in [83]. Thus, the description of transport in nanochannels is reduced to the description of diffusion in a spatially inhomogeneous high-density one-dimensional system.

For a weakly nonequilibrium system, the problem of computing fluxes in 1D channel is reduced to the calculation of relaxation frequency spectra for density fluctuations of mixture components. Spectra  $\omega_i(k)$  were determined by using the response functions derived in Section 2.4.1. Analysis of the dependences of  $\omega_i$  on  $k$  and on fill factor  $\theta$  proved that a hydrodynamic spectrum  $\omega_i(k) = c_i k$  is typical of clusters ( $\theta \sim 1$ , finite values of  $k$ ), while for transport of excitations over distances much longer than the characteristic size of clusters ( $k \ll 1$ ), the spectrum is of the diffusion type,  $\omega_i(k) \propto D_i k^2$ , for an arbitrary fill factor. In accordance with the dependences of spectra and fluxes on the fill factor obtained here, three regimes of particle transport can be singled out. For  $\theta \ll 1$ , we have diffusion of solitary particles. As the value of  $\theta$  increases, the flux and the diffusion coefficient increase due to the barrier-free (hydrodynamic) transport of particles along the increasing part of the length of a 1D channel filled with short-lived clusters formed in it. As the value of  $\theta$  increases further and the potential barrier ( $E_i$ ) stabilizing the clusters arises, particle fluxes decrease exponentially since the value of  $E_i$  increases with  $\theta$ . Thus, an increase in the fill factor gives rise to the new property of 1D two-component systems (transport blocking by the clusters formed). A comparison of the theory with experimental data and discussion of results was carried out (Section 2.4.3). The obtained dependences of the fluxes on the mixture composition (fill factor) and of the selectivity on pressure successfully describe the experimental data known to the authors.

We have also considered an infinite quasi-1D system and showed by means of statistical methods [102] that in spite of the absence of phase transitions in an infinite quasi-1D system it can be in two states due to collective effects [33]. These two states of a quasi-1D system are characterized by the formation of clusters with finite lifetimes but different structural properties [33]. Clusters in a quasi-1D system can be interpreted as density fluctuations that can exhibit macroscopic lifetimes. As a concrete example, we estimate the lifetime, interatomic distances for 1D gold clusters and compare them to the available experimental and theoretical data on monoatomic gold chains. Depending on the density of the quasi-1D gold system, clusters with either large

(3.5 ÷ 4.0 Å) or smaller Au-Au separations (2.5 ÷ 2.9 Å) can have an observable lifetime. Also we have estimated the minimal number of atoms in a 1D chain and a force required to break a chain with a minimal number of atoms in it for different metals (Au, Ag, Ni, and Pt). Thus we show that the methods of statistical mechanics, in some cases, can be used to investigate the properties of finite systems. In particular, these methods allow one to explain experimentally observed anomalously large interatomic distances in monoatomic Au chains and to predict its maximal length and to estimate its lifetime. The described approach was applied to analyze the interatomic distances and lifetimes of quasi-1D structures of different materials such as Ag, Ni, and Pt. The obtained results successfully describe the experimental data.

#### 4. Conclusions

The paper is devoted to the analysis of the correlation effects and manifestations of general properties of 1D systems (spatial heterogeneity that is associated with strong density fluctuations, the lack of phase transitions, the presence of frozen disorder, confinement, and blocked movement of nuclear particle by its neighbours) in nonequilibrium phenomena by considering the four examples. The anomalous transport in zeolite channels is considered. The mechanism of the transport in carbon nanotubes and MOF structures, relaxation, mechanical properties, and stability of nonequilibrium states of free chains of metal atoms, non-Einstein atomic mobility in 1D atomic systems is considered.

Description of molecular transport in zeolite membranes is reduced to the description of transport in 1D system in which strong density fluctuations with a finite lifetime of the clusters are presented. Response function method for density functional allows us to calculate the spectrum of density fluctuations and the diffusion coefficient of the particle with arbitrary density and arbitrary laws of interaction between particles and between a particle and a wall of the channel. Systematic account of correlation effects leads to the following physical picture of transport and mobility in strong fluctuating 1D confinement system.

Thus, if the interaction between particles in the 1D system is low ( $u \leq 1$ ), at low densities  $\theta \leq 0.1$  at times  $t < l_0^2/D_0$  particles move independently of each other, and, therefore, their mobility is of the Einstein type  $\langle x^2 \rangle \sim t$ . At the times  $t > l_0^2/D_0$ , the motion of the particles is limited due to blocking by other particles that results in the SFD regime  $\langle x^2 \rangle \sim t^{1/2}$ . 1D system becomes spatially inhomogeneous due to collective effects in it by increasing of density of system. This state is characterized by the presence of clusters with a finite lifetime. In such a system, the diffusion of a particle is the result of its moving in a confined space between clusters with subsequent transfer of momentum to a cluster. This effect results in a disintegration of a cluster and a disconnection of the particles from the other side of the cluster. For identical particles, this process is a result of diffusion due to the “excitation” transfer along the chain of closely spaced particles and leads to an increase of a diffusion coefficient with increasing density of particles in 1D clustered system.

A further increase of the filling factor leads to the increase of a cluster lifetime, to the simultaneous decrease in the average distance between these clusters, and to the increase of diffusion coefficient. In this case, the dependence of the mean square displacement of particles at the large times ( $t \rightarrow \infty$ ) is of the Einstein type with an increased diffusion coefficient  $D(\theta) \sim D_0/(1 - \theta)^2$ ,  $\theta \sim 1$ . If the pair interaction between particles is large, the cluster formation occurs at low densities, so that all the discussed above becomes true for small filling factors zeolite channels also.

Cluster of atomic particles that forms in 1D systems allows to describe and explain the phenomena observed in experiments, such as the formation of atomic chains with two different interatomic distances, mechanical properties, and stability of the nonequilibrium free chains, and allows to calculate the minimal number of atomic particles of different metals in free chains. In this case, it is not necessary to use impurity atoms, the presence of which requires experimental confirmation in the chain to explain the large interatomic distances in the 1D chains of gold.

The description of the practically important transport of two-component mixture in membranes with subnanometer channels by the response function method allowed to show that in 1D system of two types of particles at high filling factors, a phase transition in an inhomogeneous state with the formation of clusters of a finite size components may occur due to an effective particle attraction.

In the framework of the response function method, the equation of motion of the order parameter of the system is derived. The order parameter is the Fourier component of the density fluctuations. Analysis of this equation shows that two-component mixture in the channels passes into a spatially inhomogeneous state with the increase of  $\theta$  that results in formation of a short-lived clusters, the size and the lifetime of which increase with increasing of  $\theta$ .

A new result here was the occurrence of a minimum of a dependence of fluctuation part of the free energy on the wave vector and the Fourier component of the order parameter. Thus, at high filling factors in the two-component mixture, there is a new feature: the clusters of a certain size in the channels stabilizes by a potential barrier due to the effective attraction of particles.

Such a situation is typical for the transition to an inhomogeneous state. The lifetime of the clusters increases exponentially according to the Arrhenius law, and the clusters can be locked for transport of the particles of the mixture at sufficiently low temperature channels. The observed increase of the separation factor with conductivity of 1D channels in case of blocking a channel by stable clusters with a certain concentration is described. The dependence of the separation coefficient on the concentration, temperature, and density is defined.

A comparison of the theory with experimental data and results is discussed. The resulting fluxes depending on the composition of the mixture (the filling factor) and selectivity depending on pressure describe the experimental data presented in the literature.

## Acknowledgments

The study was supported by The Ministry of Education and Science of Russian Federation, Project no. 16.740.11.0536 and state Grants no. 2.6310.2011 and no. 2.5466.2011.

## References

- [1] A. Kumar, A. Kumar, and P. K. Ahluwalia, "Ab initio study of structural, electronic and dielectric properties of free standing ultrathin nanowires of noble metals," *Physica E*, vol. 46, pp. 259–269, 2012.
- [2] P. Makk, D. Tomaszewski, J. Martinek et al., "Correlation analysis of atomic and single-molecule junction conductance," *ACS Nano*, vol. 6, no. 4, pp. 3411–3423, 2012.
- [3] K. Tsysar, D. Bazhanov, A. Saletsky, O. Brovko, and V. Stepanyuk, "Influence of hydrogen impurities on atomic and electronic structure of palladium nanowires and nanocontacts," *Physical Review B*, vol. 84, no. 8, Article ID 085457, 8 pages, 2011.
- [4] D. Çakır and O. Gülseren, "Effect of impurities on the mechanical and electronic properties of Au, Ag, and Cu monatomic chain nanowires," *Physical Review B*, vol. 84, no. 8, Article ID 085450, 10 pages, 2011.
- [5] E. H. Huisman, M. L. Trouwborst, F. L. Bakker, B. J. van Wees, and S. J. van der Molen, "The mechanical response of lithographically defined break junctions," *Journal of Applied Physics*, vol. 109, no. 10, Article ID 104305, 7 pages, 2011.
- [6] P. Vélez, S. A. Dassie, and E. P. M. Leiva, "Kinetic model for the long term stability of contaminated monoatomic nanowires," *Physical Review B*, vol. 81, no. 12, Article ID 125440, 2010.
- [7] M. Zelený, M. Šob, and J. Hafner, "Ab initio density functional calculations of ferromagnetism in low-dimensional nanostructures: from nanowires to nanorods," *Physical Review B*, vol. 79, no. 13, Article ID 134421, 10 pages, 2009.
- [8] T. Kizuka and K. Monna, "Atomic configuration, conductance, and tensile force of platinum wires of single-atom width," *Physical Review B*, vol. 80, no. 20, Article ID 205406, 2009.
- [9] A. Hasmy, L. Rincón, R. Hernández, V. Mujica, M. Márquez, and C. González, "On the formation of suspended noble-metal monatomic chains," *Physical Review B*, vol. 78, no. 11, Article ID 115409, 5 pages, 2008.
- [10] A. Thiess, Y. Mokrousov, S. Blügel, and S. Heinze, "Theory and application of chain formation in break junctions," *Nano Letters*, vol. 8, no. 8, pp. 2144–2149, 2008.
- [11] T. Shiota, A. I. Mares, A. M. C. Valkering, T. H. Oosterkamp, and J. M. Van Ruitenbeek, "Mechanical properties of Pt monatomic chains," *Physical Review B*, vol. 77, no. 12, Article ID 125411, 2008.
- [12] T. Kizuka, "Atomic configuration and mechanical and electrical properties of stable gold wires of single-atom width," *Physical Review B*, vol. 77, no. 15, Article ID 155401, 2008.
- [13] F. Pauly, M. Dreher, J. K. Viljas, M. Häfner, J. C. Cuevas, and P. Nielaba, "Theoretical analysis of the conductance histograms and structural properties of Ag, Pt, and Ni nanocontacts," *Physical Review B*, vol. 74, no. 23, Article ID 235106, 2006.
- [14] S. López-Moreno, A. H. Romero, A. Muñoz, and U. Schwingenschlögl, "First-principles description of atomic gold chains on Ge(001)," *Physical Review B*, vol. 81, no. 4, Article ID 041415, 4 pages, 2010.
- [15] P. C. Snijders, "Colloquium: electronic instabilities in self-assembled atom wires," *Reviews of Modern Physics*, vol. 82, no. 1, pp. 307–329, 2010.
- [16] D. H. Wei, C. L. Gao, Kh. Zakeri, and M. Przybylski, "Pd atomic chain formation as a result of submonolayer deposition of 3d metals on Pd(110)," *Physical Review Letters*, vol. 103, no. 22, Article ID 225504, 2009.
- [17] H. Garbouj, M. Said, F. Picaud, C. Ramseyer, D. Spanjaard, and M. C. Desjonquères, "Growth of perfect and smooth Ag and Co monatomic wires on Pt vicinal surfaces: a kinetic Monte Carlo study," *Surface Science*, vol. 603, no. 1, pp. 22–26, 2009.
- [18] C. Liu, T. Uchihashi, and T. Nakayama, "Self-alignment of Co adatoms on in atomic wires by quasi-one-dimensional electron-gas-mediated interactions," *Physical Review Letters*, vol. 101, no. 14, Article ID 146104, 2008.
- [19] K. D. Ryang, P. G. Kang, H. W. Yeom, and S. Jeong, "Structures and defects of atomic wires on Si(553)-Au: an STM and theoretical study," *Physical Review B*, vol. 76, no. 20, Article ID 205325, 2007.
- [20] J. Gascon, F. Kapteijn, B. Zornoza, V. Sebastián, C. Casado, and J. Coronas, "Practical approach to zeolitic membranes and coatings: state of the art, opportunities, barriers, and future perspectives," *Chemistry of Materials*, vol. 24, no. 15, pp. 2829–2844, 2012.
- [21] D. A. Fedosov, A. V. Smirnov, E. E. Knyazeva, and I. I. Ivanova, "Zeolite membranes: synthesis, properties, and application," *Petroleum Chemistry*, vol. 51, no. 8, pp. 657–667, 2011.
- [22] A. García-Suárez, *Computational study of adsorption and diffusion in zeolites with cations [Ph.D. thesis]*, Universidad Pablo de Olavide, Seville, Spain, 2011.
- [23] J. A. Thomas and A. J. H. McGaughey, "Water flow in carbon nanotubes: transition to subcontinuum transport," *Physical Review Letters*, vol. 102, no. 18, Article ID 184502, 2009.
- [24] J. Su and H. Guo, "Effect of nanotube-length on the transport properties of single-file water molecules: transition from bidirectional to unidirectional," *Journal of Chemical Physics*, vol. 134, no. 24, Article ID 244513, 2011.
- [25] A. Berezhkovskii and G. Hummer, "Single-file transport of water molecules through a carbon nanotube," *Physical Review Letters*, vol. 89, no. 6, Article ID 064503, 4 pages, 2002.
- [26] H. Kumar, B. Mukherjee, S. T. Lin, C. Dasgupta, A. K. Sood, and P. K. Maiti, "Thermodynamics of water entry in hydrophobic channels of carbon nanotubes," *Journal of Chemical Physics*, vol. 134, no. 12, Article ID 124105, 2011.
- [27] J. K. Holt, H. G. Park, W. Yinmin et al., "Fast mass transport through sub-2-nanometer carbon nanotubes," *Science*, vol. 312, no. 5776, pp. 1034–1037, 2006.
- [28] M. Kac, G. E. Uhlenbeck, and P. C. Hemmer, "On the van der Waals theory of the vapor-liquid equilibrium. I. Discussion of a one-dimensional model," *Journal of Mathematical Physics*, vol. 4, no. 2, pp. 216–228, 1963.
- [29] M. Kac, G. E. Uhlenbeck, and P. C. Hemmer, "On the van der Waals theory of the vapor-liquid equilibrium. III. Discussion of the critical region," *Journal of Mathematical Physics*, vol. 5, no. 1, article 60, 10 pages, 1964.
- [30] V. D. Borman, I. V. Tronin, V. N. Tronin, V. I. Troyan, B. Johansson, and N. V. Skorodumova, "Formation of high- and low-density clusters in a 1D system," *Physica E*, vol. 40, no. 3, pp. 643–648, 2008.
- [31] V. D. Borman, V. V. Teplyakov, V. N. Tronin, I. V. Tronin, and V. I. Troyan, "Molecular transport in subnanometer channels," *Journal of Experimental and Theoretical Physics*, vol. 90, no. 6, pp. 950–963, 2000.

- [32] V. D. Borman, B. Johansson, N. V. Skorodumova, I. V. Tronin, V. N. Tronin, and V. I. Troyan, "Diffusion and particle mobility in 1D system," *Physics Letters A*, vol. 359, no. 5, pp. 504–508, 2006.
- [33] V. D. Borman, V. N. Tronin, I. V. Tronin, and V. I. Troyan, "Transport of a two-component mixture in one-dimensional channels," *Journal of Experimental and Theoretical Physics*, vol. 98, no. 1, pp. 102–122, 2004.
- [34] L. D. Landau and E. M. Lifshitz, *Statistical Physics*, part 1, Pergamon Press, Oxford, UK, 1980.
- [35] V. N. Bogomolov, "Capillary phenomena in extremely thin zeolite channels and metal-dielectric interaction," *Physical Review B*, vol. 51, no. 23, pp. 17040–17045, 1995.
- [36] S. Yu. Krylov, A. V. Prosyantov, and J. J. M. Beenakker, "One dimensional surface diffusion. II. Density dependence in a corrugated potential," *Journal of Chemical Physics*, vol. 107, no. 17, pp. 6970–6979, 1997.
- [37] J. J. M. Beenakker, V. D. Borman, and S. Y. Krylov, "Molecular transport in the nanometer regime," *Physical Review Letters*, vol. 72, no. 4, pp. 514–517, 1994.
- [38] Yu. N. Devyatko and V. N. Tronin, "Kinetics of the relaxation of gas-like systems to equilibrium," *Journal of Experimental and Theoretical Physics*, vol. 71, no. 5, pp. 880–887, 1990.
- [39] V. D. Borman, S. Yu. Krylov, and A. V. Prosyantov, "Theory of nonequilibrium phenomena at a gas-solid interface," *Journal of Experimental and Theoretical Physics*, vol. 70, pp. 1013–1022, 1990.
- [40] K. K. Sirkar, "Membrane separation technologies: current developments," *Chemical Engineering Communications*, vol. 157, pp. 145–184, 1997.
- [41] S. T. Hwang and K. Kammermeyer, *Membranes in Separations*, Wiley, New York, NY, USA, 1975.
- [42] J. M. Van de Graaf, "Permeation and Separation Properties of Supported Silicalite-1 Membranes," [Ph.D. thesis], University of Delft, Delft, The Netherlands, 1999.
- [43] F. Kapteijn, W. J. W. Bakker, G. Zheng, J. Poppe, and J. A. Moulijn, "Permeation and separation of light hydrocarbons through a silicalite-1 membrane. Application of the generalized Maxwell-Stefan equations," *The Chemical Engineering Journal and The Biochemical Engineering Journal*, vol. 57, no. 2, pp. 145–153, 1995.
- [44] J. M. Ziman, *Models of Disorder: The Theoretical Physics of Homogeneously Disordered Systems*, Cambridge University Press, Cambridge, UK, 1979.
- [45] I. Z. Fisher, *Statistical Theory of Liquids*, University of Chicago Press, Chicago, Ill, USA, 1964.
- [46] R. Balescu, *Equilibrium and Nonequilibrium Statistical Mechanics*, Wiley, New York, NY, USA, 1975.
- [47] P. Resibois and M. De Leener, *Classical Kinetic Theory of Fluids*, Wiley, New York, NY, USA, 1977.
- [48] Y. N. Devyatko and V. N. Tronin, "Kinetics of the relaxation of gas-like systems to equilibrium," *Soviet Physics. Journal of Experimental and Theoretical Physics*, vol. 98, pp. 1570–1584, 1990.
- [49] G. K. L. Chan and R. Finken, "Time-dependent density functional theory of classical fluids," *Physical Review Letters*, vol. 94, no. 18, Article ID 183001, 2005.
- [50] R. E. Richards and L. V. C. Rees, "Sorption and packing of n-alkane molecules in ZSM-5," *Langmuir*, vol. 3, no. 3, pp. 335–340, 1986.
- [51] W. J. W. Bakker, G. Zheng, F. Kapteijn, M. Makke, and J. A. Moulijn, *Precision Process Technology*, Kluwer, Amsterdam, The Netherlands, 1993.
- [52] H. Van Bekkam, E. M. Flanigen, J. C. Jansen et al., Eds., *Introduction to Zeolite Science and Practice*, vol. 58, Elsevier, Amsterdam, The Netherlands, 1991.
- [53] L. J. P. Van den Broeke, W. J. W. Bakker, F. Kapteijn, and J. A. Moulijn, "Binary permeation through a silicalite-1 membrane," *AIChE Journal*, vol. 45, no. 5, pp. 976–985, 1999.
- [54] G. T. Kokotailo, S. L. Lawton, D. H. Olson, and W. M. Meier, "Structure of synthetic zeolite ZSM-5," *Nature*, vol. 272, no. 5652, pp. 437–438, 1978.
- [55] D. H. Olson, W. O. Haag, and R. M. Lago, "Chemical and physical properties of the ZSM-5 substitutional series," *Journal of Catalysis*, vol. 61, no. 2, pp. 390–396, 1980.
- [56] R. Krishna, "A unified approach to the modelling of intraparticle diffusion in adsorption processes," *Gas Separation and Purification*, vol. 7, no. 2, pp. 91–104, 1993.
- [57] F. Kapteijn, W. J. W. Bakker, G. Zheng, and J. A. Moulijn, "Temperature- and occupancy-dependent diffusion of n-butane through a silicalite-1 membrane," *Microporous Materials*, vol. 3, no. 3, pp. 227–234, 1994.
- [58] W. J. W. Bakker, F. Kapteijn, J. C. Jansen, H. van Bekkam, and J. A. Moulijn, "Hoge permeabiliteit en selectiviteit bereikt. Doorbraak in ontwikkeling zeolietmembranen," *Procestechologie*, vol. 3, no. 12, pp. 7–16, 1993 (Dutch).
- [59] A. Tselik, *Quantum Field Theory in Condensed Matter Physics*, Cambridge, UK, 1998.
- [60] H. van Beijeren, K. W. Kehr, and R. Kutner, "Diffusion in concentrated lattice gases. III. Tracer diffusion on a one-dimensional lattice," *Physical Review B*, vol. 28, no. 10, pp. 5711–5723, 1983.
- [61] G. Hummer, J. C. Rasaiah, and J. P. Noworyta, "Water conduction through the hydrophobic channel of a carbon nanotube," *Nature*, vol. 414, no. 6860, pp. 188–190, 2001.
- [62] V. Gupta, S. S. Nivarthi, A. V. McCormick, and H. T. Davis, "Evidence for single file diffusion of ethane in the molecular sieve AlPO<sub>4</sub>-5," *Chemical Physics Letters*, vol. 247, no. 4–6, pp. 596–600, 1995.
- [63] V. Kukla, J. Kornatowski, D. Demuth et al., "NMR studies of single-file diffusion in unidimensional channel zeolites," *Science*, vol. 272, no. 5262, pp. 702–704, 1996.
- [64] H. Jobic, K. Hahn, J. Kärger et al., "Unidirectional and single-file diffusion of molecules in one-dimensional channel systems. A quasi-elastic neutron scattering study," *Journal of Physical Chemistry B*, vol. 101, no. 30, pp. 5834–5841, 1997.
- [65] S. Vasenkov and J. Kärger, "Different time regimes of tracer exchange in single-file systems," *Physical Review E*, vol. 66, no. 5, Article ID 052601, 4 pages, 2002.
- [66] J. B. Delfau, C. Coste, C. Even, and M. Saint Jean, "Single-file diffusion of interacting particles in a finite-sized channel," *Physical Review E*, vol. 82, no. 3, Article ID 031201, 2010.
- [67] J.-B. Delfau, "Christophe Coste, and Michel Saint Jean. Single-file diffusion of particles in a box: transient behaviors," *Physical Review E*, vol. 85, no. 6, Article ID 061111, 14 pages, 2012.
- [68] P. A. Fedders, "Two-point correlation functions for a distinguishable particle hopping on a uniform one-dimensional chain," *Physical Review B*, vol. 17, no. 1, pp. 40–46, 1978.
- [69] J. Kärger, "Straightforward derivation of the long-time limit of the mean-square displacement in one-dimensional diffusion," *Physical Review A*, vol. 45, no. 6, pp. 4173–4174, 1992.
- [70] M. Kollmann, "Single-file diffusion of atomic and colloidal systems: asymptotic laws," *Physical Review Letters*, vol. 90, no. 18, Article ID 180602, 2003.

- [71] K. Hahn, J. Kärger, and V. Kukla, "Single-file diffusion observation," *Physical Review Letters*, vol. 76, no. 15, pp. 2762–2765, 1996.
- [72] C. Rödenbeck, J. Kärger, and K. Hahn, "Exact analytical description of tracer exchange and particle conversion in single-file systems," *Physical Review E*, vol. 55, no. 5, pp. 5697–5712, 1997.
- [73] C. Rodenbeck, J. Kärger, and K. Hahn, "Calculating exact propagators in single-file systems via the reflection principle," *Physical Review E*, vol. 57, no. 4, pp. 4382–4397, 1998.
- [74] N. Nilius, T. M. Wallis, and W. Ho, "Localized molecular constraint on electron delocalization in a metallic chain," *Physical Review Letters*, vol. 90, no. 18, Article ID 186102, 4 pages, 2003.
- [75] N. Agraït, A. L. Yeyatib, and M. van Ruitenbeek, "Quantum properties of atomic-sized conductors," *Physics Reports*, vol. 377, no. 2-3, pp. 281–279, 2003.
- [76] H. Ohnishi, Y. Kondo, and K. Takayanagi, "Quantized conductance through individual rows of suspended gold atoms," *Nature*, vol. 395, no. 6704, pp. 780–783, 1998.
- [77] V. Rodrigues and D. Ugarte, "Real-time imaging of atomistic process in one-atom-thick metal junctions," *Physical Review B*, vol. 63, no. 7, Article ID 073405, 4 pages, 2001.
- [78] Y. Takai, T. Kawasaki, Y. Kimura, T. Ikuta, and R. Shimizu, "Dynamic observation of an atom-sized gold wire by phase electron microscopy," *Physical Review Letters*, vol. 87, no. 10, Article ID 106105, 4 pages, 2001.
- [79] T. Kizuka, S. Umehara, and S. Fujisawa, "Metal-insulator transition in stable one-dimensional arrangements of single gold atoms," *Japanese Journal of Applied Physics*, vol. 40, no. 1, pp. L71–L74, 2001.
- [80] C. Untiedt, A. Yanson, R. Grande et al., "Calibration of the length of a chain of single gold atoms," *Physical Review B*, vol. 66, no. 8, Article ID 085418, 6 pages, 2002.
- [81] N. V. Skorodumova and S. I. Simak, "Spatial configurations of monoatomic gold chains," *Computational Materials Science*, vol. 17, no. 2–4, pp. 178–181, 2000.
- [82] N. V. Skorodumova, S. I. Simak, A. E. Kochetov, and B. Johansson, "Ab initio study of electronic and structural properties of gold nanowires with light-element impurities," *Physical Review B*, vol. 75, no. 23, Article ID 235440, 2007.
- [83] N. V. Skorodumova and S. I. Simak, "Stability of gold nanowires at large Au-Au separations," *Physical Review B*, vol. 67, no. 12, Article ID 121404, 4 pages, 2003.
- [84] V. Rodrigues, T. Fuhrer, and D. Ugarte, "Signature of atomic structure in the quantum conductance of gold nanowires," *Physical Review Letters*, vol. 85, no. 19, pp. 4124–4127, 2000.
- [85] S. R. Bahn, N. Lopez, J. K. Nørskov, and K. W. Jacobsen, "Adsorption-induced restructuring of gold nanochains," *Physical Review B*, vol. 66, no. 8, Article ID 081405, 2002.
- [86] S. B. Legoas, D. S. Galvão, V. Rodrigues, and D. Ugarte, "Origin of anomalously long interatomic distances in suspended gold chains," *Physical Review Letters*, vol. 88, no. 7, pp. 761051–761054, 2002.
- [87] S. Di Napoli, A. Thiess, S. Blügel, and Y. Mokrousov, "Modeling impurity-assisted chain creation in noble-metal break junctions," *Journal of Physics*, vol. 24, no. 13, Article ID 135501, 2012.
- [88] M. Kiguchi, R. Stadler, I. S. Kristensen, D. Djukic, and J. M. van Ruitenbeek, "Evidence for a single hydrogen molecule connected by an atomic chain," *Physical Review Letters*, vol. 98, no. 14, Article ID 146802, 2007.
- [89] C. Q. Sun, C. M. Li, S. Li, and B. K. Tay, "Breaking limit of atomic distance in an impurity-free monatomic chain," *Physical Review B*, vol. 69, no. 24, Article ID 245402, 2004.
- [90] C. Kittel, *Introduction to Solid State Physics*, Wiley, New-York, NY, USA, 1995.
- [91] T. Hill, *Statistical Mechanics*, McGraw-Hill Book Company, New York, NY, USA, 1956.
- [92] E. M. Lifshitz and L. P. Pitaevskii, *Statistical Physics*, part 2, Pergamon Press, Oxford, UK, 1980.
- [93] A. Calzolari, C. Cavazzoni, and M. B. Nardelli, "Electronic and transport properties of artificial gold chains," *Physical Review Letters*, vol. 93, no. 9, pp. 1–96404, 2004.
- [94] G. M. Francis, L. Kuipers, J. R. A. Cleaver, and R. E. Palmer, "Diffusion controlled growth of metallic nanoclusters at selected surface sites," *Journal of Applied Physics*, vol. 79, no. 6, pp. 2942–2947, 1996.
- [95] E. Y. Zarechnaya, N. V. Skorodumova, S. I. Simak, B. Johansson, and E. I. Isaev, "Theoretical study of linear monoatomic nanowires, dimer and bulk of Cu, Ag, Au, Ni, Pd and Pt," *Computational Materials Science*, vol. 43, no. 3, pp. 522–530, 2008.
- [96] L. D. Landau, L. P. Pitaevskii, E. M. Lifshitz, and A. M. Kosevich, *Course of Theoretical Physics*, vol. 7 of *Theory of Elasticity*, Butterworth-Heinemann, 3 edition, 1986.
- [97] J. M. Van de Graaf, F. Kapteijn, and J. A. Moulijn, "Modeling permeation of binary mixtures through zeolite membranes," *AIChE Journal*, vol. 45, no. 3, pp. 497–511, 1999.
- [98] Yu. L. Klimontovich, *Statistical Physics*, Harwood Academic, New-York, NY, USA, 1986.
- [99] D. N. Voskresenskii, *Multiparticle Effects in Solids*, Energoatomizdat, Moscow, Russia, 1983.
- [100] O. G. Bakunin, "Mysteries of diffusion and labyrinths of destiny," *Physics-Uspekhi*, vol. 46, no. 3, pp. 309–313, 2003.
- [101] G. N. Sarkisov, "Approximate equations of the theory of liquids in the statistical thermodynamics of classical liquid systems," *Physics-Uspekhi*, vol. 42, no. 6, pp. 545–561, 1999.
- [102] F. Baletto and R. Ferrando, "Structural properties of nanoclusters: energetic, thermodynamic, and kinetic effects," *Reviews of Modern Physics*, vol. 77, no. 1, pp. 371–423, 2005.

## Research Article

# Electrical Resistivity of Pristine and Functional Single-Wall Carbon Nanotubes

Yijiang Lu,<sup>1</sup> Jing Li,<sup>1</sup> and Haiping Hong<sup>2</sup>

<sup>1</sup> Nanotechnology Branch, NASA Ames Research Center, Moffett Field, Sunnyvale, CA 94035, USA

<sup>2</sup> Department of Material and Metallurgical, South Dakota School of Mines and Technology, Rapid City, SD 57701, USA

Correspondence should be addressed to Haiping Hong; [haiping.hong@sdsmt.edu](mailto:haiping.hong@sdsmt.edu)

Received 6 January 2013; Accepted 16 February 2013

Academic Editor: Yun Zhao

Copyright © 2013 Yijiang Lu et al. This is an open access article distributed under the Creative Commons Attribution License, which permits unrestricted use, distribution, and reproduction in any medium, provided the original work is properly cited.

The resistance of several pristine and functional single-wall carbon nanotubes (SWNTs) deposited and dried on interdigitated electrode (IDE) chips was investigated to better understand how functional groups influence their resistivity. Without the external electrical field, the resistance was generally increased for the sulfonated and fluorinated SWNTs but not for COOH-SWNTs. With a 3 V electric field applied during depositing, while no change in resistance was found for the purified pristine SWNTs, fluorinated SWNTs, COOH SWNTs, and Ni-SWNTs, a significant decrease in resistance was observed in sulfonated SWNTs and unpurified pristine SWNTs, which could be due to the alignment of SWNTs in an electric field. The alignment of the sulfonated SWNTs is most likely due to the charge of the sulfate functional group. It is interesting to note that the alignment was found in the unpurified pristine SWNTs but not in the purified pristine ones which have lessened resistivity. The lower resistivity in the purified pristine SWNTs may be due to the smaller number (<5%) of impurities. The significance of this research is that hydrophilic COOH-SWNTs could be a better candidate than the hydrophobic pristine SWNTs for being used in many applications, especially in polymer nanocomposites.

## 1. Introduction

Carbon nanotubes have attracted extensive attention recently because of their extraordinary thermal, electrical, and mechanical properties [1–3]. Due to these unique properties, they have the potential to be used in electrical devices [4], nanofluids [5, 6], grease [7], and sensors [8–10].

Measuring the electrical properties of carbon nanotubes in solutions is not easy because it is difficult to get a homogeneous solution with carbon nanotubes. It is very hard to dissolve or disperse the carbon nanotubes in their pristine form in the hydrophilic fluids, such as water and ethylene glycol, simply because carbon nanotubes are inorganic solids (hydrophobic) [11]. Usually chemical surfactants are added to disperse the nanotubes. But the added chemical surfactant is always a concern in such measurements because it would complicate the interpretation of electrical conductivity results.

An alternative approach to improve the solubility of carbon nanotubes in water or organic solvents is by surface

modification, such as covalent, noncovalent, free-radical, and electrochemical modification or plasma treatments [12]. The most used and efficient method is chemical functionalization, through which carboxyl groups or other functional groups such as fluorinated groups and sulfonated groups are attached to the sidewall or the ends of the single-walled carbon nanotubes (SWNTs), leading to a reduction of the strong van der Waals interactions among carbon nanotubes and strongly facilitating the separation of SWNT bundles into individual tubes [12]. For example, recently, Dr. Billups' group at Rice University has synthesized highly exfoliated, water soluble, and single-walled carbon nanotubes with functional aryl sulfonated group [13]. Therefore, no chemical surfactant is necessary to disperse the nanotubes, thus eliminating the influence of chemical surfactants and simplifying the experimental procedure. The addition of the functional groups to the SWNTs causes a change of the electronic structure from a trigonal-planar local bonding geometry to a tetrahedral geometry, leading to the transformation of  $sp^2$ - into  $sp^3$ -hybridized carbon atoms [12], which may affect the intrinsic

electronic properties of SWNTs and their potential application in electronic devices and sensors. Therefore, it is interesting to investigate the effect of the added functional groups on electrical resistance to better understand how the chemical bonds and geometric/electronic configuration affect the electrical properties of the SWNTs.

In this paper, the electrical resistance of several pristine and functionalized SWNTs was investigated with and without an electric field to better understand the relationship between nanotube structure and physical properties (thermal, electrical, and mechanical).

## 2. Experimental and Procedure

The functional sulfonated SWNTs were obtained from Dr. Billups' group, Rice University. The details for the synthesis of these materials can be found in [13]. The COOH SWNTs were obtained from School of Mines and Nankai University respectively. (fluorinated single-wall carbon nanotubes) F-SWNTs were purchased from Carbon Nanotechnologies Incorporation (CNI, Houston, TX, USA). The surfaces have not been treated chemically or physically. Ni-coated SWNTs were prepared using the methodology as reported previously [14, 15]. A handheld sonic probe (Sonic Dismembrator, Model 100) was used to efficiently disperse the nanotubes into solvents. All flocculation of the nanotubes visible to the eye was removed by this process.

The nanotube coatings on the interdigitated electrode (IDE) chips were applied by a Nanoject II (Drummond Scientific Co.). The smallest drop distributed by this device is 2.3 nL. Ten drops of each sample were put to each IDE chip to ensure a uniform 23 nL SWNTs coating. When an electrical field was applied, 3 V or 5 V was added to the IDE chips before dropping the solution droplets on the electrodes. At the same time, the IDE sensor chip is heated up to 60°C. The electric field is removed once the SWNTs are dried. The IDE is made by a P-type boron-doped silicon (100) wafer with a resistivity of 0.006–0.01 ohm-cm and thickness of  $500 \pm 25 \mu\text{m}$ . A layer of 0.5  $\mu\text{m}$  silicon dioxide was thermally grown on top of the Si substrates. A layer of 200 nm platinum on top of 20 nm titanium was deposited on the SiO<sub>2</sub> layer with the designed finger patterns. These patterns consisted of 4, 8, 12, and 50  $\mu\text{m}$  finger gaps with 10  $\mu\text{m}$  finger width [16]. The IDE used for the conductivity measurement is shown in Figure 1 with a finger width of 10  $\mu\text{m}$  and a gap width of 12  $\mu\text{m}$ .

The electrical conductivities of various fillers (nanotubes) in solid phase were measured by Keithley 2002/7001 High performance DMM/Multiplexer and Agilent 34401 DMM (precisely calibrated). A Keithley 237 High voltage measure unit was used to measure the voltage of the electric field when the nanotube coating was applied.

## 3. Results and Discussion

In order to better understand the influence of functional groups on the conductivity (resistivity) of nanotubes, the electrical resistivity of various fillers (nanotubes) in solid phase was measured. Table 1 lists seven nanofillers (nanotubes) with different functional groups and chemical structures. All solutions were prepared to make SWNTs in the similar

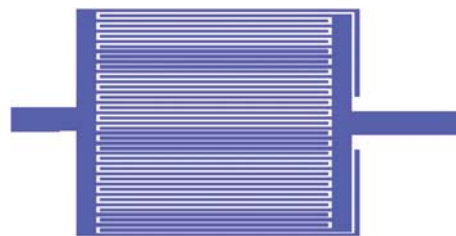


FIGURE 1: Interdigitated electrode (IDE) chip for measuring the resistance of different SWNTs.



FIGURE 2: Picture of five nanofiller (nanotube) solutions with different functional groups and chemical structures. (1) Unpurified pristine SWNT, (2) fluorinated SWNT, (3) COOH SWNT (school of mines), (4) COOH SWNT (outside campus), and (5) sulfonated SWNT.

TABLE 1: Types of nanofillers, concentrations, and solvents.

| No. | Type of nanofiller          | Concentration, wt% | Solvent type |
|-----|-----------------------------|--------------------|--------------|
| 1   | Unpurified pristine SWNT    | 0.0324%            | DMF          |
| 2   | Fluorinated SWNT            | 0.0364%            | DMF          |
| 3   | COOH SWNT (school of mines) | 0.0363%            | DMF          |
| 4   | COOH SWNT (outside campus)  | 0.0365%            | DMF          |
| 5   | Sulfonated SWNT             | 0.0366%            | DMF          |
| 6   | Ni-SWNT                     | 0.037%             | DMF          |
| 7   | Purified pristine SWNT      | 0.037%             | DMF          |

concentration by wt% in order to control the amount of nanotubes deposited on each IDE.

Pristine SWNTs were not distributed as well as the others in Dimethylformamide (DMF) even after being set in an ultrasonicator for 15 minutes, see Figure 2. The possible reason is that the pristine nanotube is hydrophobic. The other functional SWNTs dispersed better in DMF because they are hydrophilic.

Table 2 lists the conductivity (resistivity) data of the SWNTs with and without an applied electric field when depositing the nanotubes onto the electrodes.

TABLE 2: Resistance of SWNTs with and without an applied electric field.

| Coating sample            | Agilent<br>34401 DMM | Keithley<br>2002 DMM | Comments       |
|---------------------------|----------------------|----------------------|----------------|
| Unpurified pristine SWNT  | 256 K $\Omega$       | 270 K $\Omega$       |                |
| Unpurified pristine SWNT* | 29.9 $\Omega$        | 29.9 $\Omega$        | Applied<br>3 V |
| Fluorinated SWNT          | 41.2 K $\Omega$      | 40.5 K $\Omega$      |                |
| Fluorinated SWNT*         | 39.1 K $\Omega$      | 39.2 K $\Omega$      | Applied<br>3 V |
| COOH SWNT(S3)             | 12.0 $\Omega$        | 12.0 $\Omega$        |                |
| COOH SWNT(S3)*            | 16.1 $\Omega$        | 16.2 $\Omega$        | Applied<br>3 V |
| COOH SWNT(S4)             | 18.5 $\Omega$        | 18.2 $\Omega$        |                |
| COOH SWNT(S4)*            | 17.8 $\Omega$        | 17.8 $\Omega$        | Applied<br>3 V |
| Sulfonated SWNT           | 5.34 K $\Omega$      | 5.29 K $\Omega$      |                |
| Sulfonated SWNT*          | 25.6 $\Omega$        | 25.7 $\Omega$        | Applied<br>3 V |
| Ni-SWNT                   | 17.6 $\Omega$        |                      |                |
| Ni-SWNT*                  | 26.5 $\Omega$        |                      | Applied<br>3 V |
| Purified pristine SWNT    | 21.5 $\Omega$        |                      |                |
| Purified pristine SWNT*   | 34.1 $\Omega$        |                      | Applied<br>3 V |

\* An electric field of 3 V across the fingers with a gap size of 12 mm was applied while the SWNT samples were being coated on the IDE.

Instrument used for the resistance measurement: Keithley 2002 digital multimeter and Agilent 34401 DMM.

When no electric field is applied, the resistance of the sulfonated SWNTs and fluorinated SWNTs is 5.34 k $\Omega$  and 41.5 k $\Omega$ , respectively, which are about two to three orders of magnitude higher than that of purified pristine ones with a value of 21.5  $\Omega$ , indicating that functionalization generally increases the resistance except for COOH-SWNTs and Ni-SWNTs, with a resistance range from 12.0  $\Omega$  to 17.8  $\Omega$ , close to or even lower than 21.5  $\Omega$  of purified pristine ones. It is reported that coating nickel on the SWNT aids in exfoliation of SWNTs agglomerates and enables good dispersions [17]. The enhanced dispersions and formation of continuous interconnections between SWNTs lead to the low electrical resistance of Ni-SWNTs. In addition, coating the SWNTs with nickel will not diminish the sidewall properties and affect the electrical properties as in sulfonated SWNTs and fluorinated SWNTs [17], resulting in a much lower electric resistance in Ni-SWNTs than that of other functional SWNTs.

When a 3 V electric field was applied during coating the SWNTs onto IDE chips, the resistance decreased from 5.34 k $\Omega$  to 25.6  $\Omega$  for sulfonated SWNTs and from 256 k $\Omega$  to 29.9  $\Omega$  for unpurified pristine SWNTs, respectively. The decrease in resistance is most likely caused by the nanotubes alignment. In our previous study [15, 18], a significantly increase in thermal conductivity was observed in the nanofluids containing magnetic-metal-coated carbon nanotubes when a magnetic field was applied. Real images showed that

the initial randomly dispersed Ni-coated SWNTs gradually stretched and finally aligned to form chains and clusters which are longer than the real length of individual nanotubes [18]. The contact between the individual nanotubes in these chains and clusters leads to the increase in thermal conductivity of the nanofluids. Similarly, since the sulfated SWNTs have charged sulfate functional groups, these charges could make SWNTs align in an electric field, leading to the contact enhancements among the nanotubes, thus decreasing the electrical resistance. No change in resistance was found in the purified pristine SWNTs when they were applied in an electric field, which indicates that there is no alignment for the purified pristine SWNTs in an electric field because there is no charged functional group. The same thing (no alignment) should also be expected for the unpurified pristine SWNTs because they are the same except that there are more impurities (e.g., metal catalysts and their oxides and graphite) in the unpurified ones. Therefore, these impurities in the unpurified pristine SWNTs could be the reason for the unexpected alignment.

The resistance of the Ni-SWNTs does not change in a 3 V electric field but change in a 5 V electric field (data is not listed) because Ni-SWNTs are slightly polarized in nature due to the addition of Ni. These slightly polarized Ni-SWNTs will align along the electric field when the field is strong enough (5 V in this study) and leads to the decrease in electric resistance. It was reported that Cu and Ti atoms adsorbed on SWNTs are positively charged and the two nearest carbon atoms carry a little negative charge based on the model using pseudo-potential plane wave method [19]. Such charge transfer increased several times when an electric field was applied. The binding energy of Ni to SWNT is very close to that of Ti but larger than that of Cu [20]. Therefore, similar charge transfer would be expected in Ni-SWNTs, and it would increase with the strength of an electric field, leading to the polarization of the Ni-SWNTs and their alignment.

No significant change was observed for the resistance of the fluorinated SWNTs and COOH SWNTs after an electric field was applied to the IDE during SWNTs deposition. This is due to that the COOH and fluorine functional groups have no charges, and, therefore, they were not aligned under an electric field. It is also worth noting that the resistance of COOH SWNTs is three magnitudes lower than that of fluorinated SWNTs. The much lower resistance of COOH-SWNTs is because that, during the well-controlled carboxyl functionalization, the chemical modification is limited mostly to the opening of the tube caps at the ends and the formation of functional groups at defect sites along the sidewall. SWNTs functionalized in this manner basically retain their pristine electronic properties [12]. Therefore, the resistance of the COOH-SWNTs is very similar to that of the purified pristine ones. It was found using the density functional theory that vacancy-COOH pairs with a strong covalent bond are energetically favorable on the zigzag nanotube sidewall after acid treatment, and the electrical conductivity would be enhanced [21]. This is the case in the present study as seen from Table 2, the resistance of the COOH-SWNTs is pretty close to and even lower than that of the pristine ones with an applied electric field or not. By comparison, addition

reactions enable the direct coupling of functional groups such as fluorine onto the  $\pi$ -conjugated carbon framework of the tubes. It is known that the formation of carbon-heteroatom bonds will transform a  $sp^2$ -hybridized configuration to that of a  $sp^3$ -hybridized structure, leading to the disruption of the pseudo-one-dimensional lattice of the SWNTs and increase in resistance [12]. This is consistent with the results in the present study that the resistance of the fluorinated SWNTs is three magnitudes higher than that of the pristine SWNTs and COOH-SWNTs.

Previous study showed that the tensile strength of the cross-link membrane with 5 wt% of sulfonated SWNTs and sulfonated polystyrene is only 35 MPa, which is much lower than the expected value by considering the extremely high tensile strength of SWNTs (around 60 GPa) [22]. Assuming that nanotubes disperse very well in the polymer matrix, ideally, a 5 wt% nanotube loading in a film would have a tensile strength of around  $\approx 3$  GPa. One possible explanation of the lower than expected values is that the inserted functional groups interfere with the conjugate structure of the nanotube, thereby reducing its macromechanical strength. The effective electrical conductivity measurement of sulfonated SWNTs solution [11] provides strong evidence and support to this. No percolation threshold phenomenon is observed in the experiments. The linear conductivity increase versus the weight percentage indicates that the dominant conduction mechanism might be the ionic conduction, which is in agreement with the chemical structure of sulfonated SWNTs (anion  $SO_3^-$  group).

The existence of anion  $SO_3^-$  group in sulfonated SWNTs is also proved in the present study. The resistivity of the SWNTs is 5.34 k $\Omega$ , which are about two orders of magnitude higher than that of purified pristine ones with a value of 21.5  $\Omega$ . It decreased from 5.34 k $\Omega$  to 25.6  $\Omega$  under the external electrical field, probably caused by the nanotubes alignment due to the existence of the anion  $SO_3^-$  groups.

The motivation of the resistivity measurement of pristine and functionalized SWNTs is to better understand the relationship between nanotube structure and physical properties (thermal, electrical, and mechanical). Our study indicated that macrophysical strength is damaged by addition (insertion) of functional group [22]. Electrical conductivity measurement could provide additional information of structure of SWNTs. COOH-SWNTs have a resistance around 12.0  $\Omega$ , even lower than that of purified pristine ones with a value of 21.5  $\Omega$ , indicating that COOH group would maximally reduce the interfacial influence and keep the unbroken nanotube conjugate structure.

Changing the SWNTs from hydrophobic to hydrophilic with COOH group, while keeping its excellent electrical conductivity, makes it a better choice than pristine one to be used as nanofillers for various applications, especially in polymer composites [23].

#### 4. Conclusions

The electrical resistivity of several pristine and functional SWNTs in solid phase was investigated with and without an applied electric field.

Without an applied electric field, the resistance generally increased for the sulfonated and fluorinated SWNTs but not for COOH-SWNTs. With an applied electric field, no change was observed in resistance for purified pristine SWNTs, COOH-SWNTs, and fluorinated SWNTs. A significant decrease in resistance was observed from sulfonated SWNTs and unpurified pristine SWNTs when an electric field was applied, indicating that they both align within an electric field. The alignment of the sulfonated SWNTs is most likely due to the charged sulfonate groups. Alignment was found in the unpurified pristine SWNT but not the purified pristine SWNTs, which indicates that the alignment of unpurified pristine SWNTs is probably due to the impurities within its structure. The lower resistivity in the purified pristine SWNTs may be due to the smaller number (<5%) of impurities.

The results in this study show that the resistance of pristine and functional singlewall nanotubes is correlated to the type of functional groups and the alignment of the nanotubes. The significance of this research is that the hydrophilic COOH-SWNTs show relative low resistivity, which indicates that conjugated  $\pi$  structure of nanotubes (sidewall properties) is alive. These results demonstrate that hydrophilic COOH-SWNTs could be a better candidate than the hydrophobic pristine SWNTs for being used in many applications, especially in polymer nanocomposites.

#### Acknowledgments

H. Hong would like to thank NASA EPSCoR (award no. NNX09AU83A) for financial support. Jing Li would like to thank for DHS HSARPAR (IAA no. HSHQDC-08-x-00870) for financial support. Thanks are due to Mianliang Huang for his useful comments and corrections.

#### References

- [1] S. Berber, Y. K. Kwon, and D. Tomanek, "Unusually high thermal conductivity of carbon nanotubes," *Physical Review Letters*, vol. 84, no. 20, pp. 4613–4616, 2000.
- [2] C. Zhou, J. Kong, and H. Dai, "Intrinsic electrical properties of individual single-walled carbon nanotubes with small band gaps," *Physical Review Letters*, vol. 84, no. 24, pp. 5604–5607, 2000.
- [3] M. S. Dresselhaus, G. Dresselhaus, J. C. Charlier, and E. Hernández, "Electronic, thermal and mechanical properties of carbon nanotubes," *Philosophical Transactions of the Royal Society A*, vol. 362, no. 1823, pp. 2065–2098, 2004.
- [4] A. Javey, R. Tu, D. B. Farmer, J. Guo, R. G. Gordon, and H. Dai, "High performance n-type carbon nanotube field-effect transistors with chemically doped contacts," *Nano Letters*, vol. 5, no. 2, pp. 345–348, 2005.
- [5] H. Hong, X. Luan, M. Horton, C. Li, and G. P. Peterson, "Alignment of carbon nanotubes comprising magnetically sensitive metal oxides in heat transfer nanofluids," *Thermochimica Acta*, vol. 525, no. 1–2, pp. 87–92, 2011.
- [6] J. Wensel, B. Wright, D. Thomas et al., "Enhanced thermal conductivity by aggregation in heat transfer nanofluids containing metal oxide nanoparticles and carbon nanotubes," *Applied Physics Letters*, vol. 92, no. 2, Article ID 023110, 3 pages, 2008.
- [7] H. Hong, D. Thomas, A. Waynick, W. Yu, P. Smith, and W. Roy, "Carbon nanotube grease with enhanced thermal and electrical

- conductivities,” *Journal of Nanoparticle Research*, vol. 12, no. 2, pp. 529–535, 2010.
- [8] Y. Lu, J. Li, J. Han et al., “Room temperature methane detection using palladium loaded single-walled carbon nanotube sensors,” *Chemical Physics Letters*, vol. 391, no. 4–6, pp. 344–348, 2004.
- [9] J. Li, Y. Lu, Q. Ye, M. Cinke, J. Han, and M. Meyyappan, “Carbon nanotube sensors for gas and organic vapor detection,” *Nano Letters*, vol. 3, no. 7, pp. 929–933, 2003.
- [10] J. Li and Y. Lu, “Carbon nanotube based chemical sensors for space and terrestrial applications,” *ECS Transactions*, vol. 19, no. 6, pp. 7–15, 2009.
- [11] B. Glover, K. W. Whites, H. Hong, A. Mukherjee, and W. E. Billups, “Effective electrical conductivity of functional single-wall carbon nanotubes in aqueous fluids,” *Synthetic Metals*, vol. 158, no. 12, pp. 506–508, 2008.
- [12] K. Balasubramanian and M. Burghard, “Chemically functionalized carbon nanotubes,” *Small*, vol. 1, no. 2, pp. 180–192, 2005.
- [13] F. Liang, J. M. Beach, P. K. Rai et al., “Highly exfoliated water-soluble single-walled carbon nanotubes,” *Chemistry of Materials*, vol. 18, no. 6, pp. 1520–1524, 2006.
- [14] Y. Zhang, N. W. Franklin, R. J. Chen, and H. Dai, “Metal coating on suspended carbon nanotubes and its implication to metal–tube interaction,” *Chemical Physics Letters*, vol. 331, no. 1, pp. 35–41, 2000.
- [15] B. Wright, D. Thomas, H. Hong et al., “Magnetic field enhanced thermal conductivity in heat transfer nanofluids containing Ni coated single wall carbon nanotubes,” *Applied Physics Letters*, vol. 91, no. 17, Article ID 173116, 3 pages, 2007.
- [16] J. Li, Y. Lu, Q. Ye, L. Delzeit, and M. Meyyappan, “A gas sensor array using carbon nanotubes and microfabrication technology,” *Electrochemical and Solid-State Letters*, vol. 8, no. 11, pp. H100–H102, 2005.
- [17] D. K. Chakravarthi, V. N. Khabashesku, R. Vaidyanathan et al., “Carbon fiber-bismaleimide composites filled with nickel-coated single-walled carbon nanotubes for lightning-strike protection,” *Advanced Functional Materials*, vol. 21, no. 13, pp. 2527–2533, 2011.
- [18] M. Horton, H. Hong, C. Li, B. Shi, G. P. Peterson, and S. Jin, “Magnetic alignment of Ni-coated single wall carbon nanotubes in heat transfer nanofluids,” *Journal of Applied Physics*, vol. 107, no. 10, Article ID 104320, 4 pages, 2010.
- [19] L. Wang and Y. Zhang, “Electronic and magnetic properties of metal atom adsorption on SWNT,” *Physica E: Low-Dimensional Systems and Nanostructures*, vol. 43, no. 4, pp. 889–892, 2011.
- [20] E. Durgun, S. Dag, V. M. K. Bagci, O. Gülseren, T. Yildirim, and S. Ciraci, “Systematic study of adsorption of single atoms on a carbon nanotube,” *Physical Review B*, vol. 67, no. 20, Article ID 201401, 4 pages, 2003.
- [21] C. Wang, G. Zhou, J. Wu, B. L. Gu, and W. Duan, “Effects of vacancy-carboxyl pair functionalization on electronic properties of carbon nanotubes,” *Applied Physics Letters*, vol. 89, no. 17, Article ID 173130, 3 pages, 2006.
- [22] Y. Dai, H. Hong, M. Guiver, and J. S. Welsh, “Reinforced films based on cross-linked water-soluble Sulfonated carbon nanotubes with Sulfonated Polystyrene,” *Journal of Nanoscience and Nanotechnology*, vol. 9, no. 9, pp. 5150–5156, 2009.
- [23] Z. Han and A. Fina, “Thermal conductivity of carbon nanotubes and their polymer nanocomposites: a review,” *Progress in Polymer Science*, vol. 36, no. 7, pp. 914–944, 2011.

## Research Article

# Synthesis and Characterisation of Calcium Carbonate Aragonite Nanocrystals from Cockle Shell Powder (*Anadara granosa*)

Abdullahi Shafiu Kamba,<sup>1</sup> Maznah Ismail,<sup>1</sup>  
Tengku Azmi Tengku Ibrahim,<sup>2</sup> and Zuki Abu Bakar Zakaria<sup>1</sup>

<sup>1</sup> Laboratory of Molecular Biomedicine, Institute of Bioscience, Universiti Putra Malaysia, 43400 Serdang, Malaysia

<sup>2</sup> Faculty of Veterinary Medicine, Universiti Putra Malaysia, 43400 Serdang, Malaysia

Correspondence should be addressed to Zuki Abu Bakar Zakaria; mdzukiabubakar@gmail.com

Received 24 November 2012; Accepted 24 March 2013

Academic Editor: Yun Zhao

Copyright © 2013 Abdullahi Shafiu Kamba et al. This is an open access article distributed under the Creative Commons Attribution License, which permits unrestricted use, distribution, and reproduction in any medium, provided the original work is properly cited.

The synthesis of pure calcium carbonate nanocrystals using a high pressure homogeniser (HPH) via a microemulsion system produced uniform nanosized particles, which were characterised using transmission electron microscopy (TEM), field-emission scanning electron microscopy (FESEM), X-ray diffraction (XRD), Fourier transform infrared spectroscopy (FTIR), and thermogravimetric analysis (TGA). The identified particles were aragonite polymorphs with a rod shape and were approximately 50 nm in size. The aragonite polymorph of calcium carbonate was prepared from biogenic materials, cockle shells, and exhibited unique characteristics (i.e., a higher density than that of calcite), which makes it biocompatible and potentially suitable for applications in the medical, pharmaceutical, cosmetic, and paint industries. The methods adopted and the nonionic surfactant used in the synthesis of calcium carbonate nanocrystalline aragonite polymorphs were environmentally friendly and can be scaled up for industrial production. The sources are naturally available materials that are by-products of the seafood industry, which offers an opportunity for exploitation in numerous industrial applications.

## 1. Introduction

Calcium carbonate nanoparticles are abundant inorganic biomaterials with different morphological structures that have attracted the interest of researchers in different fields. This interest is due to the wider application of these nanoparticles in many industries, such as the paint, rubber, and plastics industries. With the present focus of interest in nanotechnology, calcium carbonate nanoparticles have been observed to be biocompatible for use in medicine, pharmaceutical industries, and drug delivery systems [1, 2]. The most important aspect with respect to the synthesis of nanoparticles is control of the particle size, polymorphism, and morphology of the desired material. Control of this parameter has led to the development of new materials with unique properties that differ from those in the bulk material [3]. Many studies have been conducted to mimic nature in the synthesis of nanomaterial with the aim of analysing the biogenic materials

and identifying how nature controls the morphology, size, and polymorphism in organisms.

Biomineralization is the process by which a living organism secretes inorganic material in the form of a skeleton, a shell, teeth, or bone [1]. These processes are natural, are often performed with a high level of spatial control, and usually occur in a confined reaction environment. The organic matter or biopolymers observed in the hard tissue, such as the bones, teeth, and shells of living organisms, have the unique capacity to control the morphology, crystal size, polymorphism, and structure of the inorganic material. These biopolymers are usually soluble and are referred to as a functional matrix [1–3]. Biomaterials are highly optimised materials with remarkable properties, and they serve as natural archetypes for future materials [1]. These unusual properties have recently attracted the attention of numerous researchers, including both materials chemists and researchers in the medical and pharmaceutical sciences because of the biogenic origin and

potential biocompatibilities of these materials [3]. Biomaterials with an optimised structure exhibit better performance, durability, and appearance, which offers valuable opportunities for the development of new techniques for the synthesis and control of nanostructures materials with potential applications in pharmaceuticals, cosmetics, drug delivery, medicine, microelectronics, and energy technology [3].

Biological systems are capable of producing inorganic materials such as calcium carbonate with different structures, morphologies, and polymorphs. Such biological systems are observed in numerous marine organisms such as oyster shells, coral, ivory sea urchin, and mollusc shell bivalve nacre, whereby the main components of the shells are calcium carbonate and other organic components, such as anionic protein and glycoprotein [4].

Currently, research with respect to cockle shells, in which the primary component is approximately 98-99% calcium carbonate, is in its infancy [5, 6]. Calcium carbonate has three anhydrous crystalline phases: calcite, which is thermodynamically stable under ambient conditions; aragonite, which is a high-pressure polymorph that is less stable than calcite; and vaterite, which is the least stable among the three polymorphs and has the ability to transform into one of the other two polymorphs [7]. Different techniques for the preparation of calcium carbonate nanoparticles have been reported, including the precipitation of homogeneous solutions [8], water-in-oil-in-water emulsions [9], mechanochemical and sonochemical syntheses [10] and water-in-oil (W/O) microemulsions [11]. Other preparation methods include the high-pressure homogeniser (HPH) technique and high-gravity precipitation. For precipitation methods, two different routes have been reported with the only difference being the chemicals used. The first method is based on the carbonation process, whereby carbon dioxide gas is bubbled through aqueous slurry of calcium hydroxide at specific temperature in present of organic additive such as surfactant thereby inducing precipitation of calcium carbonate. The second method is known as double decomposition and involves the combination of salt of calcium ions with salt of carbonate ions, such as the reaction of calcium chloride or calcium nitrate with sodium carbonate or ammonium carbonate [12].

Most researchers are now diverting their attention to the microemulsion route for the synthesis of different types of nanoparticles. Microemulsions are a thermodynamically stable, optically transparent, isotropic dispersion of two immiscible liquids, such as water and oil, stabilised by an interfacial film of a surfactant molecule [13]. The system is a single optical dispersion of thermodynamically stable liquids that typically consists of small particle droplets with diameters in the range of less than from 10 nm to 100 nm [14]. A microemulsion serves as a special microreactor that inhibits the growth of nanosized particles [15]. The advantage of this method is that it increases the homogeneity of the chemical decomposition at the nanolevel and allows the easy preparation of nanocrystals of comparatively equal sizes [16].

The research in this paper was focused on the synthesis of calcium carbonate nanocrystals from cockle shells by the microemulsion route using a HPH. The process is a top-down

technique that occurs in a special homogenising valve at the heart of homogenising equipment. The fluid passes through a minute gap in the homogenising valve [17], which creates conditions of high turbulence and shear, combined with compression, acceleration, and a pressure drop. The impact causes disintegration of particles and dispersion throughout the sample [17]. After homogenisation, the particles are uniform in size, and their sizes depend on the number of cycles, the processing, and the operating pressure. The homogeniser is the most efficient device for the reduction of particle and droplet sizes.

To the best of our knowledge, no research related to the synthesis of calcium carbonate nanocrystals from biogenic origins or its reservoir using calcium carbonate as the main source of calcium and carbonate ions has been reported. Most research has focused on the use of chemical reactions, whereby the salts of calcium and carbonate ions act as the precursors for the synthesis of calcium carbonate nanocrystals.

## 2. Experimental

*2.1. Synthesis of Calcium Carbonate Powder.* Cockle shells were obtained from market. The calcium carbonate powders were prepared from the cockle shells according to the procedure described by Islam et al. [18]. Samples of the cockle shells were dried in an oven at 50°C for 7 days, and the shells were then crushed and blended into a fine powder, which was sieved through a 90- $\mu$ m laboratory stainless steel sieve (Endecott, London, England). The calcium carbonate powders were finally packed into a polyethylene plastic bag for further analyses.

*2.2. Synthesis of Calcium Carbonate Nanocrystals.* The synthesis of calcium carbonate nanocrystals was performed through oil-in-water (O/W) microemulsions using a HPH. In this technique, the particles sizes are reduced after leaving the homogenising gap by cavitations, particle collisions, and shear forces [19, 20].

The calcium carbonate nanocrystals were prepared by the dissolution of 2 g of dry cockle shell powder in a formulated oil-in-water (O/W) microemulsion, which was moderately stirred by a magnetic stirrer for 5 min at 100 rpm to form a calcium carbonate suspension. The formulated suspension was passed through the liquid inlet of a HPH for premilling at a moderate pressure of 300 and 500 bars for three cycles each. The premilled suspension was collected at the HPH outlet and was again passed through the HPH liquid inlet at a high pressure of 1500 bars for 25 homogenising cycles to obtain the desired product. The product of the crystal suspension was filtered and dried in an oven at 105°C for 24 hours.

*2.3. Characterisation of Calcium Carbonate Nanocrystals.* The following instruments were employed for the observation and characterisation of the calcium carbonate nanocrystals. The morphology and particle size of the nanocrystals were analysed using a transmission electron microscope (TEM, Hitachi H-7100) and a field-emission scanning electron microscope (FESEM, JOEL 7600F) operated at a voltage of

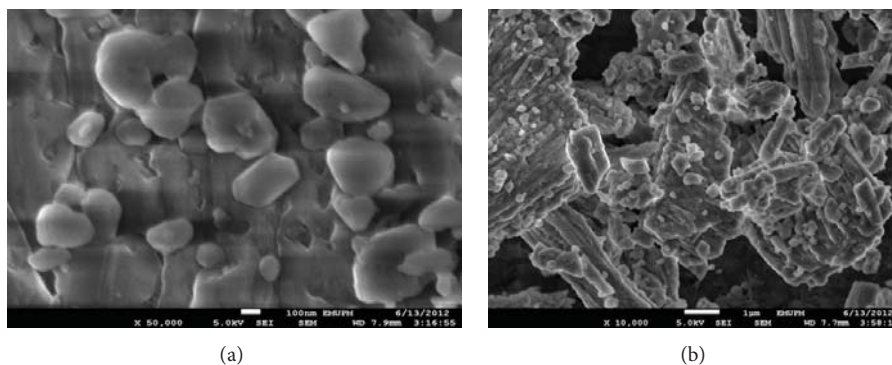


FIGURE 1: FESEM micrographs of (a) cockle shell calcium carbonate nanocrystals and (b) cockle shell powder.

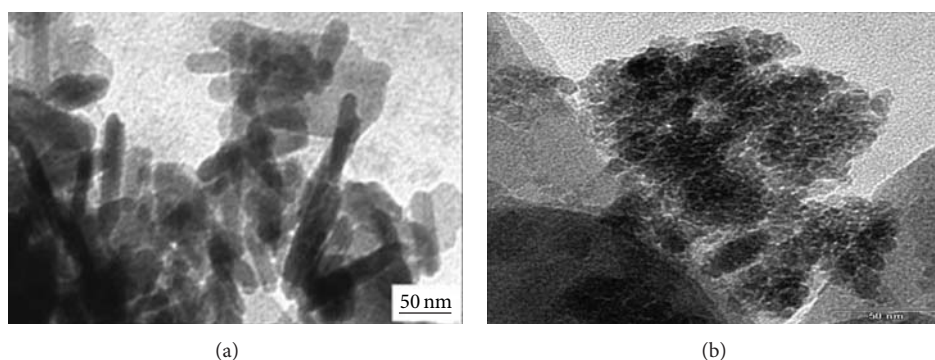


FIGURE 2: TEM images of (a) rod-shaped nanocrystals synthesised via microemulsion routes and (b) cockle shell powder without organic additive added.

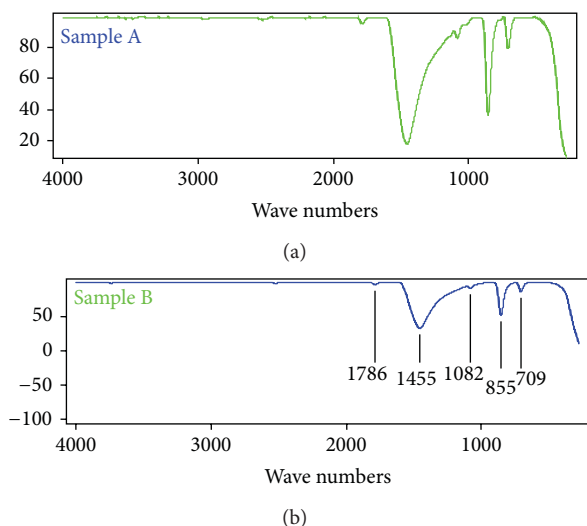


FIGURE 3: FTIR spectra of calcium carbonate nanocrystals (a) and cockle shell powder (b).

5 kV and equipped with an energy-dispersive X-ray spectroscopy (EDX) unit. The crystal powder was characterised by X-ray powder diffraction (XRD) using a Rigaku X-ray diffractometer equipped with a Cu  $K\alpha$  ( $\lambda = 0.15406$  nm) radiation source; samples were scanned at a rate of 40/min.

Pellets of the calcium carbonate nanocrystals were calibrated in a weight proportion of 1 wt% in Ker, and analyses were performed with a Fourier-transform infrared spectrometer (FTIR, model 100, Perkin Elmer, 710 Bridgeport Avenue, Shelton, CT, USA) in the range of 400–4000  $\text{cm}^{-1}$ . Thermogravimetric analysis of the calcium carbonate nanocrystals was performed using a TG-DTA instrument (Netzsch STA449C) with an air flow of 100 mL/min and a heating rate of 10 K/min from room temperature to 1000°C.

### 3. Results and Discussion

**3.1. FESEM and TEM Characterisation of Calcium Carbonate Nanocrystals.** The morphological characteristics of the calcium carbonate nanocrystals presented in Figures 1(a) and 1(b) are typical FESEM micrographs of the samples under study. The nanometre-sized and rod-shaped particles in Figure 1(a) were synthesised in the confined microemulsion system, whereas Figure 1(b) shows micrographs of a cockle shell powder without any organic additives. These results indicate a natural ability of the biological system to control specific size and morphology, which is very difficult to achieve using classical methods or colloid-chemistry routes [21]. A living organism has the ability to secrete macromolecules, such as in oyster shells, coral, mollusc shells and bivalve nacre. Living organisms achieve this natural

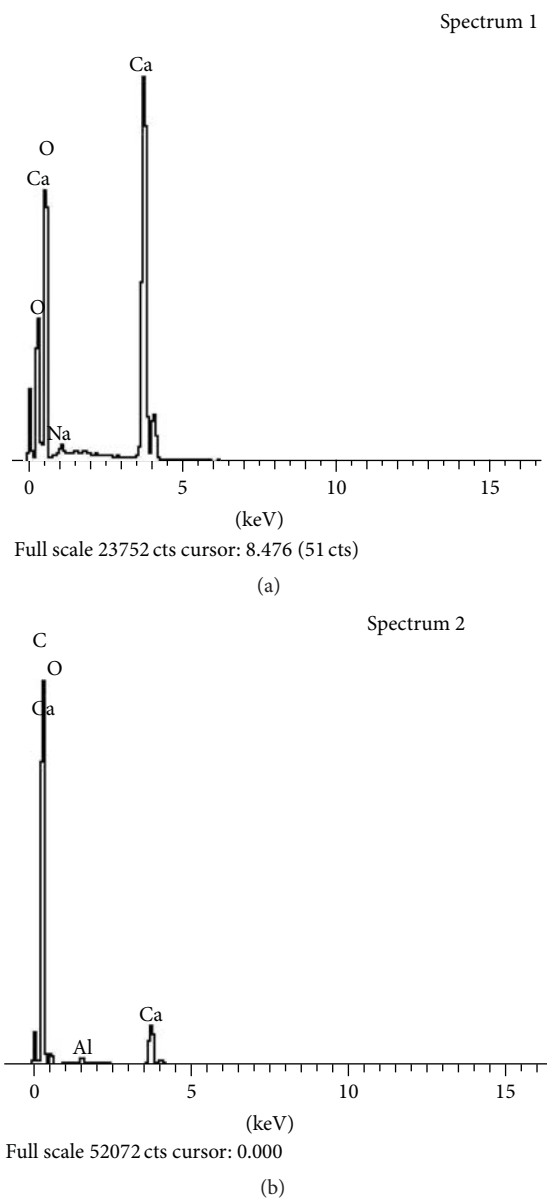


FIGURE 4: EDX spectral data for calcium carbonate nanocrystals and cockle shell powder.

phenomenon by utilising the secreted macromolecules (proteins, polysaccharides, and acidic macromolecules) as the nucleators (usually in the form of phospholipid membranes) to modulate the formation of a unique inorganic-organic material with a special morphology and function [21].

TEM was also used to study the calcium carbonate crystal particles. The images of the crystal presented in both Figures 2(a) and 2(b) reveal a rod shape of calcium carbonate aragonite polymorphs. The particles in Figure 2(a) are uniformly distributed at the nanometre scale and were formed in the microemulsion system; this system is considered an ideal medium for the preparation of inorganic nanoparticles [22]. The nanocrystal particles synthesised in the microemulsion

system presented in Figure 2(a) differ in size, being approximately 50 nm with individual particles measuring 12–30 nm; in addition, the shape of the particles is clear, and the difference in the particle size may result from the presence of Tween 80 used in the prepared microemulsion. In contrast, the particles shown in Figure 2(b) agglomerated, and the rod shape was not clear compared with the shape in Figure 2(a), which may be due to the differences in the preparation conditions and the additional surfactant (Tween 80) used. Surfactants, both ionic and nonionic, have been reported to strongly affect the size and morphology of calcium carbonate nanoparticles during synthesis [23]. However, nonionic surfactants have a weaker effect on the morphology than do ionic surfactants [23]. This result is most likely due to the weak interactions between a nonionic surfactant and  $\text{Ca}^{2+}$  and  $\text{CO}_3^{2-}$  ions [24]; in addition, the microemulsion route, when used for the synthesis of nanoparticles, enables control of the size and morphology of the obtained materials [23].

**3.2. FTIR Spectra of Calcium Carbonate Nanocrystals.** FTIR spectra of the calcium carbonate nanocrystals are presented in Figures 3(a) and 3(b). FTIR spectroscopy is an important instrument used to identify different phases of organic and inorganic compounds and, specifically, calcium carbonate phases due to the differences in their carbonate ions,  $\text{CO}_3^{2-}$ . Carbonate ions and similar molecules have four normal modes of vibration peaks:  $\nu_1$ , symmetric stretching;  $\nu_2$ , out-of-plane bending;  $\nu_3$ , doubly degenerate planar asymmetric stretching; and  $\nu_4$ , doubly degenerate planar bending [25]. The spectral data obtained for the samples reveal a broad absorption peak of  $\text{CO}_3^{2-}$  at  $\sim 1455\text{ cm}^{-1}$ ,  $\sim 1082\text{ cm}^{-1}$ ,  $\sim 1786\text{ cm}^{-1}$ ,  $\sim 855\text{ cm}^{-1}$ , and  $\sim 709\text{ cm}^{-1}$ , which have been reported to be the common characteristic features of the carbonate ions in calcium carbonate and are the fundamental modes of vibration for this molecule [26]. However, the observed bands at  $\sim 1082\text{ cm}^{-1}$  and  $\sim 855\text{ cm}^{-1}$  were carefully assigned as  $\nu_1$  symmetric stretching and  $\nu_2$  out-of-plane bending modes of  $\text{CO}_3^{2-}$ , respectively. The peak at  $\sim 1082\text{ cm}^{-1}$  was only observed in the spectrum of aragonite-phase calcium carbonate, whose  $\text{CO}_3^{2-}$  ions are inactive in the infrared region. This observation was verified by other reports in the literature on characteristic infrared bands, which are experimentally not observed in the spectrum of calcite [26]. In contrast, the doubly degenerate peak that appears at  $\sim 709\text{ cm}^{-1}$  can be attributed to the  $\nu_4$  in-plane bending mode of  $\text{CO}_3^{2-}$  ions, which indicates a structural change in the calcium ions from the symmetry of the calcite phase. This degeneracy can only be removed by splitting the band into two; thus, the band is attributed to the aragonite phase only, which has been confirmed in the literature [26]. This assertion was also supported by a very broad doubly degenerate band  $\nu_3$  at  $\sim 1452\text{ cm}^{-1}$ , which confirms the structural changes in the symmetry of the  $\text{CO}_3^{2-}$  molecular ions that correspond to the asymmetric stretching mode of  $\text{CO}_3^{2-}$ . A similar result was also reported by Cheng et al. [27]. The fundamental changes in the positions of the vibration mode of a molecule are caused by a modification of the electrostatic valence of the Ca–O bond due to changes in

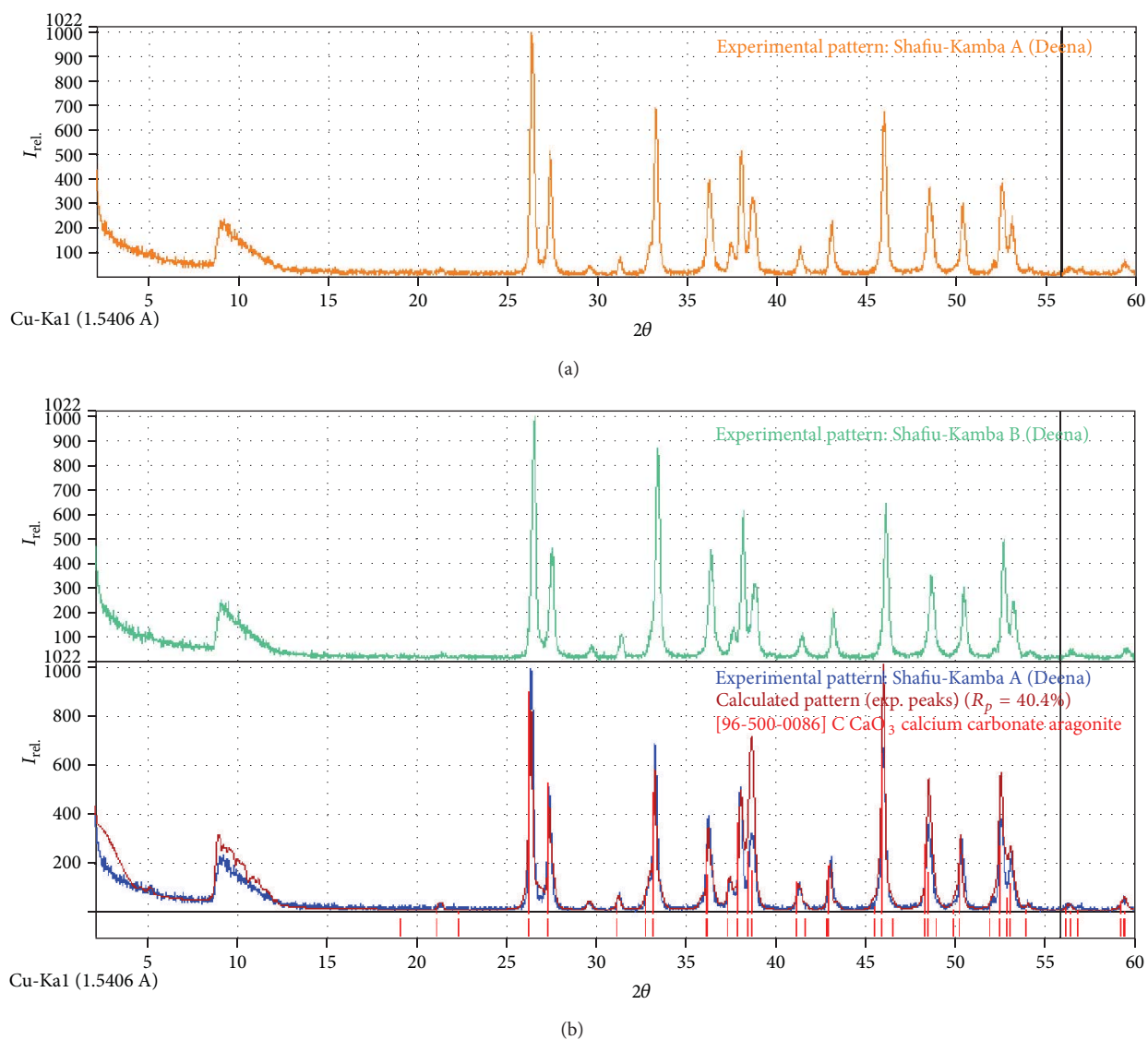


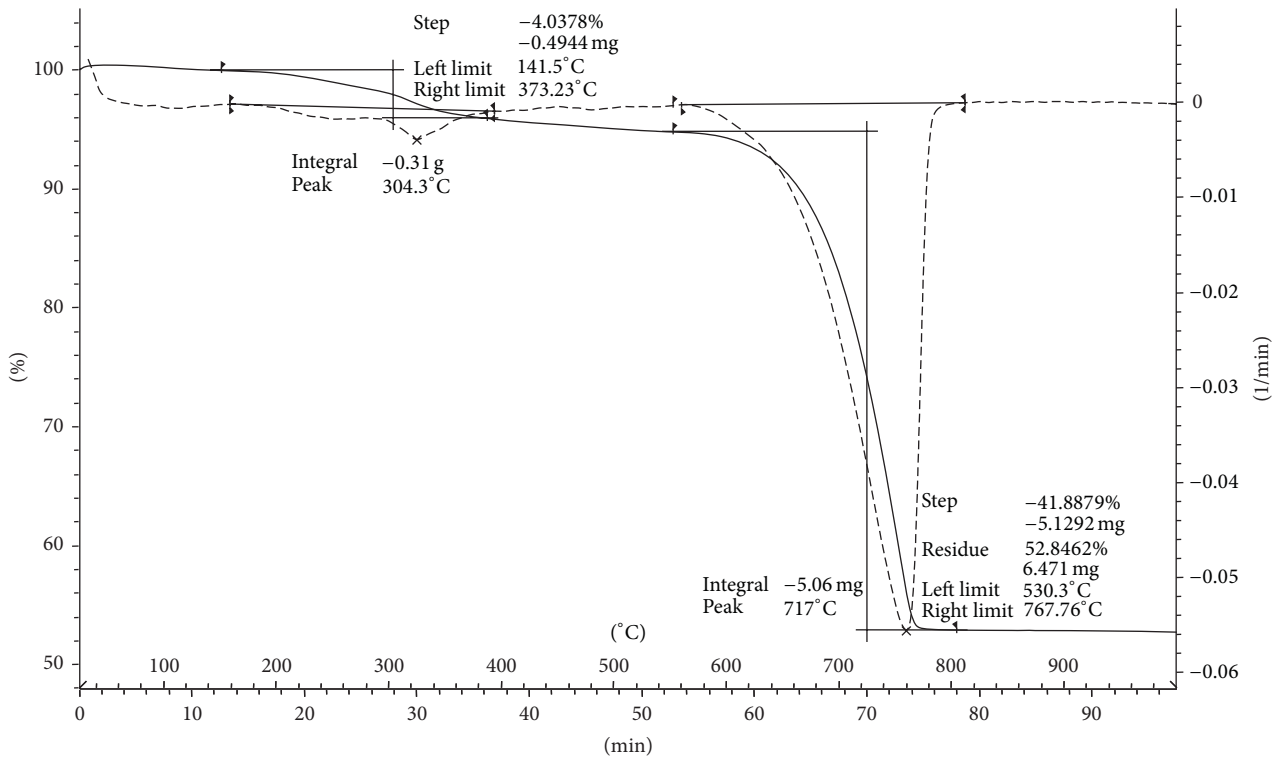
FIGURE 5: X-ray diffraction patterns of calcium carbonate nanocrystals (a) and cockle shell powder (b).

the coordination; the Ca–O bond alteration occurs because the displacement of the carbonate vibration mode changes in the environment of oxygen atoms [26–28]. This evidence further demonstrates that the synthesis involves a single phase of calcium carbonate aragonite crystals. The observed IR frequencies at  $\sim 1786\text{ cm}^{-1}$  and  $\sim 252\text{ cm}^{-1}$  are due to the combination of the fundamental vibration frequencies of the carbonate ions assigned between ( $\nu_1$  and  $\nu_4$ ) and ( $\nu_1$  and  $\nu_3$ ), respectively, as reported in the literature [26–28].

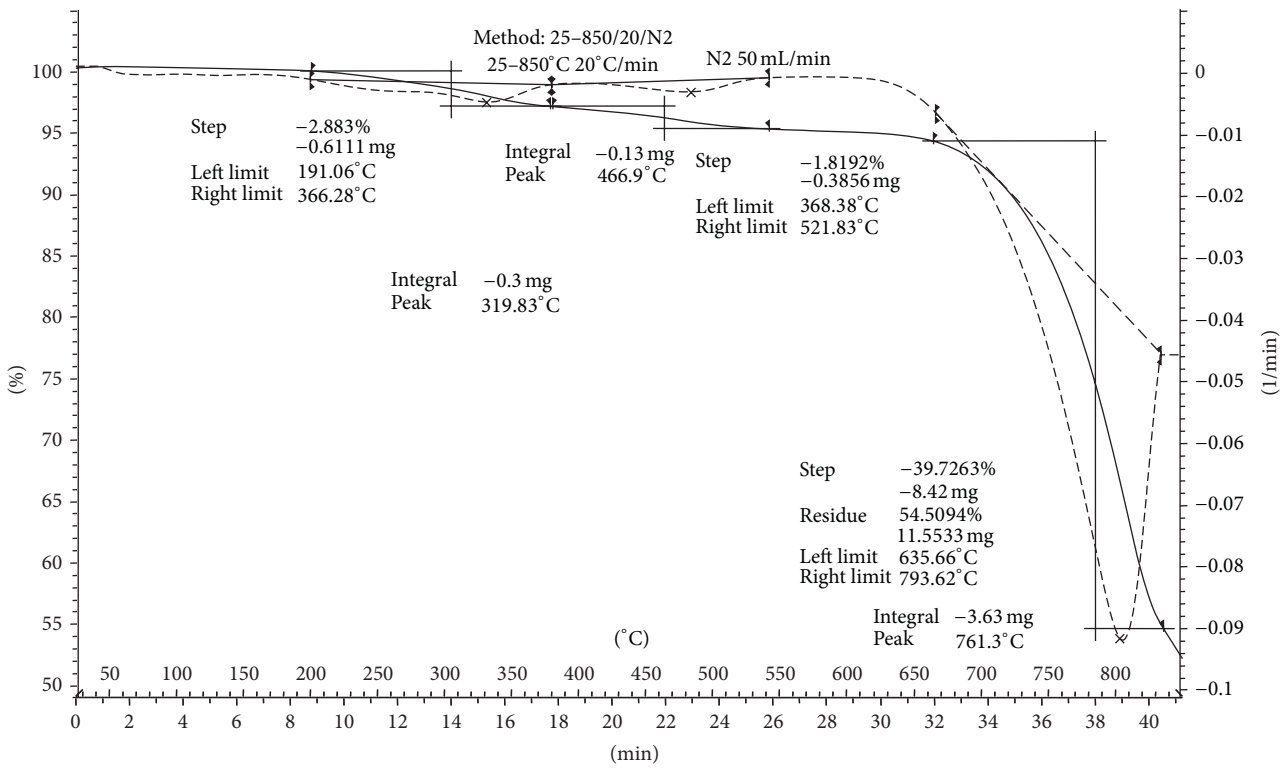
Both the cockle shell powder and the synthesised calcium carbonate nanocrystals possess the same vibration frequencies as observed in the FTIR data obtained in Figure 3(a). The results demonstrate that the nonionic surfactant (Tween 80) used in the preparation of the microemulsion does not affect the vibration frequencies because no additional peaks were observed when the spectrum of the calcium carbonate nanocrystals was compared with that of the cockle shell

powder in Figure 3(b). The cockle shell powder was prepared in distilled water only and without the use of additional organic additives or surfactants. This result may be due to the presence of a natural or organic matrix composed of an elastic biopolymer, such as the silk-like protein chitin; this organic matrix secreted by marine shell plays an important role in controlling the inorganic structure, morphology, size, and polymorphism [28, 29].

**3.3. Elemental Compositions of Synthesised Nanocrystals and Cockle Shell Powder.** The chemical compositions of the samples were analysed using EDX, which revealed the presence of individual elements in the samples. As indicated in Tables 1(a) and 1(b), the samples contained almost identical elements, with no significant differences observed between the elements detected in the two samples analysed. Both



(a)



(b)

FIGURE 6: (a) Graphical representation of nanocrystal TGA results. (b) Graphical representation of cockle shells powder TGA data.

TABLE 1: (a) Elemental compositions of calcium carbonate nanocrystals and (b) elemental compositions of cockle shell powder.

| (a)                |        |        |        |         |  |           |
|--------------------|--------|--------|--------|---------|--|-----------|
| Spectrum           | Carbon | Oxygen | Sodium | Calcium |  | Total (%) |
| Spectrum 1         | 20.18  | 59.51  | 0.53   | 19.78   |  | 100.00    |
| Spectrum 2         | 14.44  | 46.73  | 0.30   | 38.53   |  | 100.00    |
| Spectrum 3         | 13.57  | 28.14  | 0.18   | 58.11   |  | 100.00    |
| Mean               | 16.06  | 44.79  | 0.34   | 38.81   |  | 100.00    |
| Standard deviation | 3.59   | 15.78  | 0.17   | 19.17   |  |           |
| Max.               | 20.18  | 59.51  | 0.53   | 58.11   |  |           |
| Min.               | 12.65  | 28.14  | 0.18   | 19.78   |  |           |

| (b)                |        |        |        |         |           |           |
|--------------------|--------|--------|--------|---------|-----------|-----------|
| Spectrum           | Carbon | Oxygen | Sodium | Calcium | Aluminium | Total (%) |
| Spectrum 1         | 22.18  | 50.51  | 0.53   | 27.60   | 0.17      | 100.00    |
| Spectrum 2         | 12.44  | 46.32  | 0.30   | 30.53   | 0.41      | 100.00    |
| Spectrum 3         | 13.57  | 37.14  | 0.18   | 58.11   |           | 100.00    |
| Mean               | 16.06  | 44.79  | 0.34   | 38.81   |           | 100.00    |
| Standard deviation | 3.59   | 15.78  | 0.17   | 19.17   |           |           |
| Max.               | 19.82  | 69.52  | 0.36   | 58.11   |           |           |
| Min.               | 13.57  | 26.42  | 0.16   | 23.87   |           |           |

samples contained negligible traces of elemental sodium, and a minute percentage of aluminium was recorded only in the cockle shell powder (Figure 4(b)). This analysis proves that the composition of the calcium carbonate in the cockle shell powder is not 100% pure due to the presence of other elements such as aluminium and sodium.

**3.4. X-Ray Diffraction Pattern of Calcium Carbonate Nanocrystals.** X-ray diffraction is a sensitive instrument used for the identification of crystalline phases of inorganic compounds. The data obtained from the X-ray diffraction patterns in Figures 5(a) and 5(b) demonstrate the crystalline nature and phase composition of both samples under analysis. The X-ray diffraction pattern of the synthesised calcium carbonate nanocrystals and cockle shell powder in Figures 3(a) and of 3(b) exhibits characteristics peaks of aragonite at  $2\theta$  values of  $26.34^\circ$ ,  $33.24^\circ$ ,  $45.98^\circ$  and  $26.31^\circ$ ,  $33.24^\circ$ ,  $45.98^\circ$ , and respectively, which correlate with (hkl) indices of (111), (012), (221), and (021), (012), and (221), respectively. These are the strongest peaks observed in the X-ray diffraction patterns of the analysed samples. However, peaks are also observed at  $26.71^\circ$ ,  $26.87^\circ$ ,  $27.02^\circ$ ,  $27.38^\circ$ ,  $27.57^\circ$ ,  $27.72^\circ$ ,  $41.28^\circ$ ,  $45.62^\circ$ ,  $46.54^\circ$ ,  $48.84^\circ$ , and  $52.53^\circ$ . These values also correspond with calcium carbonate aragonite polymorphs reported in the PDF-4+ data bank of the International Centre for Diffraction Data [30]. All the reflections can be attributed to the pure aragonite phase of calcium carbonate, which validates the FTIR results of the aragonite polymorph of calcium carbonate.

**3.5. Thermal Decomposition of Calcium Carbonate Nanocrystals.** Thermogravimetric analyses of the cockle shell powder and the nanocrystals synthesised from the powder were

performed using the shrinking core model (SCM), whereby the reaction usually begins from the outer layer of the particles and moves toward the solid, which yields an ash solid as the converted material [5]. Therefore, Figures 6(a) and 6(b) illustrate the weight losses of the samples analysed during the process. Both samples were stable until  $300^\circ\text{C}$  and then decomposed in two steps. The first step was the initial process, which started with a very small weight loss of 4.0% due to the moisture content in the samples [31]; a similar result has been reported by Yu et al. [32] for bulk or microcalcium carbonate, and this value would also be the loss for nanoparticles of the same material, as reported as by Mohamed et al. [5]. Endothermic behaviour was also observed in the temperature range from  $304$  to  $373^\circ\text{C}$ , which may be due to the removal of water molecules from the carbonate lattice and the phase transformation of aragonite to calcite due to its unstable nature, as described previously. The phase transition of aragonite to calcite in coral and other marine shells occurs at a lower temperature than that of the phase transition in aragonite of mineral origin [26]. Second, a rapid weight loss of 41.88% and endothermic behaviour from  $600$  to  $800^\circ\text{C}$  were observed in both samples; in this temperature range, volatile minerals in the sample began to decompose, thereby releasing  $\text{CO}_2$ . For the cockle shell powder, the rate of decomposition was slower compared with that of the nanocrystals, as shown in Figure 6(a); this result has been reported in the literature, whereby particles of smaller size decompose faster than larger particles [5] because smaller-sized particles have a greater surface area than larger particles. However, both samples remained unchanged when the temperature reached  $900^\circ\text{C}$ . This result indicates the total decomposition of calcium carbonate to  $\text{CaO}$  and signifies the release of  $\text{CO}_2$  from calcium carbonate, leaving only the product, that is, "ash" [5]. This assumption

derived from the TGA analysis is also supported by the XRD data shown in Figure 5.

#### 4. Conclusions

Cockle shells consist of a higher percentage of calcium carbonate aragonite polymorphs, as described in the introduction of this paper. On the basis of the analysis of calcium carbonate nanocrystals from the cockle shell powder and that of the powder itself, the shells are composed of the aragonite form of calcium carbonate, which is less stable and denser than calcite. These properties make it a potential biomaterial for medical applications. The thermogravimetric analyses of the two samples revealed the solid-state phase transformation of aragonite to calcite. The transformation of aragonite began at approximately at 300–373°C and at 600–700°C; the complete removal of volatile substances occurred, and the phase transformation of aragonite to calcite was completed with a loss of 41% of the initial weight of the sample. These results also demonstrate that smaller particles decompose faster than larger particles within a short time at low temperatures.

The methods adopted and the nonionic surfactant used in the synthesis of aragonite nanocrystals are environmentally friendly and could be scaled up for industrial production, thereby permitting a greener synthesis from naturally available materials and utilising the waste shells that are a by-product of the seafood industry. This method thus offers a great opportunity for exploitation in numerous industrial applications.

#### Conflict of Interests

The authors would like to confirm that there is no conflicts of interests associated with this paper submitted for publication, and there has been no significant financial support for this work that could have affected its outcome. The authors confirm that the paper has been read and approved by all named authors and that there are no other persons who satisfy the criteria for authorship but who are not listed. The authors further confirm that the order of authors listed in the paper has been approved by all of the authors. The authors confirm that they have given due consideration to the protection of intellectual property associated with this work and that there are no impediments to publication, including the timing of publication, with respect to intellectual property. In so doing, The authors confirm that they have followed the regulations of their institutions concerning intellectual property.

#### References

- [1] A. Xu, Y. Ma, and H. Colfen, "Biomimetic mineralization," *Journal of Material Chemistry*, vol. 17, pp. 415–449, 2006.
- [2] Y. Fukui and K. Fujimoto, "Bioinspired nanoreactor based on miniemulsion system to create organic-inorganic hybrid nanoparticle and nanofilm," *Journal of Material Chemistry*, vol. 22, no. 8, pp. 3493–3499, 2012.
- [3] Q. L. Feng, G. Pu, Y. Pei, F. Z. Cui, H. D. Li, and T. N. Kim, "Polymorph and morphology of calcium carbonate crystals induced by proteins extracted from mollusk shell," *Journal of Crystal Growth*, vol. 216, no. 1, pp. 459–465, 2000.
- [4] R. Velázquez-Castillo, V. Reyes-Gasga, D. I. García-Gutierrez, and M. Jose-Yacaman, "Nanoscale characterization of nautilus shell structure: an example of natural self-assembly," *Journal of Materials Research*, vol. 21, no. 6, pp. 1484–1489, 2006.
- [5] M. Mohamed, S. Yusup, and S. Maitra, "Decomposition study of calcium carbonate in cockle shells," *Journal of Engineering Science and Technology*, vol. 7, no. 1, pp. 1–10, 2012.
- [6] A. J. Awang-Hazmi, A. B. Z. Zuki, M. M. Nordin, A. Jalila, and Y. Norimah, "Mineral composition of the cockle (*Anadara Granosa*) shells of west coast of peninsular Malaysia and its potential as biomaterial for use in bone repair," *Journal of Animal and Veterinary Advances*, vol. 6, no. 5, pp. 591–594, 2007.
- [7] Y. Guowei., L. Wang, and H. Jianhua, "The crystallization behavior of calcium carbonate in ethanol/water solution containing mixed nonionic/anionic surfactants," *Powder Technology*, vol. 192, no. 1, pp. 58–64, 2009.
- [8] R. Gupter, *Synthesis of Precipitated Calcium Carbonate Nanoparticles Using Modified Emulsion Membranes [M.S. thesis]*, Georgia Institute of Technology, Atlanta, Ga, USA, 2004.
- [9] G. X. Wu, J. Ding, and J. M. Xue, "Synthesis of calcium carbonate capsules in water-in-oil-in-water double emulsions," *Journal of Materials Research*, vol. 23, no. 1, pp. 140–149, 2008.
- [10] T. A. Hassan, V. K. Rangari, V. Fallon, Y. Farooq, and S. Jeelani, "Mechanochemical and sonochemical synthesis of bio-based nanoparticles," in *Proceedings of the Nanotechnology Conference*, pp. 278–281, June 2010.
- [11] A. Georgieva, B. Georgieva, Z. Bogdanov, and D. K. Stefanov, "Microemulsion water-in-oil (W/O)—microreactor for synthesis of ultrafine carbonate nanostructures," *University of Ruse Union of Scientists-Ruse*, vol. 50, no. 9, pp. 34–38, 2011.
- [12] R. Babou-Kammoe, S. Hamoudi, F. Larachi, and K. Belkacemi, "Synthesis of calcium carbonate nanoparticles by controlled precipitation of saturated carbonated and calcium Nitrate aqueous solution," *The Canadian Journal of Chemical Engineering*, vol. 90, pp. 26–33, 2012.
- [13] Y. H. Cho, S. Kim, E. K. Bae, C. K. Mok, and J. Park, "Formulation of a cosurfactant-free O/W microemulsion using nonionic surfactant mixtures," *Journal of Food Science*, vol. 73, no. 3, pp. E115–E121, 2008.
- [14] S. Talegaonkar, A. Azeem, F. J. Ahmad, R. K. Khar, S. A. Pathan, and Z. I. Khan, "Microemulsions: a novel approach to enhanced drug delivery," *Recent Patents on Drug Delivery and Formulation*, vol. 2, no. 3, pp. 238–257, 2008.
- [15] K. C. Song and J. H. Kim, "Synthesis of high surface area tin oxide powders via water-in-oil microemulsions," *Powder Technology*, vol. 107, no. 3, pp. 268–272, 2000.
- [16] C. Karagiozov and D. Momchilova, "Synthesis of nano-sized particles from metal carbonates by the method of reversed mycelles," *Chemical Engineering and Processing*, vol. 44, no. 1, pp. 115–119, 2005.
- [17] GEA.Niro-Soavi, "Laboratory Manual for Higher pressure Homogenizer," 2011, <http://www.nirosoavi.com/index.asp>.
- [18] N. Islam, Z. B. A. Bakar, M. M. Noordin, M. Z. B. Hussain, N. S. B. A. Rahman, and E. Ali, "Characterisation of calcium carbonate and its polymorphs from cockle shells (*Anadara granosa*)," *Powder Technology*, vol. 213, no. 1–3, pp. 188–191, 2011.
- [19] K. Mitri, R. Shegokar, S. Gohla, C. Anselmi, and R. H. Müller, "Lutein nanocrystal as antioxidant formulation for oral and

- dermal delivery," *International Journal of Pharmaceutics*, vol. 420, pp. 141–146, 2011.
- [20] R. Shegokar and R. H. Müller, "Nanocrystals: industrially feasible multifunctional formulation technology for poorly soluble actives," *International Journal of Pharmaceutics*, vol. 399, no. 1-2, pp. 129–139, 2010.
- [21] B. Cheng, M. Lei, J. Yu, and X. Zhao, "Preparation of monodispersed cubic calcium carbonate particles via precipitation reaction," *Materials Letters*, vol. 58, no. 10, pp. 1565–1570, 2004.
- [22] Y. Dong, Y. Chu, L. Dong, and Z. Yu-jiang, "Controllable synthesis of CaCO<sub>3</sub> micro/nanocrystals with different morphologies in microemulsion," *Chemical Journal of Chinese Universities*, vol. 26, no. 5, pp. 678–682, 2010.
- [23] A. Szcześ, "Influence of the surfactant nature on the calcium carbonate synthesis in water-in-oil emulsion," *Journal of Crystal Growth*, vol. 311, no. 4, pp. 1129–1135, 2009.
- [24] Y. Tang, B. Du, L. Li, J. Yang, and Y. Zhang, "Effects of Tx-100-SDS on crystal growth of calcium carbonate in reverse microemulsion solution," *Chinese Science Bulletin*, vol. 52, no. 1, pp. 78–83, 2007.
- [25] Y. Wang, Y. X. Moo, C. Chen, P. Gunawan, and R. Xu, "Fast precipitation of uniform CaCO<sub>3</sub> nanospheres and their transformation to hollow hydroxyapatite nanospheres," *Journal of Colloid and Interface Science*, vol. 352, no. 2, pp. 393–400, 2010.
- [26] C. Linga Raju, K. V. Narasimhulu, N. O. Gopal, J. L. Rao, and B. C. V. Reddy, "Electron paramagnetic resonance, optical and infrared spectral studies on the marine mussel *Arca burnesi* shells," *Journal of Molecular Structure*, vol. 608, no. 2-3, pp. 201–211, 2002.
- [27] B. Cheng, W. Cai, and J. Yu, "DNA-mediated morphosynthesis of calcium carbonate particles," *Journal of Colloid and Interface Science*, vol. 352, no. 1, pp. 43–49, 2010.
- [28] V. Vongsavat, P. Winotai, and S. Meejoo, "Phase transitions of natural corals monitored by ESR spectroscopy," *Nuclear Instruments and Methods in Physics Research B*, vol. 243, no. 1, pp. 167–173, 2006.
- [29] Y. Hu, Y. Ma, Y. Zhou, F. Nie, X. Duan, and C. Pei, "Hen eggwhite-mediated stack crystallization of calcium carbonate," *Journal of Crystal Growth*, vol. 312, no. 6, pp. 831–836, 2010.
- [30] C. A. Korash, "Mechanical properties of a Nanostructure Poly (KAMPS)/Aragonite composite," in *Mechanic of Biological System and Materials. Volume 2*, Conference proceedings of the society for experimental mechanic series, pp. 131–136, 2011.
- [31] *Powder Diffraction File-4 Release*, International Centre for Diffraction Data (ICDD), Newton square, Pa, USA, 2012.
- [32] J. Yu, H. Guo, S. A. Davis, and S. Mann, "Fabrication of hollow inorganic microspheres by chemically induced self-transformation," *Advanced Functional Materials*, vol. 16, no. 15, pp. 2035–2041, 2006.

## Research Article

# Improved Processing of Carbon Nanotube Yarn

Chaminda Jayasinghe,<sup>1</sup> Trent Amstutz,<sup>1</sup> Mark J. Schulz,<sup>2</sup> and Vesselin Shanov<sup>1</sup>

<sup>1</sup> Department of Chemical and Material Science Engineering, University of Cincinnati, Cincinnati, OH 45221-0012, USA

<sup>2</sup> Department of Mechanical Engineering, University of Cincinnati, Cincinnati, OH 45221-0072, USA

Correspondence should be addressed to Vesselin Shanov; [Vesselin.Shanov@uc.edu](mailto:Vesselin.Shanov@uc.edu)

Received 22 October 2012; Accepted 10 March 2013

Academic Editor: Qian-Ming Gong

Copyright © 2013 Chaminda Jayasinghe et al. This is an open access article distributed under the Creative Commons Attribution License, which permits unrestricted use, distribution, and reproduction in any medium, provided the original work is properly cited.

We compared mechanical and electrical properties of carbon nanotube (CNT) yarns formed from four different spinning methods. In these methods, a yarn was spun from two aligned CNT arrays. CNT yarns fabricated from each method were tested quantitatively through the mechanical and electrical properties and reported. This improvement is considered to be caused by multiple factors, such as reduction of the yarn diameter, densification, water evaporation, and CNT orientation. The best electrical and mechanical property of CNT yarn was observed from the fourth spinning method where heating and tension during spinning were applied. The introduced yarn spinning methods are appropriate for continuous mass production of high strength carbon nanotube yarns with controlled diameter, strength, and electrical conductivity.

## 1. Introduction

Carbon nanotubes (CNTs) are considered one of the strongest and stiffest materials known. They have unique atomic structure with interesting related properties such as high tensile strength and Young's modulus, high aspect ratio, and good electrical and thermal conductivities. These unique properties open up various applications in different areas, for example, in advance electronics, biotechnology, and nanomechanics.

Research efforts have been carried out to fabricate macroscopic threads and yarn structures to make the use of the CNTs unique properties. However there are technical challenges to transfer individual CNT properties into spun yarn structures because CNT bundles tend to slide in yarn microstructures. Therefore may be promising techniques have been implemented to improve the strength of the CNT yarn. One practical application is polymer dip coating which will improve the mechanical properties of CNT yarns structures but it will not help to improve the electrical properties of the yarn. Other is high temperature annealing which will help to improve the electrical and thermal properties of the CNT yarn. However, the disadvantage of thermal annealing is high cost and brittle behavior of the yarn structures.

There are mainly two methods of CNT yarn production: liquid-state spinning and solid-state spinning. Most synthetic fibers are created from a concentrated, viscous liquid. In liquid based spinning, CNTs are dispersed into fluids and either extruded or coagulation spun into fibers [1–3]. The major issue with applying this approach to CNTs is that there is a relatively high fraction of remaining polymer and using of short CNTs, which limits the overall strength and electrical and thermal conductivity of the produced fiber [4]. The solid-state spinning can be done in two methods. One is spinning CNT yarns directly from a furnace using floating catalyst [5]. The second method is substrate base spinning. Spinning directly from a furnace is a very efficient approach for continuous production of yarn that has good properties [6, 7]. Limitations of this method are the nanotubes used relatively short and there are catalyst impurities deposited in the final product.

Cotton and wool are naturally made fibers that are made by solid-state spinning. In solid state spinning, CNTs are assembled into either yarns or sheets without the use of any chemical additives. This process is practiced by a handful of research groups [2, 5, 8–11]. The posttreatment methods play an important role to improve the properties of CNTs. Zhang et al. showed substantial increase in the strength of

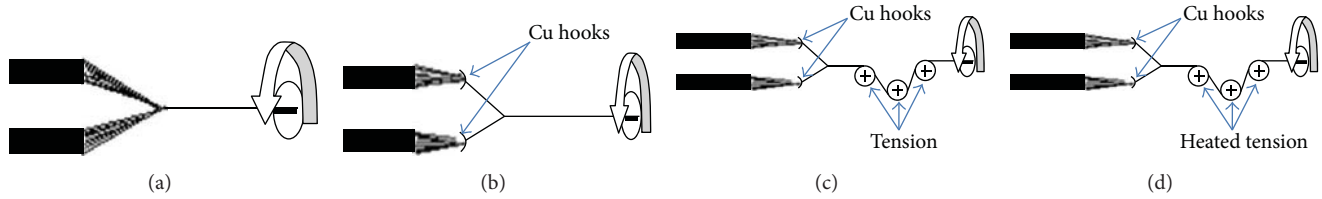


FIGURE 1: Schematic of the four different spinning methods (Methods 1 to 4) illustrated in the schematic corresponding to figures (a) to (d).

the CNT threads after infiltration with a polymer [10]. Zhu et al. reported that CNT yarn load capacity can be improved by postspun twisting which is affected by two factors: bringing the CNTs into closer contact with one another and therefore enhancing the van der Waals forces and higher radial compressive stress [5]. Other posttreatments involve densification with organic solvents such as ethanol and acetone, or heating the thread at high temperatures by applying an electric current [12]. Those posttreatment techniques require extra processing time [13–15]. In this paper, four improved methods for spinning CNT yarns are presented. The mechanical and electrical properties of CNT yarns made by each method are compared.

## 2. Experimental Procedure

We introduce four comparative methods of CNT yarn spinning. Spinnable carbon nanotube arrays were grown on silicon wafers using Chemical Vapor Deposition (CVD) at 750°C for 30 minutes [16]. CNT arrays about 325  $\mu\text{m}$  in height were spun into yarns at about a 2000 rpm twisting rate and a 324 mm/minute pulling speed.

Based on Method 1 (spinning yarn from two CNT arrays), two CNT forests were drawn out forming two ribbons which were directly spun into a two-ply thread without any further treatment (Figure 1(a)). This spinning technique has been used by several other groups [2, 5, 8–11] and served in our experiments as a reference (baseline) to which all the other techniques were compared in the present work. Method 2 (two arrays with copper hooks) was designed to employ two copper hooks which applied small tension force to the ribbons prior to spinning (Figure 1(b)). This arrangement forced the ribbons to condense and spin into low tension threads before they were combined into the final thread. Method 3 (two arrays with copper hooks and tension rods) improves the second method by using the same hook system but also implementing several tensioning rods along the spun yarn (Figure 1(c)). The rods applied tension to the thread in order to increase the interactions between the CNTs and to enhance the van der Waals forces between the individual carbon nanotubes. The intention of this arrangement was to increase the strength and decrease the resistivity of the thread. Method 4 (two arrays with copper hooks and heated tension rods) is a modification of the third one, where the tensioning rods were modified to heat the thread simultaneously while applying tension (Figure 1(d)). This the method we call heating and tension spinning (HTS).

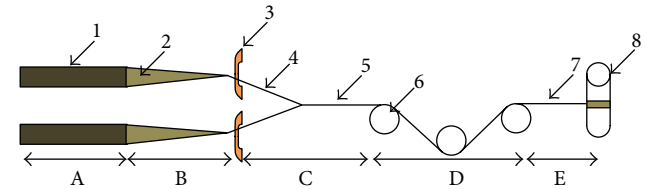


FIGURE 2: Schematic of the setup used in the proposed improved spinning process: A: CNT forest; B: web formation zone; C: partially twisted thread and yarn formation zone; D: tension and heat zone; E: twisting zone; (1) spinnable CNT forest; (2) CNT web; (3) copper hook; (4) partially twisted thread; (5) low twisted yarn; (6) heated rod for applying tension; (7) high twisted yarn; (8) spool.

The produced yarns were collected on spools. The samples were tested to determine their electrical resistivity and ultimate tensile strengths. Scanning electron microscopy (SEM) was used to measure the diameters of the tested yarns. The tensile strength measurement was conducted with a 3345-Instron stress-strain instrument. A four-probe setup was employed to determine the electrical properties of the yarn using a Keithley 6220 current source and a 2182A nanovoltmeter. All the tests were conducted multiple times to verify consistency of the acquired data.

## 3. Results and Discussion

**3.1. Production of Carbon Nanotube Yarn.** Currently, dry spinning of CNTs is conducted by twisting the formed web while pulling CNTs from a single substrate [2, 5, 8–11]. This process can be improved by introducing different spinning techniques. Recently, Hu et al. tested a modified spinning process attempting to improve the mechanical properties of CNT yarns [17]. They formed CNT threads under tension spinning in a high volume heated environment. Here we introduced resistive heating tension rods which can be used as tension rods as well as heat sources. Therefore the process is really simple and cost effective. This paper also provides a detailed characterization and explanation of the improved spinning process. Figure 2 shows the main components of the improved spinning setup. The main steps in the process for spinning thread are described next.

**3.1.1. Web Formation.** CNTs initially pulled from the forest form a web. As the CNT bundles are pulled away from the forest they form a long “line” in which all the CNT centerlines are

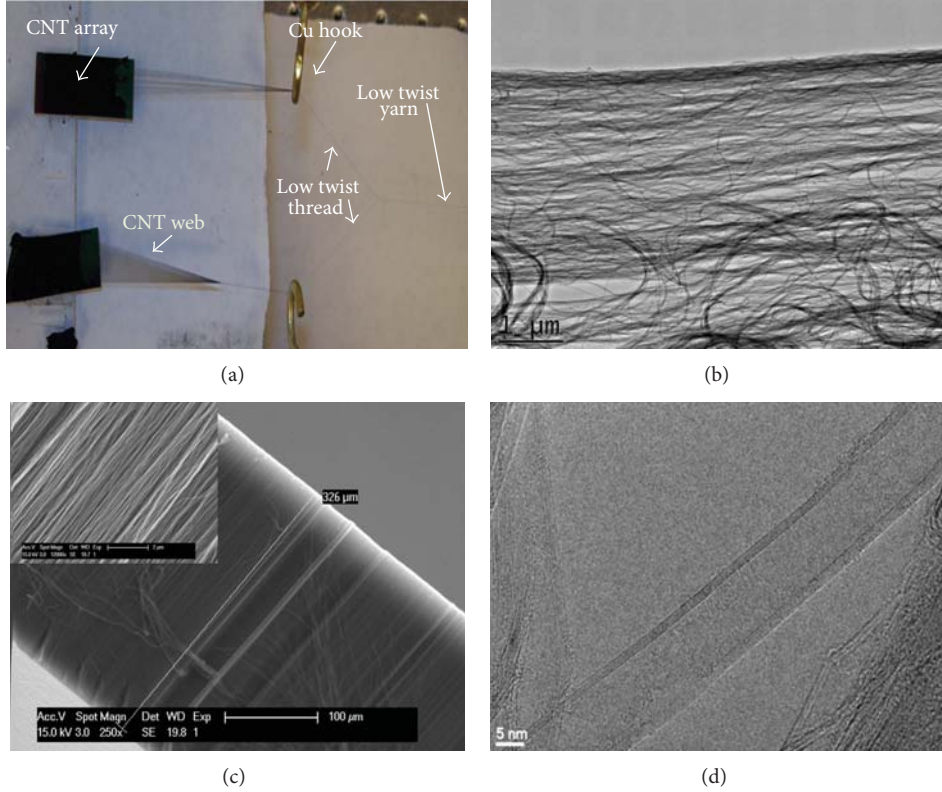


FIGURE 3: (a) Two CNT arrays spun into a yarn using the improved spinning method, (b) TEM image of CNT web, (c) SEM image of aligned CNT array (inset shows the forest cross-section at high magnification) and (d) HRTEM image of individual CNT with diameter  $\sim 15$  nm.

aligned and parallel. The CNT web is orthogonal to the initial nanotube direction in the array and parallel to the substrate surface. The web must be kept stable during the spinning process in order to yield well-formed yarn. As shown in Figure 3(a), smooth copper hooks are placed between the first tension rod and the substrates. This improves the contact between the loosely attached CNT bundles within the web. The portion between the CNT forest and the copper hooks is the CNT web, and just after the copper hook it is transformed into a low twist thread. During the spinning process, those low twisted threads are combined to form one yarn. The joining point is called the convergence point. The convergence point is located before the first tension rod. The portion of the yarn shown in Figure 2 at position 5 is called low twisted yarn. In general, the web is “fluffy” and for this reason it needs to be compacted before spinning. Transmission electron microscopy (TEM) images show that the CNT web consists of poorly aligned and randomly orientated CNT bundles (Figure 3(b)). The thickness of the web ranges from 50 nm to 100 nm. According to the capstan equation from the rope theory, when yarn passes through a pulley, the change in tension and the corresponding radial pressure on the yarn can be written as follows [17, 18]:

$$\frac{T_2}{T_1} = e^{\mu\varphi}, \quad (1)$$

$$N_1 = \frac{T_2}{\mu} (e^{\mu\varphi} - 1), \quad (2)$$

where  $T_1$ ,  $T_2$ ,  $\mu$ ,  $\varphi$ , and  $N_1$  are the low incoming tension and high outgoing tension, the frictional coefficient, the contact angle, and the radial pressure on the yarn, respectively.

**3.1.2. Thread Formed under Tension.** Figure 4 illustrates the arrangement of two copper hooks which apply a small initial tension force to the ribbons prior to the spinning. This force helps the ribbons to condense and spin together slightly before they combine into partially twisted yarn. This part of the fiber is called “low twisted yarn.” When the CNT web passes through the copper hooks, tension increases according to the capstan equation (1). This tension causes convergence of the web which is observed at a point close to the copper hooks. Further, Figure 4 displays the system using spinning under tension, where  $T_w$ ,  $T_1$ ,  $T_5$ ,  $\Omega_1$ , and  $\Omega_5$  are the web tension (incoming and outgoing after copper hook), final tension (near the CNT yarn winding spool), twisting of pre-formed thread, and twisting of final yarn, respectively. As the yarn passes through different stages, it is subjected to gradually increasing tension. The magnitude of the tension for a 3-tension rod arrangement increases accordingly:  $T_w < T_1 < T_2 < T_3 < T_4 < T_5 < T_3 < T_4 < T_5$ . Thus, for the tested spinning system, the change in tension after the last tension rod ( $T_5$ ) and the corresponding final radial pressure ( $N_5$ ) on the yarn is given by the following two equations, respectively:

$$\begin{aligned} T_5 &= 2 \cos \theta T_1 e^{\mu \sum_{i=1}^n \theta_i}, \\ N_5 &= \frac{T_5}{\mu} (e^{\mu\varphi_i} - 1), \end{aligned} \quad (3)$$

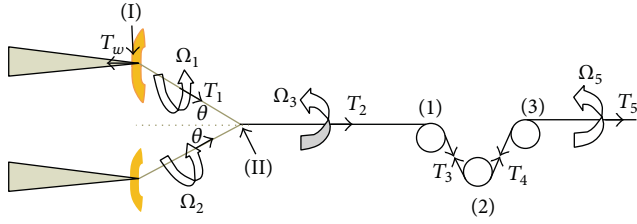


FIGURE 4: Schematic of heating and tension spinning system (HTS) with incorporated tension rods showing related process parameters:  $T_w$ ,  $T_1$ ,  $T_5$ ,  $\Omega_1$ , and  $\Omega_5$  denoted as the web tension (incoming and outgoing after copper hook), final tension (near the CNT yarn winding spool), twisting of pre-formed thread and twisting of final yarn respectively.

where  $\theta$  is the angle between partially twisted thread and the initially formed yarn at the convergent point (near II). Lastly, Figure 4 illustrates various stages in yarn formation leading to the final tension. Alignment and slip occur at the copper hooks, where tension is first applied to the thread. This causes increased CNT interaction in the bundles and yarn. Higher alignment of the CNTs and bundles results in more compact yarn. Therefore, the net effect of the multistage system is to increase the mechanical and electrical properties of the CNT yarn. However, we have observed after a certain maximum tension, further increase in this parameter leads to decreased yarn strength.

**3.2. Twisting and Heating Effect on Yarn Formation.** For short bundles of CNT drawn from the forest, in the absence of twisting action applied to the yarn, the strength of yarn is limited because of absence of significant transverse forces to bind the CNT assembly together [5]. In order to achieve higher mechanical and electrical properties, the CNTs and bundles need to have maximum contact with one another. This makes twisting a very important part in spinning CNT yarns. At low twist, there is considerable cohesion between the CNTs that can provide reasonable strength to the web. As twisting increases, cohesion also increases, and at a very high level of twisting, brittle behavior is observed [19]. The variation in diameter of CNT yarn is shown in Figures 5(a) to 5(d) at different stages (I to IV) of the HTS process. The SEM images indicate that the diameter of the yarn suddenly decreased as it passed through stage I to stage II (from  $14.2 \mu\text{m}$  to  $12.1 \mu\text{m}$ ) and then stage II to stage III ( $12.1 \mu\text{m}$  to  $10.9 \mu\text{m}$ ) and remained relatively unchanged afterwards. It was observed from the SEM images (Figures 5(a) to 5(c)) that the twisting angle of the fibers gradually increased with the yarn passing through the stages. We have observed when both heating and tension are applied the diameters of the CNT yarn decreased by about 23% from  $14$  to  $10.3 \mu\text{m}$  (see Figures 5(a) and 5(d)). SEM images demonstrated that the HTS technique improved the uniformity along the CNT yarn (Figure 5(d)). This technique provides two benefits. First, it increases the alignment of the carbon nanotubes in the thread and also the interbundle lateral cohesion. Second, it reduces the intertube distance and increases the van der Waals force interaction between all the CNTs. Figure 5(e) illustrated the schematic of different

positions of heating and tension spinning (HTS) stages are illustrated in Figure 5(f). Raman spectroscopy performed on both CNT yarn formed from treatment 1 and treatment 4 (see Figure 5(f)) do not show important differences that can be readily related to morphological differences in the CNTs for different treatments.

Figure 6(a) shows the resistivity (left  $y$ -axis) and strength (right  $y$ -axis) as a function of the tested four different methods of spinning. Substantial improvements in both the electrical and mechanical properties of the threads occurred when applying these methods. Method 4 was carried out using an HTS system temperature of about  $225^\circ\text{C}$ . Figure 6(b) shows that the strength and electrical conductivity of CNT yarn improve 61% and 71%, respectively, when employing Method 4 as opposed to the Method 1. Method 1 is state of art of spinning yarn which is practiced by most of the research groups [8] and is used in this study as a baseline for comparison. Spinning under tension brings the CNTs in closer contact to each other and therefore enhances the van der Waal interactions. The later causes increased friction between the CNTs, which improves the load transfer between the tubes.

The experimental results showed that treatments 2–4 brought improvement in the mechanical and electrical properties of the CNT yarns relative to treatment 1. The highest percentage improvement compared to the baseline treatment 1 was observed for treatments 3 and 4. This effect is obviously due to applying tension during spinning. However we also noticed that there is a considerable improvement of CNT yarn in treatment 4 compared to treatment 3. Figures 5(c) and 5(d) display SEM images of CNT yarns formed from treatment 3 and Method 4. Treatment 4 utilized three tension rods preheated up to  $225^\circ\text{C}$ . It shows that the diameter of the CNT yarn formed from treatment 4 decreases from  $10.9$  to  $10.2 \mu\text{m}$ . We assume that the applied simultaneous heating and tension during spinning improve the thread structure by stretching the CNT bundles and enabling more effective thread compactions.

Another interpretation of the results is based on the hypothesis of collapsing the CNTs under tension, which may be enhanced by the applied heating. It was observed by Motta et al. that double walled tubes in yarn corresponding to diameters larger than  $\sim 5 \text{ nm}$  collapse into structures with dog-bone cross-sections thus forming stacks of parallel graphene layers [7]. The applied tension and radial force change the microscopic structure of the CNTs which tend to polygonize from circular to hexagonal shape.

In the experiments, the mechanical and electrical properties of the CNT yarns substantially improved. This could be due to two reasons. The first reason is the applied heat may have caused evaporation of the absorbed water molecules within the CNT bundles thus increasing the friction and decreasing the air gaps between them. The second is associated with the possible CNT collapse due to the radial pressure incurred from the HTS action. In this scenario stacks of flattened nanotubes can share maximum contact area which will cause increased yarn cohesion. The nanotubes used in this study are double walled with diameters in the range of  $8$  to  $12 \text{ nm}$  which qualifies them for collapsing according to

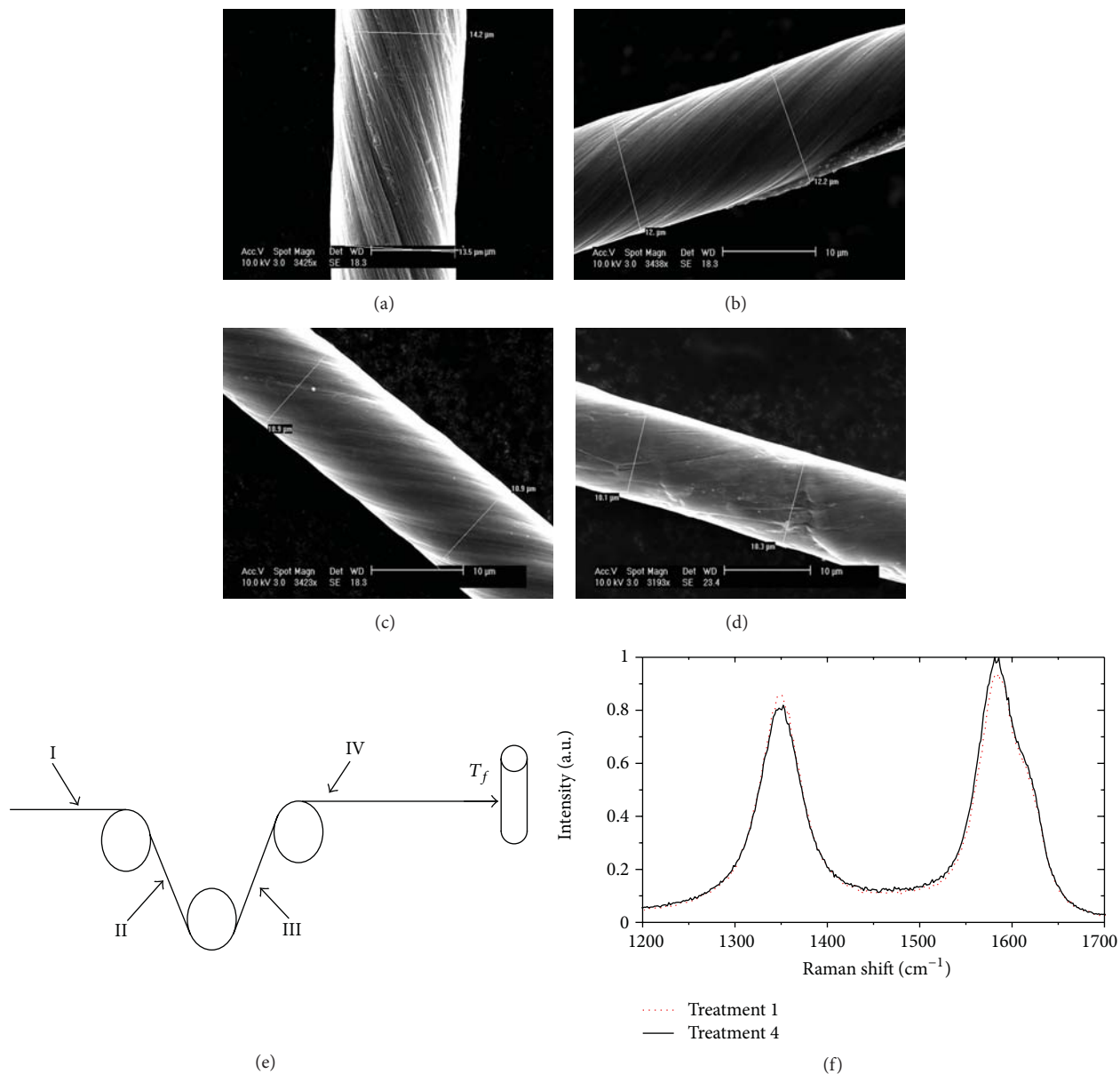


FIGURE 5: SEM images of CNT yarn at different stages of the spinning process. Stage I (a), Stage II (b), Stage III (c), and Stage IV (d), schematic of the applied heating and tension spinning (HTS) stages (e). I-denotes the position before 1st applied tension; II before 2nd tension; III before 3rd tension; IV before winding on the spool; Raman spectra of CNT yarn formed from treatment 1 and treatment 4(f).

[17]. Thorough High Resolution TEM studies of the CNT yarn may be able to confirm such a phenomenon.

#### 4. Conclusions

This work introduced new and improved methods for dry spinning of CNT yarns, which helped to positively affect the yarn structure by stretching the CNT bundles and enabling more effective yarn compaction. The preliminary results for spinning CNT yarn under tension showed an improvement of the fiber mechanical and electrical properties with respect to a standard spinning method used as a baseline. Further

enhancement of the CNT yarn quality was observed by introducing a heating and tension spinning (HTS) technique. The tensile strength of the spun yarn when employing HTS improved about 61% and the electrical conductivity increased by ~71%. Optimization of the new spinning techniques has not been fully achieved and will require further studies to understand the entire temperature and tension effect on the quality of HTS spun yarns. Further optimization of the spinning parameters employing the HTS environment is required, since the results obtained are promising for manufacturing high performance CNT-based yarns. Such experiments are in progress and will be reported in the near future.

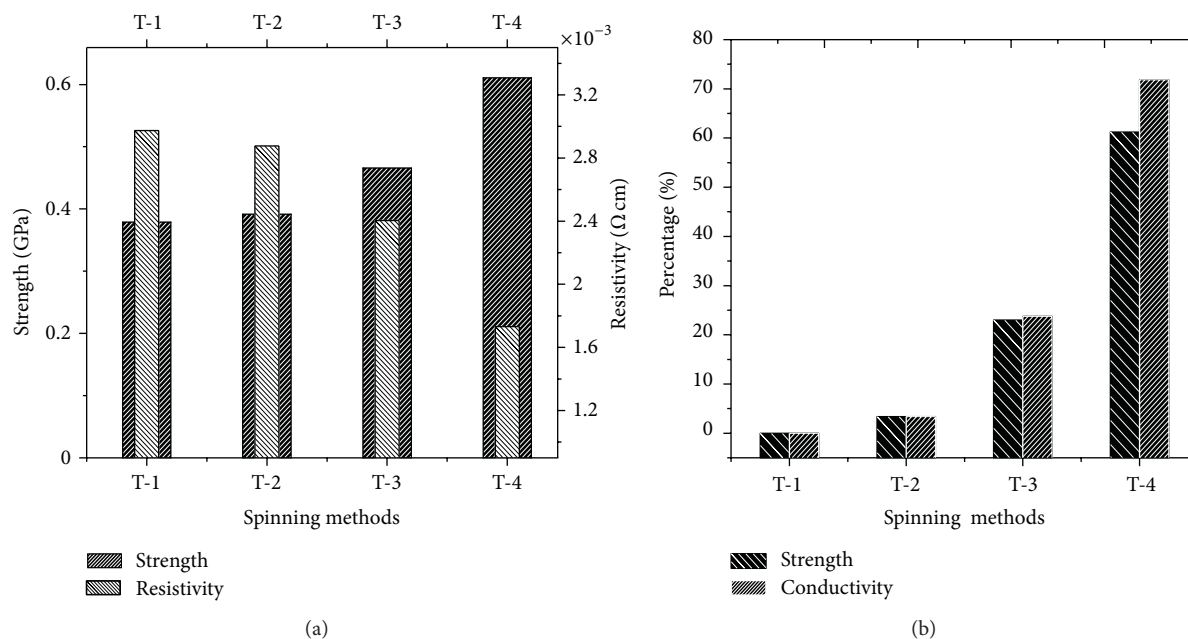


FIGURE 6: (a) Stress (left  $y$ -axis) and resistivity (right  $y$ -axis) versus spinning methods, (b) strength and electrical conductivity improvement in percentage versus spinning methods.

## Supporting Data

See Movie 1 in supplementary material available online at <http://dx.doi.org/10.1155/2013/309617>.

## Acknowledgments

The authors would like to acknowledge Dr. Sergey Yarmolenko and Svetlana Fialkova from North Carolina A&T State University for providing instrumentation to test the mechanical properties of the CNT threads and Mr. Doug Hurd for helping to design and manufacture the spinning machine. The financial support from NSF through Grant CMMI-07272500 program officer Dr. Haris Domanidis and from NCA&T through the ONR is highly appreciated.

## References

- [1] L. M. Ericson, H. Fan, H. Peng et al., "Macroscopic, neat, single-walled carbon nanotube fibers," *Science*, vol. 305, no. 5689, pp. 1447–1450, 2004.
- [2] M. E. Kozlov, R. C. Capps, W. M. Sampson, H. Von Ebron, J. P. Ferraris, and R. H. Baughman, "Spinning solid and hollow polymer-free carbon nanotube fibers," *Advanced Materials*, vol. 17, no. 5, pp. 614–617, 2005.
- [3] B. Vigolo, A. Penicaud, C. Coulon et al., "Macroscopic fibers and ribbons of oriented carbon nanotubes," *Science*, vol. 290, no. 5495, pp. 1331–1334, 2000.
- [4] X. Zhang, Q. Li, Y. Tu et al., "Strong carbon-nanotube fibers spun from long carbon-nanotube arrays," *Small*, vol. 3, no. 2, pp. 244–248, 2007.
- [5] H. W. Zhu, C. L. Xu, D. H. Wu, B. Q. Wei, R. Vajtai, and P. M. Ajayan, "Direct synthesis of long single-walled carbon nanotube strands," *Science*, vol. 296, no. 5569, pp. 884–886, 2002.
- [6] M. Motta, A. Moiala, I. A. Kinloch, and A. H. Windle, "High performance fibres from "dog bone" carbon nanotubes," *Advanced Materials*, vol. 19, no. 21, pp. 3721–3726, 2007.
- [7] M. Motta, Y. L. Li, I. Kinloch, and A. Windle, "Mechanical properties of continuously spun fibers of carbon nanotubes," *Nano Letters*, vol. 5, no. 8, pp. 1529–1533, 2005.
- [8] R. H. Baughman, A. A. Zakhidov, and W. A. De Heer, "Carbon nanotubes—the route toward applications," *Science*, vol. 297, no. 5582, pp. 787–792, 2002.
- [9] K. Koziol, J. Vilatela, A. Moiala et al., "High-performance carbon nanotube fiber," *Science*, vol. 318, no. 5858, pp. 1892–1895, 2007.
- [10] M. Zhang, K. R. Atkinson, and R. H. Baughman, "Multi-functional carbon nanotube yarns by downsizing an ancient technology," *Science*, vol. 306, no. 5700, pp. 1358–1361, 2004.
- [11] Q. Li, X. Zhang, R. F. DePaula et al., "Sustained growth of ultralong carbon nanotube arrays for fiber spinning," *Advanced Materials*, vol. 18, no. 23, pp. 3160–3163, 2006.
- [12] X. Zhang, Q. Li, T. G. Holesinger et al., "Ultrastrong, stiff, and lightweight carbon-nanotube fibers," *Advanced Materials*, vol. 19, no. 23, pp. 4198–4201, 2007.
- [13] C. Feng, K. Liu, J. S. Wu et al., "Flexible, stretchable, transparent conducting films made from superaligned carbon nanotubes," *Advanced Functional Materials*, vol. 20, no. 6, pp. 885–891, 2010.
- [14] M. Naraghi, T. Filleter, A. Moravsky, M. Locascio, R. O. Loutfy, and H. D. Espinosa, "A multiscale study of high performance double-walled nanotube-polymer fibers," *ACS Nano*, vol. 4, no. 11, pp. 6463–6476, 2010.
- [15] S. Fang, M. Zhang, A. A. Zakhidov, and R. H. Baughman, "Structure and process-dependent properties of solid-state spun carbon nanotube yarns," *Journal of Physics Condensed Matter*, vol. 22, no. 33, Article ID 334221, 2010.
- [16] C. Jayasinghe, S. Chakrabarti, M. J. Schulz, and V. Shanov, "Spinning yarn from long carbon nanotube arrays," *Journal of Materials Research*, vol. 26, pp. 1–7, 2011.

- [17] L. Hu, D. S. Hecht, and G. Grüner, "Infrared transparent carbon nanotube thin films," *Applied Physics Letters*, vol. 94, no. 8, Article ID 081103, 2009.
- [18] J. H. Jung, T. J. Kang, and J. R. Youn, "Effect of bending rigidity on the capstan equation," *Textile Research Journal*, vol. 74, no. 12, pp. 1085–1096, 2004.
- [19] S. Hutton, C. Skourtis, and K. Atkinson, "Tensile and electrical properties of carbon nanotube yarns and knitted tubes in pure or composite form," *International Journal of Technology Transfer and Commercialisation*, vol. 7, no. 2-3, pp. 258–264, 2008.

## Research Article

# A Comparative Study of Three Different Chemical Vapor Deposition Techniques of Carbon Nanotube Growth on Diamond Films

Betty T. Quinton,<sup>1,2</sup> Paul N. Barnes,<sup>3</sup> Chakrapani V. Varanasi,<sup>4</sup> Jack Burke,<sup>5</sup>  
Bang-Hung Tsao,<sup>5</sup> Kevin J. Yost,<sup>1</sup> and Sharmila M. Mukhopadhyay<sup>2</sup>

<sup>1</sup> Air Force Research Laboratory (AFRL), Wright-Patterson, Air Force Base, OH 45433, USA

<sup>2</sup> Wright State University, Dayton, OH 45420, USA

<sup>3</sup> Army Research Laboratory, Adelphi, MD 20783, USA

<sup>4</sup> Army Research Office, Research Triangle Park, NC 27709, USA

<sup>5</sup> University of Dayton Research Institute (UDRI), Dayton, OH 45469, USA

Correspondence should be addressed to Betty T. Quinton; [bettyyanguic@gmail.com](mailto:bettyyanguic@gmail.com)

Received 28 November 2012; Accepted 17 February 2013

Academic Editor: Lijun Ji

Copyright © 2013 Betty T. Quinton et al. This is an open access article distributed under the Creative Commons Attribution License, which permits unrestricted use, distribution, and reproduction in any medium, provided the original work is properly cited.

This paper compares between the methods of growing carbon nanotubes (CNTs) on diamond substrates and evaluates the quality of the CNTs and the interfacial strength. One potential application for these materials is a heat sink/spreader for high-power electronic devices. The CNTs and diamond substrates have a significantly higher specific thermal conductivity than traditional heat sink/spreader materials making them good replacement candidates. Only limited research has been performed on these CNT/diamond structures and their suitability of different growth methods. This study investigates three potential chemical vapor deposition (CVD) techniques for growing CNTs on diamond: thermal CVD (T-CVD), microwave plasma-enhanced CVD (MPE-CVD), and floating catalyst thermal CVD (FCT-CVD). Scanning electron microscopy (SEM) and high-resolution transmission electron microscopy (TEM) were used to analyze the morphology and topology of the CNTs. Raman spectroscopy was used to assess the quality of the CNTs by determining the  $I_D/I_G$  peak intensity ratios. Additionally, the CNT/diamond samples were sonicated for qualitative comparisons of the durability of the CNT forests. T-CVD provided the largest diameter tubes, with catalysts residing mainly at the CNT/diamond interface. The MPE-CVD process yielded non uniform defective CNTs, and FCT-CVD resulted in the smallest diameter CNTs with catalyst particles imbedded throughout the length of the nanotubes.

## 1. Introduction

Carbon nanotubes (CNTs) are lightweight materials that express superior mechanical, electrical, and thermal properties [1–4]. Diamond films are well known for their hardness and scratch resistance combined with excellent thermal conductivity [5, 6]. Successful CNT growth on a diamond substrate creates a unique all-carbon structure that can be beneficial for advanced power and electronic applications. Various methods such as chemical vapor deposition (CVD), laser ablation, thermal evaporation, arc discharge, and glow discharge have been used to grow CNTs on different surfaces [7–9] including diamond substrates and nanoparticles [9–11].

Among these methods, CVD is perhaps the most promising and scalable approach for future power and electronic devices.

There are many different varieties of CVD used to grow CNTs. The variations depend on power sources, type of catalyst deposition, gas composition, and operating temperatures. In addition to variations of the CVD process, CNT growth is expected to depend significantly on the chemistry, morphology, and activity of the substrate. Catalyst and substrate interactions can create differences in root growth or tip growth mechanisms, size distribution, and defects in CNTs growth [12–14].

Several CVD approaches have been investigated and documented on common electronic substrates such as silicon, but no work seems to have been reported on specialty substrates such as CVD diamond. It is desirable to test the applicability of these techniques on diamond substrates and compare the CNTs obtained from different CVD growth techniques. This would enable future device manufacturers to select the most appropriate technique for a specific application. This study compares three types of CVD techniques believed to be the most probable candidate techniques to be scaled up and utilized for future power devices. They all utilize transition metal catalysts that can readily form metastable carbides needed for CNT growth on any substrate [15–17]. The three CVD approaches selected were thermal CVD (T-CVD) with presputtered metal catalyst, microwave plasma-enhanced CVD (MPE-CVD) with presputtered metal catalyst, and floating catalyst thermal CVD (FCT-CVD) with xylene and ferrocene liquid mixture without any prior catalyst deposition. T-CVD is a low-cost system that can easily be set up to grow CNTs. In comparison to arc discharge, T-CVD operates at a lower temperature which increases the range of substrate material selections. However, the resulting CNTs' structure may be defective compared to arc discharge or laser ablation [18]. MPE-CVD is very suitable for large surface CNT production and can grow CNTs at even lower temperatures than T-CVD [19]. Both these techniques involve predeposition of catalyst on the substrate. The FCT-CVD introduces the carbon and catalyst simultaneously on the substrate via a gas mixture. This approach cuts out the first step of catalyst deposition giving it a potential economic advantage for future scale-up. However, it coats everything in the growth chamber and may be problematic when selective area growth is required [20].

The CNT forests grown have been investigated in detail, and each sample has been analyzed using a scanning electron microscope (SEM), transmission electron microscope (TEM), Raman spectroscopy, and energy dispersive X-ray spectroscopy (EDS) to fully characterize the structures.

## 2. Experimental Methods

**2.1. Sample Preparation.** Polished free-standing diamond substrates grown by a CVD technique were purchased from SP<sup>3</sup> Diamond Technologies Inc. The substrate measurements were  $5 \times 5 \text{ mm}^2$ , with a  $400 \mu\text{m}$  thickness. The surface roughness was determined to be 5 nm as measured by an atomic force microscope. Three CVD-based CNT growth techniques have been investigated: (i) T-CVD, (ii) MPE-CVD, and (iii) FCT-CVD. The first two techniques involved predeposition of seed catalysts prior to CNT growth and were optimized first on an electronic grade silicon substrate with a layer of thermal silicon dioxide layer on the surface. The last one had the catalyst source combined with the carbon source in the feeder gas and had been optimized earlier on graphitic carbon substrates.

Due to limited quantities of CVD diamond substrates, each -of the growth methods described below were first tested and optimized using other standard substrates before

deposition on the diamond. While it is recognized that optimization of parameters on identical diamond substrates would be ideal, the large number of diamond substrates necessary for such an undertaking was not available. It was, however, verified that the growth conditions on standard substrates were repeatable on other available substrates. As for growth parameters of CNTs on the diamond available in the literature the values reported for T-CVD and MPE-CVD were found to be very comparable to ones derived in house on standard substrates [10, 21]. There is no reported growth on CNTs on diamond substrate using the FCT-CVD method. However, this technique involves precoating the substrate with a plasma-enhanced oxide layer, which is expected to make the CNT growth more independent of the underlying substrate. Additional optimization and refinement on specific diamond substrates may be performed in the future as more varieties of diamond substrates become available in larger quantities. At the current time, Raman spectroscopy was used as an indicator of CNT quality, and the *D*-peak to *G*-peak intensity ratios from CNTs obtained on all samples were more than satisfactory. Successful and repeatable experiments from earlier research indicated that the best CNT forests were obtained by using T-CVD and MPE-CVD growth processes with nickel and iron catalysts, respectively. For the FCT-CVD approach, ferrocene is used as an iron source to promote CNT growth. Based on these repeatable results, the CNT growth parameters were used to grow CNTs on the diamond films.

**2.2. T-CVD Method.** Polished free-standing CVD diamond substrates were cleaned in an ultrasonic acetone bath for 5 minutes followed by 5 minutes in an ultrasonic isopropanol bath. After cleaning, the samples were placed into a radio frequency (RF) sputtering system loaded with a 99.999% pure nickel target. The sputtering system uses RF power to create a plasma plume that deposits material from the target to the substrate surface. The substrate was first sputtered with a 10 nm thin film of nickel in a sputter chamber. Then, the nickel-sputtered sample then placed into a T-CVD furnace. The furnace was heated from room temperature to the growth temperature of  $800^\circ\text{C}$  in 20 minutes with an argon/5% hydrogen (Ar/5% H<sub>2</sub>) gas mixture at a flow rate of 300 standard cubic centimeters per minute (sccm). Upon reaching the growth temperature, the sample was held for 10 minutes to allow the thin nickel film to break up into nanoscale islands. Then 400 sccm of argon/10% methane (Ar/10% C<sub>2</sub>H<sub>2</sub>) was introduced as the carbon feedstock source at the end of the 10-minute heat treatment. The growth process continued for 2 hours followed by a slow cool to room temperature again using a flow of 300 sccm of a (Ar/5% H<sub>2</sub>) gas mixture. The entire growth process was performed at a pressure of 90 torr.

**2.3. MPE-CVD Method.** The same sample cleaning procedures discussed above were followed here. The sputtering process was used again, but with a 99.999% pure iron target to form a 10 nm thin film of iron on the CVD diamond samples. The sample was loaded into the MPE-CVD chamber. The furnace was heated from room temperature to  $400^\circ\text{C}$  with pure hydrogen gas flowing at 150 sccm. Once the

temperature reached 400°C, a microwave frequency was used on the hydrogen gas to induce a hydrogen plasma within the chamber. The sample was held for 5 minutes with the hydrogen plasma at 400°C to allow iron island formation. After 5 minutes of annealing in plasma, the temperature was increased to the 650°C growth temperature, followed by the introduction of 15 sccm of methane gas as a carbon source. Methane gas was allowed to flow for 5 minutes for growth to take place. After that, the methane gas was shut off. With hydrogen gas still flowing into the chamber, the current source for the plasma was also shut off. Finally, the heating unit was turned off to allow the system to cool naturally.

**2.4. FCT-CVD Method.** The free-standing CVD diamond samples were treated with microwave plasma containing dimethyl sulfoxide (DMSO) to deposit a thin film of silica, 100 nm in thickness, onto the CVD diamond substrate. Note that there is a correlation between the silica thickness and the quality of CNTs and that this silica layer is required in order for CNTs to grow using FCT-CVD methods [22, 23]. The FCT-CVD system is a two-stage furnace with Ar gas flowing at 600 sccm and hydrogen gas flowing at 45 sccm. The low-temperature furnace is kept at 250°C, while the high-temperature furnace is ramped up to the growth temperature of 750°C. Ferrocene was dissolved into a xylene solvent in a 0.008 : 1 molar volume ratio. The xylene/ferrocene liquid mixture serves as a carbon feed stock as well as an iron catalytic particle source carrier. During growth, xylene/ferrocene was introduced at a flow rate of 3 mL/hr via a syringe pump. The growth time was 20 minutes followed by a cooldown with 600 sccm of Ar gas. Details of silica treatment as well as the CNT growth parameters can be found in earlier publications [24].

**2.5. Characterization.** The resulting samples were characterized using a FEI Sirion high-resolution SEM for analysis of carpet surface and nanotube morphology. Cross-sectional views of the interfaces are needed to understand how catalyst particles play a role during CNT growth. A thin TEM foil of the cross section of interest was made using a DB235 FEI focused ion beam. To protect CNTs from the gallium ion etching, a layer of platinum cap was sputtered on top of the CNT before the trenching process began for a lift out sample. The resulting foil was attached to a molybdenum TEM grid for final thinning until a transparent foil was formed. The TEM foil was first analyzed using a Philips CM200 TEM for general appearances and identified the different layers that it contains. The foils containing CNTs with both catalyst and substrate intact were then analyzed for elemental compositions by energy dispersive X-ray spectroscopy (EDS) using the FEI Titan 80–300 TEM. In addition to the imaging analysis, Raman spectroscopy analysis was used to provide a qualitative value for the growth structures of CNTs. It uses the intensity ratio of the disorder peak (*D*-peak) over the graphite peak (*G*-peak) to determine this qualitative value [25]. In order to monitor the durability and strength of bonding between CNTs and the diamond substrate, a sonication test was performed on samples made from each growth method.

This test uses Branson 3210, an ultrasonic cleaner with 40 kHz frequency. The samples were sonicated for 15 minutes while submerged in deionized water. The results from the previous analyses are discussed in the next section.

### 3. Results and Discussions

**3.1. Initial Catalyst Distribution in Preseeded Samples.** It is well established that the underlying catalysts play a big role in the structure and properties of the resulting CNTs. The three different techniques compared here have two different approaches of introducing the catalyst: T-CVD and MPE-CVD involve predeposition of nickel and iron catalysts, respectively, while FCT-CVD technique introduces catalyst with the feeder gas during CNT growth. In the first two cases, the morphology of the starting catalyst film could be analyzed prior to CNT growth. For the last case, there is no precursor catalyst film, and catalyst morphology can only be seen after the CNT layer is formed, as discussed later.

Figure 1(a) shows that thermal treatment of the 10 nm nickel film covering the polished diamond surface resulted in nanoislands with average diameters of 53 nm distributed uniformly across the substrate surface. According to Homma et al. [26], the resulting particle size can be modified and is dependent on the film thickness. A thinner film thickness using the procedure mentioned above provided a low CNTs growth yield. Because of this, the study uses 10 nm film thicknesses as the testing film thickness.

Figure 1(b) shows the SEM surface analysis of a sample treated at 400°C with hydrogen plasma inside the MPE-CVD system for 5 minutes. The image shows that the iron catalyst agglomerated into a continuous uneven film rather than solidified as isolated nanoparticles.

**3.2. Nanotube Morphology.** Figure 2 shows SEM images of the CNT layer formed on diamond film using the three different techniques. Figure 2(a) is the image of T-CVD grown CNTs which have an average tube diameter of 61 nm ± 12 nm, with smooth and uniform tubular structure. This correlates well with the uniform size distribution of nickel islands of similar sizes seen in Figure 1(a).

Figure 2(b) is an SEM image of MPE-CVD-grown CNTs that indicates that the CNTs are not uniform and contain various defects as well as variation in diameters. This may be the result of the seed catalyst layer consisting of irregular-shaped particles. The nonuniformity of individual tubes may also be influenced by defects developed during formation. The MPE-CVD method uses a hydrogen plasma that forms a reducing environment within the chamber. The SEM image taken can be compared to the study done by Behr which indicates that hydrogen can etch CNTs during the growth process. This can create surface defects throughout the growth process [27]. Some studies suggest that exposing growing CNTs to hydrogen-rich environments convert them into diamonds [28, 29]. Figure 2(b) shows the MPE-CVD CNTs tubes with defects similar to the ones reported by Behr after exposure to the hydrogen-rich environment.

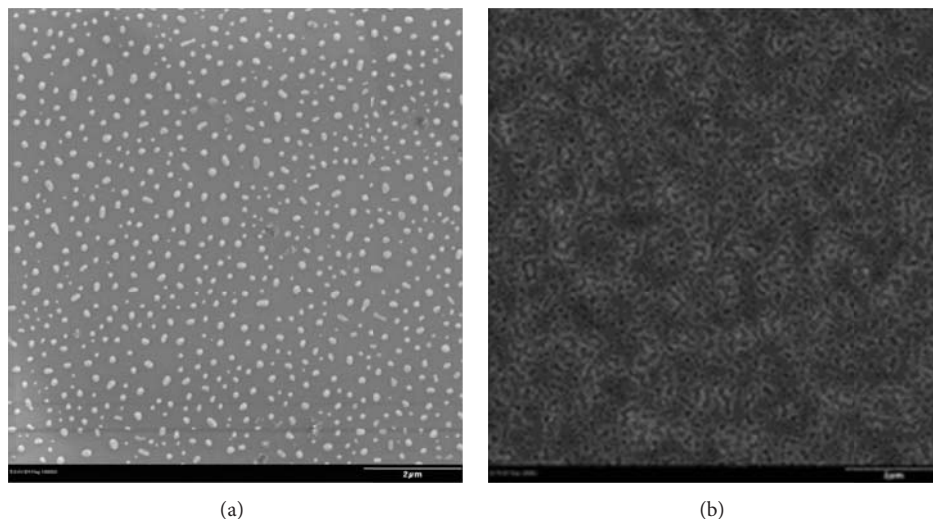


FIGURE 1: (a) Ni catalyst after thermal treatment in T-CVD. (b) Fe catalyst after thermal treatment in MPE-CVD with hydrogen plasma.

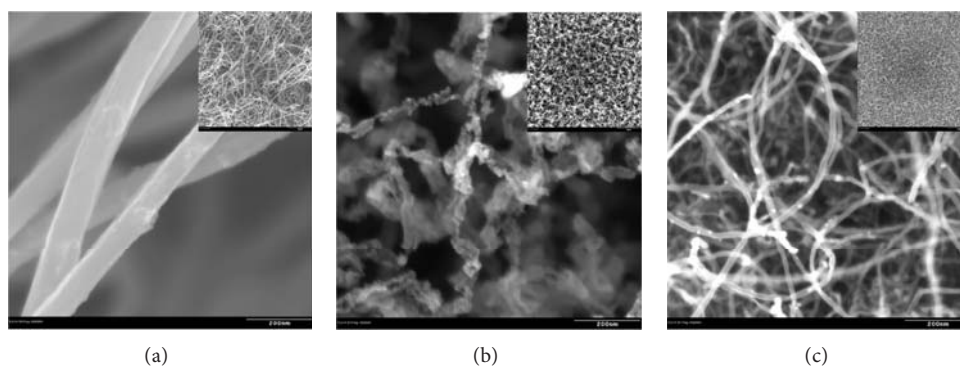


FIGURE 2: (a) T-CVD-grown CNTs. (b) MPE-CVD-grown CNTs. (c) FCT-CVD-grown CNTs.

Figure 2(c) shows an image of FCT-CVD-grown CNTs. This figure indicates that the CNTs are uniform in diameter and grow as densely entangled forests. These CNTs have average diameters of  $12 \text{ nm} \pm 1.8 \text{ nm}$ , making them the smallest of the three growth methods. The image also suggests that there are particles residing on the outer surface of the CNTs. This is expected because the xylene/ferrocene mixture provides continuous source of iron particles throughout the entire process, some of which are expected to attach to the growing CNT surface. The diameter of the outer particles can provide an estimate of iron catalyst size, and they have an averaging diameter size of  $12 \text{ nm} \pm 2.2 \text{ nm}$ .

**3.3. Catalyst Distribution in the Final CNT-Covered Diamond Structure.** Figures 3–5 show high-resolution TEM images with EDS elemental mapping. Figure 3 indicates that in T-CVD, nickel particles are encapsulated with a layer of carbon, and CNT growth originates from the outer carbon layer. This explains why the average CNT diameter is slightly higher than the average nickel catalyst diameter as shown later. The encapsulated catalyst particle remains anchored at the diamond-CNT interface implying the predominant growth

mechanism is root growth. There are a few instances where the catalyst particle moved several nanometers into the CNT length, away from the interface. Growth patterns similar to this indicate a small probability of catalyst lift-off.

Figure 4 shows an energy-filtered transmission electron microscope (EF-TEM) image of an MPE-CVD film. It can be seen that iron particles in this case do not reside along the interface, but rather move easily into the CNT, away from the interface. The mobility of nonanchored catalytic particles at the interface may also contribute to disordered CNT growth.

As seen in Figure 5, EF-TEM analysis of the FCT-CVD sample indicates a high distribution of iron particles residing at the diamond CNT interface which has the silica functional layer. There are additional iron particles found further away in the CNT forest. This is expected due to the continuous iron particle introduction throughout the CNT growth phase. The large number of iron catalysts at the interface suggests that the silica nanolayer keeps them anchored and prevents them from migrating during CNT growth.

Figure 6 shows the average particle size distribution taken with Image J software. This software provides qualitative values for the catalyst particle size and tube diameter comparison taken from the resulting TEM images. For T-CVD, the

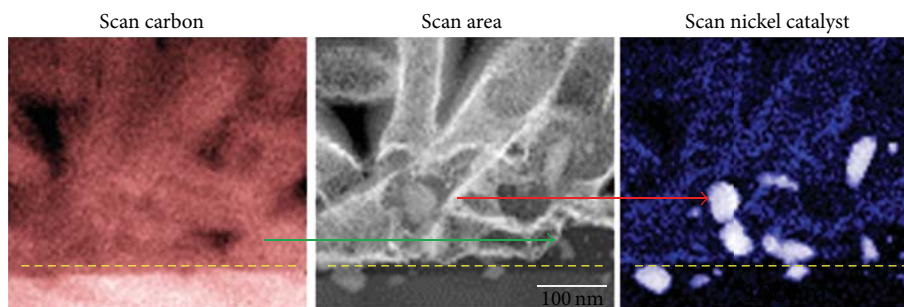


FIGURE 3: Cross-sectional TEM image of T-CVD-grown CNTs, the scale bar is 100 nm.

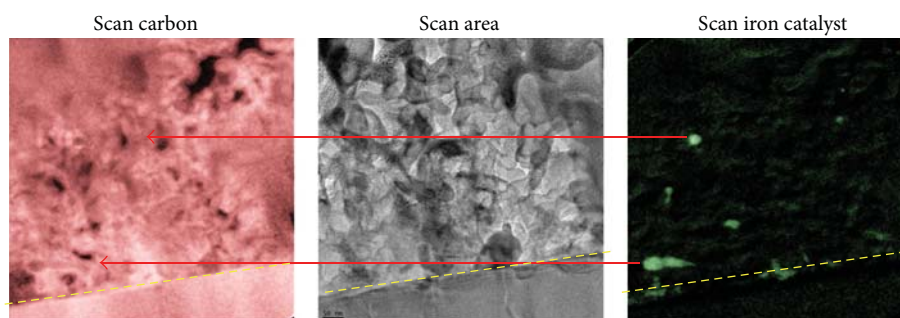


FIGURE 4: Cross-sectional TEM image of MPE-CVD-grown CNTs, the scale bar is 50 nm.

average catalyst particle diameter was measured to be  $53 \text{ nm} \pm 16 \text{ nm}$ , and the average tube diameter was  $61 \text{ nm} \pm 12 \text{ nm}$ . Thus, the catalyst diameters measured using TEM images are within the margin of error with the top view images seen by SEM. For MPE-CVD, the average catalyst particle diameter was  $21 \text{ nm} \pm 7 \text{ nm}$ , and the average tube diameter was  $40 \text{ nm} \pm 18 \text{ nm}$ . For the FCT-CVD method, the average catalyst particle size was  $12 \text{ nm} \pm 2 \text{ nm}$ , and the average tube diameter was  $12 \text{ nm} \pm 2 \text{ nm}$ . Cross-sectional TEM images provided additional information about particle location and concentration relative to the interface. For T-CVD, the image indicated that catalyst particles are the largest of all growth methods and reside close to the interface. For MPE-CVD, the catalyst particles are distributed away from the interface. This migration may be due to either the fact that they are smaller in size compared to T-CVD samples, the excess energy provided by the hydrogen plasma, or both. For FCT-CVD, the image indicates that the majority of the iron particles used as catalysts are anchored along the  $\text{SiO}_2$  layer and the iron particles that arrived later reside outside the growing CNTs. The anchoring of smaller nanoparticles may be caused by the silica functional layer and may assist in uniform CNT growth. It can be seen that the nanocatalyst particle size in each case correlates with the CNT diameters observed by SEM and TEM and further validates the hypothesis that the CNT size is largely governed by catalyst particles.

**3.4. Raman Spectrograph Results.** Raman spectroscopy was performed on samples produced by the different growth methods. The results are presented in Figure 7. According to the Handbook of Raman Spectroscopy and Dresselhaus

et al., Raman spectroscopy can be used as a guide to describe different carbon structures, such as diamond-like carbon which has C–C  $\text{sp}^3$  bonding, graphitic carbon which has  $\text{sp}^2$  bonding, and glassy/amorphous carbon which has C–H and disordered mixed bonds [25, 30, 31]. The peaks found around  $1350\text{--}1365 \text{ cm}^{-1}$  are called *D*-peaks, resulting from the disorderly network of  $\text{sp}^2$  and  $\text{sp}^3$  carbon clusters, whereas the peaks found around  $1580\text{--}1620 \text{ cm}^{-1}$  are called *G*-peaks as a result of graphite, and finally the peak found at  $1332 \text{ cm}^{-1}$  is the diamond peak [30–32]. The most interesting finding from our experiment concerned the calculated intensity of the *D*-peak to *G*-peak ratios ( $I_D/I_G$ ). This ratio matched the CNT morphology in terms of defect appearance in the SEM. The  $I_D/I_G$  ratios are given as follows: T-CVD = 0.30; MPE-CVD = 1.94; FCT-CVD = 0.84. Note that the T-CVD has the lowest  $I_D/I_G$  ratio; its SEM images indicated that this tube structure looks the smoothest. In contrast, the  $I_D/I_G$  for MPE-CVD is the highest and its SEM images indicated that the tube structure appears damaged and full of defects. Earlier, we stated that hydrogen may etch the CNT and introduce defect sites that can raise the intensity of the *D*-peak. Another possibility that causes high *D*-peak is when CNT is introduced to a hydrogen rich environment; the hydrogen alters CNT's C–H bonding and transforms them into diamond or disordered carbon [27, 33]. If this is the case, it explains why the disordered bonding peak, the *D*-peak, is much higher in the MPE-CVD sample.

Since the CNTs were grown on diamond substrates, one might suggest that the high intensity of *D*-peak resulted from signals coming from the diamond substrate underneath. However, the recorded *D*-peak intensity lies around

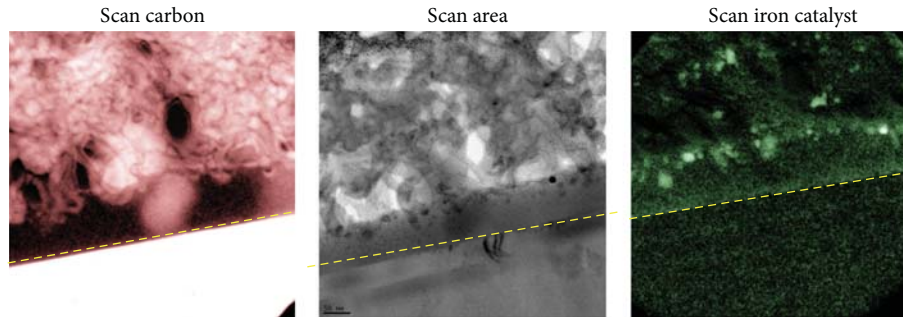


FIGURE 5: Cross-sectional TEM image of FCT-CVD-grown CNTs, the scale bar is 50 nm.

Average catalytic particle size and CNTs diameter distribution

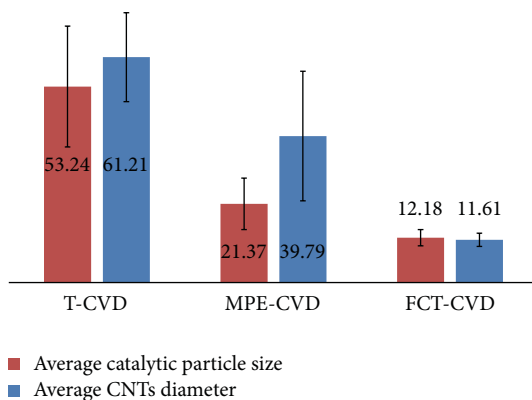


FIGURE 6: Particle size and CNTs tube diameter distribution chart.

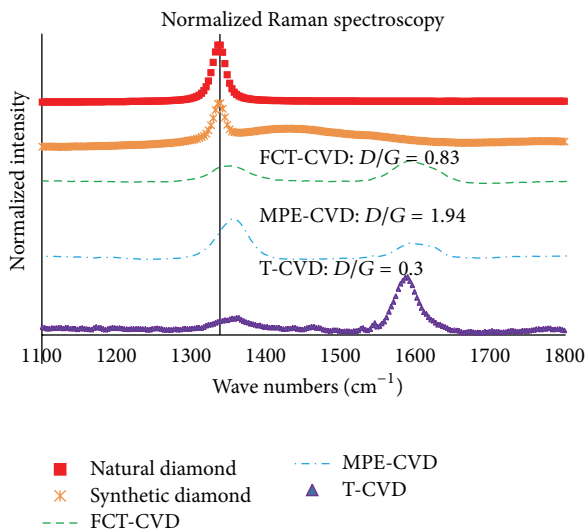


FIGURE 7: Raman spectroscopy signals for natural diamond, synthetic diamond, and CNTs from the three CVD methods.

(1354  $\text{cm}^{-1}$ ), whereas known diamond  $D$ -peaks are detected at (1332  $\text{cm}^{-1}$ ), indicating that the peak signal did not result from the diamond substrate. For confirmation, a razor blade was used to scrape away the CNTs from a sample and expose

the diamond substrate underneath. The Raman spectra taken from the exposed diamond surface has a peak intensity at (1338  $\text{cm}^{-1}$ ), which closely matches the published Raman peak for diamond (1332  $\text{cm}^{-1}$ ). This additional test further indicates that the (1354  $\text{cm}^{-1}$ ) peak is indeed the  $D$ -peak from the disordered CNT and not from the diamond substrate.

**3.5. Sonication Results.** If the sample was used in a commercial device, it would be important to know if the CNTs had the strength to stay intact within the substrate. The sonication test was used as a qualitative comparison of the forces needed to detach CNT from the substrate [34–36]. SEM images were taken before and after the sonication tests as shown in Figure 8. The images in the top row of Figure 8 were taken prior to sonication, and the bottom row images were taken after the test. Figures 8(a) were from the T-CVD, Figures 8(b) were from the MPE-CVD, Figures 8(c) were from FCT-CVD, and Figures 8(d) were optical images taken from MPE-CVD sample. The before sonication image seen in Figure 8(d) can also be used to represent T-CVD and FCT-CVD, because there were no visual differences observed after the sonication test. It can be seen that the nanotubes were intact even after sonication and that there were no noticeable differences seen in the before and after images from SEM. The low-magnification optical images show a difference for the MPE-CVD sample. Before sonication, all samples look identical at this magnification as seen in Figure 8(d) top image. The optical images after the sonication test were unchanged for T-CVD and FCT-CVD which are also represented by Figure 8(d) top image. The MPE-CVD after sonication sample was different as shown in Figure 8(d) bottom image. While postsonication SEM images of MPE-CVD sample show that CNTs were present on the scanned regions, the low-magnification optical images show exposed diamond substrate on the corners of the sample. This indicates detachment of CNTs at the corners of this sample, implying that the bonding between CNTs and substrate may be the weakest in this fabrication method. It must be noted that because of the extremely high length/diameter ratio of the nanotubes, agitation in an ultrasonic bath produces concentrated stresses at the root of the CNT. Survival under these conditions indicates that these materials will be robust in many service conditions. Among the three samples, MPE-CVD specimen may be the weakest, and detachment begins

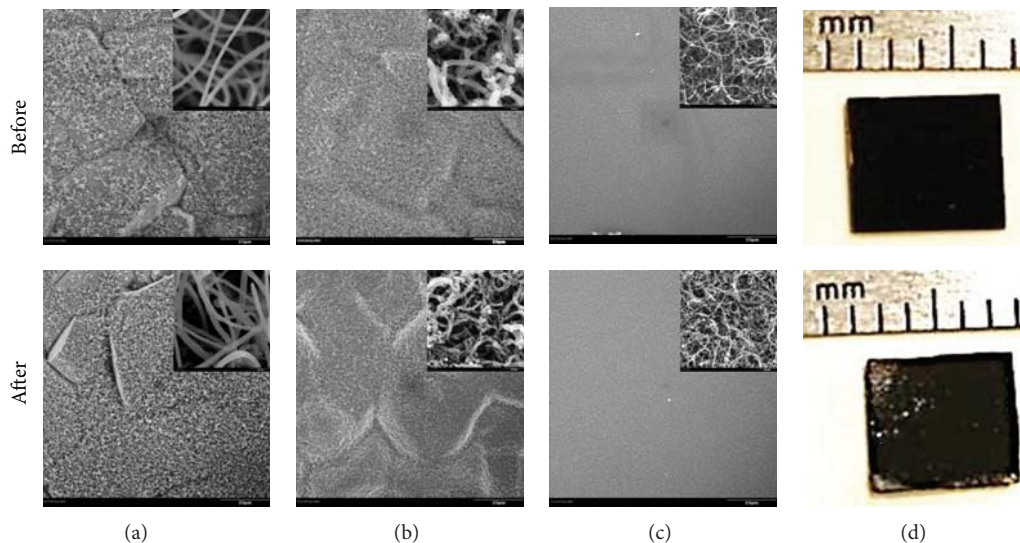


FIGURE 8: (a), (b), and (c) are SEM images, and (d) is the optical image. The images in the top row were taken prior to sonication, and those in the bottom row were taken after the test. (a) is the T-CVD sample. (b) is the MPE-CVD sample. (c) is the FCT-CVD sample, and (d) is taken from MPE-CVD Sample. There were no visual changes seen after the sonication test for the T-CVD and the FCT-CVD sample. Therefore, the before image from (d), can also be used to represent before and after sonication test for T-CVD and FCT-CVD sample.

to occur at the corners, which are the most vulnerable regions of the sample.

**3.6. Overall Comparison.** It is seen that very different types of CNT layers can be grown on diamond film by different techniques. It must be noted that T-CVD and MPE-CVD are multistep processes that separate the catalyst deposition step from the CNT growth step. The catalytic particles in the T-CVD growth are found to be the largest of the three types of growth for the conditions used. These particles were found to reside at the interface with minimal migration into the CNT layer. The resulting CNT structures were found to be the smoothest with the largest tube diameters of all three growth types. This smooth structure may be useful for electronic and thermal applications that require minimal defects.

The SEM images show the CNTs that resulted from the MPE-CVD method contains kinks and defects on the individual tubes. The defects may be the result of hydrogen plasma and excess hydrogen in the chamber. The excess hydrogen can etch the surface of CNTs as it grows, which results in a defected surface. The hydrogen plasma may also provide excess energy that inadvertently promotes catalyst migration. If this migration occurs during CNT growth, it may be another underlying reason as to why those CNT structures are kinked. It can be proposed that as the CNTs are growing with the migrating catalytic particles, a straight path for growth was not provided, which resulted in a kinked-type growth. Therefore, this approach which is suitable for large area growth will be useful only in situations where defective and kinked CNTs are acceptable. It would be interesting to determine if the defective CNTs grown under energetic conditions are more reactive than their smoother counterparts. Another noticeable difference provided by the MPE-CVD method is that it has the weakest bonding with the

substrate compared to the other two methods. Images from the three growth methods were compared after the sonication test. The images from the sonication test show the corners of the diamond substrate were exposed after the test, which is not seen in the other samples. The benefit of using FCT-CVD is that it is a one step process where catalyst and carbon source are introduced together. The resulting CNTs grown by this process had the smallest diameter, averaging 12 nm, with uniform and dense growth patterns. While this may be a very suitable approach in many applications, the disadvantage is the possibility of excess iron particles arising from continuous catalyst deposition. This may be mitigated by modifying the process to cut off ferrocene during the latter part of CNT growth.

Since each method has its unique advantages and disadvantages, these studies indicate that the selection of the CNT growth method is heavily influenced by the intended application.

## 4. Conclusions

In this paper, we have compared the growth of CNTs forests on synthetic diamond substrates using three different CVD growth methods. The CNTs were characterized using electron microscope imaging (SEM and TEM), elemental analysis (EDS), Raman spectroscopy, and the sonication test. The SEM and TEM images indicated each method produces CNTs with a distinctly different diameter and morphology. Raman spectroscopic analysis suggested that T-CVD had the lowest disordered carbon to graphite intensity ratio of 0.3 followed by FCT-CVD of 0.83 and the highest by MPE-CVD of 1.94. T-CVD also produces large diameter CNTs that are otherwise clean, with minimal tubular defects or additional catalytic contaminants. MPE-CVD is sometimes

the preferred method for larger scaled applications; however, the excess hydrogen plasma energy during growth may cause migrations of catalytic particles, surface etching, and defective CNTs that may be detrimental to precision applications. MPE-CVD has the highest probability for catalytic mobility, the most defective CNTs structure morphology, and the weakest interfacial bonding strength. It may be possible to improve this situation through extensive processing parameter changes, but not certain. FCT-CVD has the advantage of being a one-step CNT growth method that does not need a separate catalyst deposition step, yet produces dense uniform CNTs. This technique provided the finest CNT diameter, and intermediate diamond/graphite ratio in the Raman signal. This method does produce some excess metal particles due to continuous catalyst nucleation. However, this issue can be easily addressed in the future if needed, by stopping the catalytic source after a certain growth time. Finally, this study indicates that there is a clear correlation between the size of catalyst particle and the CNT diameters.

### Conflict of Interests

B. Quinton, as the author of this paper, does not have a direct financial relation with the incorporation and software mentioned in this paper and that might lead to a conflict of interests for any of the authors.

### Acknowledgments

The authors of the paper would like to thank the funding support of Air Force Office of Scientific Research, Air Force Research Laboratory Propulsion Directorate, Wright State University, and Ohio Board of Regents. The authors would like to acknowledge Dr. Robert Wheeler for his guidance on TEM and EDS.

### References

- [1] M. Meyyappan, *Carbon Nanotubes: Science and Applications*, CRC Press, Boca Raton, Fla, USA, 2004.
- [2] S. Iijima, "Helical microtubules of graphitic carbon," *Nature*, vol. 354, no. 6348, pp. 56–58, 1991.
- [3] R. Saito, M. Fujita, G. Dresselhaus, and M. S. Dresselhaus, "Electronic structure of chiral graphene tubules," *Applied Physics Letters*, vol. 60, no. 18, pp. 2204–2206, 1992.
- [4] P. Calvert, "Strength in disunity," *Nature*, vol. 357, no. 6377, pp. 365–366, 1992.
- [5] N. V. Novikov and S. N. Dub, "Hardness and fracture toughness of CVD diamond film," *Diamond and Related Materials*, vol. 5, no. 9, pp. 1026–1030, 1996.
- [6] S. V. Kidalov and F. M. Shakhov, "Thermal conductivity of diamond composites," *Materials*, vol. 2, pp. 2467–2495, 2009.
- [7] C. J. Lee, S. C. Lyu, Y. R. Cho, J. H. Lee, and K. I. Cho, "Diameter-controlled growth of carbon nanotubes using thermal chemical vapor deposition," *Chemical Physics Letters*, vol. 341, no. 3–4, pp. 245–249, 2001.
- [8] E. T. Thostenson, Z. Ren, and T. W. Chou, "Advances in the science and technology of carbon nanotubes and their composites: a review," *Composites Science and Technology*, vol. 61, no. 13, pp. 1899–1912, 2001.
- [9] N. Tumilty, L. Kasharina, T. Prokhoda, B. Sinelnikov, and R. B. Jackman, "Synthesis of carbon nanotubes on single crystal diamond," *Carbon*, vol. 48, no. 11, pp. 3027–3032, 2010.
- [10] C. Varanasi, J. Petry, L. Brunke et al., "Growth of high-quality carbon nanotubes on free-standing diamond substrates," *Carbon*, vol. 48, no. 9, pp. 2442–2446, 2010.
- [11] D. Takagi, Y. Kobayashi, and Y. Homma, "Carbon nanotube growth from diamond," *Journal of the American Chemical Society*, vol. 131, no. 20, pp. 6922–6923, 2009.
- [12] Y. Li, W. Kim, Y. Zhang, M. Rolandi, D. Wang, and H. Dai, "Growth of single-walled carbon nanotubes from discrete catalytic nanoparticles of various sizes," *Journal of Physical Chemistry B*, vol. 105, no. 46, pp. 11424–11431, 2001.
- [13] S. Helveg, C. López-Cartes, J. Sehested et al., "Atomic-scale imaging of carbon nanofibre growth," *Nature*, vol. 427, no. 6973, pp. 426–429, 2004.
- [14] R. T. K. Baker, M. A. Barber, P. S. Harris, F. S. Feates, and R. J. Waite, "Nucleation and growth of carbon deposits from the nickel catalyzed decomposition of acetylene," *Journal of Catalysis*, vol. 26, no. 1, pp. 51–62, 1972.
- [15] C. T. Wirth, S. Hofmann, and J. Robertson, "State of the catalyst during carbon nanotube growth," *Diamond and Related Materials*, vol. 18, pp. 940–945, 2009.
- [16] J. Y. Raty, F. Gygi, and G. Galli, "Growth of carbon nanotubes on metal nanoparticles: a microscopic mechanism from ab initio molecular dynamics simulations," *Physical Review Letters*, vol. 95, no. 9, Article ID 096103, 4 pages, 2005.
- [17] S. Hofmann, G. Csányi, A. Ferrari, M. Payne, and J. Robertson, "Surface diffusion: the low activation energy path for nanotube growth," *Physical Review Letters*, vol. 95, Article ID 036101, 4 pages, 2005.
- [18] K. Koziol, B. O. Boskovic, and N. Yahya, *Carbon and Oxide Nanostructures: Synthesis, Characterisation and Applications*, Henry Dickens, Columbia, SC, USA, 2011.
- [19] Y. C. Choi, D. J. Bae, Y. H. Lee et al., "Growth of carbon nanotubes by microwave plasma-enhanced chemical vapor deposition at low temperature," *Journal of Vacuum Science and Technology A*, vol. 18, no. 4, pp. 1864–1868, 2000.
- [20] Teo, B. K. Kenneth, C. Singh, M. Chhowalla, and W. Milne, *Encyclopedia of Nanoscience and Nanotechnology*, 2003.
- [21] A. J. S. Fernandes, M. Pinto, M. A. Neto, F. J. Oliveira, R. F. Silva, and F. M. Costa, "Nano carbon hybrids from the simultaneous synthesis of CNT/NCD by MPCVD," *Diamond and Related Materials*, vol. 18, no. 2–3, pp. 160–163, 2009.
- [22] A. Cao, P. M. Ajayan, G. Ramanath, R. Baskaran, and K. Turner, "Silicon oxide thickness-dependent growth of carbon nanotubes," *Applied Physics Letters*, vol. 84, no. 1, pp. 109–111, 2004.
- [23] S. M. Mukhopadhyay, A. Karumuri, and I. T. Barney, "Hierarchical nanostructures by nanotube grafting on porous cellular surfaces," *Journal of Physics D*, vol. 42, no. 19, Article ID 195503, 2009.
- [24] S. M. Mukhopadhyay, P. Joshi, and R. V. Pulikollu, "Thin films for coating nanomaterials," *Tsinghua Science & Technology*, vol. 10, no. 6, pp. 709–717, 2005.
- [25] J. L. Lauer, *Handbook of Raman Spectroscopy from the Research Laboratory to the Process Line*, Marcel Dekker, West Yorkshire, UK, 1st edition, 2001.

- [26] Y. Homma, Y. Kobayashi, T. Ogino et al., "Role of transition metal catalysts in single-walled carbon nanotube growth in chemical vapor deposition," *Journal of Physical Chemistry B*, vol. 107, no. 44, pp. 12161–12164, 2003.
- [27] M. J. Behr, E. A. Gaulding, K. A. Mkhoyan, and E. S. Aydil, "Hydrogen etching and cutting of multiwall carbon nanotubes," *Journal of Vacuum Science & Technology B*, vol. 28, no. 6, pp. 1187–1194, 2010.
- [28] L. T. Sun, J. L. Gong, Z. Y. Zhu et al., "Nanocrystalline diamond from carbon nanotubes," *Applied Physics Letters*, vol. 84, no. 15, pp. 2901–2903, 2004.
- [29] Q. Yang, S. Yang, C. Xiao, and A. Hirose, "Transformation of carbon nanotubes to diamond in microwave hydrogen plasma," *Materials Letters*, vol. 61, no. 11-12, pp. 2208–2211, 2007.
- [30] M. S. Dresselhaus, G. Dresselhaus, R. Saito, and A. Jorio, "Raman spectroscopy of carbon nanotubes," *Physics Reports*, vol. 409, no. 2, pp. 47–99, 2005.
- [31] M. S. Dresselhaus, A. Jorio, A. G. Souza Filho, and R. Saito, "Defect characterization in graphene and carbon nanotubes using Raman spectroscopy," *Philosophical Transactions of the Royal Society A*, vol. 368, no. 1932, pp. 5355–5377, 2010.
- [32] L. C. O'Brien, R. L. Kubicek, and J. J. O'Brien, "Laser raman spectroscopy of diamond," *Journal of Chemical Education*, vol. 71, no. 9, pp. 759–760, 1994.
- [33] G. Zhang, P. Qi, X. Wang et al., "Hydrogenation and hydrocarbonation and etching of single-walled carbon nanotubes," *Journal of the American Chemical Society*, vol. 128, no. 18, pp. 6026–6027, 2006.
- [34] Q. Zhang, J. Liu, R. Sager, L. Dai, and J. Baur, "Hierarchical composites of carbon nanotubes on carbon fiber: influence of growth condition on fiber tensile properties," *Composites Science and Technology*, vol. 69, no. 5, pp. 594–601, 2009.
- [35] M. F. De Riccardis, D. Carbone, T. D. Makris, R. Giorgi, N. Lisi, and E. Salernitano, "Anchorage of carbon nanotubes grown on carbon fibres," *Carbon*, vol. 44, no. 4, pp. 671–674, 2006.
- [36] I. T. Barney, *Fabrication and Testing of Hierarchical Carbon Nanostructures For Multifunctional Applications*, Wright State University, 2012.

## Research Article

# Photoluminescence of Hexagonal ZnO Nanorods Hydrothermally Grown on Zn Foils in KOH Solutions with Different Values of Basicity

Nuengruethai Ekthammathat,<sup>1</sup> Titipun Thongtem,<sup>1,2</sup>  
Anukorn Phuruangrat,<sup>3</sup> and Somchai Thongtem<sup>2,4</sup>

<sup>1</sup> Department of Chemistry, Faculty of Science, Chiang Mai University, Chiang Mai 50200, Thailand

<sup>2</sup> Materials Science Research Center, Faculty of Science, Chiang Mai University, Chiang Mai 50200, Thailand

<sup>3</sup> Department of Materials Science and Technology, Faculty of Science, Prince of Songkla University, Hat Yai, Songkhla 90112, Thailand

<sup>4</sup> Department of Physics and Materials Science, Faculty of Science, Chiang Mai University, Chiang Mai 50200, Thailand

Correspondence should be addressed to Titipun Thongtem; [ttphongtem@yahoo.com](mailto:ttphongtem@yahoo.com) and Anukorn Phuruangrat; [phuruangrat@hotmail.com](mailto:phuruangrat@hotmail.com)

Received 18 November 2012; Revised 19 February 2013; Accepted 25 February 2013

Academic Editor: Yun Zhao

Copyright © 2013 Nuengruethai Ekthammathat et al. This is an open access article distributed under the Creative Commons Attribution License, which permits unrestricted use, distribution, and reproduction in any medium, provided the original work is properly cited.

Aligned hexagonal ZnO nanorods on pure Zn foils were hydrothermally synthesized in 30 mL solutions containing 0.05–0.50 g KOH. The products were characterized by X-ray diffraction (XRD), scanning electron microscopy (SEM), transmission electron microscopy (TEM), and photoluminescence (PL) spectroscopy. In this research, wurtzite hexagonal ZnO nanorods grown along the [002] direction with green light emission at 541 nm caused by singly ionized oxygen vacancies inside were detected.

## 1. Introduction

One-dimensional (1D) semiconducting materials are able to be used for a number of potential applications in short wavelength optical, nanoelectronic, and optoelectronic devices due to their tunable electronic and optoelectronic properties controlled by morphologies and dimensions [1–3]. Compared to two-dimensional (2D), three-dimensional (3D), and zero-dimensional (0D) nanostructures, the 1D nanostructure has unique characteristic: large aspect ratio, single crystalline structure, and oriented growth [3]. Zinc oxide is an important low-cost II–VI basic semiconductor with 3.37 eV wide band gap and strong exciton binding energy of 60 meV at room temperature [4–7]. It possesses unique catalytic, electrical, optoelectronic, and photochemical properties—very interesting for a number of potential applications as room-temperature UV lasers, sensors, light-emitting diodes, optical switches, solar cells, and photocatalysis due to its low dielectric constant, high chemical stability, good photoelectric, and piezoelectric behaviors [4, 6, 8].

In the paper, hexagonal ZnO nanorods on Zn foils were hydrothermally synthesized in solutions containing 0.05–0.50 g KOH at 120°C. Their phase, morphology, and photoluminescence were investigated and discussed in more details.

## 2. Experimental Procedure

Reagents of the research were of analytical grade and used without further purification. The hexagonal prism ZnO nanorods were grown on Zn foils by the following. Several 10 × 10 mm square Zn foils with 0.25 mm thick were cleaned with deionized water and absolute alcohol in an ultrasound bath and put in 30 mL of 0.05, 0.10, 0.20, 0.30, 0.40, and 0.50 g KOH aqueous solutions, containing 1, 2, 4, 6, 8, and 10 times of KOH in sequence. All of the solutions and zinc foils were transferred into 50 mL Teflon-lined stainless steel autoclaves, which were tightly closed, heated at 120°C in a laboratory electric oven for 24 h, and naturally cooled to room temperature. In the end, the zinc foils were thoroughly rinsed by

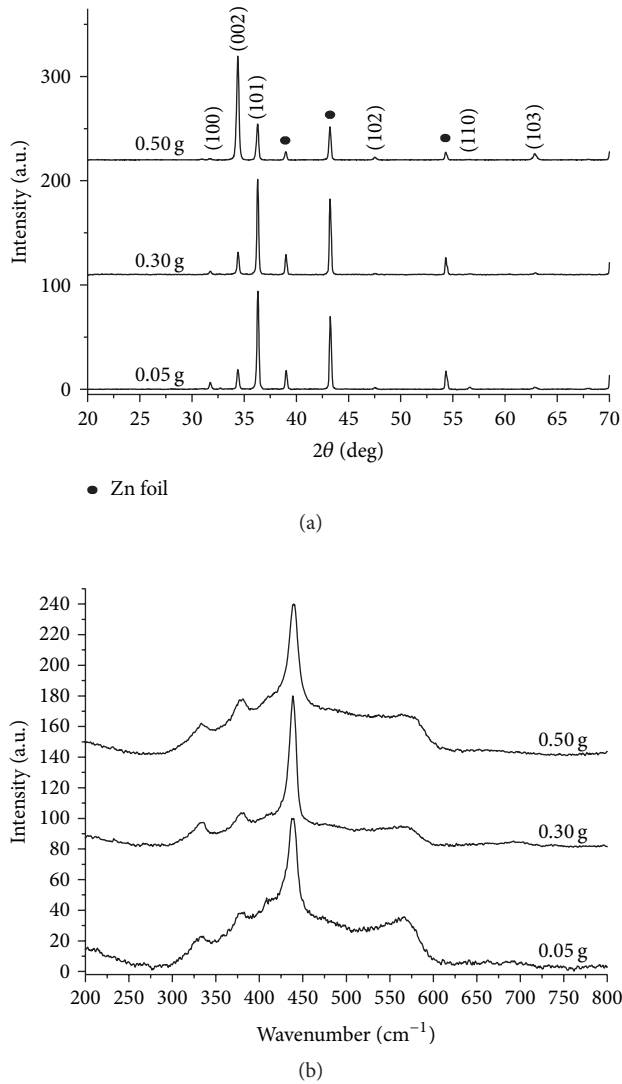


FIGURE 1: (a) XRD patterns and (b) Raman spectra of the as-synthesized ZnO in 30 mL solutions containing 1 (0.05 g), 6 (0.30 g) and 10 times (0.50 g) of KOH.

deionized water several times and alcohol, and dried at 70°C in an electric oven for 12 h for further characterization.

X-ray diffraction (XRD) operated on Philips X'Pert MPD X-ray diffractometer with Cu  $K_{\alpha}$  radiation in the  $2\theta$  of 20–70 deg with a scanning rate of 0.02 deg per step and Raman spectroscopy on T64000 HORIBA Jobin Yvon at 50 mW Ar Laser with 514.5 nm wavelength were used to determine phase, crystalline degree, purity, and vibration modes. Their morphologies were characterized by scanning electron microscopy (SEM, JEOL JSM-6335F) with an accelerating voltage of 15 kV across the LaB<sub>6</sub> cathode. Their nanostructures and growth direction were further investigated by transmission electronic microscopy (TEM) and selected area electronic diffraction (SAED) on a JEOL JEM-2010 TEM at 200 kV with LaB<sub>6</sub> gun. At the end, optical properties of the products were analyzed by a LS50B Perkin Elmer fluorescence spectrometer in the wavelength range of 450–700 nm.

### 3. Results and Discussion

Figure 1(a) exhibits typical XRD patterns of the as-grown ZnO on Zn foils, revealing that all diffraction peaks were explicable in term of wurtzite ZnO structure with  $a = b = 3.251 \text{ \AA}$  and  $c = 5.208 \text{ \AA}$  (JCPDS No. 36-1451) [9]. Sharp diffraction peaks indicate good crystalline degree of the as-synthesized crystals without other impurities detection.

Degree of  $c$  orientation of the as-synthesized ZnO samples was explained by the relative texture coefficient (TC) [10, 11] of the (002) peak calculated using the formula

$$TC_{002} = \frac{(I_{002}/I_{002}^0)}{[I_{002}/I_{002}^0 + I_{100}/I_{100}^0]} \quad (1)$$

$TC_{002}$  is the relative texture coefficient of the (002) over (100) diffraction peaks.  $I_{002}$  and  $I_{100}$  are the measured diffraction intensities of the (002) and (100) peaks, including the corresponding  $I_{002}^0$  and  $I_{100}^0$  values of the randomly oriented standard powder, respectively. For randomly crystallographic orientation, the texture coefficient of ZnO is 0.5. In the solution containing 0.50 g KOH, calculated  $TC_{002}$  was 0.86, which supported the preferential orientation of the as-synthesized ZnO nanorods grown along the [002] direction on the Zn foil.

Wurtzite ZnO structure belongs to  $C_{6v}^4$  ( $P6_3mc$ ) space group with two formula units per primitive cell, and all atoms occupy the  $C^{3v}$  sites. Group theory of wurtzite ZnO structure predicts eight sets of phonon modes:  $A_1 + E_1 + 2E_2$  (Raman active),  $2B_2$  (Raman silent), and  $A_1 + E_1$  (IR active). Moreover, the  $A_1$  and  $E_1$  symmetry are split into longitudinal (L) and transverse (T) optical (O) components due to the macroscopic electric fields associated with the LO phonons. Figure 1(b) shows Raman spectra of the as-synthesized ZnO nanorods. They show a dominant peak of typical characteristic of the wurtzite ZnO structure at  $439 \text{ cm}^{-1}$ , assigned to be the optical phonon  $E_{2H}$  mode. The weak peak at  $332 \text{ cm}^{-1}$  was assigned to be the second-order Raman scattering arising from the zone/zero boundary phonons  $E_{2H}-E_{2L}$  of multiphonon process, while the Raman peak at  $379 \text{ cm}^{-1}$  is attributed to  $A_1$  symmetry with the TO mode. Furthermore, Raman spectra of ZnO samples at  $567 \text{ cm}^{-1}$  are a contribution of the  $E_1$  (LO) mode which is directly associated with oxygen vacancies. The stronger  $E_1$  (LO) mode indicates the presence of higher oxygen vacancies inside [5, 12–14].

SEM images as shown in Figure 2 were investigated on surfaces of Zn foils after hydrothermal treatment in 30 mL solutions containing 1 (0.05 g), 2 (0.10 g), 4 (0.20 g), 6 (0.30 g), 8 (0.40 g), and 10 times (0.50 g) of KOH. An interesting feature of the nanostructures grown on the bottom surfaces exhibited the presence of aligned nanorods of ZnO with the diameter ranging from 400 nm to 700 nm without the detection of other nanostructures. The lengths of the ZnO nanorods are in the range of several micrometers to even longer than 5–7  $\mu\text{m}$ . These nanorods were enlarged and lengthened in sequence with an increase in the degree of basicity. The inset of Figure 2(f) demonstrates the hexagonal

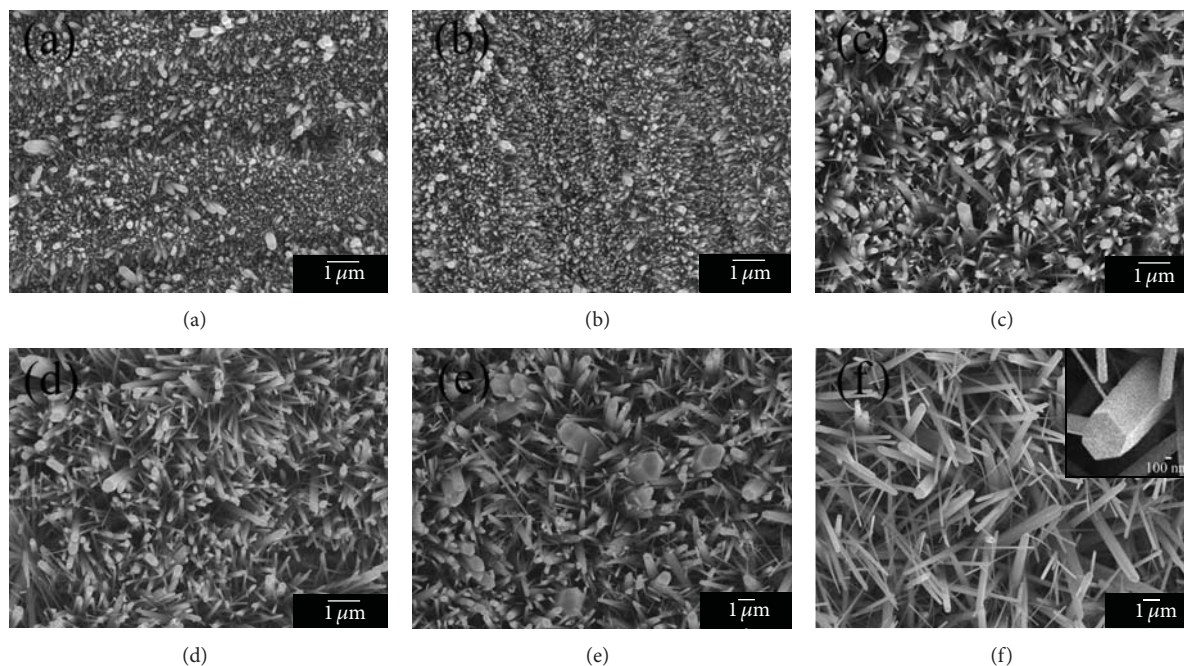


FIGURE 2: SEM images of the as-synthesized ZnO samples in 30 mL solutions containing (a) 1 (0.05 g), (b) 2 (0.10 g), (c) 4 (0.20 g), (d) 6 (0.30 g), (e) 8 (0.40 g), and (f) 10 times (0.50 g) of KOH.

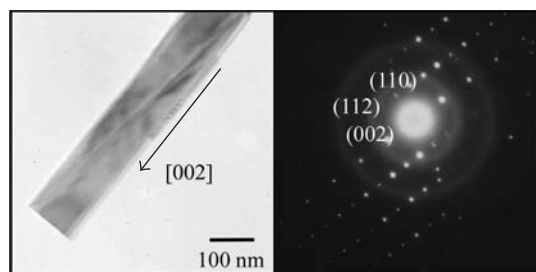
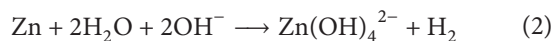


FIGURE 3: TEM image and SAED pattern of hexagonal ZnO nanorod in 30 mL solution containing 10 times (0.50 g) of KOH.

ZnO nanorod which was fully grown on Zn foil in the solution containing 0.50 g KOH.

The hexagonal ZnO nanorods were also characterized through TEM and SAED (Figure 3). TEM image reveals a single hexagonal ZnO nanorod with smooth surface and the preferred growth in the [002] direction. It shows the SAED pattern of bright spots corresponding to hexagonal wurtzite ZnO [9].

Based on the previous discussion, mechanism of the growth and morphology of ZnO nanostructure can be proposed as follows:



The formation of  $\text{Zn}(\text{OH})_4^{2-}$  ions from  $\text{Zn}^{2+}$  and  $\text{OH}^-$  ions by a hydrothermal reaction is a key role in the formation of hexagonal wurtzite ZnO nanorods. The primary ZnO

nanoparticles began to nucleate on Zn foil by the dissolution of Zn atoms into the solution and the cause of concentration gradient of  $\text{Zn}^{2+}$ . The intrinsic electric fields of the polar ZnO lattice could be responsible for further growth of ZnO crystals, described as alternating planes of  $\text{Zn}^{2+}$  and  $\text{O}^{2-}$ , stacked along the  $c$ -axis. The oppositely charged ions produced positively charged and negatively charged surfaces, resulting in polarization along the  $c$ -axis. The preferred  $c$ -axis orientation of ZnO nanostructure is driven by electrostatic interaction between the polar charges to minimize surface energy. Finally, ZnO nanorods grew on Zn foil as substrate [15].

The main emission of ZnO nanorods can be assigned as the recombination of free excitons. Other peaks probably originated from position of band-edge emission of ZnO of relatively large dimensions with different concentration of native defects [16]. It is well known that visible photoluminescence mainly originates from defect states of Zn interstitials, zinc vacancies, and oxygen vacancies [17]. Photoluminescence (PL) of ZnO nanorods grown on Zn foils was investigated using excitation wavelength of 214 nm at room temperature as shown in Figure 4. PL spectrum of hexagonal ZnO nanorods using 0.50 g KOH shows the highest strong green light emission at 541 nm, due to the singly ionized oxygen vacancies of ZnO, in accordance with other reports [16–18].

#### 4. Conclusions

In summary, densely aligned hexagonal ZnO nanorods on Zn foils were synthesized by a 120°C and 24 h hydrothermal reaction. The XRD, SEM, and TEM analyses showed that the

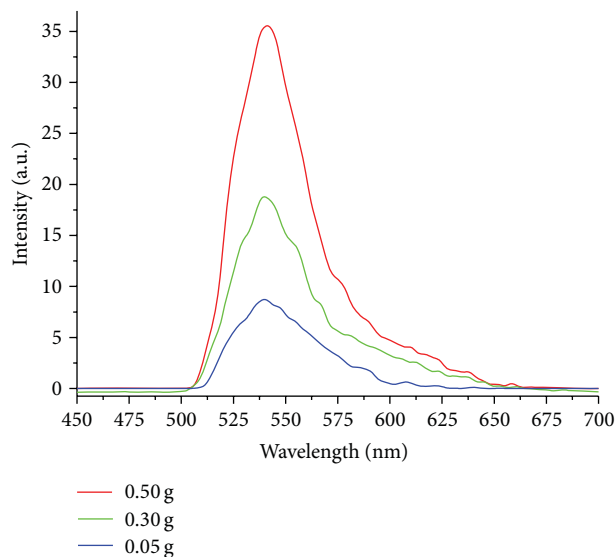


FIGURE 4: PL spectra of the as-synthesized ZnO in 30 mL solutions containing 1 (0.05 g), 6 (0.30 g), and 10 times (0.50 g) of KOH.

as-synthesized products were pure wurtzite ZnO nanorods with uniform hexagonal structure of 400–700 nm diameter and 5–7  $\mu\text{m}$  long. Room temperature PL spectrum of the ZnO nanorods exhibited one strong green light emission at 541 nm due to the singly ionized oxygen vacancies inside.

## Acknowledgments

The authors wish to thank the Thailand's Office of the Higher Education Commission for providing financial support through the National Research University (NRU) Project for Chiang Mai University (CMU) and the Human Resource Development Project in Science Achievement Scholarship of Thailand (SAST) and the Thailand Research Fund (TRF) for providing financial support through the TRF Research Grant BRG5380020, including the Graduate School of CMU through a general support.

## References

- [1] L. Z. Pei, H. S. Zhao, W. Tan, H. Y. Yu, Y. W. Chen, and Q. F. Zhang, "Single crystalline ZnO nanorods grown by a simple hydrothermal process," *Materials Characterization*, vol. 60, no. 9, pp. 1063–1067, 2009.
- [2] Z. Li, X. Huang, J. Liu, Y. Li, and G. Li, "Morphology control and transition of ZnO nanorod arrays by a simple hydrothermal method," *Materials Letters*, vol. 62, no. 10–11, pp. 1503–1506, 2008.
- [3] X. Wu, H. Chen, L. Gong, F. Qu, and Y. Zheng, "Low temperature growth and properties of ZnO nanorod arrays," *Advances in Natural Sciences*, vol. 2, Article ID 035006, 2011.
- [4] H. Zhang, J. Feng, J. Wang, and M. Zhang, "Preparation of ZnO nanorods through wet chemical method," *Materials Letters*, vol. 61, no. 30, pp. 5202–5205, 2007.
- [5] J. H. Yang, J. H. Zheng, H. J. Zhai, L. L. Yang, J. H. Lang, and M. Gao, "Growth mechanism and optical properties of ZnO nanosheets by the hydrothermal method on Si substrates," *Journal of Alloys and Compounds*, vol. 481, no. 1–2, pp. 628–631, 2009.
- [6] X. Ren, D. Han, D. Chen, and F. Tang, "Large-scale synthesis of hexagonal cone-shaped ZnO nanoparticles with a simple route and their application to photocatalytic degradation," *Materials Research Bulletin*, vol. 42, no. 5, pp. 807–813, 2007.
- [7] S. Suwanboon, R. Tanattha, and R. Tanakorn, "Fabrication and properties of nanocrystalline zinc oxide thin film prepared by sol-gel method," *Songklanakarinn Journal of Science and Technology*, vol. 30, no. 1, pp. 65–69, 2008.
- [8] D. Wang, C. Song, Z. Hu, W. Chen, and X. Fu, "Growth of ZnO prisms on self-source substrate," *Materials Letters*, vol. 61, no. 1, pp. 205–208, 2007.
- [9] Powder Diffract. File, JCPDS Internat. Centre Diffract. Data, PA, 19073–3273, U.S.A, 2001.
- [10] J. H. Park, P. Muralidharan, and D. K. Kim, "Solvothermally grown ZnO nanorod arrays on (101) and (002) single- and polycrystalline Zn metal substrates," *Materials Letters*, vol. 63, no. 12, pp. 1019–1022, 2009.
- [11] F. Li, Z. Li, and F. J. Jin, "Structural and luminescent properties of ZnO nanorods," *Materials Letters*, vol. 61, no. 8–9, pp. 1876–1880, 2007.
- [12] L. I. Yang, J. H. Yang, D. D. Wang et al., "Photoluminescence and Raman analysis of ZnO nanowires deposited on Si(100) via vapor-liquid-solid process," *Physica E*, vol. 40, no. 4, pp. 920–923, 2008.
- [13] O. Lupan, L. Chow, L. K. Ono et al., "Synthesis and characterization of Ag- or Sb-doped ZnO nanorods by a facile hydrothermal route," *Journal of Physical Chemistry C*, vol. 114, no. 29, pp. 12401–12408, 2010.
- [14] S. J. Chen, Y. C. Liu, Y. M. Lu, J. Y. Zhang, D. Z. Shen, and X. W. Fan, "Photoluminescence and Raman behaviors of ZnO nanostructures with different morphologies," *Journal of Crystal Growth*, vol. 289, no. 1, pp. 55–58, 2006.
- [15] J. Y. Kim, H. Jeong, and D. J. Jang, "Hydrothermal fabrication of well-ordered ZnO nanowire arrays on Zn foil: room temperature ultraviolet nanolasers," *Journal of Nanoparticles Research*, vol. 13, no. 12, pp. 6699–6706, 2011.
- [16] W. Li, Y. Sun, and J. Xu, "Controllable hydrothermal synthesis and properties of ZnO hierarchical micro/nanostructures," *Nano-Micro Letters*, vol. 4, no. 2, pp. 98–102, 2012.
- [17] Y. J. Gao, W. C. Zhang, X. L. Wu et al., "Hydrothermal self-assembly of ZnO nanorods into sphere-like superstructures and their optical characteristics," *Applied Surface Science*, vol. 255, no. 5, pp. 1982–1987, 2008.
- [18] G. Z. Wang, N. G. Ma, C. J. Deng et al., "Large-scale synthesis of aligned hexagonal ZnO nanorods using chemical vapor deposition," *Materials Letters*, vol. 58, no. 16, pp. 2195–2198, 2004.

## Research Article

# Growth and Physical Property Study of Single Nanowire (Diameter $\sim 45$ nm) of Half Doped Manganite

Subarna Datta,<sup>1</sup> Sayan Chandra,<sup>2</sup> Sudeshna Samanta,<sup>1</sup> K. Das,<sup>1</sup>  
H. Srikanth,<sup>2</sup> and Barnali Ghosh<sup>1</sup>

<sup>1</sup> Unit for Nanoscience, Department of Condensed Matter Physics and Material Sciences, S.N. Bose National Centre for Basic Sciences, Salt Lake, Kolkata 700098, India

<sup>2</sup> Department of Physics, University of South Florida, Tampa, FL 33620, USA

Correspondence should be addressed to Barnali Ghosh; barnali@bose.res.in

Received 11 December 2012; Accepted 17 February 2013

Academic Editor: Lijun Ji

Copyright © 2013 Subarna Datta et al. This is an open access article distributed under the Creative Commons Attribution License, which permits unrestricted use, distribution, and reproduction in any medium, provided the original work is properly cited.

We report here the growth and characterization of functional oxide nanowire of hole doped manganite of  $\text{La}_{0.5}\text{Sr}_{0.5}\text{MnO}_3$  (LSMO). We also report four-probe electrical resistance measurement of a single nanowire of LSMO (diameter  $\sim 45$  nm) using focused ion beam (FIB) fabricated electrodes. The wires are fabricated by hydrothermal method using autoclave at a temperature of  $270^\circ\text{C}$ . The elemental analysis and physical property like electrical resistivity are studied at an individual nanowire level. The quantitative determination of Mn valency and elemental mapping of constituent elements are done by using Electron Energy Loss Spectroscopy (EELS) in the Transmission Electron Microscopy (TEM) mode. We address the important issue of whether as a result of size reduction the nanowires can retain the desired composition, structure, and physical properties. The nanowires used are found to have a ferromagnetic transition ( $T_C$ ) at around 325 K which is very close to the bulk value of around 330 K found in single crystal of the same composition. It is confirmed that the functional behavior is likely to be retained even after size reduction of the nanowires to a diameter of 45 nm. The electrical resistivity shows insulating behavior within the measured temperature range which is similar to the bulk system.

## 1. Introduction

Nanowires of functional oxide materials because of their unique one-dimensional-like structural characteristics and size effects exhibit many novel physical properties that are different from their bulk counterparts. It had been shown before that down to size range of 40 nm the ferromagnetic  $T_C$  is enhanced in nanowires of  $\text{La}_{0.67}\text{Ca}_{0.33}\text{MnO}_3$  [1]. In past studies nanowires of  $\text{La}_{0.67}\text{Ca}_{0.33}\text{MnO}_3$  were grown within templates [1, 2]. The enhancement in  $T_C$  of nanowires corroborates the enhancement in  $T_C$  of nanoparticles of same materials [3]. Our motivation is to investigate to what extent nanowires of complex oxides such as manganites retain their functionality and physical properties on size reduction when the wires are grown by hydrothermal method. The 1D nanostructures with well-controlled size, phase purity, crystallinity, and chemical composition are synthesized by

hydrothermal method in this paper. As a result, the retention of the composition and structural and physical properties on size reduction are important issues that need to be established. Often such structural characterizations are done at average level on an ensemble of nanowires. However, characterizations at the level of a single nanowire using spatially resolved tools are needed. In the present work we have used spatially resolved technique like TEM-based EELS to investigate the chemical composition along with other structural and microscopic tools. Importantly we are able to carry out four-probe electrical measurement using FIB grown contacts on a single nanowire of diameter  $\sim 45$  nm.

The nanowires of functional oxides can be fabricated by different methods like template-assisted growth along with chemical solution processing [4], laser-assisted vapor-liquid-solid phase growth [5], lithography, solvothermal method [6], hydrothermal process [7], and so forth. All the

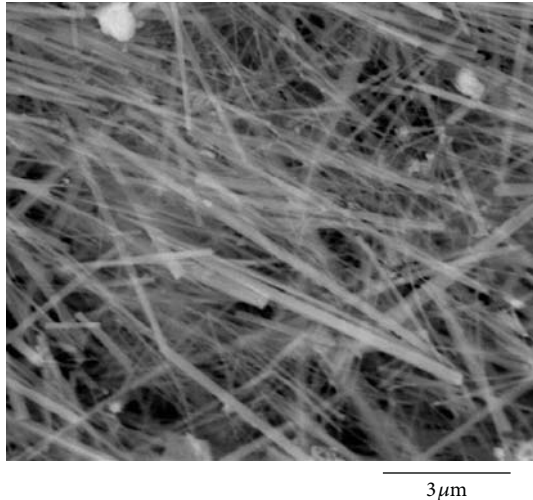


FIGURE 1: SEM image of collection of nanowires.

above-mentioned methods have their own advantages and disadvantages. We have already reported template-assisted growth of functional oxide nanowires by sol-gel synthesis method and magnetic properties of such nanowires [3, 8]. We report here template free fabrication of single-crystalline nanowires ( $\sim 50$  nm, length  $\sim 1\text{--}10$   $\mu\text{m}$ ) of hole doped manganite of  $\text{La}_{0.5}\text{Sr}_{0.5}\text{MnO}_3$  (LSMO) using hydrothermal method. Though this method is suffering from size (diameter) dispersion, it has the advantage of high throughput.

## 2. Experimental Details

Functional oxide nanowires of hole doped manganite  $\text{La}_{0.5}\text{Sr}_{0.5}\text{MnO}_3$  (LSMO) were fabricated by hydrothermal synthesis using autoclave.  $\text{MnCl}_2$ ,  $4\text{H}_2\text{O}$ ,  $\text{La}(\text{NO}_3)_3$ ,  $6\text{H}_2\text{O}$ , and  $\text{Sr}(\text{NO}_3)_2$  were used as precursor materials;  $\text{KOH}$  served as mineralizer, while  $\text{KMnO}_4$  was used as oxidizer. The precursor materials were dissolved in deionized water, and  $\text{KOH}$  was added while stirring to adjust the alkalinity of the solution [7]. The initial mole ratios of the input species were  $0.6\text{KMnO}_4 : 1.4\text{MnCl}_2 \cdot 4\text{H}_2\text{O} : 1.0\text{La}(\text{NO}_3)_3 \cdot 6\text{H}_2\text{O} : 1.0\text{Sr}(\text{NO}_3)_2 : 400\text{H}_2\text{O} : 70\text{KOH}$ . The reaction mixture was vigorously stirred and poured into an autoclave. The main reaction was done in a Teflon vessel which has to be placed in a stainless steel autoclave for higher temperature hydrothermal treatment. The Teflon vessel was filled till 80% of its volume, and then this vessel was placed in the stainless steel container. The crystallization reaction was performed at  $270^\circ\text{C}$  for 30 hours. After the reaction, the autoclave was cooled and depressurized; the products were washed with deionized water and dried in an oven at  $120^\circ\text{C}$  for overnight. A black powder that contains the nanowires was finally obtained.

Nanowires were characterized by using different characterization tools like X-ray diffraction, Scanning Electron Microscope (SEM), Energy Dispersive Analysis of X-ray (EDAX), and High Resolution Transmission Electron Microscopy (HRTEM). The phase formation and phase purity were confirmed by powder diffraction X-ray. The data was taken by PANalytical X'Pert PRO Laboratory powder

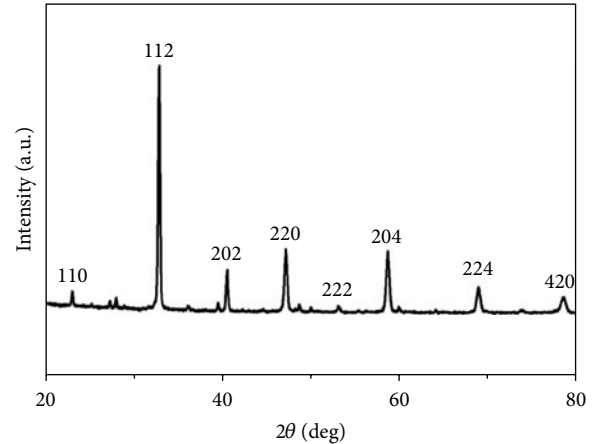


FIGURE 2: XRD pattern of  $\text{La}_{0.5}\text{Sr}_{0.5}\text{MnO}_3$  nanowires confirms the phase formation and phase purity.

X-ray diffractometer with  $\text{Cu K}\alpha$  radiation. The diameter and length of the wires are around  $20\text{--}50$  nm and  $1\text{--}10$  micron, respectively, confirmed by Quanta FEI 200 Scanning Electron Microscope (SEM) and 200 KV Tecnai G2 TF-20 Transmission Electron Microscope. The stoichiometry of the compound LSMO was determined using TEM-EDAX.

To establish the retention of composition on size reduction, we have used TEM-based Electron Energy Loss Spectroscopy (EELS) to investigate the chemical composition at a single nanowire level [9]. 200 kV Tecnai G2-TF-20 TEM with a Gatan parallel detection EELS spectrometer was used for this study. The unknown Mn valency of LSMO nanowire is estimated from EELS. Energy Filtered Transmission Electron Microscopy (EFTEM) mode was done to image the distribution of constituent elements within the nanowire. In addition to the basic characterizations the magnetic nature of the nanowires was determined by a commercial Physical Property Measurement System (PPMS).

To make the four-wire electrical contacts on a single nanowire, we have dispersed the nanowires on  $\text{SiO}_2$  substrate. A single nanowire of LSMO of diameter  $\sim 45$  nm was connected to Cr/Au contact pads by interconnectors made of Pt deposited by FIB (FEI-HELIOS 600) using Ga ions at a voltage of 30 keV and beam current of 80 pA. The temperature variation of resistivity of a single nanowire down to liquid helium temperature (5 K) was done by using cryogenic cryocooler model SRDK 305.

## 3. Results and Discussions

**3.1. Structural and Elemental Characterization.** A typical collection of nanowires obtained from autoclave is given in Figure 1. Phase formation and phase purity were checked with X-ray diffraction measurement shown in Figure 2. It is the tetragonal structure of the space group  $I4/mcm$ , it compares well with bulk values [10], and it matches well with the data reported in ICSD pattern (ref. code: 01-089-0786). The lattice parameters are  $a = 0.545$  nm,  $b = 0.545$  nm, and  $c = 0.770$  nm. From the structural characterization (shown

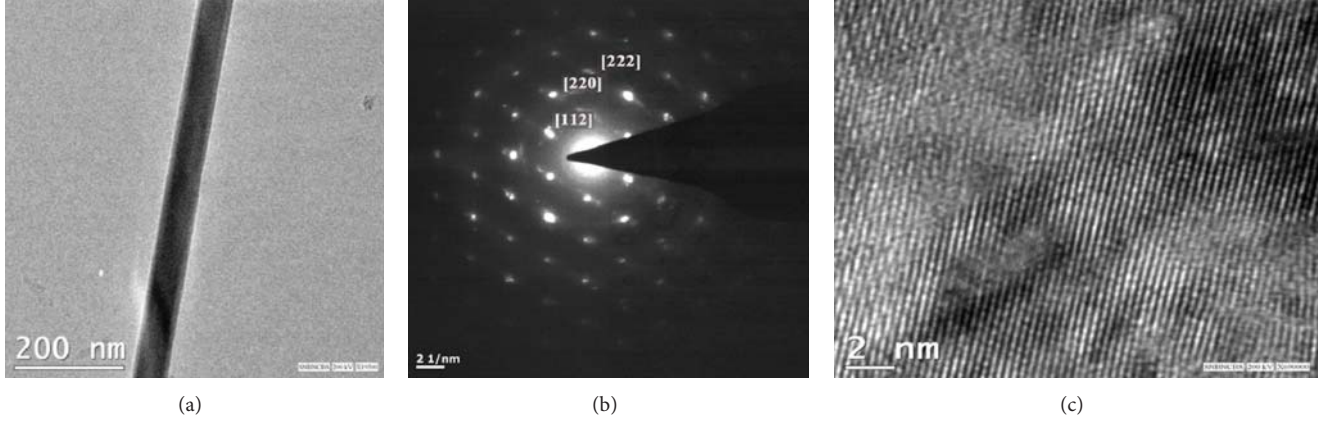


FIGURE 3: (a) Single nanowire of diameter around 45 nm, (b) the selected area diffraction pattern taken with a Transmission Electron Microscope, and (c) HRTEM image shows the single crystalline nature of LSMO nanowires.

in Figure 2) of hydrothermally grown nanowires, it has been observed that we could form single tetragonal phase of LSMO ( $x = 0.5$ ) nanowires which has no impurity.

**3.2. Transmission Electron Microscopy.** The wires were grown of different diameters and lengths ranging 20–50 nm and 1–10 micron, respectively. The TEM image of a single nanowire is shown in Figure 3(a). The single crystalline nature of the nanowires was confirmed from the diffraction pattern and HRTEM images shown in Figures 3(b) and 3(c). The lattice spacing is around 3.11 Å, and (hkl) values are estimated from diffraction pattern data. Nanowires fabricated are of pure phase and single crystalline in nature. It has been observed from the TEM-EDAX data that the atomic percentage ratio (La : Sr) : Mn : O is approximately 1 : 1 : 3 which is the desired composition. We have done the TEM analysis on many single nanowires across the length of the nanowires, and it shows single crystallinity throughout the length.

**3.3. Elemental Analysis Using EELS.** The elemental analysis of these nanowires was done by EELS on different single nanowires repeatedly and estimated the valency of Mn from the calibration curve shown in Figure 4(a). We have determined Mn valency using the white lines ( $L_2$ ,  $L_3$  ionization edges of Mn) and the intensity ratio of  $L_3$  and  $L_2$  lines [11]. The intensities of  $L_3$  and  $L_2$  lines are related to the unoccupied states in the 3d bands. Transition from Mn 2p shell is actually split into two components separated by spin orbit splitting of the ionized 2p core level. Transitions from  $2p^{3/2}$  to  $3d^{3/2}$   $3d^{5/2}$  and from  $2p^{1/2}$  to  $3d^{1/2}$  are  $L_3$  and  $L_2$  lines, respectively. Comparing the intensity  $L_3/L_2$  ratio of Mn of LSMO nanowire and that of Mn with known valency of some compounds, quantitative determination of Mn valency of our sample was evaluated [9]. The intensity ratios of  $L_3$  and  $L_2$  lines of different Mn oxide compounds as a function of their known valency are plotted in Figure 4(a). This curve serves as the calibration curve from which the valence state of unknown materials can be obtained by using the observed intensity ratios. From the calibration curve, we have estimated the valency of Mn of LSMO nanowire. The Mn

TABLE 1: Comparison of  $T_C$  and valency of LSMO nanowires with the bulk.

| Sample        | $T_C$ (K) | Mn valency |
|---------------|-----------|------------|
| LSMO bulk     | 330       | 3.5        |
| LSMO nanowire | 325       | 3.5        |

valency is of the order of  $\sim 3.5$ , and it is very close to its bulk value as shown in Table 1. Energy Filtered TEM image was taken to check the homogeneity of the elemental distribution in each nanowire. Figure 4(b) shows the EFTEM image of LSMO nanowire, where red, green, blue, and yellow colors are used for elements O, Mn, La, and Sr, respectively. The EFTEM analysis shows that all the constituent elements La, Sr, Mn, and O are homogeneously distributed within the nanowire.

**3.4. Magnetic Measurements.** The results of magnetic measurements are shown in Figure 5. It has been observed from the temperature variation of magnetization data that the LSMO nanowires undergo a transition from ferromagnetic (FM) to paramagnetic (PM) phase around 325 K shown in Figure 5(a). The observed  $T_C$  was compared with the phase diagram of bulk LSMO [12], shown in Table 1. Field variations of magnetization ( $M$  versus  $H$ ) were done at 300 K and 5 K in Figure 5(b). The nanowires show ferromagnetic behavior with large coercivity  $\sim 645$  Oe at 5 K shown in the inset of Figure 5(b).

Based on the magnetic data and the work on magnetocaloric study on these LSMO ( $x = 0.5$ ) nanowires [13], we have observed the signatures of three distinct magnetic transitions from the change in magnetic entropy  $-\Delta S_M(T)$ : two maxima at 290 K and 45 K and a minimum at 175 K. The maximum at 290 K arises due to PM-FM transition, and around 175 K the transition is due to antiferromagnetic (AFM) transition. The above two transitions are also observed in bulk LSMO ( $x = 0.5$ ) sample [14–16]. Around 45 K there is one maximum in the magnetization curve; this behavior is not seen in bulk. We have explained this transition as

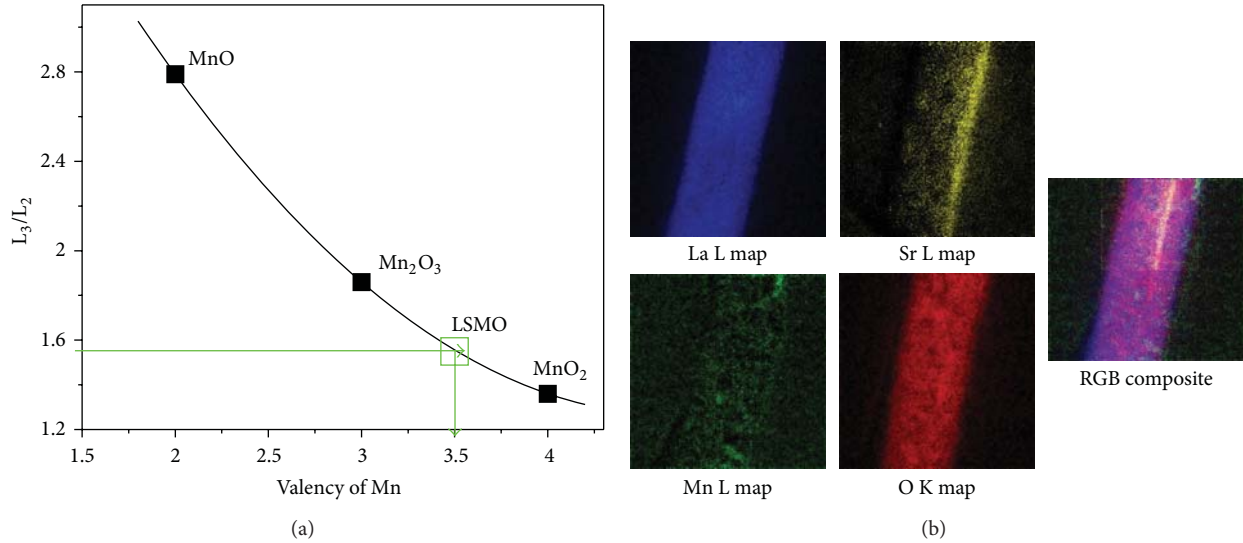


FIGURE 4: (a) Intensity ratios of  $L_3$  and  $L_2$  lines of different Mn oxide compounds as a function of their known valency in the energy range 600–1000 eV and (b) Energy Filtered Transmission Electron Microscope (EFTEM) image of each constituent element: L map of La, Sr, and Mn and K map of O in LSMO nanowire. The red, green, blue, and yellow colors represent the distribution of elements O, Mn, La, and Sr, respectively in the nanowire in the RGB composite map.

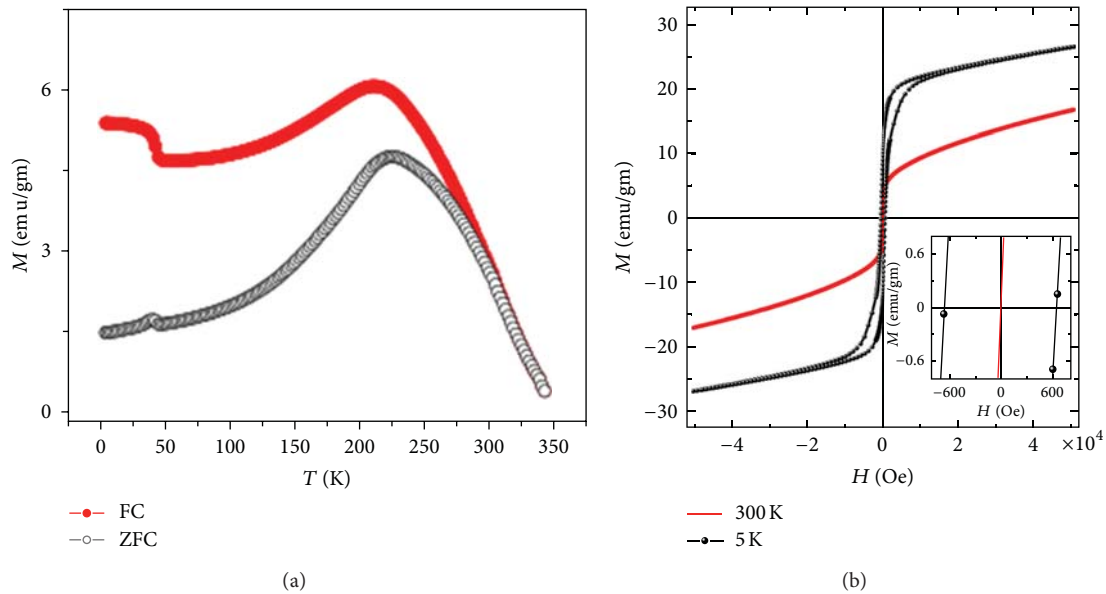


FIGURE 5: (a) Temperature variation of magnetization data of LSMO at 100 Oe and (b) plot of field variation magnetization of LSMO at 5 K and 300 K.

FM transition as observed in the magnetic entropy change plot [13]. From the magnetic measurements and from our previous magnetocaloric study [13], we can infer that the hydrothermally grown nanowires show the basic ferromagnetic property as seen in bulk.

### 3.5. Electrical Resistivity Measurement

**3.5.1. Fabrication of Contact Pads Using FIB.** For resistivity measurement Cr/Au contact pads are deposited on  $SiO_2$

substrate by thermal evaporation using hard mask as shown in Figure 6(a). Using Helios Dual Beam System consisting of an FEG source and an ion beam source, we have located one single nanowire of diameter  $\sim 45$  nm as shown in Figure 6(b). The electrical contact pads were deposited by using a Pt source by Focused Electron Beam (FEB), and then these four pads were finally connected to the prefabricated gold contact pads by FIB, shown in Figure 6(c). The separation between two consecutive probes is around  $\sim 300$  nm. Each contact pad has width of  $\sim 300$  nm.

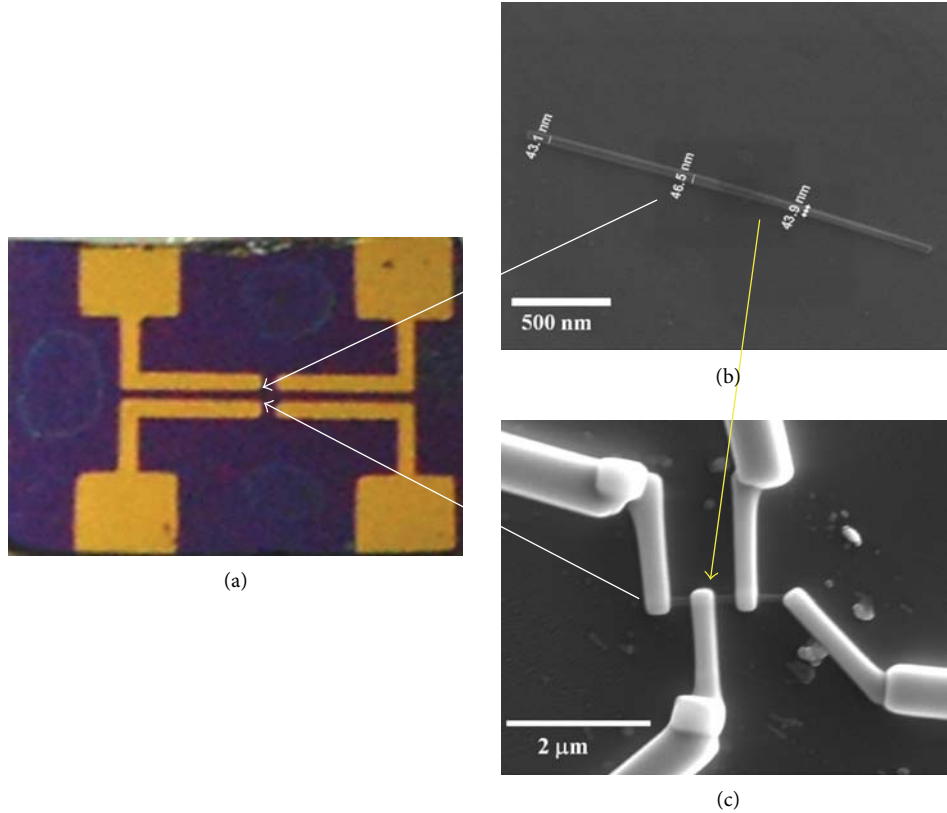


FIGURE 6: (a) Cr/Au contact pads deposited on  $\text{SiO}_2$  substrate by thermal evaporation using hard mask, (b) SEM image of single nanowire of diameter  $\sim 45$  nm, and (c) SEM image of four-wire electrical contact made of Pt by using FIB. The white lined arrows in (a) indicate the area where the nanowires are dispersed and made contact with FIB. The yellow lined arrow indicates that nanowire is connected to four contact pads by Focused Electron Beam (FEB), and after that these are connected to gold contact pads by FIB.

**3.5.2. Transport Measurement on Single Nanowire.** The resistivity data are plotted in Figure 7(a) as a function of temperature which were taken at a current of  $1 \mu\text{A}$ .

We are able to make proper electrical contact and have measured the resistivity of single nanowire of LSMO ( $x = 0.5$ ). Variation of resistivity as a function of temperature plotted in Figure 7(a) shows insulating behaviour within the measured temperature range. The behaviour is similar to that seen in the bulk LSMO ( $x = 0.5$ ) system [14]. The comparison of the resistivity of nanowire compared to the bulk ceramic sample is depicted quantitatively in Figure 7(b). The bulk sample was prepared by ceramic method which shows quite higher resistivity than the nanowire. The  $\rho$  at 5 K is around  $2.7 \times 10^{-3} \Omega\text{-m}$  measured at  $1 \mu\text{A}$  current, and the resistivity at the highest temperature (310 K) is  $4 \times 10^{-5} \Omega\text{-m}$ . We have fitted our conductivity data with variable range hopping model ( $\sigma = \sigma_0 \exp(-(T_0/T))^{1/4}$ ) appropriate for whole temperature ranges ( $\sim 10$  K–310 K) as shown in inset of Figure 7(a) [17]. We have found the characteristic temperature ( $T_0$ ) and density of states (DOS) at Fermi level ( $N(E_F)$ ) from the fitted equation. From the slope of the fitted curve the estimated  $T_0$  is  $\sim 2.4 \times 10^4$  K.  $N(E_F)$  is related to  $T_0$  by the relation  $N(E_F) = (24/\pi a^3 K_B T_0)$ , where  $a$  is localization length ( $\sim 0.39$  nm) which is around one unit cell. From measured  $T_0$ , we obtain  $N(E_F) \sim 6.22 \times 10^{22} \text{ eV}^{-1} \text{ cm}^{-3}$

or  $1.55 \times 10^{43} \text{ J}^{-1} \text{ mole}^{-1}$ . From heat capacity data for a similar compound (LSMO  $x = 0.3$ ) we obtain  $N(E_F) \sim 0.96 \times 10^{43} \text{ J}^{-1} \text{ mole}^{-1}$  [18]. The two DOS values are quite comparable, and this validates the use of VRH model for the electrical conduction in the nanowire.

## 4. Conclusions

We have demonstrated the fabrication of functional oxide nanowires of Sr doped lanthanum manganite system using autoclave and have used EELS as a tool to study the elemental composition of LSMO nanowires of diameter  $\sim 45$  nm. From the EELS and magnetic measurements it has been observed that the nanowires retain the desired composition as well as basic ferromagnetic property, though  $H_C$  increases even after the size reduction down to  $\sim 45$  nm. Finally we are able to make four-probe contacts to a single nanowire and perform the electrical transport measurements on a single nanowire down to 5 K. The resistivity from 310 K down to 10 K shows variable range hopping.

## Acknowledgments

B. Ghosh wants to thank DST, Government of India, under UNANST Phase II for financial support. S. Datta would like to thank DST for financial support. The work has been done

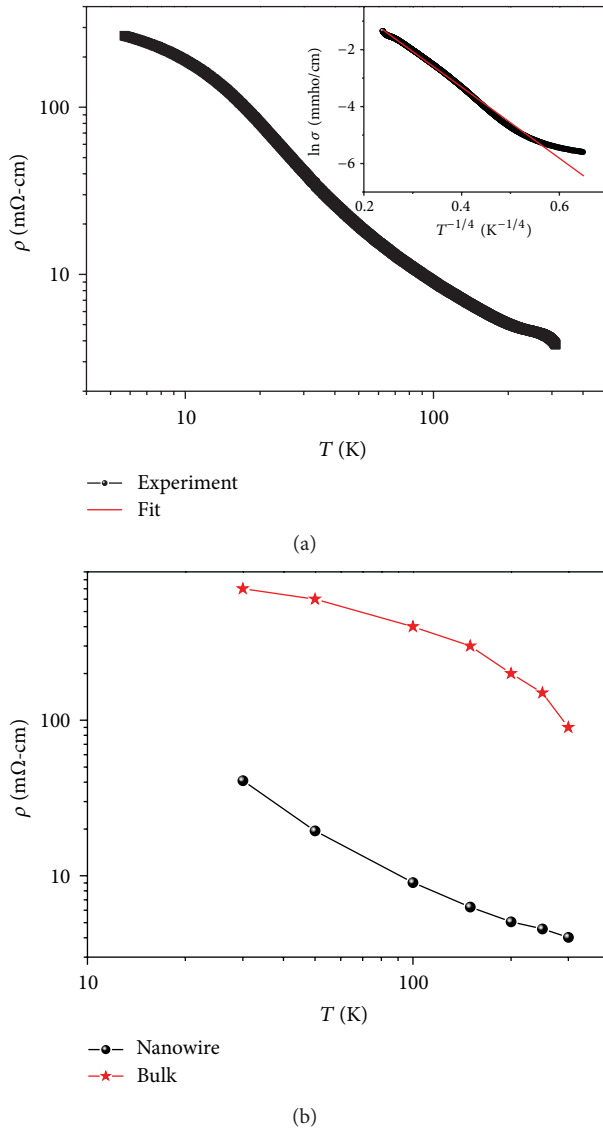


FIGURE 7: (a) Temperature variation of resistivity of single nanowire of  $\text{La}_{0.5}\text{Sr}_{0.5}\text{MnO}_3$  measured in the temperature range from 5 K to 310 K. Inset curve ( $\ln \sigma$  versus  $T^{-1/4}$ ) shows that conductivity data fitted with variable range hopping model for the whole temperature ranges and (b) quantitative comparison of resistivity of LSMO nanowires and bulk [14].

in the DST supported Unit for Nanoscience. S. Chandra and H. Srikanth would like to thank US Department of Energy (Grant no. DE-FG02-07ER46438), for the work at USF.

## References

- [1] B. Ghosh and A. K. Raychaudhuri, "Synthesis and physical properties of ordered arrays of nanowires of complex functional oxides," *Journal of Nanoscience and Nanotechnology*, vol. 9, no. 9, pp. 5533–5536, 2009.
- [2] K. S. Shankar, S. Kar, A. K. Raychaudhuri, and G. N. Subbanna, "Fabrication of ordered array of nanowires of  $\text{La}_{0.67}\text{Ca}_{0.33}\text{MnO}_3$  ( $x=0.33$ ) in alumina templates with enhanced ferromagnetic transition temperature," *Applied Physics Letters*, vol. 84, no. 6, pp. 993–995, 2004.
- [3] T. Sarkar, A. K. Raychaudhuri, A. K. Bera, and S. M. Yusuf, "Effect of size reduction on the ferromagnetism of the manganite  $\text{La}_{1-x}\text{Ca}_x\text{MnO}_3$  ( $x=0.33$ )," *New Journal of Physics*, vol. 12, Article ID 123026, 2010.
- [4] A. K. Raychaudhuri, *Nanolithography and Nanomanipulation, the Chemistry of Nanomaterials Synthesis Properties and Applications*, vol. 2 of edited by C. N. R. Rao, A. Muller, and A. K. Cheetham, Wiley-VCH, Berlin, Germany, 2004.
- [5] Y. Chen, J. Li, Y. Han, X. Yang, and J. Dai, "The effect of Mg vapor source on the formation of MgO whiskers and sheets," *Journal of Crystal Growth*, vol. 245, no. 1-2, pp. 163–170, 2002.
- [6] J. R. Heath and F. K. LeGoues, "A liquid solution synthesis of single crystal germanium quantum wires," *Chemical Physics Letters*, vol. 208, no. 3-4, pp. 263–268, 1993.
- [7] D. Zhu, H. Zhu, and Y. H. Zhang, "Hydrothermal synthesis of single-crystal  $\text{La}_{0.5}\text{Sr}_{0.5}\text{MnO}_3$  nanowire under mild conditions," *Journal of Physics: Condensed Matter*, vol. 14, no. 27, pp. L519–L524, 2002.
- [8] S. Chandra, A. I. Figueroa, B. Ghosh et al., "Fabrication and magnetic response probed by RF transverse susceptibility in  $\text{La}_{0.67}\text{Ca}_{0.33}\text{MnO}_3$  nanowires," *Physica B: Condensed Matter*, vol. 407, no. 1, pp. 175–178, 2012.
- [9] R. F. Egerton, "Electron energy-loss spectroscopy in the TEM," *Reports on Progress in Physics*, vol. 72, no. 1, Article ID 016502, 2009.
- [10] P. M. Woodward, T. Vogt, D. E. Cox et al., "Influence of cation size on the structural features of  $\text{Ln}_{1/2}\text{A}_{1/2}\text{MnO}_3$  Perovskites at room temperature," *Chemistry of Materials*, vol. 10, no. 11, pp. 3652–3665, 1998.
- [11] Z. L. Wang, J. S. Yin, and Y. D. Jiang, "EELS analysis of cation valence states and oxygen vacancies in magnetic oxides," *Micron*, vol. 31, no. 5, pp. 571–580, 2000.
- [12] A. Urushibara, Y. Moritomo, T. Arima, A. Asamitsu, G. Kido, and Y. Tokura, "Insulator-metal transition and giant magnetoresistance in  $\text{La}_{1-x}\text{Sr}_x\text{MnO}_3$ ," *Physical Review B*, vol. 51, no. 20, pp. 14103–14109, 1995.
- [13] S. Chandra, A. Biswas, S. Datta et al., "Multiple magnetic transitions and magnetocaloric effect in hydrothermally synthesized single crystalline  $\text{La}_{0.5}\text{Sr}_{0.5}\text{MnO}_3$  nanowires," *Materials Research Society Symposium Proceedings*, vol. 1454, 2012.
- [14] Z. Jirak, J. Hejtmanek, K. Knmzek, M. Marysk, V. Smma, and R. Sonntag, "Ferromagnetic-antiferromagnetic transition in tetragonal  $\text{La}_{0.50}\text{Sr}_{0.50}\text{MnO}_3$ ," *Journal of Magnetism and Magnetic Materials*, vol. 217, no. 1–3, pp. 113–119, 2000.
- [15] I. Dhiman, A. Das, P. K. Mishra, and L. Panicker, "Influence of A-site ionic radii on the magnetic structure of charge-ordered  $\text{La}_{0.5}\text{Ca}_{0.5-x}\text{Sr}_x\text{MnO}_3$  manganites," *Physical Review B*, vol. 77, no. 9, Article ID 094440, 11 pages, 2008.
- [16] J. Spooren, R. I. Walton, and F. Millange, "A study of the manganites  $\text{La}_{0.5}\text{M}_{0.5}\text{MnO}_3$  ( $M = \text{Ca}, \text{Sr}, \text{Ba}$ ) prepared by hydrothermal synthesis," *Journal of Materials Chemistry*, vol. 15, no. 15, pp. 1542–1551, 2005.
- [17] N. F. Mott and E. A. Davis, Eds., *Electronic Processes in Non-Crystalline Materials*, Clarendon Press: Oxford University Press, Oxford, UK, 2nd edition.
- [18] J. M. D. Coey, M. Viret, L. Ranno, and K. Ounadjela, "Electron localization in mixed-valence manganites," *Physical Review Letters*, vol. 75, no. 21, pp. 3910–3913, 1995.

## Research Article

# Spin-Filtering Effects in Würtzite and Graphite-Like AlN Nanowires with Mn Impurities

G. A. Nemnes

Faculty of Physics, “Materials and Devices for Electronics and Optoelectronics” Research Center, University of Bucharest, P.O. Box MG-II, Ilfov 077125 Magurele, Romania

Correspondence should be addressed to G. A. Nemnes; [nemnes@solid.fizica.unibuc.ro](mailto:nemnes@solid.fizica.unibuc.ro)

Received 14 December 2012; Accepted 28 February 2013

Academic Editor: Yun Zhao

Copyright © 2013 G. A. Nemnes. This is an open access article distributed under the Creative Commons Attribution License, which permits unrestricted use, distribution, and reproduction in any medium, provided the original work is properly cited.

Spin transport properties of magnetic nanowire systems—atomic-sized AlN nanowires with additional Mn impurities—are investigated employing *ab initio* constrained spin density functional theory calculations and nonequilibrium Green's functions formalism. The analyzed nanowire structures exhibit a stress-induced phase transition, between würtzite and graphite-like configurations. In these quasi-one dimensional systems, the surface states ensure the basic prerequisite in establishing spin and charge transfer, by reducing the relatively large bandgap of the group III nitride semiconductor. The results show in how far this phase transition affects the surface states, focusing on the consequences which appear in the spin-filtering processes.

## 1. Introduction

Group-III nitride nanowires provide nowadays a vast number of applications, ranging from chemical [1, 2] and temperature sensors to nanomechanical resonators, thermoelectrical [3] and field emitter [4] applications. In particular, since AlN is a wide bandgap (~6.2 eV) semiconductor, it has become a strong candidate for optoelectronic devices in the UV regime. AlN nanowires are currently produced by a number of techniques, such as self-patterning [5], direct arc discharge [6], or from Al powder [7]. Moreover, inserting transitional metal (TM) impurities (e.g., Mn), attempts have been made in order to produce ferromagnetic quasi-one dimensional diluted magnetic semiconductors [8].

Although the native structure of bulk AlN is würtzite (WZ, space group  $P6_3mc$ ), it was established that ultrathin nanowires occur naturally in a graphite-like (GL, space group  $P6_3/mmc$ ) phase [9–11]. However, upon applying pulling stress, the structures may retain the WZ configuration. Switching between these two configurations can occur due to thermal fluctuations or mechanically induced stress and this has a large impact in both charge and thermal transport.

The surface states play a significant role in the conduction properties of the nanowires, as they reduce the wide bandgap, which is found in the bulk semiconductor. In contrast to

bulk AlN, which has rather good insulating properties, the atomic sized nanowires can achieve reasonable conduction. Therefore, the structures can be regarded as viable solutions for the active region in field effect applications. It is also important to emphasize that it is essential for the nanowire systems to retain a small band gap (up to ~1-2 eV), that is, semiconducting behavior, in order to have an efficient field effect control exerted by an external gate.

The AlN nanowires may also provide the low dimensional building blocks for the future spintronic devices, since ferromagnetic ordering has been observed in the bulk semiconductor, doped with Mn impurities [12]. Specific studies on nanowire systems report experimental observation of ferromagnetic ordering [8], as well as the influence of the wire passivation on the stability of the ferromagnetic ground state using *ab initio* investigations [13]. Nonmagnetic dopants, for example, Mg, can produce unconventional magnetism in AlN nanowire systems, due to the interplay between the low dimensional effects generated by confinement and surface states [14].

In this paper the spin filtering effects are investigated in AlN atomic-sized nanowires with additional Mn impurities, with the main focus on the differences which arise by switching between the two structural configurations, WZ and GL. The GL phase corresponds to the freestanding nanowire,

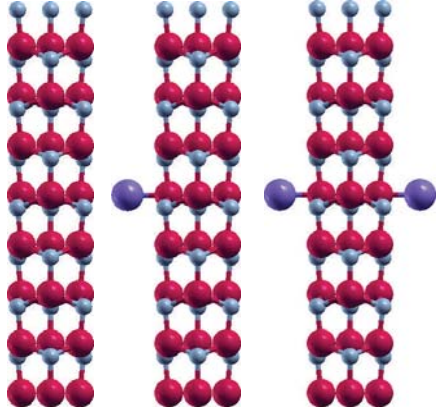


FIGURE 1: Pristine WZ nanowire and structures with one or two Mn impurities.

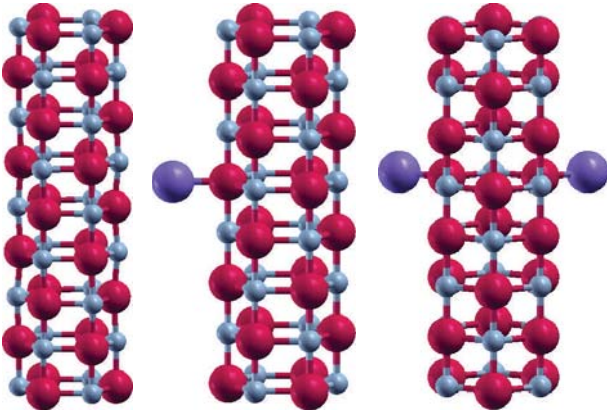


FIGURE 2: Pristine GL nanowire and structures with one or two Mn impurities.

while the WZ phase is obtained by tuning the applied axial stress. The contribution of the surface states to the spin transport is comparatively analyzed. The results convey the possibility of using AlN nanowires as nanomechanical spintronic devices, where the spin detection can indicate the magnetic and structural state of the system.

## 2. Structures and Methods

The structures considered are AlN nanowires with one or two additional impurities, depicted in Figures 1 and 2. The GL configurations correspond to free-standing wires, while the WZ structures are obtained by applying an external pulling stress. The nanowires are functionalized by introducing additional Mn impurities on the surface. Depending on the magnetic moments of the impurities the two components of spin current are scattered differently. For the systems considered here it is expected that the transmission is less affected compared to structures with substitutional TM impurities. However, one needs to assess in how far the adatoms can still produce a reasonable spin current polarization and, furthermore, evaluate the potential differences introduced by switching between the two structural configurations.

The *ab initio* calculations are performed in the framework of density functional theory (DFT), using the SIESTA package [15]. The magnetic structures are investigated using constrained spin-DFT calculations, in the local spin density approximation (LSDA), with the parametrization proposed by Ceperley and Alder. In the supercell approach implemented by SIESTA, the real space grid was set by a cutoff energy of 300 Ry, and a Monkhorst-Pack scheme to  $1 \times 1 \times 5$   $k$ -points was considered. In order to obtain the atomic coordinates, structural relaxations are performed. The starting point is the pristine AlN nanowire in the WZ phase, which is the native configuration of the bulk material. The initial lattice parameters correspond to the bulk system, that is,  $a_0^{\text{WZ}} = 3.112 \text{ \AA}$ ,  $c_0^{\text{WZ}} = 4.982 \text{ \AA}$ . The system is relaxed using a maximum displacement of  $0.1 \text{ \AA}$  until the forces are less than  $0.04 \text{ eV/\AA}$ . The final configuration obtained for the free-standing wire is the hexagonal GL phase. In the GL structure the Al and N atoms are placed in alternating positions in hexagonal layers, with the lattice constant  $a^{\text{GL}} = 1.97 \text{ \AA}$ , that is, the in-plane distance between two successive Al and N atoms. The distance between the hexagonal layers, which are equally spaced, is  $c^{\text{GL}} = 1.87 \text{ \AA}$ . The lattice constant along the wire direction is therefore reduced from  $4.982 \text{ \AA}$  to  $2c^{\text{GL}} = 3.74 \text{ \AA}$ . However, by applying a pulling force of  $0.40 \text{ nN}$ , the wire retains the original WZ configuration, with slightly modified lattice parameters,  $a^{\text{WZ}} = 2.79 \text{ \AA}$ ,  $c^{\text{WZ}} = 4.86 \text{ \AA}$ . The lattice parameters generally depend on the applied axial stress.

The spin dependent transmission functions are extracted using the non-equilibrium Green's functions (NEGF) formalism, which is implemented in TRANSIESTA [16]. The scattering region consists of four unit cells, with a total of 48 atoms and it is coupled to the left/right semi-infinite electrodes. The effects introduced by the additional Mn impurities, which are present on the nanowire surface, can be observed in the calculated transmission functions corresponding to the two spin channels,  $T_{\uparrow}$  and  $T_{\downarrow}$ . The total transmission function can be found for a total energy  $E$  using the relation

$$T(E) = \text{Tr} [\Gamma_L G^r \Gamma_R G^a], \quad (1)$$

where  $G^{r/a}$  are the retarded/advanced Green's functions and  $\Gamma_{L/R}$  are the self-energies corresponding to the couplings with the two contacts. In linear regime, the efficiency of a spin-filter device can be defined using the transmission of each spin component [17]:

$$p^s = \frac{T_{\uparrow} - T_{\downarrow}}{T_{\uparrow} + T_{\downarrow}}, \quad (2)$$

where  $s$  indicates the structural configuration,  $s = \text{WZ, GL}$ .

## 3. Results and Discussion

As it was already pointed out in the introduction, the surface states which appear in the considered quasi-one-dimensional structures effectively reduce the bandgap of the aluminium nitride. Figure 3 shows the total and partial densities of

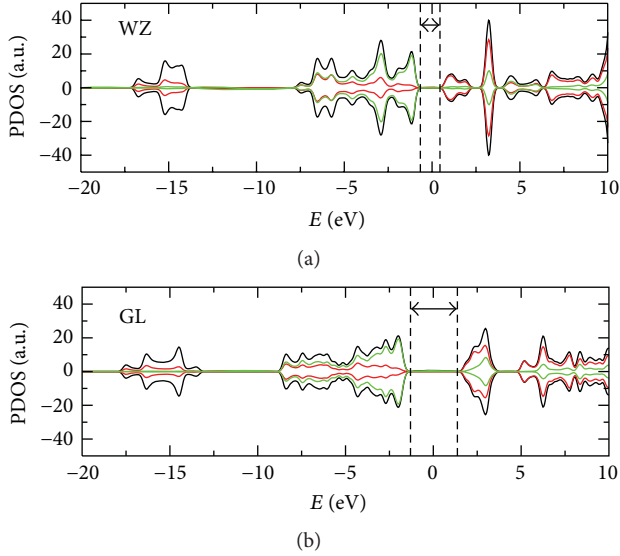


FIGURE 3: Total (black) and partial density of states for WZ and GL structural configurations. The contribution of the  $p$  orbitals of nitrogen (green) and  $s, p$  orbitals of aluminium (red) are represented. The arrows mark the minibandgaps between the valence band and the first group of surface states.

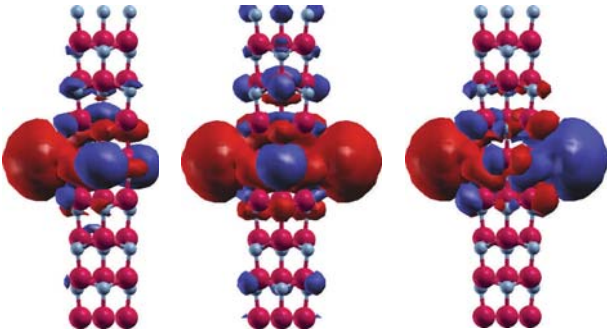


FIGURE 4: Spin densities for nanowires in the WZ configuration, with one and two Mn impurities. Both ferro- and antiferromagnetic configurations are indicated.

states (DOS) of the ideal nanowires, for the two structural configurations. One can see that the mini-bandgaps which appear,  $E_g^{WZ} \approx 1.2$  eV and  $E_g^{GL} \approx 2.5$  eV, are significantly smaller than the bandgap of bulk AlN. In both WZ and GL phases, the valence band is formed by  $p$  orbitals of nitrogen. For the WZ nanowire the first group of surface states is formed by both  $s$  and  $p$  orbitals of aluminium, while for the GL configuration there is also a noticeable contribution from the  $p$  orbitals of nitrogen. It is important to note that in the case of WZ nanowire there is an effective bandgap comparable with the one of bulk silicon, which suggests the atomic sized structure is suitable for spin and charge transfer applications.

Next, by introducing the Mn adatoms, the spin densities are comparatively analyzed for WZ and GL structures and a clear qualitative difference can be observed in Figures 4 and

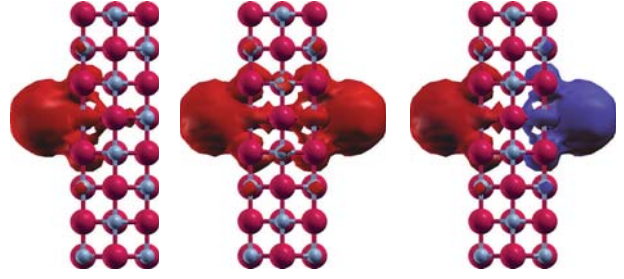


FIGURE 5: Spin densities for nanowires in the GL configuration, with one and two Mn impurities. Both ferro- and antiferro-magnetic configurations are indicated.

5. For the two impurity cases, both ferro- (FM) and antiferromagnetic (AFM) configurations of the magnetic moments are investigated. As expected, the spin polarization is maximum at the location of the magnetic impurities. In the case of WZ nanowire, there is also a large polarization of neighboring Al and N atoms, which are otherwise nonmagnetic. Opposite spin polarizations can be observed at the first and second order neighbors. This is in contrast with the case of the GL structure, which has better insulating properties and the net spin density remains confined at the magnetic adatoms. In the case of two impurities, placed symmetrically to one of the planes which bisect the structures in two identical halves, a mirrored symmetry in the spin density can be noticed. This has consequences in the spin transport, where both components of spin current are equally transmitted, that is, the net spin current is zero. Thermal excitations as well as small magnetic fields can switch the magnetic state of the impurities from FM to AFM, turning on and off the spin current. This suggests the possibility of using the considered magnetic nanowires as building blocks for high sensitivity temperature and magnetic field sensors.

The spin resolved transmission is depicted in Figures 6 and 7, for systems with one and two magnetic impurities, respectively. The pristine non-magnetic nanowires are first analyzed in both WZ and GL configurations. In this case each propagating mode adds one unit plateau to the total transmission. The ideal transmission follows closely the density of states plotted in Figure 3. The adatoms placed on the nanowire surface introduce a selective scattering on the two spin components, depending on the preset magnetic configuration. Contrary to the situation where the magnetic impurities are placed substitutional, in this case the transmission is rather close to ideal. More significant scattering is visible in the energy range corresponding to the first group of surface states. The mini-gaps are consistent with the previously obtained values from the DOS analysis. For the systems with the pair of magnetic impurities in the AFM configuration, there is a rather similar transmission function with the one indicated in Figures 6 and 7, with major qualitative difference that in this case one has  $T_{\uparrow} = T_{\downarrow}$ .

The spin polarization depends on the intricate scattering processes, which follow from the addition of magnetic impurities and which are also dependent on the magnetic configuration. Due to the sharp variations present in the transmission

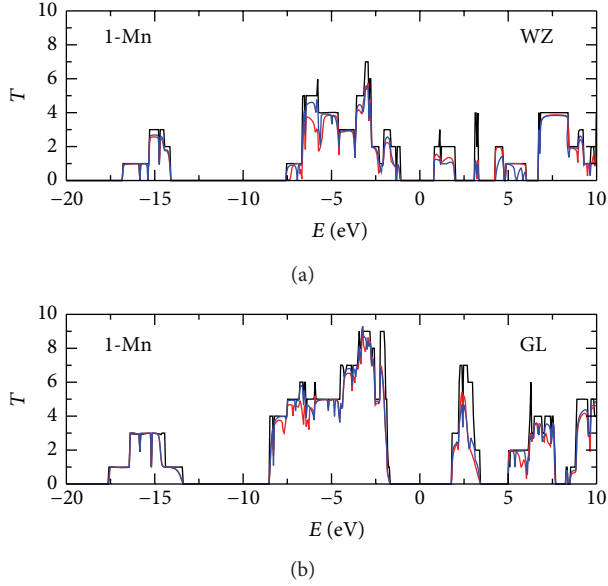


FIGURE 6: Transmission versus energy for nanowires in the WZ and GL configurations: pristine nanowire (black) and nanowires with one Mn impurity;  $T_{\uparrow}$  (red) and  $T_{\downarrow}$  (blue) are represented. The Fermi level is located at  $E = 0$ .

functions, polarizations close to unity are possible. However, they occur on small energy ranges. Therefore the data indicated in Figure 8 was averaged on energy intervals of  $\sim 25$  meV, consistent with realistic thermal fluctuations. By this procedure, spin polarizations above 20% can still be achieved for the GL structures. Focusing on the first group of surface states, one can notice that the differences between the one- and two-impurity cases are smaller for the GL structure, when compared to its WZ counterpart. This indicates the potential robustness of the spin characteristics with respect to adding one extra impurity.

To conclude, both WZ and GL structures with Mn adatoms exhibit reasonable transmission and are able to produce detectable spin polarization. The reduced bandgaps offer the possibility of using the magnetic AlN nanowires in spintronic field effect applications.

#### 4. Conclusions

AlN nanowires with Mn adatoms are investigated using constrained spin-DFT calculations. The phase transition between the wurtzite and graphite-like configurations is discussed in the context of exploring the spin transport properties. A general feature of the analyzed quasi-one dimensional structures is the reduction of the band gap, down to  $\sim 1.2$  eV for the WZ nanowire. Consequently, although bulk AlN is a wide bandgap semiconductor, it is suitable for atomic sized devices which employ the field effect. With the additional impurities placed on the surface of the nanowires, the scattering is reduced and the transmission is at a significant ratio, when compared with the ideal case. However, one or two Mn impurities in the ferromagnetic configuration still provide a reasonable spin separation and the net current may be further

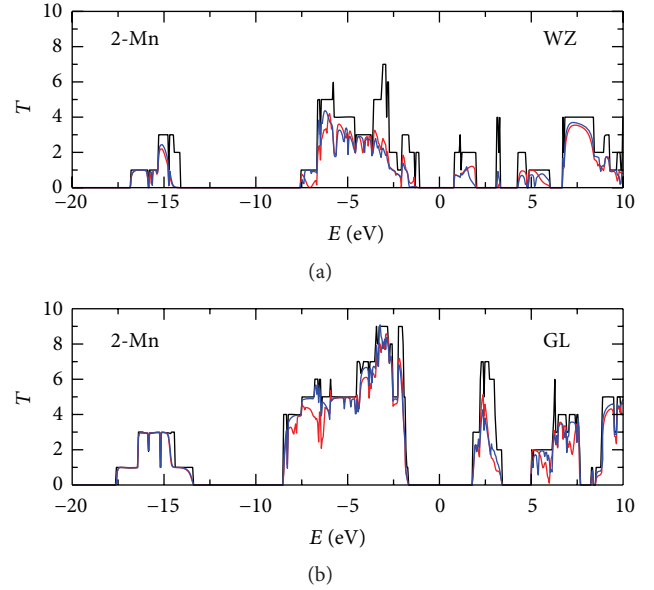


FIGURE 7: Similar data as in Figure 6 for nanowires with two Mn impurities, in the ferromagnetic configuration.

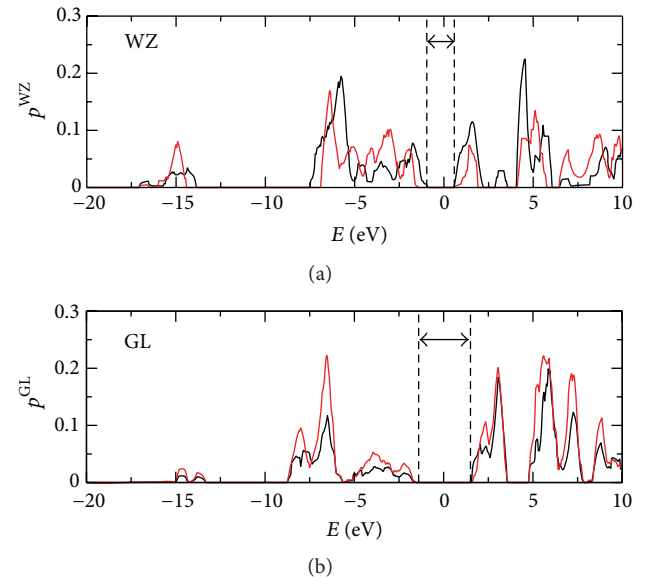


FIGURE 8: Spin polarization (absolute value) for WZ and GL nanowires with one (black) or two (red) impurities. The arrows indicate the mini-bandgaps.

manipulated in a spintronic device. Taking advantage of the symmetries, it was shown that the considered structures in the antiferro magnetic configurations provide zero net spin current. By switching the magnetic states of the impurities, a detection mechanism is provided. Applying axial stress, the changes in the spin transfer characteristics can be pointed out. The analyzed nanowire systems can therefore provide the building blocks for integrating both nanomechanical and spintronic devices.

## Acknowledgments

This work was supported by the Romanian National Authority for Scientific Research, CNCS-UEFISCDI, Projects nos. PN-II-RU-PD-2011-3-0044 and PN-II-ID-PCE-2011-3-0960 and in part by the European Commission under EU FP7 Project HP-SEE (under Contract no. 261499).

## References

- [1] S. Chattopadhyay, C. S. Shih, H. L. Zon, F. C. Chia, K. H. Chen, and L. C. Chen, "Molecular sensing with ultrafine silver crystals on hexagonal aluminum nitride nanorod templates," *Journal of the American Chemical Society*, vol. 127, no. 9, pp. 2820–2821, 2005.
- [2] Z. Zhou, J. Zhao, Y. Chen, P. von Ragu Schleyer, and Z. Chen, "Energetics and electronic structures of AlN nanotubes/wires and their potential application as ammonia sensors," *Nanotechnology*, vol. 18, Article ID 424023, 2007.
- [3] G. A. Nemnes, C. Visan, and S. Antohe, "Thermopower of atomically sized wurtzite AlN wires," *Physica E*, vol. 44, p. 1092, 2012.
- [4] C. Xu, L. Xue, C. Yin, and G. Wang, "Formation and photoluminescence properties of AlN nanowires," *Physica Status Solidi (A)*, vol. 198, no. 2, pp. 329–335, 2003.
- [5] G. R. Yazdi, M. Syvajarvi, and R. Yakimova, "Aligned AlN nanowires and microrods by self-patterning," *Applied Physics Letters*, vol. 90, Article ID 123103, 2007.
- [6] L. H. Shen, X. F. Li, J. Zhang et al., "Synthesis of single-crystalline wurtzite aluminum nitride nanowires by direct arc discharge," *Applied Physics A*, vol. 84, pp. 73–75, 2006.
- [7] R. K. Paul, K. H. Lee, B. T. Lee, and H. Y. Song, "Formation of AlN nanowires using Al powder," *Materials Chemistry and Physics*, vol. 112, no. 2, pp. 562–565, 2008.
- [8] Y. Yang, Q. Zhao, X. Z. Zhang et al., "Mn-doped AlN nanowires with room temperature ferromagnetic ordering," *Applied Physics Letters*, vol. 90, Article ID 092118, 2007.
- [9] L. H. Shen, X. F. Li, Y. M. Ma et al., "Pressure-induced structural transition in AlN nanowires," *Applied Physics Letters*, vol. 89, Article ID 141903, 2006.
- [10] Y. Wu, G. Chen, H. Ye, Y. Zhu, and S. H. Wei, "Origin of the phase transition of AlN, GaN, and ZnO nanowires," *Applied Physics Letters*, vol. 94, Article ID 253101, 2009.
- [11] T. L. Mitran, A. Nicolaev, G. A. Nemnes, L. Ion, and S. Antohe, "Ab initio vibrational and thermal properties of AlN nanowires under axial stress," *Computational Materials Science*, vol. 50, no. 10, pp. 2955–2959, 2011.
- [12] H. Li, H. Q. Bao, B. Song et al., "Ferromagnetic properties of Mn-doped AlN," *Physica B*, vol. 403, pp. 4096–4099, 2008.
- [13] Y. Zhang, H. Shi, R. Li, and P. Zhang, "Magnetic coupling properties of Mn-doped AlN nanowires: first-principles calculations," *Physics Letters A*, vol. 375, no. 15, pp. 1686–1689, 2011.
- [14] Z.-K. Tang, L. Wang, L.-M. Tang et al., "Ferromagnetic coupling in Mg-doped passivated AlN nanowires: a first-principles study," *Physica Status Solidi B*, vol. 249, pp. 185–189, 2012.
- [15] J. M. Soler, E. Artacho, J. D. Gale et al., "The SIESTA method for ab initio order-N materials simulation," *Journal of Physics Condensed Matter*, vol. 14, no. 11, pp. 2745–2779, 2002.
- [16] M. Brandbyge, J. L. Mozos, P. Ordejon, J. Taylor, and K. Stokbro, "Density-functional method for nonequilibrium electron transport," *Physical Review B*, vol. 65, Article ID 165401, 17 pages, 2002.
- [17] G. A. Nemnes, "Spin current switching and spin-filtering effects in Mn-doped boron nitride nanoribbons," *Journal of Nanomaterials*, vol. 2012, Article ID 748639, 5 pages, 2012.

## Research Article

# Investigation and Estimation of Structure of Web from Electrospun Nanofibres

**Jolanta Malašauskienė and Rimvydas Milašius**

*Department of Textile Technology, Kaunas University of Technology, Studentu 56, 51424 Kaunas, Lithuania*

Correspondence should be addressed to Jolanta Malašauskienė; [jolanta.malasauskiene@stud.ktu.lt](mailto:jolanta.malasauskiene@stud.ktu.lt)

Received 12 December 2012; Accepted 17 February 2013

Academic Editor: Lijun Ji

Copyright © 2013 J. Malašauskienė and R. Milašius. This is an open access article distributed under the Creative Commons Attribution License, which permits unrestricted use, distribution, and reproduction in any medium, provided the original work is properly cited.

During the electrospinning process the web of nanofibres is manufactured by means of electrostatic forces between two electrodes. The diameters of nanofibres usually differ and they depend on various parameters. The different fineness of fibres influences the structure of the web and herewith the end-use properties of such kind of nanomaterial. Analysis of nanofibres diameters distribution also shows big differences; even more, the distributions are not spread along the normal distribution. Understanding the influence of electrospinning parameters and the reason why the shapes of distributions are so sophisticated is very important. The goal of this paper is to analyse the distribution of diameter and to propose the new criterion for nanofibres diameter comparison and web of nanofibres estimation. In this paper the influence of covering time of support material on structure of PA6.6 nanofibre web has been investigated. It was estimated that this parameter does not have a significant influence on the average diameter of nanofibres, and only the structure of web has been influenced by the changes in covering time. According to the results provided the phenomena of nanofibres sticking on the support material at the time of electrospinning can be proved and explained.

## 1. Introduction

Electrospinning is one of the most common processes used for nonwovens production. The diameters of electrospun fibres diameter may range from 10 nm to 1500 nm [1]. It has been discovered that the diameter of nanofibres and the final properties of the produced nonwovens depend on type of polymer, solution properties (viscosity, conductivity, surface tension, etc.), applied voltage, distance between electrodes, coating time of support material, air humidity, and temperature [2–5]. The diameter of the fibre is arguably the most important factor for determining the quality of nonwoven structure. So, it is very important to understand how the diameter of fibre and its distribution is affected by various parameters [6].

There are a lot of studies analyzing the influence of various parameters on nonwoven structure. The analysis of such studies shows that in some cases the different researches, analyzing the influence of the same factor on the structure of nanofibres, obtain different results. The reasons of different conclusions can be explained in several ways. According to

one of them, in some cases the authors do not analyze the dispersions of nanofibres diameter. The other reason—quite often the authors skip the description of the main parameters which may have a significant influence on nonwoven structure. It is possible that the mismatches of the results occur because of the lack of common methodology for nanofiber diameter characterization.

While analyzing the literature sources we noticed that the measurements of nanofibres diameter are distributed in unclear distribution and the shapes of all distributions always differ. Ellison et al., Tsimliaraki et al., and Gu et al. [7–9] state that the measurements of nanofibres diameter are distributed by log normal distribution. Dosunmu et al. [10] states that distribution of electrospun nanofibres could be well fitted as normal distribution in log normal scale. But log normal distribution does not have the theoretical background in electrospinning process, because this process does not depend on the time and all nanofibers in the web are being manufactured simultaneously. Usually the values of fibres diameter of various textile materials are distributed by normal distribution [11]. But sometimes the

shapes of the distributions of nanofibres diameter are not similar to this one.

It is impossible to compare the average values when dispersions of diameter are different, so it is absolutely wrong way to estimate the web of nanofibres, in order to compare parameters having different kinds of distribution. According to mathematical statistic point the average value of nanofibres diameter (if they are distributed in not normal distribution) cannot characterize the nanofibres precisely, because changes in average values do not suppose changes in modal value and other characteristics. It means that in order to compare the diameter of nanofibres with an average value it is necessary to use the other characteristics too.

In our previous study [12] the similarity of empirical distribution of nanofibres diameters to the compound distribution, consisting of several normal distributions, has been noticed. The compound distribution is a characteristic of blended spun yarns, received from several kinds of fibres. It means that the web of nanofibres consists from nanofibres of different diameter. There is no single opinion about the reasons of this phenomenon. It is possible that the web of nanofibres forms when nanofibres in the distance from Taylor cone to the other electrode do not separate completely. Although the possibility also exists that the web of several kinds of fibres forms depending on the sticking of nanofibres at the time when they are moved to other electrode. The goal of this paper is to analyse the dispersion of nanofibres diameter and to check the hypothesis about the possibility of the sticking of several nanofibres.

## 2. Method of Distribution Calculation

In our previous study [12] the method of dividing the compound distribution into several normal distributions had been presented. The first normal distribution was calculated using the following method: empirical values up to the modal value of the total distribution were set as the points of the left part of the first normal distribution. It has been considered that the diameter of nanofibres had been distributed in normal distribution, so the right part of the first normal distribution was marked as symmetrical points of the left side. The first normal distribution has been calculated according to the probability density. The left part of the second normal distribution has been calculated as a difference between empirical measurements and measurements calculated by the first normal distribution. The right part of empirical values and the second normal distribution have been calculated similarly as in the previous case. All normal distributions have been calculated using this method. Finally the compound distribution has been calculating by summarising the values of all normal distributions. The coefficient of determination confirmed the correlation of empirical curve with the compound distribution. This method can be used for dividing a compound distribution into several normal distributions.

The main disadvantage of this method is sophistication of compound distribution calculation. For this reason the short-cut method of the quality of nonwoven structure

estimation has been presented [13]. The short-cut method is more straightforward and is based on the modal value of empirical values. The points of the modal value of the empirical distribution are called the points of left part of the first normal distribution. It has been considered that diameter of nanofibres is distributed by normal distribution, and in the other side of modal value the symmetrical points were marked. The results calculated by both methods were identical.

The obtaining of compound distribution confirms that the web of nanofibres at the electrospinning process consists of different kinds of nanofibres.

## 3. Material and Methods

An 8% solution of PA6.6 in 85% formic acid was gently stirred at ambient temperature for 12 hours until the polymer granules dissolved completely. The nonwoven web from PA6.6 nanofibres had been formed using the electrospinning equipment "Nanospider" (Figure 1). The principle of this equipment includes the rotating roller which is submerged in a bath filled with polymer solution. The Taylor cones with increasing electrostatic forces are formed on the rotating roller. When electrostatic forces overcome the surface tension, a jet of polymer solution is ejected from the Taylor cone and it is directed up to the support material [14]. During this experiment the electrode with narrower tines has been selected as it is easier to form PA6.6 nanofibres. The sufficiently powerful electric field is not formed by means of the cylindrical electrode; consequently the continuous flow of Taylor cones cannot be formed. According to the electric field theory, the major supply of electric charge has been collected on the top of tines, where the surface curvature is greater and the surface electric field density in these places is higher. As a result, the continuous flow of Taylor cones can be formed on the tines [15].

During all experiments, the ambient temperature was  $T = 24 \pm 2^\circ\text{C}$ , the humidity was  $\phi = 50 \pm 2\%$ . The distance between electrodes was 13 cm. The applied voltage was 70 kV. Experiment has been carried out by changing the duration of support material covering. The speed of support material was  $v = 0.010$  m/s, the time of covering  $t = 25$  s (indicate I);  $v = 0.006$  m/s,  $t = 41$  s (II);  $v = 0.002$  m/s,  $t = 125$  s (III).

The structure of received nanofibres web has been analyzed by Scanning Electron Microscopy (SEM)—SEM-FEI Quanta 200 (Netherlands). The value of diameter of PA6.6 nanofibres was measured from SEM images by LUCIA Image 5.0 programme, with an accuracy  $\pm 0.01$  nm. Nanofibres have been measured using the 5 different SEM images.

## 4. Results

Nanofibres have been manufactured from PA6.6 solution of 8% concentration. The first series of experiments were carried out at the speed of support material 0.010 m/s, the second 0.006 m/s, and the third 0.002 m/s. With decreasing in speed the covering time of support material increased from 25 s to 125 s. The influence of the speed (and herewith the

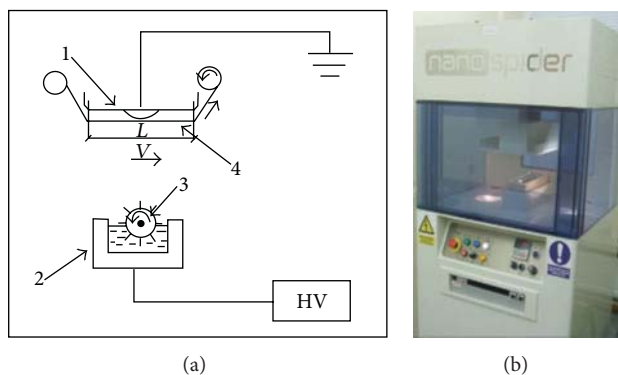


FIGURE 1: Principal scheme and photo of electrospinning technique “Nanospider”: 1: upper electrode, 2: bath with polymer solution, 3: rotating roller with tines, 4: support material,  $L$ : the distance of support material, which is covered with a layer of nanofibres (250 mm).

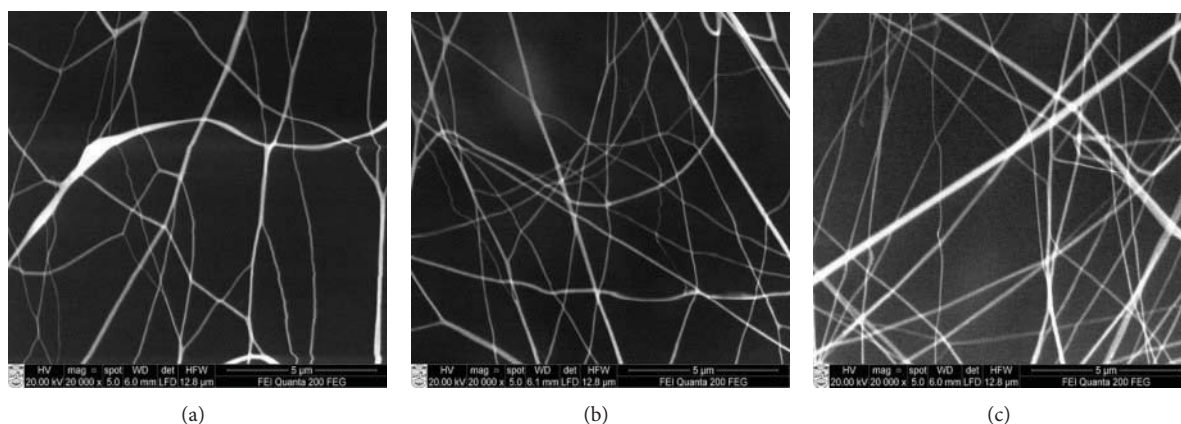


FIGURE 2: SEM images of electrospun PA6.6 mats when the speed of support material was (a)  $v = 0.010$  m/s,  $t = 25$  s (I); (b)  $v = 0.006$  m/s,  $t = 42$  s (II); (c)  $v = 0.002$  m/s,  $t = 125$  s (III).

covering time) of support material on PA6.6 nanofibres web morphology is presented in Figure 2.

As is seen from Figure 2, at the higher speed of support material fewer nanofibres cover it. During the tests the 5 SEM images for each variant of speed have been analysed. The 165 diameters of PA6.6 nanofibres for the I variant, 200 diameters of nanofibres for II variant, and 288 nanofibres for III variant were found and measured. The density of nanofibres was calculated by number of nanofibres in SEM images. The following density has been established—23 nanofibres for I variant, 29 nanofibres for II variant, and 42 nanofibres for III variant in  $100 \mu\text{m}^2$ . The results showed that the speed (also the covering time) of support material does not have significant influence on the average value of PA6.6 nanofibres diameter, as the difference is less than  $\pm 3.5\%$  (I  $d_{\text{average}} = 357$  nm; II  $d_{\text{average}} = 373$  nm; III  $d_{\text{average}} = 382$  nm), while the density of fibres depends on the speed. That means that the structure of web needs a deeper analysis. In the next step of investigations the dispersions of PA6.6 nanofibres have been studied. The frequency distributions of all series of experiment are presented in Figure 3.

First of all Figure 3 demonstrates that the diameter of nanofibres in all cases is distributed in different distributions.

In histogram which is presented in Figure 3(c) only one peak of distribution when the diameter of nanofibres is around 350 nm is observed. It is evident that this value is the modal value of this distribution too. Therefore we can make the assumption that this distribution is very close to normal distribution, because the average value is 382 nm. In the histogram presented in Figure 3(a) two peaks are observed: the first peak is around 200 nm, while the second peak is around 300 nm. A similar view, the distribution with several peaks, may be observed in Figure 3(b): first peak is around 200 nm, the second around 300 nm, and the third 400 nm. In Figure 4 more comprehensive analysis of measurements dispersion of I variant is presented—the interval of nanofibre diameter is distributed not by 50 nm as in Figure 3, but by 25 nm. As is seen from Figure 4 it is evident that the histogram really has not one peak—the first peak is around 212.5 nm, the second—around 312.5 nm. So, values are distributed not by normal but by compound distribution from several normal distributions.

According to the results it is possible to assume that at the lowest speed of support material, the thicker nanofibres were formed and at the higher speed the thinner nanofibres were formed.

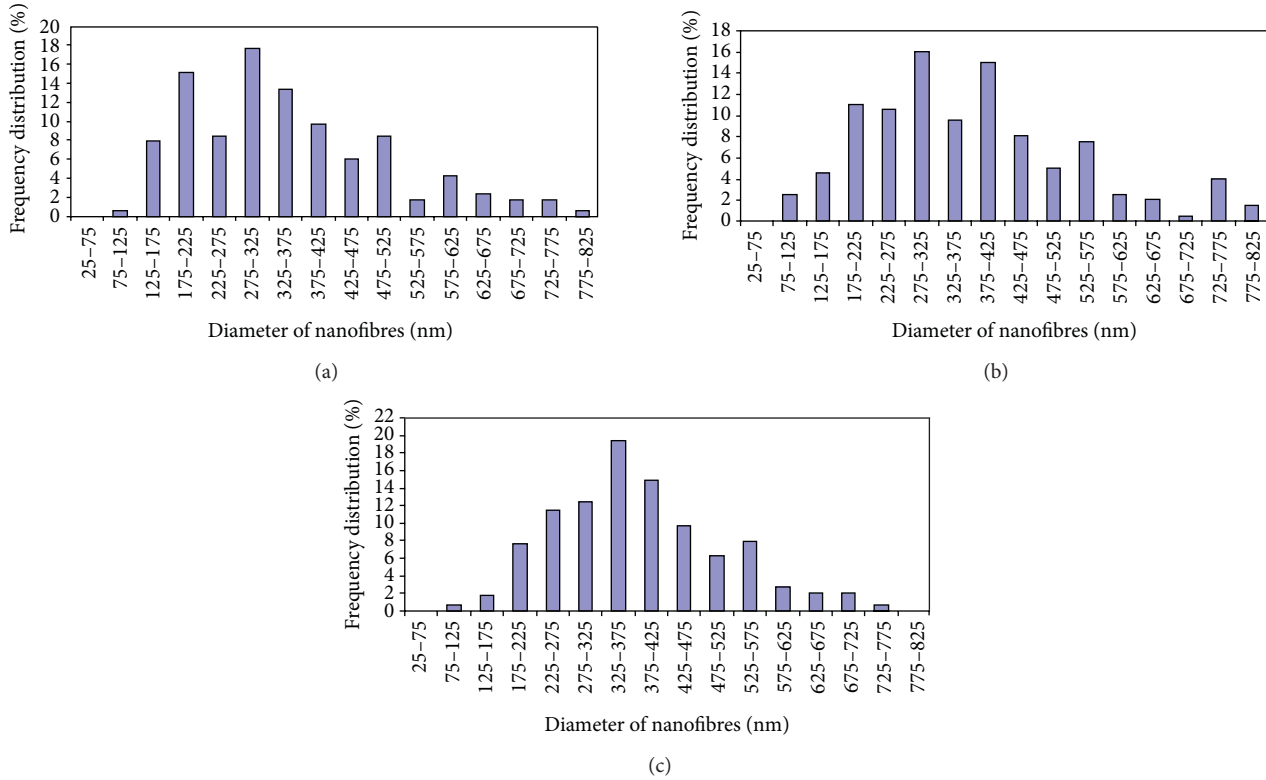


FIGURE 3: Distributions of PA6.6 nanofibres during the experiment: (a)  $v = 0.010$  m/s,  $t = 25$  s (I); (b)  $v = 0.006$  m/s,  $t = 42$  s (II); (c)  $v = 0.002$  m/s,  $t = 125$  s (III).

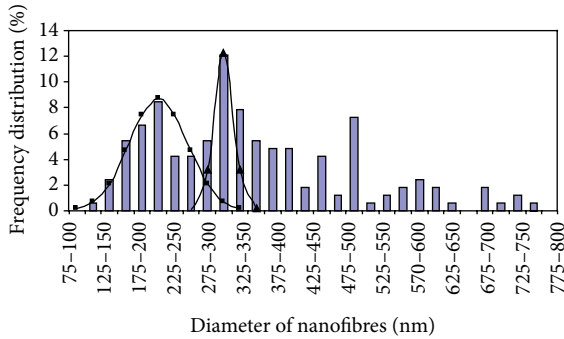


FIGURE 4: Detailed distributions of the results of the I variant.

In previous work [12] it was proved that in the case when the diameter of nanofibres is distributed in compound distribution from several normal distributions, the modal value of the first distribution and the percentage quantity of measurements of the first distribution can be used as a criterion of nanofibres diameter and measurement dispersion estimation. The more the percentage increases, the more unique the structure of the web obtained as well. Using this method we can determine the influence of covering speed (the covering time too) on the structure of manufactured web.

The following results have been received using the histograms presented in Figure 3. As is seen, in the variant I mostly single and no stucked nanofibres had been formed. The percentage quantity of nanofibres distributed in the first

distribution is 32.2%. As in the II variant the quantity of nanofibres distributed in the first distribution has been just 24.04%. It means that in this case less single nanofibres were formed. The modal value of the first distribution in both cases is 200 nm. In this work the new criterion is proposed for estimation of web structure. This criterion may conclude the average of two values—modal values and value of the second highest peak, and it can be calculated using the formula:  $d' = (d_{\text{modal}} + d_{2\text{modal}})/2$  (where  $d_{\text{modal}}$  is the modal value of all distribution;  $d_{2\text{modal}}$  is the second value, close to modal value of this distribution). During the analysis of the results, we noticed that the diameter  $d'$  decreased along with a speed of support material increase. Using the histograms in Figure 3 the following data has been calculated: (III)  $d' = 375$  nm; (II)  $d' = 350$  nm; (I)  $d' = 250$  nm. It means that thinner fibres are formed at a higher speed (lower time).

The next stage of our investigation has been aimed to check the hypothesis that the web from different diameter of nanofibres forms from single nanofibres which stick together on the support material. It is known that the surface area of cross-section of single nanofibre may be calculated using formula:  $S_1 = (\pi d_1^2)/4$ . A surface area of cross-section of stucked nanofibres makes  $S_n = nS_1$ . As a result, the diameter of stucked nanofibres is calculated using  $d_n = d_1 \sqrt{n}$ . So, if the modal value of the diameter of a single fibre is  $d_{\text{modal}} = 200$  nm (see Figures 3(a) and 3(b)), the diameter of a double fibre would be about  $d_2 = 283$  nm. As is seen from Figure 3(a), the second peak is when diameter of nanofibres is about  $d_{2\text{emp}} = 300$  nm. The relative error in both

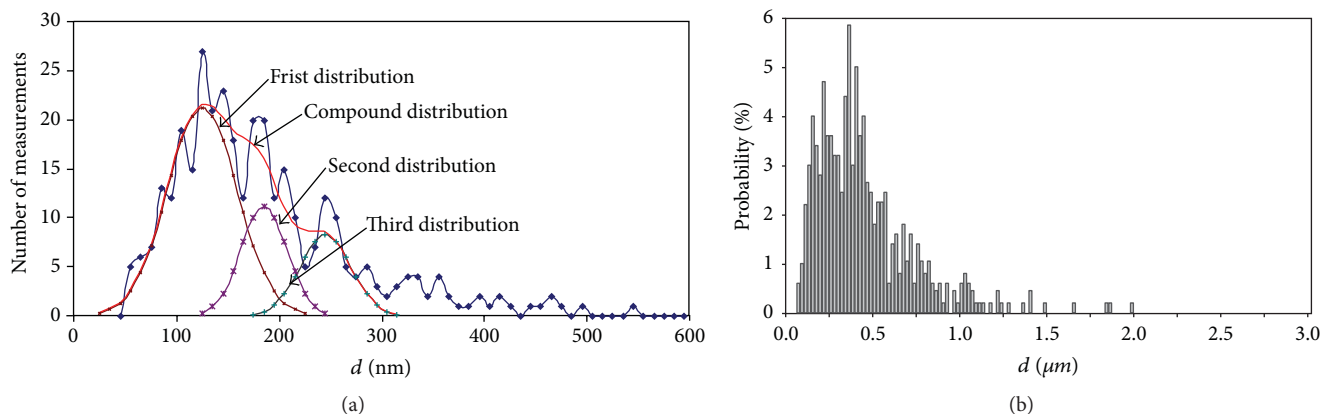


FIGURE 5: Fibre diameter distributions (a) from PVA [12]; (b) from PP [10].

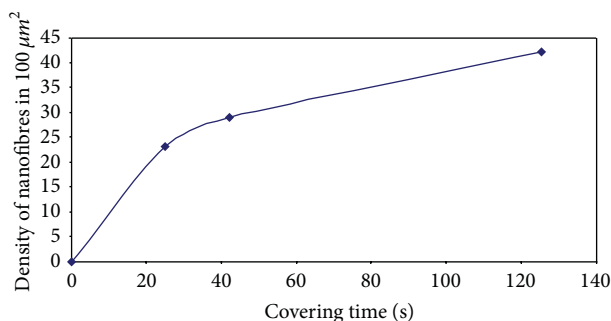


FIGURE 6: Dependence of the density of nanofibres (in  $100 \mu\text{m}^2$ ) on the covering time.

cases is  $\delta = 6\%$ . The recurrent values of nanofibres diameter confirm the hypothesis about the sticking of nanofibres on the web. The similar conclusions about the sticking were approved in our previous work, when the structure of PVA web was analysed [12]. The histograms of this article (especially of Figures 3(a) and 3(b)) can be compared with histogram from literature sources as well [10] (Figure 5).

In this figure few peaks can be noticed as well. According to this data one can guess that these peaks appeared for the sticking of PP nanofibres on the web. It means that this problem is typical for the whole electrospinning process regardless of the type of polymer—the similar results can be observed with PA6.6, PVA, and PP nanofibres.

At the last step of this study, the dependence of the density of nanofibres (in  $100 \mu\text{m}^2$ ) on the covering time is presented in Figure 6.

During the analysis of the data presented in Figure 6, it has been stated that during 1 second of the electrospinning process the support material is covered approximately by 1 nanofibre. According to this, we can state that as the covering time increases, the density of nanofibres should increase linearly. At the same time it is obvious that the curve in Figure 6 is not linear. It is very well visible that at the highest covering time there were not 120 nanofibres, just 42. That also confirms the phenomenon of fibres sticking on the support material. Such data make us sure that the covering time is a

very important parameter for the structure of nanofibre web, and, using the higher covering time, more stucked fibres are forming.

## 5. Conclusions

- (i) The distributions of electrospun nanofibres diameter are always different and the shapes of such distributions usually do not differ from the compound distribution, which consists of several normal distributions.
- (ii) The speed of support material from 0.002 m/s till 0.010 m/s does not have a significant influence on the average value of PA6.6 nanofibres diameter. It only influences the structure of nanofibre web; that is, as the speed of the support material decreases, the more stucked nanofibres are formed.
- (iii) For the web structure estimation the modal value of the first distribution, the percentage quantity of the first distribution, and the average diameter of two peaks of distribution—modal value and the value of the second highest peak—may be used.
- (iv) The results of the tests confirm that the web of nanofibres consists of various nanofibres due to the sticking of several nanofibres during the process of their manufacturing.

## Conflict of Interests

The authors declare no possible conflict of interests.

## References

- [1] M. Chowdhury and G. Stylios, "Effect of experimental parameters on the morphology of electrospun Nylon 6 fibres," *International Journal of Basic and Applied Sciences*, vol. 10, no. 6, pp. 116–131, 2010.
- [2] W. Sambaer, M. Zatloukal, and D. Kimmer, "The use of novel digital image analysis technique and rheological tools to characterize nanofiber nonwovens," *Polymer Testing*, vol. 29, no. 1, pp. 82–94, 2010.

- [3] X. M. Mo, C. Y. Xu, M. Kotaki, and S. Ramakrishna, "Electrospun P(LLA-CL) nanofiber: a biomimetic extracellular matrix for smooth muscle cell and endothelial cell proliferation," *Biomaterials*, vol. 25, no. 10, pp. 1883–1890, 2004.
- [4] E. Adomavičiūtė and R. Milašius, "The influence of applied voltage on poly(vinyl alcohol) (PVA) nanofibre diameter," *Fibres and Textiles in Eastern Europe*, vol. 15, no. 5-6, pp. 69–72, 2007.
- [5] E. Adomavičiūtė, R. Milašius, and A. Žemaitaitis, "The influence of main technological parameters on the diameter of poly(vinyl alcohol) (PVA) nanofibre and morphology of manufactured mat," *Materials Science (Medziagotyra)*, vol. 13, no. 2, pp. 152–155, 2007.
- [6] M. Ziabari, V. Mottaghitalab, and A. K. Haghi, "Simulated image of electrospun nonwoven web of PVA and corresponding nanofiber diameter distribution," *Korean Journal of Chemical Engineering*, vol. 25, no. 4, pp. 919–922, 2008.
- [7] C. J. Ellison, A. Phatak, D. W. Giles, C. W. Macosko, and F. S. Bates, "Melt blown nanofibers: fiber diameter distributions and onset of fiber breakup," *Polymer*, vol. 48, no. 11, pp. 3306–3316, 2007.
- [8] A. Tsimliaraki, I. Zuburtikudis, S. I. Marras, and C. Panayiotou, "Optimizing the nanofibrous structure of non-woven mats of electrospun bio-degradable polymer nanocomposites," in *Proceeding of the Latest Advances in High Tech Textiles and Textile-Based Materials*, pp. 128–133, Ghent, Belgium, September 2009.
- [9] S. Gu, Q. Wu, and J. Ren, "Preparation and surface structures of carbon nanofibers produced from electrospun PAN precursors," *Carbon Materials*, vol. 23, no. 2, pp. 171–176, 2008.
- [10] O. O. Dosunmu, G. G. Chase, W. Kataphinan, and D. H. Reneker, "Electrospinning of polymer nanofibres from multiple jets on a porous tubular surface," *Nanotechnology*, vol. 17, no. 4, pp. 1123–1127, 2006.
- [11] G. A. V. Leaf, *Practical Statistics for the Textile Industry: Part I*, The Textile Institute, Manchester, UK, 1984.
- [12] J. Malašauskienė and R. Milašius, "Mathematical analysis of the diameter distribution of electrospun nanofibres," *Fibres and Textiles in Eastern Europe*, vol. 18, no. 6, pp. 45–48, 2010.
- [13] J. Malašauskienė and R. Milašius, "Short-cut method of electrospun nanofibres diameter distribution estimation," in *Book of Proceedings of Magic World of Textiles: 6th International Textile Clothing & Design Conference*, Dubrovnik, Croatia, pp. 522–525, 2012.
- [14] J. Šukytė, E. Adomavičiūtė, and R. Milašius, "Investigation of the possibility of forming nanofibres with potato starch," *Fibres and Textiles in Eastern Europe*, vol. 18, no. 5, pp. 24–27, 2010.
- [15] A. Banuškevičiūtė, E. Adomavičiūtė, R. Milašius, and S. Stanys, "Formation of thermoplastic polyurethane (TPU) nano/micro fibers by electrospinning process using electrode with tines," *Materials Science (Medziagotyra)*, vol. 17, no. 3, pp. 287–292, 2011.